UNIVERSITÉ LAVAL

Roles of poly(ADP-ribose) polymerase-1 in the ultraviolet radiation-induced skin carcinogenesis

Thèse

Nupur Purohit

Doctorat en biologie cellulaire et moléculaire
Philosophiæ doctor (Ph. D.)

Québec, Canada

Roles of poly(ADP-ribose) polymerase-1 in the ultraviolet radiation-induced skin carcinogenesis

Thèse

Nupur K. Purohit

Sous la direction de :

Girish M. Shah, directeur de recherche

Résumé

L'exposition aux rayons ultraviolets (UV) est essentielle à la vie et bénéfique pour la santé humaine. Cependant, la surexposition aux UV solaires, en particulier aux UVB, rayons les plus énergétiques atteignant la surface terrestre, peut entrainer des cancers de la peau chez l'être-humain comme les cancers de la peau de type non-mélanome (NMSC). La capacité des UVB à initier des NMSC provient principalement de leurs habilités à causer des dommages directs à l'ADN, tels que les dimères cyclobutyliques de pyrimidine (CPD) et les produits pyrimidine-pyrimidone (6-4PP), qui sont pris en charge par le mécanisme de réparation par excision de nucléotide (NER). L'incidence croissante de NMSC chez les patients déficients pour l'une des protéines de la NER souligne l'importance d'un processus fonctionnel. Par conséquent, une meilleure compréhension des mécanismes moléculaires de la NER permettrait de mettre en évidence de nouvelles cibles thérapeutiques pour la prévention ou le traitement des cancers de la peau.

L'une des premières réponses cellulaires aux dommages CPD/6-4PP induits par UVB dans la peau des mammifères est l'activation de l'enzyme nucléaire poly(ADP-ribose) polymérase-1 (PARP1) qui catalyse la formation de polymères d'ADP-ribose. Les précédents travaux de notre laboratoire et d'autres équipes ont démontré que PARP1 et son activité enzymatique facilitent la NER en collaboration avec la protéine UV-damaged DNA binding protein 2 (DDB2), qui va aussi s'accumuler rapidement aux sites CPD/6-4PP pendant la phase de reconnaissance des dommages à l'ADN de la NER. Cependant, plusieurs aspects des interactions de PARP1 avec DDB2 et avec les dommages directs à l'ADN sont inconnus. Ainsi, le premier objectif de mon projet de doctorat a été de caractériser précisément la nature de la liaison de PARP1 aux dommages CPD/6-4PP induits par UV vis-à-vis la protéine DDB2. Mes recherches ont mis en évidence l'empreinte asymétrique formée par PARP1 de -12 à +9 nucléotides de chaque côté des dommages CPD/6-4PP en présence ou en absence de DDB2. Nous avons également démontré que PARP1 augmente l'affinité de DDB2 pour les dommages CPD/6-4PP. De plus, les résultats de notre étude indiquent un rôle de PARP1 indépendant de DDB2 pendant la phase de reconnaissance des dommages à l'ADN.

Cibler PARP1 et son rôle dans les voies de réparation des dommages à l'ADN est l'une des stratégies les plus efficaces développées ces dernières années pour le traitement des cancers des ovaires et du sein. L'application translationnelle de mon projet de doctorat a alors été de comprendre le rôle de PARP1 dans la NER dans le contexte des NMSC. À cet égard, nous avons développé un modèle PARP1-KO dans la lignée de souris SKH-1, qui est un modèle largement adopté pour étudier les NMSC induits par UVB. Puisque les souris SKH-1 développent principalement des carcinomes spinocellulaires (CSC) cutanés après une exposition chronique aux UVB, notre étude rapporte le rôle

de PARP1 dans le développement des CSC. En utilisant les souris nouvellement créées SKH-1 PARP1-KO et les souris SKH-1 PARP1-WT avec ou sans application topique d'inhibiteurs de PARP, nous avons mis en évidence que l'absence de PARP1 ou de son activité dans la peau des souris SKH-1 mâles et femelles réduit significativement le fardeau tumoral des CSC et prolonge la période de latence du développement tumoral. L'étude hebdomadaire de l'apparition et de la croissance de tumeurs tout au long du protocole révèlent aussi que cibler PARP1 est très efficace pour ralentir, à l'étape pré-maligne, le développement de CSC. Nos résultats sont surprenants à la lumière des propriétés onco-suppressives rapportées de PARP1 et de son activité catalytique dans des cas de cancérogenèse induits par des dommages à l'ADN causés par des agents alkylants, ainsi que de la susceptibilité croissante des souris knock-out pour d'autres protéines de la NER à développer des CSC induits par UVB. Le rôle de PARP1 dans les mécanismes cellulaires induits par UVB autres que la NER, comme la mort cellulaire et les modulations immunes, pourrait expliquer nos observations. Alors que d'autres analyses sont nécessaires pour comprendre le rôle de PARP1 dans ces mécanismes, notre étude met en avant l'utilisation potentielle d'inhibiteurs de PARP comme nouvel agent chimio-préventif contre les CSC induits par UVB.

Abstract

The exposure to solar ultraviolet radiation (UV) is essential to life and beneficial to human health. However, an overexposure to terrestrial solar UV, especially its most energetic component UVB, can cause skin cancers including the non-melanoma skin cancers (NMSC) in humans. The NMSC initiating properties of UVB arise predominantly from their ability to cause direct DNA damage such as cyclobutane pyrimidine dimers (CPD) and 6-4photoproducts (6-4PP), which are repaired via nucleotide excision repair (NER) pathway. The increased incidence of NMSC in patients with hereditary defects in NER pathway proteins underscores the importance of efficient NER in humans. Therefore, detailed understanding of the molecular operation of NER pathway can provide novel therapeutic targets for the prevention or treatment of skin cancers.

One of the earliest responses of the mammalian skin cells to UVB-induced CPD or 6-4PP is the activation of the nuclear enzyme poly(ADP-ribose) polymerase-1 (PARP1), which catalyzes the formation of polymers of ADP-ribose (PAR). The previous work from other teams and our laboratory have shown that PARP1 and its enzymatic activity facilitate NER in collaboration with UV-damaged DNA binding protein 2 (DDB2), which also rapidly accumulates at the CPD/6-4PP site during the DNA damage recognition stage of NER. However, many aspects of interaction of PARP1 with DDB2 and direct DNA damage are not understood. Therefore, the first aim of my doctoral project was to characterize the precise nature of binding of PARP1 vis-à-vis DDB2 at UV-induced CPD/6-4PP. My doctoral research demonstrates that PARP1 casts asymmetric footprint from −12 to +9 nucleotides on either side of the CPD/6-4PP in presence or absence of DDB2. We also demonstrated that PARP1 facilitates the binding of DDB2 to CPD/6-4PP. Moreover, our study reports DDB2-independent role of PARP1 during the DNA damage recognition phase in NER.

Targeting the role of PARP1 in DNA strand break repair pathways has emerged as one of the successful strategies for the treatment of ovarian and breast cancers in last decade. Consequently, the ultimate translational goal of my doctoral project was to understand the implication of NER facilitating role of PARP1 in NMSC. In this regard, we first developed a PARP1-KO model in the albino hairless SKH-1 mouse strain, which is a widely adopted mouse model to study UVB-induced NMSC. Since SKH-1 mice mainly develop cutaneous squamous cell carcinoma (SCC) upon chronic UVB-exposure, our present study reports the role of PARP1 in development of SCC. Using the newly developed PARP1-KO and PARP1-WT SKH-1 mice with or without topical application of PARP inhibitor, we report that the absence of PARP1 or its activity in skin of both male and female SKH-1 mice significantly reduces the SCC tumor burden and prolongs the tumor latency period. The analyses of appearance and growth of individual tumors on a weekly basis during this protocol also revealed

that targeting of PARP1 was most effective in suppressing the premalignant stage of the SCC development. Our results are surprising in light of the reported onco-suppressive property of PARP1 and its catalytic activity in alkylating DNA damage-induced tumorigenesis and the increased susceptibility of other NER protein knock-out mice to UVB-induced SCC. We reason that the roles of PARP1 in UVB-induced cellular processes other than NER, such as cell death and immune modulations, can account for our observation. While further studies are required to understand these roles of PARP1 in UVB-induced cellular processes, our study underscores the potential for use of PARP inhibitors as a novel chemopreventive agents against UVB-induced SCC.

Table of contents

List of figures

List of tables

List of abbreviations

$^{\bullet}OH$	hydroxyl radical
1D	one dimension
$^{1}O_2$	singlet oxygen
3-AB	3-aminobenzamide
5'-P	5′-phosphate
5′-dRP	5′-deoxyribose phosphate
6-4PP	pyrimidine (6-4) pyrimidone photoproducts
8-oxoG	8–oxo–7,8–dihydroguanine
A	adenine
aa	amino acids
aa-ADPr	accepter aa-linked ADP-ribose
ADP	adenosine diphosphate
ADPr	ADP-ribose
AK	actinic keratosis
AKT	phosphoinositide-dependent serine/threonine protein kinase or PKB
ALC1	amplified in liver cancer 1
AP	apurinic-apyrimidinic
AP-1	activator protein-1
APC	antigen presenting cells
APE1	apurinic-apyrimidinic endonuclease 1
APLF	aprataxin-and-PNKP-like factor
Arg	arginine
ARH1	ADP-ribosylhydrolase 1
ARH3	ADP-ribosylhydrolase 3
ART	ADP-ribosyl transferase
Asp	aspartic acid
ATM	ataxia telangiectasia-mutated
ATP	adenosine triphosphate
ATR	ataxia telangiectasia and Rad3-related protein kinase
BCC	basal cell carcinomas

BD	Bowen's disease
BER	base excision repair
bp	base pair
BRCA	breast cancer type 1/2 susceptibility protein
BRCT	BRCA C-terminus
Bregs	regulatory B cells
C	cytosine
CDC25A	cell division cycle 25 homolog A
CDKN2A	cyclin dependent kinase inhibitor 2A
CHS	contact hypersensitivity
COX-2	cyclooxygenase-2
CPD	cyclobutane pyrimidine dimers
CRLCSA	E3-ubiquitin ligase complex with CSA, DDB1, Cul4A and Rbx1
CRLDDB2	complex with UV-DDB, Cul4A and Rbx1
CS	cockayne syndrome
CSB	cockayne syndrome complementation group B
Cul4A	cullin 4A
Cys	cysteine
DAMP	damage associated molecular patterns
DDB1	UV-damaged DNA binding protein 1
DDB2	UV-damaged DNA binding protein 2
dDC	dermal dendritic cells
DEW	Dewar valence isomers
DNA	deoxyribonucleic acid
DNA-PKc	DNA-dependent protein kinase catalytic subunit
DR	death receptor
DSB	double strand breaks
DSBR	double strand break repair
dsDNA	double strand DNA
DTH	delayed type hypersensitivity
EGFR	epidermal growth factor receptor

ENPP1	ectonucleotide pyrophosphatase/phosphodiesterase 1
ERK1/2	extracellular signal-regulated kinases
FapyG	[2,6-diamino-4-hydroxy-5-formamidopyrimidine]
FEN1	flap endonuclease 1
FICZ	6-formylindolo[3,2-b]carbazole
G	guanine
GAR	glycine/arginine-rich
GG-NER	global genomic nucleotide excision repair
Glu	glutamic acid
H_2O_2	hydrogen peroxide
HCR	host cell reactivation
HD	helical
His	histidine
HMGN1	high mobility group nucleosome binding domain containing protein 1
hOGG1	human 8-oxoG glycosylase 1
HPF1	histone PARylation factor 1
HRR	homologous recombination repair
Hr	hairless
HR23B	UV excision repair protein RAD23 homolog B
H-Y-E	His862-Tyr896-Glu988
IARC	International Agency for Research on Cancer
IL-10	interleukin-10
IL-1β	interleukin-1β
IL-4	interleukin-4
JNK	c-Jun N-terminal kinases
KA	keratocanthoma
KC	keratinocytes
KO	knockout
KR	lysine/arginine
LC	Langerhans cells
Lig IIIa	DNA ligase IIIa

LigI	DNA ligase I
LOH	loss of heterozygosity
LP	long-patch
Lys	lysine
Macro D1	macrodomain type I
Macro D2	macrodomain type II
MAPK	mitogen-activated protein kinase
MAR	monomer of ADP-ribose
MARylation	mono-ADP-ribosylation
MC1R	melanocortin 1 receptor
MDM2	ubiquitin-protein ligase mouse double minute 2 homolog
MED	minimal erythemal dose
MEF	mouse embryonic fibroblasts
MKPs	MAPK phosphatases
MMEJ	microhomology-mediated end-joining
MMP	matrix metalloproteinases
MMR	DNA mismatch repair
NAD^+	nicotinamide adenine dinucleotide
NER	nucleotide excision repair
NFκB	nuclear factor kappa-light-chain-enhancer of activated B cells
NHEJ	non-homologous end-joining
NKT	natural killer T cells
NLS	nuclear localization signal
NMSC	non-melanoma skin cancers
nt	nucleotide
NUDIX	nucleoside diphosphate linked moiety
$O_2^{\bullet-}$	superoxide anion
OB-fold	oligonucleotiode/oligosaccharide-binding fold
p21	cyclin-dependent kinase inhibitor 1
p38	p38 mitogen-activated protein kinases
PAF	platelet activating factors

PAR	polymers of ADP-ribose
PARG	PAR glycohydrolase
PARP1	poly(ADP-ribose) polymerase-1
PARPi	poly(ADP-ribose) polymerase inhibitors
PARylation	poly-ADP-ribosylation
PBM	PAR binding motifs
PBZ	PAR-binding zinc fingers
PCNA	proliferating cell nuclear antigen
pDC	plasmacytoid dendritic cells
PGE2	prostaglandins
PI3K	phosphoinositide 3 kinase
PIKK	phosphoinositide 3 kinase-related kinases
PIN	PilT protein N-terminus
PKB	protein kinase B or AKT
PNKP	polynucleotide kinase-3'-phosphatase
Polβ	DNA polymerase β
polζ	DNA polymerase zeta
polη	DNA polymerase eta
polι	DNA polymerase iota
polκ	DNA polymerase kappa
Polλ	DNA polymerase λ
PRR	pattern recognition receptors
pSer	phospho-Serine
PTM	posttranslational modifications
PTP	protein tyrosine phosphatases
PUA	α,β unsaturated aldehyde
RAD4	radiation sensitive 4 protein
RANK-L	receptor activator of nuclear factor kappa-B ligand
Rbx1	RING box protein 1
RFC	replication factor C
RNA	ribonucleic acid

RNAPII	RNA polymerase II
RNAPIIo	elongating RNA polymerase II
ROS	reactive oxygen species
RPA	replication protein A
RRM	RNA recognition motif
SALT	skin associated lymphoid tissue
SBC	sunburn cells
SCC	squamous cell carcinoma
Ser	serine
SIS	skin immune system
SP	short-patch
SR	serine/arginine
SSB	single strand breaks
SSBR	single strand break repair
ssDNA	single strand DNA
STAT3	signal transducer and activator of transcription 3
STUbL	SUMO-targeted E3 ligase
SUMO	small ubiquitin-like modifier
T	thymine
T4NV	T4 endonuclease V
TARG1	terminal ADPr protein glycohydrolase 1
Tc	$CD8^+$ T cytotoxic cells
TC-NER	transcription coupled nucleotide excision repair
TERT	telomerase reverse transcriptase
TFIIH	transcription factor IIH
TFIIS	transcription factor IIS
T_H1	$CD4^+$ T helper 1
T_H17	$CD4^+$ T helper 17
T_H2	$CD4^+$ T helper 2
Thr	threonine
TLR	Toll-like receptors

TLS	translesion DNA synthesis
TNBC	triple-negative breast cancer
TNF	tumor necrosis factor
TNFR	tumor necrosis factor receptor
TNFα	tumor necrosis factor alpha
TRAIL	tumor necrosis factor related apoptosis inducing ligand
TRAILR	tumor necrosis factor related apoptosis inducing ligand receptor
Tregs	regulatory T cells
Tyr	tyrosine
U	uracil
UCA	urocanic acid
USP7	ubiquitin specific processing protease 7
UV	ultraviolet radiation
UV-DDB	UV-DNA damage binding complex
UVSSA	UV-stimulated scaffold protein A
USP7	ubiquitin specific processing protease 7
WGR	tryptophan-glycine-arginine
WT	wild type
XAB2	XPA-binding protein 2
XPA	*Xeroderma pigmentosum* group A-complementing protein
XPB	*Xeroderma pigmentosum* group B-complementing protein
XPC	*Xeroderma pigmentosum* group C-complementing protein
XPD	*Xeroderma pigmentosum* group D-complementing protein
XPE	*Xeroderma pigmentosum* group E-complementing protein
XRCC1	X-ray repair cross-complementing protein 1
α-MSH	alpha-melanocyte stimulating hormone

Acknowledgements

The completion of this doctoral project was a long adventure dotted with challenges but also full of successes. It is the culmination of a chapter of my life for which I cannot thank enough all the people without whom this journey wouldn't have been possible. First and foremost, I would like to express my deepest gratitude to my research director, Dr Girish M. Shah, for giving me an opportunity to pursue PhD. studies in his laboratory. I am grateful for his timely inputs in my research work, for believing in my abilities so that I can believe in them too and for allowing me to develop sense of initiative and autonomy in my research projects. I have benefitted immensely from his enthusiasm to share his scientific knowledge and life experiences throughout my PhD. I highly appreciate the opportunities given by him to present my scientific findings at the prestigious international meetings such as Gordon Conference on the DNA repair and others. I also thank him for the warm relationship that made me forget that he was my director, thanks to his friendliness, his human side, our social activities and many diverse and varied topics of conversation.

I would also like to thank our amazing collaborators Dr. Jean-Mathieu Beauregard, Dr. Thomas Klonisch and Dr. Sabine Hombach-Klonisch, who were not only actively involved in my research projects but were also always there for discussing ideas, troubleshooting and provided invaluable feedback. I will always cherish the summer BBQ hosted by Dr. Jean-Mathieu Beauregard at his summer cottage. I cannot thank enough to Dr. Thomas, Dr. Sabine and the lab members for the good time and comfortable stay in Winnipeg.

I would like to thank all the present and past members of my laboratory who have contributed to my well-being, both scientific and personal. I will never forget our discussions during coffee breaks, whether scientific or non-scientific, which were very enriching. I especially want to thank Rashmi Shah, who mentored me initially and taught me the discipline required to carry out any experimental protocol. She has become more than a colleague, a true friend, over the years. I would like to thank Dr. Mihaela Robu for all the help and guidance that she provided me during my PhD. Thanks, Mihaela for all the long scientific discussions during my thesis writing. It really helped me. I would also like to thank Dr. Marc Bazin, without whose assistance and help the major part of my research work wouldn't have been possible. I will never forget the long arguments and discussion we had. It was always interesting to understand the different outlook of yours for various subjects. Thank you, Marine Merlin for being a good friend and colleague. I learned a lot from you while training you. Thank you for bearing with my impromptu scientific blabbering during my thesis writing days. It really allowed me to convert my thoughts into scientific writing. I would also like to thank the past lab member, Dr. Febitha Kandan-Kulangara, with whom I first started working in lab. I learned a

lot from you. I would also like to thank Dr. Alicia Montoni. I also learnt a lot from Dr. Samuel Adant, Elisa Fernández Castillo and Maude Lagacé, who worked with me as summer trainee.

The commencement and the completion of this journey was impossible without the unconditional support of my parents, Kaushik Purohit and Rohini Purohit as well as parents in law, Rasibhai Gevariya and Kantaben Gevariya. I would also like to thank my uncle Dr. Shree Kumar Dave and my cousin Mr. Nilay Pathak, without whose financial help the commencement of my PhD. studies in Canada would have been very difficult. Last but not the least, I would like to thank my husband, Dr. Nikunj Gevariya, who motivated me to start PhD. in Canada. This journey wouldn't have been easy without you being around.

I would also like to express my deepest gratitude to the family away from home, Dr. Niraj Joshi, Supreet Wantamutte, Dr. Emilie Dubois, Dr. Lillian Lee and Sebastien Le Batteux, who made my stay in Quebec city enjoyable. I would also like to specially thank Praveena Uppari, Chandrakanth Pothraj, Dr. Angana Mukherjee and Dr. Prasad Padmanabhan, who generously offered their place for me to stay during last month of my PhD. Thanks to all the Indian community in Quebec City, with whom I enjoyed celebrating all the Indian festivals away from India.

May this thesis be a pleasure to read for all of you!

Preface

The previous work from our laboratory and other teams began to reveal a hitherto unsuspected role of PARP1 in global genome nucleotide excision repair (GG-NER) of the ultraviolet radiation (UV)-induced direct DNA damage without strand breaks, namely cyclobutane pyrimidine dimers (CPD) and 6-4 photoproducts (6-4PP). It was reported that PARP1 facilitates repair of these DNA damage by participating from the initial DNA damage recognition to final post-incision steps of the GG-NER pathway. My doctoral project in the laboratory of Dr. Girish Shah was aimed at further characterizing the role of PARP1 in GG-NER of UV-induced direct DNA damage and in long-term biological consequence of unrepaired UV-induced direct DNA damage, that is cutaneous squamous cell carcinoma (SCC) development. These studies allowed me to contribute as 'first', 'co-first' and 'second' author to the chapters 1-4 presented in this thesis. The research work in the present thesis was made possible with the help of many people, whose contributions are detailed in the preface of each chapter.

In the present thesis, the first half of **Introduction section** describes the current knowledge on the solar UV-induced cellular processes, which contributes to the pathogenesis of SCC with the emphasis on NER pathway. The second half reports the current state of knowledge on the role of PARP1 in the UV-induced cellular processes with the focus on its novel role in the NER pathway. This section ends with **context, hypothesis and objective**s, which are addressed in the following chapters.

The research in **Chapter 1** uses two novel assays to characterize the binding of PARP1 to UV-induced direct DNA damage at the nucleotide level. This study accounts for the concurrent recruitment as well as interaction of PARP1 and DDB2 at the UV-damaged chromatin. It also envisions the mechanism by which DDB2 can stimulate the catalytic activity of PARP1 in the presence of UV-damaged DNA. This research led to the publication of article titled « **Characterization of the interactions of PARP-1 with UV-damaged DNA *in vivo* and *in vitro*** » (Nupur K. Purohit, Mihaela Robu, Rashmi G. Shah, Nicholas E. Geacintov and Girish M. Shah) in Scientific Reports (2016). Its PDF version is available in **Annexe 1** of this thesis. My research work in characterizing the DDB2-independent role of PARP1 in NER was published as a research article titled « **Poly(ADP-ribose) polymerase 1 escorts XPC to UV-induced DNA lesions during nucleotide excision repair** » (Mihaela Robu#, Rashmi G. Shah#, Nupur K. Purohit, Pengbo Zhou, Hanspeter Naegeli et Girish M. Shah) in Proceedings of the National Academy of Sciences of the United States of America (2017). I contributed as second author for this publication and its PDF version is available in the **Annexe 4**.

The **chapter 2 and 3** are the by-products of my main project presented in chapter 4. They report the development, refinement, characterization and validation of the methods employed for the acquisition of weekly tumor data used in the measurement of severity of UVB-induced cancer severity, which is described in **chapter 4.** The research study in **chapter 2** was published as a research article titled « **Comprehensive Measurement of UVB-Induced Non-Melanoma Skin Cancer Burden in Mice using Photographic Images as a Substitute for the Caliper Method** » (Marc Bazin, Nupur K. Purohit, and Girish M. Shah) in PLoS One (2017). Its PDF version is available in **Annexe 2** of this thesis. The research study in **chapter 3** was published as a research article titled « **A panel of criteria for comprehensive assessment of severity of ultraviolet B radiation-induced non-melanoma skin cancers in mice** » (Marc Bazin, Nupur Purohit, Marine Merlin, Girish Shah) in the Journal of Photochemistry & Photobiology, B: Biology Its PDF version is available in **Annexe 3** of this thesis.

The **chapter 4** presents the major work carried out by me during my doctoral studies. For conducting this research, we transferred PARP1-KO genotype from the C57BL/6 mice to the SKH-1 strain of mice, which took around 3 years. Using this PARP1-KO and PARP1-WT SKH-1 mice with or without topical application of PARP inhibitor, we demonstrate the role of PARP1 in UVB-induced SCC. The manuscript titled « **Decreased susceptibility of PARP1-knockout or PARP inhibitor-treated SKH-1 mice to develop UVB-induced non-melanoma skin cancers**» (Nupur K. Purohit, Marc Bazin, Marine A. Merlin, Julie Brind'Amour, Yulian Niu, Sabine Hombach-Klonisch, Girish M. Shah) is under preparation.

Finally, the advances in the field as a result of my work described in the chapters 1-4 are discussed in **chapter 5**. The **conclusion** section of this thesis provides the working models for the role of PARP1 in NER pathway and UVB-induced SCC based on my original contributions described here placed in the context of current literature. At the end, the **perspectives** describe the approaches for more in-depth study towards the roles of PARP1 and PARylation in the NER and UVB-induced skin cancer.

Apart from the studies described in the thesis, I also took a lead in examining the role of PARP1 in potentiating the peptide receptor radionucleotide therapy (PRRT) for the treatment of neuroendocrine tumors. This led to the publication of a research article titled « **Potentiation of ^{177}Lu-octreotate Peptide Receptor Radionuclide Therapy of Human Neuroendocrine Tumor Cells by PARP Inhibitor** » (Nupur K Purohit, Rashmi G Shah, Samuel Adant, Michael Hoepfner, Girish M Shah, Jean-Mathieu Beauregard) in Oncotarget (2018). I contributed as first author in this manuscript and its PDF version is available in **Annexe 5**.

I also contributed as co-author in the publication of a review article titled « **PARP Inhibitors in Cancer Therapy: Magic Bullets but Moving Targets** » (Girish M Shah, Mihaela Robu, Nupur K Purohit, Jyotika Rajawat, Lucio Tentori and Grazia Graziani) in Frontiers in Oncology (2013). PDF versions of this review is available in **Annexe 6**.

Introduction

A. Skin

From a histological point of view, the skin is composed of three superimposed layers, the epidermis, the dermis and the hypodermis (Fig. A) [1-3]. The outermost layer of the skin, the epidermis is a self-renewing tissue, which is mainly (~90 %) composed of keratinocytes (KC) that are arranged in four distinct layers representing their stage of differentiation: the lowermost is basal cell layer (stratum basale), followed by the squamous cell layer (stratum spinosum), the granular cell layer (stratum granulosum) and the uppermost corneocyte or horny cell layer (stratum corneum). The KC originate from mitotic divisions of the stem cells in the basal layer and migrate through squamous and granular layers to the stratum corneum while undergoing morphological and biochemical differentiation into corneocytes, which are dead, enucleated, keratin-packed and flattened cells. The corneocytes are then shed from the stratum corneum (a process known as desquamation) every 12–14 days accounting for renewal of the epidermis. The outermost keratin-filled stratum corneum of the epidermis provides barrier function, which protects the internal milieu from the external environment.

Epidermis also contains Merkel cells and melanocytes which together accounts for 5-10 % of epidermal cells. Merkel cells have mechanoreceptors, which are responsible for tactile sensation. Melanocytes are scattered throughout the basal cell layer of the epidermis and produce the melanin pigment, which is responsible for skin color. Melanocytes come into contact with as many as fifty neighboring KC through dendritic extensions to form an “epidermal melanin unit” and transfer the melanin to adjacent KC in cellular organelles called melanosomes.

The basement membrane zone forms an interface between the epidermis and dermis, holds these two layers together and allows the exchange of fluids. The dermis, a connective tissue layer of skin, is mostly composed of an extracellular matrix produced by dermal fibroblasts scattered in this layer. It is divided into two layers, papillary and reticular with former having less and latter having high density of collagen fibers. The dermis harbors vascular plexus, lymph nodes, nerves, hair follicles, sebaceous glands and sweat glands. The blood vessels in the dermis also nourish epidermis, which is devoid of vasculature. Beneath the dermis lies the hypodermis, which is a layer of subcutaneous tissue containing adipocytes.

Skin also serves as the primary immunological barrier of the body to the external environment. It is rich in immune cells, forming a complex network called the “skin immune system” (Fig. A) [4-7]. The immune cells residing in the epidermis are the antigen presenting cells (APC), Langerhans cells (LC) and the rare $CD8^{+}$T cytotoxic (Tc) cells. Although the epidermal KC are not classical immune

cells, they serve as one of the main immune effector cells in skin in response to stimulus. The underlying dermis contains more diverse population of immune cells: (a) two types of APC, i.e., dermal dendritic cells (DC) and plasmacytoid DC (pDC), (b) T cell subsets such as $CD4^+$ T helper (T_H) 1, T_H2 and T_H17, γδT cells and natural killer T (NKT) cells, and (c) macrophages and mast cells. Moreover, distinct circulating immune cells such as, neutrophils, macrophages, mast cells, subsets of T- and B-cell, etc. are also recruited into skin by lymph nodes and blood vessels in dermis upon stimulus, as explained by the concept of skin associated lymphoid tissue [6, 8]. Taken together, all the three layers of the skin make a strong physical barrier and an immunological gatekeeper that protect the host from the harmful effects of surrounding environment such as solar ultraviolet radiations.

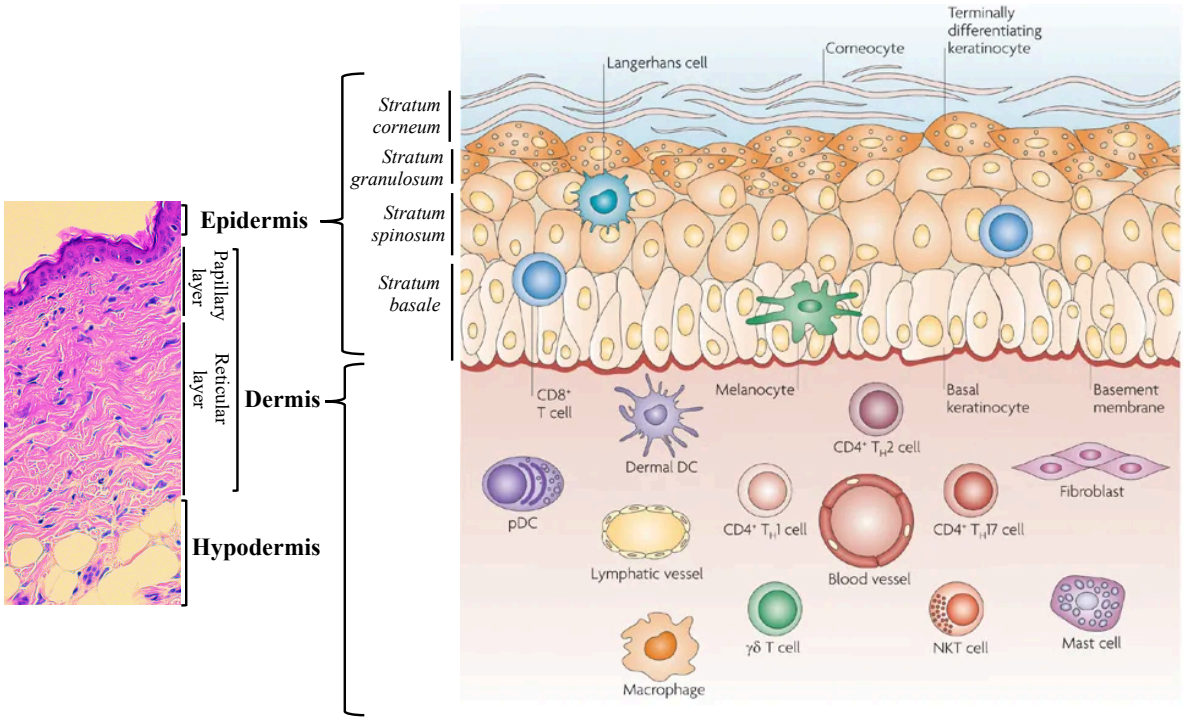

Figure A. Histology and cellular composition of the skin
Please refer to the section A for the full forms of the abbreviations. Figure modified from Nestle et al., 2009 [4].

B. Solar ultraviolet radiation (UV)

The term ultraviolet means "higher than violet" and refers to solar electromagnetic radiation with a wavelength shorter than visible violet light but longer than X-rays (Fig. B) [9]. The non-ionizing solar UV (100-400 nm) can be subdivided into three components: UVA (320-400 nm), UVB (280-320 nm)

and UVC (100-280 nm). UVA has been further divided into UVA-I (340-400 nm) and UVA-II (320-340 nm) [10]. The energy of each UV is inversely related to its wavelength with UVC being the most energetic, UVA the least energetic and UVB having energy in between UVC and UVA [2]. Since the stratospheric ozone and atmospheric oxygen absorb all the UV wavelengths below 310 nm, only 5 % of the solar UV reaches earth's surface. Hence terrestrial UV mainly comprises UVA (90-95 %) and a part of UVB (5-10 %) [2, 9]. The intensity of these radiations varies with time and location and is dependent on a range of factors, including hour of the day, season, latitude, altitude weather and degree of surface reflection [10].

The skin, being human's primary interface with surrounding environment, hinders UV from penetrating into deeper tissues, thereby protecting the rest of the organism from the deleterious effects of UV. However, when UV photons strike the skin, part of its energy is reflected whereas another part is transmitted and finally absorbed in the layers of skin. UV penetrates the skin in a wavelength-dependent manner (Fig. B), with UVA penetrating up to and absorbed by the deeper portion of the dermis (~1000 µm), and UVB absorbed by the epidermis and the upper part of the dermis (160-180 µm) [11-13].

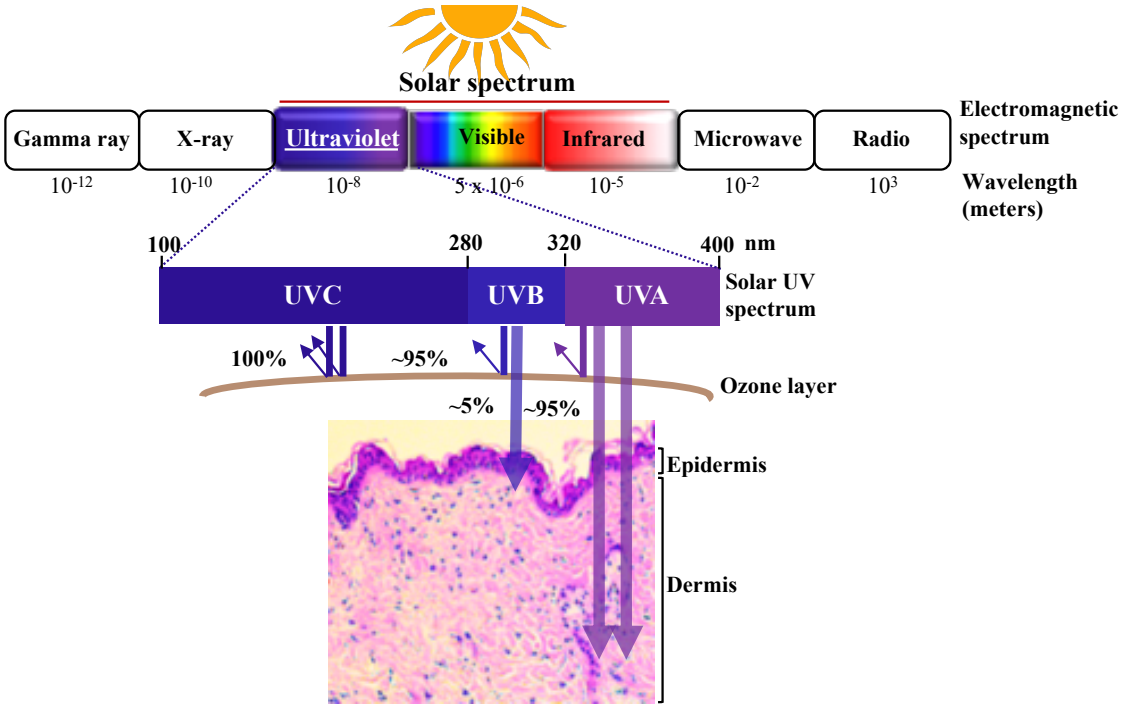

Figure B. The solar UV and its absorption in skin
Figure created by Nupur Purohit.

Exposure to UV is essential to life and beneficial to human health. Solar UV is absolutely required for biosynthesis of vitamin D and endorphins in human body [14, 15]. Moreover, UV is used in the phototherapy of several skin disorders such as psoriasis, eczema and vitiligo [16, 17]. However, a fine line exists between adequate UV exposure for vitamin D synthesis and a risk of UV-induced harmful effects on the skin. Often the exposure to solar UV due to leisure or profession related outdoor activities is beyond what is required for vitamin D synthesis and causes clinically harmful effects on the human skin. These effects are either acute (such as sunburn, tanning and modulation of skin immune system) or chronic (such as ageing and skin cancer) [18]. The research work presented in this thesis focuses on the harmful effects of the most energetic component of terrestrial UV, namely UVB on the skin.

C. Chromophores in skin that absorb UVB

The harmful clinical effects of UVB on the skin are initiated when the epidermal chromophores, i.e., the regions of biomolecules, absorb the energy of UVB photons [19], resulting in transition of their electrons from ground state into an excited state. Upon UVB-absorption, some chromophores in the skin undergo direct structural alteration [19, 20], such as the conversion of trans-urocanic acid (trans-UCA) to cis-UCA in the stratum corneum [21, 22], 7-dehydrocholestrol (7-DHC; the precursor of vitamin D) to 1,25(OH)2D3 (active form of vitamin D) in the epidermal cells [20] and dimerization of adjacent pyrimidines in the DNA [23]. Alternatively, some chromophores such as vitamins (riboflavin, nicotinic acid, vitamin E, D, A and K), heme groups in catalase and oxidase enzymes, lipids as well as aromatic amino acids (tryptophan and tyrosine) act as photosensitizers, which upon UVB-absorption, undergo photosensitization reactions or photoionization to generate reactive oxygen species (ROS) such as singlet oxygen ($^1O_2$), hydroxyl radical ($^{\bullet}OH$) and peroxyl radical [19, 24-27]. The ROS in turn cause DNA damage such as 8-oxo-7,8-dihydroguanine (8-oxoG) and single-strand breaks (SSB) [27], membrane lipid peroxidation-induced formation of platelet activating factors (PAF) and PAF-like lipid ligands [28, 29], formation of tryptophan photoproduct, i.e., 6-formylindolo[3,2-b]carbazole (FICZ) [30], as well as oxidation of proteins [31]. Altogether these UVB-induced immediate products, of which most importantly UVB-induced DNA damage, cause harmful clinical effects on the skin.

D. UVB-induced DNA damage

The primary chromophore that absorbs UVB in the skin is DNA. Due to its penetration power, UVB can cause direct and indirect damage to DNA in the cells of epidermis and upper layer of the dermis (Fig. C) [27, 32, 33].

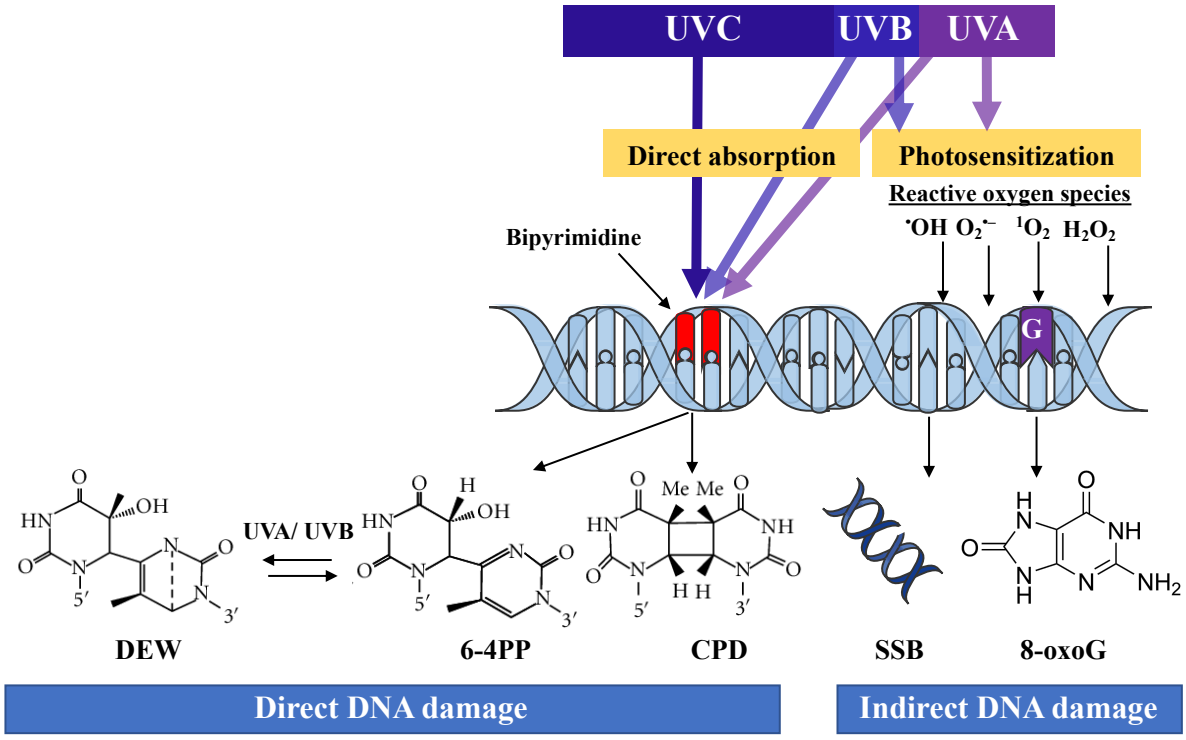

Figure C. UV-induced DNA damage
Please refer to the sections C and D for the full forms of the abbreviations. Figure created by Nupur Purohit.

D.1. Direct DNA damage

The direct DNA damage arise from the direct absorption of all the UV wavelengths by DNA (Fig. C, right). Owing to the maximum absorption of DNA at 260 nm (UVC) [27], the yield of direct DNA damage decreases from UVC to UVA. UV-absorption by DNA mainly results in dimerization of adjacent pyrimidines (thymine (T) and/or cytosine (C)) to form either cyclobutane pyrimidine dimers (CPD), pyrimidine (6-4) pyrimidone photoproducts (6-4PP) or Dewar valence isomers (DEW). In addition to these, formation of minor direct DNA lesions such as adenine dimer and adenine-thymine dimer have been reported [34-36]. Amongst these UV-induced direct DNA damage, the most frequent are the CPD and 6-4PP [37].

CPD are formed ~1 picosecond after UV excitation of the adjacent pyrimidines [38], and structurally consist of a cyclobutane ring with covalent double bond between the C4 and C5 carbons of the adjacent pyrimidines [39, 40]. They can potentially be formed at each of the four pyrimidine doublets in DNA, that is at TT, TC, CC or CT [41], have half-life of few hours [42] and can exist as two diastereoisomers: cis-isomers in double strand (ds) DNA and trans-isomers in single stranded (ss)

DNA [43, 44]. Due to the high photoreactivation capacity of thymine base, the most frequent UVB-induced CPD in the DNA of mammalian cells or skin is the TT, followed by CT, TC and CC [45-47]. CPD exhibit an absorption maximum in the UVC range, i.e., at 230 nm [48]. Since absorption of UVC by CPD results in its reversion to free adjacent pyrimidines with high efficiency, prolonged irradiation with high dose UVC leads to an equilibrium between the formation and reversion of CPDs, especially for C-containing CPD [41].

Structurally, 6-4PP consist of single covalent bond between the C6 carbon of the 5' pyrimidine and C4 carbon of the 3' pyrimidine [49]. Like CPD, they can potentially be formed at each of the four bipyrimidine doublets with TC 6-4PP being the most frequent, followed by TT 6-4PP while CC and CT 6-4PP are hardly detectable [41]. Their formation requires 4 milliseconds, which is 1000 times slower than CPD [50], and they are produced at a ratio of 1:3-1:5 as compared to CPD [41, 45]. They have a maximum absorption at 320 nm and their subsequent exposure to UVA or UVB result in their photoisomerization into the DEW [51-53]. However, very low levels of DEW are detected in cells and skin at biologically relevant doses of UVB [54].

The yield of all these direct DNA damage depends on the organization of DNA structure and medium in which the DNA is present during its exposure to UVB or UVC. The yield of all the three types of direct DNA damage is highest when DNA is in an aqueous solution, followed by their yield in cellular DNA and then that in skin DNA [46, 49]. In the skin, the distribution of UVB-induced CPD is homogenous throughout all the epidermal layers [55]. In the genome, the distribution of CPD and 6-4PP is not homogeneous and they occupy different regions in chromatin [49]: CPD are distributed in the eu- and heterochromatin, while 6-4PP are mainly in the euchromatin regions and their formation is greatly reduced by DNA condensation in heterochromatin [56]. In nucleosomes, the 6-4PP are mainly formed in the linker region [57] whereas the CPD are formed in both, linker and intra-nucleosomal regions, albeit with higher yield in linker region [58-60]. The telomeres are found to be more sensitive to UV-induced direct DNA damage than the bulk of the genome [61]. The local DNA sequences also affect the pyrimidine dimer formation [49]. CPD are more frequent within pyrimidine tracks [62, 63]. The flanking bases of a bipyrimidine site also drastically modify its photoreactivity. Formation of CPD at GTTG is much less efficient than in tetrads containing C at 5′- or 3′-end and that of 6-4PP is favored downstream C and upstream adenine (A) [48, 64]. The bipyrimidine sites containing 5-methylcytosine, such as those found in the CpG islands of the genome, are more prone to CPD formation [65, 66]. The pyrimidine dimers also distort the DNA double helix. The 6-4PP is a deforming lesion and bends DNA backbone by an angle of 44°, while the CPDs creates just a small distortion of 7° to 9° [67]. DNA distortion induced by 6-4PP is associated with a more permissive

chromatin environment, facilitating their recognition by DNA repair proteins, and hence their rapid repair. CPD are eliminated at a slower rate than 6-4PP and their repair efficiency is in the order of CT CPD> TC CPD/CC CPD> TT CPD [68]. Because the CPD persist longer than 6-4PP in DNA, they are more responsible for the harmful effects of UVB in the skin [49].

D.2. Indirect DNA damage

UVB can also induce indirect oxidative DNA damage via the ROS generated by various endogenous photosensitizers (section C and Fig. C, left), albeit to a much lesser extent than that by UVA [27, 69]. The UV-induced ROS such as H_2O_2 and $^{\bullet}OH$ can modify purines and pyrimidines indiscriminately, thereby resulting in formation of 8-oxoG, thymine glycol, 5'-hydroxycytosine and 2,6-diamino-4-hydroxy-5-formamidopyrimidine [27, 49, 70]. The $^{\bullet}OH$ can also attack the 2'-deoxyribose unit of DNA resulting in the formation of SSB [71], which are the discontinuities in one strand of the DNA double helix, usually accompanied by loss of a single nucleotide (nt) [72]. UVB-induced singlet oxygen ($^1O_2$) [24-26, 73-75] creates exclusively 8-oxoG in cellular DNA [76]. Owing to its lowest ionization potential, guanine (G) is the most susceptible target base, and hence 8-oxoG is the major type of UVB-induced oxidative DNA damage in mammalian cells and skin [77]. Notably, all these indirect DNA damage account for only 1 % of the UVB-induced DNA damage in the cellular DNA [37, 78]. The number of each type of lesions per 10^6 nucleobases per kJm^{-2} UVB are: 77 CPD, 0.31 8-oxoG, 0.19 SSB and 0.18 oxidized pyrimidine bases [37].

Interestingly, the ROS-induced oxidation of melanin and its precursors in melanocytes after UVB or UVA exposure can indirectly induce CPD by a process of chemisensitization [79]. These CPD are formed 2-4 h after UV exposure, and hence called dark CPD. Since this process is dependent on the presence of melanin, it can contribute to UVB-genotoxicity in KC [79, 80], which receives melanin from melanocytes (Section A). The direct formation of double-strand breaks (DSB) by UVB remains controversial [81-83]. However, unrepaired CPD could be converted to DSB during replication [84]. Notably, UVC rarely induce oxidative DNA damage [27].

In conclusion, UVB can cause different types of DNA damage in the skin cells: to a major extent, direct DNA damage such as pyrimidine dimers (CPD, 6-4PP and DEW) and to a minor extent, indirect oxidative DNA damage (8-oxoG and SSB) [27]. These DNA damage can mediate both acute and chronic harmful effects (erythema, skin immune system modulation and skin cancer) of UVB on skin [33, 85-87]. In response to UVB exposure, the epidermal cells initiate a DNA damage response which involves molecular and cellular processes such as DNA repair (Section E), cell cycle arrest and cell death (Section F) [32].

E. Repair of UVB-induced DNA damage

Mammalian skin cells are equipped with evolutionarily conserved DNA repair mechanisms to remove all types of DNA damage induced by UVB. The base excision repair (BER) and single strand break repair (SSBR) eliminate UVB-induced oxidative DNA damage, whereas the nucleotide excision repair (NER) eliminates UVB-induced direct DNA damage.

E.1. Repair of UVB-induced indirect DNA damage

The major types of UVB-induced indirect DNA damage, 8-oxoG and SSB are repaired via BER and SSBR pathways, respectively (Fig. D). In general, depending on the cell cycle phase and the type of complementary base present opposite 8-oxoG, BER of this non-bulky lesion involves DNA damage recognition and processing by the specific DNA glycosylases and/or endonucleases, resulting in single nt gap or "SSB" in DNA [88, 89]. At this point, the classical BER converges with the SSBR pathway to repair SSB [90, 91]. The single nt gap is filled either via short-patch (SP) or long-patch (LP) repair sub-pathways, which involve direct insertion of a single nt in this gap or replacement and insertion of 2-12 nt, respectively [92].

E.1.1. Base excision repair (BER) of 8-oxoG

ROS-induced oxidation of G in the context of C:G base pair (bp) in DNA results in C:8-oxoG, which are recognized in mammalian cells by the DNA glycosylase, 8-oxoG DNA glycosylase 1 (OGG1) (Fig. D.1a) [89, 93]. OGG1 serves two enzymatic functions: (i) its glycosylase activity cleaves N-glycosyl bond to release 8-oxoG, thereby creating an abasic site and (ii) its apurinic (AP) lyase activity cleaves the abasic site resulting in the formation of a SSB containing α,β unsaturated aldehyde (PUA) at the 3′-end [94]. The 3′-PUA group is removed by the diesterase activity of apurinic-apyrimidinic endonuclease 1 (APE1) to form single nt gap with 3′-OH and 5′- phosphate (5′-P) moieties [95, 96]. The OGG1 initiated BER follows the SP-BER sub-pathway [97, 98] in which the OGG1 recruits the scaffold protein X-ray repair cross-complementing protein 1 (XRCC1). The latter protein recruits DNA polymerase β (Polβ) and DNA ligase IIIa (Lig IIIa) [99-102]. Polβ utilizes its polymerase activity to insert one nt into the gap and Lig IIIa ligates the resulting 3′OH of the newly inserted nt with the downstream 5′-phosphate (5'-P), thereby concluding the repair of 8-oxoG [103-105].

If the C:8-oxo-G bp escapes recognition by OGG1 or the oxidation of G occurs in cells which are in

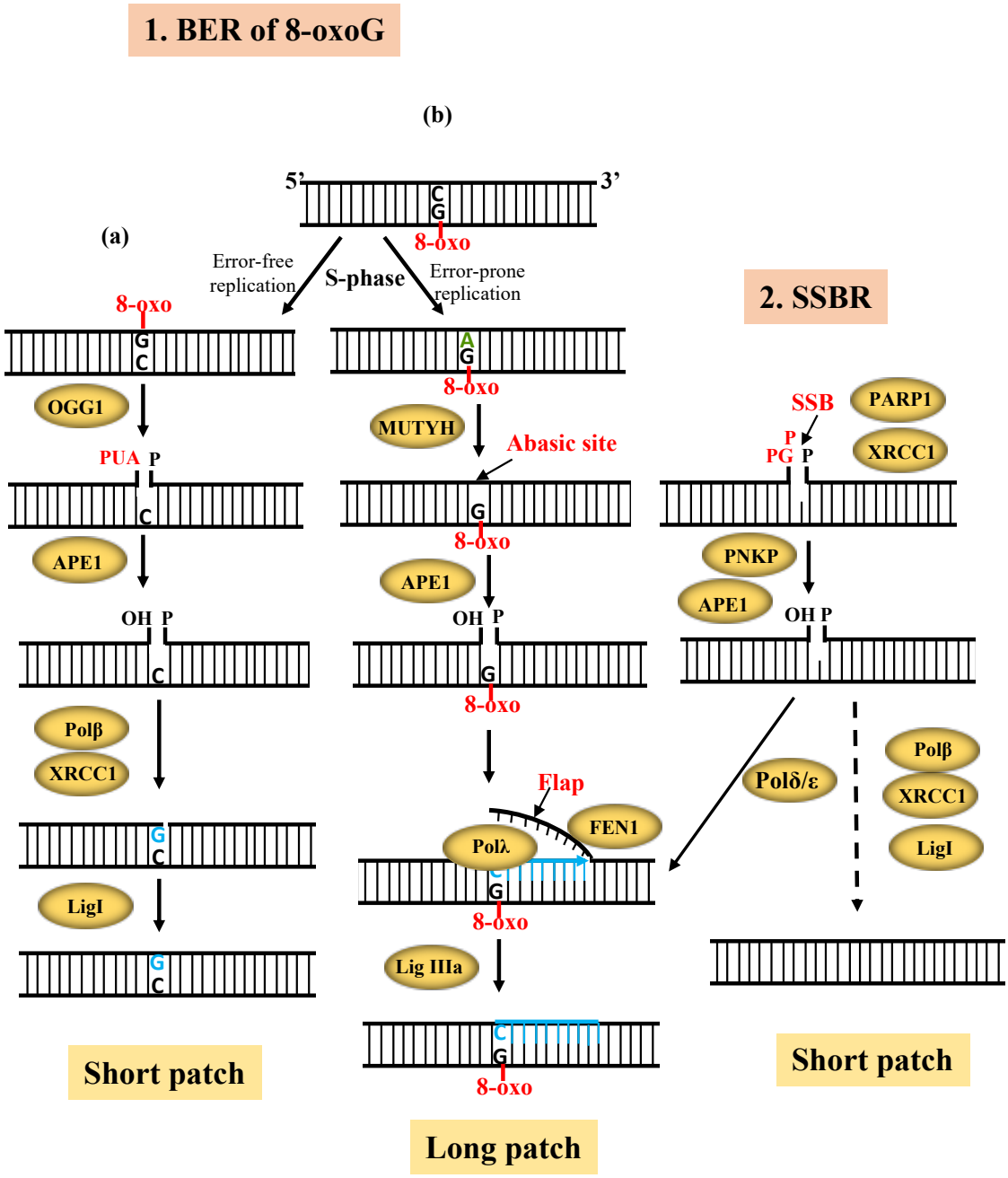

Figure D. Graphical outline of BER and SSBR pathways
Please refer to the section E.1 for the full forms of the abbreviations. Figure created by Nupur Purohit.

S-phase (Fig. D.1b), the replication of 8-oxoG can have two outcomes [89]. The error-free bypass of 8-oxoG during replication results in C:8-oxoG bp, which is recognized by OGG1 and repaired as described above [106, 107]. On the contrary, the error-prone bypass of 8-oxoG results in insertion of an A opposite 8-oxoG (A:8-oxoG), which is a mispair [108-112]. If left uncorrected, it could result

in C:G → A:T transversion mutation during second round of replication. To remove the A from this mispair, cells utilize the adenine DNA glycosylase (MUTYH) [113]. It serves only one enzymatic function, i.e., the cleavage of N-glycosyl bond to release the A. The resulting apurinic site is then cleaved by APE1 to form SSB with 3′-OH and 5′-P ends, where DNA polymerase λ (polλ) can insert correct C opposite 8-oxoG [96, 109, 114, 115] and two or more correct nt via LP-BER sub-pathway [116]. This results in the displacement of the downstream DNA strand (flap), which is recognized and cleaved by flap endonuclease 1 (FEN1) [117, 118]. The resulting 5′-P end is ligated by DNA ligase I (LigI) to yield an intact ds-DNA containing C:8-oxo-G, which is then repaired via OGG1 mediated SP-BER.

E.1.2. Single strand break repair (SSBR)

Unlike 8-oxoG, UVB-induced SSB pose greater threat to the cellular homeostasis because they can stall and collapse replication forks and create cytotoxic DSB in DNA [108, 119, 120]. The SSB are repaired via SSBR pathway (Fig. D.2) [121]. Two proteins key in orchestrating SSBR are poly(ADP-ribose) polymerase 1 (PARP1) and XRCC1. The first step, detection and signaling of the SSB, is carried out primarily by PARP1 [122-125]. The binding of PARP1 at SSB stimulates its catalytic activity resulting in synthesis of polymer of ADP-ribose (PAR) that modify several proteins present at the site of damage, including PARP1 itself. The PAR formation is absolutely necessary for the recruitment of XRCC1 at the SSB site and thereby accelerates SSBR kinetics in cellular DNA [121, 126-131]. The domain of XRCC1 that is PARylated, also mediates its interaction with DNA through separate and non-overlapping binding sites [131, 132]. The exact mechanism by which PARP1 plays a role in the repair of SSB generated during BER is under debate as described in section N.1.1.

XRCC1 is a critical scaffold protein that coordinates and accelerates the repair of SSB by interacting with, and in some cases stabilizing and/or stimulating several downstream enzymatic components [133]. Most of the ROS-induced SSB in DNA contains 3'-P and 3'-phosphoglycolate (PG) termini [72], which are restored to 3'-OH by polynucleotide kinase-3'-phosphatase (PNKP) and APE1 enzymes, respectively [134-141]. This is then followed by gap filling, which like BER proceeds either via SP- or LP-repair sub-pathways. To note, LP-repair in SSBR uses polymerases δ or ε (polδ/ε) for gap filling. The overlap in the repair of SSB arising via direct sugar disintegration in DNA and as intermediates of BER results in extensive intersection between the enzymes employed for SSB removal. Therefore, SSBR is considered as specialized sub-pathway of BER [142].

E.2. Nucleotide excision repair pathway

NER is a versatile DNA repair pathway that eliminates variety of structurally unrelated helix distorting DNA lesions including direct DNA damage induced by UV and bulky chemical adducts caused by environmental mutagens or chemotherapeutic agents such as benzo[a]pyrene and cisplatin [143]. Bacteria, yeasts, plants and marsupial mammals can eliminate UV-induced direct DNA damage via multiple mechanisms: NER, DNA photolyases which directly reverts CPD and 6-4PP or via UV DNA endonucleases that incise DNA adjacent to the CPD or 6-4PP [144]. In contrast, placental mammals including humans and mice rely solely on the NER pathway to eliminate UV-induced CPD and 6-4PP lesions [23]. Studies have established that mammalian NER removes CPD and 6-4PP in a highly orchestrated fashion involving multiple proteins in following defined steps [145-148]: (I) DNA damage recognition, (II) DNA unwinding around the damage and its verification, (III) excision of a 26-30 nt fragment containing the damage, gap filling and ligation (Fig. E). For the sake of simplicity, the CPD and 6-4PP are referred as UV-lesion or UV-damage in this section. The research in the chapter 1 and Annexe 3 of this thesis requires the detailed understanding of NER pathway.

E.2.1. DNA damage recognition

The mammalian NER pathway begins with the recognition of UV-lesion in DNA by two distinct sub-pathways (Fig. E-I): (1) the transcription coupled NER (TC-NER) that recognizes UV-lesions from the transcribed strands of transcriptionally active genes and (2) the global genomic NER (GG-NER), that identifies lesions throughout the genome [23, 149]. Even though TC-NER removes UV-lesions more rapidly from the actively transcribed DNA strands than that by GG-NER throughout the genome, it repairs < 10 % of the total UV-lesions, while > 90 % are repaired by GG-NER in the mammalian cells [150-154].

(1) TC-NER*:* The proposed molecular events of DNA damage recognition during TC-NER in the mammalian cells can be summarized as follows (Fig. E.2) [23, 149, 153, 155-157]. The primary sensor of UV-lesion during transcription of mRNA coding genes is the elongating RNA polymerase II (RNAPIIo), which may loosely interact with Cockayne syndrome (CS) complementation group B (CSB) protein as well as with the complex of UV-stimulated scaffold protein A (UVSSA) and ubiquitin specific processing protease 7 (USP7) deubiquitinase (UVSSA/USP7) [158-161]. Upon encountering UV-lesion in the transcribed strand, RNAPIIo stalls at the UV-lesion site [162, 163], thereby stabilizing RNAPIIo-CSB and RNAPIIo-UVSSA/USP7 interactions [149, 155, 158, 164]. CSB is a SWI/SNF ATP dependent chromatin remodeler. It binds to the DNA upstream of RNAPIIo

and using its ATPase activity pulls DNA towards itself to verify if RNAPIIo is just paused or truly stalled at the lesion site, and also mediates chromatin remodeling either directly or via recruitment of Cockayne syndrome (CS) complementation group A (CSA) protein and histone acetyltransferase p300 (p330) [156, 157, 164-168]. As a part of an E3-ubiquitin ligase (CRLCSA) complex consisting of DNA damage-binding protein 1 (DDB1), Cullin 4A (Cul4A) and RING box protein 1 (Rbx1) proteins, CSA ubiquitinates itself, CSB, and RNAPIIo at the DNA damage site [169, 170]. The ubiquitination of CSB results in its degradation [171]. Therefore, to allow sufficient time for CSB to perform its functions, the CSB ubiquitination is counteracted by the deubiquitinase USP7 in UVSSA/USP7 complex [159, 160]. This complex can also be recruited by CSA [172]. The recruitment of factors such as transcription factor IIS (TFIIS), high mobility group nucleosome binding domain containing protein 1 (HMGN1) and XPA-binding protein 2 (XAB2) are dependent on both CSB and CSA [168]. Following the DNA damage recognition, the accessibility of the lesion by the core NER factors such as transcription factor IIH (TFIIH) and Xeroderma pigmentosum (XP) group A-complementing protein (XPA) is likely to be achieved by displacement of RNAPIIo from the damage site. Amongst the several proposed mechanisms for RNAPIIo displacement, the most accepted one is its back tracking, which is facilitated by TFIIS and/or TFIIH [153, 155, 157, 173] and the required sliding or disassembly of upstream nucleosomes is facilitated by various chromatin remodelers including CSB, p300 and HMGN1 [174-183]. The XAB2 is indispensable for TC-NER, but its exact role is yet unknown [184, 185]. To note, TC-NER but not GG-NER is absent in cell lines deficient in CSB, CSA, UVSSA, XAB2 or HMGN1 [159, 161, 172, 179, 184-188]. Since CSB is the master regulator of TC-NER, the CSB-deficient cells are often used as model cell line to study GG-NER [157].

(2) GG-NER: The research presented in chapter 1 and annex 2 of this thesis involves GG-NER. The UV- damage recognition in GG-NER is mediated by the interplay between two DNA damage sensor complexes: UV-damaged DNA-binding protein (UV-DDB) and XPC-HR23B-Centrin2 (Fig. E.1) [189-192]. Since the recruitment of subsequent NER proteins to UV-lesion sites throughout the genome (except the transcribed strand of active genes) is abolished in XPC-deficient cells (XP-C cells), XPC (Xeroderma pigmentosum group C-complementing protein) is indispensable for GG-NER. Hence XP-C cells are deficient in GG-NER and are used as a model cell line to study TC-NER [154, 193]. The XPC-HR23B-Centrin2 complex binds to UV-lesion via XPC [190-192]. HR23B (UV excision repair protein RAD23 homolog B) protects XPC from proteasomal degradation and stimulates DNA damage binding by XPC. However, HR23B dissociates from the complex after XPC binds to UV-lesion, possibly due to overlap of binding site in XPC protein for HR23B and DNA [194-

198]. Centrin2 (C2) probably remains attached to XPC during the NER and stimulates damage repair but its exact biological role is yet unknown [199, 200].

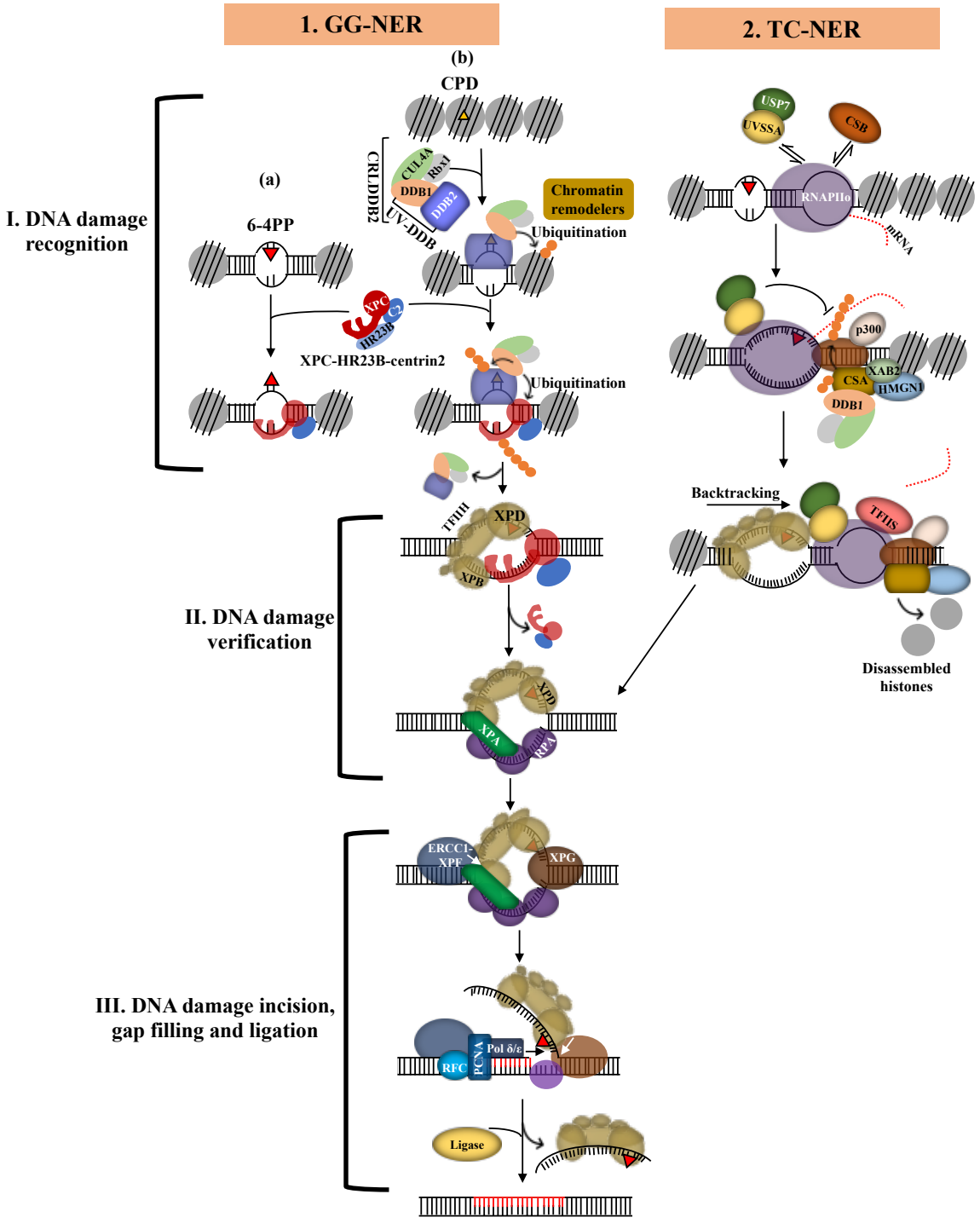

Figure E. Graphical outline of nucleotide excision repair pathway
Step I. DNA damage recognition: The protein complexes involved in damage recognition are the UV-DDB (DDB2 and DDB1) and XPC-HR23B-centrin2 for the direct DNA damage located in the

entire genome (GG-NER) and the RNAPIIo-CSB for those on the strand of transcriptionally active genes (TC-NER). For GG-NER sub-pathway, 6-4PP can be directly recognized by XPC (a), whereas recognition of CPD by XPC requires UV-DDB (b). Once the damage has been recognized, the two sub-pathways of the NER converge to the following steps. Step II. DNA damage verification: The transcription factor TFIIH opens the DNA helix with its helicases XPB and XPD (step II. DNA damage verification). The blockage of XPD by the lesion allows the complete opening of the "bubble" and the recruitment of the XPA and RPA complex proteins which leads to the formation of the open complex. Step III. DNA damage incision, gap filling and ligation: The XPF protein is recruited by XPA via its partner ERCC1 and initiates the incision at 5 'of the UV-lesion. This generates the formation of a free 3'OH group which acts as a primer for the δ/ε polymerases. The synthesis of the new strand is probably the signal which triggers the activation of XPG, which incises at 3'-end of the UV-lesion bearing strand. (step C). The repair is completed when the newly synthesized strand is ligated by ligases. Please refer to the section E.2 for the full forms of the abbreviations. Figure created by Nupur Purohit.

XPC recognizes with a high affinity the DNA damage including UV-induced 6-4PP, which cause significant distortion of the DNA helix (Fig. E.1a) [201-204]. Recent studies with the yeast orthologue of XPC (RAD4), and UV-DNA bound XPC fragments or XPC-HR23B provide insight into the mechanism by which XPC can search and bind to the helix-distorting DNA damage [205-209]. While RAD4 scans DNA by both, 3D hopping and 1D sliding mechanisms [208], the human XPC does the same by only 1D hopping to avoid protein obstacles on the DNA [209]. By either mechanism, XPC tests the integrity of DNA by twisting/bending the DNA backbone resulting in formation of labile nucleoprotein intermediate [205, 207, 208, 210]. The presence of a damage-induced helical distortion allows longer retention of XPC at this site and lowers the energy barrier that has to be overcome to form a stable DNA-XPC complex [206]. At the damage site, XPC does not directly contact the UV-lesion but binds to the junction of ds- and ss-DNA around the UV-lesion while interacting with the unpaired nt located on the strand opposite the UV-lesion [210-215]. In this interaction, the UV-lesion-containing bases are dislocated from the duplex inducing a flipped-out configuration [198, 210]. This characteristic of XPC to employ indirect strategy to recognize damage based on the DNA double helix distortions explains the great variety of lesions recognized and repaired by GG-NER [201-204]. However, the same feature limits the ability of XPC to detect CPD, which cause minor distortion to the DNA double helix [67]. *In vitro* studies show that XPC has none or very little ability to initiate repair at the CPD-sites [201, 202, 216, 217]. Consistently, a recent single molecule visualization study showed that XPC identifies CPD inefficiently and binds to them with limited stability [209].

To recognize and repair CPD in the constrained chromatin environment of mammalian cells, XPC requires UV-DDB complex (Fig.E.1b) [218-222], a heterodimer of DDB1 and DDB2 proteins. DDB2 (UV-damaged DNA binding protein 2) is encoded by the Xeroderma pigmentosum group E (*XPE)* gene and is absent in yeast. After UV-irradiation, it is one of the earliest proteins to co-localize with

UV-lesions [218, 219]. The UV-DDB complex searches for 6-4PP or CPD via 3D-diffusion by hopping from one DNA molecule to another, allowing it to scan the DNA quickly while avoiding the problems associated with DNA slippage due to the presence of other proteins and nucleosomes [223]. *In vitro* studies have shown that the affinity of UV-DDB complex for UV-lesions is 100 to 1000 times greater than that of XPC [221, 224]. The formation of a dimer with another UV-DDB complex via the N-terminal domain of DDB2 results in its immobilization at the UV-lesion site and increases its affinity for the damaged DNA [225]. Crystallography studies show that, unlike XPC, the UV-DDB complex binds directly to these lesions via the WD40 domain of DDB2 [169, 189, 225], which wedges itself into the DNA duplex at the lesion site causing CPD/6-4PP to flip out into its shallow binding pocket. DDB2 makes a footprint of 2 nt on the 5'-side of the lesion. Binding of DDB2 to UV-lesion bends DNA at an angle of 40-45º [169, 189]. DDB2 can bind to UV-lesions not only in naked DNA but also in nucleosomes [169, 189, 226, 227]. Although DDB1 does not directly interact with DNA, its importance in GG-NER is underscored by the existence of XPE diseases caused by mutations affecting its interaction with DDB2 [228, 229].

The stable binding of DDB2 to UV-lesions stimulates the translocation of XPC from nucleoplasm to chromatin and facilitates the recruitment of XPC not only at CPD sites but also at 6-4PP sites [218, 220-222]. This observation is supported by the fact that cells from individuals with mutations in the *XPE* gene do not repair CPD and slowly repair 6-4PP, most likely due to direct recognition of 6-4PP by XPC [218, 221, 230, 231]. DDB2 facilitates the recruitment of XPC at the UV-lesion site by either directly interacting with XPC [217, 232-234] or by UV-DDB complex mediated chromatin remodeling around the UV-damage site. Since distorted DNA is the substrate of XPC, DDB2 binding-induced helix distortion at the site of UV-damage could be a signal to facilitate damage detection by XPC. It has been shown that the greater the distortion in DNA, the higher the number of XPC molecules bound to DNA [235]. The UV-DDB can open chromatin around the UV-lesion site directly via DDB2 [236], by recruitment of various chromatin remodeling factors [237-242] and by ubiquitination activity to facilitate the damage detection via XPC.

In addition to UV-damage recognition, UV-DDB forms a ubiquitin ligase complex with Cul4A and Rbx1 proteins (CRLDDB2 complex) (Fig.E.1b), and ubiquitinates proteins within a radius of about 100 Å around the UV-lesion site [169, 170, 189]. Its main targets for ubiquitination are histones, XPC, DDB2 and Cul4A [170, 217, 243-246]. The ability of HR23B to recognize ubiquitin chains of histones, can facilitate the recruitment of XPC-HR23B-centrin-2 complex to damage site [243, 247]. The ubiquitinated histones are displaced or evicted thereby giving XPC an access to damaged site [244, 246, 248]. The ubiquitination of XPC, following its recruitment at the UV-damage site, doubles

its affinity for intact or damaged DNA [217], and stabilizes it at this site. On the contrary, ubiquitination of DDB2 results in loss of its affinity for DNA and in its degradation [169]. This is important for handover of damage site to XPC for the subsequent repair [192, 249, 250]. Finally, XPC is also modified by SUMO (small ubiquitin-like modifier) residues, that target XPC for second round of ubiquitination mediated by the SUMO-targeted E3 ligase (STUbL) RNF11/Arkadia [251-253]. These modifications have been shown to be important for the timely removal of XPC from damaged DNA and handover of damage to downstream NER factors to accomplish the subsequent repair steps [192, 246, 250].

E.2.2. DNA damage verification and open complex formation

Once the damage is recognized by either TC-NER or GG-NER factors, both the pathways converge and follow common molecular mechanism until the final step of the repair [23]. The TC-NER and GG-NER DNA damage recognition factors, UVSSA and XPC recruit the TFIIH [148, 254-258], which in turn recruits XPA (Fig. E-II) [259]. TFIIH is a 10-subunit transcription factor which includes the two ATP-dependent helicases with opposite polarities, XPB and XPD along with other subunits [257]. In GG-NER, XPC, TFIIH and XPA collaborate to mediate DNA damage verification using the helicase activities of XPD and XPB subunits [192, 260-265]. This results in the formation of an open complex, which is an unwound structure of approximately 25-30 nt with ~22 nt on the 5’ and ~5 nt on the 3’of CPD, respectively [266, 267]. In TC-NER, TFIIH is also proposed to mediate RNAPII backtracking while forming an open complex [157]. XPA interacts with the eukaryotic ssDNA binding replication protein A (RPA), and their recruitment to damage site, either individually or as a pre-formed XPA–RPA complex promotes the dissociation of the XPC from the damage site [268, 269]. Binding of RPA to undamaged DNA strand partially unwound by TFIIH, leads to a separation of the DNA strands around the lesion [270]. Altogether, these steps lead to the stabilization of open complex and formation of pre-incision complex in which the lesion site is demarcated by XPA and TFIIH binding.

E.2.3. Excision of UV-lesion, Gap filling and ligation

The incision of UV-lesion is mediated via two endonucleases that specifically cut at the junction of ds- and ss- DNA around the UV-lesion (Fig. E-III), but have opposite polarities: the DNA excision repair protein (ERCC1)-xeroderma pigmentosum group F-complementing (XPF) protein complex (ERCC1-XPF) cuts the DNA at 5’ of the lesion and the xeroderma pigmentosum group G-complementing (XPG) protein at 3' [271]. The recruitment and proper positioning of ERCC1-XPF on the 5’ side of the damage is mediated via XPA [272-274], whereas that of XPG is via TFIIH

complex [275-277]. The first incision is made by ERCC1-XPF, which requires the presence but not the catalytic function of XPG [278]. The resulting 3'OH residue can be used by the polymerases to initiate the synthesis of a new strand. To do this, the endonuclease XPG recruits replication factor C (RFC)-proliferating cell nuclear antigen (PCNA) protein complex (RFC-PCNA), which is positioned at 5' of the damage by the RPA. Depending on the status of cell cycle, this is accompanied by the recruitment of polymerases δ, ε or κ and XRCC1 which begin the synthesis of the new strand [279, 280]. In order to conclude the synthesis of the new fragment, XPG cleaves at the 3'-end of the UV-lesion in the presence of the catalytic activity of XPF [281] to liberate a TFIIH bound fragment of ~26-30 nt containing the UV-damage [282, 283]. The nicks are sealed by either DNA ligase I or III, which are recruited by PCNA or XRCC1 respectively, depending on the stage of the cell cycle [279, 284].

F. UVB-induced signaling pathways decides the fate of epidermal cells

The UVB-induced DNA damage and/or ROS activate a complex signal transduction network in epidermal cells that decides their fate: repair the damage and survive or undergo apoptosis (Fig. F) [285, 286]. DNA damage, either directly or indirectly via their repair pathways, triggers DNA damage checkpoints, which are mediated by ataxia telangiectasia and Rad3-related protein kinase (ATR) and ataxia telangiectasia-mutated (ATM). The ATR and ATM have overlapping functions and cross talk with each other [286-296]. The UVB-activated ATM and ATR initiate a signaling cascade that leads to the activation and stabilization of cellular tumor antigen p53 (p53) and inhibition of cell division cycle 25 homolog A (CDC25A) activity, which results in cell cycle arrest at G1/S and G2/M phases [286]. Alternatively, prolonged activation of ATM/ATR results in apoptosis as described below. The UVB-induced ROS also cause activation of mitogen-activated protein kinase (MAPK) family members, MAPKp38 (p38) and c-Jun N-terminal kinases (JNK) [285, 286] via oxidation-mediated inactivation of MAPK phosphatases (MKPs) [297] and activation of ATM/ATR pathway (Fig. F) [298-300]. These UVB-activated MAPK also use p53 dependent and independent signaling pathways to induce cell cycle arrest and apoptosis in UVB-damaged KC [301].

p53 plays a central role in deciding the fate of UVB-damaged skin cells. The activated p53 mediates its transcriptional activity by binding to the enhancer/ promoter elements of downstream target genes in the nucleus [302, 303]. The UVB-activated p53 cause the upregulation of cyclin-dependent kinase inhibitor 1 (p21) in the cultured KC and mouse epidermis [32, 304, 305]. p21 mediates cell-cycle arrest at G1-phase [104, 306]. Simultaneously, activated p53 also promotes optimal NER and BER via its transcription-dependent and independent functions [307]. It facilitates NER by inducing the transcription of DNA damage recognizing proteins DDB2 and XPC [230, 308-312] as well as by

transcription-independent chromatin relaxation that facilitates the accessibility of NER machinery at the DNA damage site [313]. It also modulates BER in a cell cycle specific manner by enhancing BER during G1 phase of the cell cycle and inducing apoptosis in the G2-M phase [314]. It facilitates the BER of 8-oxoG by enhancing the transcription of OGG1 and MUTYH and also by transcription-independent functions [315-319].

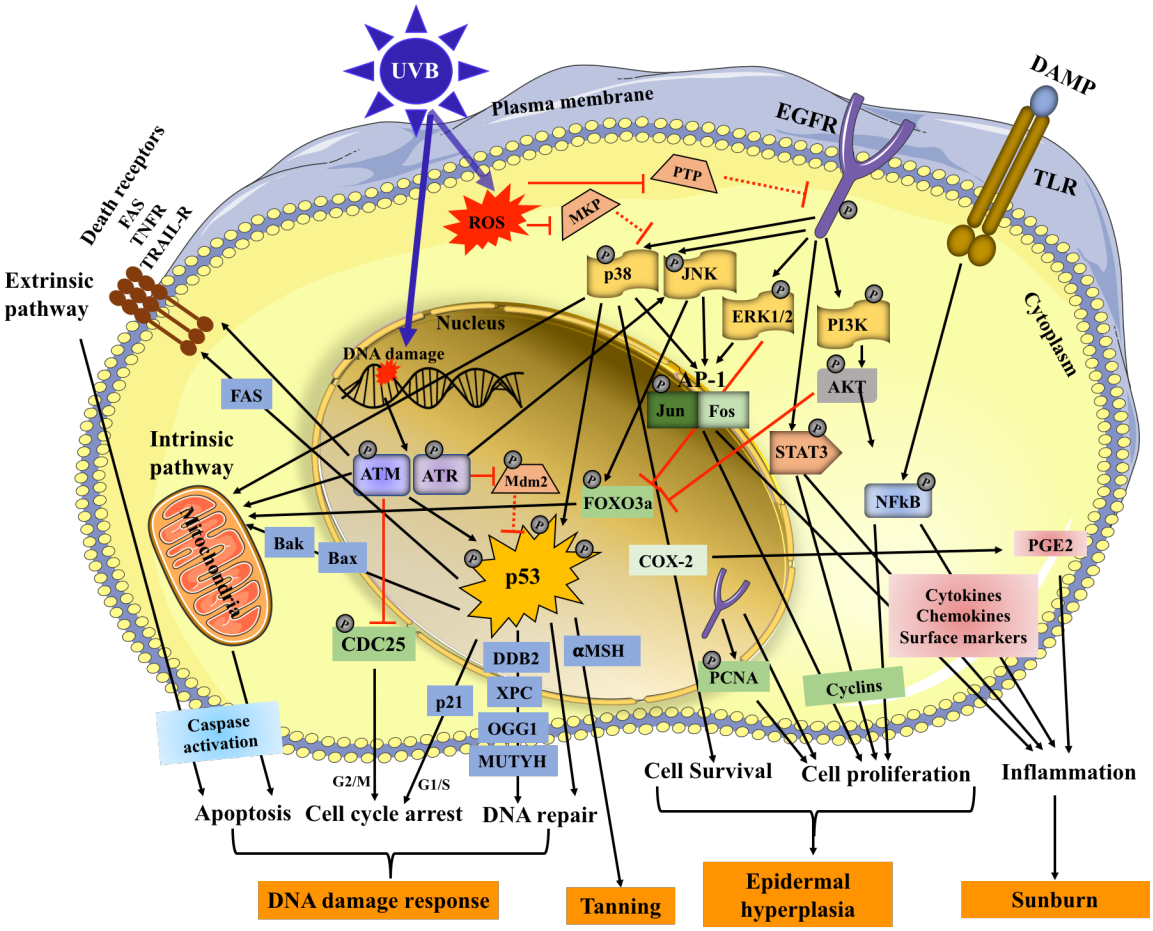

Figure F. UVB-induced signaling pathways
Please refer to the section F, G and I.1 for the full forms of the abbreviations. Figure created by Nupur Purohit.

The UVB-irradiated KC bearing high or persistent DNA damage die via apoptosis [304]. The apoptotic KC or sunburn cells (SBC) are identified in the epidermal layers of UVB-irradiated skin by their eosinophilic cytoplasm and a pyknotic nuclei [320]. UVB-induced apoptosis of KC is mediated primarily via intrinsic pathway initiated at the mitochondria, but can also be mediated via extrinsic death receptor-dependent pathway initiated at the plasma membrane (Fig. F) [286, 321]. The significant reduction in UVB-induced SBC in the epidermis of $p53^{-/-}$ mouse underscores the role of

p53 in UVB-induced apoptosis [322]. p53 mediates apoptosis by transactivating several genes involved in the extrinsic (Fas) and intrinsic (Bax, Bak, Bid, etc.) pathways [323], as well as via its transcription independent activities [324, 325]. Since UVB-induced SBC are reduced but not abolished in $p53^{-/-}$ mouse [322], it suggests the existence of p53-independent apoptotic pathways in KC [286, 321, 326]. These pathways are mediated via the members of tumor necrosis factor (TNF) superfamily and TNF receptor (TNFR) superfamilies: FAS-L/FAS [327], TNFα/TNFR [328, 329] and tumor necrosis factor related apoptosis inducing ligand (TRAIL)/TRAILR [330]. In addition, p53-independent intrinsic pathway of apoptosis can be mediated via UVB-activated ATR/ATM [331, 332], p38 [333-335] and JNK [336, 337] signaling.

The fate of UVB-damaged KC is decided by the level of DNA damage. Mice that are irradiated with high doses of UVB or those deficient in the repair of UVB-induced direct DNA damage show increased number of apoptotic cells in their skin [32, 86]. High or persistent DNA damage results in the prolonged activation of ATM/ATR, and hence increased levels of accumulated p53 [286]. It has been reported that the promoters/enhancers of p53-transcriptional target genes involved in cell cycle and DNA repair often have high affinity binding sites for p53, whereas those involved in the apoptosis have variable affinity that requires co-operative binding via tetramerization and therefore, higher amounts of p53 [338, 339]. Hence at low level of DNA damage after the low doses of UVB (50 J/m^2), the level of p53 accumulated and activated is just enough to mediate cell cycle arrest and DNA repair but not apoptosis in the murine skin cells [304, 340, 341]. However, at the higher UVB doses (100-400J $/m^2$), excessive p53 accumulation directly corroborates with increased apoptosis.

To conclude, UVB-induced DNA damage response in the skin results in cell cycle arrest that not only facilitates DNA repair but also provides enough time for the epidermal cells to repair the damaged DNA before its replication. Whereas, cell death via apoptosis eliminates the cells in which DNA damage is high or persistent. The p53 regulates this cell fate decision, and hence it is considered as guardian of the genome [342]. Following the DNA damage response, the regenerative and adaptive processes such as epidermal hyperplasia and tanning are initiated in the UVB-irradiated skin.

G. UVB-induced epidermal hyperplasia

Following the phases of UVB-induced cell cycle arrest, DNA repair and apoptosis, is the regeneration phase, i.e., increase in proliferation of KC resulting in epidermal thickening or hyperplasia [305, 343]. It is observed between 48 and 72 h after single exposure to UVB and is marked by increased cell layers [86], thickness of skin [344] or PCNA and Ki67 positive cells in the basal and suprabasal layers of the epidermis [305]. It is dependent on the activation via phosphorylation of epidermal growth

factor receptor (EGFR) [345, 346] in ligand-independent manner due to ROS-induced inactivation of protein tyrosine phosphatases (PTP) [347-350] in UVB-irradiated human KC [351] and murine skin (Fig. F) [345]. UVB-induced inflammatory mediators (Section I.1) result in ligand-dependent activation of EGFR [352]. The downstream effectors of EGFR activation include the MAPK family members: ERK1/2, p38 and JNK as well as phosphoinositide 3-kinase (PI3K)/protein Kinase B (PKB or AKT), which mediate proliferation as well as suppression of apoptosis [286]. The activated MAPKs subsequently lead to upregulation and activation of the transcription factor activator protein-1 (AP-1) that is composed of Jun and Fos subunits. AP-1 promotes cell proliferation by increasing the transcription of cell cycle genes such as cyclin D1, cyclin A, cyclin E, etc., [353, 354]. ERK1/2 [355] and AKT [356, 357] suppress apoptosis by inhibiting proapoptotic transcription factor Forkhead box protein O3a (FOXO3a) [358, 359] while p38 inhibits apoptosis by inducing expression of anti-apoptotic cyclooxygenase-2 (COX-2) [360, 361]. UVB also induces translocation of activated EGFR to the nucleus [362, 363], where it transactivates the transcription of genes such as cyclin D1 [364] and COX-2 [365] as well as phosphorylates and consequently stabilizes chromatin-bound PCNA via its tyrosine kinase activity, contributing to prolonged cell proliferation [366]. The UVB-induced epidermal hyperplasia is not only a regenerative response which replaces the dead epidermal cells but also an adaptive response, because thickening of epidermis reduces the penetration of UVB during subsequent exposures [367].

H. Tanning

In addition to its effects on KC, UVB also affects melanocytes in murine and human skin, thereby resulting in increased skin pigmentation or tanning. It causes delayed tanning in humans, which occurs 3-4 days after the exposure [368]. Tanning is mediated via p53-induced increased synthesis of alpha-melanocyte stimulating hormone (α-MSH) in KC (Fig. F), which upon its release, binds to its receptor, melanocortin 1 receptor (MC1R) on neighboring melanocytes [369-372]. The resulting signaling cascade leads to transcriptional upregulation of genes required for melanin synthesis and melanocyte proliferation, thereby resulting in increased melanin pigment in melanocytes and its eventual transfer to neighboring KC via melanosomes [373-378]. To note, the factors released from fibroblasts and endothelial cells also contribute to this UVB-mediated tanning response [376, 379]. The UVB-acquired tanning is a skin adaptive response, providing protection against subsequent UVB damage [372, 376, 380-382]. The melanin scatters or absorbs 50-70% of UV reaching the skin surface and reduces the extent of UV rays penetrating through the epidermal layers [383-385]. Within individual KC, melanosomes localize in the perinuclear area to form “supranuclear melanin caps” [386], which shield the nuclear DNA from UVB-induced damages [387]. Moreover, melanin provides

protection against oxidizing effects of UVB by quenching free radicals [388]. Owing to its photoprotective effects on skin, melanin is considered as "natural sunscreen" [2, 384].

Overall, these regenerative and adaptive processes restore the skin homeostasis after a single exposure to UVB and reduce the damages in skin during subsequent UVB exposures.

I. Effects of UVB on skin immune system

UVB affects the skin immune system (Section A), which encompasses both the innate and the adaptive immune systems [6, 389-393]. The innate immune responses are rapid, serve as first line of defense and are mediated in the skin via KC, neutrophils, macrophages, mast cells, LC, dDC and pDC [6]. In contrast, adaptive immune responses are slow, create immunological memory, serve as second line of defense and are mediated via T- and B-cell subsets [6]. The bridge between innate and adaptive immune responses are APC (LC, dDC, mast cells and macrophages, etc.), which process the antigens and present them to T- and B-cells to determine the development of active or tolerogenic adaptive immune response to particular antigen or stimulus [6]. It is now well established that UVB stimulates the innate immunity to initiate inflammatory response resulting in sunburn and modulate immune recognition directly or via inflammatory mediators, resulting in suppression of adaptive immune responses (photoimmunosuppression) [389, 390].

I.1. UVB-induced stimulation of the innate immune response results in sunburn reaction

Amongst all the innate immune cells in the skin, the epidermal KC act as primary pro-inflammatory effector cells in response to UVB [389, 390, 393]. Excessive UVB exposure results in formation and/or release of damage-associated molecular patterns (DAMPs) from the damaged KC [394-397]. These bind to and activate a signaling pathway through the pattern recognition receptors (PRR) such as Toll-like receptors (TLR) present on the neighboring KC and other innate immune cells in the skin (Fig. F) [6]. Moreover, UVB-induced immediate products (cis-UCA, $1,25(OH)_2D3$, PAF and PAF-like lipid ligands and FICZ) in the skin bind to their receptors on the KC, LC, mast cells, etc., and initiate various pathways, which culminate in activation of EGFR signaling [389, 390]. Activation of transcription factors, nuclear factor kappa-light-chain-enhancer of activated B cells (NFκB), signal transducer and activator of transcription 3 (STAT3) and AP-1 as well as enzyme COX-2 [286, 389, 398] are the combined downstream effects of TLR- and EGFR-signaling pathways (Fig. F). These transcription factors induce the expression of inflammatory mediators such as cytokines (TNFα, IL-6, IL-10, IL-1β, etc.), chemokines and surface markers (RANK-ligand (RANK-L) and VEGF) whereas COX-2 increases the synthesis of prostaglandins (PGE2) [286, 361, 389, 398-403], altogether resulting in sunburn [389].

Clinically, sunburn is characterized by perceptible erythema (redness), edema (swelling) and pain [404, 405]. The erythema results from the inflammatory mediators-induced local vasodilatation and increased blood flow in UVB-exposed skin [406, 407]. These mediators also mediate the perivascular infiltration of neutrophils, monocytes and macrophages [32, 408-410] in dermis and/or epidermis, resulting in edema [406, 411]. The infiltrating immune cells conclude the innate immune response and also mediate repair in the skin, such as, phagocytosis of sunburn cells by the macrophages [409, 410]. Moreover, they prevent infections that might occur due to the penetration of bacteria through the UVB-compromised epidermal barrier of the skin [411-415]. The UVB-induced inflammation is a sterile inflammatory response because it is triggered in the absence of any microbial/pathogen infection [416]. The inflammatory transcription factors such as NFκB and STAT3 as well as inflammatory mediators also promote survival and proliferation of KC by regulating the expression and function of a number of genes that regulate cell cycle and cell death [356, 417].

Sunburn is the most conspicuous acute cutaneous response to UVB, particularly in fair-skinned individuals [418]. Hence, it is used to determine an individual's skin sensitivity to UVB [406]. The minimum dose of UVB required to produce barely perceptible erythema (skin reddening) is termed as minimal erythemal dose (MED) and is variable amongst humans. It should be noted that a dose of UVB lower than 1 MED (sub-erythemal dose) can also induce upregulation of inflammatory mediators via epidermal chromophore mediated pathways [399].

I.2. UVB-induced suppression of adaptive immunity

The direct evidence that UVB acts as an immunosuppressant came from a classic series of experiments in mouse which showed that it prevents the immunologic rejection of transplanted highly immunogenic UVB-induced skin tumors [419, 420]. Since then extensive research has made it clear that UVB exerts immunosuppressive effects on skin via APC such as LC, dDC, mast cells and macrophages [389-392, 421, 422]. UVB-induced DNA damage in epidermal LC undermine their antigen presenting capacities or trigger their apoptosis-mediated depletion in epidermis [423]. In addition, UVB-induced immediate products from the epidermal chromophores and the inflammatory mediators also modulate the APC functions [389, 390]. UVB triggers the migration of these impaired APC to the draining lymph nodes, where they generate regulatory T- and B-cells (Treg and Breg) and natural killer T (NKT)-cells [389-392, 421, 422].

Under normal circumstances, cutaneous exposure to antigens, such as contact allergens or tumor antigens expressed on skin cancers, results in the generation of antigen-specific effector T-cells and Treg [424]. While the effector cells promote an immune response against the antigen, the Treg

dampen the reaction and the overall magnitude of the immune response is a net result of these two responses. However, UVB modulates the skin immune system to favor the induction of adaptive immune cells (Treg, Breg and NKT cells) which have immunosuppressive activities via the release of IL-10 and IL-4 cytokines [389-392, 421, 422]. This is directly evident from the reported suppression of typical T- and B-cell mediated responses, contact hypersensitivity (CHS) and delayed type hypersensitivity (DTH) to specific antigens in the UVB-irradiated mouse skin [392, 425-429]. Furthermore, this UVB-induced immunosuppression was observed not only at the same site as the UVB-irradiation (local immunosuppression) but also at the distal non-irradiated site such as spleen (systemic immunosuppression) and is mediated via dermal lymph nodes [392, 430]. Since skin is directly exposed to the environment all the time, immunosuppression prevents allergic and autoimmune responses in it, post single or acute UVB-exposure [392].

To conclude, a single exposure to UVB perturbs the skin homeostasis in multiple ways. The skin responds to these threats by launching multiple protective cellular processes to not only restore the homeostasis but also adapt changes that would reduce the damage during subsequent UVB exposures. However, repeated and long-term (chronic) exposure of skin to UVB overwhelms and deregulates these repair, regenerative and adaptive responses resulting in harmful consequences, such as photoaging and cancer. The present thesis emphasizes on the UVB-induced skin cancer.

J. UVB-induced skin cancers

Chronic solar UV exposure is one of the major risk factors for skin cancer, which is one of the most common malignancies among Caucasians [431, 432]. The skin cancers are classified into two types, melanoma and non-melanoma skin cancers (NMSC), depending on whether they arise from melanocyte or not, respectively [433]. Even though melanoma is the most aggressive type resulting in 75 % of all skin cancer-related deaths, the incidence of NMSC is highest [432-435]. NMSC comprise of various types of carcinoma, such as basal cell carcinoma (BCC), squamous cell carcinoma (SCC), baso-SCC, infiltrative carcinoma, Merkel cell carcinoma, adnexal tumors, cutaneous lymphoma, etc. [436]. However, the SCC and BCC are the two major types of NMSC that arise from the KC, and hence termed as keratinocyte carcinomas [437, 438]. Since the research in the chapters 2 to 4 uses a mouse model which mainly develops SCC in response to chronic UVB irradiation, the following sections introduce the mechanism by which chronic UVB-exposure induces SCC.

J.1. Cutaneous squamous cell carcinoma

Among NMSC, BCC account for 70% incidence whereas SCC account for 20% incidence [439, 440]. However, unlike BCC that largely stay confined to skin, the SCC pose a greatest threat to metastasize and mortality rates are high in SCC patients [440, 441]. In fact, 20 % of the skin cancer deaths are attributable to SCC [442]. The epidemiological data show that SCC incidence is 15–35/100,000 person-years [443]. 3–7 % of SCC patients develop metastasis, of which more than 70 % die from disease [444] and SCC incidence is expected to increase by 2–4 % each year [445]. However, epidemiologic data of SCC incidence is underrepresented because of dearth of their reliable registration due to its relatively low mortality rate and the practical difficulties in ascertaining the large number of NMSC cases [431]. Owing to its increasing worldwide incidence, NMSC including SCC carry a substantial economic burden with it being the costliest cancer in Australia [446]. In the USA, the estimated total annual NMSC-related expenditure is 650 million USD [447].

Today, epidemiological studies have made it clear that one of the major risk factors for SCC in humans is the cumulative exposure to terrestrial solar UV [448]. The SCC incidence in humans is directly associated with factors such as stratospheric ozone depletion, geographical locations with lower latitudes (i.e. nearer to equator) or higher altitudes, increased occupational or recreational outdoor activities, increased popularity of tanning devices and increasing age, which contribute to increased UV exposure [443, 449-454]. Moreover, SCC arise on chronic sun-exposed skin areas, such as head, neck and dorsal aspects of the upper limb in ~90 % of cases [436, 455, 456] and these can be reduced by application of sunscreen [457, 458]. Finally, the direct experimental evidence of involvement of UV in SCC development comes from the fact that they can be produced in mouse by chronic UV irradiation [459, 460]. Since both UVA and UVB can cause SCC in humans, they are classified as “Group I carcinogens” by International Agency for Research on Cancer (IARC) [461, 462]. Moreover, the UV-action spectrum for induction of SCC in mice and humans falls in UVB range [460].

J.2. Pathogenesis of UVB-induced SCC

The fact that SCC incidence is strongly linked to cumulative lifetime solar UV exposure and most common among elderly Caucasians indicate that development of SCC in response to chronic UVB-exposure is a complex process involving stepwise accumulation of cellular and molecular changes in skin over years or decades [431, 432, 454, 463]. Consistently in humans, the multistep process of SCC formation is a continuum of precursors such as actinic keratosis (AK), Bowen’s disease (BD), and keratocanthoma (KA) [464-467]. AK are the well- established precancerous lesions, of which 5-

10 % may progress to SCC [465, 467-469]. BD, also known as SCC in situ, represents the pre-invasive stage of SCC, of which 3-5 % may progress to invasive SCC [464, 467, 468]. KA, the benign cutaneous squamous neoplasia, are arguably the genetically incomplete SCC and can regress after 3-6 months [464, 466, 470]. Finally, the chronic UVB irradiation studies in mouse skin have been helpful in understanding the genetic and molecular changes during the UVB-induced SCC development and led to a proposal of the multistage carcinogenesis model for SCC development (Fig. G), which proceeds via three stages, namely initiation, promotion and progression [417, 471].

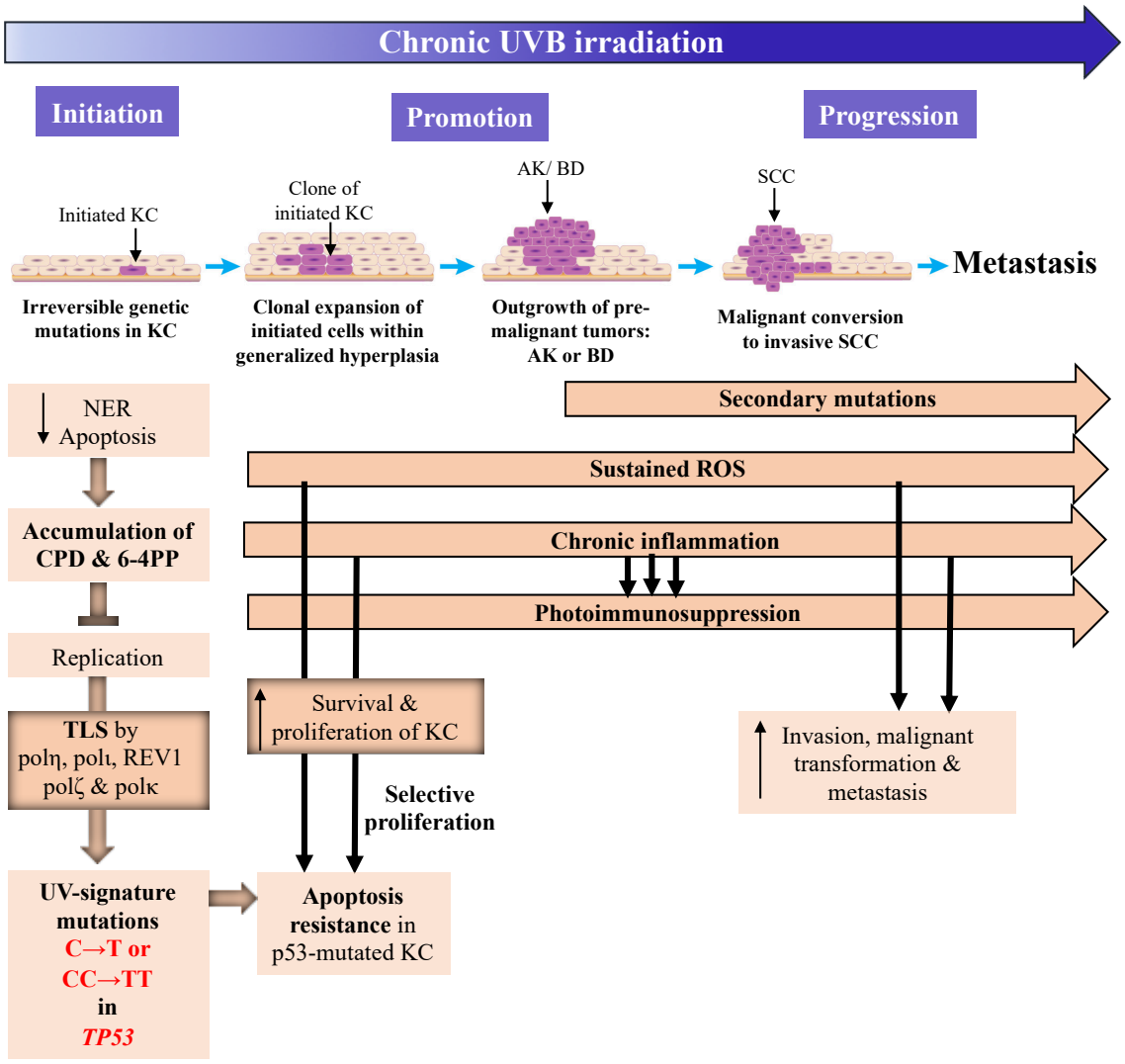

Figure G. Multistage carcinogenesis model of chronic UVB-induced SCC
Please refer to the section J for the full forms of the abbreviations. Figure created by Nupur Purohit.

J.2.1. Initiation

Initiation of SCC is an earliest and irreversible process by which UVB-irradiated KC acquire genetic mutations that trigger inactivation of their tumor suppressor genes and/or activation of their oncogenes (Fig. G) [13, 27, 417, 471]. The hallmark of UVB-induced mutagenesis is the high frequency of C → T (≥60 %) and CC → TT (≥5 %) transition mutations at the dipyrimidine sites where UVB induces direct DNA damage [472, 473]. These mutations are considered "UV signature" mutations, especially CC → TT, which are an absolute specific marker of UV signature [473]. Moreover, UVB can also induce other minor mutations such as triplet mutations at dipyrimidine sites [474-479] and G → T or A → G transversion mutations possibly due to unrepaired 8-oxoG [480-482]. Since UVB mainly induces UV-signature mutations [480, 483] which play predominant role in initiating UVB-induced skin carcinogenesis, this section describes the mechanisms by which this mutation arise at unrepaired direct DNA damage site and initiate SCC (Fig. G).

(1) Accumulation of direct DNA damage in chronic UVB-exposed skin: After single exposure to UVB, the direct DNA damage are completely eliminated from the mouse and human skin by 2-4 days [32] and 10 days [484], respectively, whereas they accumulate in the mouse epidermis after chronic UVB exposure [485]. This reduced repair after chronic UVB exposure [485, 486] is due to the inhibitory effects of UVB-induced immediate products such as cis-UCA, PAF or ROS-mediated oxidation of proteins on the NER machinery [487-489]. Furthermore, the apoptosis of KC, a mechanism by which skin eliminates highly damaged cells after single UVB-exposure (Section F), also decreases very early (1st week) during chronic UVB-irradiation of the skin [490-493]. Thus, chronic UVB-induced repetitive DNA damage, impaired capacity to remove this damage and reduced death of damaged KC together results in persistence of KC with the accumulated direct DNA damage, which are the potential SCC progenitors or premutagenic cells in which "UV-signature mutations" can arise. Therefore, an efficient NER of UVB-induced direct DNA damage and the apoptosis of highly damaged cells are very important to prevent the SCC initiation. This is evidenced by the increased photosensitivity and susceptibility to solar UV-induced skin cancers including SCC in the xeroderma pigmentosum (XP) patients, who have hereditary defects in NER pathway protein [494-496]. Similarly, mice deficient in NER [87, 497-500] and apoptosis [322] pathway proteins are also highly susceptible to UVB-induced skin cancer.

(2) Formation of UV-signature mutations at direct DNA damage: The direct DNA damage in the template strand prevents the replicative DNA polymerases from passing, thereby stalling replication forks [501]. The mammalian cells employ translesion DNA synthesis (TLS), which uses TLS polymerases such as polη, polι and REV1 to restart the stalled replication forks across the direct DNA

damage [479, 502]. This TLS can be error-prone and eventually result in C → T or CC → TT transition mutations at the lesion site during the second round of replication [479]. Since the NER of CPD is slower than that of 6-4PP and DEW [503-505], the mutagenicity of CPD is highest [506] and is the principle cause of UV-signature mutations and skin tumorigenesis in mouse [507]. Nonetheless, few genetic studies have also established the significant involvement of 6-4PP and DEW in UV-mutagenesis [508, 509]. Notably, the estimated mutation frequency per CPD in the mouse epidermis is very low, i.e., 1.82 $x10^{-4}$ after single exposure to UVB [510]. This mutation frequency increases due to chronic UVB-induced accumulation of CPD and can affect the tumor suppressor genes or protooncogenes.

(3) Formation of UV-signature mutations is an early event and primarily affects TP53 gene: During chronic UVB irradiation, the induction of UV-signature mutations is one of the earliest events that occurs well before the appearance of skin tumors in mouse and human skin [303]. The most frequent and one of the earliest targets of UVB-mutagenesis is *TP53* (encodes p53 protein) gene [471] in which the UV-signature mutations have been detected as early as 1^{st} and 6^{th} week of chronic UVB irradiation in mouse and human skin, respectively [303, 490]. In addition to *TP53*, mutations in other genes, i.e., *NOTCH1/2* can also be an early event as observed from the gene mutation analysis of sun-exposed human skin [511-513].

(4) The stem cells of epidermal basal layer: cells of origin of SCC: While SCC can arise from any keratinocyte in the epidermis, there is an emerging evidence that the stem cells in the basal layer of epidermis are the precursors of SCC [514-516]. The chronic UVB-induced accumulation of direct DNA damage in these stem cells in mouse [517, 518] provides the basis for UVB-induced mutagenesis in them. Consistently, it was shown that the repair of UVB-induced direct DNA damage specifically in the cells of epidermal basal layer reduces SCC formation to the similar level as that when the direct DNA damage are repaired from the KC of entire epidermis in mouse [519]. While the epidermal stem cells could be the prominent target for initiating chronic UVB-induced skin carcinogenesis and the cells of origin of SCC, more work is needed to fully understand and exploit their role in the initiation of SCC for diagnostic and therapeutic purposes.

J.2.2. Promotion

UVB-induced promotion entails the clonal expansion of initiated KC resulting in visible outgrowth of pre-malignant tumors, referred as AK or Bowen's disease (BD) (Fig. G) [417]. Since this process can be reversed at many stages, not all initiated KC finally form SCC. The chronic UVB drives the clonal expansion of initiated KC in mouse and human skin [303]. In mouse, the patches of p53-

mutated (initiated) KC were detected within 2-3 weeks of chronic UVB-irradiation [520-522]. These patches increased in size and density with continued UVB-irradiation but declined if the irradiation was ceased [521]. The patches of p53-mutated KC are also frequently present in the sun-exposed human skin [523, 524]. Since p53 plays an important role in mediating and/or facilitating cell cycle arrest and apoptosis in response to UVB (Section H), the p53-mutated KC are more resistant to these cellular processes as compared to normal KC [322, 474]. Therefore, p53-mutated KC have proliferative advantage to undergo chronic UVB-induced selective clonal expansion [303]. Indeed, single exposure to UVB stimulates the proliferation of p53-mutant cells whereas it induces apoptosis in normal KC [322, 521, 525]. Furthermore, clonally expanding p53 mutated KC were shown to colonize adjacent epidermal stem-cell compartments [522], during which the physical constraint for expansion of p53-mutated KC in epidermis is counteracted by UVB-induced apoptosis of normal neighboring KC [526, 527].

Successive UVB exposures result in the formation of visible skin tumors (outgrowth), which also have UV-signature mutation in *TP53*, suggesting that p53-mutated patches are precursor to AK [528, 529]. However, only a small proportion of p53-mutated patches may progress to form visible tumors [530]. In mouse, the induction kinetics of epidermal p53-mutated patches directly correlate with that of tumors [521]. The human AK or BD also show UV-signature mutation in *TP53* [322, 531-533] and all the cells within a single AK or BD have same *TP53*-mutation fingerprint [322, 531], further validating the clonal basis for SCC development. NOTCH1/2-mutated patches are also observed in sun-exposed normal human skin [511]. Moreover, other genes such as *CDKN2A*, *NOTCH1/2*, *RAS*, etc. are found to be mutated in the AK or BD from humans [511, 534] and mice [529]. To note, the mutations in *CDNK2A* gene is not reported in mouse AK or SCC [529] whereas the activating mutations in *RAS* protooncogene appears to be strain specific in mouse SCC [535-537]. Finally, the reversible nature of the promotion stage of SCC development is demonstrated by the observed reduction in p53-mutated patches in mouse skin when the UVB-irradiation is ceased [520, 521, 538] or by the regression of AK or BD in humans [465, 467-469].

J.2.3. Progression

UVB-induced progression phase in SCC development involves increase in size, invasion in the dermal layers and malignant transformation of the premalignant tumors such as AK or BD to SCC (Fig. G) [417]. The clinical observation that some of the AK or BD may eventually progress to SCC with continued UVB-exposure is validated by the presence of identical mutated genes (*TP53*, *NOTCH1/2*, *CDKN2A*, *RAS* etc.) in AK or BD and SCC from humans [534, 539, 540] and mice [529]. In addition to the clonal evolution, the subclonal evolution of AK or BD from p53-mutated patches

and that of SCC from AK or BD is also demonstrated [534]. A histopathological study identified that ~70 % of the tumors with >3 mm diameter are SCC whereas ~70 % of tumors with <2 mm diameter were found to be AK or BD in chronic UVB-irradiated mice, further suggesting that progression AK or BD to SCC is accompanied by increase in size of tumors [541]. Among the genetic changes that can mediate transition from AK or BD to invasive or metastatic SCC in humans are: an increase in frequency of mutations in *TP53* [539], activating UV-signature mutations in promoter of TERT (a rate-limiting component of telomerase complex that replicates telomeres) [542] and loss of heterozygosity (LOH) in the chromosomes carrying *TP53* and *CDKN2A* genes [543]. For the LOH of *TP53*, chronic UVB-induced carcinogenesis studies in $p53^{+/-}$ mouse demonstrated that allelic loss of p53 enhances progression to a higher grade of SCC malignancy [537]. Overall, UVB-driven progression of SCC involves multiple genetic mutations that might accumulate early or progressively during the course of cancer development [544].

J.2.4. UVB-induced ROS and inflammation drive the promotion and progression of SCC

The observation that the topical application of antioxidants and anti-inflammatory agents on mouse skin during chronic UVB-irradiation reduces the tumor formation [545-552] highlights the role of UVB-induced ROS and inflammation in SCC development (Fig. G). Consistently, irradiation with dose of UVB higher than the MED results in a faster development and more number of tumors in mice [541]. Furthermore, enhanced tumor growth in mice is also associated with an influx of inflammatory cells and its proinflammatory mediators [553] and these cells are also present in the microenvironment of human SCC [554]. As explained earlier in sections G and I.1, UVB-induced ROS and inflammation drive regenerative proliferation of KC in the skin, resulting in epidermal hyperplasia post single UVB exposure [491]. However, this process is tightly regulated and epidermis returns to substantially normal structure by 2 weeks. On the other hand, chronic UVB-induced sustained ROS production and persistent inflammation dysregulates controlled regenerative proliferation [417, 491], thereby causing continuous proliferation of KC, especially of apoptosis resistant p53-mutated KC, in the skin.

The main mediator of ROS and inflammation-induced proliferation is the EGFR signal transduction pathway (Fig. F). The important role of EGFR in the promotion and progression to SCC is directly corroborated by the mouse models in which deletion, pharmacological inhibition or expression of dominant negative form of EGFR [346], its downstream effector kinase p38 [555] and its downstream transcription factors AP-1 [556], STAT3 [557] or NFκB [558] suppressed UVB-induced skin tumors. The role of UVB-induced proinflammatory mediators in promotion and progression to SCC is evidenced by the reduced UVB-induced SCC development in mice with deletion or inhibition of

COX-2 [546, 559] or the receptors of TNFα and PGE2 [560, 561]. The UVB-induced proinflammatory mediators also upregulate the synthesis of matrix metalloproteinases (MMP) [562, 563], which degrade collagen in the basement membrane and dermis. This is required not only for the invasion of SCC in underlying dermal connective tissue but also for the epithelial-mesenchymal transition of KC and metastases of invasive SCC to lymph nodes [564]. Consistently, the expression of MMP is found to be high in human SCC stroma [565]. Thus, chronic UVB-induced ROS and inflammation result in increased survival, proliferation, migration and invasion of mutated KC during promotion and progression stages of SCC development [286, 417, 566].

J.2.5. Photoimmunosuppression facilitates the promotion and progression of SCC

The cancer cells are eliminated from the body by adaptive immunity [567]. However, UVB suppresses adaptive immunity (I.2), thereby allowing the persistence of cancer cells during the tumorigenesis. The role of UVB-induced immunosuppression in facilitating the UVB-induced SCC development was recognized very early in the photocarcinogenesis research [419, 420]. This is corroborated by the higher risk, incidence, metastatic potential and aggressive progression of UV-induced SCC in people who receive immunosuppressive drugs such as organ transplant recipients [568-575] and patients with chronic lymphocytic leukemia, non-Hodgkin lymphoma or HIV [576-580]. Furthermore, the mice lacking Treg, a key immune cell that mediates UVB-induced immunosuppression, shows reduced UVB-induced SCC development as compared to WT mice [581]. Conversely, the mice lacking the Tc cells, which are important for the antitumor immunity, shows increased chronic UVB-induced SCC development [581]. Moreover, there was a direct correlation between the aggressiveness of the SCC in humans and the intra-tumoral infiltration of Treg, high expression of immunosuppressive cytokine IL-10 and low Tc:Treg ratio [582-586]. Since UVB-activated innate immune cells and proinflammatory mediators also contribute towards suppressing the adaptive immune response (Section I.2), the chronic UVB-induced sustained inflammation can also facilitate the SCC development by maintaining persistent immunosuppressive environment in the skin [587].

K. SKH-1 hairless albino mouse: a widely adopted model to study UVB-induced SCC

Since the availability of their outbred stock in 1960, the SKH-1 hairless mouse strain has been extensively used and proven to be well suited for experimental UV-skin carcinogenesis studies [460, 588]. The existence and phenotype of SKH-1 mouse strain was first described in 1926 by H.C. Brooke [589]. Genotypically, they have autosomal recessive mutation in the *Hairless (Hr)* gene resulting from the insertion of murine leukemia virus *pmv43* in exon 6 of *hr allele* (Hr^{hr}) [590]. *Hr* encodes

HR protein that is necessary for normal hair growth but this mutation results in aberrant splicing of ~95 % of *Hr* transcripts, which translates into hairless phenotype [591]. In SKH-1 mice, the first hair coat develops normally within 4-5 days of their birth. However, beginning 13-14 days after their birth, there is rapid hair loss, which progresses from the head to tail end [588, 592]. They become completely hairless by 3 weeks of age.

Their hairless and albino phenotype makes them ideal subjects for the research associated with skin ailments such as physical wounding [593], photoaging [563, 594, 595] and photocarcinogenesis [460, 588]. The furlessness allows better imaging via *in vivo* bioluminescence and florescence-based techniques [596, 597]. Use of these mice also compare favorably with that of other hairy mouse strains, such as C57BL/6, FVB/NJ which need to be frequently depilated with chemical or physical approaches in experimental protocols [593, 598, 599], because hair forms an impenetrable and inconvenient shield for skin treatments such as UV-irradiation or topical application of agents [460]. More importantly, the depilation procedures are time consuming, cause irritation and inflammation which can confound the results in the studies using hairy mice. The routine procedures such as breeding (repeated backcrossing) with transgenic mice [85, 556] or microinjection into the pronuclei of their fertilized oocytes [600], can be used to create SKH-1 mice with specific gene deletion or mutation. This allows study of the role of specific proteins in UVB-induced skin carcinogenesis as described in the chapter 4.

SKH-1 mouse represents an ideal model for human photocarcinogenesis [460, 588]. Their repeated long-term (16-25 weeks) exposure to sub-erythematic or MED of UVB results in formation of skin tumors, which are mainly SCC [541, 601-603]. This further validates the role of cumulative solar UV exposure in human SCC development. Similar to that in humans, the UVB-induced tumorigenesis progresses from epidermal hyperplasia to AK or BD and finally to invasive SCC in these mice [541]. Moreover, cellular and molecular alterations such as UV-signature mutation in *TP53* or *NOTCH1*, formation of p53-mutated patches and COX-2 upregulation during the UVB-induced SCC development in SKH-1 mice resembles that reported in human SCC [520-522, 529, 604, 605]. In contrast to the nude mice, their immune-competency enables UVB-induced immunological responses such as inflammation [32, 411] and immunosuppression [606, 607] in their skin, which are similar to those in human skin at cellular and molecular levels [588]. Hence SKH-1 mouse is by far the widely adopted model for studies of UVB-induced SCC development.

Upon chronic UVB-irradiation, the SKH-1 mouse can bear more than 40 tumors depending on the cumulative dose of UVB by the end of the protocol [541]. These tumors are readily noticeable at very small sizes (<1 mm diameter) by a trained observer and can be followed in their progression

throughout the protocol to allow the quantification of tumor burden in terms of tumor incidence (proportion of mice with or without tumor) and multiplicity (number of tumors) [460, 541]. The tumor size (diameter, area and volume) can also be measured using vernier calipers [608] or more accurately via photography [609] as well as magnetic resonance [610] or ultrasound imaging [611]. These measurement criteria have allowed assessment and comparison of severity of UVB-induced SCC development in SKH-1 mice in presence or absence of genetic, pharmacological or other interventions [85, 546, 608, 612, 613].

To summarize, UVB acts as a complete carcinogen driving all three stages of SCC development in a complex process involving genetic mutations, chronic inflammation and immunosuppression in skin. Hence, identifying and understanding the function of proteins which play a critical role in these processes, can lead to discovery of novel targeted therapeutic approaches for SCC. The multifunctional mammalian nuclear enzyme, poly(ADP-ribose) polymerase-1 (PARP1) is one such protein, and the present thesis describes research on its role in the NER of UVB-induced direct DNA damage (Chapter 1) and SCC development (Chapter 4).

L. Poly(ADP-ribose) polymerase-1

PARP1 is a highly abundant (0.5 to 2 × 10^6 molecules per cell [614]) chromatin-associated enzyme found in all higher eukaryotes and absent in yeast [615]. It is the founding member of a 18 membered PARP family of enzymes that share a conserved catalytic core ("PARP signature") [616]. Their enzymatic activity catalyzes the posttranslational modification (PTM) "ADP-ribosylation" in mammalian cells. Most of the PARP family members catalyze mono(ADP-ribosyl)ation (MARylation) reaction, i.e., the transfer and covalent attachment of the ADP-ribose (ADPr) moiety from nicotinamide adenine dinucleotide (NAD^+) to specific amino acids (aa), thereby posttranslationally modifying substrate proteins with monomer of ADP-ribose (MAR) [616, 617]. In addition, subset of them including PARP1 catalyze poly(ADP-ribosyl)ation (PARylation) reaction, i.e., the successive transfer of multiple ADPr moieties to previously added ADPr on substrate proteins, thereby posttranslationally modifying substrate proteins with polymer of ADP-ribose (PAR). In mammalian cells, PARP1 is responsible for PARylation of 85-90 % proteins which are involved in multiple biological processes [618].

L.1. Structure of PARP1

Human PARP1 is a 113 kDa protein composed of 1014 aa that are organized into six independently folded domains connected by flexible linkers [614]. In solution and in absence of DNA binding, its global structure is proposed to resemble modular ‘‘beads on a string’’ architecture (Fig. H.1) [619].

Located at its N-terminus are the three zinc finger domains: Zn1 (6-91 aa), Zn2 (105-202 aa) and Zn3 (224-360 aa). A bipartite nuclear localization signal (NLS; 207-209 and 221-226 aa) and a caspase-3 cleavage site ($DEVD_{214}$) are located in the linker between Zn2 and Zn3 domains. Following the Zn3 domain, are the BRCA C-terminus (BRCT) fold (387-483 aa), WGR domain containing tryptophan (W)-glycine (G)-arginine (R) (530-645 aa) and C-terminal catalytic domain (CAT; 662-1014 aa). The

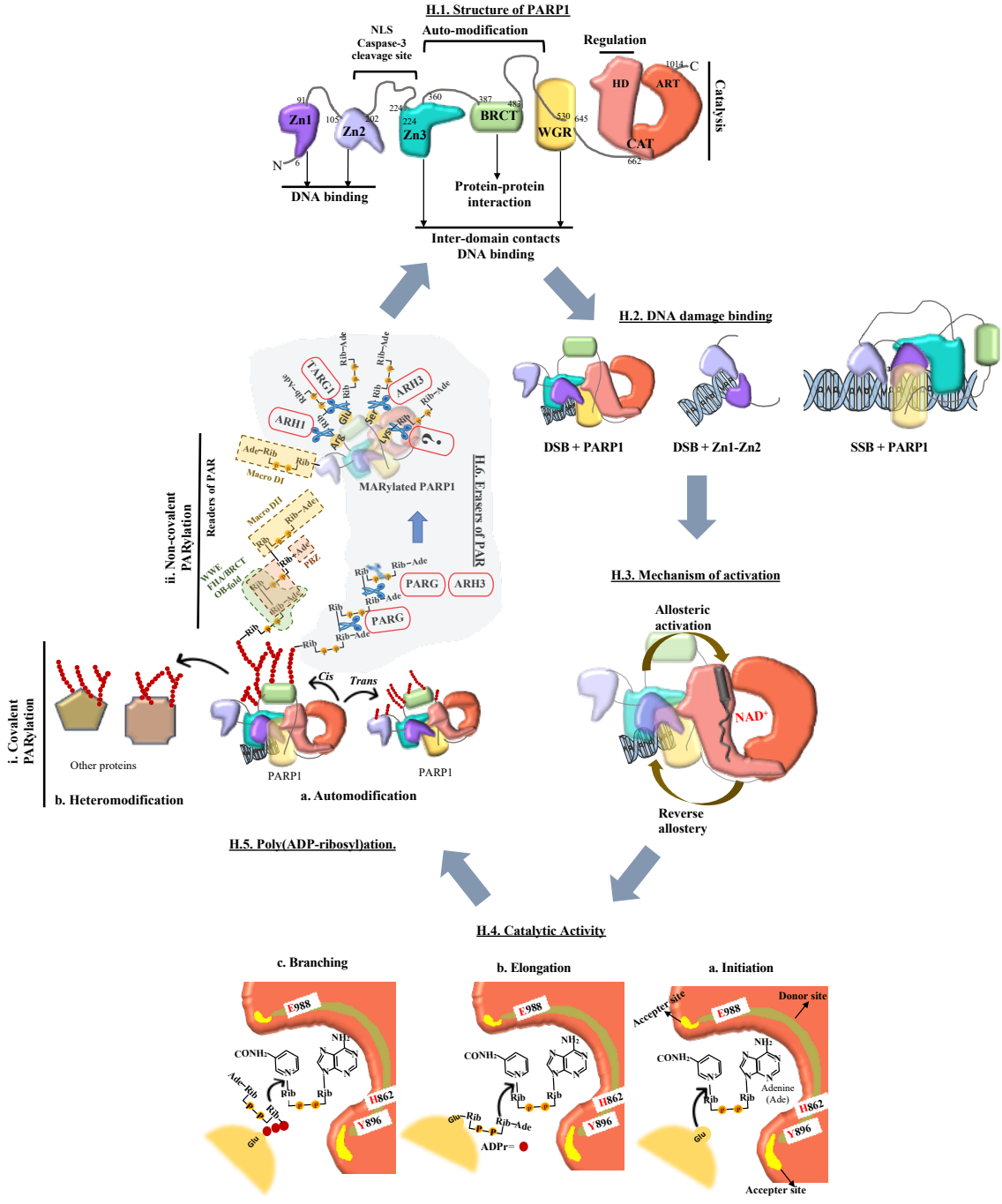

Figure H. PARP1 and poly(ADP-ribosyl)ation

Please refer to the sections L.1-4 for the full forms of the abbreviations. Figure created by Nupur Purohit.

CAT is composed of two subdomains, the helical (HD) and the ADP-ribosyl transferase (ART) subdomains. Functionally, Zn1 and Zn2 domains mediate the binding of PARP1 to DNA, while Zn3 and WGR domains mediate interdomain contacts within PARP1 and also interact with DNA. The BRCT domain often mediates interaction of PARP1 with other proteins and the HD regulates the ART subdomain, which catalyzes the synthesis of PAR [620-623].

L.2. PARP1 binds to damaged and undamaged DNA

PARP1 binds to damaged and undamaged DNA irrespective of the nucleotide sequence [624]. It binds to DNA damage with strand breaks, i.e., SSB (nicked or gapped) and DSB (blunt or with overhangs) with highest affinity [625-629] and also those without strand breaks, i.e., AP sites [630]. In undamaged DNA, it binds to altered DNA structures such as supercoil [629, 631], hairpin [632, 633], loop [633, 634] and cruciform [632, 633, 635, 636]. It is also shown to bind to the linker region of nucleosomes in undamaged chromatin [628, 637]. Moreover, the monomer [628, 638-642] or dimer [620, 643-647] of PARP1 is debated to bind to DNA.

The mode of DNA damage sensing and binding by PARP1 is revealed by the recent X-ray crystallographic and NMR studies of the structures of single or multiple domains of PARP1 bound to SSB or DSB [619, 639, 644, 648, 649]. On DNA with DSB (Fig. H.2a), monomers of PARP1 domains (Zn1, Zn3 and WGR-CAT) bind with a footprint of 7 bp upstream of DSB [619, 639]. Zn1 binds to the DNA phosphate backbone spanning 3 nt upstream of DSB and stacks on to DSB while interacting with the exposed nucleotide bases [648]. Zn3 contacts DNA phosphate backbone spanning 4 nt upstream of Zn1 and WGR domain engages 5' terminus of the DSB as well as DNA phosphate backbone spanning 3 nt on the opposite DNA strand. In the context of full length PARP1, this study proposed anchoring of Zn2 and BRCT domains away from DNA between the Zn1-Zn3 and Zn3-WGR domains, respectively. In contrast to this, two studies showed that Zn2 domain either individually [648] or in tandem with Zn1 domain (Zn1-Zn2) [644] binds to DNA containing DSB in similar fashion as Zn1 domain (Fig. H.2b). Interestingly, in the presence of Zn2, Zn1 binds to the DNA phosphate backbone on the opposite strand and instead of engaging with DSB it interacts with Zn2. On the DNA with SSB (Fig. H.2c), the monomers of Zn1 and Zn2 bind to the DNA phosphate backbones spanning 3 nt on the either side of the SSB while interacting with the exposed nucleotide bases at the SSB ends [649]. In the context of full length PARP1, the Zn3 and WGR domains bind to the DNA phosphate backbone on the Zn1 binding side of SSB, thereby suggesting bilateral footprint

of PARP1 around SSB. A previous study using DNase I footprinting had also proposed a bilateral ±7 nt footprint on the either side of the SSB, albeit for PARP1 as dimer [640].

Thus, Zn1 and Zn2 domains of PARP1 are the primary sensors of DNA strand breaks and recognize its two key features: the exposed nucleotide bases and the flanking continuous region of DNA phosphate backbone. This mode of interaction can also account for the ability of PARP1 to sense exposed or unpaired nucleotide bases without strand breaks and altered DNA structures in undamaged DNA present at the AP site, hairpins and cruciform [630, 632, 633, 635, 636]. Consistently, PARP1 was shown to have footprint at the stem-loop boundaries in the hairpins of cruciform DNA [631, 633, 636].

L.3. Mechanism of catalytic activation of PARP1

Binding of PARP1 to DNA strand breaks and other unbroken altered DNA structures results in activation of its enzymatic activity [625, 631, 633, 636, 643]. In the absence of DNA damage, HD restricts the access of NAD^+ to ART via its specific local helical regions, thus limiting the catalytic activity of PARP1 to basal level [650] (Fig. H.1, HD). Binding of Zn1 and Zn2 domains to DSB or SSB triggers the self-assembly of PARP1 domains, thereby establishing three key interdomain contacts: Zn1-WGR-HD, Zn3-WGR-HD and Zn1-Zn3, which are mediated via WGR and Zn3 [619, 639, 642, 649, 651]. This results in unfolding of restrictive helical regions within HD (Fig. H.3) allowing productive and non-restricted binding of NAD^+ to synthesize PAR [650, 651]. Interestingly, the extent of unfolding within HD is directly correlated with the degree of catalytic activation of PARP1 [650]. This can possibly explain the variations in PARP1 activation observed with different DNA structures. To summarize, the binding of Zn1 and Zn2 to DNA strand breaks is allosterically signaled to the CAT domain via Zn3 and WGR domains [650, 651]. Notably, a recent study has also demonstrated reverse allostery within the PARP1 domains (Fig. H.3) in which binding of NAD^+ analogue to the ART subdomain and the resulting unfolding within HD subdomain, increased the affinity of PARP1 for DNA containing SSB by 10-fold [652]. Alternatively, PARP1 catalytic activation can also be induced in absence of DNA, either via its physical interaction with another protein, e.g. phosphorylated ERK1/2 [653-655] or via its posttranslational modifications e.g. phosphorylation [656], acetylation [657] or MARylation [658]. It is anticipated that these DNA-independent PARP1 activating signals may also either directly or indirectly engage WGR domain to perturb HD structure [650].

L.4. Enzymatic activity of PARP1: PARylation

Upon DNA dependent or independent activation, ART subdomain of PARP1 via its donor and acceptor sites binds to and processes NAD^+ to catalyze the PARylation [659, 660]. This comprises of three chemical reactions [620]: (a) initiation, the covalent attachment of the first ADPr monomer to the acceptor aa in target protein (b) elongation, the formation of a (2'-1'') ribose-ribose glycosidic bond and (c) branching, the formation of a (2''-1''') ribose-ribose bond between ADPr units (Figs. H.4a-c) [661]. Since the ART subdomain can bind to ADPr of growing PAR chain in two orientations, PARP1 has dual specificity to catalyze both elongation and branching reactions [660]. However, elongation is preferred over branching and the latter has been predicted to take place every 20-50 ADPr units in PAR chains [662, 663].

L.5. PARP inhibitors

The observation that the by-product of ADP-ribosylation reaction, nicotinamide causes modest inhibition of PARP1 catalytic activity formed the basis for the development of PARP inhibitors (PARPi) [664, 665]. Over ~50 years, three generations of PARPi have been developed, all of which inhibit the catalytic activity of PARP1 by competing with NAD^+ for its binding site in the ART subdomain [666, 667]. Since all the PARP family members carry highly conserved ART subdomain, most of the PARPi inhibit the catalytic activity of at least two PARPs (PARP1 and PARP2) if not all of them [667, 668]. Notably, few PARPi with higher selectivity for either PARP1 or PARP2 have been identified [667]. While the first and second generation PARPi such as 3-aminobenzamide (3-AB) and PJ-34, respectively, were relatively less efficacious and exhibited off-target activities, most of the third generation PARPi including olaparib, rucaparib, veliparib, niraparib and talazoparib are more potent and highly specific [665, 669]. PARPi can also trap PARP1 on the DNA via reverse allosteric mechanism described in Section L.3 [652, 670-672]. The development of PARPi has proved to be an important tool to study not only the biological role of PARP1 in higher eukaryotes but also therapeutic targeting of PARP1 in various pathological conditions including cancer in humans (Section P).

M. PARylation: The post translational modification

By the mechanism described in section L.4, the activated PARP1 catalyzes the covalent PARylation of target proteins, which represent the "ADP-ribosyl proteome" (Fig. H.5.i) [673, 674]. Alternatively, several DNA and RNA metabolism proteins which undergo non-covalent PARylation by interacting with the free or protein-bound PAR, make up the "ADPr interactome" [617, 623, 673-677] (Fig. H.5.ii).

M.1. Cellular targets of PARP1 mediated covalent PARylation: "ADP-ribosyl proteome"

The ADP-ribosyl proteome studies show that the major target of PARP1-mediated covalent PARylation upon genotoxic stress is PARP1 itself, thereby resulting in its automodification (Fig. H.5.i-a), which occurs in *cis* (intramolecularly within the same PARP1 molecule) [647, 649, 651] and *trans* (intermolecularly in another PARP1 molecule) [645, 651, 678, 679]. PARP1 is automodified at multiple sites with prominent PARylation in the interdomain linker regions of BRCT-WGR and WGR-HD domains [680-688]. This can be structurally accounted for by close proximity of BRCT with CAT and the flexibility of these linker regions in DNA damage bound PARP1 [619, 639, 649, 650]. In addition to itself, activated PARP1 PARylates other proteins (heteromodification) involved in various aspects of DNA and RNA metabolism (Fig. H.5.i-b) [620, 688-691]. Recently, *in vitro* studies showed that PARP1 ADP-ribosyl proteome includes 167 proteins, of which 43 are exclusively PARylated by PARP1 [692]. These studies have also identified Asp, Glu, Lys, Arg, Cys, Ser, Thr, pSer (phospho-ser, via phospho group), His and Tyr as the target amino acids that are covalently PARylated in various target proteins including PARP1 itself [688-691, 693-697]. Among these, the charged aa such as Glu, Asp, Lys and Arg are most commonly PARylated [689, 694]. Apart from protein PARylation, PARP1 also covalently PARylates the ends of recessed DNA duplexes *in vitro* [698].

M.2. Readers of PAR undergo non-covalent PARylation: "ADPr interactome"

The ADPr interactome consists of ~70 proteins ("readers") that can recognize ("read") and bind to the different structural features of PAR via their structurally distinct and evolutionarily conserved "PAR binding modules" (Fig. H.5.ii) [617, 623, 675-677, 691, 699]. The positively charged PAR binding module known as PAR binding motif (PBM) recognizes and binds to the negatively charged long and branched PAR chains possibly through electrostatic interactions [700, 701]. Similar mode of PAR binding could also be exhibited by other positively charged PAR binding modules such as RNA recognition motif (RRM), serine/arginine (SR) repeats and lysine and arginine (KR)-rich motifs, the PilT protein N-terminus (PIN) domains and glycine-arginine-rich (GAR) domains [677, 691]. The PAR-binding zinc fingers (PBZ) recognize and bind to 2'-1''-glycosidic bond, adjacent ADP groups and the adenine ring of the distal ADPr units [702]. The macrodomain type II and I (MacroD2 and D1) bind to the terminal ADPr of PAR or protein-bound MAR, respectively [703-705]. The WWE domains [706], FHA/BRCT [707] and oligonucleotide/oligosaccharide-binding fold (OB-fold) [708, 709] recognize iso-ADPr of PAR. To note, a single protein can have more than one PAR binding modules [691] or can be both, covalently and non-covalently PARylated [690, 697, 710].

M.3. PARylation reprograms protein function

Since the first report of the discovery of PAR formation in mammalian cells by P. Chambon in 1963 [711], a great deal of work has been done to determine its structural and biochemical properties [615]. Structurally, PAR is a complex and branched polymer of up to 200-400 ADPr units [712-714]. It is postulated to form a secondary helical structure that is reminiscent of DNA and RNA [715]. Chemically, PAR bears two molecules of negatively charged phosphate groups per ADPr; therefore, is twice as negatively charged as DNA or RNA [716, 717]. Owing to these structural and biochemical characteristics, PARylation dramatically alters or "reprograms" the function of an acceptor/binding protein, thereby allowing them to respond appropriately to the stimuli [674, 677]. Indeed, PARylation sites in proteins often coincide with their functional domains including protein-protein interaction, DNA binding and nuclear localization domains [700]. Moreover, PARylation can also change protein's topological features. Therefore, covalent and/or non-covalent PARylation can recruit important proteins for particular process, regulate intracellular transport of proteins, modulate protein-protein and protein-DNA/RNA interactions, modulate the biochemical/enzymatic activity of protein, and also influence other PTM of proteins such as phosphorylation and ubiquitination [623, 674, 677, 706, 718-720]. In addition, the free PAR, that is generated by the enzymatic activities of PAR hydrolases (Section M.4), is proposed to diffuse out of nucleus [721] and modulate protein functions in the cellular compartments such as cytoplasm [718] and mitochondria [722]. The role of PARylation in reprogramming protein function is exemplified by PARP1 itself. The auto-PARylation of PARP1 eventually result in its release from DNA [622, 651, 723], possibly due to PAR induced charge repulsion with DNA [724, 725].

M.4. Erasers of PARylation

As with any other PTM, PARylation is a transient event with the degradation of PAR starting immediately after the beginning of its synthesis [726]. In cells, the half-life of 85 % of PAR is ~40 seconds and that of the remaining 15 % is ~6 minutes [727]. The main enzymes responsible for degrading most of the PAR in the mammalian cells are the PAR glycohydrolase (PARG) isoforms [726, 728-731]. PARG possesses both, the less effective endo- and highly effective exo-glycohydrolase activities that catalyze the hydrolysis of the ribose-ribose glycosidic bond between internal and proximal ADPr units of PAR, respectively, thereby generating mostly free ADPr and some oligo-ADPr (Fig. H.6) [732-734]. However, PARG is unable to remove the ADPr linked covalently to accepter aa of the PARylated proteins, thereby leaving the proteins MARylated.

ADP-ribosylhydrolase3 (ARH3) can also hydrolyze free or protein-bound PAR via its exo-glycohydrolase activity in mammalian cells, but exhibits only 10 % of PARG's activity, (Fig. H.6) [730, 735-737]. ARH1, the isoform of ARH3, also mediates PAR catabolism [738]. As opposed to PARG, ARH1 and ARH3 can specifically remove the terminal ADPr linked to Arg [730, 739, 740] and Ser [740-742], respectively in MARylated proteins and thus complement PARG. Another PARG complementing enzyme is the terminal ADP-ribose protein glycohydrolase 1 (TARG1)/C6orf130, which hydrolyzes the Glu/Asp-ADPr ester bond to release MAR or entire PAR from the protein (Fig. 1.8F) [684]. MacroD1/2 can also reverse MARylation at the Glu/Asp residues [743, 744]. Recent studies have identified additional enzymes such as nudix hydrolase 16 (NUDT16) and ectonucleotide pyrophosphatase/phosphodiesterase 1 (ENPP1) which can cleave the pyrophosphate bonds within PAR or protein linked ADPr *in vitro*, thereby generating ribose-5'-phosphate tags on proteins [745-747]. While the enzymes that specifically cleave the Lys-ADPr or Cyst-ADPr bond have not yet been identified, NUDIX, NUDT16 and ENPP1 might be responsible for removal of ADPr from these aa [748].

Interestingly, PARG, MacroD1/2 and TARG1 utilize macrodomain not only to non-covalently interact with the PAR or MAR but also to exert ADP-ribosyl hydrolase activity [726]. These enzymes are present in nucleus (PARG, ARH3, TARG1 and MacroD1/2), mitochondria (PARG and ARH3) and cytoplasm (PARG, ARH1, ARH3, TARG1 and MacroD1/2) [617], thereby providing spatial control of PAR metabolism, and hence a mechanism for tight regulation of PAR-dependent downstream signaling events. The importance of PAR catabolism in the well-being of mammals is highlighted by the embryonic lethality of *Parg*$^{-/-}$ mice [749] and severe neurodegeneration in TARG1 mutated patients [684].

N. Biological functions of PARP1: focus on its role in UVB-induced cellular responses

Collectively, PARP1, its ADP-ribosyl proteome, ADPr interactome and PAR degrading enzymes constitute a signal transduction network that serves the cells in "peace" (normal physiological conditions) and in "war" (genotoxic stress) [750]. The normal physiological functions of PARP1 include the chromatin organization [751-753], regulation of gene expression [618, 754-757], cell cycle progression and immunoglobulin class switching [758, 759]. However, PARP1 appears to be dispensable for these functions because knocking out PARP1 in mice (PARP1-KO mice) did not result in any embryonic lethality or any other severe abnormal phenotype under normal conditions [760-763]. On the contrary, PARP1-KO mice exhibited severe hypersensitivities to genotoxic and inflammatory stress [763] as well as accelerated aging and spontaneous carcinogenesis in old age [764], thereby suggesting that function of PARP1 in stress response is indispensable. Today, the role

of PARP1 and its catalytic activity in response to various stress signals including DNA damage is extensively recognized [618, 765-767]. During a stress response, they are implicated in DNA repair [123, 768], transcriptional regulation [618, 765], chromatin remodeling [755], inflammation [769-771] and cell death [772, 773]. Since the research in this thesis focuses on role of PARP1 in UVB-induced stress in the skin, the following sections describe the reported functions of PARP1 in various UVB-induced cellular processes involved in DNA damage response, immune modulation and skin carcinogenesis.

N.1. Role of PARP1 in the repair of UVB-induced DNA damage

Today, PARP1 and its catalytic activity are known to play multifaceted roles in the various DNA damage repair pathways, such as BER, SSBR, DSB repair (DSBR) via homologous recombination (HR), classical non-homologous end-joining (cNHEJ), alternative NHEJ and microhomology-mediated end-joining, DNA mismatch repair and NER [123, 768, 774]. Briefly, the roles of PARP1 in these repair pathways can be categorized as follows: (a) sensing of DNA damage; (b) chromatin remodeling at the DNA damage site; (c) recruitment of DNA repair proteins; and (d) modulation of biochemical activities of the DNA repair proteins [622, 775]. PARP1 is usually one of the first proteins to sense the DNA damage, which is often attributed to its sheer abundance and its capacity to bind to various types of DNA damage (Section L). Furthermore, two recent studies suggested that PARP1 can rapidly scan the otherwise intact genome for the DNA damage by 3D-diffusion across the DNA, possibly via “monkey bar” mechanism [641, 776]. Its catalytic activation at the DNA damage site and the resulting PARylation account for the rest of its roles. Recently, it was proposed that local PAR formed at the DNA damage site mediates liquid demixing and seeds the formation of subnuclear structures composed of proteins with low complexity domains interacting via their non-covalent interactions with PAR [691, 777]. This phase separation phenomenon allows the selected repair factors to access the lesion and coordinates the DNA repair stages within nucleus. This section describes in detail the reported roles of PARP1 in the repair of UVB-induced direct and indirect DNA damage.

N.1.1. Role of PARP1 in BER/SSBR

Among various DNA repair pathways, the role of PARP1 in SSBR is the most explored and well-established. PARP1 has been shown to accelerate SSBR in mammalian cells [126, 778]. It is the earliest protein to arrive at SSB in DNA [779], where PARP1 domains exhibit cooperative and stepwise self-assembly, resulting in destabilization of HD subdomain and activation of ADP-ribosyl transferase activity of PARP1 [649]. The activated PARP1 covalently PARylates itself, other proteins

such as histones and also possibly the ends of SSB [123, 698, 768, 780]. Recent study showed that upon SSB-induced auto-PARylation, PARP1 switches its interaction with DNA from 3D-diffussive search to a less stable 1D anomalous sub-diffusion along DNA before its eventual dissociation due to charge repulsion [724, 725], thereby suggesting the possibility for an intermediate state of automodification that allows PARP1 to mediate its function at SSB site [641]. This could be accounted for by a newly identified regulator of PARP1 activity, histone PARylation factor 1 (HPF1), which upon its PARP1-dependent recruitment at the SSB sites, promotes heteromodification of histones by PARP1 over the automodification of PARP1 [781-783]. Altogether, the covalently PARylated PARP1 and histones serve as a scaffold for recruitment of critical SSBR protein, XRCC1 [125, 130, 131, 784, 785] and chromatin remodeling proteins such as amplified in liver cancer 1 (ALC1) [786] and aprataxin-and-PNKP-like factor (APLF) [787, 788], which interact non-covalently with PAR. The PARylation of core histones and chromatin remodelers result in open chromatin around the SSB to allow the access to other SSBR proteins [780]. PARP1 also stabilizes XRCC1 at SSB [789], to accomplish subsequent steps of SSBR pathway (Section E.1.2).

The role of PARP1 in BER of 8-oxoG (Section E.1.1) is less clear and controversial. Unlike SSB, PARP1 is not reported to sense and bind to 8-oxoG in DNA. However, the inhibition of PARP1 activity reduced the removal of 8-oxoG in mammalian cells [790]. Furthermore, OGG1 was shown to interact with PARP1 and stimulate its catalytic activity in the presence of nicked DNA [791] whereas PARP1 reduced the glycosylase/AP lyase activity of OGG1. While the authors proposed that OGG1 may stimulate PARP1 activity by creating SSB which would serve to recruit XRCC1, they did not provide any functional significance for the PARP1-mediated inhibition of OGG1 activity. Furthermore, PARP1 can also bind to DNA with AP-sites [630, 641, 792, 793], which are generated as an intermediate during BER initiated via monofunctional glycosylases such as MUTYH. However, PARP1 is only weakly activated upon binding to DNA with AP-site, and requires strand incision by APE1 for its strong activation [630]. While PARP1 can stimulate strand incision activity of APE1 [794], it also possesses AP lyase activity and can thus perform strand incision at the AP-site [630] to accomplish BER in the absence of APE1 [794]. Indeed, recent studies showed that PARP1 and APE1 colocalize at AP-sites while interacting with each other directly [641], and APE1 can also be covalently and non-covalently PARylated [795]. In this case also, the functional role of APE1-mediated stimulation of PARP1's catalytic activity is proposed to be the recruitment of XRCC1 [641].

However, the role of PARP1 and its catalytic activity in the recruitment of XRCC1 during BER of 8-oxoG is contentious. While an earlier study showed that the recruitment of XRCC1 at the SSB intermediates during the BER of 8-oxoG is independent of PARP1 and its catalytic activity [785], a

recent study demonstrated the opposite [796]. Furthermore, it has been shown that SSB sensor role of PARP1 as described for SSBR of "direct SSB" (those generated by direct disintegration of DNA phosphate backbone) might have limited utility during BER because SSB are the scheduled intermediates of this pathway and are most likely channeled through the pathway until they are ligated [797]. However, PARP1 might be required if these SSB intermediates become uncoupled from the BER pathway. In the two sub-pathways of BER/SSBR, PARylated PARP1 interacts with Polβ to ensure the efficient polymerization during LP-repair [798-800]. In the final DNA ligation step, the required ATP was shown to be generated from PAR [801, 802].

N.1.2. Role of PARP1 in NER

The participation of PARP1 in NER was not anticipated for a long time. Initially, multiple studies had reported the formation of PAR in human cells including skin fibroblasts in response to UVC irradiation [803-808], as well as human keratinocytes [809] and mouse skin [810] in response to UVB-irradiation. Since NER deficient XP-A or XP-C cells, which are unable to perform incision step of NER, failed to show increase in PAR formation in response to UVC [804], UV-induced PARP1 activation was thought to be linked to the incision step of NER pathway [804, 807, 808]. Moreover, the depletion or knockout (KO) of PARP1 or inhibition of PARP catalytic activity in UVC-irradiated cells did not significantly affect their NER capacity (as measured by unscheduled DNA synthesis in UVC-irradiated cells) [760, 806, 807, 811, 812] or their growth and viability [813], thereby dismissing the requirement of PARP1 for efficient NER. Nonetheless, the reduced NER capacity of PARP1-KO mouse embryonic fibroblasts (MEF) was observed in reporter gene assay in one of these studies [760]. Subsequently, pre-treatment of UVB-irradiated rodent cells with PARPi was shown to reduce the repair of CPD and 6-4PP (as determined by quantifying the SSB generated by T4 endonuclease V (T4NV) at these damages) [790]. However, it still remained unclear whether PARP1 was activated by UV-induced CPD and 6-4PP or by the intermediate SSB and ssDNA gaps generated during NER of these DNA damage.

This controversy was resolved by the colleagues from my laboratory [814] and is considered to be one of the initial convincing findings clearly suggesting the role of PARP1 and its activity in NER [775]. They showed biphasic activation of PARP1 in UVB-irradiated MEF, i.e., a very rapid first activation within few seconds in response to direct DNA damage followed by a second activation, 1-2 h later in response to indirect DNA damage. The first activation was corroborated by the monophasic early (~15 seconds) activation of PARP1 in UVC-irradiated MEF. They also demonstrated that PARP1 binds to UVB-irradiated dsDNA *in vitro* and was enriched in chromatin containing TT CPD in UVB-irradiated cells. Using the local irradiation technique, which allows the

creation of 3-5 μm local irradiation zones surrounded by non-irradiated regions in the nuclei [815], they also showed that PAR colocalizes with the TT sites in the nucleus and pointed out the concurrence between the swiftness of PARP1 activation and that of DDB2 accumulation at this site [218, 816], thereby suggesting the involvement of PARP1 in the damage recognition phase of NER. In another study, they examined if the role of PARP1 was in GG-NER and/or TC-NER sub-pathways [817]. They used PARP1-depleted normal human fibroblast transfected with UVB- and UVC-irradiated viruses containing reporter gene in host cell reactivation technique to show that PARP1 facilitated repair in both, GG-NER deficient XP-C and TC-NER deficient CS-B cells and its depletion rendered these cells hypersensitive to UVC- and UVB-irradiation.

Although these studies strongly indicated that PARP1 is required for efficient NER, they used "indirect techniques", such as T4NV induced SSB at direct DNA damage [817] or host cell reactivation that measures the transcriptional consequences of the repair [790]. Moreover, a study that was able to demonstrate the reduced NER capacity of PARP-inhibited or PARP1-depleted cells using a "direct technique", i.e., by specific antibodies-based detection of CPD or 6-4PP, used BRCA1-mutant triple-negative breast cancer (TNBC) cells [818], which are inherently defective in GG-NER [819]. In view of these confounding results, the colleagues from my laboratory used UVC-irradiated NER proficient human skin fibroblasts and SKH-1 mouse skin to clearly show that PARP inhibition delays the repair kinetics of direct DNA damage, as measured by specific antibody-based detection of TT or 6-4PP [820]. Since the delay in TT repair kinetics for UVC-irradiated cells was similar for PARP1-depleted and PARP-inhibited human skin fibroblasts, my colleagues concluded that PARP1 is likely to be the main PARP implicated in this repair process. Nonetheless, a previous study did report inefficient CPD repair but not 6-4PP repair in PARP2-depleted TNBC cells [819]. Around the same time, two independent studies in human skin fibroblasts and human keratinocytes demonstrated similar effect of PARP inhibition or depletion on NER kinetics by direct technique [821, 822].

These studies along with others also provided mechanistic insight into the roles of PARP1 in facilitating GG-NER [236, 820-823]. My colleagues showed that DDB2 and PARP1 arrive independently at the direct DNA damage site. At this site, DDB2 directly interacts with PARP1, stimulates its catalytic activity and get PARylated [820]. PARPi treatment decreased the interaction of DDB2 with both XPC and PARP1, increased its tendency to persist at the UVC-damaged chromatin and decreased level of XPC recruitment/ localization and modification at the UVC-lesion. Based on this, they suggested that catalytic activity of PARP1 could be involved in recruitment of XPC, promotion of chromatin remodeling by DDB2 and in ubiquitination activity of CRLDDB2

ligase complex [820]. Interestingly, it was shown that XPC has a putative PBM in silico [701] and XPC-HR23B were non-covalently and covalently PARylated *in vitro*, which was most efficient in the presence of UV-irradiated plasmid DNA [710]. *In vivo* covalent PARylation of XPC has also been reported, albeit in response to oxidative DNA damage [690, 697].

Similar to the study from my laboratory, another group showed reduced XPC recruitment at the direct DNA damage sites in PARP-inhibited cells [236]. They demonstrated that PARylation promotes ATP-dependent chromatin decondensation function of DDB2 and proposed that DDB2 in concert with PARylation could facilitate the recruitment of chromatin-modifying factors, which eventually facilitates the recruitment of XPC to the DNA damage site. The subsequent study showed this chromatin modifying factor to be the ATP-dependent chromatin remodeler ALC1 [821], which was already known to possess PAR binding macrodomain [786, 824]. While corroborating with and further extending the findings of my laboratory [820], they showed that DDB2-stimulated PARylation by PARP1 at the UV-damaged site is involved in recruitment of ALC1. They also found that DDB2 is PARylated. Additionally, they identified that it is PARylated within the first 40 N-terminal amino acids, which also include lysine residues that are targets of ubiquitination [169]. In contrast to that observed by my colleagues [820], they reported that PARylation of DDB2 increased its stability and prolonged its chromatin retention time. Based on their *in vitro* and *in vivo* data, they proposed that PARylation of DDB2 suppresses its ubiquitylation at the Lys residues in its N-terminal, and thus its degradation [169]. However, this still needs to be demonstrated experimentally. This study also reported the PARylation of DDB1 by PARP1.

Thus, the working model for role of PARP1 during the DNA recognition step of GG-NER can be proposed as follows (Fig. I.1) [123, 775, 825]. Upon UV-induced direct DNA damage in the cells, PARP1, due to its sheer abundance [614], is likely to be one of the first proteins to arrive at the CPD/6-4PP [820] and be basally activated within seconds [814]. DDB2, in a CRLDDB2 complex also arrives at and binds to CPD/6-4PP in a similar time frame as PARP1 [218] and stimulates PARP1 catalytic activity, resulting in PARylation of many proteins including PARP1 and DDB2. PARP1 interacts with DDB2 via PAR at this site [820, 821]. The PARylation of DDB2 suppresses its ubiquitination, and hence rapid degradation to allow enough time for its subsequent functions including CRLDDB2-mediated ubiquitination of histones to promote chromatin remodeling at the damage site [244, 246, 248, 821]. Furthermore, DDB2 and PARylation collaborate to recruit ALC1, which opens the chromatin around the damage by nucleosome sliding [821]. Additionally, PARP1 can PARylate the histones to disrupt the chromatin structure around the damage [821, 826]. Altogether, the chromatin remodeling around the damage site facilitates the recruitment of XPC [236,

821], which could be also further facilitated by the interaction of its putative PBM with the PAR chains at this site [701, 710]. Eventually, the degradation of PAR chain by PAR erasers allows the ubiquitination, and hence degradation of DDB2, resulting in the handover of the damage site to XPC.

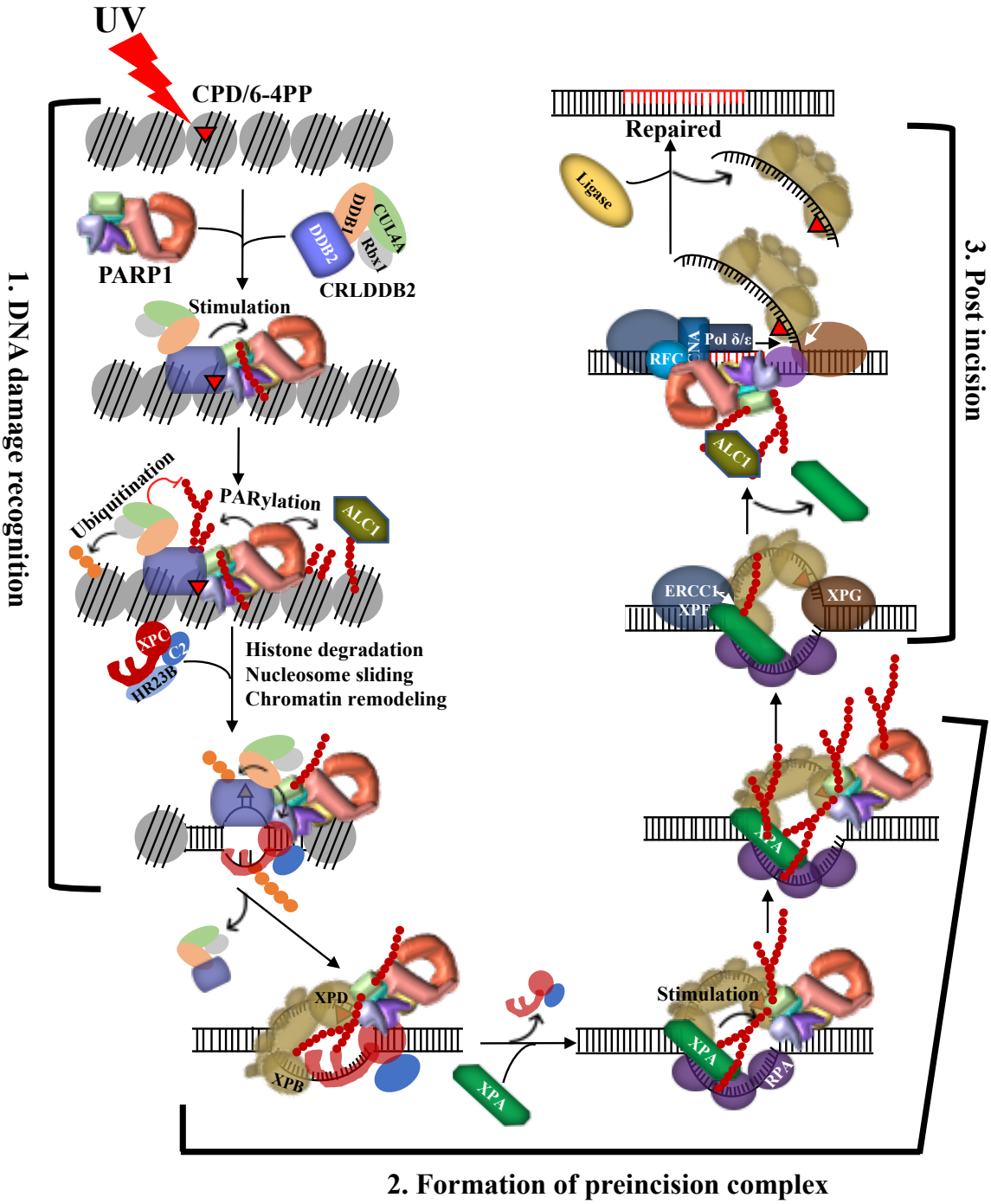

Figure I. Graphical outline of the proposed model for role of PARP1 in facilitating NER
Figure created by Nupur Purohit.

Two independent studies showed that PARP1-mediated PARylation is also required for the recruitment of XPA at direct DNA damage site in cells [822, 823]. XPA also has PBM that binds to long PAR chains with high affinity [700, 823, 827, 828]. The authors proposed that PARylation is important in the early phase of XPA recruitment at the damage site (Fig. I.2) [823]. The subsequent XPA-PARP1 interaction can further stimulate PARP1 activity and the resulting increased PAR synthesis can lead to dissociation of XPA from the damage site during the later course of NER. The observed second wave of PARylation at the post-incision stage of NER when ssDNA gaps are generated, suggest the involvement of PARP1 during this stage of NER (Fig. I.3) [821]. However, the function of this second PARylation wave remains enigmatic. While it was shown to recruit ALC1 in DDB2 independent manner [821], it did not affect recruitment of the XRCC1–LigIII complex or the disassembly kinetics of NER complexes [284].

To conclude, PARP1 facilitates the GG-NER of CPD and 6-4PP by participating during the DNA damage recognition, pre-incision complex formation and post-incision stages [123, 775, 825]. The participation of PARP1 in the latter two stages could also account for the observed reduced TC-NER capacity of PARP1-depleted XP-C cells [817] because these stages are common between GG-NER and TC-NER. However, its role in initial DNA damage recognition step during TC-NER merits further studies in the view of observed requirement of PARP1 and its catalytic activity for the transcription elongation by RNAPIIo [692] and cooperation between PARP1-mediated PARylation and CSB after oxidative stress [829].

N.2. Role of PARP1 in cell fate decision after UVB-induced DNA damage

As a stress sensor protein, PARP1 has been suggested to function as a “cellular rheostat”, at least in response to oxidative stress-induced DNA damage [618, 765, 766]. Depending on the level of DNA damage, PARP1 can determine the outcome of cell fate via PARylation, similar to that exhibited by p53 in response to UV-induced DNA damage (Section G). The mild or moderate level of DNA damage results in adequate PARP1 activation, which is required to facilitate DNA repair and thus cell survival. If the DNA damage is irreparable, the apoptotic pathways are triggered, leading to the cleavage of PARP1 by the activated caspases [830]. On the other hand, severe or sustained DNA damage hyperactivates PARP1. This excessive PARylation, which either via PAR or due to PARP1 hyperactivation-induced energy (NAD+/ATP) depletion triggers cell death via parthanatos or necrosis, respectively [772, 773, 831].

The role of PARP1 and its catalytic activity in facilitating the repair of UV-induced DNA damage in skin cells is clearly demonstrated by inhibiting PARP activity and/or silencing PARP1 (Section

N.1.2). However, a direct implication of this role of PARP1 in facilitating the survival of skin cells is controversial. Previous studies have reported both, the protective and sensitizing effects of PARP-inhibition and/or PARP1 silencing on the UVB- and/or UVC-induced cytotoxicity in human skin fibroblasts [817, 821, 832], keratinocytes [833] and SKH-1 mouse skin [810, 834]. As described in section F, p53 plays a crucial role in determining the fate of UV-damaged cells. Our group showed that the topical application of PARPi in mice resulted in reduced number of p53-positive cells in the epidermal layer in response to single UVB-exposure [834], whereas other study reported that absence of PARP1 in MEF had no effect on the UVC-induced p53 accumulation [835]. Consistently, PARP1-mediated PARylation of p53 promotes its UVC-induced stabilization in the human hepatoma cells [836] and its nuclear retention [837]. p53 has been reported to be both covalently and non-covalently PARylated [838, 839] and this enhanced p53 functions including transactivation of CDKN1A gene (codes for p21) expression [839]. Furthermore, PARP1 can also modulate and/or be modulated by the biochemical activities of the kinases such as ATM, AKT, JNK and p38, which are also involved in phosphorylation mediated stabilization and activation of p53 in response to UVB [624]. Altogether, these studies suggest that PARP1 can serve its stress sensing function to determine fate of UVB-damaged cells.

N.3. Role of PARP1 in UVB-related immunological modulations

To date, only few studies have examined the role of PARP1 in UVB-induced immunological modulations (Section I). The role of PARP1 has not been examined for UVB-induced inflammation in the skin. However, there is an indirect indication for its role in UV-induced inflammation in the skin. It was suggested that UV-induced vitamin D synthesis results in anti-inflammatory effects on the skin possibly by inhibition of PARP1 activity [840], which is known to play proinflammatory role under different pathological conditions in different organs including skin [770, 833, 841-844]. Furthermore, activated PARP1 is shown to promote NFκB-dependent expression of proinflammatory cytokines such as TNFα, IL-6, IL-1β, etc. in various type of cells including innate immune cells [770]. Beyond NFκB, PARP1 was shown to enhance the DNA binding of other inflammatory transcription factors including AP-1 [845]. Furthermore, the PARP1 overactivation induced necrosis and parthanatos can also triggers inflammation [846, 847]. Interestingly, extracellular PAR is reported to be recognized as DAMP by the TLR on the macrophages [848]. These proinflammatory roles of PARP1 are further corroborated by the observed alleviation of lipopolysaccharide-induced inflammation in PARP1-KO mice [849].

Concerning role of PARP1 in UVB-induced immunosuppression, topical application or oral administration of nicotinamide, a weak PARPi, mitigated UV(B+A)-induced immunosuppression in

human skin [850] and chronic UVB-induced immunosuppression in BALB/c mouse skin [851, 852]. Paradoxically, nicotinamide is not only the inhibitor of PARP activity but also a precursor of PARP substrate NAD^+, suggesting that it may prevent PARP hyperactivation rather than complete inhibition of PARP1 activity [853]. Additionally, reduced photoimmunosuppression due to nicotinamide is also suggested to be a consequence of its role in enhancing the repair of UV-induced DNA damage [853-855]. Nonetheless, a different PARPi, BGP-1, is also shown to alleviate immunosuppression in SKH-1 mouse skin within few hours of UVB irradiation [810], thereby indicating that PARP1 activity might facilitate photoimmunosuppression. However, this is in contrast to: (a) observed increase in the immunosuppressive Treg in spleen, thymus and the peripheral lymph nodes of PARP1-KO mice [856]; (b) role of PARP1 in easing immunosuppressive capacity of Tregs [857] and (c) relatively reduced oxazolone-induced CHS (a T-cell mediated response) in the PARP1-KO mouse skin [858].

O. Role of PARP1 in development of cancers including UVB-induced SCC

Carcinogenesis is a complex and multistep process, which can be summarized as the acquisition of eight biological capabilities that are the hallmarks of cancer: sustaining proliferative signaling, evading growth suppressors, resisting cell death, enabling replicative immortality, reprogramming of energy metabolism, inducing angiogenesis, evading immune destruction and activating invasion and metastasis [859]. Genome instability and inflammation accelerate and foster the acquisition of these hallmarks during carcinogenesis [859]. Owing to their multifunctionality in various cellular responses to genotoxic stress [860] including that caused by UVB (Section N), PARP1 and its catalytic activity are implicated in all of the processes linked to the acquisition of these cancer hallmarks [861, 862].

In general, PARP1 maintains the genetic stability of the normal cells by facilitating the DNA repair pathways [775], and hence protects against the formation of oncogenic genetic mutations [861]. Furthermore, excessive genotoxic stress-induced overactivation of PARP1 triggers the death of normal cells via PAR-induced parthanatos or the rapid energy depletion-induced necrosis [772, 773, 831], thereby eliminating potential premutagenic cells [863]. Consistently, PARP1-KO mice show increased susceptibility to spontaneous and/or alkylating agent induced mutagenesis and tumorigenesis as compared to WT mice [764, 861, 864-870]. On the contrary, in cancer cells, DNA repair function of PARP1 can be co-opted for their survival. Furthermore, PARP1, being a transcription regulator, modulates the expression of oncogenes, tumor suppressor genes and pro-inflammatory genes, which are implicated in tumor promotion, progression, metastasis and angiogenesis [862, 871]. Moreover, PARP1-mediated cell death can paradoxically contribute to the tumor promoting inflammation [846, 847]. Interestingly, PARP1 and/or its catalytic activity have been reported to be upregulated in multiple cancer cell lines and in patient-derived tumors from

different tissues including skin [862, 872, 873]. In some of these cancers, it has been linked to malignant transformation, tumor aggressiveness and poor survival or resistance to therapy in patients [872]. Altogether, these findings indicate that PARP1 plays two paradoxical roles in cancer [872]: it acts as a barrier against the tumorigenesis by maintaining genomic stability in the normal cells whereas it promotes the survival, progression and metastasis of the established tumors. Recently, this was demonstrated for the alkylation-triggered colorectal cancer in mice, where DNA repair function of PARP1 protected against tumor initiation whereas its pro-inflammatory function promoted the tumor growth [874].

In skin cancers, PARP1 overexpression has been linked to aggressive cutaneous malignant melanoma in humans [873]. In mice, depletion of PARP1 is shown to significantly compromise the tumorigenic potential of melanoma cells due to reduction in tumor-associated angiogenesis and inflammation [875]. This was subsequently validated by the use of PARPi, which suppressed angiogenesis, invasion and metastasis of melanoma in mice [876]. For NMSC, knocking out PARP1 increases the incidence and multiplicity of X-ray-induced BCC-like tumors in the BCC mouse model [877]. With respect to SCC, it was shown that the absence of PARP1 (PARP1-KO) or topical application of PARPi in mice reduces their susceptibility to the chemical carcinogen-induced skin papilloma [841, 842]. To date, only few studies have assessed the role of PARP1 in the development of UVB-induced SCC. The treatment of MEF with PARPi 3-AB inhibit their UVC-induced malignant transformation [878]. Conversely, topical application of 3-AB in SKH-1 mice increases the incidence and severity of UVB-induced SCC [879]. While these studies show contradictory effects of PARP inhibition, to date, no studies have examined the effect of the absence of PARP1 protein on UVB-induced SCC development.

P. Therapeutic targeting of PARP1 in cancer

Killing cancer cells by inducing DNA damage is the basis for radiotherapy and chemotherapy of cancer [665, 880, 881]. However, the repair of DNA damage presents a mechanism by which cancer cells develop resistance to these therapies. Therefore, inhibiting the repair along with DNA damaging therapeutics became an attractive strategy to enhance the efficacy of these cancer therapies. The idea of targeting PARP1 to inhibit the DNA repair in cancer cells stems from the seminal work by Sydney Shall's group in 1980, which demonstrated that the inhibition of PARP activity impedes the BER/SSBR of DNA damage caused by alkylating agent and enhances its cytotoxicity (chemosensitization) [882]. Subsequently, exploiting PARPi for radiosensitization of cancer cells was also suggested based on its similar mode of action in response to ionizing radiation-induced DNA strand breaks and cytotoxicity [883, 884]. Since then, multiple preclinical and clinical studies have

demonstrated the chemo- and radiosensitizing effects of PARPi in combination therapy with conventional cytotoxic or targeted chemotherapeutic drugs and radiations for different types of cancer [665, 860, 871, 880, 885-887]. The emerging insights into the immune functions of PARP1 have also resulted in implication of PARPi in combination therapy with immunotherapeutic drugs in clinical studies [888]. However, PARPi combination therapies in various clinical trials pose major challenges, such as complicated nature of combination regimens, severe side effects due to overlapping toxicities and difficulty in establishing biologically appropriate dosages [665, 860, 871, 880, 885, 886]. Nonetheless, the continued reports of the improved anti-cancer efficacy of PARPi in combination with various new generation cancer therapeutics in cellular and preclinical studies have kept the interest alive in the medical community as seen from the ongoing multiple clinical trials (https://www.clinicaltrials.gov).

The major impetus for the use of PARPi in clinic as a monotherapy for cancer was provided by two seminal studies, which suggested that it can be utilized for the DNA repair deficient cancers such as HR repair (HRR)-defective BRCA1/2-mutated cancers [889, 890]. These studies reported that PARP inhibition exhibits synthetic lethal interaction with BRCA1/2 mutations. By definition, synthetic lethality, a concept first described by Dobzhansky in 1946, is a situation where an individual defect in two genes/proteins is compatible with cell viability but combination of both defects (synthesized) in the same cell results in death [891]. The mechanism by which PARP inhibition displays synthetic lethal interaction with BRCA1/2 mutations is not clearly understood, but proposed mechanisms include PARPi-induced suppression of BER/SSBR, PARP1 trapping at the DNA strand break site, replication fork collapse, defective recruitment of BRCA1 or activation of error prone NHEJ pathway [892-895]. Any one or all of these effects of PARPi in the background of BRCA1/2 mutation-induced defective HRR pathway, ultimately result in cell death.

Since this ground breaking discovery, a decade of clinical studies and development of new PARPi have led the FDA to approve olaparib, rucaparib, niraparib and talazoparib as “fourth line of treatment” or maintenance therapy for somatic or germinal BRCA1/2-mutated breast and ovarian cancers as well as platinum-sensitive recurrent epithelial ovarian, fallopian tube or primary peritoneal cancers [896-903]. Olaparib and rucaparib have “breakthrough designation” from FDA for the treatment of BRCA1/2-mutated prostate cancers [904]. The application of PARPi as a monotherapy has also been extended for cancers with BRCAness [905], i.e., those with mutations in genes other than BRCA1/2 that show similar HRR defect (HRD) as germline BRCA1/2 mutated cancers [906]. More recent clinical trials suggest that PARPi monotherapy can also be used as “first line of treatment” for BRCA1/2 mutated cancers and also for those with BRCAness or HRD [907].

Q. Context, hypothesis and objectives

The WHO reported cancer as the second leading cause of death accounting for estimated 9.6 million deaths globally in 2018 [908]. Underpins of cancer are the genetic mutations, which arise due to disruption of genomic integrity. The creation of PARP1-KO mouse models and their studies led to the realization that PARP1 is a "guardian angel" protecting the genome and thus suppressing tumorigenesis [909]. Since then, characterization of the roles of PARP1 in genome maintenance has kept the scientists busy (Sections N-P).

One of the research areas of my laboratory is to study the role of PARP1 in mammalian NER [814, 817, 820], which restores genomic integrity following solar UV-induced insults in DNA. In 2012-2013, two other teams from Europe and colleagues from my laboratory resolved the ambivalence surrounding role of PARP1 in NER pathway [236, 820, 821]. They showed that PARP1 collaborated with DDB2 during the DNA damage recognition step of NER (Section N.1.2). However, this was not the only missing piece of the puzzle because many aspects of PARP1 participation during this step remained to be understood. One of them was the lack of nucleotide level information for the whereabouts of PARP1 binding on the DNA containing direct damage that could account for the observed similar time frame for its recruitment as DDB2 and their interaction at the UV-damaged chromatin [820]. Moreover, mechanism by which DDB2 was stimulating catalytic activity of PARP1 in the presence of UV-damaged DNA was also unaddressed [820, 821].

As described in section P, targeting the role of PARP1 in DNA strand break repair has emerged as one of the successful strategies for the treatment of HRR-deficient ovarian and breast cancer in last decade. The defects in NER pathway in Xeroderma pigmentosum patients renders them highly susceptible to solar UV-induced skin cancer including SCC [494-496]. Therefore, understanding the role of PARP1 in facilitating NER can have important implication in skin carcinogenesis and the use of FDA approved PARPi for therapy of solar UV-induced skin cancers. Few previous studies using PARPi to understand the role of PARP1 in UV-induced transformation of cells or SCC in mice have led to the contradictory observations ([878, 879] and Section O). Therefore, the only way to validate these reports is by the use of PARP1-KO mouse model.

The absence of BER/SSBR function of PARP1 in PARP1-KO mice rendered them highly susceptible to alkylating agent-induced tumorigenesis. Since the mice deficient in NER pathway proteins also exhibited higher susceptibility to UVB-induced SCC [85, 87, 497-500], it was tempting to anticipate that PARP1-KO mice will be highly susceptible to UVB-induced SCC. However, in addition to DNA repair, PARP1 also plays roles in cellular processes such as cell death (Section N.2) and immune-

modulation (Section N.3), which are also involved in pathogenesis of UVB-induced SCC (Section J). Therefore, I hypothesized that PARP1 can influence the outcome at multiple steps of UVB-induced skin carcinogenesis.

The major problem in testing this hypothesis was that the available PARP1-KO mouse models were created in the background of C57BL/6 strain of mice. In addition to the problem posed by their hairy phenotype (Section K), these mice require non-physiological dose of UVB and prolonged periods of irradiation to develop skin tumors [497, 499, 500]. The most widely adopted model for studying UVB-induced SCC is SKH-1 hairless mouse (Section K). Since this type of study requires a large number of mice to obtain the statistically significant results and each SKH-1 mouse can develop up to more than 40 tumors during the protocol, it was important to develop a technique to accelerate the process of tumor data acquisition on weekly basis to allow accurate determination of cancer severity. Finally, the conventional tumor measurement criteria used to determine the cancer severity have some inherent limitations; therefore, they needed refinement to be able to provide more detailed biological insights for the observed skin cancer phenotype in response to specific genetic or chemical manipulation. To address these hypotheses and problems, the **specific objectives** of my doctorate studies were:

1. *To determine the precise nature of binding of PARP1 with respect to DDB2 at UV-induced CPD/6-4PP (Chapter 1).*
2. *To create PARP1-KO SKH-1 mouse model by transferring the Parp1$^{-/-}$ genotype from the existing C57BL/6 strain to SKH-1 strain of mice (Chapter 4).*
3. *To develop and/or refine methods and criteria for the acquisition of weekly tumor data and measurement of UVB-induced cancer severity, respectively (Chapters 2 and 3).*
4. *To compare the susceptibility of PARP1-KO and PARP1-WT SKH-1 mice treated or not with PARPi to UVB-induced skin cancers (Chapter 4).*

Chapter 1. Characterization of the interactions of PARP-1 with UV-damaged DNA *in vivo* and *in vitro*

Nupur K. Purohit[1#], Mihaela Robu[1#], Rashmi G. Shah[1#], Nicholas E. Geacintov[2] and Girish M. Shah[1*]

[1]Laboratory for Skin Cancer Research, CHU-Q (CHUL) Quebec University Hospital Research Centre & Laval University, 2705, Laurier Boulevard, Québec (QC) Canada G1V 4G2.

[2]New York University, Department of Chemistry, New York, NY, USA

[*]To whom correspondence should be addressed.

Tel: [1-418-525-4444/ext. 48259]; Email: [girish.shah@crchul.ulaval.ca]

[#] These authors contributed equally to this work.

1.1. Preface

In light of the previously reported role of PARP-1 in facilitating the DNA damage recognition step of NER (section N.1.2), research in this chapter (published in January 2016 in the journal Scientific Report and its PDF format is attached Annexe 1) further characterizes the interaction of PARP-1 with UVC-damaged DNA and DDB2 using two novel techniques. By developing and using the first technique, i.e., "*in situ* fractionation" in combination with immunocytochemistry and local UVC-irradiation, an equal co-author of this article, Dr. Mihaela Robu demonstrated for the first time the recruitment of PARP-1 protein at the local UVC-damaged sites in the nucleus (Fig. 1.1e & 1.2a). Owing to the abundance of PARP-1 protein in the mammalian cells, this was otherwise nearly impossible to do using conventional immunocytological methods that are used for visualizing the recruitment of other NER proteins at these sites (Fig.1.1a-b). Using this novel technique, she also showed that the N-terminal Zn1 and Zn2 domains of PARP-1 are sufficient for its recruitment (Fig. 1.2b). This technique as well as previous studies from others and our team (section N.1.2) had shown that, (i) PARP-1 binds to UVC-damaged large oligonucleotide (oligo) *in vitro* or to chromatin fragments containing T-T lesions in cells, (ii) PARP-1 interacts with DDB2 on the same DNA strand in UVC-irradiated cells and (iii) DDB2 stimulates catalytic activity of PARP-1 in the presence of UVC-damaged DNA. However, we still did not know whether PARP-1 was bound directly to the CPD/6-4PP or to any other base in those long pieces of DNA and whether PARP-1 and DDB2 have sufficient space to co-exist around UV- lesion. Therefore, I, in collaboration with the other equal co-author of this article, Rashmi Shah, created and characterized the second tool, an oligo with defined and unique UVC-induced TT as well as with overlapping unique restriction sites (Fig. 1.3), which allowed us to determine the binding, footprint and catalytic activation of PARP-1 around T-T, alone or in presence of DDB2 (Fig. 1.4 & 1.5). I also took part in writing the manuscript, reviewing it and editing the figures. Another oligo containing unique chemically synthesized T-T or 6-4PP used in Fig. 1.5a was provided by Dr. Nicholas Geacintov.

1.2. Résumé

Les méthodes existantes pour étudier les réponses de la poly(ADP-ribose) polymérase-1 (PARP-1) aux dommages à l'ADN de type cassures simple- ou double-brin sont souvent inadaptées pour examiner ses réponses plus subtiles face à de l'ADN altéré par rayonnement UV sans cassure. Nous présentons ici deux nouveaux outils avec lesquels nous avons caractérisé l'interaction de la PARP-1 avec l'ADN endommagé par rayons UV *in vivo* et *in vitro*. En utilisant la technique de fractionnement *in situ* qui élimine sélectivement la PARP-1 libre tout en conservant la PARP-1 liée à l'ADN, nous avons démontré le recrutement direct de la PARP-1 endogène ou exogène sur le site de lésions induites *in vivo* par les UV après irradiation locale. De plus, en utilisant un modèle d'oligonucléotide portant une seule lésion causée par rayonnement UV, encadrée de plusieurs sites de reconnaissance d'enzymes de restriction, nous avons démontré *in vitro* que la protéine DDB2 et la PARP-1 peuvent se lier simultanément à l'ADN endommagé par les UV, et que la PARP-1 a une empreinte bilatérale asymétrique de -12 à +9 nucléotides de chaque côté du dommage. Ces techniques permettront de caractériser les différents rôles de la PARP-1 dans la réparation de l'ADN altéré par les UV et ses rôles constitutifs impliquant l'ADN non endommagé.

1.3. Abstract

The existing methodologies for studying robust responses of poly(ADP-ribose) polymerase-1 (PARP-1) to DNA damage with strand breaks are often not suitable for examining its subtle responses to altered DNA without strand breaks, such as UV-damaged DNA. Here we describe two novel assays with which we characterized the interaction of PARP-1 with UV-damaged DNA *in vivo* and *in vitro*. Using an *in situ* fractionation technique to selectively remove free PARP-1 while retaining the DNA-bound PARP-1, we demonstrate a direct recruitment of the endogenous or exogenous PARP-1 to the UV-lesion site *in vivo* after local irradiation. In addition, using the model oligonucleotides with single UV lesion surrounded by multiple restriction enzyme sites, we demonstrate *in vitro* that DDB2 and PARP-1 can simultaneously bind to UV-damaged DNA and that PARP-1 casts a bilateral asymmetric footprint from -12 to +9 nucleotides on either side of the UV-lesion. These techniques will permit characterization of different roles of PARP-1 in the repair of UV-damaged DNA and also allow the study of normal housekeeping roles of PARP-1 with undamaged DNA.

1.4. Introduction

The abundance of poly(ADP-ribose) polymerase-1 (PARP-1) in mammalian cells and its rapid catalytic activation to form polymers of ADP-ribose (PAR) in the presence of various types of DNA damages with or without strand breaks has made it an ideal first responder at the lesion site to influence downstream events [1, 2]. Apart from DNA damages, PARP-1 is also recruited to DNA during normal physiological processes such as transcription and chromatin remodeling [3], which do not involve overt DNA damage but just altered DNA structures. While we know much more about how PARP-1 rapidly recognizes and binds to single or double strand breaks in DNA, we know very little about how PARP-1 interacts with DNA damages or altered DNA structures without strand breaks. The key reason is that the existing methodologies that readily identify interactions of PARP-1 with DNA strand breaks are not sufficiently sensitive to study the relatively weaker responses of PARP-1 to DNA damage without strand breaks. The response of PARP-1 to UVC-induced direct photolesions, such as cyclobutane pyrimidine dimers (CPD) that are formed without any DNA strand breaks exemplifies this problem.

Recent studies from others and our team have shown the involvement of PARP-1 in the host cell reactivation [4] and specifically in the nucleotide excision repair (NER) of UV-damaged DNA through its interaction with early NER protein DDB2 [5-7]. Additional studies have shown that downstream NER proteins XPA [8, 9] and XPC [10] are PARylated. Thus, PARP-1 possibly has multiple roles in NER, but we do not yet fully understand its interactions with UV-damaged DNA or other NER proteins due to two major challenges. The first challenge is that unlike for many NER proteins, the abundance of endogenous PARP-1 in the nucleus makes it nearly impossible to visualize its dynamics of recruitment to UV-damaged DNA *in situ* using conventional immunocytological methods. To circumvent this challenge, the detection of its activation product PAR has been used as a proxy for PARP-1 recruitment at UV-lesion [5, 11]. However, PAR may underestimate the role of PARP-1 in response to UV-damage due to weak activation of PARP-1 by UV [4, 12], short half-life of PAR [2], and technical limitations in combining the detection of PAR with other proteins [13, 14]. PAR detection will also not reveal participation of PARP-1 in protein-protein interactions without formation of PAR. Thus, there is a need for methods that permit direct visualization of recruitment of PARP-1 to UV-induced DNA lesions.

The second major challenge is that we do not know the exact footprint of PARP-1 at the UV-lesion site that could explain its interaction with different NER proteins. We have earlier shown that PARP-1 binds to UV-damaged large oligonucleotide *in vitro* or to chromatin fragments containing T-T lesions *in vivo* [11]. We also showed that PARP-1 and DDB2 associate with each other on the

chromatin of UV-irradiated cells and that DDB2 stimulates catalytic activity of PARP-1 in the presence of UV-damaged DNA [7]. However, these assays lack the nucleotide level resolution to reveal whether PARP-1 was bound directly to the UV-damaged bases or to any other base in those long pieces of DNA and whether PARP-1 and DDB2 have sufficient space to co-exist around UV-induced DNA lesion. To address these challenges, here, we describe two novel assays. The first assay is an *in situ* fractionation technique that allows a direct visualization of PARP-1 recruited to UV-damaged DNA *in vivo*. The second assay involves use of model oligonucleotides with a defined UV-damage surrounded by multiple restriction enzyme sites that reveals a bilateral asymmetric footprint of PARP-1 around the UV-lesion.

1.5. Results and discussion

1.5.1. Novel *in situ* fractionation protocol to reveal recruitment of endogenous PARP-1 to UV-induced DNA lesion

We first determined whether different permeabilization-fixation protocols conventionally used for PARP-1 could reveal a direct recruitment of PARP-1 to UVC-induced DNA photolesions *in situ*. There was no change in the pattern of abundant PARP-1 signal before or after global UVC-irradiation using formaldehyde-methanol protocol despite using three different antibodies to PARP-1 (Fig. 1.1a, left panel). Unlike global irradiation, local UVC-irradiation produces defined size subnuclear spots of UV-damaged DNA that could be identified either by immunodetection of T-T lesions or DDB2 that is recruited very rapidly to these lesions (Supplementary Fig. S1.1a). Therefore, we examined whether the formaldehyde-methanol protocol could reveal localization of PARP-1 to subnuclear UV-damaged DNA spots after local irradiation. Once again, we could not observe colocalization of PARP-1 with the subnuclear spots of DDB2 (Fig. 1.1a, right panel). Next, we tried previously described formaldehyde-Triton protocol [8] which was shown to display a punctate pattern of PARP-1. However, we noted that this pattern did not correlate with recruitment of PARP-1 to UV-damaged DNA, because it was observed in both the unirradiated control and globally UVC-irradiated cells; and none of the spots of PARP-1 were co-incident with DDB2, i.e., UV-damaged DNA in the cells after local UVC-irradiation (Supplementary Fig. S1.1b).

In view of these challenge in the immunocytological detection of PARP-1 bound to UV-damaged DNA due to the background "noise" created by rest of the nuclear PARP-1, we designed a novel *in situ* fractionation technique to selectively deplete unbound or "free" PARP-1 from the nuclei while leaving behind the PARP-1 that is bound and cross-linked to the UV-damaged DNA. We used CSK buffer (C) with Triton (C+T) as the basic conditions, which have been used earlier to extract majority of the cellular proteins without destroying the cellular architecture and permit visualization of NER and other repair proteins recruited to the damaged DNA [15-18]. To this buffer, we added 0.42 M NaCl (C+T+S), since we had earlier seen that 0.42 M NaCl retained chromatin-bound PARP-1 during cell fractionation *in vitro* [7] whereas 1.6 M NaCl was shown to strip almost all PARP-1 from cells [19]. We first compared the efficiency of these three protocols (i.e., C, C+T and C+T+S) for the extraction of PARP-1 and DDB2 from unirradiated control cells. The immunoblotting of cell pellet and supernatant from each protocol revealed that while C+T protocol could efficiently remove majority of the free DDB2, a significant extraction of the free PARP-1 from cell pellet required C+T+S protocol (Fig. 1.1c). Next, we compared the capacity of these three protocols for the *in situ* extraction of PARP-1 from control and global UVC-irradiated cells. The immunocytological

visualization confirmed that C+T+S buffer extracted most of the "free" PARP-1 from the control and UVC-irradiated cells, while leaving behind residual PARP-1 that would be interacting with DNA for normal physiological functions in control cells and relatively stronger punctate pattern of PARP-1 in UV-irradiated nuclei (Fig. 1.1d).

When the three protocols were compared after local irradiation, we observed that the C+T+S protocol offered the best extraction condition for visualization of the recruitment of PARP-1 to the subnuclear spots of DDB2 (Fig. 1.1e, left panel). The pooled data from at least 100 subnuclear spots revealed that each additional step of extraction with detergent and salt improved our ability to discern colocalization of PARP-1 with DDB2 (Fig. 1.1e, left chart). Since the initial irradiation conditions were identical prior to extraction with each of the protocols, the improved detection of colocalization of PARP-1 with DDB2 could only be due to a more efficient removal of rest of the nuclear "free PARP-1" by the C+T+S protocol. This was evident when PARP-1 signal at the irradiated site was corrected for the background signal from an equivalent area of the unirradiated part of the same nucleus for all techniques (Fig. 1.1e, right chart).

1.5.2. Validation of the *in situ* fractionation protocol with GFP-tagged exogenous PARP-1 or its N-terminal DNA binding domain

We compared the efficiency of each of the three protocols in revealing the recruitment of exogenous GFP-tagged PARP-1 to UV-induced T-T lesion in locally UV-irradiated cells (Fig. 1.2a). The C protocol was inefficient in revealing the co-localization of GFP signal with T-T spots especially in the cells expressing higher levels of exogenous PARP-1. The C+T and C+T+S protocols increasingly resolved this problem by removing "free" PARP-1; thus giving a background-corrected signal for GFP-PARP-1 at T-T lesion that was 1.9 and 2.7 times better than the C protocol, respectively (Fig. 1.2a, chart). The additional advantage was that this co-localization could be readily observed whether these cells initially expressed high or low levels of GFP-PARP-1.

The N-terminal DNA binding domain (DBD) of PARP-1 containing first two zinc fingers was shown to be sufficient for its recruitment to different types of DNA damages caused by laser irradiation of cells [20, 21]. In the cells transiently transfected with GFP-DBD, the colocalization of DBD with T-T was evident only in low DBD-expressers, as shown in low and high exposure panels of C-protocol (Fig. 1.2b). The ability to discern co-localization of GFP-DBD to T-T lesion sites was significantly improved by 1.5 and 2.1 times with C+T protocol and C+T+S protocol, respectively (Fig. 1.2b, chart). Immunoblotting for GFP-DBD and endogenous untagged PARP-1 in control cell pellets in these extraction protocols revealed that the extent of removal of exogenous GFP- DBD at each step was

similar to that of the endogenous cellular PARP-1 (Supplementary Fig. S1.1c). Our results show that the N-terminal DBD of PARP-1 is sufficient to recognize and bind to UVC-induced DNA damage.

To assess the specificity of the new protocol, we examined the status of UV-induced colocalization of unrelated proteins, such as the exogenous tag protein GFP (Fig. 1.2c) or the cellular DNA double strand break-repair protein Rad51 (Fig. 1.2d) at UV-lesion spots after processing with all three protocols. Although C+T and C+T+S protocols progressively removed both of these proteins from the cells, neither GFP nor Rad51 colocalized with UV-induced T-T lesions. Thus, our results show that the C+T+S protocol does not cause an artifact of random colocalization of unrelated proteins with UV-damaged DNA. This simple yet selective *in situ* fractionation protocol to reveal PARP-1 at UV-lesion site would be useful in studying other NER-related roles of PARP-1 with or without its catalytic activation at the site of UV-damaged DNA.

1.5.3. An oligo with defined UV-lesion for restriction mapping of PARP-1

To determine the exact footprint of PARP-1 at the UV-lesion site, we created biotin-tagged 40mer oligonucleotides with or without a single defined UV-lesion surrounded by multiple unique restriction enzyme sites (Supplementary Fig. S1.2a). The UVC-irradiation of the top strand of the oligo, which has only one pair of adjacent Ts and no other adjacent pyrimidines (T or C), resulted largely in the formation of T-T rather than 6-4PP lesions (Supplementary Fig. S1.2b). The inability of restriction enzymes to digest through UV-induced CPD [22, 23] was exploited for purification of UV-DNA with VspI enzyme to remove all DNA molecules that did not form T-T at this site (Supplementary Fig. S1.2c). The biotin-tagged complementary strand for both control and UV-DNA allowed a common procedure for their immobilization to streptavidin beads (Fig. 1.3a). We reasoned that any protein bound at or around the UV-lesion site would prevent the restriction enzyme from digesting the DNA at that site; and thus decrease the quantity of non-biotinylated 5'-restriction fragment released from bead-bound DNA into the supernatant. This model allowed us to compare the extent of binding of proteins to control versus UV-DNA and also provide a non-isotopic method to footprint proteins on UV-DNA.

1.5.4. PARP-1 and DDB2 bind more to UV-DNA than control DNA

We had shown in the cells and *in vitro* that PARP-1 not only binds to UV-damaged DNA [11], but also interacts with DDB2 in the vicinity of UV-induced DNA lesions [7]. Using the model oligo described in Fig. 2.3a, we examined the extent of binding of PARP-1 and DDB2 to control and UV-DNA at two different molar ratios of protein : DNA (Fig. 1.3b). The 2.1-2.2x fold higher binding of DDB2 to UV-DNA than the control-DNA at these two molar ratios is in agreement with a previous

report [24]. The binding of PARP-1 to UV-DNA was also 1.5-1.7x fold more than the control-DNA (Fig. 1.3b). We confirmed that PARP-1 did not bind to the beads per se unless DNA was attached to it (Supplementary Fig. S1.3a: left panel). To determine the site of PARP-1 binding to the control DNA without UV-lesion, we digested PARP-1-bound control DNA with VspI or NspI and noted that PARP-1 was attached more to the bead-bound 3'-end than to the 5'-end that is released after the restriction digestion (Supplementary Fig. S1.3a: right panel). This could be due to the linker attached biotin providing a pseudo-overhang at the 3'-end unlike blunt 5'-end, because PARP-1 has higher affinity for overhangs as compared to the blunt ends of DNA [25]. However, since the same 3' and 5'-ends exist in both control and UV-DNA, any increase in PARP-1 binding to UV-DNA as compared to control-DNA must be due to the interaction of PARP-1 with UV-lesion, which we footprinted using a series of restriction enzymes that digest on either side of the lesion.

1.5.5. Restriction protection profile of PARP-1 is distinct from that of DDB2 on either side of the T-T lesion

We established the optimal amount of DNA required in the assay for detection of DNA fragments released after digestion with restriction enzyme (Supplementary Fig. S1.3b) and also confirmed that both the control and UV-DNA without bound protein could be digested by all the restriction enzymes used in our footprinting assays (Supplementary Fig. S1.3c-d). Thus, any restriction protection offered to DNA after reaction with protein could be attributed to the footprint of the protein. During the restriction digestion by NspI and MslI that recognize sequences from -2 to -12nt on the 5'-side of the T-T lesion, PARP-1 offered more protection to UV-DNA than control DNA, as seen from a significant PARP-1 dose-dependent decrease in the corresponding 5'-fragments released by these enzymes (Fig. 1.4a). Thus, the footprint of PARP-1 on UV-DNA extended from 2-12nt upstream of the lesion site. In contrast, DDB2 failed to protect UV-DNA against NspI (-2 to -7 nt), indicating that its footprint stays within 2nt on the 5'-side of T-T, as reported earlier [26].

PARP-1 has been shown to have a bilateral footprint of 7 nt on either side of DNA single strand breaks [27]. Therefore, we compared the protections offered by PARP-1 and DDB2 against the restriction enzymes ApaII and Bsp1286I that target from 3 to 9 nt on the 3'-side of the T-T lesion. The DDB2 did not offer any protection to control or UV-DNA against ApaII (Fig. 1.4b), indicating that its footprint does not exceed beyond 3nt on 3'-side of T-T, as reported earlier [26]. In contrast, PARP-1 offered a strong but equal protection to both UV and control oligos against both the enzymes, possibly due to PARP-1 bound to 3'-ends of both types of DNA, as noted earlier (Supplementary Fig. S1.3a: right panel). Thus using 40mer oligo, it was difficult to discern additional protection, if any,

offered by PARP-1 that is bound at or near T-T site from the protection offered by PARP-1 that is bound to the 3'-end of the oligo.

To resolve this issue, we extended the size of 40mer oligo on either ends to create a 60mer, in which 3'-end was significantly separated from these two restriction sites and added a new RsaI restriction site at +11 nt from T-T (Fig. 1.4c, top panel). PARP-1 significantly protected 60mer UV-DNA against digestion by Bsp1286I as compared to control DNA, confirming its footprint up to +9nt from T-T lesion. Moreover, the lack of any additional protection by PARP-1 to UV-DNA against digestion by RsaI defined that PARP-1 footprint does not reach up to +11nt from T-T site (Fig. 1.4c). Thus using restriction-mapping technique on our model oligo, we show that PARP-1 bound at or near the T-T lesion extends asymmetric bilateral protection against restriction digestion from -12 to +9nt around the lesion.

Next, we examined whether PARP-1 and DDB2 can simultaneously bind to UV-DNA and whether DDB2 bound at the T-T lesion would alter the footprint of PARP-1 around the lesion. Using 60mer oligo, we noted that when incubated together, both DDB2 and PARP-1 could bind to UV-DNA (Fig. 1.4d, left panel). We observed in two independent experiments that the presence of PARP-1 increased the binding of DDB2 to UV-DNA, whereas that of DDB2 reduced the binding of PARP-1. However, the presence of DDB2 did not affect the restriction footprint of PARP-1 on UV-DNA, because PARP-1 offered identical protection to UV-DNA against restriction digestion on either side of the lesion site by MslI and Bsp1286I in the absence or the presence of DDB2 (Fig. 1.4d, right panel). Thus, the footprint of PARP-1 around the lesion was not compromised in the presence of DDB2 whereas DDB2 was more stabilized in the presence of PARP-1.

1.5.6. No effect of PARP-1 and DDB2 binding on CPD-photolyase mediated repair of T-T in UV-DNA

Unlike restriction enzymes that cleave the DNA in the sugar phosphate backbone, the CPD photolyase directly removes the cross-linking of adjacent pyrimidines in the CPD photolesions such as T-T [28]. Structural studies have revealed that DDB2 has a protein fold that flips out and maintains contact with T-T [26], and our results indicate that PARP-1 also remains in the vicinity of T-T lesion. Hence, we examined whether binding of DDB2 or PARP-1 to UV-DNA could influence the repair of T-T by CPD photolyase (Fig. 4e). The immunodot-blot of DNA with or without photolyase treatment revealed that binding of DDB2 or PARP-1 to DNA could not inhibit the ability of photolyase to repair the T-T lesions, indicating that these two proteins do not exclude other repair proteins from accessing

the lesion. This is also in agreement with a previous report that binding of DDB2 to UV-DNA does not prevent CPD photolyase from repairing the UV-lesion [29].

1.5.7. Catalytic activation of PARP-1 is stronger with 6-4PP than T-T lesion

We used the model oligos for further characterization of the interaction of PARP-1 with UV-damaged DNA. Since the catalytic activation of PARP-1 is more with damaged DNA than with undamaged DNA [14], we examined the extent of activation of PARP-1 with 40mer control or UV-oligo *in vitro* as an additional indicator of the extent of binding of PARP-1 to these DNA. A stronger PARP-1 activation with UV-DNA was observed as compared to control-DNA at two different molar ratios of PARP-1 to DNA (Fig. 1.5a, left panel). Thus the binding of PARP-1 to UV-lesion caused stronger stimulation of its catalytic activity as compared to its binding to either the 3' or 5'-ends of both the control and UV-DNA. To compare the capacity of different UV-induced direct damages for activation of PARP-1, we assessed the efficacy of 24mer oligo containing a single chemically synthesized T-T or 6-4PP lesion [28] in the PARP-1 activation assay *in vitro* (Fig. 1.5a, right panel). Both the DNA containing defined UV-lesions were stronger activator of PARP-1 than the 24mer control-DNA at two different molar ratios of PARP-1 to DNA. Moreover, 6-4PP, which is known to cause a higher degree of helical distortion, was a stronger stimulator of the catalytic activity of PARP-1 than T-T.

1.5.8. Model for the interaction of PARP-1 and DDB2 with UV-damaged DNA

Based on the current results of *in situ* visualization and footprinting of PARP-1 and DDB2 at UV-induced DNA lesion site, we propose that DDB2 attaches directly at the UV-lesion site whereas PARP-1 makes an asymmetric bilateral contact from -12 to +9nt around the lesion (Fig. 1.5b). This footprint is compatible with either one or two PARP-1 molecules enveloping around the UV-lesion, similar to the reported binding of either one [29] or two [21] PARP-1 molecules binding at the site of DNA strand breaks. The N-terminal DNA binding domain of PARP-1 that is known to be recruited to DNA strand breaks [20] was also recruited to UV-lesions without strand breaks, indicating more general property of this domain of PARP-1 to bind to different types of DNA damages. Our model is also consistent with previously reported interactions of DDB2 and PARP-1 at the UV-lesion site [5, 7]. We have earlier shown that PARP-1 and DDB2 co-immunoprecipitate at the UV-damaged chromatin in the presence of ethidium bromide, indicating their direct interaction on the same DNA strand [7]. Here, we confirm that PARP-1 and DDB2 can co-exist at the UV-lesion site and the presence of DDB2 does not alter the footprint of PARP-1 around the lesion. Our results do not exclude the possibility that PARP-1 footprint may vary when the damaged DNA is in the context of chromatin or when there are multiple UV-lesions in close proximity. We had earlier shown that PARP-1 is

weakly activated by UV in the DDB2-deficient XP-E cells, but introduction of DDB2 in these cells strongly stimulates PARP-1 catalytic activity in response to UV [7]. Moreover, we had also observed that DDB2 stimulates catalytic activity of PARP-1 *in vitro* with UV-damaged DNA that largely contains T-T lesions [7], and here we show that PARP-1 activation was much stronger with 6-4PP than with T-T. Since the 6-4PP by itself causes larger distortion of DNA as compared to T-T, whereas the binding of DDB2 to T-T increases the distortion of DNA [26], collectively these results indicate that the extent of DNA distortion could be the determinant for PARP-1 activation with UV-damaged DNA. Our results show that PARP-1 and DDB2 do not prevent access to the lesion site by other repair proteins such as CPD photolyase, and may even be more flexible and accommodating *in vivo* conditions as compared to our *in vitro* condition in which damaged DNA is anchored to beads and interacting proteins are cross-linked to the DNA. Together, these two novel assays will open new avenues to study the ever-expanding roles of PARP-1 in NER and housekeeping functions in which PARP-1 shows subtle interactions with DNA without strand breaks.

1.6. Figures and legends

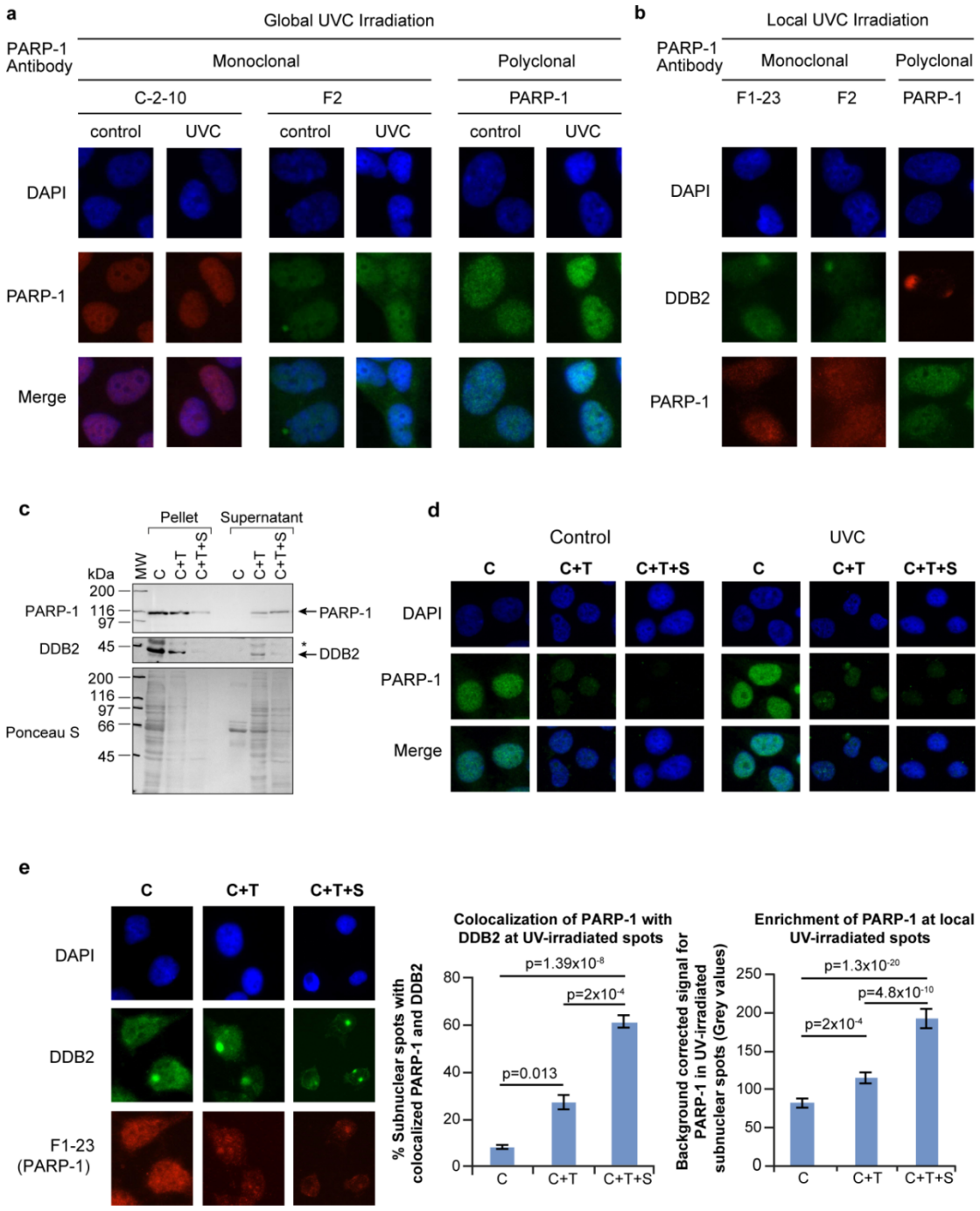

Figure 1.1. *In situ* fractionation to reveal the recruitment of endogenous PARP-1 to UV-induced DNA lesion site

(a-b) Unchanged pattern of nuclear staining for PARP-1 after global or local UVC-irradiation of cells processed with conventional immunocytological techniques. Human skin fibroblasts were exposed either to global (panel a) or local (panel b) irradiation with UVC, fixed with formaldehyde-methanol and probed for PARP-1 (global and local UVC) and DDB2 (local UVC) using specified antibodies. DAPI staining was carried out to define nuclei. (c) Efficiency of extraction of free PARP-1 and DDB2

from adherent control GMU6 cells. The pellets and supernatants obtained from equivalent cell numbers after extraction with CSK buffer (C), CSK+0.5 % Triton (C+T) or CSK + 0.5 % Triton + 0.42 M NaCl (C+T+S) were immunoblotted for PARP-1 and DDB2. The * refers to non-specific signal in DDB2 probing and Ponceau S staining reflected the residual protein content in cell pellets and supernatant at the end of each protocol. (d) Comparison of the efficiency of three protocols for extraction of the endogenous PARP-1 from adherent control and UV-irradiated cells. The GMU6 human skin fibroblasts were globally irradiated with 10 J/m^2 UVC (or control), extracted 10 min later with the three protocols and probed for PARP-1 using polyclonal PARP-1 antibody. (e) Colocalization of endogenous PARP-1 with DDB2 at local UVC-induced DNA damage. GMU6 cells were irradiated locally with 100 J/m^2 and after 10 min subjected to the three protocols (C, C+T and C+T+S) followed by visualization of PARP-1 (F1-23, red) and DDB2 (green). The left chart represents the percent of subnuclear PARP-1 spots that colocalize with DDB2. The right chart represents the quantification of the PARP-1 intensity at the DDB2 spots after subtraction of background signal intensity for PARP-1 from an equivalent area of unirradiated part of the same nucleus. Data of the charts are pooled from three experiments (n = 120 -150 spots, data points are mean ± s.e.).

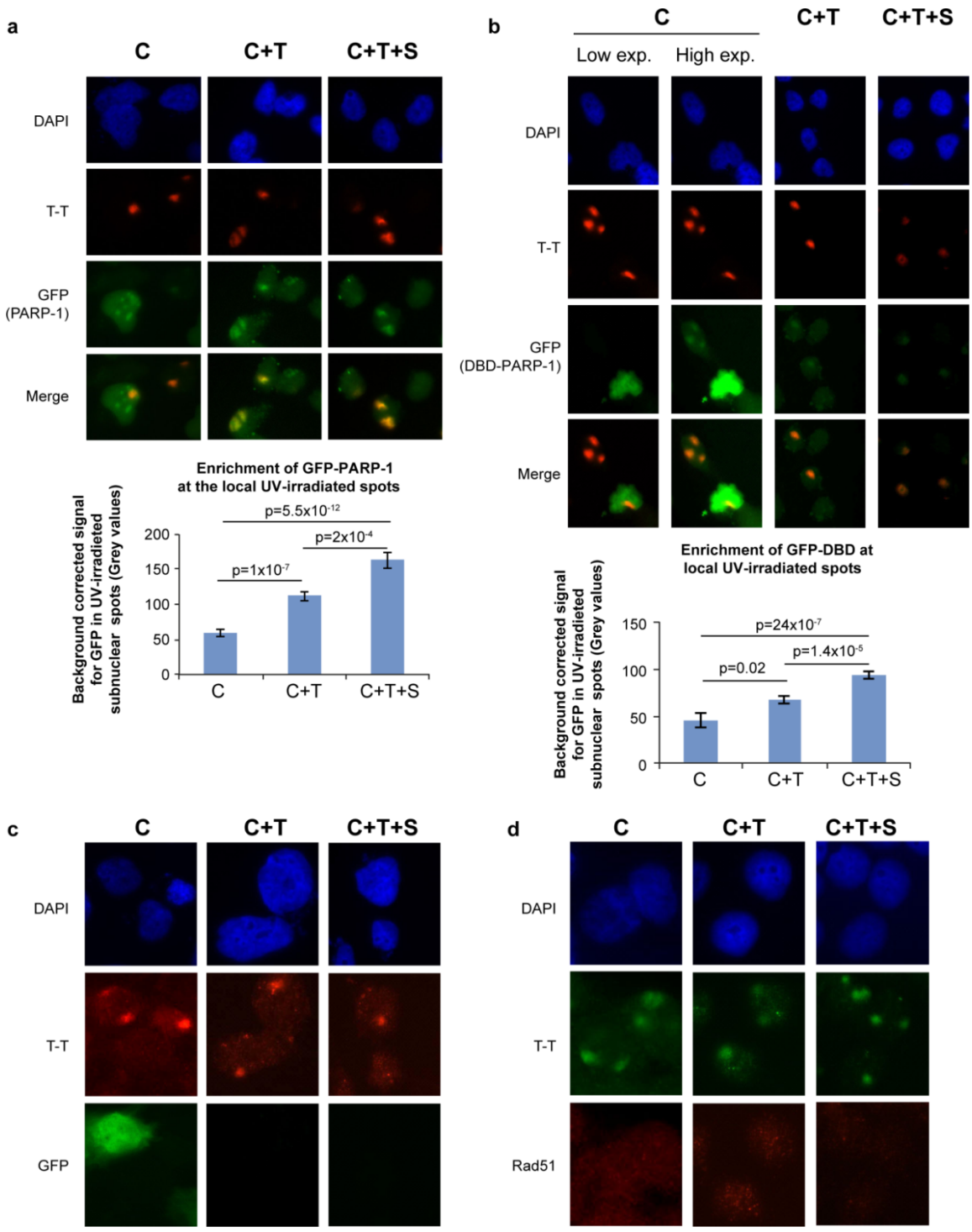

Figure 1.2. In situ fractionation improves detection of exogenous GFP-PARP-1 or its DNA binding domain at local UV-irradiated spots

(a-b) Recruitment of GFP-PARP-1 or its DBD to UV-induced T-T lesions. GMU6 cells were transfected with GFP- PARP-1 or GFP-DBD of PARP-1 for 24 h. The cells were locally irradiated and processed by C, C+T or C+T+S protocols. GFP-PARP-1 or GFP-DBD (green) and T-T (red) were visualized in DAPI-stained nuclei by immunofluorescence microscopy. The charts represent the quantification of GFP intensity for GFP- PARP-1 or GFP-DBD of PARP-1 at the T-T spots after

background correction. (n = 80–150 spots, data points are mean ± s.e.). (c-d) Specificity of in situ extraction protocol: unrelated nuclear proteins (GFP and Rad51) do not colocalize with UV-damaged DNA. GMU6 cells were locally irradiated with 100 J/m2 UVC and subjected 10 min later to in situ fractionation using the three protocols. For panel-c, the cells were transfected with GFP expressing plasmid 24 h before irradiation and protein extraction. The cells were processed for immunofluorescence detection of GFP, Rad51 (green) and T-T (red). DAPI staining was carried out to define nuclei.

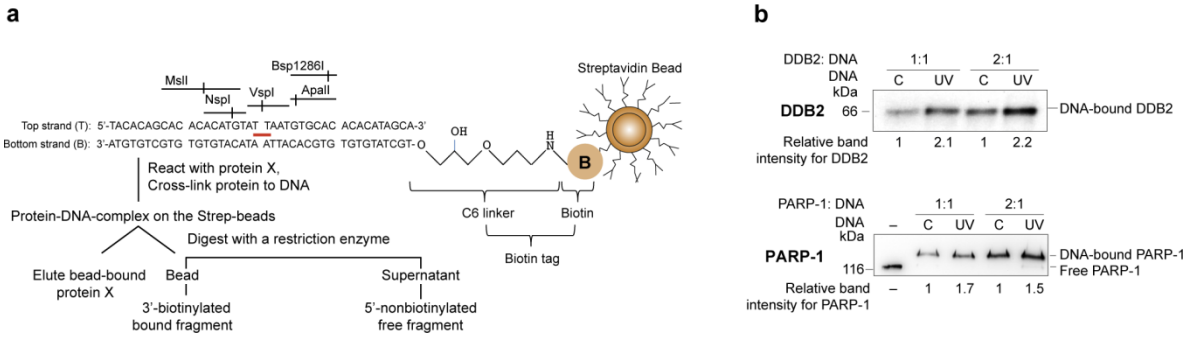

Figure 1.3. Strategy to study binding and footprint of proteins on UV-DNA

(a) The experimental design for determining the extent of binding of proteins to UV-DNA and analyses of protection of DNA during restriction digestion. The control and UV-DNA were immobilized on streptavidin beads via their biotin tag and reacted with purified PARP-1 or DDB2. The unreacted proteins were removed and bound proteins were cross-linked. The beads were then either analysed for bound-proteins by eluting the protein in Laemmli buffer, followed by SDS-PAGE, transfer and probe with specific antibodies or they were subjected to restriction digestion followed by analyses of the released DNA fragments on 10-15 % native PAGE stained with gel red. (b) DDB2 and PARP-1 bind more to UV-DNA than control DNA. PARP-1 and DDB2 were reacted with 50 ng of control or UV-DNA at 1:1 or 1:2 (DNA:protein) molar ratios. The proteins were eluted from the beads, resolved on SDS-PAGE and analyzed by immunoblotting as shown in Fig. 2.3a. The band intensities of protein bound to UV-DNA are shown as relative to signal for protein bound to control DNA.

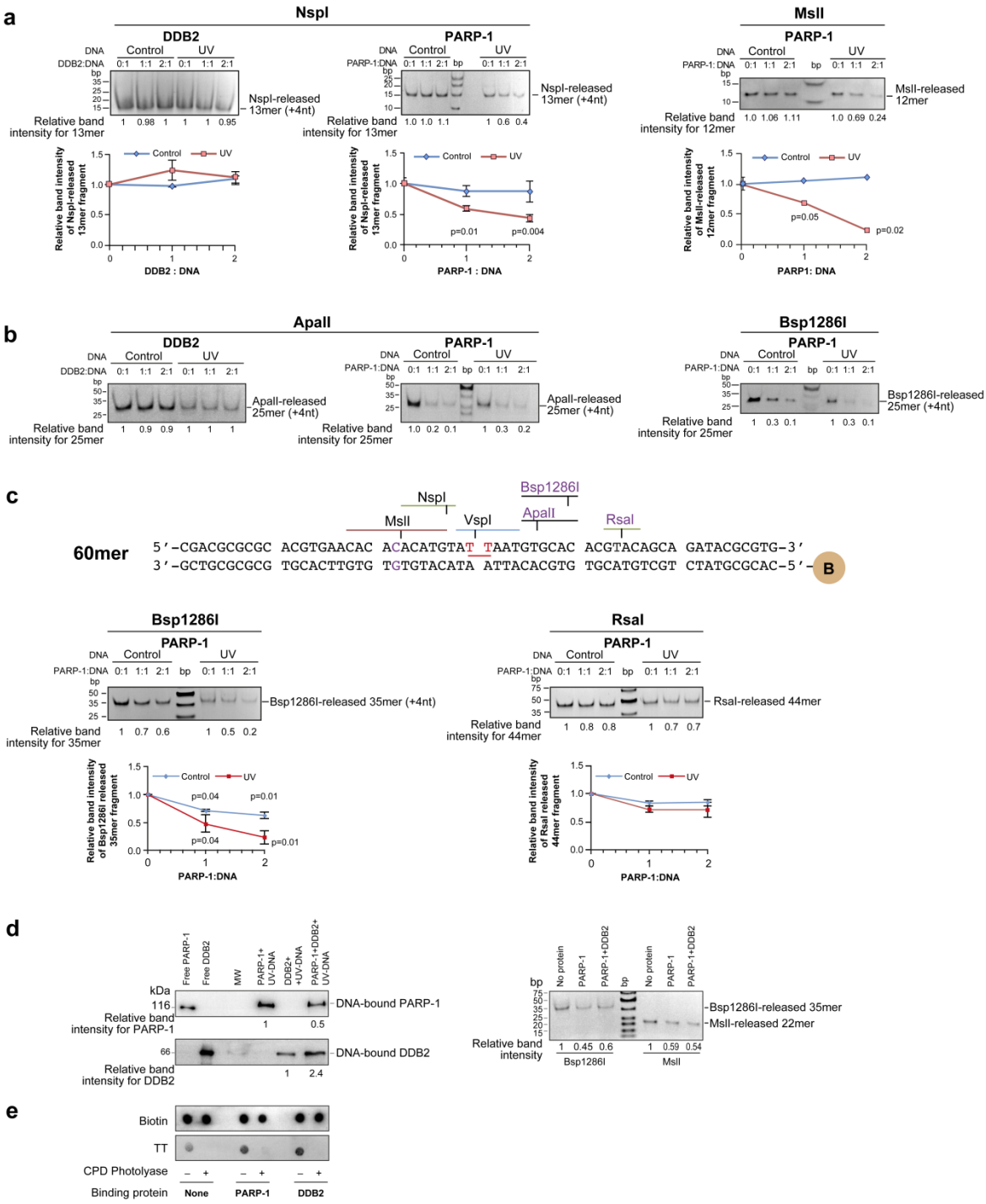

Figure 1.4. Footprinting of PARP-1 and DDB2 at UV-lesion site

(a) Restriction mapping of proteins on the 5'of the UV-lesion on 40mer DNA. 100 ng of bead-bound control or UV-DNA were reacted with DDB2 or PARP-1 at different DNA: protein ratios and digested at 37° C with NspI (30 min) or MslI (15 min). The released 5'-fragments were resolved on 15 % native PAGE and band intensities were measured. Each data point derived from three independent experiments represents mean ± s.d. for relative band intensity from three experiments for the fragment released from protein-bound versus protein-free DNA, with *P* values shown in the

chart. (b) Mapping of proteins on the 3'-side of the UV-lesion on 40mer DNA. The protein-bound DNA was digested with ApaII (60 min) and Bsp1286I (20 min), and released 5'-fragments were resolved on 12 % native PAGE. The data derived from two independent experiments is represented in the chart as described in panel-a. (c) *Top panel*-Structure of 60mer oligo with defined UV-damage. The 60mer oligo sequence was based on 40mer oligo but with a new RsaI site near 3'-end. *Bottom panels*- Restriction mapping of proteins on the 3'-side of the UV-lesion on 60mer DNA. The protein-bound DNA was digested with Bsp1286I (20 min) and RsaI (30 min) and released 5'-fragments were analysed by 12 % native PAGE. The data derived from three independent experiments is represented in the chart as described in panel-a. (d) Simultaneous binding and footprint of DDB2 and PARP-1 on 60mer UV-DNA. PARP-1 and DDB2 were reacted either separately or together with bead-bound UV-DNA (50 ng), at 2:1 molar ratio of protein:DNA. The proteins bound to the beads were detected by immunoblotting (left panels), and footprint of proteins on DNA was examined by restriction digestion with Bsp1286I and MsII (right panels). (e) Repair of T-T by CPD photolyase despite binding of DDB2 or PARP-1 to UV-DNA. Bead-bound 40mer UV-DNA was reacted (or not) with DDB2 or PARP-1, and subjected to repair (or not) by CPD photolyase. The DNA was eluted and immunodot-blotted for T-T. The data represents identical results obtained in three independent experiments.

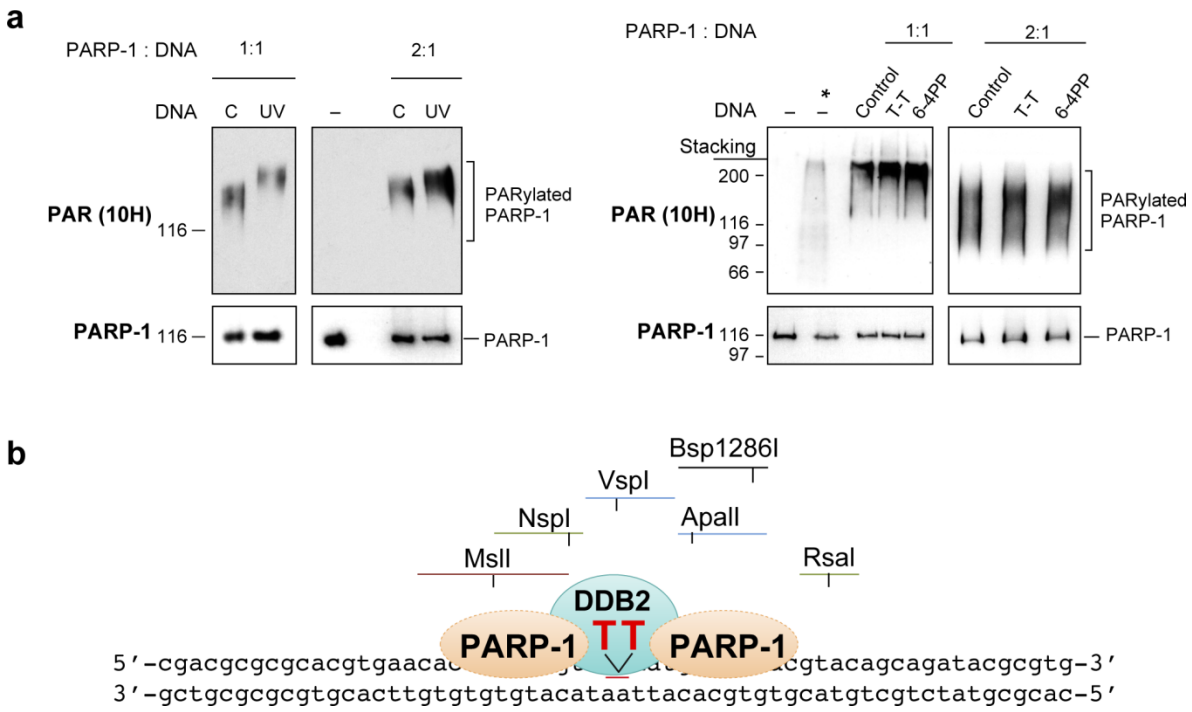

Figure 1.5. Catalytic activation of PARP-1 with defined UV-damaged DNA and a model for footprint of PARP-1 and DDB2 on UV-lesion site

(a) Stimulation of catalytic activity of PARP-1 by various defined UV-damaged DNA *in vitro*. PARP-1 activation assay was performed using 40mer control or UV-DNA (left panel) or using 24mer DNA with no damage (control) or with a single defined T-T and 6-4PP (right panel) at 1:1 or 1:2 molar ratio of DNA:protein. After resolution on SDS-PAGE, immunoprobing for PARP-1 and PARylated PARP-1 (10H antibody) was carried out. The * refers to the cell extract containing H_2O_2-activated PARP-1. Panel represents one of three identical experiments. (b) Model for binding of PARP-1 and DDB2 to the UV-lesion site on 60mer oligo (see Results and Discussion section for details).

1.7. Supplementary figures

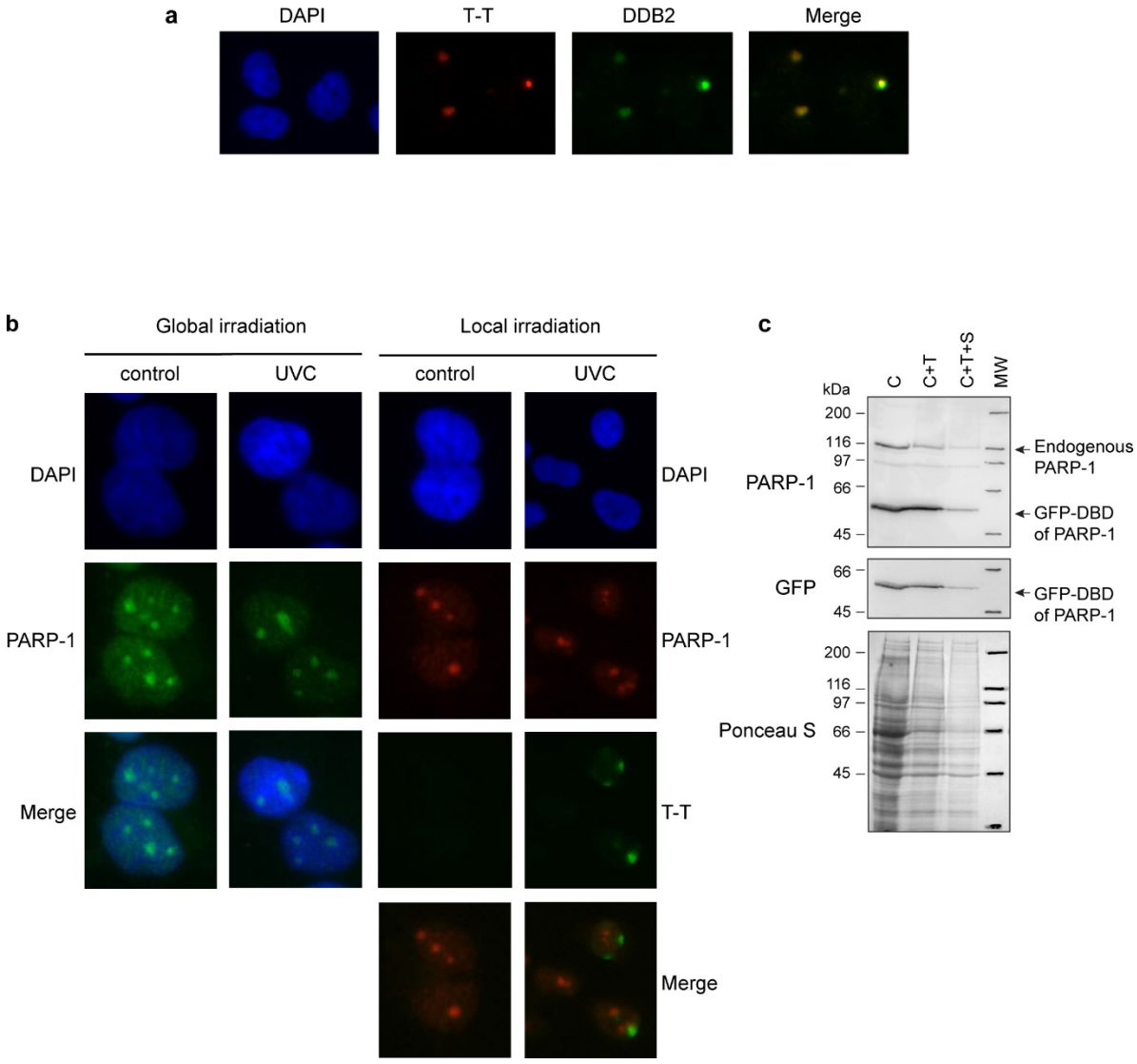

Figure S1.1. Controls for in situ fractionation protocol
(a) DDB2 colocalizes with T-T spots. GMU6 cells locally irradiated with 100 J/m2 UVC were probed after 10 min for DDB2 (green) and T-T (red) in DAPI stained cells. (b) PARP-1 spots after formaldehyde-Triton protocol do not colocalize with T-T. Human skin fibroblasts growing on coverslips were exposed either to global (10 J/m2) or local (100 J/m2) irradiation with UVC and 10 min later fixed with formaldehyde for 10 min followed by 5 min permeabilization with 0.5 % Triton. The globally irradiated cells were probed for PARP-1 (green) and the locally irradiated cells for PARP-1 (red) and T-T (green). The nuclear DNA was stained with DAPI. (c) Verification of the in situ protocol for extraction of GFP-DBD and endogenous PARP-1 in control cells by Western blot. The GMU6 cells were transfected with GFP-DBD of PARP-1 and 24 h later extracted with C, C+T and C+T+S buffers. The cell pellets from equivalent number of cells for each of the three protocols were immunoblotted for GFP and PARP-1. Ponceau S staining reflected the residual protein content in cell pellets at the end of each protocol.

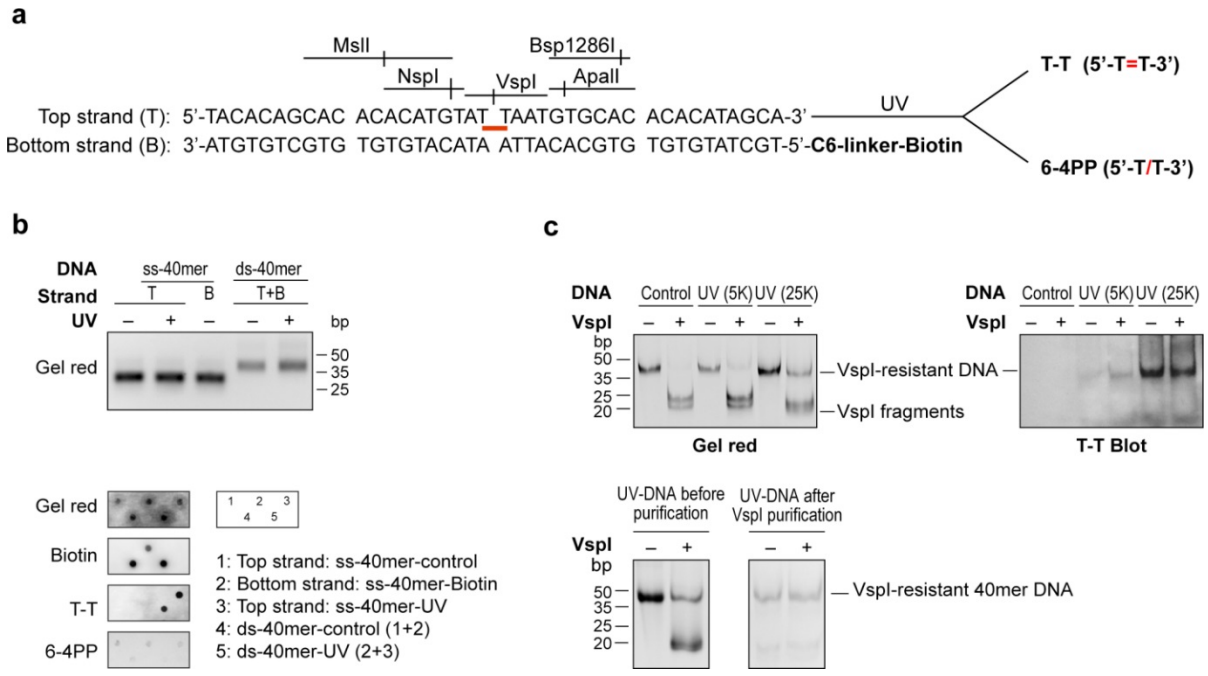

Figure S1.2. Preparation and characterization of double stranded (ds) 40mer DNA
(a) Construction of biotinylated ds 40mer with and without defined T-T. The top single strand (ss) 40mer sequence was designed to carry only one adjacent pair of Ts, and no other pair of pyrimidines, i.e., T or C. The complementary bottom ss 40mer contained a biotin tag at its 5'-end attached via a 6-carbon linker chain. For UV-DNA with defined T-T, the top strand was irradiated in TE at 25,000 J/m^2 UVC at the fluence rate of 51.2 J/m^2/sec in Spectrolinker XL1000. Where specified, top strand was also irradiated with lower UVC-dose (5,000 J/m^2) at the fluence rate of 10 J/m^2/sec. The control and UV-irradiated top ss oligos were annealed with biotin tagged complementary bottom strand to form control and UV ds 40mer oligos, respectively. (b) *Top panel*-The ss 40mer and ds 40mer were verified on agarose gel. *Bottom panel*- 25 ng of the individual ss and the resulting ds 40mer were spotted on charged nylon membrane, and probed for T-T, 6-4PP, biotin and stained with gel red (to indicate the loading of DNA). (c) Enrichment of 40mer UV-DNA using VspI. Top left panel- Control, 5,000 and 25,000 J/m^2 UVC irradiated DNA were digested (37˚ C for 1 hr) with VspI (or undigested) and resolved on 12 % native PAGE. Top right panel- Same as top left, but the native PAGE resolved DNA was transferred on charged nylon membrane for 75 min at 0.2 A (45-60V) and probed for T-T. *Bottom left and right panel*-Purification of T-T containing DNA using VspI digestion. The undigested and VspI-digested 25,000 J/m^2 UV-DNA were run on 12 % native PAGE before (bottom left) and after purification (bottom right).

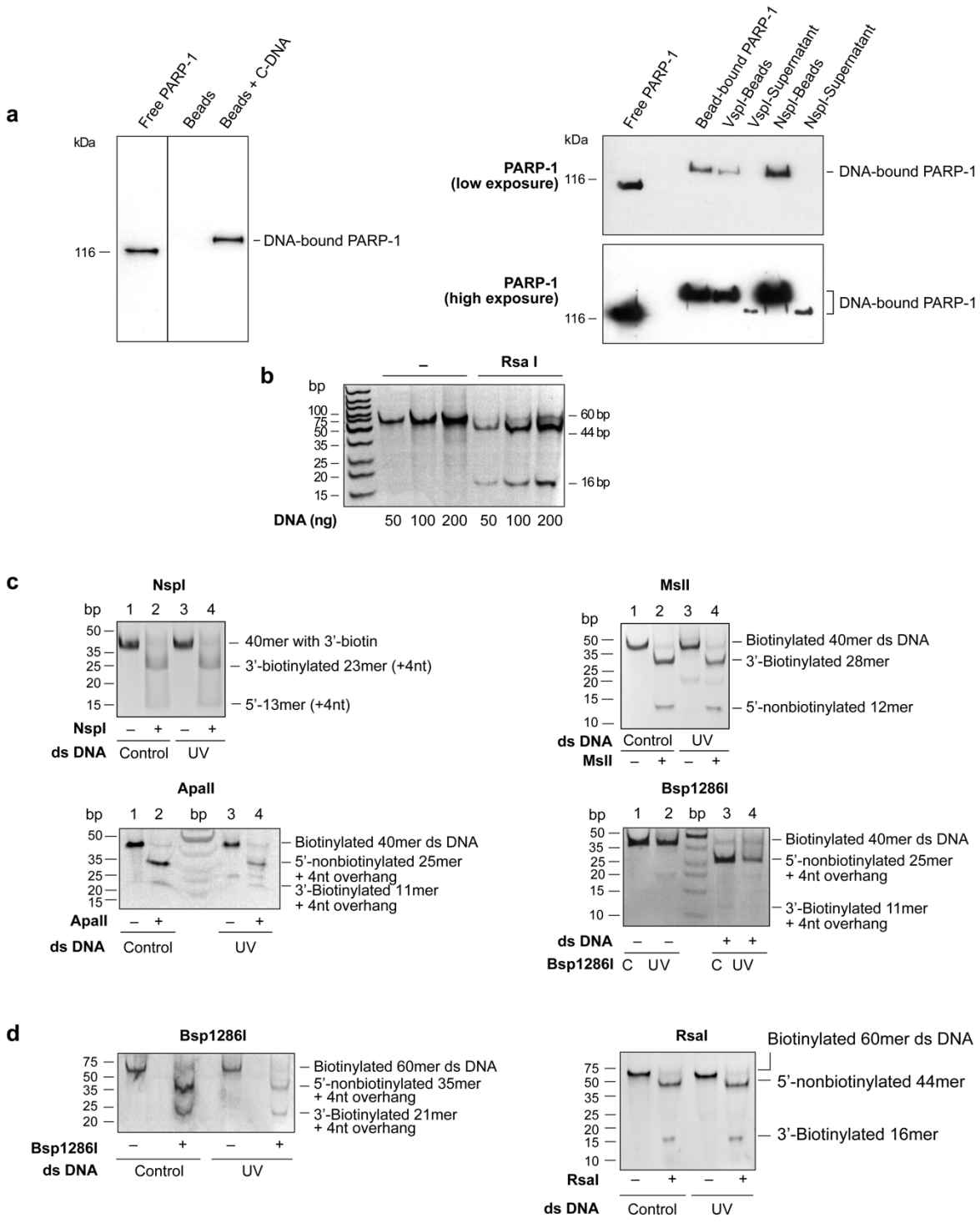

Figure S1.3. Optimization of protein binding and restriction assays with control and UV-DNA
(a) PARP-1 binds to bead-bound 40mer control DNA mainly at 3'-end of oligo and does not bind to streptavidin beads per se. *Left panel*- PARP-1 was reacted with either free streptavidin beads or beads bound to control DNA. The bound-protein was immunoblotted for PARP-1. *Right panel*- Bead-bound control DNA was reacted with PARP-1 and the reaction mixture divided in three equal aliquots. One aliquot was not reacted with any restriction enzyme (bead-bound PARP-1) and other two aliquots

were digested with VspI or NspI. Immunoblotting was carried out to detect PARP-1 that was attached to the bead-bound undigested 40mer, the 5'-restriction fragment of DNA released in the supernatant and 3'-restriction fragment of DNA bound to the beads. (b) Optimization of DNA concentration in restriction digestion assay. The 50-200 ng control 60mer DNA were digested with RsaI and the resulting 3' and 5' DNA fragments were resolved on 15 % native PAGE and visualized using gel red. (c) Digestion of protein-free 40mer control or UV-DNA with different restriction enzymes. Both DNA were digested at 37˚ C with NspI for 30 min (top left panel), MslI for 15 min (top right panel), ApaII for 1h (bottom left panel) and Bsp1286I for 20 min (bottom right panel). The DNA or its fragments recovered from undigested and enzyme digested samples were resolved on native PAGE prior to detection with gel red. (d) Digestion of protein-free 60mer control or UV-DNA with different restriction enzymes. Both the DNA were digested at 37˚ C with Bsp1286I for 20 min (left panel) or RsaI for 30 min (right panel), followed by detection of DNA or its fragments as described above.

1.8. Material and methods

Antibodies: For Western blotting: Monoclonal 6-4PP (KTM50) and T-T (KTM53) (1:5,000), polyclonal PARP-1 (1:5,000), PARP-1 monoclonal (F2, 1:500), GFP monoclonal (1:5,000), DDB2 anti goat (1:500), PAR monoclonal (10H, 1:1,000), HRP-conjugated secondary antibodies (1:2,500). For immunocytology: T-T (KTM53, 1:2,000), polyclonal PARP-1 (1:5,000), PARP-1 monoclonal F2 (1:500), PARP-1 monoclonal C2-10 (1:500), F1-23 monoclonal (1:500), DDB2 anti goat (1:200), Rad51 polyclonal (1:500) and secondary fluorescent antibodies (1:500).

Cell culture: Cells were grown in 5 % humidified incubator at 37º C in □MEM medium supplemented with 10 % FBS, penicillin and streptomycin and 200 µg/ml hygromycin. The creation of GM637-derived PARP-1 replete GMU6 cells were described earlier [30].

Expression Plasmids: The pGFP-hPARP-1 was a gift from V. Schreiber, pGFP-DBD of PARP-1 was generated by subcloning the 0.7 kb SacI (blunted) and HindIII-fragment of PARP31 cDNA into NheI (blunt)/HindIII sites of pEGFP-N1 plasmid.

Transfection and UVC-irradiation: GMU6 cells were transfected with pEGFP-hPARP-1, pEGFP-DBD-PARP-1 and pEGFP-N1 plasmid using Turbofect reagent. After 24 h, cells were irradiated for global UVC (10 J/m^2) or through polycarbonate filter with 5 µm pores for local (100 J/m^2) UVC [11].

Indirect immunofluorescence detection *in situ*: The cells adherent on the coverslip were processed by one of the three protocols: *C protocol:* After washing with CSK buffer (100 mM NaCl, 300 mM sucrose, 10 mM PIPES pH 6.8, 3 mM $MgCl_2$, 1 mM EGTA), cells were fixed with 3 % formaldehyde (10 min, ambient temperature), rinsed with PBS, permeabilized with 100 % methanol (-30º C, 10 min), rinsed with PBS, blocked for 30 min with 5 % BSA in PBS-0.1 % Triton-X-100 followed by reaction with primary antibodies given below. *C+T protocol:* Cells were washed twice with CSK buffer, extracted with 0.5 % Triton in CSK buffer for 8 min at ambient temperature, fixed and blocked as in C protocol. *C+T+S protocol:* After C+T protocol fixation step, cells were washed and extracted with 0.5 % Triton in high salt CSK buffer (420 mM NaCl, 300 mM sucrose, 10 mM PIPES pH 6.8, 3 mM $MgCl_2$, 1 mM EGTA) for 20 min on ice. After DNA denaturation in 0.07 N NaOH for 8 min at ambient temperature, immunoprobing was carried out for all three protocols as follows: The cells were incubated for 1 h with primary antibodies in the blocking buffer, washed with PBS containing 0.1 % Tween 20 and incubated for 30 min with Alexa 488 or 594-linked secondary antibodies. After washing with PBS-0.1 % Tween 20, coverslips were incubated in PBS-0.25 µg/ml DAPI for 5 min and mounted with ProLong Gold Antifade. Images were captured with Zeiss Axiovert 200 and AxioCam MRm and the brightness and contrast were uniformly adjusted across the panels with

Photoshop CS5.5. The fluorescent intensity of PARP-1 at the irradiated spots was analyzed with AxioVision 4.7 and corrected for background signal for similar area in the unirradiated zone of nucleus, where specified.

Statistical analyses for immunocytology: Data for intensity of at least 100 foci from three independent experiments were pooled to create mean $\pm$ s.e., and subjected to the unpaired two-tailed t-tests to determine the significance of difference. The significant *P*-values <0.05 are stated in the charts.

Oligos: The ss-24mer oligos with T-T or 6-4PP were chemically synthesized and hybridized with the complementary ss-24mer to get 24mer ds oligo with T-T or 6-4PP lesions. The creation of 40 or 60mer oligos are described in Figs. 2.3a, 2.4c, and Supplementary Fig. S2.2a.

VspI-purification of 25 kJ/m^2 UVC irradiated oligo: The UVC irradiated 40mer or 60mer ds oligos were digested with VspI for 1 h at 37° C, followed by VspI-inactivation at 65° C for 5 min. The VspI-resistant 40 or 60mer UV-DNA were separated on 12 % PAGE from the digested fragments of DNA without UV-damage, cut from the gel and eluted with PAGE elution buffer (0.5 M ammonium acetate, 10 mM magnesium acetate and 1 mM EDTA) overnight at 37° C. The eluted UV-DNA were cleaned by passage through ULTRAFREE–DA filter units, concentrated in Microcon YM-10 followed by purification in Zymo Research oligo clean and concentrator columns.

The protein-DNA interactions, restriction mapping and CPD photolyase assays for bead-bound oligos with proteins: The control or UV-DNA with biotin tag was immobilized on Dynabeads MyOne streptavidin T1. (i) The binding of PARP-1 or DDB2 to control or UV-oligos immobilized on the magnetic streptavidin beads: The bead-bound oligos (50-100 ng) were reacted with PARP-1 or DDB2 at 1:1 or 1:2 molar ratio. PARP-1 was reacted at 25° C for 15 min in 10 µL of Na-PO_4 reaction mixture (20 mM of Na-PO_4 buffer pH 7.4, 5 mM $MgCl_2$, 150 mM NaCl, 5 % glycerol, 1 mM DTT, 0.01 % Triton, 20 µM Zn-acetate and 1X protease inhibitor). DDB2 was reacted at 25˚ C for 30 min in Tris reaction mixture (100 mM Tris buffer pH 8.0, 10 mM $MgCl_2$, 10 % glycerol, 150 mM NaCl, 1.5 mM DTT and 1X protease inhibitor). The simultaneous binding of PARP-1 and DDB2 was carried out in Tris reaction mixture for 15 min at 25˚ C. The unbound proteins were removed and the bound proteins were crosslinked to oligo with 1 % formalin in Na-PO_4 reaction mixture for 10 min at ambient temperature. After quenching formalin with 250 mM Tris-HCl pH 8.0, the beads were washed twice with Tris-reaction mixture and subjected to following steps.

(ii) Assessment of binding of proteins with DNA: The proteins that were attached to bead-bound DNA were extracted with Laemmli buffer at 95° C for 10 min. The eluted proteins were resolved on

SDS-PAGE for immunoblotting of the protein. The band quantification for immunoblots was carried out with ChemiGenius 2 using SynGene software.

(iii) Restriction protection assay of protein-bound oligos: For the restriction protection assay, the magnetic streptavidin beads bound control or UV-DNA with or without bound protein were digested with the specified Fast-digest or CutSmart restriction enzyme in 10 µL reaction buffer at 37° C for specified time. The DNA fragments released in the supernatant were resolved on 10-15 % native PAGE and stained with gel red for identification and quantification with ChemiGenius2 using SynGene software. The relative band intensities were derived by comparing the intensities of the fragments released from the protein-bound DNA with that from protein-free DNA. The significance was calculated by unpaired two-tailed t-test and the *P* values <0.05 were considered significant.

(iv) CPD photolyase repair assays: The bead-bound UV-DNA with or without attached proteins was split into two aliquots; one subjected to repair by CPD photolyase and the other was mock-treated. The CPD repair was carried out in 20 µL CPD photolyase binding mix (20 mM Tris buffer pH 7.5, 1 mM DTT, 0.2 mg/ml BSA, 125 mM NaCl) with 0.2 µL Oryza sativa CPD photolyase and incubated for 15 min in dark at ambient temperature, followed by exposure for 15 min to UVA (Spectrolinker XL-1500, 363 nm, 15 watts). DNA was eluted with 95 % formamide, 10 mM EDTA pH 8.0 for 5 min at 95° C, dot-blotted on the Hybond N^+ and probed for T-T.

PARP-1 activation assay *in vitro* : In a 10 µL reaction mixture containing 100 mM Tris-HCl pH 8.0, 10 mM $MgCl_2$, 10 % glycerol, 1.5 mM DTT, 1X protease inhibitor and 10 µM NAD, purified PARP-1 was reacted at 25° C for 30 min with specified DNA for each reaction. After adding an equal volume of 2X Laemmli buffer, samples were resolved on SDS-PAGE and immunoblotted for PAR (10H) and PARP-1 [14].

Immuno-Dot-blot: DNA samples were heated at 95° C for 5 min, chilled on ice for 5 min and adjusted to final concentration of 6X SSC. Samples were dot-blotted on Hybond N+ membrane, baked at 80° C for 1-2 h and processed for antibody probing.

1.9. References

1. Robert, I., et al., Functional aspects of PARylation in induced and programmed DNA repair processes: Preserving genome integrity and modulating physiological events. Mol. Aspects Med., 2013. **34**(6): p. 1138-52.

2. Pascal, J.M. and T. Ellenberger, The rise and fall of poly(ADP-ribose): An enzymatic perspective. DNA Repair (Amst), 2015. **32**: p. 10-16.

3. Kim, M.Y., et al., NAD+-dependent modulation of chromatin structure and transcription by nucleosome binding properties of PARP-1. Cell, 2004. **119**(6): p. 803-14.

4. Ghodgaonkar, M.M., et al., Depletion of poly(ADP-ribose)polymerase-1 reduces host cell reactivation for UV-treated adenovirus in human dermal fibroblasts. DNA Repair (Amst), 2008. **7**: p. 617-632.

5. Pines, A., et al., PARP1 promotes nucleotide excision repair through DDB2 stabilization and recruitment of ALC1. J. Cell Biol., 2012. **199**(2): p. 235-49.

6. Luijsterburg, M.S., et al., DDB2 promotes chromatin decondensation at UV-induced DNA damage. J. Cell Biol., 2012. **197**(2): p. 267-81.

7. Robu, M., et al., Role of poly(ADP-ribose) polymerase-1 in the removal of UV-induced DNA lesions by nucleotide excision repair. Proc. Natl. Acad. Sci. U.S.A. , 2013. **110**(5): p. 1658-1663.

8. King, B.S., et al., Poly(ADP-ribose) contributes to an association between Poly(ADP-ribose)polymerase-1 and Xeroderma pigmentosum complementation group A in nucleotide excision repair. J. Biol. Chem., 2012. **287**: p. 39824-33.

9. Fischer, J.M., et al., Poly(ADP-ribose)-mediated interplay of XPA and PARP1 leads to reciprocal regulation of protein function. FEBS J., 2014. **281**(16): p. 3625-41.

10. Maltseva, E.A., et al., Poly(ADP-ribose)polymerase 1 Modulates Interaction of the Nucleotide Excision Repair Factor XPC-RAD23B with DNA via Poly(ADP-ribosyl)ation. J. Biol. Chem., 2015. **290**(36): p. 21811-20.

11. Vodenicharov, M.D., et al., Mechanism of early biphasic activation of poly(ADP-ribose) polymerase-1 in response to ultraviolet B radiation. J. Cell Sci., 2005. **118**(Pt 3): p. 589-99.

12. Berger, N.A. and G.W. Sikorski, Poly(adenosine diphosphoribose) synthesis in ultraviolet-irradiated xeroderma pigmentosum cells reconstituted with Micrococcus luteus UV endonuclease. Biochemistry, 1981. **20**(12): p. 3610-4.

13. Kawamitsu, H., et al., Monoclonal antibodies to poly(adenosine diphosphate ribose) recognize different structures. Biochemistry, 1984. **23**: p. 3771-3777.

14. Shah, G.M., et al., Approaches to detect PARP-1 activation in vivo, in situ, and in vitro. Methods Mol. Biol., 2011. **780**: p. 3-34.

15. Mirzoeva, O.K. and J.H. Petrini, DNA damage-dependent nuclear dynamics of the Mre11 complex. Mol. Cell. Biol., 2001. **21**(1): p. 281-8.

16. Balajee, A.S. and C.R. Geard, Chromatin-bound PCNA complex formation triggered by DNA damage occurs independent of the ATM gene product in human cells. Nucleic Acids Res., 2001. **29**(6): p. 1341-51.

17. Zhu, Q., et al., Chromatin restoration following nucleotide excision repair involves the incorporation of ubiquitinated H2A at damaged genomic sites. DNA Repair, 2009. **8**(2): p. 262-73.

18. Fey, E.G., K.M. Wan, and S. Penman, Epithelial cytoskeletal framework and nuclear matrix-intermediate filament scaffold: three-dimensional organization and protein composition. J. Cell Biol., 1984. **98**(6): p. 1973-84.

19. Kaufmann, S.H., et al., Association of poly(ADP-ribose) polymerase with the nuclear matrix: the role of intermolecular disulfide bond formation, RNA retention, and cell type. Exp. Cell Res., 1991. **192**(2): p. 524-35.

20. Mortusewicz, O., et al., Feedback-regulated poly(ADP-ribosyl)ation by PARP-1 is required for rapid response to DNA damage in living cells. Nucleic Acids Res., 2007. **35**(22): p. 7665-75.

21. Ali, A.A., et al., The zinc-finger domains of PARP1 cooperate to recognize DNA strand breaks. Nat. Struct. Mol. Biol., 2012. **19**(7): p. 685-92.

22. Hall, R.K. and L.L. Larcom, Blockage of restriction endonuclease cleavage by thymine dimers. Photochem. Photobiol., 1982. **36**(4): p. 429-32.

23. Cleaver, J.E., Restriction enzyme cleavage of ultraviolet-damaged simian virus 40 and pBR322 DNA. J. Mol. Biol., 1983. **170**(2): p. 305-17.

24. Wittschieben, B.O., S. Iwai, and R.D. Wood, DDB1-DDB2 (xeroderma pigmentosum group E) protein complex recognizes a cyclobutane pyrimidine dimer, mismatches, apurinic/apyrimidinic sites, and compound lesions in DNA. J. Biol. Chem., 2005. **280**(48): p. 39982-9.

25. Clark, N.J., et al., Alternative modes of binding of poly(ADP-ribose) polymerase 1 to free DNA and nucleosomes. J. Biol. Chem., 2012. **287**(39): p. 32430-9.

26. Fischer, E.S., et al., The molecular basis of CRL4DDB2/CSA ubiquitin ligase architecture, targeting, and activation. Cell, 2011. **147**(5): p. 1024-39.

27. Menissier-de Murcia, J., et al., Zinc-binding domain of poly(ADP-ribose)polymerase participates in the recognition of single strand breaks on DNA. J. Mol. Biol., 1989. **210**(1): p. 229-33.

28. Hendel, A., et al., Reduced efficiency and increased mutagenicity of translesion DNA synthesis across a TT cyclobutane pyrimidine dimer, but not a TT 6-4 photoproduct, in human cells lacking DNA polymerase eta. DNA Repair (Amst), 2008. **7**(10): p. 1636-46.

29. Langelier, M.F. and J.M. Pascal, PARP-1 mechanism for coupling DNA damage detection to poly(ADP-ribose) synthesis. Curr. Opin. Struct. Biol., 2013. **23**: p. 134-43.

30. Shah, R.G., et al., DNA vector-based RNAi approach for stable depletion of poly(ADP-ribose) polymerase-1. Biochem Biophys Res Commun, 2005. **331**(1): p. 167-74.

1.10. Acknowledgements

We are thankful to V. Schreiber for GFP-PARP-1, K. Hitomi for the CPD photolyase and J. Brind'Amour for creating cDNA for GFP-DBD. We thank M. Miwa, National Cancer Center Research Institute, Tokyo, for permission to receive 10H hybridoma through the Riken cell bank. This work was supported equally by the two grants to GMS: Discovery Grant 155257-2011 from NSERC, Canada and Grant IMH-131569 from the Canadian Institutes of Health Research: Priority Announcement of Musculoskeletal Health, Arthritis, Skin and Oral Health. The work related to the site-specifically modified oligonucleotides was supported by the National Institutes of Health Grant CA-168469 to NEG. NP received the scholarship support from Quebec Government and Shastri Indo-Canadian Institute from foreign student fee waiver program and MR received graduate scholarship from the Fonds de recherche du Québec-Santé.

Author contributions statement

The first three authors (NKP, MR and RGS) contributed equally to performing all the experiments and preparing the figures. NEG provided material support and guidance in planning the experiments with synthetically defined UV-damaged oligo. All authors contributed towards writing and reviewing the manuscript.

Competing Financial Interest Statement: The authors declare no competing financial interests.

Chapter 2. Comprehensive Measurement of UVB-Induced Non-Melanoma Skin Cancer Burden in Mice using Photographic Images as a Substitute for the Caliper Method

Marc Bazin[1], Nupur K. Purohit[1], and Girish M. Shah[1]*

[1]Laboratory for Skin Cancer Research, CHU-Q (CHUL) Quebec University Hospital Research Centre, Laval University, Québec (QC), Canada

Short Title: Measurement of skin tumor burden by photographic method

*To whom correspondence should be addressed.

Email: girish.shah@crchul.ulaval.ca (GS)

2.1. Preface

Soon after the initiation of the protocol for studying the role of PARP1 in UVB-induced SCC tumorigenesis, I realized that it was not only important to carefully measure the number and the dimensions of the developing tumors on the mouse skin, but also to note the site of the tumor so that each of them can be individually followed throughout the protocol. Intuitively, I came up with a method of carefully mapping the site of tumors each week on the sheet of paper bearing mouse diagram while measuring the dimensions of tumor with vernier caliper. Later on, we realized that similar method was also employed by the pioneers of the photocarcinogenesis studies in the SKH-1 mice. However, this method is tedious, time-consuming and stressful for the animals as well as the operator when used for measuring multiple tumors in a large number of animals, which was the case in our protocol. Upon explaining this problem to my physicist colleague and the first author of this article, Dr. Marc Bazin (published in January 2017 in the journal PLoS One, and is available in PDF format in Annexe 4), he devised a photographic technique that allowed us to not only record the course of tumor development on individual mice during the protocol but also measure the dimensions of tumors from this photographs. For this article, I contributed for the tumor data collection presented in the all the tables 2.1-3, supplementary tables S2.1-3 as well as in the graph of Fig. 2.2B. I also participated in editing manuscript and figures. This technique of Dr. Marc Bazin has allowed us to procure and analyze the tumor measurement data in various ways as presented in chapter 3 and 4 of this thesis.

2.2. Résumé

Le vernier est la méthode de référence pour mesurer la longueur, la largeur et la hauteur de tumeurs cutanées afin de calculer leur surface et leur volume. Cette méthode simple pour collecter des données sur quelques tumeurs devient fastidieuse et stressante pour les animaux et le manipulateur quand il s'agit de mesurer un grand nombre de tumeurs sur de multiples animaux dans certains protocoles, comme celui des cancers de la peau de type non-mélanome chez les souris SKH-1. Dans cet article, nous avons démontré que les photographies de ces souris prises en condition optimale en quelques minutes peuvent être soumises à une analyse par logiciel pour déterminer le volume et la surface de tumeurs avec la même précision que la méthode vernier. A l'inverse du vernier, la méthode par photographie permet également de calculer l'incidence et la multiplicité des tumeurs permettant ainsi une mesure complète de la charge tumorale chez l'animal. La simplicité et l'aisance de cette méthode permet un contrôle plus fréquent de la charge tumorale tout au long du protocole, résultant en la création de données supplémentaires sur la progression du cancer ou l'efficacité des interventions thérapeutiques. Cette méthode photographique peut substituer la méthode vernier pour quantifier des pathologies cutanées.

2.3. Abstract

The vernier caliper has been used as a gold standard to measure the length, width and height of skin tumors to calculate their total area and volume. It is a simple method for collecting data on few tumors at a time, but becomes tedious, time-consuming and stressful for the animals and the operator when used for measuring multiple tumors in a large number of animals in protocols such as UVB-induced non-melanoma skin cancer (NMSC) in SKH-1 mice. Here, we show that photographic images of these mice taken within few minutes under optimized conditions can be subjected to computerized analyses to determine tumor volume and area as accurately and precisely as the caliper method. Unlike caliper method, the photographic method also records the incidence and multiplicity of tumors, thus permitting comprehensive measurement of tumor burden in the animal. The simplicity and ease of this method will permit more frequent monitoring of tumor burden in long protocols, resulting in creation of additional data about dynamic changes in progression of cancer or the efficacy of therapeutic intervention. The photographic method can broadly substitute caliper method for quantifying other skin pathologies.

2.4. Introduction

In mouse models that examine the causes and cures of chronic ultraviolet B (UVB)-induced non-melanoma skin cancers (NMSC), the tumor burden is quantified as the incidence (proportion of mice with or without tumor), multiplicity (number of tumors), tumor area and tumor volume [1-7]. While the first two parameters are visually noted and recorded, the last two parameters are measured using the vernier caliper, which is a simple yet accurate instrument to manually measure the length, width and height of tumors. The use of digital calipers with 0.01 mm accuracy is perfect for collecting data for one or two tumors per animal and for few animals at a time. However, it becomes time-consuming and challenging for measuring dimensions of hundreds of tumors. For example, the chronic UVB-irradiated SKH-1 albino hairless mice develop numerous papillomas, keratocanthomas, carcinomas-in-situ and carcinomas over a period of 10-40 weeks; and caliper method would take 5-30 min per mouse and several days for each cycle of measurement for a large number of mice. Moreover, the repetitive and tedious nature of this work and stress-related movements of forcibly restrained mice increase the chances of errors in caliper measurement. Therefore, although frequent measurement of tumor dimensions throughout the NMSC protocol would provide valuable information about the dynamic state of the disease, few studies report weekly or biweekly measurement of tumor volume [2,3], while most studies measure tumor volume only at the end of the protocol [4-7]. Some studies do not measure smaller tumors [1,8] or height of the tumors [1,9], while others do not report any measurement of tumor size but only the incidence [10]. All these studies produced valid data, but availability of a convenient yet accurate and reproducible alternative to caliper method would permit frequent measurement of tumor area and volume revealing more information about the disease.

In subcutaneous tumor models, the magnetic resonance imaging [11] or ultrasound imaging [12] were shown to be more accurate in measuring tumor volume than caliper method. However, these techniques would be expensive, require each mouse to be anesthetised and impractical for NMSC protocol with large number of mice. In studies related to healing of skin wounds, the area measurements are made with a foot-ruler or tracing of wound shapes on transparent sheets with a grid and scale-pattern, or by spectrophotogrammetry or spectrophotography methods that use multiple cameras or video-camera with customized software in a special equipment [13-16]. For NMSC measurement, the transparency method would not save much time over caliper method, and photo or videography-based methods would be costly and perhaps even more time consuming than caliper method. Nonetheless, the photographic methods were more accurate in measurement of wound area, and an earlier NMSC study reported use of photography to determine tumor area [9], although the technique was not validated with caliper method, and it did not report tumor volume possibly because

height could not be measured in their technique. Here, we provide detailed description of a fully validated simple photography method that allows measurement of area and volume of skin tumors as accurately as the caliper method, while avoiding potentially error-inducing limitations of the caliper method. This method also permits measurement of the incidence and multiplicity of tumors, thus providing a comprehensive method to measure tumor burden in UVB-induced NMSC protocols, and could broadly substitute caliper method for quantifying other skin pathologies.

2.5. Results

2.5.1. Photographic method accurately reflects caliper method for total tumor burden in terms of area and volume per mouse

In a single mouse with 30 tumors of different sizes, the photographic and caliper methods were used for measuring length, width and height of each tumor (Fig 2.1A). Evidently, the top picture of the mouse enlarged on the computer screen allowed us to note the tumor incidence and identify and count tumor multiplicity. The three dimensions of each tumor were used for determining total tumor volume and area by each method. Both the methods produced statistically similar values for total tumor burden, measured as total area or volume of all the tumors in the mouse (Tables 2.1 and S2.1). To examine whether photographic method was accurate for all sizes of tumors, we sorted these tumors by volume as small (<2 mm^3) or large (>2 mm^3); and observed that the photography and caliper methods once again produced statistically similar total collective volume or area for small or large size tumors (Table 2.1, bottom panel). We noted that volume of individual smaller tumors often differed significantly between two methods because of differences in height rather than length or width values (S2.1 Table). This could be attributed to approximation of heights assigned to smaller tumors below 0.5 mm in caliper method (see Materials and Methods), whereas the photographic method using enlarged images allowed precise determination of heights below 0.5 mm. Nonetheless, the global impact of the differences in heights of smaller tumors by two methods was negligible to the total tumor burden on the mouse, which is mostly determined by larger tumors. Thus, photographic method allowed measurement of all four parameters of tumor burden, namely the incidence, multiplicity, area and volume, with last two parameters accurately reflecting the values obtained by the caliper method.

The individual volume and area measurements of 30 tumors were derived from the data of all three dimensions of each tumor by both the methods as shown in S2.1 Table. The small and large tumors (2 mm cut-off by caliper volume) are separated by a double-line. The two methods were compared for measuring the total volume or area for all (n = 30), small (n = 24) or large (n = 6) tumors. The statistical significance of difference between two methods was calculated using Wilcoxon signed rank test.

To confirm our observation that the tumor dimensions measured by photographic method are comparable to those measured by caliper; we examined total tumor area in five additional mice by both the methods. The mice had variable tumor area that ranged from 34 to 200 mm^2. Once again the

photography method produced statistically similar tumor burden data as the caliper method for each mouse (Table 2.2 and S2.2 Table).

Total tumor area for 6 mice was calculated from the length and width of all tumors measured by the caliper and photographic methods. The data for individual tumors in each mouse is shown in S2.2 Table. The differences between two methods for total tumor burden varied from 0.05-6.5%, but it was statistically not different, as determined by Wilcoxon signed rank test.

Finally, we compared the two methods for measuring the changes in total tumor burden in three mice over a period of six weeks (Fig 2.2B). Although the total tumor area changed in each mouse by 5-7 fold from 20^{th} to 25^{th} week, both the methods produced similar values for total tumor burden at three different time-points in this period. Thus the photography method produced total tumor burden data similar to the caliper method in multiple mice carrying different sizes of tumors and for assessing growth of the same set of tumors over several weeks in a given mouse.

2.5.2. Accuracy and precision of photography and caliper methods

Next, we compared the accuracy and precision of photography and caliper method by taking 10 replicate measures of the length of a small tumor (~1 mm) and a medium size tumor (~5 mm) by two methods (Table 2.3 and S2.3 Table). The average length from 10 measurements by photography method accurately reflected within 1% the average length derived by the caliper method. The precision of a method refers to the reproducibility of result in repeated measurements, and this is derived from relative standard deviation of replicate values (SD / mean × 100) with lower value showing greater precision. The relative standard deviation values revealed that measurements by both the methods were less precise with smaller tumors as compared to larger tumors. Interestingly, the photography method showed better precision than the caliper method for both 1 and 5 mm dimensions. In summary, if caliper is the gold standard for measurement of tumor dimensions, then photography method accurately and precisely measures the true dimensions of the tumors.

The length of a small and medium size tumors were measured 10 times by the same operator under optimum conditions, and averages shown here were derived from the dataset shown in S2.3 Table. Accuracy of photography method was reflected in providing average length value that is very close to the mean obtained by the caliper method. The precision was derived from the relative standard deviation of repeat measures (SD as % of mean value), which decreases when precision increases.

2.6. Discussion

Our results clearly show that the photographic method is simple, cheap and accurate alternative to the caliper method for measuring tumor burden in terms of area and volume of all sizes of NMSC. In addition, the photographs allow measurement of the incidence as well as multiplicity of tumors, thus providing a comprehensive measure of tumor burden in the animal. Most importantly, our photography method allows measurement of the tumor height and therefore the tumor volume. Since height of NMSC often indicates its degree of progression, measuring the actual height of each tumor has an advantage of integrating the severity of cancer in the volume data. The biggest advantage of photography method is that it splits the total task of caliper method in two distinct components. The first one involves handling of the animals to collect raw data in the form of pictures which are taken within few minutes; while the second task of tumor dimension measurement is handled away from the animals and using computerized methods which can be performed at any other time by the operator who handled the animal or by anybody else with computer skills. Thus, a quick photo session is less stressful to the animal and decreases the operator fatigue. Moreover, the photography method offers more reproducibility and accuracy than the caliper method in volume measurement of even smaller tumors with heights below 0.5 mm. In our experience, the operators who are properly trained in both the methods are able to generate unbiased data for total tumor volume or area from multiple tumors that differ by less than 5% between two methods for each mouse. Thus, while being as accurate as the caliper method, photographic method avoids major error-inducing factors of caliper method even when used for measuring the tumor burden in a large number of animals.

The photography method offers additional advantages, such as reducing the cost associated with using the animal house facilities during long hours of caliper measurement in time-shared laminar flow cabinets. The splitting of tasks for animal handling for picture session and computerized measurement of tumor dimensions permits better work distribution and time-management among personnel with animal and computer skills. Most importantly, the photographs serve as a permanent record of data for regulatory purposes, and could be subjected to repeated analyses for verification or correction of data, as well as for any additional analyses in future. A series of weekly photographs during the protocol could provide useful data for determining the growth rate of tumors from pre-neoplastic foci to full tumors or for regression of tumors in response to therapy. Among few limitations of photography method is the need for a skilled photographer and a well-trained person in computer skills for dimension measurement, as well as the creation of simple photography set-up in the animal facility. In view of its simplicity, the photography method would also be suitable for quantification

of skin lesions in the models of melanoma, subcutaneous tumors, wound healing, inflammatory responses and other pathologies of skin.

2.7. Figures and legends

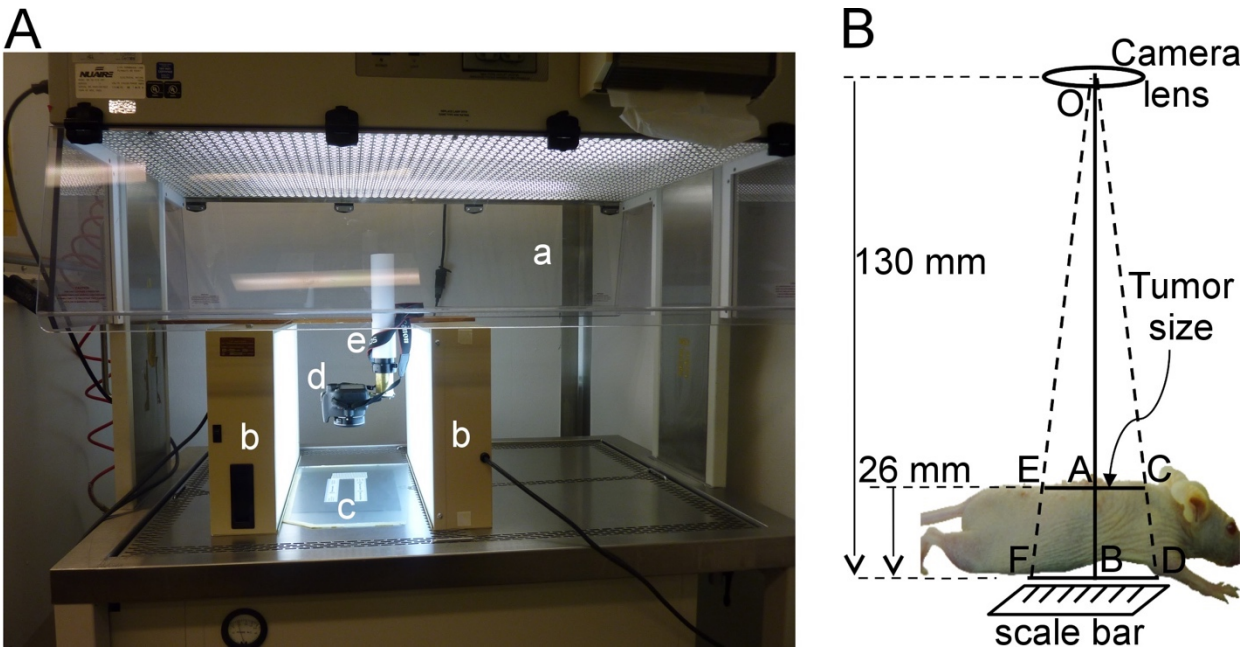

Figure 2.1. The optimized photography set-up for imaging mice
(A) The photography set-up. In a laminar flow cabinet with dual opening (a), illuminated by two additional fluorescent lights on the side (b), mice were placed one at a time on a frosted glass plate with a broad-grid fabric tape that was positioned above black paper and two scale bars (c). The remote shutter controlled camera (d) was positioned 130 mm above the glass plate on a telescopic support (e). (B) Representation of the imaging set-up with distances. The camera lens (O) was placed 130 mm above the glass plate, which resulted in a height difference of 26 mm between the scale bar below the glass plate (BD) and tumor (AC) on the dorsal skin of the mouse from the camera lens. The length or width dimension of the tumor (AC) was calculated using Thales' theorem to determine the scale factor of OA/OB =0.8=AC/BD. Since tumors were distributed broadly over the dorsal skin of the mouse, each tumor was carefully calibrated against the nearest portion of the scale bar for better accuracy of measurement. For example, the tumors in EC region of the skin were calibrated against FD segment of the scale.

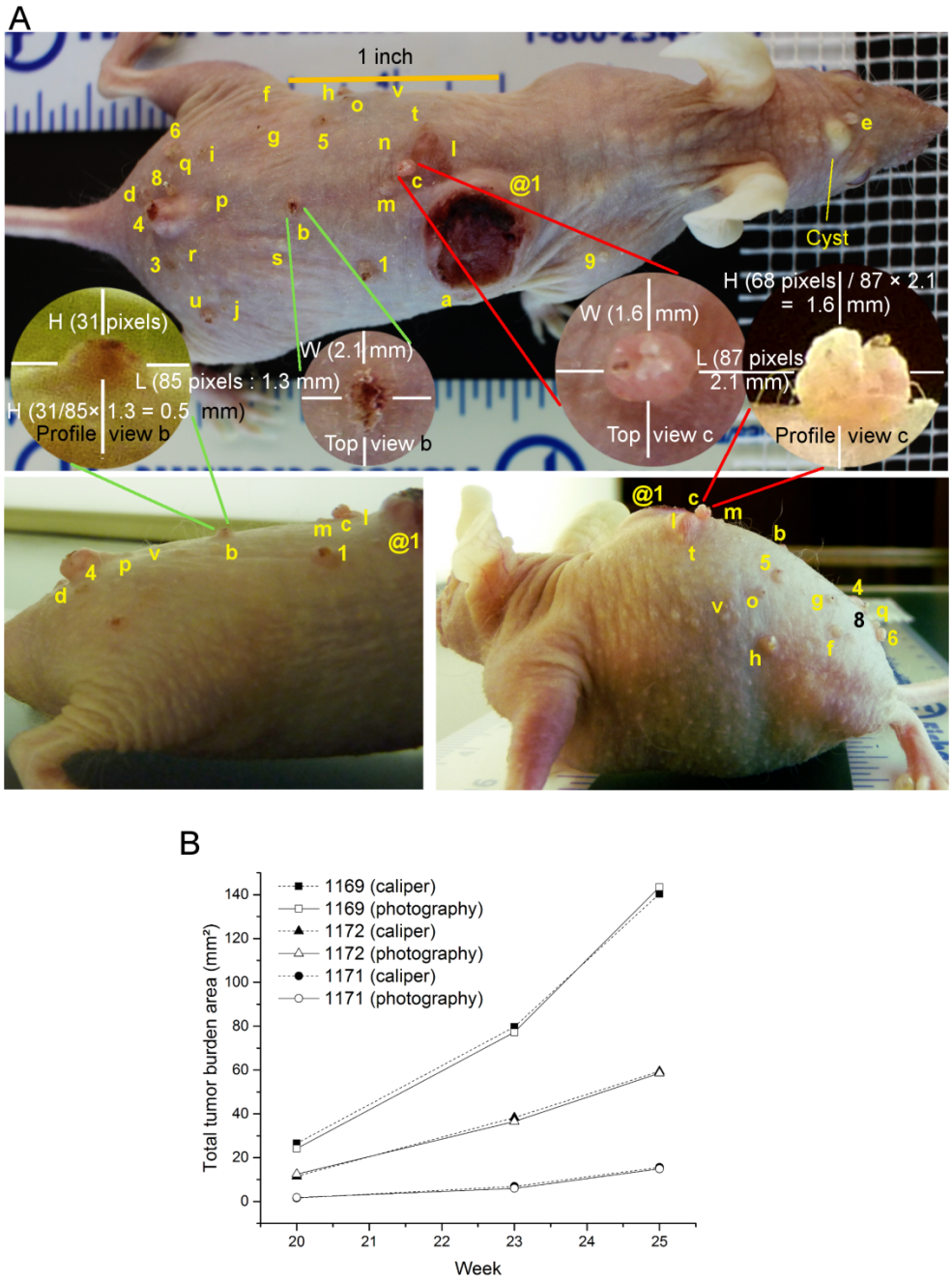

Figure 2.2. Measurement of tumor dimensions and total tumor burden in mice by two methods (A) Top and profile view pictures of a mouse with multiple UVB-induced skin cancers for photographic method of measuring tumor dimensions. The top views of the mouse with scale bars (top image) were used for detecting tumors (incidence) and for counting the tumors to determine the multiplicity. The magnified images of individual tumors from top view, as shown here for tumors # b and c, were used for measuring the length and width of tumors. The profile pictures of the mouse (bottom images) allowed measurement of heights of all tumors, as shown here for encircled magnified images of these two tumors in different profile images. The calibration of pixel to distance in profile pictures was achieved by comparing either the length or width dimension of a given tumor in both top and profile magnified images. The newly calibrated pixel distances in profile picture now allowed

accurate measurement of height of this tumor in profile images. The cysts such as the one seen between eyes were identified as described in the caliper method were excluded in tumor counts. (B) Comparison of time-course of increasing total tumor burden (area) in mice as measured by the caliper and photography methods. The total tumor burden (area) in three different mice was monitored from 20 to 25 weeks of the protocol by caliper and photography methods.

2.8. Tables

	Volume (mm^3)		Area (mm^2)	
Tumor ID	**Caliper**	**Photography**	**Caliper**	**Photography**
v	0.05	0.08	0.82	0.57
o	0.07	0.28	1.04	1.41
j	0.09	0.09	1.38	1.41
3	0.13	0.13	1.88	1.90
r	0.14	0.04	0.85	0.57
m	0.16	0.30	0.95	1.13
9	0.17	0.19	0.50	0.95
8	0.18	0.35	1.10	1.33
i	0.22	0.31	1.30	1.56
n	0.22	0.04	1.33	0.63
p	0.27	0.45	1.63	1.70
g	0.46	0.65	1.38	2.42
e	0.55	0.90	0.64	1.13
t	0.79	0.37	2.36	1.84
a	0.85	1.20	5.09	4.52
8	0.89	1.27	0.64	0.95
l (letter)	0.98	1.35	5.87	6.74
q	1.07	1.33	1.34	1.53
f	1.23	0.80	1.84	2.00
5	1.39	0.66	2.97	2.47
h	1.65	1.42	2.47	2.67
b	1.72	0.71	3.68	2.14
d	1.76	1.68	2.94	2.51
1	1.85	1.91	3.97	4.08
u	2.17	1.76	3.61	3.30
6	2.26	2.40	2.26	2.40
c	2.67	2.81	2.67	2.64
k	3.18	3.36	5.96	5.61
4	35.26	31.76	19.59	17.01
@1(2+7)	276.08	274.66	118.32	121.17
All tumors n = 30	338.5	333.3	200.4	200.3
% Difference	1.5%		0.05%	
P-value	0.98		0.97	
Small tumors n = 24, <2 mm^3	16.9	16.5	48.0	48.2
% Difference	0.2%		0.4%	
P-value	0.23		0.84	
Large tumors n = 6, >2 mm^3	321.6	316.8	152.4	152.1
% Difference	1.5%		0.2%	
P-value	0.44		0.69	

Table 2.1. Comparison of tumor volume and area of 30 tumors by caliper and photographic methods

Mouse #	Number of tumors	Total area by caliper (mm^2)	Total area from photography (mm^2)	*P-value*	% Difference
1151	10	34.3	33.0	0.30	3.9%
1154	17	132.3	140.9	1	6.5%
1157	12	43.4	458	0.31	5.4%
1158	22	67.5	68.7	0.36	1.7%
1152	24	69.9	72.5	0.30	3.7%
1680	30	200.4	200.3	0.97	0.05%

Table 2.2. Comparison of total tumor burden on 6 mice using photographic and caliper methods

		Small tumor (~1 mm length)		Large tumor (~5 mm length)	
		Caliper	Photography	Caliper	Photography
Mean Length (mm)		1.03	1.04	5.36	5.32
Standard Deviation		0.16	0.10	0.19	0.10
Precision	Relative standard variation	15.9	9.30	3.50	1.90
Accuracy	(Photography/Caliper) × 100	100.97		99.30	

Table 2.3. Accuracy and precision of the photography and caliper methods

2.9. Supplementary tables

								Volume ($\frac{\pi}{6} \times \mathcal{L} \times \mathcal{W} \times \mathcal{H}$) mm³		Area ($\frac{\pi}{4} \times \mathcal{L} \times \mathcal{W} \times \mathcal{H}$) mm²	
	Tumor ID	Caliper			Photography			Volume-Caliper	Volume-Photography	Area-Caliper	Area-Photography
		L	W	H	L	W	H	(Vc)	(Vp)	(Ac)	(Ap)
Less than 2 mm³	v	1.5	0.7	0.1	1.2	0.6	0.2	0.05	0.08	0.82	0.57
	o	1.2	1.1	0.1	1.5	1.2	0.3	0.07	0.28	1.04	1.41
	j	1.6	1.1	0.1	1.5	1.2	0.1	0.09	0.09	1.38	1.41
	3	2	1.2	0.1	2.2	1.1	0.1	0.13	0.13	1.88	1.90
	r	1.2	0.9	0.25	0.9	0.8	0.1	0.14	0.04	0.85	0.57
	m	1.1	1.1	0.25	1.2	1.2	0.4	0.16	0.30	0.95	1.13
	9	0.8	0.8	0.5	1.1	1.1	0.3	0.17	0.19	0.50	0.95
	s	1.4	1	0.25	1.3	1.3	0.4	0.18	0.35	1.10	1.33
	i	1.5	1.1	0.25	1.8	1.1	0.3	0.22	0.31	1.30	1.56
	n	1.3	1.3	0.25	1	0.8	0.1	0.22	0.04	1.33	0.63
	p	1.6	1.3	0.25	1.8	1.2	0.4	0.27	0.45	1.63	1.70
	g	1.6	1.1	0.5	2.2	1.4	0.4	0.46	0.65	1.38	2.42
	e	0.9	0.9	1.3	1.2	1.2	1.2	0.55	0.90	0.64	1.13
	t	2	1.5	0.5	1.8	1.3	0.3	0.79	0.37	2.36	1.84
	a	2.7	2.4	0.25	2.5	2.3	0.4	0.85	1.20	5.09	4.52
	8	0.9	0.9	2.1	1.1	1.1	2	0.89	1.27	0.64	0.95
	l	3.4	2.2	0.25	3.3	2.6	0.3	0.98	1.35	5.87	6.74
	q	1.7	1	1.2	1.5	1.3	1.3	1.07	1.33	1.34	1.53
	f	1.8	1.3	1	1.7	1.5	0.6	1.23	0.80	1.84	2.00
	5	2.1	1.8	0.7	2.1	1.5	0.4	1.39	0.66	2.97	2.47
	h	2.1	1.5	1	2	1.7	0.8	1.65	1.42	2.47	2.67
	b	2.6	1.8	0.7	2.1	1.3	0.5	1.72	0.71	3.68	2.14
	d	2.2	1.7	0.9	2	1.6	1	1.76	1.68	2.94	2.51
	1	2.3	2.2	0.7	2.6	2	0.7	1.85	1.91	3.97	4.08
More than 2 mm³	u	2.3	2	0.9	2.1	2	0.8	2.17	1.76	3.30	2.17
	6	1.8	1.6	1.5	1.7	1.8	1.5	2.26	2.40	2.40	2.26
	c	2	1.7	1.5	2.1	1.6	1.6	2.67	2.81	2.64	2.67
	k	3.3	2.3	0.8	3.4	2.1	0.9	3.18	3.36	5.61	3.18
	4	5.8	4.3	2.7	5.7	3.8	2.8	35.26	31.76	17.01	35.26
	@1 (2+7)	13.1	11.5	3.5	13.3	11.6	3.4	276.08	274.66	121.17	276.08
							Volume range (mm³)	n	(Vc)	(Vp)	(Ac)	(Ap)
							Sum (All)	30	338.5	333.3	200.4	200.3
							Sum (0-2 mm³)	24	16.9	16.5	48.0	48.2
							Sum (> 2mm³)	6	321.6	316.8	152.4	152.1

Table S2.1. Three dimensions of 30 individual tumors measured by the caliper and photography methods

Mouse #	1151		1152		1154		1157		1158		1680	
Method	C	P	C	P	C	P	C	P	C	P	C	P
Tumor #												
1	1.4	1.5	116.5	128.8	5.9	5.6	1.8	2.7	0.8	0.8	0.5	1
2	4.4	4.4	2.3	2.6	0.8	1	1.2	1.6	1.8	1.3	0.6	1
3	1.2	1.3	6	6.5	2.4	3.8	4	4	1.3	1.4	0.6	1.1
4	3.2	3.1	6.3	6.4	9.3	8.6	1.8	2.1	4.6	5.5	0.8	0.6
5	4.8	4.4	3.8	4.5	0.8	1	2.1	2.4	1.9	1.7	0.9	0.6
6	3	1.8	3.4	3.4	1.8	3.2	2.2	2.4	1.9	2.2	1	1.1
7	11.8	11.2	4	3.5	13.7	14	1.2	1.4	2.2	3.3	1	1.4
8	2.3	1.8	3.4	3.4	11.2	10.5	1.7	2.3	4	3.7	1.1	1.3
9	2	1.7	3	2.4	0.9	0.8	10.7	12.5	1.2	1.9	1.3	1.6
10	9.6	10.8	3.4	3.2	5	5.3	16.8	14.8	1.7	1.8	1.3	0.6
11			1.9	2.7	2	2.7	2.1	2.1	0.5	1.3	1.3	1.5
12			2.4	2.8	1.5	1.8	2.3	2	0.4	1.2	1.4	2.4
13			3.2	1.7			2.9	3.6	3.8	3.5	1.4	1.4
14			1.8	1.4			2.8	4.8	0.8	1	1.6	1.7
15			3.2	3.1			2	3.2	1.8	1.8	1.8	2
16			2.1	1.6			0.8	0.5	0.9	2	1.9	1.9
17			1.8	1.4			11.2	7.8	2.7	2.2	2.3	2.4
18							2.5	2.7	1	0.8	2.4	1.8
19							4.4	3.2	4.4	4.6	2.5	2.7
20							8.1	6.5	5.2	5.5	2.7	2.6
21							1.7	2.3	40.2	39	2.9	2.5
22							1.7	2.6	1.8	2.1	3	2.5
23									2.1	1.6	3.6	3.3
24									2	2.1	3.7	2.1
25											4	4.1
26											5.1	4.5
27											5.9	6.7
28											6	5.6
29											19.6	17
30											118.3	121.2
Total area	**34.3**	**33.0**	**132.3**	**140.9**	**43.4**	**45.8**	**67.5**	**68.7**	**69.9**	**72.5**	**200.5**	**200.2**
Number of tumors	10		17		12		22		24		30	

Mouse #	Number of tumors	Total area by caliper (mm²)	Total area from photography (mm²)	Wilcoxon test	|photography-caliper|/caliper
1151	10	34.3	33	0.3	3.90%
1154	12	43.4	45.8	0.31	5.40%
1157	22	67.5	68.7	0.36	1.70%
1158	24	69.9	72.5	0.3	3.70%
1152	17	132.3	140.9	1	6.50%
1680	30	200.4	200.3	0.97	0.05%

Table S2.2. The total tumor area (mm^2) by the caliper (C) and photography (P) methods for six mice bearing 10-30 tumors

Supplementary Table S-III			
		Small Tumor	Large Tumor
Method	Repeat #	Length (mm)	Length (mm)
CALIPER	1	0.8	5.1
	2	0.9	5.1
	3	0.9	5.6
	4	1.0	5.6
	5	1.0	5.5
	6	1.1	5.5
	7	1.3	5.2
	8	0.9	5.3
	9	1.2	5.3
	10	1.2	5.4
	Mean	**1.03**	**5.36**
	Standard deviation	0.16	0.19
	Relative standard deviation	15.89	3.54
PHOTOGRAPHY	1	1.0	5.5
	2	1.1	5.4
	3	1.1	5.3
	4	1.1	5.3
	5	0.9	5.3
	6	0.9	5.4
	7	1.0	5.1
	8	1.1	5.3
	9	1.2	5.3
	10	1.0	5.3
	Mean	**1.04**	**5.32**
	Standard deviation	0.10	0.10
	Relative standard deviation	9.29	1.94

Table S2.3. Ten replicate measurements of length of a small and a medium size tumor to determine accuracy and precision of the photography and caliper methods

2.10. Materials and Methods

Chronic UVB-induced NMSC in SKH-1 hairless mice

All animal studies were approved by the Animal Protection Committee of Laval University and were conducted by the personnel who were trained and certified for animal work. The 5-week old SKH-1 albino hairless mice obtained from Charles River Canada were irradiated thrice a week for 20 weeks at 800 J/m^2 UVB (280-320 nm). Five weeks after last irradiation, mice were sacrificed under anaesthesia with isoflurane followed by exposure to CO_2 and cervical dislocation. The unrestrained mice were irradiated in an open cage placed in a Spectrolinker XL-1500 (Spectronics Corp.) equipped with six 15W UVB tube-lights, which delivered 800 J/m^2 within 2 to 3 min at a flux of 5.9 J/m^2/sec. During irradiation, the cages were covered from the top with Kodacel filter to remove the contaminating UVC radiations (230-280 nm) [17]. The UVA wavelengths (320-400 nm) accounted for 20% of the energy, as measured by UVX radiometer (UVP Inc.) equipped with UV-A, B and C-specific probes. Mice were monitored weekly for tumor burden, as described below.

Caliper method to measure tumor dimensions

The tumors were visible from 12-15 weeks and all data presented in this study are from measurements between 20 to 25 weeks. The pre-neoplastic foci that persisted and progressed over time to form proper tumors were taken into account for the final tumor burden. In contrast, very few cysts that appeared on the skin were identified and excluded from data sets as they either did not change in appearance or disappeared in few weeks. Mice were held in hand for measuring all three dimensions of each tumor using the digital caliper with 0.01 mm precision (Mitutoyo). The length was measured along its longest linear dimension on the skin and the width was measured along the axis perpendicular to the length axis. The height was measured at the tallest point of the tumor. For the length and width that are measured along the flat skin, we could maintain the accuracy of 0.1 mm. However, the heights below 0.5 mm posed practical difficulties in judging accurate placement of the caliper jaws from skin to the top of the tumor; therefore using visual cues and caliper readout, the near-flat tumors were assigned 0.1 mm height and progressively raised tumors were assigned 0.25 or 0.5 mm heights. All heights above 0.5 mm were actual caliper readouts. Assuming hemi-ellipsoidal shape of the tumors, the tumor burden was determined as the area ($\frac{\pi}{4} \times length \times width$) and volume ($\frac{\pi}{6} \times length \times width \times height$) [6]. The statistical difference in values by two methods was derived using Origin Pro 2015 with the Wilcoxon signed rank test.

Photographic method to measure tumor dimensions

Photography set-up for mice in laminar hood. The measurement of tumor dimensions with photographs requires a set-up with known distances from the camera to the mouse skin and reference scale-bars, as well as an environment that keeps the mouse calm for few minutes to take the pictures of the tumors (Fig 1A). We used a laminar flow cabinet open on both sides for the ease of operations by two persons standing on either side of the cabinet. The cabinet was illuminated with diffused light from a top fluorescent lamp and two 5000 K fluorescent tubes from the sides. We designed a stand that permitted the camera to be steadily positioned so that the lens of the camera was exactly 130 mm above the frosted glass plate that was placed in the cabinet on top of a black paper and two rulers that would flank the mouse in the picture (Fig 1B). Since mouse becomes restless on the glass that does not provide any grip for their paws, we affixed a broad grid fabric tape on which mouse could obtain a secure grip and remain steady for the duration of the photography session. We used a reflex Canon EOS Rebel T5 camera equipped with a Canon EFS 24 mm lens having a fixed focal length and took all the pictures without flash. To avoid shaking the camera or alarming the mouse with hand movement, the pictures were taken using a commercially available remote shutter control cable for the camera.

Photography of mice. The mouse was gently placed over the glass plate and the tail was slightly tugged, which resulted in a relatively stable posture of the mouse with a straight spine and nearly flat dorsal skin containing almost all the tumors. In this situation, the tumors on back of mouse were at an average distance of 104 mm from the camera, whereas the reference scales below the glass plate were at 130 mm from the camera; and these two values were taken into account for calculation of scale factor in images (Fig 1B). Within 30 seconds, 3-5 top view pictures were taken without flashlight that would allow measurement of length and width (Fig 2A, top image). The camera was then removed from the stand to rapidly take several profile pictures of the mouse within 2 min from various angles that would allow measurement of heights of tumors (Fig 2A, bottom images). For profile pictures, it was impractical to use vertical scales or keep a fixed distance between camera and the tumors, as this would unduly prolong picture session. Moreover, the distances in profile pictures could be calibrated against the top picture, as described below.

Measurement of the length, width and height of tumors from the top and profile pictures. We used freely available AxioVision SE64-4.9.1 image analysis software (Zeiss) to process the pictures for determining the tumor dimensions, although any other image analyses software that allows correlation of pixel distances in the pictures with actual size based on a scale bar in the same picture is suitable for this analysis. For each mouse, the top picture with scale bars was analyzed first to establish the correlation of pixel to distance in mm using Scaling wizard function in the

“Measure/Scaling” menu of the software (Fig 3.2A, top image). A scale correction factor of 0.8 was applied to account for the difference in the distance from camera to the tumors (OA = 104 mm) and the nearest scale bar (OB=130 mm) as per Thales' intercept theorem that OA/OB = AC/BD, where AC is the tumor dimension on the back of mouse and BD is distance on the scale below the glass plate (Fig 1B). The calibrated pixel distance in the picture allowed measurement of length and width of the tumor using the measure “length” menu of the software (Fig 2A). The photographic method with zooming of pictures on the computer screen allowed better definition of the tumor boundaries and more accurate measurement of distances. For profile pictures, since scale bars and distances were not fixed, we calibrated the pixel distance of either the length or width of the tumor in profile image with the known value of this parameter in the top picture and used the revised scale to measure height of the tumor in the profile picture (Fig 2A, circled images of tumors #b and c in top and profile images). For multiple tumors in close proximity, the calibration made with one tumor could be easily applied to measure dimensions of other tumors of similar size. The area and volume of tumors and statistical analyses were carried out as described for caliper method. The average time for measuring dimensions of a single tumor on the computer by the photography method was about 1-2 min, which is similar to the time required for the caliper method. However, for a mouse with 30 tumors, the actual photography session with mouse would take about 3 min and tumor measurements on computer would be about 30-60 min, whereas in the caliper method, the entire period of 30-60 min would have to be spent with a mouse in hand.

2.11. References

1. Thomas-Ahner JM, Wulff BC, Tober KL, Kusewitt DF, Riggenbach JA, et al. (2007) Gender differences in UVB-induced skin carcinogenesis, inflammation, and DNA damage. Cancer Res 67: 3468-3474.

2. Lou YR, Peng QY, Li T, Medvecky CM, Lin Y, et al. (2011) Effects of high-fat diets rich in either omega-3 or omega-6 fatty acids on UVB-induced skin carcinogenesis in SKH-1 mice. Carcinogenesis 32: 1078-1084.

3. Lu YP, Lou YR, Xie JG, Peng QY, Liao J, et al. (2002) Topical applications of caffeine or (-)-epigallocatechin gallate (EGCG) inhibit carcinogenesis and selectively increase apoptosis in UVB-induced skin tumors in mice. Proc Natl Acad Sci U S A 99: 12455-12460.

4. Katiyar SK, Korman NJ, Mukhtar H, Agarwal R (1997) Protective effects of silymarin against photocarcinogenesis in a mouse skin model. J Natl Cancer Inst 89: 556-566.

5. Pentland AP, Schoggins JW, Scott GA, Khan KN, Han R (1999) Reduction of UV-induced skin tumors in hairless mice by selective COX-2 inhibition. Carcinogenesis 20: 1939-1944.

6. Vaid M, Singh T, Prasad R, Katiyar SK (2014) Intake of high-fat diet stimulates the risk of ultraviolet radiation-induced skin tumors and malignant progression of papillomas to carcinoma in SKH-1 hairless mice. Toxicol Appl Pharmacol 274: 147-155.

7. Tsai KD, Lin JC, Yang SM, Tseng MJ, Hsu JD, et al. (2012) Curcumin Protects against UVB-Induced Skin Cancers in SKH-1 Hairless Mouse: Analysis of Early Molecular Markers in Carcinogenesis. Evid Based Complement Alternat Med 2012: 593952, DOI: 593910.591155/592012/593952.

8. Gaddameedhi S, Selby CP, Kaufmann WK, Smart RC, Sancar A (2011) Control of skin cancer by the circadian rhythm. Proc Natl Acad Sci U S A 108: 18790-18795.

9. Chilampalli C, Guillermo R, Zhang X, Kaushik RS, Young A, et al. (2011) Effects of magnolol on UVB-induced skin cancer development in mice and its possible mechanism of action. BMC Cancer 11: 456.

10. Singh A, Singh A, Sand JM, Bauer SJ, Hafeez BB, et al. (2015) Topically applied Hsp90 inhibitor 17AAG inhibits UVR-induced cutaneous squamous cell carcinomas. J Invest Dermatol 135: 1098-1107.

11. Sapi J, Kovacs L, Drexler DA, Kocsis P, Gajari D, et al. (2015) Tumor Volume Estimation and Quasi-Continuous Administration for Most Effective Bevacizumab Therapy. PLoS One 10: e0142190.

12. Ayers GD, McKinley ET, Zhao P, Fritz JM, Metry RE, et al. (2010) Volume of preclinical xenograft tumors is more accurately assessed by ultrasound imaging than manual caliper measurements. J Ultrasound Med 29: 891-901.

13. Wysocki AB (1996) Wound measurement. Int J Dermatol 35: 82-91.

14. Griffin JW, Tolley EA, Tooms RE, Reyes RA, Clifft JK (1993) A comparison of photographic and transparency-based methods for measuring wound surface area. Phys Ther 73: 117-122.

15. Gilman T (2004) Wound outcomes: the utility of surface measures. Int J Low Extrem Wounds 3: 125-132.

16. Chang AC, Dearman B, Greenwood JE (2011) A comparison of wound area measurement techniques: visitrak versus photography. Eplasty 11: e18 PMCID: 3080766.

17. Vodenicharov MD, Ghodgaonkar MM, Halappanavar SS, Shah RG, Shah GM (2005) Mechanism of early biphasic activation of poly(ADP-ribose) polymerase-1 in response to ultraviolet B radiation. J Cell Sci 118: 589-599.

2.12. Acknowledgements

This work was supported by the grants to GMS from Natural Sciences and Engineering Research Council of Canada (Discovery Grants #RGPIN-2016-05868 and Discovery Accelerator Grant # RGPAS-492875-2016). NKP received a foreign student fee-waiver scholarship from Quebec Government and Shastri Indo-Canadian Institute. NKP was also a recipient of the graduate scholarships from the Neuroscience Axis of CR- CHU-Q. The funders had no role in study design, data collection and analysis, decision to publish, or preparation of the manuscript.

Competing interests: The authors have declared that no competing interests exist.

Chapter 3. A panel of criteria for comprehensive assessment of severity of ultraviolet B radiation-induced non-melanoma skin cancers in SKH-1 mice

Marc Bazin[a,c], Nupur K. Purohit[a,c], Marine A. Merlin[a,c] and Girish M. Shah[a,b,c*]

[a] CHU de Quebec-Laval University Research Center, Neuroscience and Cancer Axes, Laboratory for Skin Cancer Research, 2705, Boulevard Laurier, Quebec (QC), Canada

[b] Department of Molecular Biology, Medical Biochemistry and Pathology, Faculty of Medicine, Laval University, Quebec (QC), Canada

[c] Université Laval Cancer Research Center, Quebec (QC), Canada

* Correspondence should be addressed to: girish.shah@crchul.ulaval.ca

Highlights

Measuring severity of UV-induced NMSC burden in mice is a challenge

Current four criteria to assess severity of NMSC provide inconsistent results

Three new more accurate criteria for assessment of NMSC burden are described

Proposed panel of seven criteria provides a comprehensive assessment of NMSC burden

New panel distinguishes between tumor burden due to initiation or growth of NMSC

Keywords

Ultraviolet B (UVB) radiation; non-melanoma skin cancers (NMSC); SKH-1 mouse model, assessment of cancer burden; methods/tools/techniques.

3.1. Preface

The present manuscript is published in Journal of Photochemistry & Photobiology, B: Biology. During the analysis of the tumor measurement data obtained from the photographic images of the mice as described in the previous chapter, it was realized by Dr. Marc Bazin (the first author) and me (the second author) that the four conventional criteria (prevalence, multiplicity, area and volume of tumors) used for the measurement of severity of skin cancer present inherent limitations (Fig 3.1). Most importantly, Dr. Marc Bazin identified that the tumor size measured by area and volume either ignores or overcompensates the tumor height at the cost of planar dimensions, respectively, thereby introducing unintended bias in interpretation of the severity of cancer based on the tumor size. This problem was resolved by Dr. Marc Bazin by demonstrating and validating the use of the already known Knud Thomsen tridimensional surface formula (KT-3D surface) that apportions optimal weightage to three tumor dimensions (Fig. 3.2 and Suppl. Fig. S3.2). In addition to this, I also realized that the criteria such as tumor multiplicity and tumor size can be further adapted to determine the frequency of initiation of measurable tumors and changes in growth characteristic of the skin cancer with time. Upon explaining this problem to Dr. Marc Bazin, he came up with a mathematical solution to demonstrate the former by plotting the occurrence of only new tumors appearing each week during the protocol and the latter by measuring the change in KT-3D surface per week during different time frames (Fig. 3.3). Furthermore, we also understood that tumor-free survival is generally determined based on the appearance of the first tumor, but we surmised that appearance of a minimum of two tumors could be a better indicator of a stable disease for this criterion (Fig. 3.4). Overall, as a second author, I contributed to the conceptualization of this manuscript by identifying and explaining the specific problems and possible ways of interpretation of tumor data to Dr. Marc Bazin. I also participated in writing and reviewing the manuscript. Marine Merlin, the third author, was involved in the tumor data collection as well as in the correction and editing of the manuscript.

3.2. Résumé

L'étude des cancers de la peau de type non-mélanome induits par le rayonnement ultraviolet B (UVB) a été grandement facilitée par l'utilisation des souris glabre albinos SKH-1. Ces souris développent de multiples tumeurs de différentes tailles, et la gravité du cancer est souvent mesurée à partir d'un ou plusieurs critères parmi les quatre généralement admis, à savoir la prévalence, la multiplicité, la surface et le volume des tumeurs. Cependant, il existe plusieurs limitations inhérentes à chaque critère : la prévalence et le nombre ne tiennent pas compte des différences de taille entre les tumeurs, la mesure de surface ignore la hauteur des tumeurs, alors que la mesure du volume néglige les dimensions planaires au profit de la hauteur. En utilisant les données de notre étude en cours sur les cancers de la peau de type non-mélanome, nous discutons ici des limitations de ces quatre critères et suggérons des améliorations pour la mesure de prévalence. Nous recommandons également l'utilisation de trois nouveaux critères. Il s'agit de la surface tridimensionnelle de Knud-Thomsen qui prend en considération les trois dimensions de la tumeur de manière optimale, le taux d'apparition hebdomadaire de nouvelles tumeurs, ainsi que le taux de croissance tumorale pour mettre en évidence l'initiation et la croissance des tumeurs dans le temps. L'utilisation combinée de ces sept critères conduit à une meilleure estimation de la sévérité des cancers de la peau de type non-mélanome et permet de vérifier si les manipulations expérimentales sur les souris ont affecté la phase d'initiation ou la croissance tumorale.

3.3. Abstract

The study of causes and cures for ultraviolet B radiation (UVB)-induced non-melanoma skin cancers (NMSC) has been greatly facilitated by use of the albino SKH-1 hairless mice. These mice develop multiple tumors of different sizes and the severity of cancer is often measured by one or more of the four criteria, namely the prevalence, multiplicity, area and volume of tumors. However, there are inherent limitations of each criterion: the prevalence and number do not account for size differences among tumors, area measurement ignores the tumor height, and volume measurement overcompensates for the height at the cost of planar dimensions. Here, using our dataset from an ongoing NMSC study, we discuss the limitations of these four criteria, and suggest refinements in measuring prevalence. We recommend the use of three more criteria, namely the Knud Thomsen tridimensional surface that apportions optimal weightage to three tumor dimensions, weekly occurrence of new tumors and tumor growth-rate to reveal initiation and growth of tumors in early and late phase of NMSC development, respectively. Together, use of this comprehensive panel of seven criteria can provide an accurate assessment of severity of NMSC and lead to a testable hypothesis whether the experimental manipulation of mice has affected the early initiation or growth phase of NMSC tumors.

3.4. Introduction

All studies that examine the genetic, pharmacological and other causes or cures for different cancers in animal models need to assess and compare severity of the disease with or without the proposed intervention. Unlike cancers that are within the body, skin cancers offer multiple options to physically measure its severity. As an example, the study of various factors influencing solar ultraviolet B radiation (UVB)-induced non-melanoma skin cancers (NMSC) has been greatly facilitated by use of the albino SKH-1 hairless mouse model [1-4]. This model results in mice carrying variable number of small to large, flat or raised tumors appearing at different time in the protocol, and severity of their cancer burden is routinely assessed by one or more of the following four criteria. The first criterion is the prevalence [5, 6] or the tumor-free survival fraction [7, 8] that represents the fraction of mice carrying tumors or free from tumors in a given group, respectively. Second criterion is the multiplicity or the average number of tumors per mouse [7, 9]. The last two criteria describe the size of the tumor burden in the form of average tumor area per mouse measured from the length and width [10] or diameter [5] of the tumors, or the average tumor volume per mouse derived from the length, width and height of the tumors [6, 8].

Each criterion provides key information about the severity of the disease, but inherently contains limitations that restrict its capacity to represent the full picture of tumor burden. The prevalence and multiplicity account for the presence of a tumor but ignore the difference in size of tumors. The area measurement ignores height, whereas volume measurement places more emphasis on height at the expense of contributions from length and width of tumor, although clinically all three dimensions contribute significantly to the severity of NMSC. Since most published papers with this model do not provide all four criteria of tumor burden, it is a significant challenge to compare conclusions drawn from studies that use different criterion for measuring the severity of cancer. Hence, it is important to assess the advantages and limitations of each of these criteria and improve the panel to more accurately reflect the status of disease.

Here, using selected dataset from our ongoing experiments with UVB-induced NMSC model, we highlight the problem that each of these four routinely used criteria may not always lead to an identical conclusion about the severity of tumor burden. We demonstrate that a more accurate estimate of tumor size can be obtained by using a fifth criterion, namely Knud Thomsen three-dimensional (KT-3D) tumor surface area, which is used in many other disciplines but not in NMSC research. We also show that analyzing the weekly appearance of new tumors during the protocol and a modified version of a rarely used criterion of tumor growth-rate [5] together should be used to measure the frequency of initiation of measurable tumors and changes in the growth characteristics of cancer with time.

Together, the four old and three new criteria can provide not just a numerical but a more comprehensive picture of the UVB-induced NMSC.

3.5. Results and discussion

3.5.1. Discordance among assessment criteria for determining the severity of NMSC

We first examined whether all four conventionally used assessment criteria, i.e., prevalence, multiplicity, area and volume, would provide an identical conclusion regarding differences in the severity of tumor burden among different groups that were chosen from our large ongoing experimental dataset using this model. We selected five groups of 9-12 mice that had a predominance of small (groups 1 and 2), medium (group 3), large and flat (group 4) or large and raised (group 5) tumors (Suppl. Fig. S3.1). For each group, the weekly tumor data for all four criteria were collected using our photographic method [11]. We divided these five groups of mice in three pairs for comparison, namely pair A (groups 1 and 2), pair B (groups 2 and 3) and pair C (groups 4 and 5). For each pair, we compared the difference in severity of cancer by each of the four criteria.

In pair A containing groups 1 and 2 with mainly small tumors, all four criteria revealed an identical conclusion that there was no significant difference in severity of cancer in these two groups (Fig. 3.1, pair A). In pair B, when we compared the group 2 mice with smaller tumors to group 3 mice with moderate size tumors, once again all four criteria unequivocally identified that group 3 had significantly more severe cancer as compared to group 2 (Fig. 3.1, pair B). Thus, if there are two groups with either very similar or distinctly different size tumors, all four conventional criteria would provide an identical conclusion about severity of cancer in these groups.

In contrast, when we compared group 4 mice carrying mainly large flat tumors with group 5 mice having largely tall tumors with small footprint on the skin (Fig 3.1, pair C), the four criteria produced three different conclusions regarding which group had more severe cancer burden. The prevalence criterion indicated no significant difference with the mean tumor-free survival period around 13.5 weeks for both the groups. The multiplicity criterion at week 20 revealed that average number of tumors per mouse was 2.6 times more in group 4 (19.7 tumors) than in group 5 (7.6 tumors). The area criterion also gave similar indication that group 4 (45.1 mm2) had significantly higher (1.6 times) average area of tumors per mouse than group 5 (28.6 mm2). In contrast, the tumor volume criterion produced a diametrically opposite result that group 5 (29.1 mm3) had almost 3.5 times more severe cancer burden than group 4 (8.4 mm3).

This discrepancy among four commonly used criteria in the estimation of severity of cancer poses a significant challenge in drawing an accurate conclusion about the influence of genes and other interventions on the susceptibility to NMSC that tend to generate situation such as that described in pair C. As we described earlier [11], this problem is even more acute since many studies do not report

all four criteria but report the results with only prevalence and number of tumors, whereas other studies report area and that too after excluding tumors below an arbitrary cut-off dimension, and very few studies report volume of tumors. Thus, reporting of results based on only one or two criteria could introduce an unintended bias in the interpretations of results. In addition, even the use of all four conventional criteria does not guarantee a uniform conclusion for at least some of the data in NMSC studies, such as pair C. Hence, there is a need for additional criteria for a more reliable and consistent estimate of severity of cancer burden.

3.5.2. Knud Thomsen three-dimensional surface as a fifth criterion of tumor burden

The formulae for area and volume measurement are made with an assumption of a hemi-ellipsoidal shape for NMSC tumors. However, for such a shape, the KT-3D formula to calculate the tridimensional surface area strikes an optimum balance between the contributions by the length and width against its height. This formula, developed by Knud Thomsen [13] through optimization of the original formula of Klamkin [12] for ellipsoid shapes, is extensively used in many different disciplines ranging from medicine [14-16], veterinary medicine [17], medical imaging [18], cell biology [19, 20], immunology [21], plant biology [22], plant pathogen interactions [23, 24], evolutionary ecology [25], biophysics [26], oceanography [27], physical chemistry [28], engineering and applied sciences [29], aeronautics [30], geology [31], hydrodynamic [32], and thermodynamics [33]. More specifically in the above studies, the KT-3D formula was used for calculating the three-dimensional surface area of a vast variety of ellipsoid or hemi-ellipsoid objects, such as osteosarcoma, retinal myocytes, zone affected by mitral valve regurgitation, areas of brain, dendritic cells in brain, bacterial shape during cell-cycle, insect puparium, beetles, plasma membrane of plant cells that transport nutrients, rhodolith beds of algae in marine sediments, and gas-filled airships.

In view of the widespread acceptance of KT-3D formula as a true measure of tridimensional surface area of a hemi-ellipsoid object, we used it as a fifth criterion for measuring NMSC tumor burden in the same three comparison groups (Fig. 3.2). First of all, this criterion validated the observations described in Fig. 3.1 that there was no significant difference between groups 1 and 2 (Fig. 3.2A); and that group 3 had a significantly higher tumor burden than group 2 (Fig. 3.2B). On the other hand, KT-3D surface measurement revealed no statistically significant difference between groups 4 and 5 (Fig. 3.2C), an assessment of tumor burden that was a compromise between two opposite results observed with area and volume criteria in Fig. 3.1C. In view of the limitations of the formulae used for area and volume, we propose that conclusion drawn by KT-3D surface criteria is a more reasonable comparison of tumor burden between these two groups.

To more clearly demonstrate how each of the three dimensions of tumor influence the estimation of severity of burden as measured by area, volume and KT-3D surface, we compared the severity of cancer burden in two mice, one (mouse #1) carrying multiple small and near-flat tumors and another (mouse #2) carrying one very large and few small tumors (Suppl. Fig. S3.2). The mouse #1 had 4.9 times more tumor burden by area but 11.4 times less burden by volume than mouse #2, whereas KT-3D surface once again moderated between these two criteria to indicate that mouse #1 had 1.9 times more severe tumor burden than mouse #2. Thus, the area measurement undervalues the importance of a large and tall tumor with small footprint on the skin, whereas volume measurement undervalues contribution of numerous small but flat tumors to tumor burden. Since all three dimensions are clinically important determinants of severity of cancer, and since KT-3D surface criterion is universally recognized to apportion optimal weightage to all three dimensions of ellipsoid and hemi-ellipsoid structures, we propose that KT-3D surface represents the most accurate estimation of the severity of cancer in this model.

3.5.3. Occurrence of new tumors and growth-rate of tumors as two additional criteria

The net increase in tumor burden over time is due to two distinct factors, the number of new tumors added each week which represents continuing cancer initiation events, and weekly increase in size of tumors which represents growth of tumors at different stages after initiation. However, these two key aspects of cancer burden are not readily discernible in the cumulative weekly data for different criteria, as presented in Figs. 3.1 and 3.2. The presentation of weekly multiplicity data in Fig. 3.1 reveals a total number of tumors each week, irrespective of whether they were pre-existing tumors from earlier weeks or new tumors that appeared in that week. Similarly, weekly tumor area and volume data shown in Fig. 3.1 or weekly KT-3D surface area curves shown in Fig. 3.2 provide an average growth rate of newly formed tumors during that week pooled with that of the tumors that had appeared weeks earlier in the protocol.

Here, we propose two more criteria to measure occurrence of new tumors and growth rate of new versus old tumors by mining our exhaustive weekly dataset on multiplicity and KT-3D surface area as shown in Figs. 3.1 and 3.2. The weekly data for the multiplicity in pair C was transformed to determine the occurrence of new tumors each week during the protocol (Fig. 3.3, left panel). While both groups developed ~1-2 new tumors each week up to 16th week, the occurrence of new tumors jumped significantly from week 17 for group 4 but not for group 5. These results suggest that the experimental intervention in group 4 had influence over tumor initiation events, as compared to intervention in group 5.

The variation in growth-rate of cancers after their initial appearance on the skin was determined by analyses of tumor dimension data collected on weekly basis, as suggested by Gruijl et al. [5]. We used KT-3D surface data to determine the average tumor growth-rate per week in entire period of 13-20 weeks, or only in the initial (13-16 weeks) or late (17-20 weeks) phase of tumor growth (Fig. 3.3, middle panel). The global average growth-rate for the tumors from their first appearance in 13th week to the last week of the protocol (week 20) showed no significant difference between groups 4 and 5. However, stratification of this data into early (13-16 weeks) and late (17-20 weeks) phases revealed that tumors in group 5 had a significantly higher growth-rate than group 4 tumors only in the late phase but not in the initial phase.

Next, we examined if initial 4-week growth-rate of tumors would be same in a given group whether tumors appeared either early (13th week) or late (17th week) period of the protocol (Fig. 3.3, right panel). The main difference between these two tumors would be that late appearing tumors would have received four extra weeks of irradiation before they first appeared as tumors in the 17th week. The initial growth-rate of early and late tumors was not significantly different in group 4, but for tumors in group 5, growth-rate of late tumors was significantly higher as compared to early tumors. Collectively, these two new criteria revealed key mechanistic differences in development of NMSC in these two groups of mice. Mice in group 4 had tendency to promote more frequent appearance of new tumors but not alter the growth-rate of tumors over time. In contrast, mice in group 5 exhibited stable occurrence of new tumors throughout the protocol, but accelerated the growth of tumors at later stage of the protocol. Thus, use of these two new criteria could reveal experimentally testable hypothesis for explaining the differences in NMSC development in groups 4 and 5.

3.5.4. Improved method to calculate tumor-free survival fraction

Gruijl et al. had earlier shown a mathematical relationship between the prevalence and multiplicity in UVB-induced NMSC in SKH-1 mice [34]. In Fig. 3.1, this correlation of higher prevalence and multiplicity was evident for comparison pairs A and B. However, for pair C, although prevalence was not different, the multiplicity was more in group 4 than in group 5. Normally, prevalence is based on the appearance of the first tumor, but we noted that appearance of a minimum of two tumors is a better indicator of a stable disease. Therefore, we recalculated the prevalence based on the presence of two tumors in a mouse rather than the first tumor (Fig. 3.4). This revised method of calculating prevalence or tumor-free survival correlated very well with multiplicity in all three pairs described in Fig. 3.1. Thus, our results indicate that tumor-free survival fraction based on two-tumor cut-off could serve as a better criterion for prevalence that is more aligned with multiplicity measure of tumor burden.

The SKH-1 mouse model has been very useful to study solar UVB-induced NMSC despite its limitations. These experiments are time-consuming, expensive and require a significant manpower. As a result, it is understandable that many studies do not analyze tumor burden each week and report only few criteria to assess and compare severity of cancer in different groups. Earlier, we have shown that the use of a simple yet accurate photographic method to capture weekly three-dimensional tumor data for measuring tumor burden on an ongoing basis can solve most of the manpower and time problem in collecting the weekly tumor data from a large number of mice in this protocol [11]. Here, we show that our combined panel of seven criteria can provide a comprehensive picture of NMSC severity and lead to further studies to understand mechanistic explanations for the influence of experimental treatment on development of NMSC. Our panel could also be applied for the study of NMSC in other mouse strains, if they develop UVB-induced NMSC because not all mouse strains have similar photosensitive response to UVB [35]. Finally, our panel can be more broadly used for measuring changes in other skin lesions such as psoriasis or wound or for other cancers in internal organs, as long as they can be counted and measured by any means for calculating area, volume and KT-3D surface with formulae suitable for the shape of the lesion or tumor.

3.6. Figures and legends

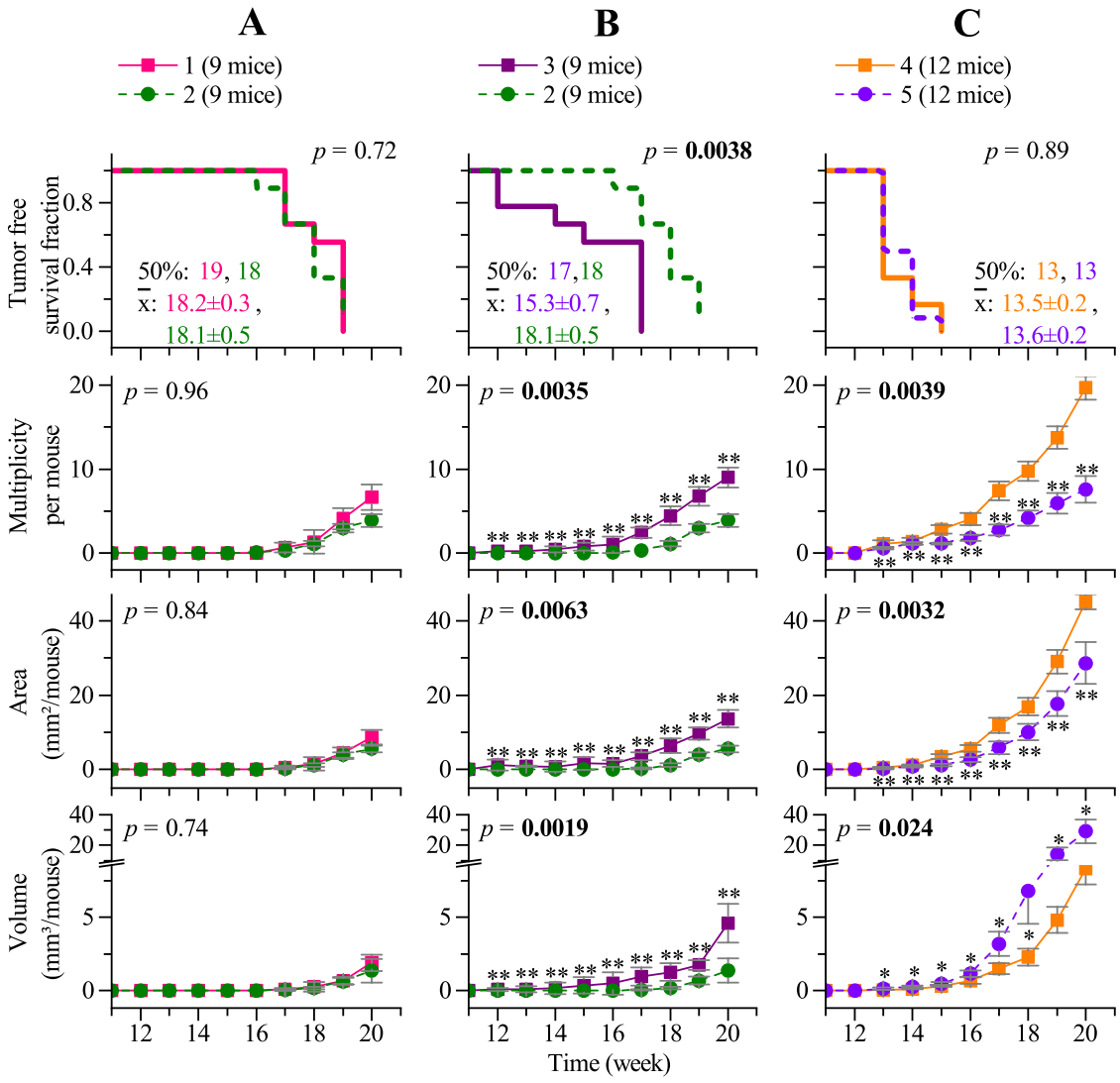

Figure 3.1. Four commonly used criteria for assessment of severity of NMSC
The severity of cancer burden mice from five groups is presented as comparison pair A (groups 1 and 2), pair B (groups 2 and 3) and pair C (groups 4 and 5). The results are presented as pairwise comparison of two selected groups with p-values (p), medians (50%) and means ($\bar{x}$). Multiple comparison results are annotated with * for significant, ** for very significant, and *** for highly significant difference. Error bars are means ± SEM.

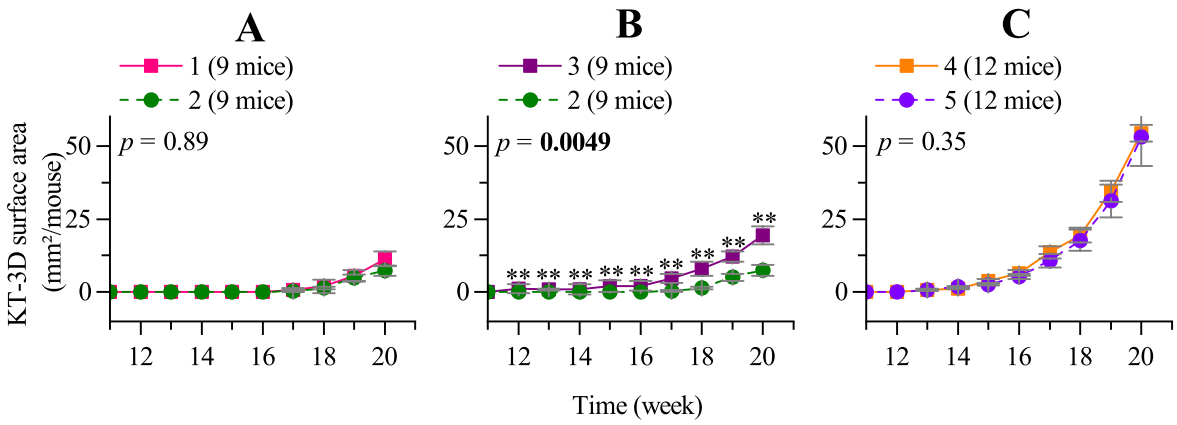

Figure 3.2. Assessment of cancer burden by KT-3D surface area
The severity of tumor burden was measured as KT-3D surface area for five groups of mice divided in three comparison pairs (A, B and C) described in Fig. 3.1.

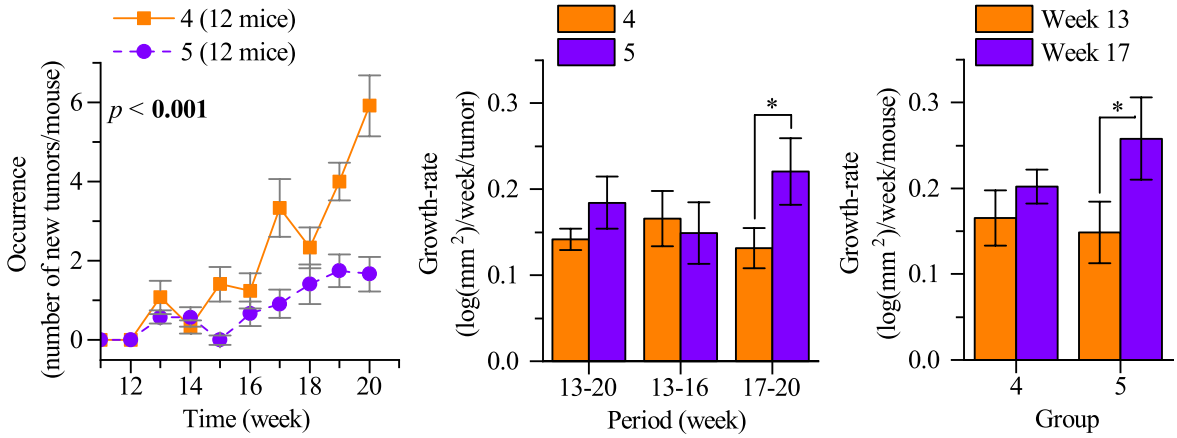

Figure 3.3. Weekly occurrence and growth-rate of tumors

Left panel: Weekly occurrence of new tumors per mouse for groups 4 and 5. The group description and p-value for difference between two groups are same as described for Fig.3.1. Middle panel: Growth-rate in initial and late phase of tumors. For the tumors in groups 4 and 5 that appeared in week 13, their growth-rates in two groups were compared for the periods of 13-20 week (total period), 13-16 weeks (initial growth) and 17-20 weeks (late growth). Right panel: Growth-rate of early and late appearing tumors within a group. Comparison within each group for only the initial growth-rate of tumors over first four weeks after their first appearance in either 13th week (early tumors) or in 17th week (late tumors). The p-value indicates the significance of the occurrence group comparison. The * indicates statistically significant difference.

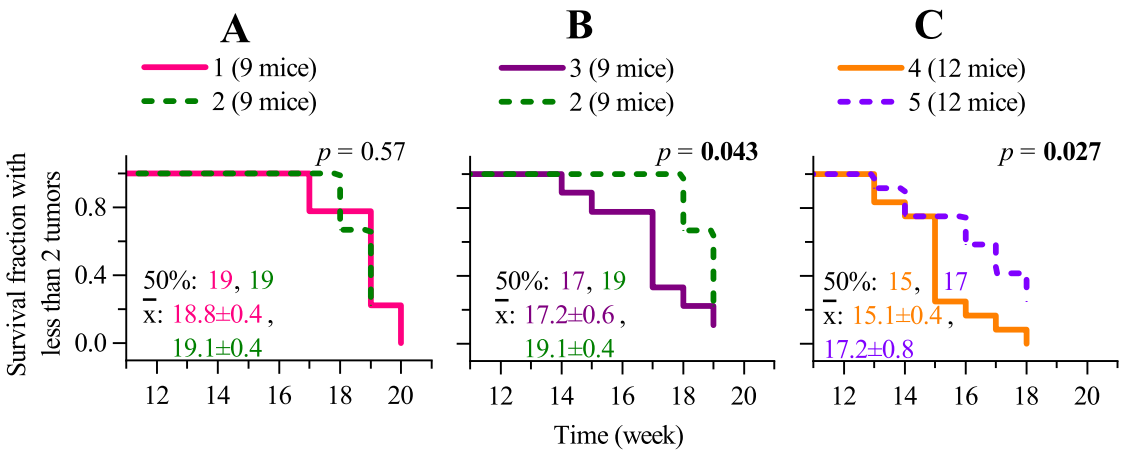

Figure 3.4. Tumor survival graphs with two-tumor cut-off
For same three comparison pairs described in Fig. 3.1.

3.7. Supplementary Figures

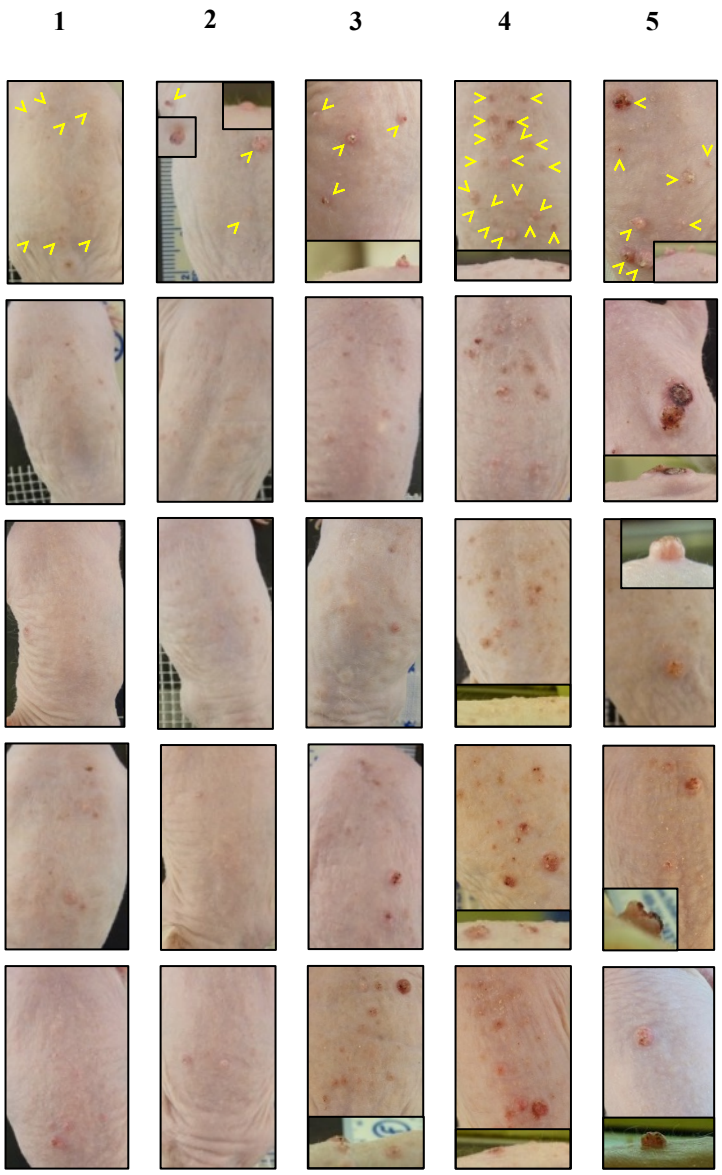

Figure S3.1. Morphology of tumors from mice in the 5 groups used in Fig. 3.1
Group differences in term of tumor size are illustrated in each column for groups 1 to 5. In the first row, yellow arrows show an example of the tumor location on the mouse back. The inset pictures are tumor profiles where tumor height is clearly visible.

Criterion of tumor burden	Mouse #1 	Mouse #2 	Difference in tumor burden between mice #1 and #2
Prevalence: week of first tumor	14	14	no difference
Prevalence: week of first two tumors	14	17	3 weeks earlier
Multiplicity (number of tumors) at week 20	46	19	2.4× more severe
Total tumor area at week 20 (mm^2)	497	101	4.9× more severe
Total tumor volume at week 20 (mm^3)	38	432	11.3× less severe
Total KT-3D surface area (mm^2)	511	275	1.9× more severe

Figure S3.2. Discrepancy in assessment of tumor burden by different criteria in two mice with heterogeneity in number and size of NMSC tumors.

3.7. Materials and Methods

Chronic UVB-induced NMSC in the albino hairless SKH-1 mice and weekly measurement of tumors

All animal studies were approved by the Animal Protection Committee of Laval University and were conducted by the personnel who were trained and certified for animal work. The animal protocol was carried out as described earlier [11]. Briefly, the 5-week old SKH-1 albino hairless mice were irradiated thrice a week with 800 J/m2 of UVB filtered through Kodacel (to remove UVC) for 20 weeks. Mice were photographed weekly at the same time to build a database of weekly tumor appearance as well as the length, width, and height of each tumor over the 20-week protocol. The transient lesions that did not last for the entire protocol were excluded and merger of adjacent tumors was accounted for to determine the multiplicity of tumors. This database was subjected to analyses by OriginPro 2015 software (OriginLab Corp.) for assessment of severity of cancers by seven different criteria, as described below. Similar analyses could be conducted using more commonly used software for statistical and linear regression analyses, such as Microsoft Excel, R and LibreOffice Calc.

Measurement of prevalence of tumors or tumor-free survival fraction

The tumor prevalence (P) is the proportion of mice with at least one or two (as improved criterion described here) tumors at a given time. The tumor-free survival fraction was calculated as 1-P. The tumor-free survival graphs were analyzed using a Kaplan-Meier estimator with a log-rank test to calculate mean time when a mouse group develops the first or first two tumors and the median time when 50% of the mice in a group are affected.

Measurement of multiplicity, area and volume of tumors

Multiplicity of tumors was determined as average number of tumors per mouse. The area and volume were derived from length, width and height of the tumors using following formulae:

$$Area = \frac{\pi}{4} \times length \times width$$

$$Volume = \frac{\pi}{6} \times length \times width \times height$$

The tumor burden per mouse for each criterion was calculated from the sum of all tumor values for each mouse in the group in a given week, and presented as time-course of the burden value over the duration of the protocol.

Knud Thomsen's tri-dimensional tumor surface area

The three-dimensional tumor surface area was determined by KT-3D formula: $KT-3D\ surface = \pi\left(\frac{length^p height^p + width^p height^p + \frac{1}{2^p} length^p width^p}{3}\right)^{\frac{1}{p}}$

where p = 1.6075. From Klamkin's mathematical expression of the boundaries of an ellipsoidal surface [12], Knud Thomsen identified the best optimization to approximate this surface (with 1.061% error) [13]. In this formula, the two first terms in the numerator are the height contribution and the last term is the base area (length and width) contribution. The collective tumor burden by KT-3D surface area for each group was measured in the same way as described in section 2.3 for area and volume criteria.

Weekly occurrence of new tumors and tumor growth-rate

The occurrence of new tumors in a given week was derived by deducting multiplicity number of the previous week from the given week. Since tumor grows exponentially with cell division, its growth-rate was defined by the exponent of the exponential growth. The KT-3D surface data for each tumor at each time was log-transformed to generate linear data from which the slope represents the growth-rate of the given tumor. The growth-rates of the merged tumors were not assessed and corresponding tumors were excluded from this analysis. The average growth-rates of tumors appearing at week 13 were calculated for three periods: 13-20 weeks (total period); 13-16 weeks (initial phase) and 17-20 weeks (late phase). We also calculated growth-rate of tumors appearing at week 17 for the period of 17-20 weeks (early phase of late appearing tumors). The statistical differences were calculated using a two-sample t-test.

Statistical analyses for comparisons of groups

For each group, the data are presented as the mean burden per animal with standard error of the mean (SEM). The tumor burden data are calculated from the week where at least one mouse in any of the experimental groups developed a tumor. The tumor burden curves for different groups were compared with the ANOVA 2 factors test for repeated measures using OriginPro 2015 software where the factors are the group treatment and time (week) of the protocol. To determine the significance of difference between two groups at any given time, data were transformed to obtain a linear response of each factor with time. First, the data were converted by small numerical values when null, otherwise by a root function: square root for areas and KT-3D surfaces, and cubical root for volumes. Next, these quantities as well as the multiplicity and new tumor numbers were transformed by a

natural logarithm function. Multiple linear regression method was performed on the transformed data to check the normality distribution. The data sphericity was calculated using the Greenhouse-Geisser and the Huynh-Feldt corrections to estimate the factor interaction. The multiple comparisons, if required, were done with a Holm-Bonferroni post-hoc test. In all the statistical tests, the p-value below 0.05 was considered as a statistically significant difference.

3.8. References

[1] F. Benavides, T.M. Oberyszyn, A.M. VanBuskirk, V.E. Reeve, D.F. Kusewitt, The hairless mouse in skin research, J Dermatol Sci, 53 (2009) 10 - 18.

[2] A.Y. Voigt, M. Michaud, K.Y. Tsai, J. Oh, J.P. Sundberg, Differential Hairless Mouse Strain-Specific Susceptibility to Skin Cancer and Sunburn, J Invest Dermatol, 139 (2019) 1837-1840 e1833.

[3] S. Chilampalli, X. Zhang, H. Fahmy, R.S. Kaushik, D. Zeman, M.B. Hildreth, C. Dwivedi, Chemopreventive effects of honokiol on UVB-induced skin cancer development, Anticancer Res, 30 (2010) 777-783.

[4] C.K. Singh, C.A. Mintie, M.A. Ndiaye, G. Chhabra, P.P. Dakup, T. Ye, M. Yu, N. Ahmad, Chemoprotective Effects of Dietary Grape Powder on UVB Radiation-Mediated Skin Carcinogenesis in SKH-1 Hairless Mice, J Invest Dermatol, 139 (2019) 552-561.

[5] F.R. de Gruijl, J.B. Van Der Meer, J.C. Van Der Leun, Dose-time dependency of tumor formation by chronic UV exposure, Photochem Photobiol, 37 (1983) 53-62.

[6] M. Vaid, T. Singh, R. Prasad, S.K. Katiyar, Intake of high-fat diet stimulates the risk of ultraviolet radiation-induced skin tumors and malignant progression of papillomas to carcinoma in SKH-1 hairless mice, Toxicol Appl Pharmacol, 274 (2014) 147-155.

[7] J.M. Thomas-Ahner, B.C. Wulff, K.L. Tober, D.F. Kusewitt, J.A. Riggenbach, T.M. Oberyszyn, Gender differences in UVB-induced skin carcinogenesis, inflammation, and DNA damage, Cancer Res, 67 (2007) 3468-3474.

[8] Y.R. Lou, Q.Y. Peng, T. Li, C.M. Medvecky, Y. Lin, W.J. Shih, A.H. Conney, S. Shapses, G.C. Wagner, Y.P. Lu, Effects of high-fat diets rich in either omega-3 or omega-6 fatty acids on UVB-induced skin carcinogenesis in SKH-1 mice, Carcinogenesis, 32 (2011) 1078-1084.

[9] R.B. Cope, C. Loehr, R. Dashwood, N.I. Kerkvliet, Ultraviolet radiation-induced non-melanoma skin cancer in the Crl:SKH1:hr-BR hairless mouse: augmentation of tumor multiplicity by chlorophyllin and protection by indole-3-carbinol, Photochem Photobiol Sci, 5 (2006) 499-507.

[10] D.M. Euhus, C. Hudd, M.C. LaRegina, F.E. Johnson, Tumor measurement in the nude mouse, J Surg Oncol, 31 (1986) 229-234.

[11] M. Bazin, N.K. Purohit, G.M. Shah, Comprehensive measurement of UVB-induced non-melanoma skin cancer burden in mice using photographic images as a substitute for the caliper method, PLoS One, 12 (2017) e0171875.

[12] M.S. Klamkin, Elementary approximations to the area of N-dimensional ellipsoids, American Mathematical Monthly, 78 (1971) 280-283.

[13] L. Cao, Biological model representation and analysis, in: Thesis of mathematics and natural science, Leiden University, Section Imaging & BioInformatics, Leiden Insitute of Advanced Computer Science, Faculty of Science, Leiden University, 2014.

[14] E. Ashikhmina, D. Shook, F. Cobey, B. Bollen, J. Fox, X. Liu, A. Worthington, P. Song, S. Shernan, Three-dimensional versus two-dimensional echocardiographic assessment of functional mitral regurgitation proximal isovelocity surface area, Anesth Analg, 120 (2015) 534-542.

[15] S.L. Cotter, V. Klika, L. Kimpton, S. Collins, A.E. Heazell, A stochastic model for early placental development, J R Soc Interface, 11 (2014) 20140149.

[16] J.J. Tukker, B. Lasztoczi, L. Katona, J.D. Roberts, E.K. Pissadaki, Y. Dalezios, L. Marton, L. Zhang, T. Klausberger, P. Somogyi, Distinct dendritic arborization and in vivo firing patterns of parvalbumin-expressing basket cells in the hippocampal area CA3, J Neurosci, 33 (2013) 6809-6825.

[17] R.A. Sternberg, H.C. Pondenis, X. Yang, M.A. Mitchell, R.T. O'Brien, L.D. Garrett, W.G. Helferich, W.E. Hoffmann, T.M. Fan, Association between absolute tumor burden and serum bone-specific alkaline phosphatase in canine appendicular osteosarcoma, J Vet Intern Med, 27 (2013) 955-963.

[18] D. Xu, J. Cui, R. Bansal, X. Hao, J. Liu, W. Chen, B.S. Peterson, The ellipsoidal area ratio: an alternative anisotropy index for diffusion tensor imaging, Magn Reson Imaging, 27 (2009) 311-323.

[19] M.K. McGahon, J.M. Dawicki, A. Arora, D.A. Simpson, T.A. Gardiner, A.W. Stitt, C.N. Scholfield, J.G. McGeown, T.M. Curtis, Kv1.5 is a major component underlying the A-type potassium current in retinal arteriolar smooth muscle, Am J Physiol Heart Circ Physiol, 292 (2007) H1001-1008.

[20] J.M. Monteiro, P.B. Fernandes, F. Vaz, A.R. Pereira, A.C. Tavares, M.T. Ferreira, P.M. Pereira, H. Veiga, E. Kuru, M.S. VanNieuwenhze, Y.V. Brun, S.R. Filipe, M.G. Pinho, Cell shape dynamics during the staphylococcal cell cycle, Nat Commun, 6 (2015) 8055.

[21] S.L. Harwood, A. Alvarez-Cienfuegos, N. Nuñez-Prado, M. Compte, S. Hernández-Pérez, N. Merino, J. Bonet, R. Navarro, P.M.P. Van Bergen en Henegouwen, S. Lykkemark, K. Mikkelsen, K. Mølgaard, F. Jabs, L. Sanz, F.J. Blanco, P. Roda-Navarro, L. Alvarez-Vallina, ATTACK, a novel bispecific T cell-recruiting antibody with trivalent EGFR binding and monovalent CD3 binding for cancer immunotherapy, in: OncoImmunology, 2017.

[22] D. Pugh, C. Offler, M. Talbot, Y.-L. Ruan, Evidence for the role of transfer cells in the evolutionary increase in seed and fiber biomass yield in cotton, Molecular Plant, 3 (2010) 1075-1086.

[23] S.A. Broski, B.H. King, Drilling-in and Chewing-out of Hosts by the Parasitoid Wasp Spalangia endius (Hymenoptera: Pteromalidae) When Parasitizing Musca domestica (Diptera: Muscidae), Environ Entomol, 44 (2015) 1116-1124.

[24] B. Mori, H. Proctor, D. Walter, M. Evenden, Phoretic mite associates of mountain pine beetle at the leading edge of an infestation in northwestern Alberta, Canada, Can Entomol, 143 (2011) 44-55.

[25] A. Ansart, A. Guiller, O. Moine, M.C. Martin, L. Madec, Is cold hardiness size-constrained? A comparative approach in land snails, Evolutionary Ecology, 28 (2014) 471-493.

[26] C. Ihueze, C. Okafor, P. Ogbobe, Finite Design for Critical Stresses of Compressed Biomaterials under Transportation, in: Proceedings of the World Congress on Engineering (WCE) July 3-5 2013, SSRN, London, U.K. Available at SSRN, 2013.

[27] K. Millar, P. Gagnon, Mechanism of stability of rhodolith beds: sedimentological aspects, Marine Ecology Progress Series, 594 (2018) 65-83.

[28] S. Manet, A.S. Cuvier, C. Valotteau, G.C. Fadda, J. Perez, E. Karakas, S. Abel, N. Baccile, Structure of Bolaamphiphile Sophorolipid Micelles Characterized with SAXS, SANS, and MD Simulations, J Phys Chem B, 119 (2015) 13113 - 13133.

[29] Noerhidajat, R. Yunus, Z.A. Zurina, S. Syafiie, T.S. Chang, Modeling and Simulation of Heat and Mass Transfer in Oil Palm Fruit Digestion Process, J Emerging Trends in Engineering and Applied Sciences, 6 (2015) 136 - 143.

[30] M. Bonnici, A. Tacchini, D. Vucinic, Long permanence high altitude airships: the opportunity of hydrogen, Eur Transp Res Rev, 6 (2014) 253-266.

[31] Z. Jin, Z.Y. Yin, P. Kotronis, Y.F. Jin, Numerical investigation on evolving failure of caisson foundation in sand using the combined Lagrangian-SPH method, Marine Georesources and Geotechnology, 37 (2018) 23-35.

[32] P.M. Mwasame, N.J. Wagner, A.N. Beris, On the macroscopic modelling of dilute emulsions under flow, J Fluid Mechanics, 831 (2017) 433 - 473.

[33] F.E. Benedetto, H. Zolotucho, M.O. Prado, Critical Assessment of the Surface Tension Determined by the Maximum Pressure Bubble Method, Materials Research, 18 (2015) 9-14.

[34] F.R. de Gruijl, P.D. Forbes, UV-induced skin cancer in a hairless mouse model, Bioessays, 17 (1995) 651-660.

[35] N. Gyongyosi, K. Lorincz, A. Keszeg, D. Haluszka, A. Banvolgyi, E. Tatrai, S. Karpati, N.M. Wikonkal, Photosensitivity of murine skin greatly depends on the genetic background: clinically relevant dose as a new measure to replace minimal erythema dose in mouse studies, Exp Dermatol, 25 (2016) 519-525.

3.9. Acknowledgements

We are thankful to Mihaela Robu and Rashmi G. Shah for help in measurement of tumor dimensions. This work was supported by the Discovery Grant (RGPIN 2016-05868) and the Discovery Accelerator Supplement Grants (RGPA-492875-2016) to GMS from the Natural Sciences and Engineering Research Council of Canada. NKP received a graduate student scholarship from the CHU de Quebec Research Centre as well as a foreign student supplemental fee waiver from Quebec Government and the Shastri Indo-Canadian Institute.

Conflict of interest

Authors have no conflict of interest to declare.

Chapter 4. Decreased susceptibility of PARP1-knockout or PARP inhibitor-treated SKH-1 mice to develop UVB-induced non-melanoma skin cancers

Nupur K. Purohit[1,3], Marc Bazin[1,3], Marine A. Merlin[1,3], Julie Brind'Amour[4], Yulian Niu[5], Sabine Hombach-Klonisch[5] and Girish M. Shah[1,2,3]*

[1]CHU de Quebec-Laval University Research Center, Neuroscience and Cancer Axes, Laboratory for Skin Cancer Research, 2705, Boulevard Laurier, Quebec (QC), Canada

[2]Department of Molecular Biology, Medical Biochemistry and Pathology, Faculty of Medicine, Laval University, Quebec (QC), Canada

[3]Université Laval Cancer Research Center, Quebec (QC), Canada

[4]Department of Medical Genetics, Life Sciences Institute, The University of British Columbia, Vancouver, BC V6T 1Z3, Canada

[5]Department of Human Anatomy and Cell Science, Max Rady College of Medicine, University of Manitoba, Winnipeg, Canada

* Correspondence should be addressed to: girish.shah@crchul.ulaval.ca

4.1. Preface

This chapter, which is due to be submitted for publication, accounts for the major part of my doctoral work. I carried out genotyping over a period of 3 years for the creation of PARP1-KO SKH-1 mice (Fig 4.1A and Suppl. Fig. S4.1). I was actively involved in planning and execution of the chronic and acute UVB-induced SCC protocol, harvesting skin and tumor samples as well as analyzing the tumor data. I also contributed to the experiment and analysis required for the Figs. 4.1B, 4.1F, 4.3C, 4.7 and Suppl. Fig. S4.4B. Dr. Marc Bazin (second author on this manuscript) also participated in the execution of these experiments, tumor measurements and harvesting of skin and tumor samples. Dr Bazin and I also actively collaborated to develop a new photographic method to measure skin tumor burden in these mice (Chapter 2) and described a comprehensive list of seven criteria to measure severity of tumor burden in these mice (Chapter 3). Consequently, majority of the tumor burden data in this chapter was collected and analyzed using techniques described in chapters 2 and 3. Dr. Bazin also created the graphs from the data using Origin software, and developed a new program linked to the Image J software for automated machine-based extraction and analyses of the data from the immunohistological images of CPD and *in situ* TUNEL (Fig. 4.7). Marine Merlin, the third author of the manuscript, participated in the experiments for Fig. 4.1B, 4.1F, 4.3C and Suppl. fig. S4.4B. The PARP activation immunoblots in Fig. 4.1E were generated by Dr. Julie Brind'Amour (fourth author) during her Masters study in our lab. All the H&E staining (Fig. 4.3A, 4.3C and Suppl. Fig. S4.4B) as well as immunohistological staining for CPD and *in situ* TUNEL (Fig. 4.8) were carried out by Yulian Niu under the guidance of Dr. Sabine Hombach-Klonisch at her histology laboratory facility in University of Manitoba, Winnipeg, Canada. The histopathology of harvested tumors was analyzed by Dr. Sabine Hombach-Klonisch (Fig. 4.3A). Being the first author, I prepared the first draft of this manuscript and all the subsequent versions of it with the help of input from my advisor Dr. Girish M. Shah as well as the co-authors, Dr. Marc Bazin and Marine Merlin.

4.2. Résumé

Le carcinome spinocellulaire cutané (CSC) causé par le rayonnement ultraviolet B (UVB) solaire est le deuxième cancer de la peau de type non-mélanome le plus fréquent, avec le taux de développement de métastases le plus élevé et représente la majorité du taux de mortalité induit par cette catégorie de cancers. Parmi les multiples mécanismes cellulaires impliqués dans les CSC induits par UVB, il y a les voies de réparation des dommages à l'ADN, les réponses immunologiques et la mort cellulaire des kératinocytes endommagés. La poly(ADP-ribose) polymérase 1 (PARP1), une protéine nucléaire abondante dans les cellules de mammifères, est impliquée dans ces mécanismes dans plusieurs types cellulaires. PARP1 a donc le potentiel d'influencer l'effet cancérigène des UVB sur les kératinocytes mais les quelques études antérieures existantes n'ont montré que des résultats contradictoires sur le rôle des inhibiteurs pharmacologiques de PARP1 sur les CSC induits par UVB. Aucun de ces effets n'a été confirmé sur un modèle animal PARP1-knockout ou KO, probablement car le seul modèle PARP1-KO disponible était dans des lignées de souris dont la peau sombre les rend hautement résistantes au développement de CSC induits par UVB. Pour contourner cette limitation, nous avons créé une souris PARP1-KO dans la lignée de souris glabres albinos SKH-1, un modèle largement utilisé dans l'étude des CSC induits par UVB. Les souris PARP1-KO nouvellement créées ainsi que les souris SKH-1 de type sauvage avec ou sans inhibiteur de la PARP ont été soumises à un protocole d'exposition chronique aux UVB permettant le développement de CSC. Nous rapportons ici que l'absence ou la suppression de l'activité de PARP1 dans la peau des souris SKH-1 mâles et femelles réduit significativement la charge tumorale des CSC et prolonge le temps de latence des tumeurs. Les analyses hebdomadaires de l'apparition et de la croissance tumorale ont également révélé que le stade précancéreux du développement de CSC était réprimé chez les souris déficientes pour PARP1 à cause d'une augmentation de l'apoptose des kératinocytes pré-mutagènes de l'épiderme. Notre étude met en évidence l'utilisation potentielle des inhibiteurs de la PARP comme nouvel agent de chimioprévention contre les CSC induits par UVB.

4.3. Abstract

Solar ultraviolet B radiations (UVB)-induced cutaneous squamous cell carcinoma (SCC) are the second most common and fastest growing non-melanoma skin cancer (NMSC) with highest metastatic rate and account for a majority of NMSC-induced mortality. Among various cellular mechanisms implicated in UVB-induced SCC are the DNA repair pathways, immunological responses and death of damaged keratinocytes. Poly(ADP-ribose) polymerase-1 (PARP1), an abundant nuclear protein in mammalian cells, is implicated in some of these pathways in different cell types. Therefore, PARP1 has the potential to influence the carcinogenic effect of UVB on skin, but few earlier reports produced discordant conclusions regarding the effect of pharmacological inhibitors of PARP1 on UVB-induced SCC. None of these studies employed PARP1-knockout or KO mouse model to confirm their results, possibly because PARP1-KO was available only in the mouse strains with dark and hairy skin background, which are highly resistant to developing UVB-induced SCC. To overcome this limitation, we created PARP1-KO mice in the albino SKH-1 hairless background, a widely adopted model to study UVB-induced SCC. We exposed PARP1-KO SKH-1 mice or its wild type counterpart with or without topical application of PARP inhibitor to chronic UVB-irradiation for development of SCC. Here, we report that the absence or suppression of PARP1 activity in both the male and female SKH-1 mice significantly reduces the UVB-induced SCC tumor burden and prolongs the latency period for tumor growth. The weekly analyses of occurrence and growth-rate of tumors also revealed that the premalignant stage of the SCC development is suppressed in PARP1-impared mice due to increased apoptosis of premutagenic keratinocytes from their epidermis. Our study reveals a potential use of PARPi as a chemopreventive agent against UVB-induced SCC.

4.4. Introduction

The squamous cell carcinoma (SCC) arising from epidermal keratinocytes (KC) are the fastest growing non-melanoma skin cancer (NMSC) with the highest metastatic rate and cause majority of death due to NMSC [1, 2]. Cumulative exposure to terrestrial solar ultraviolet (UV) radiation, composed of UVA (400-320 nm) and UVB (320-280 nm) [3], is a major environmental risk factor for SCC development in humans [4]. More specifically, the exposure to UVB is closely associated with UV-induced SCC in mice and humans [5]. Consistently, the trend for recreational exposure to UVB in the past decades has resulted in an upsurge in worldwide incidence of SCC [6-8]. Chronic UVB exposure can mediate all the three stages of UVB-induced SCC development, namely initiation, promotion and progression; thus, making it a complete carcinogen when tested in multistage carcinogenesis model of mouse skin [9, 10].

Initiation of SCC is an early and irreversible process by which KC acquire the capacity to form tumors due to UVB-induced genetic mutations [11, 12]. The tumor initiating properties of UVB arise predominantly from its ability to cause direct DNA damage such as cyclobutane pyrimidine dimers (CPD) and 6-4 photoproducts (6-4PP) at dipyrimidine sites in the DNA [12]. The replication of DNA with unrepaired damage results in C→T transitions or CC→TT tandem mutations, which are referred to as "UV-signature mutations" [11]. These mutations can trigger inactivation of tumor suppressor genes and/or activation of oncogenes in KC, and hence initiation of SCC [11, 12]. Approximately 80% of SCC harbor the "UV-signature mutations" at the dipyrimidine sites. The repair of direct DNA damage by the nucleotide excision repair (NER) pathway [13, 14], which uses multiple proteins including the *Xeroderma pigmentosum* family of proteins, is the first and critical line of defense against solar UV-induced SCC. Consistently, *Xeroderma pigmentosum* (XP) patients, who have defects in NER pathway, have an increased susceptibility to develop sunlight-induced skin cancers including SCC [15]. In addition to direct DNA damage, UVB irradiation also results in intracellular formation of reactive oxygen species (ROS) that cause indirect DNA damage, such as 8-oxo-7,8-dihydroguanine (8-oxoG) and single strand breaks (SSB) [12]. The indirect DNA damage is repaired via base excision repair (BER) and SSB repair (SSBR) pathways [13, 14]. The UVB-induced 8-oxoG account for minor type of UVB-induced mutations such as G → T or A → G [16-18], which may also contribute to SCC initiation [19, 20]. The second line of defense against UV-induced SCC is death of KC with unrepaired DNA damage.

Promotion of the initiated KC is a reversible process, which entails clonal expansion of initiated cells resulting in visible outgrowth of pre-malignant tumors referred to as papilloma or actinic keratosis (AK) [10]. Initially UVB, via ROS and mediators of inflammation, triggers proliferation of all the

cells in epidermis [10]. However, initiated KC eventually outgrow normal cells due to advantages offered via their genetic mutations, such as resistance to death or loss of cell cycle control [9]. The increase in size of premalignant outgrowth and their malignant transformation to SCC mark the progression phase of SCC tumorigenesis, which involves formation of secondary mutations. Moreover, UVB-induced chronic inflammation as well as damage to epidermal and dermal immune cells compromise the skin's adaptive immune response resulting in immunosuppression that facilitates promotion and progression stages of SCC [21]. Thus, chronic UVB-induced genetic mutations, chronic inflammation and immunosuppression trigger initiation, promotion and progression of SCC in the mammalian skin in a complex multistage process. Hence, understanding the role of different proteins which are critical for one or more of these cellular processes could lead to novel targeted therapeutic approaches for SCC.

Poly(ADP-ribose) polymerase-1 (PARP1), an abundant genotoxic stress-responsive nuclear protein in mammalian cells, could be implicated in development of UVB-induced SCC based on its reported roles in multiple cellular processes associated with this carcinogenesis. One of the earliest responses of mammalian cells to UVB-induced DNA damage is the biphasic catalytic activation of PARP1 [22]. We showed that in the UV-irradiated cells, PARP1 rapidly accumulates at the subnuclear sites of local UV irradiation and is catalytically activated within seconds to form polymers of ADP-ribose using the substrate nicotinamide adenine dinucleotide (NAD^+) at the lesion site [22, 23], whereas its second phase activation is in response to indirect DNA damage [22]. Studies from our lab and others have shown that PARP1 and its catalytic activity improve the efficiency of mammalian NER [24-28]. Similarly, PARP1 and its activity are also required for the efficient BER/SSBR of indirect DNA damage [29-32]. Multiple studies with PARP1-knockout (KO) mice have shown that BER/SSBR function of PARP1 protects against the carcinogenesis [33].

In view of the importance of NER in preventing formation of SCC in UV-irradiated skin and the known role of PARP1 in promoting efficiency of NER, it is reasonable to presume that PARP1 could offer protection against the initiation of UVB-induced SCC development. Few earlier studies addressed this question but failed to offer a definitive conclusion as to whether PARP1 promotes or suppresses UVB-induced SCC. The treatment of mouse embryonic fibroblasts (MEF) with first generation PARPi 3-aminobenzamide (3-AB) inhibited their UVC-induced malignant transformation [34]. However, topical application of 3-AB was shown to increase the incidence and severity of UVB-induced SCC in SKH-1 mice [35]. None of these studies used PARP1-KO mice to validate their results with PARPi, possibly because the existing PARP1-KO mice were generated in dark and hairy C57BL6/129Sv strain [36-38] that is resistant to developing UVB-induced SCC and require very high

non-physiological doses of UVB with a very long latency time to develop SCC [39]. On the other hand, albino SKH-1 hairless mice develop SCC upon chronic exposure to physiological doses of UVB [40]. Since the morphology and the molecular mechanisms underlying the development of UVB-induced SCC in these mice are similar to that in humans [41], they are a widely adopted *in vivo* model to study the causes and cures of SCC [40]. Therefore, we have created PARP1-KO in SKH-1 hairless mouse model and report here that the absence or inhibition of PARP1 results in a significant suppression of UVB-induced SCC in SKH-1 mice.

4.5. Results

4.5.1. Characterization of PARP1 impaired SKH-1 mice for their use in UVB-indiced SCC protocol

PARP1-KO SKH-1 mice (KO mice), which were created by transferring the *Parp1*$^{-/-}$ genotype from PARP1-KO mice in C57BL6/129Sv background [36] to SKH-1 mice in albino hairless background (Suppl. Fig. S4.1A-B). In the skin samples of these mice, the disruption of PARP1 gene was verified by PCR (Fig. 4.1A). The absence of even a trace of active PARP1 protein or PAR formation in their epidermis was confirmed by *in situ* catalytic activation of immobilized PARP1 on the membrane (Fig. 4.1B). The KO mice had a small but significant reduction in litter size (7.7 ± 0.6 pups) as compared to WT-SKH-1 mice (9.4 ± 0.4 pups; Fig. 4.1C), which is in agreement with earlier study of PARP1-KO in C57BL6/129Sv strain [37]. Unlike previous reports [37, 42], we did not find any significant change in growth rate (body weight) of our KO mice over a 14-week period (Fig. 4.1D). We also did not observe any macroscopic skin lesions in our KO mice until the age of 6 months (Suppl. Fig S4.2A), unlike that reported earlier in another strain of mice [36].

Next, we examined the status of PARP1 activation in the skin of KO and PARPi (PARP1 impaired) mice up to 72 h following acute irradiation with 4000 J/m^2 UVB. The PAR-immunoblotting of epidermis of UVB-irradiated WT mice revealed multiple phases of PARP1 activation peaking at around 5 min, 1 h and from 6-48 h (Fig. 4.1E and F, left panels). The time frame of the first two phases of PARP1 activation are in agreement with our previous observation in UVB-irradiated cultured mammalian cells [22]. A single topical application of PARPi (PJ-34), 1 h prior to irradiation significantly suppressed formation of PAR in epidermis of WT mice up to 24 h, but not at 48 h after irradiation (Fig. 4.1F, middle panel), indicating pharmacodynamic turnover of topically applied PJ-34 over 2 days. As expected, we did not observe any trace of PAR signal at all the time points in immunoblotted KO epidermis, which suggested that PARP1 activation is the major cause for formation of the PAR-modified proteins in UVB-irradiated WT epidermis (Fig 4.1F, right panel).

4.5.2. PARP1-KO or PARP inhibition increased latency and decreased burden of UVB-induced skin cancers in mice

Next, we compared the development of SCC for 24 weeks among male and female WT, PARPi-treated WT (PARPi mice) and KO mice subjected to chronic low-dose UVB irradiation (800 J/m^2 UVB, 3× by week for first 20 weeks). To compensate for the pharmacodynamic turnover of topically applied PJ-34 (Fig. 4.1F, middle panel), PARPi was applied 1 h prior to each irradiation during first 20 weeks, and thereafter each two days in post-irradiation period of 21-24 weeks. No spontaneous

skin tumors were observed until 24 weeks in unirradiated control mice of all three groups (Suppl. Fig. S4.2A). In UVB-irradiated mice, although tumors in all three experimental groups appeared macroscopically similar, the majority of tumors in KO and PARPi mice were smaller in size and less in number as compared to those in WT mice (Suppl. Fig. S4.2B).

To quantify the difference in susceptibility of these mice to develop tumors, we used our newly developed photographic method to collect weekly data on tumors appearing in these mice [43] and our recently described panel of criteria [44] to assess the severity of tumor burden. The prevalence or fraction of mice surviving with less than two tumors revealed a modest but statistically significant increase in median time by 1 week for KO and 2 weeks for PARPi-treated WT mice, as compared to WT mice (16 weeks; Fig. 4.2A). By 18 weeks, only 68 % KO and 60 % PARPi mice had developed at least two tumors unlike 100% mice in WT group. Moreover, 3.0 % of mice in both PARP1 impaired groups did not develop two tumors until the end of the protocol at 24 weeks. The multiplicity criterion revealed a significant reduction in the average number of tumors per mouse in KO (15^{th} week onwards) and PARPi (13^{th} week onwards) mice as compared to WT mice (Fig. 4.2B). Next, we compared tumor area, volume and Knud-Thomsen tri-dimensional (KT-3D) surface area [44] in these three groups, and noted that PARP1 impaired mice had tumors with significantly smaller average KT-3D surface area (Fig. 4.2C), area and volume (Suppl. Fig. S4.3A and B) as compared to WT mice. Furthermore, there was no significant difference between PARPi and KO mice for all the above described criteria (Fig. 4.2A-C). Since the topical application of PARPi on WT mice skin inhibits the catalytic activation of other PARP family members in addition to PARP1 [45], we examined the role of activity of other PARPs in UVB-induced SCC by topical application of PARPi in KO mice (PARPi + KO mice). We observed that there was no significant difference between PARPi + KO and KO mice for all the above described criteria (Suppl. Fig. 4.3C-E). Similar to that observed with KO mice, PARPi + KO mice showed significant delay in median time of appearance of first two tumors (19 weeks; Suppl. Fig. 4.3C), lesser average number (17^{th} week onwards; Suppl. Fig. 4.3D) and smaller average KT surface area of tumor (14^{th} week onwards; Suppl. Fig. 4.3C) as compared to WT mice. Thus, our data indicate that although PARPi can inhibit other PARPs [45], the observed resistance to carcinogenesis is largely due to suppression of the catalytic activity of PARP1.

4.5.3. Decreased UVB-induced SCC and its premalignant precursor actinic keratosis (AK) in KO and PARPi mice

A previous histopathological study identified majority of tumors with ≥ 3 mm in diameter as SCC, ≤ 2 mm diameter as AK and with 2-3 mm diameter (intermediate size) as the mixed population of AK and SCC. The histopathological examination of multiple tumors with ≥ 3 mm in diameter

harvested from WT, KO and PARPi mice in our study also confirmed that all of them were SCC showing hyperkeratosis and infiltrative growth, with no histological differences among different groups (Fig. 4.3A). This allowed us to classify all the tumors in these groups by diameter criteria. We observed that both KO and PARPi mice had fewer total (Suppl. Fig. S4.4A) and average (Fig.4.3B) number of tumors with less than 2 mm (AK), 2-3 mm (AK+SCC) and more than 3 mm (SCC) diameters as compared to WT mice. However, the average number of tumors per mouse was significantly different for tumors with less than 2 mm and 2-3mm diameter (Fig. 4.3B). Our results suggest that PARP1 impaired mice have reduced burden of both the SCC and AK.

4.5.4. Impairing PARP1 in mice reduces chronic UVB-induced epidermal hyperplasia

Apart from the induction of SCC, chronic UVB also causes epidermal hyperplasia in the non-tumor bearing parts of the skin [10, 46]. To analyze the influence of PARP1 on this response, we performed epidermal morphometry of the non-tumor bearing skin from WT, KO and PARPi mice and their unirradiated counterparts. The epidermis of UVB-irradiated WT mice was 1.8 times thicker than that of the unirradiated WT counterparts (Fig. 4.3C). On the other hand, the epidermal thickness in KO and PARPi mice significantly increased 1.4 and 1.1 times, respectively as compared to their respective unirradiated controls. Thus, absence of PARP1 or its catalytic activity also significantly reduced chronic UVB-induced epidermal hyperplasia in the non-tumor bearing skin.

We also noted that chronic topical application of PARPi on unirradiated mice for ~6 months did not result in any apparent macroscopic changes as compared to the WT mice (Suppl. Fig. S4.2A). Furthermore, no significant difference in the epidermal thickness was observed between the unirradiated mice in WT and PARPi groups (Fig. 4.3C). Thus, topical application of PARPi on WT mice is non-toxic for at least 6 months. On the contrary, the epidermis of unirradiated KO mice was significantly thinner than that of WT mice. Since these mice were ~6 months old when these skin samples were harvested and thinning of epidermis is observed with ageing [47], we compared the epidermal thickness measured in the skin from unirradiated young (~1 month) WT and KO mice with that in the skin from their older (~6 months) counterparts (Suppl. Fig. S4.4B). While no difference in the epidermal thickness was observed between the skin from young WT and KO mice, the age-related epidermal thinning was slightly but significantly more in KO mice than in WT mice. Thus, our data of increased age-related epidermal thinning in KO mice is in agreement with previously reported accelerated ageing in these mice [42].

4.5.5. Decreased susceptibility to develop UVB-induced SCC in PARP1 impaired mice is independent of the sex and UVB-dose

The above described data on the influence of PARP1 on SCC development was derived from pool of male and female mice in each group. Since sex could be a critical variable in development of SCC, we examined the influence of PARP1 in each sex in this model. Stratifying tumor burden data according to sex in each group revealed that the median time for fraction of mice surviving with less than two tumors was significantly longer in both male and female KO and PARPi mice as compared to WT counterparts of the same sex (Fig. 4.4A and B). While 7 % of male KO and PARPi mice did not develop at least two tumors until 24 weeks (Fig. 4.4A), all female KO and PARPi mice developed at least two tumors by 21-22 weeks (Fig. 4.4B), which was still a significantly delayed response as compared to female WT mice (18 weeks). We also observed that both male and female KO and PARPi mice developed significantly lesser number (Fig. 4.4C and D) and smaller size tumors (Fig. 4.4E and F) as compared to their WT counterparts. To note, there was no significant difference in the tumor-free survival as well as average number and KT-3D surface area of tumors between male and female populations within WT, KO and PARPi groups (Suppl. Fig. S4.5). Thus, our data indicate that reduction in UVB-induced tumor burden in KO and PARPi mice is independent of sex.

To study the effect of higher dose of UVB on the SCC development in absence of PARP1 in WT mice, we carried out a high-dose chronic UVB study in which male and female WT and KO mice were exposed to 2240 J/m^2 UVB; 3× per week for 16 weeks and observed for another 8 weeks post UVB irradiation (total 24 weeks). Analogous to low-dose UVB study, we observed that median time of appearance of first two tumors was delayed (Fig. 4.5A), average number was less (Fig. 4.5B) and average tumor size was smaller (Fig. 4.5C) in KO mice as compared to WT mice in the high-dose UVB study. Furthermore, diameter specific classification of tumors for this study also showed reduced total (Suppl. Fig. S4.6B) and average (Fig. 4.5D) number of AK and SCC in KO mice as compared to WT mice. Thus, our data indicate that effect of absence of PARP1on UVB-induced SCC development in mice was similar at both the low- and high-dose UVB.

4.5.6. Initiation and/or promotion of UVB-induced SCC is reduced in KO and PARPi mice

To further examine the stage at which the UVB-induced SCC was reduced, we used the measurement criteria such as occurrence of new tumors and growth-rate of tumors, as described by Bazin *et al.* [44]. In low-dose UVB studies, we observed a significant reduction in the occurrence of new tumors from 15th and 16th week onwards in KO and PARPi mice, respectively as compared to WT mice (Fig. 4.6A). Similarly, we also observed significant difference in the occurrence of new tumors week 14th week onwards in KO mice as compared to WT mice from the high-dose UVB studies (Fig. 4.6B). In both low and high-dose UVB protocols, the average growth-rate of tumors arising during and after chronic UVB irradiation were not significantly different in the WT, KO and PARPi mice (Suppl. Fig.

S4.7A and B). Hence, this allowed us to compare the average growth-rate of tumors between these three groups throughout the protocol irrespective of their occurrence during or after chronic UVB irradiation. When we compared the average growth-rate of tumors, which were classified as SCC in low-dose (Suppl. Fig. S4.4A) and high-dose (Suppl. Fig. S4.6B) UVB protocols between the indicated groups of mice over a period of 8 weeks, we observed no significant difference (Fig. 4.6C and D). The occurrence of new tumors represents initiation and/or promotion stage of SCC because it accounts for every new visible outgrowth of at least ~0.4 mm diameter that could have arisen from the clonal expansion of initiated KC [10]. On the other hand, the average growth-rate of tumor represents progression because it accounts for change in size of existing tumors. Therefore, our data indicate that initiation and/or promotion of UVB-induced SCC development is reduced in PARP1 impaired mice.

4.5.7. Increased apoptosis eliminates the premutagenic KC in the epidermis of UVB-irradiated KO and PARPi mice

Initiation of SCC tumorigenesis is marked by the formation of KC with UV-signature mutations in tumor suppressor genes or oncogenes [10]. Since these mutations arise from unrepaired UVB-induced direct DNA lesions [11], optimal functionality of NER pathway is required for the removal of these potential mutagenic CPD after each UVB exposure. A previous study from our lab showed that the topical application of PARPi on WT mice resulted in reduced removal of UVB-induced thymine dimers from their epidermis [26]. To determine the NER capacity in the epidermis of KO mice skin, we did IHC staining of CPD in the 5 µm skin sections up to 72 h after single UVB exposure (Fig. 4.7A). We observed a significantly higher absorbed intensity of CPD signal per CPD positive nucleus in KO epidermis at 24 h, indicating a delay in their removal as compared to that in WT mouse epidermis. This is in agreement with the previously reported role of PARP1 in facilitating NER in skin cells including transformed human KC [25, 26, 48, 49]. Intriguingly, this absorbed intensity was significantly lower as compared to that in WT mice at 48 h, thereby suggesting faster removal of CPD from the KO epidermis.

Previous studies showed that PARPi treated or PARP1-depleted transformed and/or primary human KC exhibit higher level of death by apoptosis as compared to their control counterparts [49, 50]. To verify if this was also the case in PARP1 impaired epidermis, we carried out *in situ* TUNEL analysis in skin sections of KO, PARPi and WT mice up to 72 h after single UVB exposure. In UVB-treated WT mice epidermis, we observed that the density of TUNEL positive cells and absorbed intensity per TUNEL positive nucleus were highest at 6 h and returned by 24 h to the similar background level as in untreated WT mice epidermis (Fig. 4.7B). On the other hand, in the epidermis of KO and PARPi

mice the density of TUNEL positive cells and the absorbed intensity per TUNEL positive nucleus continued to increase until 24 h and returned to the background level only at 72 h. Interestingly, the density of TUNEL positive cells and the absorbed intensity per TUNEL positive nucleus coincided with the reduced absorbed intensity per CPD positive nuclei in KO mice at 48 h. Altogether, our data indicates that PARP1 impaired mice exhibit higher level of apoptosis in their epidermis as compared to that in WT mice and, indirectly suggest that CPD positive cells, which are the potential SCC progenitors or premutagenic cells in which UV-signature mutations can arise, are eliminated by apoptosis in PARP1 impaired mice.

4.6. Discussion

SCC, for which one of the major risk factors is solar UVB, account for 20 % of skin cancer deaths and its ability to metastasize makes preventative measures and curable treatment options a priority [1]. PARP1 serves multiple functions in response to UVB-induced DNA damage including its recently discovered role in facilitating the NER of UV-induced direct DNA damage [22-28]. Therefore, we aimed at understanding the role of PARP1 in the development of chronic UVB-induced SCC by creating and using PARP1-KO mice in SKH-1 background, as well as by inhibiting PARP1 catalytic activity in SKH-1 mice by topical application of PARPi. Consistent with our previous observation in cultured cells [22], PARP1 activation was observed to be one of the earliest events after UVB exposure in the skin of WT mice. We further demonstrate that impaired PARP1 activation in the skin of PARPi and KO mice reduced their susceptibility to UVB-induced tumorigenesis irrespective of the sex as well as the dose of UVB. The analysis of the tumor burden data showed that the reduced susceptibility to SCC development in these mice is due to the reduced initiation and/or promotion of SCC tumorigenesis. Since we did not observe any difference between the susceptibilities of the KO and PARPi mice to UVB-induced SCC, we conclude that catalytic activity of PARP1 is co-opted for the initiation and/or promotion of UVB-induced SCC in SKH-1 mice.

Our results are surprising with respect to the reported roles of PARP1 as onco-suppressive and a barrier against spontaneous as well as alkylating DNA damage-induced tumorigenesis in majority of studies using PARP1-KO mice or PARPi treated mice [33, 51]. This anti-cancer property of PARP1 has generally been linked to its role in repair of alkylated DNA via BER/SSBR pathway and thus in maintaining the genome stability [33]. The occurrence of UVB-induced SCC is associated with the defective NER pathway, as demonstrated by the increased susceptibility of the knockout mouse models of key NER pathway proteins to SCC tumorigenesis [52-56]. Recently, PARP1 was shown to facilitate NER of UV-induced direct DNA damage and its depletion or inhibition resulted in delayed NER kinetics [25, 26]. While our results challenge the widely accepted role of PARP1 in suppressing tumorigenesis [51], they are in agreement with the previous study showing reduced susceptibility of PARP1-KO and PARPi treated mice (C57BL6/129Sv background) for chemical-induced development of skin papillomas [57, 58]. Notably, the molecular changes occurring during the chemical-induced skin carcinogenesis are different from that during chronic UVB-induced SCC tumorigenesis [59].

The phenotype of our newly created PARP1-KO mouse model is in agreement with the reported dispensability of PARP1 for the development of mouse in the absence of deliberate stressors [60]. Nonetheless, when PARP1-KO C57BL/6 mice were maintained under normal physiological

conditions up to 24 months, they exhibited accelerated aging and reduced life span [42]. Considering that thinning of skin epidermis represents ageing [47], our epidermal morphometry data showing relatively increased thinning of unirradiated KO mice epidermis with age (Suppl. Fig. S4.4B) is in agreement with the previous report of accelerated aging due to the absence of PARP1 [42]. Since our conclusions for the KO mouse development are based on the observations made until 6 months, we do not rule out that they might differ at older age, as reported previously for PARP1-KO C57BL/6 mice [42].

The absence of difference in any of the cancer severity criteria between KO and PARPi mice despite the different level of PAR in their skin indicated that the inhibition of catalytic activity of PARP enzymes was enough to reduce UVB-induced SCC tumorigenesis in mice. Since topical application of PARPi in KO mice did not change their susceptibility to UVB-induced SCC, we conclude that the catalytic activity of PARP1 and not any other PARP family member is implicated in UVB-induced SCC development. However, the reduced susceptibility of PARPi mice to SCC observed in our study with PJ-34 as a PARPi is in contrast to the previous study which used 3-AB [35]. This discrepancy could be due to the PARP1-independent protection of the KC from UVB-induced cell death by 3-AB [50]. In the same study, treatment with other PARPi including PJ-34 potentiated UVB-induced keratinocyte death in PARP1-dependent manner.

In cancer cells, functions of PARP1 are co-opted for their survival and promote the growth of established tumors [51]. This has led to the therapeutic targeting of PARP1 in cancers using PARPi, with FDA approval of several PARPi to use in clinic for the treatment of ovarian, breast and prostate cancer [61]. However, our experimental set up in this study involving PARPi application even before the UVB-induced skin tumor development does not allow us to comment on chemotherapeutic effect of PARPi. Hence, it is required that tumors, which are developed without any impairment of PARP1 and its activity, are treated with PARPi to examine its chemotherapeutic effect. Nonetheless, we did observe that following their occurrence, the tumors in KO and PARPi mice grow with the same speed as that in WT mice.

On the contrary, the reduced initiation and/or promotion of SCC in PARPi mice suggests that inhibiting the catalytic activity of PARP1 can have chemopreventive effect on UVB-induced SCC. To the date, only one study has demonstrated prophylactic function of PARPi in cancer based on the observed delay in mammary tumor development and increased life span of PARPi treated BRCA1-deficient mice [62]. This study suggests that the use of PARPi could be a promising chemopreventive option for women with BRCA mutation because they have a 50-80 % risk of developing breast cancer by age of 70 years. Similarly, elderly Caucasian population is highly susceptible to UV-induced

NMSC including SCC [63]. Despite growing awareness and use of sunscreens, studies have shown only a modest reduction in AK and SCC of the skin [64], thus presenting the need for better chemoprevention strategies. Hence, further studies validating the use of PARPi as a novel and targeted chemoprevention strategy for the UV-induced SCC are warranted.

The major issue which was raised with the long-term use of PARPi as a chemopreventive agent is their toxicity in the normal tissues [65]. Addressing this in our study, we did not find any macroscopic as well as microscopic changes in the skin of PARPi mice as compared to WT mice. Assuming that topical application of PARPi on mice results in PARP inhibition only in skin, our results suggest non-toxic effect of PARPi in WT mice after 26 weeks of its topical application. Hence, further studies validating the long-term use of PARPi as a novel chemoprevention strategy for the UV-induced SCC are warranted.

The chronic UVB-induced concomitant reduction in NER [66] and cell death capacity [67] results in formation of premutagenic KC. Therefore, our data of the CPD repair and cell death in PARP1 impaired mice epidermis post single exposure to UVB suggest that even though NER capacity is compromised, the increased elimination of the cells via apoptosis could reduce the number of premutagenic KC during chronic UVB protocol. Earlier studies have also associated the increased KC death post UVB with the reduction in development of chronic UVB-induced SCC [68, 69] and vice versa [68, 70]. Moreover, PARPi exerted its chemopreventive effect against breast cancer in BRCA1-deficient mice by inducing apoptosis in the mammary glands [62]. Increased elimination of premutagenic KC results in reduced formation of mutated (initiated) KC. To this front, a recent study demonstrated reduced UVB-induced mutagenesis in PARPi treated CHO cells [49]. Therefore, we propose that impaired PARP1 function could perturb the initiation of SCC tumorigenesis by promoting the death of UVB-damaged keratinocyte, thus eliminating potential premutagenic cells, and hence the frequency of mutated KC in the PARP1 impaired mice epidermis. This could also be responsible for the observed reduced chronic UVB-induced epidermal hyperplasia in non-tumor bearing part of the PARP1 impaired mice skin as compared to WT mice skin. Nonetheless, further studies are required to determine the frequency of mutated cells in the epidermis of chronic UVB-irradiated PARP1 impaired mice.

Since PARP1 is required for the inflammatory response in the skin [57, 58] and UVB-induced pro-inflammatory mediators provide signal for KC proliferation [10], it cannot be ruled out that abrogation of chronic UVB-induced inflammation in PARP1 impaired mice skin can reduce promotion of SCC. Since UVB-induced inflammatory mediators trigger immunosuppression in the skin [71], our proposal of reduced inflammatory response in PARP1 impaired skin is further

supported by previously reported reduced UVB-induced immunosuppression in PARPi treated mice skin [72]. The growth of tumors during progression phase is also facilitated by UVB-induced pro-inflammatory mediators. However, our tumor data suggest no difference in the progression of SCC. Further studies examining UVB-induced immune responses in the skin of PARP1 impaired mice will allow to determine whether the promotion stage of SCC tumorigenesis is also affected.

Solar UV cause different types of skin cancers including melanoma, the most dangerous type and basal cell carcinoma, the most common type of NMSC [73]. Interestingly, it has been shown that PARP1 facilitates the metastasis of melanoma tumors in mice [74]. Thus, further studies examining the role of PARP1 in the development of these cancers can allow to include PARPi as chemopreventive agent in sunscreens in the era when several PARPi are being approved from FDA as chemotherapeutic drug for selected cancer therapies [75].

4.7. Figures and legends

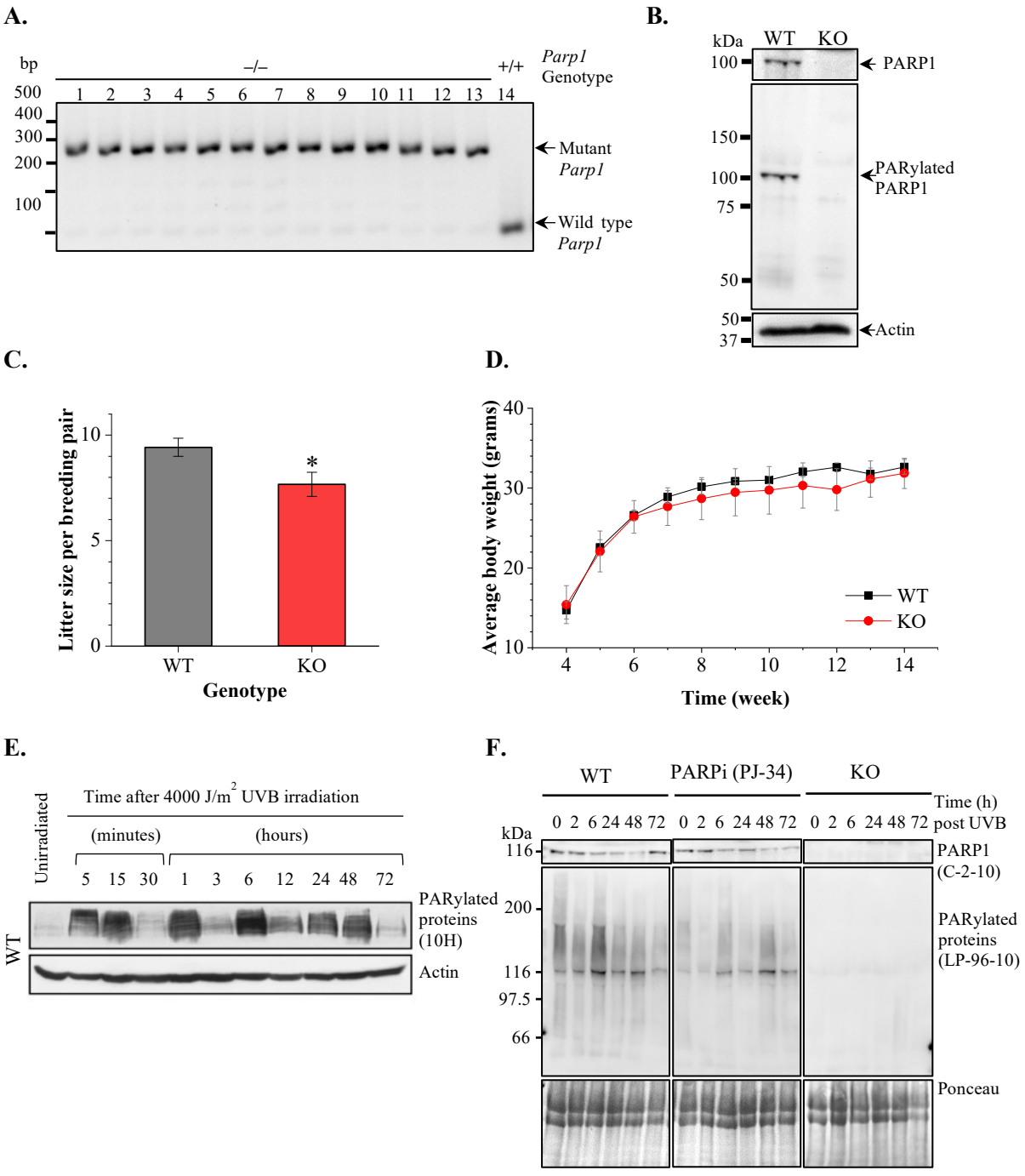

Figure 4.1. Characterization of PARP1 impaired mice

(A-D) Characterization of PARP1-KO mice (A) The DNA from ear punched skin biopsies were genotyped by PCR to validate the presence of homozygous mutant *Parp1* gene in the KO mice, which were generated by crossing male and female *Parp1*$^{+/-}$ mice. The figure represents the *Parp1* genotype of 12 mice that were used for subsequent outbreeding to create the colony of PARP1-KO SKH-1 mice. (B) PARP1 activity-western blotting. The epidermal protein extracts from untreated WT and

KO mice were used to examine the catalytic activity of PARP1 by activity western blotting technique. (C) Litter size of KO mice. The number of babies per breeding pair was determined from four to ten breeding pairs of KO and WT mice that were used in five different batches of breeding over a time of two to three years and their means ± SEM were plotted. The statistical significance was determined by Student's t-test and asterisk (*) indicates p-value ≤ 0.05. (D) Body weight of KO mice. The weighing scale (Sartorius ED2201), which is calibrated once a year in the animal facility, was used to determine the body weight of twenty KO and WT mice each week for 11 weeks. Mean ± SEM of body weight during each week were plotted. (E-F) Absence or suppression of UVB-induced catalytic activation of PARP1 in the skin of KO and PARPi treated WT mice (E) Detection of PARylated proteins in the WT mice epidermis at indicated time points after single exposure to 4000 J/m^2 UVB by western blotting. (F) Detection of PARylated proteins in the epidermis of WT mice treated or not with PARPi (PJ-34) as well as KO mice. Four mice per time point in each treatment group were irradiated (or not) with 4000 J/m^2 UVB and skin epidermis was harvested at the indicated time points. Their protein extracts were immunoblotted for detection of PAR.

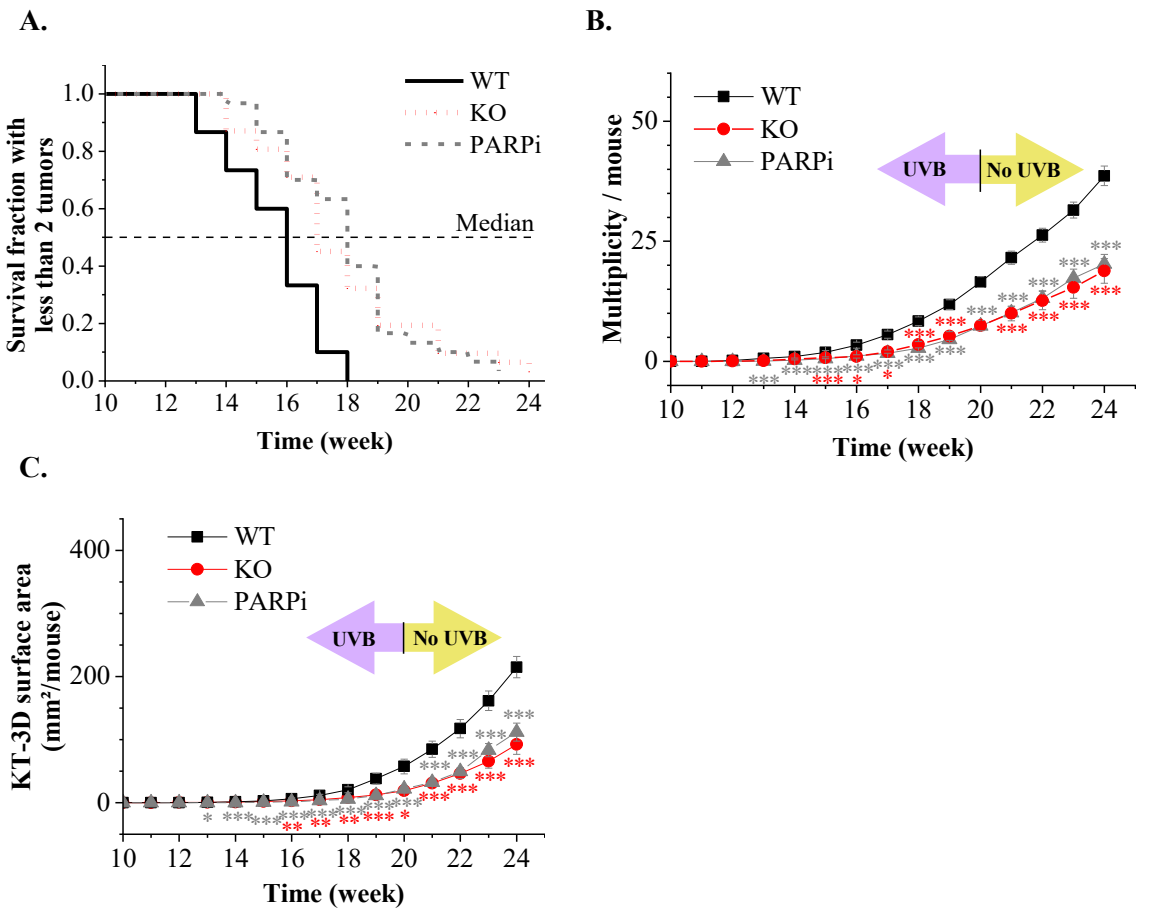

Figure 4.2. Increased tumor latency and decreased tumor burden on the skin of chronic low-dose UVB-irradiated KO and PARPi mice

The tumor measurement data from the combined population of male and female WT (n = 30), KO (n = 31) and PARPi (n = 31) mice, from chronic low-dose UVB irradiation protocol, are used for the following analyses. (A) Tumor latency. The analysis of fraction of mice surviving with less than two tumors shows significantly ($p \leq 0.001$) late tumor development in KO and PARPi mice compared to that in WT mice. (B-C) Tumor burden. The violet and yellow arrows indicate the UVB-irradiation and no UVB-irradiation phases, respectively. The tumor number (B) and KT-3D surface area (C) were determined from the acquired photographs of KO, PARPi and WT mice during each week until 24th week of the protocol and their mean ± SEM were plotted against time. The red and grey colored asterisks (*) indicate the statistical significance of KO and PARPi mice, respectively as compared to WT mice during the same week. The asterisks ***, ** and * indicate p-value ≤ 0.001, ≤ 0.01 and ≤ 0.05, respectively relative to WT group.

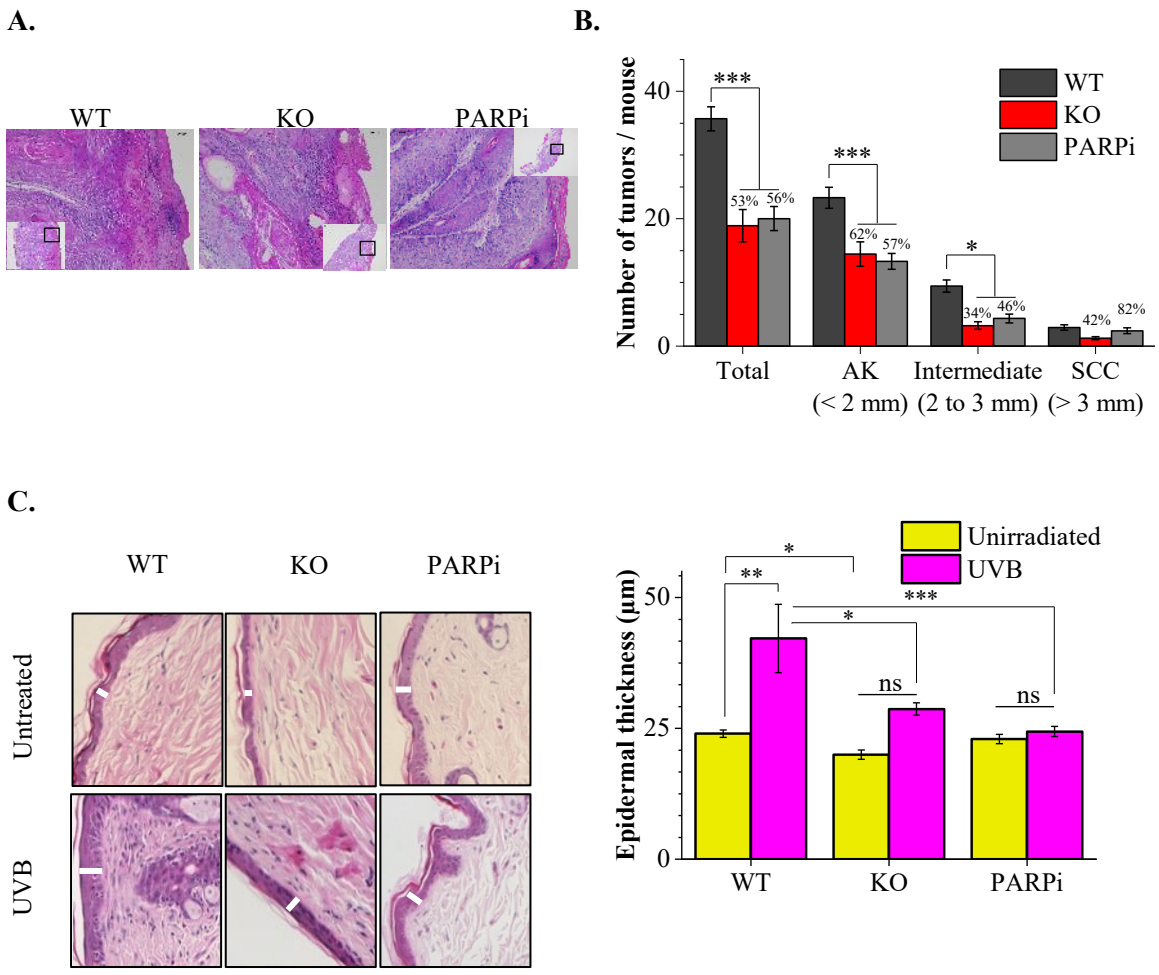

Figure 4.3. Decreased UVB-induced premalignant AK and cancerous SCC in KO and PARPi mice

(A) Histology of tumors. The H&E stained 5 µm sections of tumors (> 3 mm diameter) were harvested at week 26 from WT, KO and PARPi mice and determined to be squamous cell carcinoma (SCC) by pathologist. 30-60 tumors per treatment group were analysed. (B) Diameter specific classification of tumors. The tumors of WT, KO and PARPi mice at 24th week of the protocol were classified into three groups based on their diameter as indicated and the tumor number per mouse ± SEM of each indicated size in all the three groups of mice were plotted. The indicated percentages of tumor number per mouse in KO (n = 31) and PARPi (n = 31) mice groups are relative to WT mice (n = 30). The asterisks ***, ** and * indicate *p*-value ≤ 0.001, ≤ 0.01 and ≤ 0.05 respectively for KO and PARPi mice relative to WT group. (C) Epidermal morphometry. 10-15 20× images of H&E stained whole skin from unirradiated mice (n=4) and non-tumor bearing whole skin from chronic low-dose UVB irradiated mice (n=5) from each, WT, KO and PARPi groups were used for the measurement of epidermal thickness as explained in materials and methods section. The mean ± SEM of epidermal thickness were plotted and statistical significance between all the groups was determined by Student's t-test. Asterisk (*) represents the statistical significance between the indicated groups. The symbols ***, ** and * indicate p-value ≤ 0.001, ≤ 0.01 and ≤ 0.05, respectively.

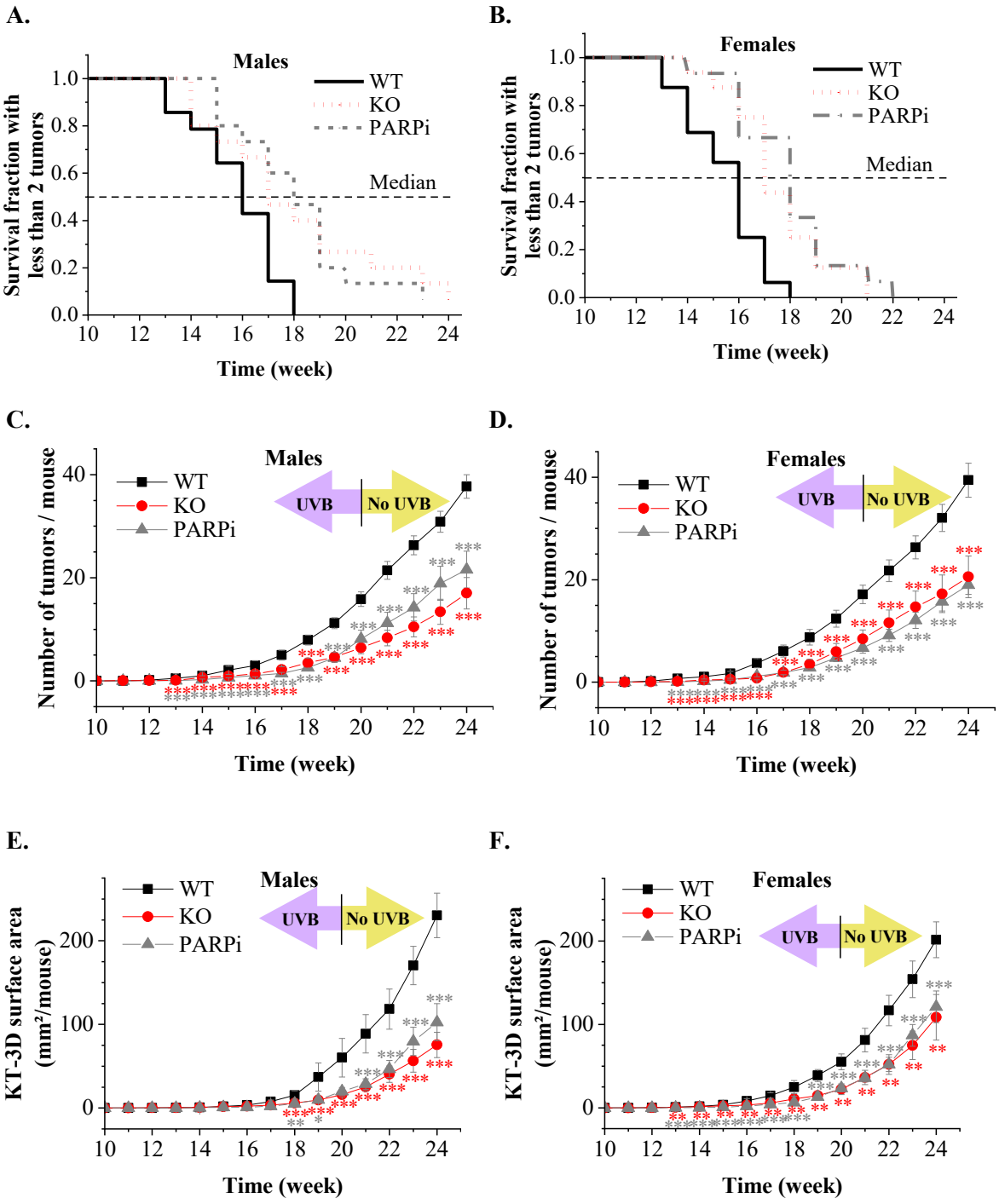

Figure 4.4. UVB-induced tumorigenesis in WT, KO and PARPi mice is independent of sex
The tumor measurement data of male and female WT (male- n = 14 & female- n = 16), KO (male- n = 15 & female- n = 16) and PARPi (male- n = 15 & female- n = 16) mice from chronic low-dose UVB-irradiation protocol were compared separately for the following analyses. (A-B) Tumor latency in male (A) and female (B) WT, KO and PARPi mice. The analysis of fraction of mice surviving with less than two tumor shows significantly ($p \leq 0.02$ for male and $p \leq 0.001$ for female) late tumor development in KO and PARPi mice with median time of 17 and 18 weeks, respectively as compared to that of 16 weeks for WT mice. (C and E) Tumor burden in male WT, KO and PARPi mice. The

mean ± SEM of tumor number (C) and KT-3D surface area (E) were plotted against time. The red and grey colored asterisks (*) indicate the statistical significance of KO and PARPi mice, respectively as compared to WT mice during the same week. (D and F) Tumor burden in female KO, PARPi and WT mice. The tumor burden data was plotted, and the statistical significance was determined as described for male KO, PARPi and WT mice in C and E. The asterisks ***, ** and * indicate p-value ≤ 0.001, ≤ 0.01 and ≤ 0.05, respectively relative to WT group.

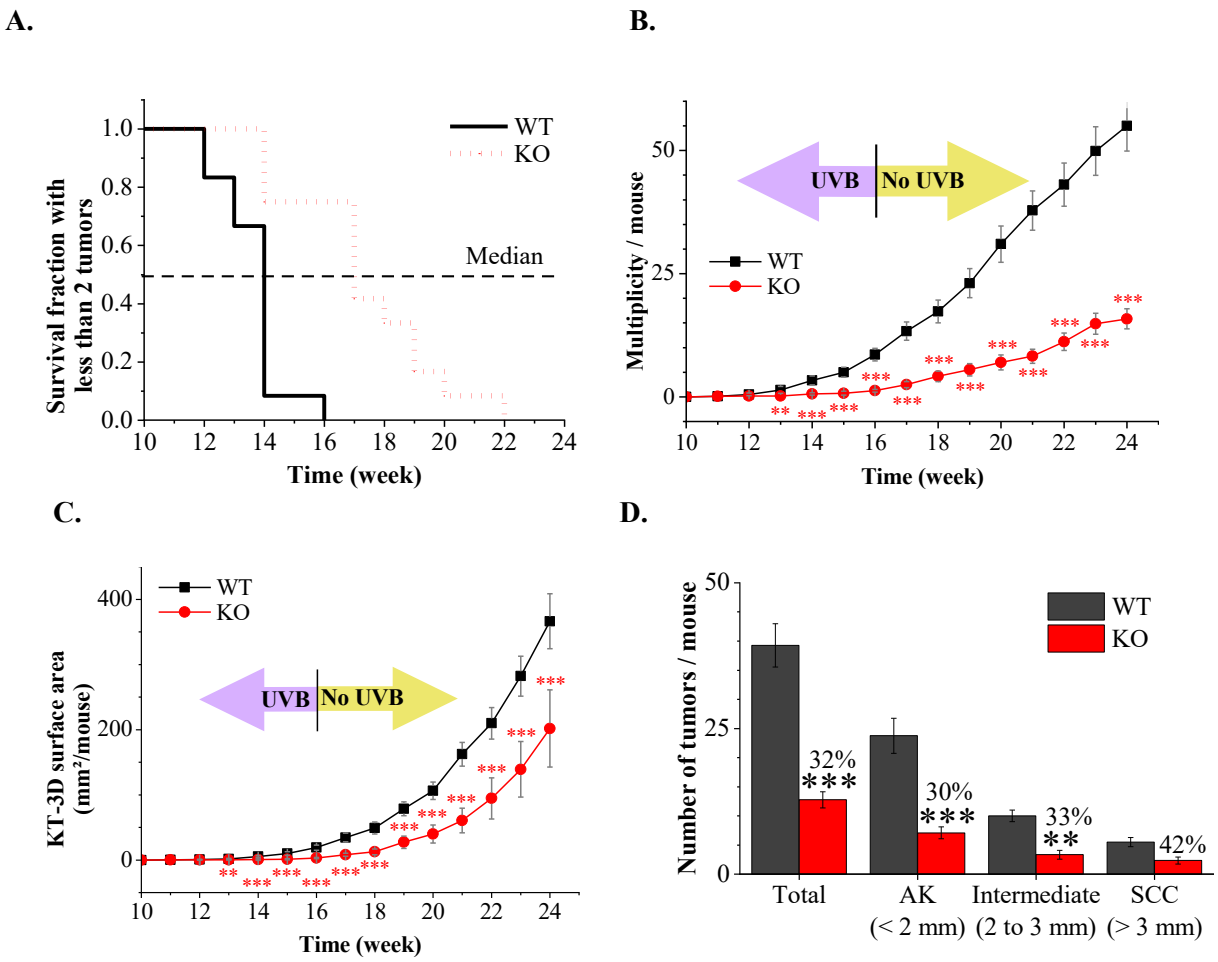

Figure 4.5. Delay of skin tumorigenesis in KO mice at high-dose UVB

The tumor measurement data from the male and female WT (n=12) and KO (n=12) mice, from chronic high-dose UVB irradiation protocol, were used for the following analyses. (A) Tumor latency in WT mice versus KO mice from high-dose chronic UVB protocol. The survival analysis of fraction of mice surviving with less than two tumors shows significantly ($p \leq 0.001$) late tumor development in KO mice with median time of 17 weeks as compared to that of 14 weeks for WT mice. (B-C) Tumor burden. The mean ± SEM of the tumor number (B) and KT-3D surface area (C) were plotted against time. (D) Size specific classification of tumors. The tumors of WT and KO mice at 24th week of the high-dose UVB protocol were classified into AK, SCC or other tumor sets based on their diameter and their number per mouse in each group were plotted. The indicated percentages of total tumor or average number in KO and PARPi mice groups are relative to WT mice. The symbols ***, ** and * indicate p-value ≤ 0.001, ≤ 0.01 and ≤ 0.05, respectively relative to WT group during the same week.

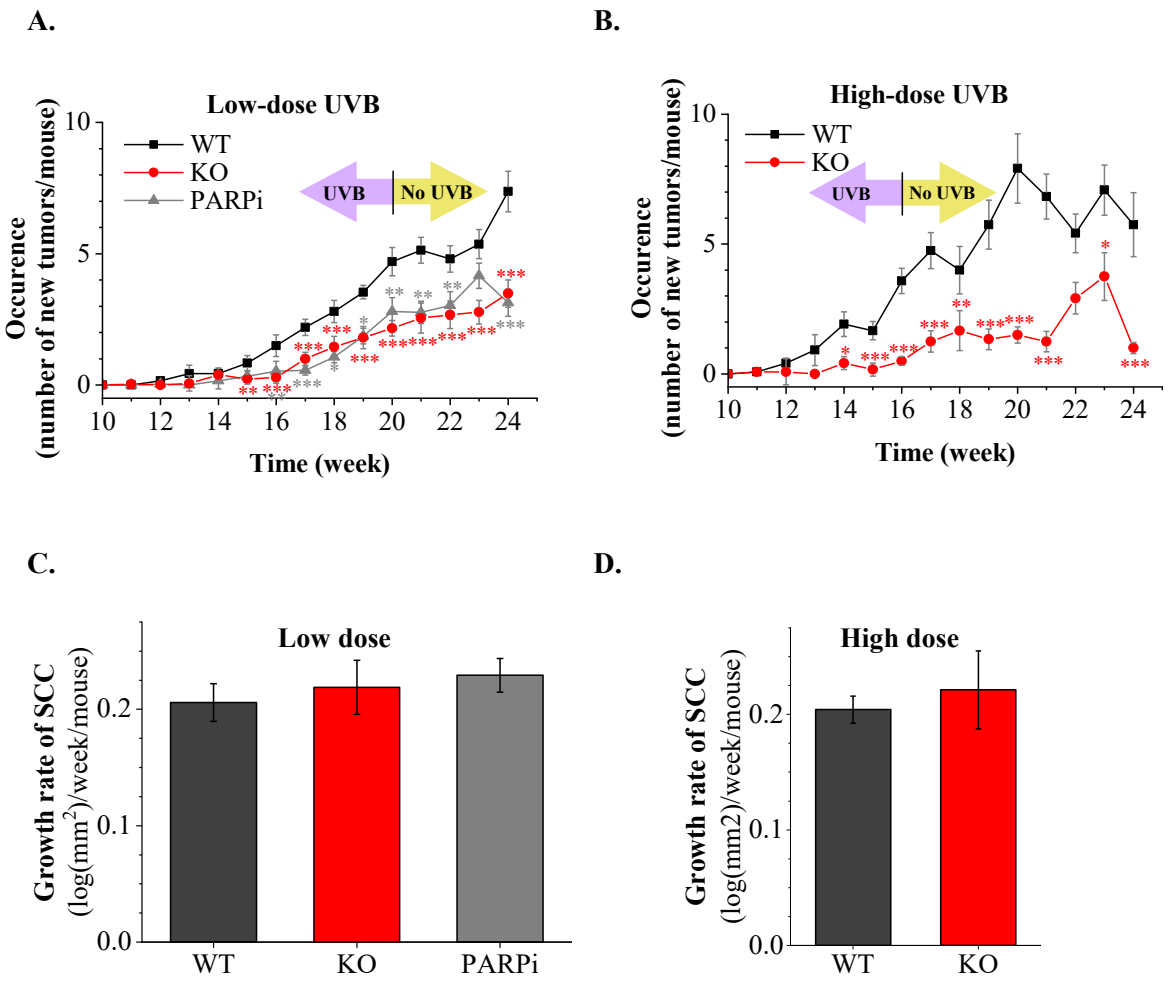

Figure 4.6. UVB-induced tumorigenesis is delayed at initiation and/or promotion stage in KO and PARPi mice

The tumor measurement data from the combined population of male and female mice, from chronic low-dose as well as high-dose UVB irradiation protocol, are used for the following analyses. (A-B) New tumor number per mouse. The mean ± SEM of the new tumor number were plotted against time for the KO, PARPi and WT mice from low-dose UVB protocol (A) and KO and WT mice from high-dose UVB protocol (B). The red and grey asterisks (*) indicate the statistical significance of KO and PARPi mice as compared to WT mice during the same week. (C) Growth rate of SCC from low-dose UVB protocol. In the WT, KO and PARPi groups, the populations of SCC (diameter specific classification of tumors in Fig. 4.3B) which developed at week 17 were compared and found to be statistically non-significant. (D) Growth rate of SCC from high-dose UVB protocol. In the WT and KO groups, the populations of SCC (diameter specific classification of tumors in Fig. 4.5D), which developed at week 17 were compared and were found to be statistically non-significant.

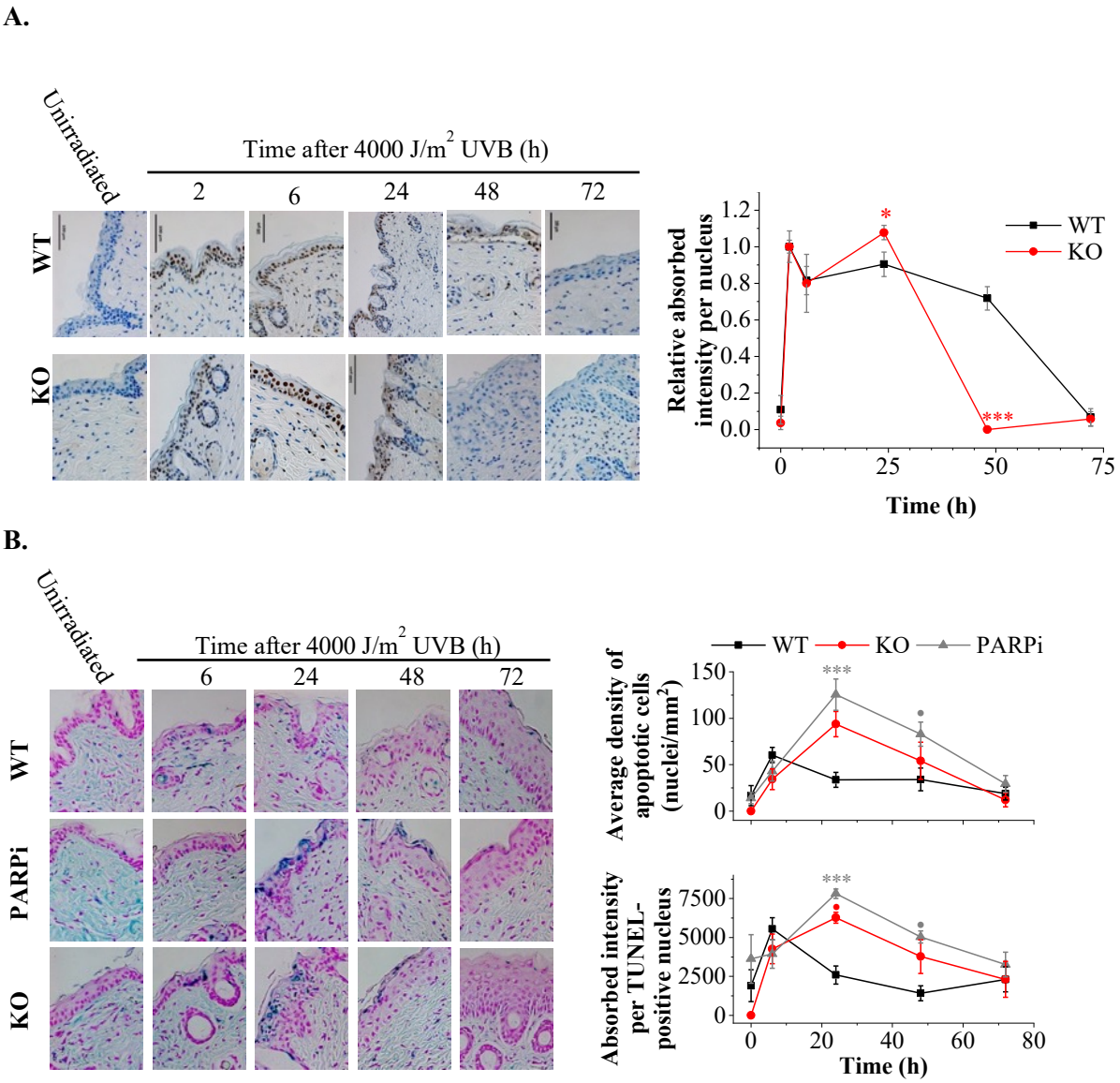

Figure 4.7. Delayed NER and increased apoptosis in the epidermis of UVB-irradiated KO and PARPi mice

(A) The CPD repair in the epidermis of KO and WT mice following single acute exposure to UVB. *Left*, The representative 200× microscopic images for the level of CPD (brown nuclei) at the indicated timepoints. The CPD in epidermis were detected by anti-CPD IHC. and *right,* The graph represents the change in mean ± SEM of absorbed intensity of CPD signal per CPD positive nucleus at indicated time points relative to that at initial 2 h damage time point. 20 images per skin sample harvested from 2 mice per time points were analyzed. (B) Apoptosis in the skin of KO and WT mice skin following single acute exposure to UVB. *Left*, The representative 200× microscopic images for the level of TUNEL positive nuclei (blue) at the indicated timepoints. The apoptotic cells in epidermis were detected by *in situ* TUNEL assay and *right,* the mean ± SEM of absorbed intensity per TUNEL positive nuclei (Top graph) as well as average density of apoptotic cells (bottom graph) were plotted against time. 10 images per skin sample harvested from 2 mice per time points were used. The symbols ***, ** and * indicate *p*-value ≤ 0.001, ≤ 0.01 and ≤ 0.05, respectively relative to WT group during the same time point.

4.8. Supplementary figures

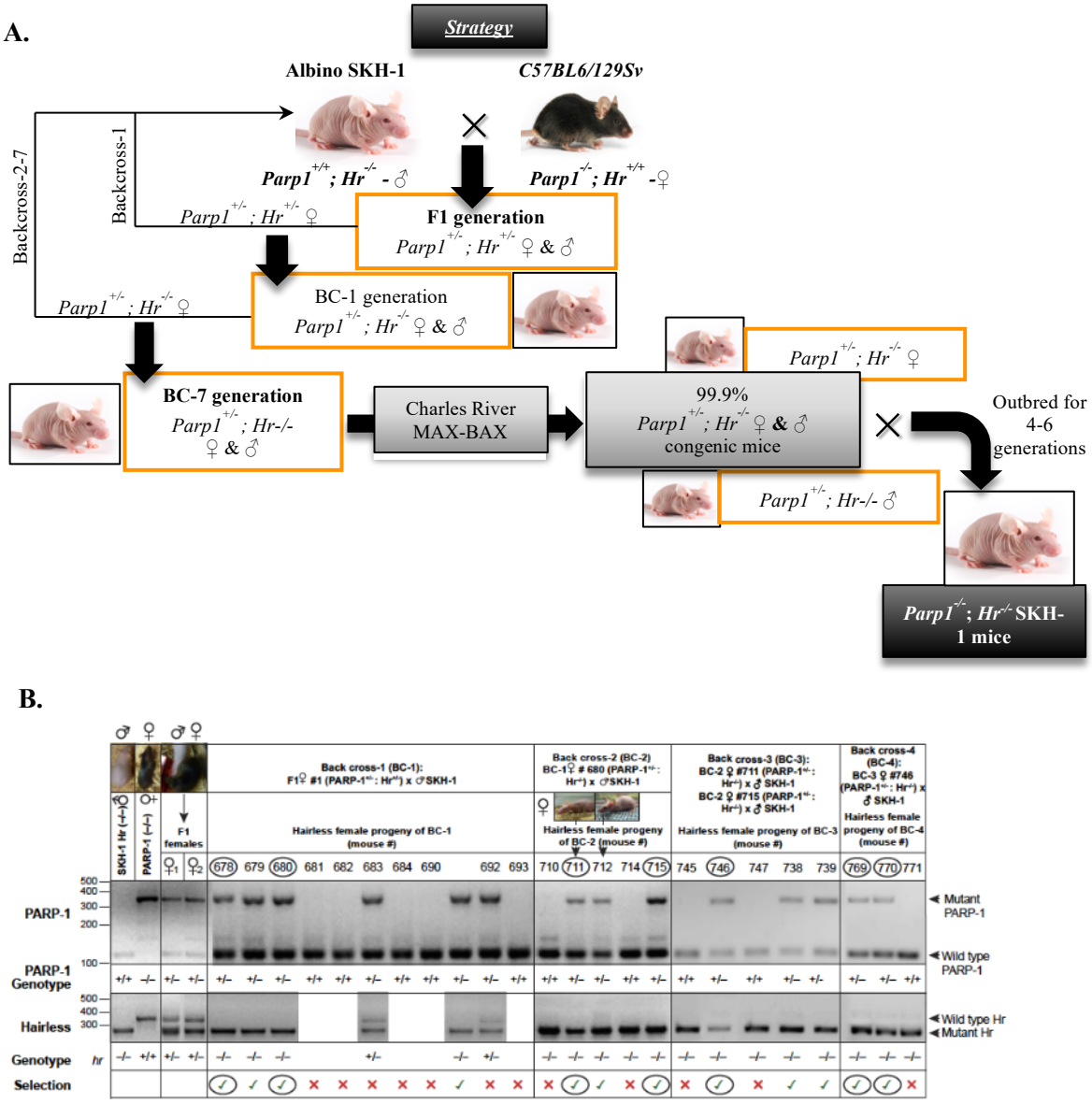

Figure S4.1. Creation of PARP1-KO mice in SKH-1 background
(A) Strategy to create PARP1-KO albino SKH-1 (KO) mice. (B) Genotyping of mice for *Parp1* and *Hr* gene during the course of *Parp1*$^{-/-}$ genotype transfer from C57BL6/1292V background to SKH-1 background. The DNA from ear punched skin biopsies were genotyped by PCR to select F1 female mice with *Parp1*$^{+/-}$ and *Hr*$^{+/-}$ genotype for BC-1 and female mice with *Parp1*$^{+/-}$ and *Hr*$^{-/-}$ genotype for subsequent back crosses.

A.

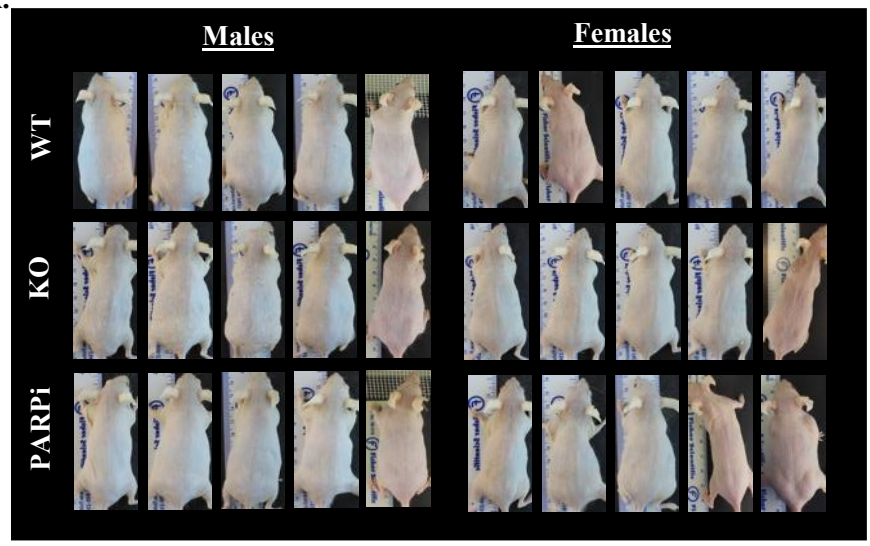
Males
Females
WT
KO
PARPi

B.

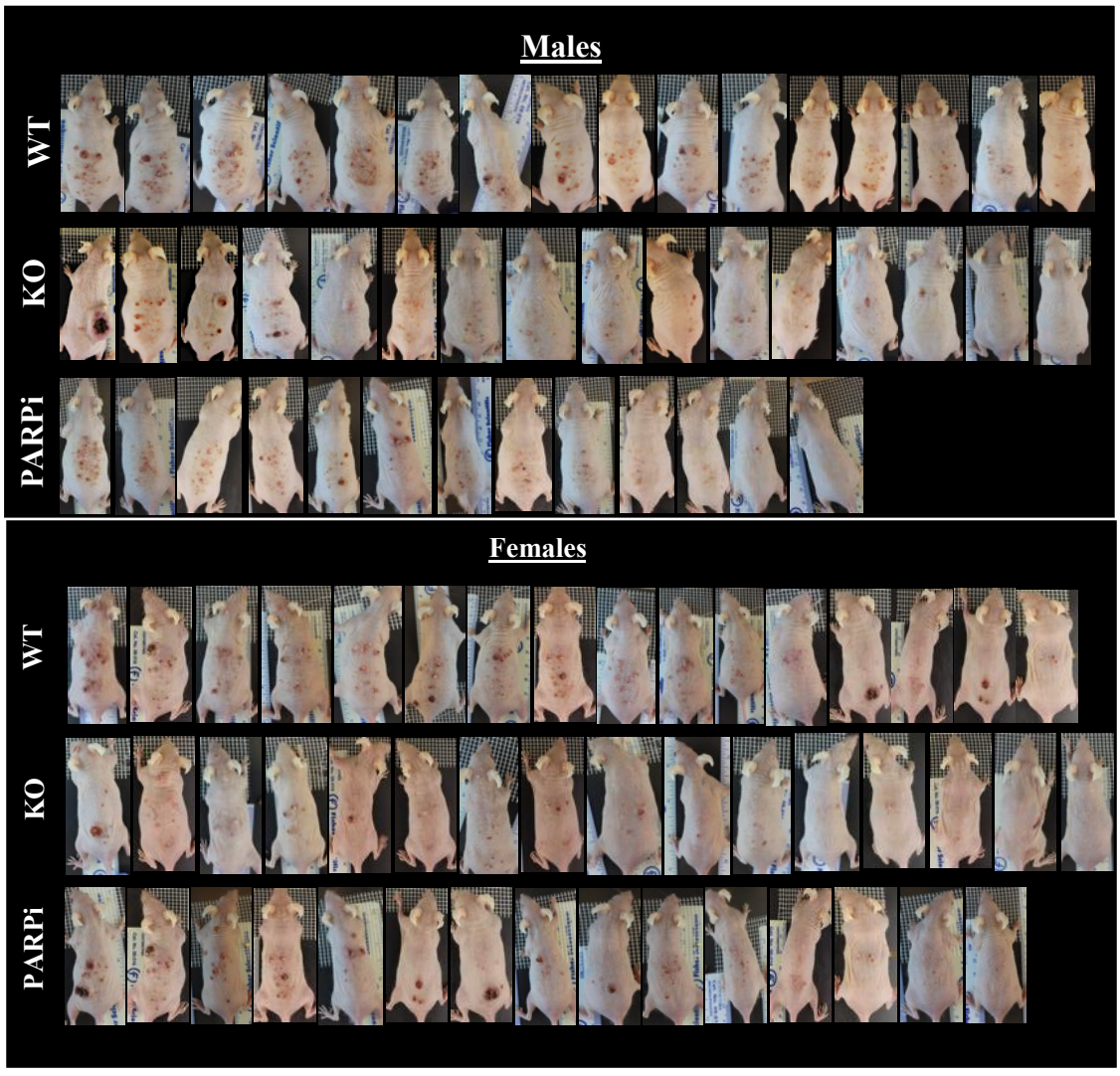
Males
WT
KO
PARPi
Females
WT
KO
PARPi

Figure S4.2. Unirradiated or UVB-irradiated WT, KO and PARPi mice at week 24 of the chronic low-dose UVB protocol

(A) Unirradiated WT, KO and PARPi mice. PARPi was applied three times per week in the PARPi group of mice until the end of the protocol at 26th week. (B) UVB-irradiated WT, KO and PARPi mice. The chronic low-dose UVB exposure results in reduced tumor burden in KO and PARPi mice as compared to WT mice.

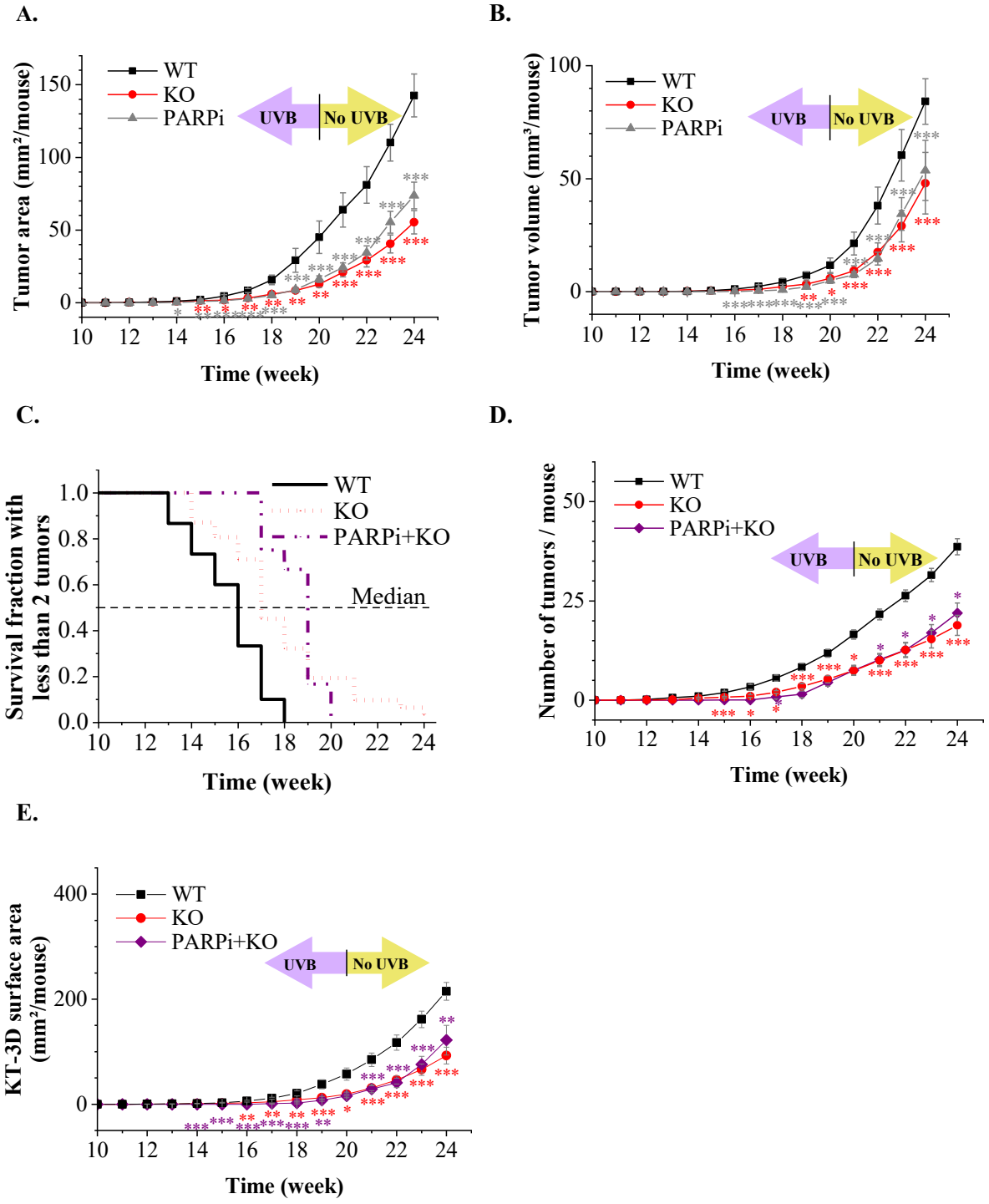

Figure S4.3. Reduced susceptibility of KO, PARPi and PARPi+KO mice to UVB-induced skin tumorigenesis

The tumor measurement data from the combined population of male and female mice, from chronic low-dose UVB irradiation protocol, are used for the following analyses. (A-B) The area and volume of tumors in WT (n = 30), KO (n = 31) and PARPi (n = 31) mice. The tumor area (A) and tumor volume (B) were determined from the acquired photographs of WT, KO and PARPi mice during each

week until 24 weeks of the protocol and their mean ± SEM were plotted against time. The red and grey colored asterisks (*) indicate the statistical significance of KO and PARPi mice, respectively relative to WT mice during the same week. (C-E) Role of catalytic activity of other PARPs in UVB-induced NMSC. (C) Tumor latency. The analysis of fraction of mice surviving with less than two tumors shows significantly ($p \leq 0.001$) late tumor development in KO (n = 31) and PARPi+KO (n = 12) mice with median time of 17 and 19 weeks, respectively as compared to that of 16 weeks for WT mice (n = 30). On the other hand, no statistical significance between KO and PARPi+KO mice is observed. (D and E) Tumor burden. The violet and yellow arrows indicate the UVB-irradiation and no UVB irradiation phases, respectively. The tumor number (D) and (KT-3D surface area (E) were determined from the acquired photographs of WT, KO and PARPi+KO mice during each week until 24 weeks and their mean ± SEM were plotted against time. The red and purple colored asterisks (*) indicate the statistical significance of KO and PARPi+KO mouse groups, respectively relative to WT mouse group during the same week. No statistical significance between KO and PARPi+KO groups was observed for these parameters of tumor burden. The asterisks ***, ** and * indicate *p*-value ≤ 0.001, ≤ 0.01 and ≤ 0.05, respectively relative to WT group.

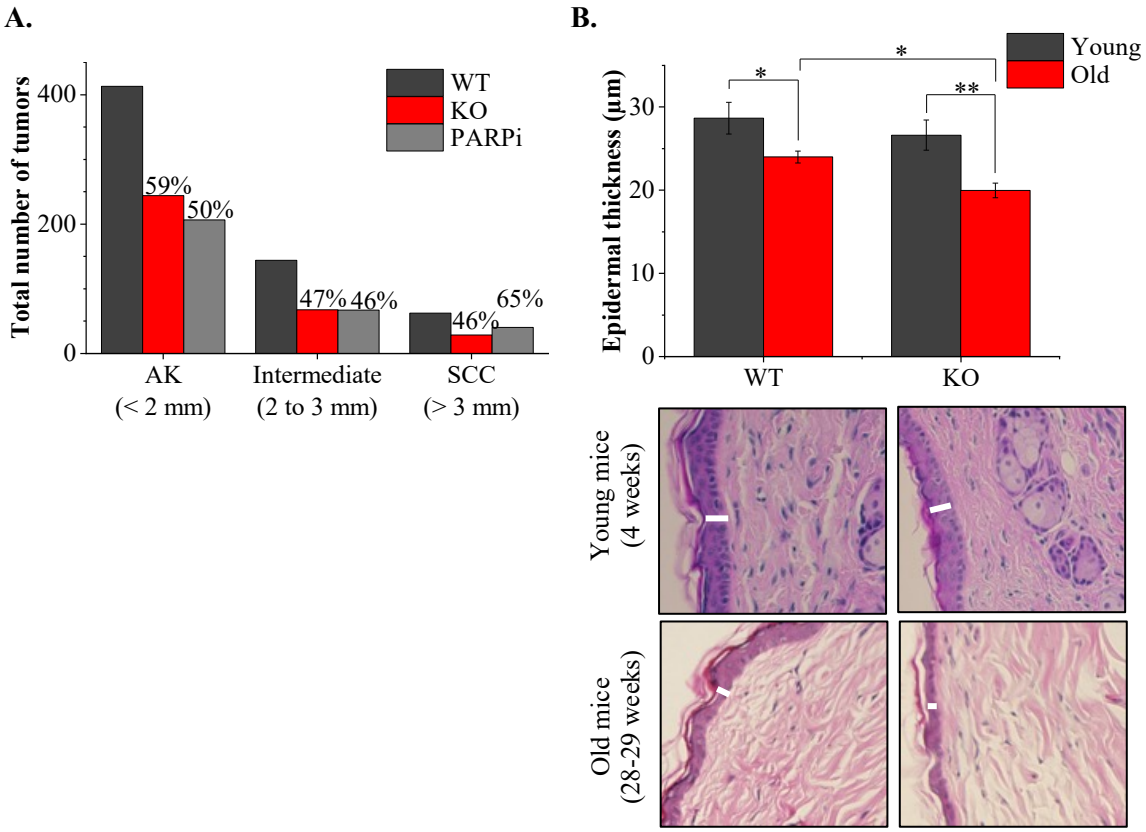

Figure S4.4. Decreased AK, SCC and epidermal thickness in PARP1 impaired mice
(A) Diameter specific classification of tumors. The tumors of WT (n = 30), KO (n = 31) and PARPi (n = 31) mice at 24th week of the low-dose UVB protocol were classified into AK, SCC or other tumor sets based on their diameter and the total tumor number in each group were plotted. The indicated percentages of total tumor number in KO and PARPi mice groups are relative to WT mice. (B) Epidermal thickness in young and old WT and KO mice. Ten to fifteen 200× images of H&E stained whole skin from three to four unirradiated young (~1 month) and old mice (~6 month) from each WT and KO groups were used for the measurement of epidermal thickness as explained in materials and methods section. The mean ± SEM of epidermal thickness was plotted and statistical significance between all the groups was determined by Student's t-test. The asterisks ***, ** and * indicates p-value ≤ 0.001, ≤ 0.01 and ≤ 0.05, respectively between the compared groups as indicated in the figure.

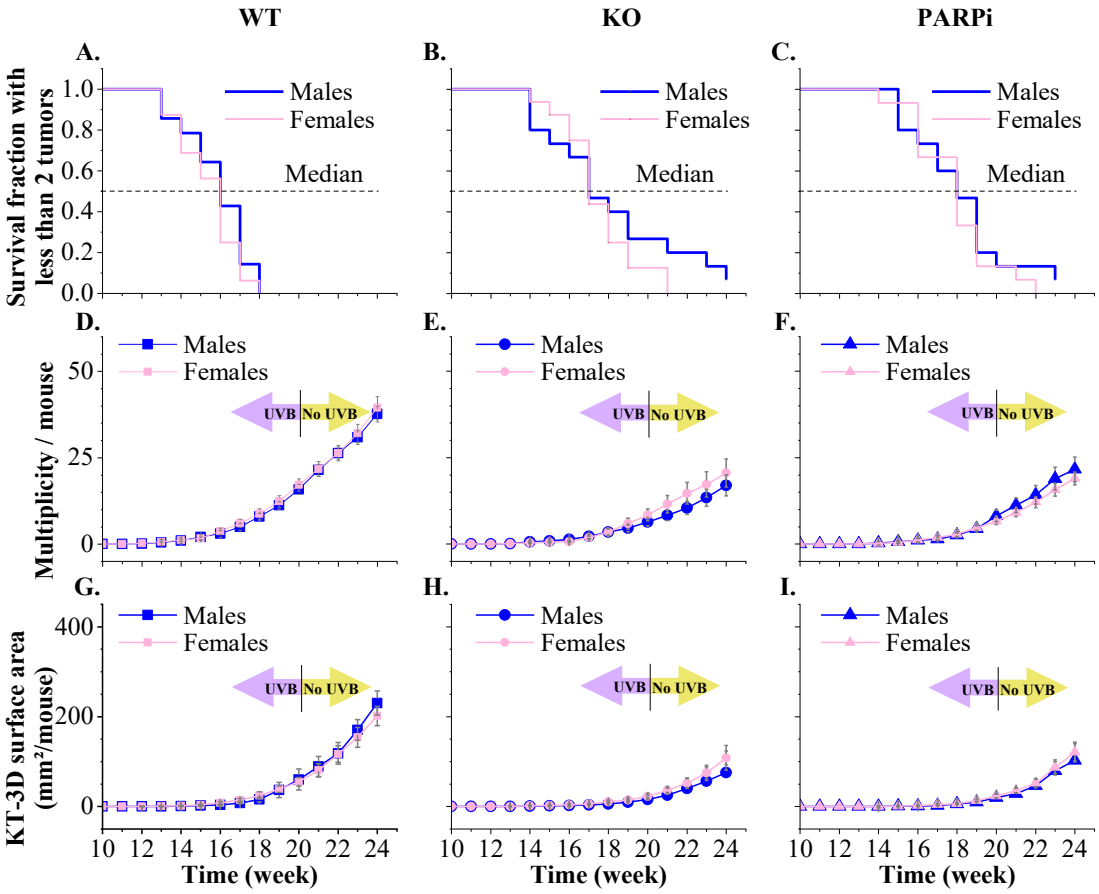

Figure S4.5. No difference in UVB-induced skin cancer severity between male and female populations within WT, KO and PARPi groups

The tumor measurement data of male and female WT (male- n=14 & female- n=16), KO (male- n=15 & female- n=16) and PARPi (male- n=15 & female- n=16) mice from chronic low-dose UVB-irradiation protocol were compared within each group separately for the tumor latency (A, B and C), multiplicity (D, E and F) and KT-3D surface area (G, H and I).

A.

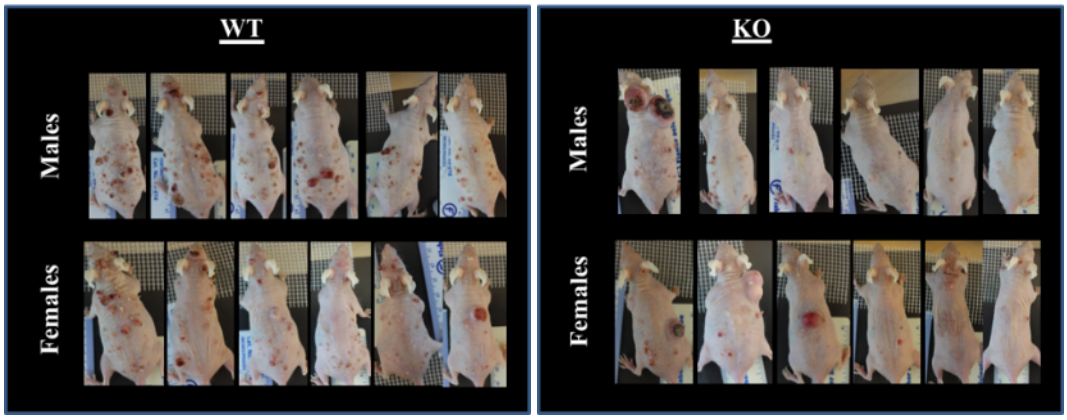

B.

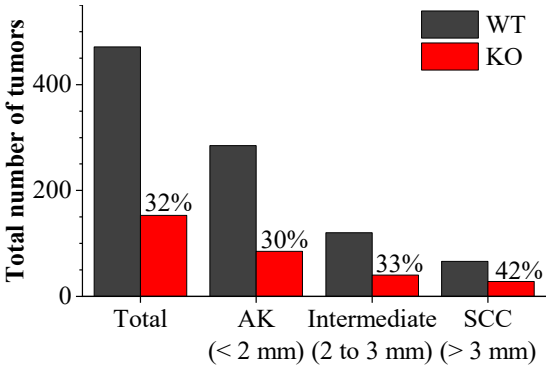

Figure S4.6. Chronic high-dose UVB-induced tumorigenesis is reduced in KO mice as compared to WT mice

(A) UVB-irradiated WT and KO mice at 24th week. (B) Size specific classification of tumors. The tumors of WT and KO mice at 24th week of the high-dose UVB protocol were classified into AK, SCC or other tumor sets based on their diameter and their total tumor number in each group were plotted. The indicated percentages of total tumor or average number in KO and PARPi mice groups are relative to WT mice.

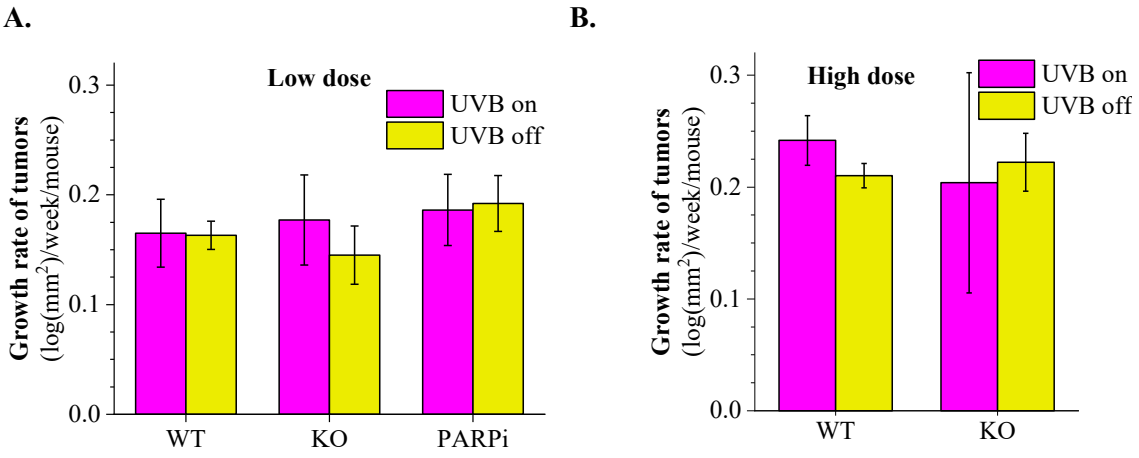

Figure S4.7. Growth rate of tumors

(A) The growth rate of tumors during and after chronic low-dose UVB irradiation phases. The growth rate of all the new tumors that appeared during UVB irradiation phase on week 17 in all the three groups of mice (WT, KO, and PARPi) were calculated over four weeks, i.e., until week 20. The mean growth rate of all the new tumors that appeared after UVB irradiation phase on week 21 in all the three groups of mice (WT, KO, and PARPi) were calculated over four weeks, i.e., until 24th week. The mean ± SEM of these growth rates were plotted and were not statistically significant. (B) The growth rate of tumors during and after chronic high-dose UVB-irradiation phases. The growth rate of all the new tumors that appeared on week 17 in all the three groups of mice (WT, KO, and PARPi) were calculated over eight weeks, i.e., until 24th week of the protocol and their mean ± SEM of these growth rates were plotted and were not statistically significant.

4.9. Materials and methods

Chemicals and other reagents

The chemicals used in preparing the buffers and other fine chemicals were purchased from Sigma. Nitrocellulose ECL membrane was from Amersham, and Immobilon western chemiluminescent HRP substrate (WBKLS0500) was from Millipore. PARP inhibitors, 1,5-dihydroxyisoquinoline (DHQ) was from Sigma and 2-(dimethylamino)N-(6-oxo-5H-phenanthridin-2-yl)acetamide (PJ-34) was from Alexis Biochemicals. Primers for genotyping were obtained from Integrated DNA Technologies.

Development of PARP-KO mice in SKH-1 hairless albino background

To create PARP1-KO albino SKH-1 mice, we used the strategy shown in Suppl. Fig. S4.1A. Briefly, the F1 generation was created by mating male inbred hairless SKH-1 mice (Charles River Labs) with female inbred PARP1-KO mice (Jackson Labs, C57 black6 background). Note that in the SKH-1 background, the "*Hr*" gene is homozygous mutant (*hr/hr*) and not a knockout ($Hr^{-/-}$). However, because both mutant *hr* and knockout $Hr^{-/-}$ have the same hairless phenotype, we have designated our homozygous *hr/hr* mutants as $Hr^{-/-}$ for the sake of simplicity. Similarly, in PARP1-KO mice, the *Parp1* gene is disrupted by replacing its exon 2 with *neo* gene, resulting in the alleles $Parp1^{tm1Zqw}$ (https://www.jax.org/strain/002779). For simplicity we have designated as $Parp1^{-/-}$. The F1 littermates were all heterozygous for the two genes *Parp1* and *hairless* (*Hr*), as determined by PCR of DNA from ear punch skin sample (Suppl. Fig. S4.1B). Selected females from F1 generation were backcrossed to male SKH-1 mice to create backcross-1 (BC-1) generation, which contained mice with albino hairless or black skin. Only those females of BC-1 generation with hairless albino skin were subjected to genotyping and mice that were $Parp1^{+/-}$ and $Hr^{-/-}$ were retained for the second backcross (BC-2) with parental male SKH-1 mice (Suppl. Fig. S4.1). The female albino hairless BC-2 progeny was all $Hr^{-/-}$. Those females, which carried *Parp1* wild type genotype (+/+), were discarded and only those females that were $Hr^{-/-}$ and $Parp1^{+/-}$ were selected for subsequent backcrosses until BC-7. The MAX-BAX (Charles River Laboratories, Troy, NY) background strain characterization procedure was used to identify BC-7 $Parp1^{+/-}$; $Hr^{-/-}$ breeders that were at least 99.9% of SKH-1 background. The outbreeding of BC-7 mice, that were selected based on MAX-BAX analysis, resulted in $Parp1^{-/-}$; $Hr^{-/-}$ mice (KO mice). The outbreeding was carried out by using four independent founder male-female pairs of KO mice from each outbred generation to create the colony of outbred KO mice. The KO mice that were used in the experiments were obtained from six or more generations of outbreeding.

Genotyping

For genotyping, the DNA was isolated from the ear punched skin samples. PCR (30 cycles) was performed using primers for wild type (WT) *Parp1* (112 bp), mutant *Parp1* (350 bp), WT *Hr* (350 bp) and mutant *Hr* (250 bp) genes and the PCR samples were separated on agarose gel. Primers for WT *Parp1*: forward- 5' CCAGCGCAGCTCAGAGAAGCCA 3' and reverse- 5' CATGTTCGATGGGAAAGTCCC 3'. Forward primer for mutant *Parp1* was same as WT *Parp1* and the sequence for reverse primer for mutant *Parp1* is 5' AGGTGAGATGACAGGAGATC 3'. Primers for WT *Hr* : forward- 5' TGTAGCCTGTGGTCGCATAG 3' and reverse- 5' CTCCTGTTTGCTTGGTCATC 3'. Forward primer for mutant *Hr* was same as WT *Hr* and the sequence for reverse primer for mutant *Hr* is 5' GCGTTACTGCAGCTAGCTTG 3'.

Animal experiment

All animal studies were approved by the Animal Protection Committee of Laval University and were conducted by the personnel who were trained and certified for animal work. The colony of SKH-1 mice (WT) which has $Parp1^{+/+}$ genotype was expanded in our animal house facility by using eight breeding pairs of SKH-1 mice, which were purchased from Charles River Canada. For the experiment four experimental groups of mice (male and female) were used: WT mice, KO mice, WT mice treated with topical application of PARPi on skin to inhibit PARP activity (PARPi mice) and KO mice treated with topical application of PARPi on skin to inhibit PARP activity (PARPi+KO mice). All the mice used in the present study were between 4 and 5 weeks of age.

Chronic UVB irradiation: Two sets of chronic UVB experiments using two different UVB doses were performed to induce skin carcinogenesis in these mice. For low dose UVB studies, 16 male and 16 female mice from all the four experimental groups were dorsally irradiated with 800 J/m2 UVB three times a week for 20 weeks. Since, the minimal erythematic dose (MED) of UVB for SKH-1 mice is ~2240 J/m2 [40], our 800 J/m2 UVB (~0.4 MED) can be considered sub-erythematic. For studies with erythematic dose of UVB, 2240 J/m2 (1 MED) UVB was used to irradiate 6 male and 6 female WT as well as KO mice 3 times a week for 16 weeks. Five animals in total or maximum 2 animals in a group died during the protocol for unknown reason. The tumor development was followed up to 4 and 7 weeks after last irradiation in low dose and high dose UVB studies, respectively. All the animals were sacrificed by 26th week from the start of both the protocols and the samples such as whole skin from unirradiated mice and tumors and non-tumor bearing skin from irradiated mice were harvested. The harvested samples were either fixed in 4% paraformaldehyde or frozen at -80 ºC.

Acute UVB irradiation: To study events after single UVB exposure, the WT, KO and PARPi mice were irradiated with 4000 J/m2 UVB (acute dose) and the animals were sacrificed for harvesting epidermis and whole skin at indicated time points in figures up to 72 h after the UVB-exposure. To harvest epidermis, the whole skin with dermis side up was placed on the dry ice frozen glass plate and the dermis was scraped out using a blade. The harvested epidermis was either fixed in 4% paraformaldehyde or frozen at -80 ºC.

UVB source

The unrestrained mice were irradiated in an open cage placed in a Spectrolinker XL-1500 (Spectronics Corp.) equipped with six 15W UVB tube-lights, referenced BLE 1T158, which delivered 800 J/m2 (within 90 s) for low dose UVB studies and delivered 2240 J/m2 (within 4 min) for high dose UVB studies. During irradiation, the cages were covered from the top with a Kodacel filter (K6805 cellulose triacetate, Eastman Kodak) to remove the contaminating UVC radiations (230–280 nm).

PARPi treatment

We used two different PARPi in our experiments: DHQ and PJ-34. Both the PARPi were diluted to 100 µM concentration in acetone and applied on the dorsal skin of SKH-1 WT mice 1 h before each irradiation. For chronic UVB irradiation protocol, only PJ-34 was used and was applied three days by week during the 20 weeks of UVB irradiation phase as well as after the UVB irradiation phase until the animals were sacrificed. For acute UVB irradiation protocol, either DHQ or PJ-34 was used as specified and applied topically on mice 1 h before UVB irradiation.

Tumor data collection and analysis

Tumor measurement method: We used our newly validated simple photographic method to record the development of tumors each week during the chronic UVB-irradiation protocol as described in our previous publication [43]. The acquired images were analyzed using AxioVision SE64-4.9.1 software (Zeiss) to measure length, width and height of each tumor on the mouse skin. All the tumors developed on the dorsal irradiated part of the mouse skin including face of mice. The visible skin lesions like wounds, cysts or other skin lesions which do not persist up to the end of the protocol were ignored in the analysis.

Tumor data analysis: A panel of seven criteria, (1) tumor free survival fraction or survival fraction with less than 2 tumors, (2) multiplicity of tumors, (3) tumor area, (4) tumor volume, (5) Knud Thomsen's three-dimensional (KT-3D) tumor surface area, (6) occurrence of new tumors and (7)

growth-rate of tumors, were used to determine and compare the cancer severity in the PARP1 impaired and WT mice. The definition and the mathematical formulae for these criteria are described in detail in chapter 3. In addition to these criteria, we also classified tumors based on their diameters. The base of a tumor on the skin is modelized by an elliptical shape having its axis defined by the tumor length and width. The mean diameter of an ellipse is the geometrical mean of the length and the width. The majority of tumors having a mean diameter lesser than 2 mm were identified as actinic keratosis (AK), and the tumors having a mean diameter greater than 3 mm were identified as squamous cell carcinomas (SCC) [76]. All the tumors with intermediate diameters (between 2 and 3 mm) were identified as a mixed population of AK, SCC and other (keratocanthoma, Bowenoid tumor and Seborrheic keratosis) tumors.

Statistical analysis: To determine the statistical significance, the quantifications such as average tumor number, average new tumor number and average tumor size (area, volume and KT-3D surface area) were converted by a root transformation followed by a logarithm transformation in order to get a linear response (cubical root for volume response, square root for area/KT-3D surface area response and no root for number response). ANOVA 2-way test with repeated measures with time and Holm-Bonferroni post-test was used on these transformed data to determine the p-values between the groups for these quantifications Multiple linear regression method was performed on the transformed data to check the distribution normality. The data sphericity was calculated using the Greenhouse-Geisser and the Huynh-Feldt corrections to estimate the factor interaction. For the tumor free survival fraction quantifications, a log-rank test on the Kaplan-Meier estimator was performed to calculate the p-values between experimental groups. Student's t-test was used to compare the litter size of two mouse populations. Depending on the number of independent factors (UVB irradiation and PARP1 treatments- KO or PARPi) implicated, the ANOVA 1-way or 2-way were used to determine the statistical significance for the average growth rate between the experimental groups. All statistical tests were done under OriginLab 2015 software.

Western blotting

The frozen epidermis samples were sonicated in 1X Laemmli SDS-PAGE buffer (Tris pH 6.8 62.5 mM, urea 6 M, glycerol 10%, SDS 2%, bromophenol blue 0.003% and 850 mM β-mercaptoethanol). The protein concentration of each sample was analysed with the Bradford method using foetal calf serum as a reference (Sigma-Aldrich, St. Louis, MI, USA). Epidermal protein extract from two to five mice were combined at each time point. An equal amount (10, 15 or 20 µg) of proteins was deposited on 6, 10 or 15% SDS polyacrylamide gels and then transferred, after electrophoresis at 100 V, onto a nitrocellulose membrane (Amersham Protran, GE Healthcare, United

Kingdom). The equality of the deposits was verified with Ponceau S (5% acetic acid, 0.5% Ponceau S powder). The membranes were blocked with a solution of 5% milk powder (Biorad, Hercules, CA, USA) and 0.1% Tween 20 (Sigma-Aldrich, St. Louis, MI, USA) in PBS for one hour. The reaction was carried out for 16 hours at 4 °C with antibodies: anti-PARP1 (C-2-10, 1:1000, Trevigen, Gaithersburg, MD, USA), anti-PAR (LP-96-10, 1:5000, Trevigen, Gaithersburg, MD, USA) and 10H (1:500, purified from the culture medium of 10H hybridoma obtained from Dr. M. Miwa, National Cancer Center Research Institute, Tokyo, through the Riken cell bank). The reaction with peroxidase-conjugated anti-mouse or anti-rabbit secondary antibodies (1:2500) was carried out for 30 min at room temperature. Western blotting was repeated two to three times for this study.

PARP1 activity-western blot

The PARP1 activity-western blot was carried out as described before [77]. Briefly, the epidermal protein extracts of the untreated WT and KO mice from acute studies were separated on the 6% SDS polyacrylamide gels along with the colored molecular weight markers for proteins. The gel was then soaked in running buffer with 5% 2-mercaptoethanol to renature proteins followed by overnight transfer of the separated proteins on the gel to a nitrocellulose membrane. Post transfer, the membrane was soaked in renaturation buffer with Zn acetate, MgCl2 and activated DNA (Sigma #D-4522) for 45 min. The membrane was then incubated with the same but fresh buffer with 100 µM NAD for 1 h for PAR synthesis, washed with renaturation buffer and then in SDS-wash buffer and followed by the processing of membrane for PAR immuno-probing with 10H antibody as described for Western blotting.

Histology and immunohistochemistry

The paraformaldehyde fixed harvested skin samples (whole skin and tumors) were embedded in paraffin. The 5 µm sections of the paraffin embedded tissues were cut and hematoxylin and eosin (H&E) staining were performed in collaboration with Dr. Sabine Hombach-Klonisch laboratory (Section Head Gross Anatomy, Department of Human Anatomy and Cell Science, Max Rady College of Medicine, Rady Faculty of Health Sciences, University of Manitoba, Winnipeg, Canada). For each experiment, skin samples from two to five mice were selected for analysis.

H&E staining: The slides with 5 µm sections of the paraffin embedded whole skin were immersed in xylene, followed by immersion in first 100% ethanol and then in 95% ethanol twice for 5 min in each solution. The slides were then washed with water and stained in a bath of hematoxylin (Harris hematoxylin) for 7 min. They were then immersed successively in water, acid alcohol (1% HCl in 70% ethanol), water and saturated lithium carbonate (1 g lithium carbonate, 100 ml water purified).

The slides are then counter-stained with eosin phloxine for 2 min soaked in water and then dehydrated by immersing successively in 70, 95 and 100% ethanol baths. The H&E stained sections on slides were then immersed in xylene twice for 5 min each and then mounted using paramount and coverslip. Hematoxylin, basic dye, will give a bluish color to acidic substances such as the chromatin of the nuclei. In contrast, eosin is a dye targeting basic substances like collagen fibres in connective tissue to stain them a pinkish-red color. These stains make it possible to discriminate the epidermis from the dermis since the high concentration of KC in the epidermis will give it a purplish color while the dermis, rich in connective tissue, will be colored in pale pink.

Epidermal morphometry: The epidermal morphometry of skin was determined in the 200× microscopy images of H&E stained skin sections and ImageJ software. With the color contrast between epidermis and dermis, ImageJ software was able to select epidermal layer of the skin and determine the parameters such as area (A), perimeter (P), and lengths of the ends (L1 and L2). The average thickness of the epidermis could thus be calculated by using these parameters as follows:

$$\text{Average thickness} = \frac{2 \times \mathrm{A}}{\mathrm{P} - \mathrm{L1} - \mathrm{L2}}$$

The Origin 2015 software (OriginLab, Northampton, MA, USA) or Microsoft excel was used to generate the graphs and statistics.

Immunohistological detection of PAR: The PAR modified proteins were detected in the whole skin sections from acute UVB dose experiment by IHC analysis of poly (ADP-ribose) using 10H antibody as described before [77]. Briefly, the harvested whole skin from WT and PARPi mice were incubated in 10% trichloroacetic acid for one hour followed by fixing them with paraformaldehyde. The fixed samples were embedded in paraffin blocks and cut in 5 µm sections and placed on microscope slides by the histology department of Université Laval. Paraffin sections on microscope slide were preheated at 60 °C, deparaffinized in toluene and rehydrated in alcohol-graduated baths (100%, 90% and 70%). The endogenous peroxidase activity was removed by incubation in 3% peroxide in methanol. The antigens were retrieved by boiling the slides for 15 min in 0.1 M Na-citrate buffer pH 6.0. Microscope slides used for immunohistochemical analyses were blocked with phosphate buffered saline (PBS) containing 10% normal goat serum (Wisent Inc.) and 0.01% Tween 20. Reaction with the primary anti-poly antibody (ADP-ribose) 10H (1:25) was performed for 16 h at 4 °C with the same blocking solution and in a humid medium (sealed box containing wet towels). The reaction with the peroxidase-conjugated anti-mouse secondary antibody (1:200) was carried out in a humid medium for 2 h at 21 °C. The antibody binding was revealed by incubation in 0.2 mg of DAB/ml of PBS. After counterstaining with hematoxylin, the slides were dehydrated by successive

baths of alcohol (70%, 90% and 100%) and then assembled with a cover glass and Paramount mounting medium. Epithelial cells with brown staining were considered as positive for 10H antibody. The counterstain (hematoxylin) gives a blue color. The IHC slides were imaged with a Nikon Eclipse E800 microscope at 600× magnification (10× eyepiece and 60× objective) and an Optronics digital camera and Picture Frame.

CPD IHC: The 5 µm sections of the paraffin embedded skin harvested from KO and WT mice of acute UVB-irradiation protocol were processed for CPD IHC, as described before for TT-IHC. The CPD were detected using 1:500 anti-CPD monoclonal antibody (Cosmo Bio Co., clone TDM-2) overnight, followed by 1:250 biotinylated goat anti mouse IgG (H+L) (Abcam, ab6668), secondary antibody and 1:500 peroxidase-conjugated streptavidin (Jackson, 016-030-084) at room temperature for 1 h and 30 min, respectively. The revelation of antibody binding at CPD was performed by using 3,3-diaminobenzidine (Thermo scientific, PI34002) for 3 minutes. The slides were counterstained with hematoxylin.

In situ TUNEL staining: For detection of apoptotic epidermis cells, the 5 µm sections of the paraffin embedded skin harvested from KO, PARPi and WT mice of acute UVB-irradiation protocol were processed for TUNEL by using the TACS•XL® Blue Label Kit (Trevigen, Gaithersburg, MD, United States). The assay was performed as per the company's protocol. The TUNEL positive cells were stained blue by TACS Blue LabelTM and the slides were counterstained pink with Nuclear Fast Red.

Quantification of CPD and TUNEL positive cells in epidermis and their statistical analysis: To quantify the CPD and TUNEL positive cells in epidermis, we first divided the acquired 200× microscopic images of skin sections into epidermis and dermis using ImageJ software. We wrote a program under the free ImageJ software that uses a modified version of IHCToolBox plugin to analyse series of hundreds of images containing only epidermis. Our program performs automatic detection of all the stained nuclei, stain color unmixing, automatic measurement of background stain intensity as well as automatic detection and intensity measurements of all the positive nuclei. Also, it parses all images in a folder and produces statistics, i.e., nucleus count, mean positive intensity and standard error of mean (SEM) recorded in a spreadsheet. Because it is a program executed by a computer, the analysis process is performed by refining the input parameters in our program as per the necessity. Objective analyses are done uniformly, i.e., without subjective technician assessments, on all images showing CPD in nuclei or apoptotic cells and therefore, they allow precise and statistical group comparisons of images. ANOVA 2-way test and Holm-Bonferroni post-test was used on these data to determine the p-values between the indicated mice groups for these quantifications.

4.10. References

1. Burton, K.A., K.A. Ashack, and A. Khachemoune, *Cutaneous Squamous Cell Carcinoma: A Review of High-Risk and Metastatic Disease.* Am J Clin Dermatol, 2016. **17**(5): p. 491-508.

2. Sanchez-Danes, A. and C. Blanpain, *Deciphering the cells of origin of squamous cell carcinomas.* Nat Rev Cancer, 2018. **18**(9): p. 549-561.

3. Kelfkens, G., F.R. de Gruijl, and J.C. van der Leun, *Tumorigenesis by short-wave ultraviolet A: papillomas versus squamous cell carcinomas.* Carcinogenesis, 1991. **12**(8): p. 1377-82.

4. Armstrong, B.K. and A. Kricker, *The epidemiology of UV induced skin cancer.* J Photochem Photobiol B, 2001. **63**(1-3): p. 8-18.

5. de Gruijl, F.R. and P.D. Forbes, *UV-induced skin cancer in a hairless mouse model.* Bioessays, 1995. **17**(7): p. 651-60.

6. Lucas, R.M., et al., *Human health in relation to exposure to solar ultraviolet radiation under changing stratospheric ozone and climate.* Photochem Photobiol Sci, 2019. **18**(3): p. 641-680.

7. Lomas, A., J. Leonardi-Bee, and F. Bath-Hextall, *A systematic review of worldwide incidence of nonmelanoma skin cancer.* Br J Dermatol, 2012. **166**(5): p. 1069-80.

8. Bray, F., et al., *Global cancer statistics 2018: GLOBOCAN estimates of incidence and mortality worldwide for 36 cancers in 185 countries.* CA Cancer J Clin, 2018. **68**(6): p. 394-424.

9. Nishisgori, C., *Current concept of photocarcinogenesis.* Photochem Photobiol Sci, 2015. **14**(9): p. 1713-21.

10. Rundhaug, J.E. and S.M. Fischer, *Molecular mechanisms of mouse skin tumor promotion.* Cancers (Basel), 2010. **2**(2): p. 436-82.

11. Wikonkal, N.M. and D.E. Brash, *Ultraviolet radiation induced signature mutations in photocarcinogenesis.* J Investig Dermatol Symp Proc, 1999. **4**(1): p. 6-10.

12. Cadet, J. and T. Douki, *Formation of UV-induced DNA damage contributing to skin cancer development.* Photochem Photobiol Sci, 2018. **17**(12): p. 1816-1841.

13. Mullenders, L.H.F., *Solar UV damage to cellular DNA: from mechanisms to biological effects.* Photochem Photobiol Sci, 2018. **17**(12): p. 1842-1852.

14. Schuch, A.P., et al., *Sunlight damage to cellular DNA: Focus on oxidatively generated lesions.* Free Radic Biol Med, 2017. **107**: p. 110-124.

15. Cleaver, J.E., E.T. Lam, and I. Revet, *Disorders of nucleotide excision repair: the genetic and molecular basis of heterogeneity.* Nat Rev Genet, 2009. **10**(11): p. 756-68.

16. Drobetsky, E.A., J. Turcotte, and A. Chateauneuf, *A role for ultraviolet A in solar mutagenesis.* Proc Natl Acad Sci U S A, 1995. **92**(6): p. 2350-4.

17. Cheng, K.C., et al., *8-Hydroxyguanine, an abundant form of oxidative DNA damage, causes G----T and A----C substitutions.* J Biol Chem, 1992. **267**(1): p. 166-72.

18. Epe, B., *Genotoxicity of singlet oxygen.* Chem Biol Interact, 1991. **80**(3): p. 239-60.

19. Kappes, U.P. and T.M. Runger, *No major role for 7,8-dihydro-8-oxoguanine in ultraviolet light-induced mutagenesis.* Radiat Res, 2005. **164**(4 Pt 1): p. 440-5.

20. Yogianti, F., et al., *Skin tumours induced by narrowband UVB have higher frequency of p53 mutations than tumours induced by broadband UVB independent of Ogg1 genotype.* Mutagenesis, 2012. **27**(6): p. 637-43.

21. Valejo Coelho, M.M., T.R. Matos, and M. Apetato, *The dark side of the light: mechanisms of photocarcinogenesis.* Clin Dermatol, 2016. **34**(5): p. 563-70.

22. Vodenicharov, M.D., et al., *Mechanism of early biphasic activation of poly(ADP-ribose) polymerase-1 in response to ultraviolet B radiation.* J Cell Sci, 2005. **118**(Pt 3): p. 589-99.

23. Purohit, N.K., et al., *Characterization of the interactions of PARP-1 with UV-damaged DNA in vivo and in vitro.* Sci Rep, 2016. **6**: p. 19020.

24. Ghodgaonkar, M.M., et al., *Depletion of poly(ADP-ribose) polymerase-1 reduces host cell reactivation of a UV-damaged adenovirus-encoded reporter gene in human dermal fibroblasts.* DNA Repair (Amst), 2008. **7**(4): p. 617-32.

25. Pines, A., et al., *PARP1 promotes nucleotide excision repair through DDB2 stabilization and recruitment of ALC1.* J Cell Biol, 2012. **199**(2): p. 235-49.

26. Robu, M., et al., *Role of poly(ADP-ribose) polymerase-1 in the removal of UV-induced DNA lesions by nucleotide excision repair.* Proc Natl Acad Sci U S A, 2013. **110**(5): p. 1658-63.

27. Robu, M., et al., *Poly(ADP-ribose) polymerase 1 escorts XPC to UV-induced DNA lesions during nucleotide excision repair.* Proc Natl Acad Sci U S A, 2017. **114**(33): p. E6847-E6856.

28. Luijsterburg, M.S., et al., *DDB2 promotes chromatin decondensation at UV-induced DNA damage.* J Cell Biol, 2012. **197**(2): p. 267-81.

29. Fisher, A.E., et al., *Poly(ADP-ribose) polymerase 1 accelerates single-strand break repair in concert with poly(ADP-ribose) glycohydrolase.* Mol Cell Biol, 2007. **27**(15): p. 5597-605.

30. Ma, W., et al., *Differential effects of poly(ADP-ribose) polymerase inhibition on DNA break repair in human cells are revealed with Epstein-Barr virus.* Proc Natl Acad Sci U S A, 2012. **109**(17): p. 6590-5.

31. Flohr, C., et al., *Poly(ADP-ribosyl)ation accelerates DNA repair in a pathway dependent on Cockayne syndrome B protein.* Nucleic Acids Res, 2003. **31**(18): p. 5332-7.

32. Caldecott, K.W., *DNA single-strand break repair.* Exp Cell Res, 2014. **329**(1): p. 2-8.

33. Masutani, M. and H. Fujimori, *Poly(ADP-ribosyl)ation in carcinogenesis.* Mol Aspects Med, 2013. **34**(6): p. 1202-16.

34. Borek, C., et al., *Inhibition of malignant transformation in vitro by inhibitors of poly(ADP-ribose) synthesis.* Proc Natl Acad Sci U S A, 1984. **81**(1): p. 243-7.

35. Epstein, J.H. and J.E. Cleaver, *3-Aminobenzamide can act as a cocarcinogen for ultraviolet light-induced carcinogenesis in mouse skin.* Cancer Res, 1992. **52**(14): p. 4053-4.

36. Wang, Z.Q., et al., *Mice lacking ADPRT and poly(ADP-ribosyl)ation develop normally but are susceptible to skin disease.* Genes Dev, 1995. **9**(5): p. 509-20.

37. de Murcia, J.M., et al., *Requirement of poly(ADP-ribose) polymerase in recovery from DNA damage in mice and in cells.* Proc Natl Acad Sci U S A, 1997. **94**(14): p. 7303-7.

38. Masutani, M., et al., *Function of poly(ADP-ribose) polymerase in response to DNA damage: gene-disruption study in mice.* Mol Cell Biochem, 1999. **193**(1-2): p. 149-52.

39. Matsumura, Y., et al., *Resistance of CD1d-/- mice to ultraviolet-induced skin cancer is associated with increased apoptosis.* Am J Pathol, 2004. **165**(3): p. 879-87.

40. Benavides, F., et al., *The hairless mouse in skin research.* J Dermatol Sci, 2009. **53**(1): p. 10-8.

41. Knatko, E.V., et al., *Whole-Exome Sequencing Validates a Preclinical Mouse Model for the Prevention and Treatment of Cutaneous Squamous Cell Carcinoma.* Cancer Prev Res (Phila), 2017. **10**(1): p. 67-75.

42. Piskunova, T.S., et al., *Deficiency in Poly(ADP-ribose) Polymerase-1 (PARP-1) Accelerates Aging and Spontaneous Carcinogenesis in Mice.* Curr Gerontol Geriatr Res, 2008: p. 754190.

43. Bazin, M., N.K. Purohit, and G.M. Shah, *Comprehensive measurement of UVB-induced non-melanoma skin cancer burden in mice using photographic images as a substitute for the caliper method.* PLoS One, 2017. **12**(2): p. e0171875.

44. Bazin, M., et al., *A panel of criteria for comprehensive assessment of severity of ultraviolet B radiation-induced non-melanoma skin cancers in SKH-1 mice.* J Photochem Photobiol B, 2020. **205**: p. 111847.

45. Wahlberg, E., et al., *Family-wide chemical profiling and structural analysis of PARP and tankyrase inhibitors.* Nat Biotechnol, 2012. **30**(3): p. 283-8.

46. Sterenborg, H.J., F.R. de Gruijl, and J.C. van der Leun, *UV-induced epidermal hyperplasia in hairless mice.* Photodermatol, 1986. **3**(4): p. 206-14.

47. Haratake, A., et al., *Intrinsically aged epidermis displays diminished UVB-induced alterations in barrier function associated with decreased proliferation.* J Invest Dermatol, 1997. **108**(3): p. 319-23.

48. King, B.S., et al., *Poly(ADP-ribose) contributes to an association between poly(ADP-ribose) polymerase-1 and xeroderma pigmentosum complementation group A in nucleotide excision repair.* J Biol Chem, 2012. **287**(47): p. 39824-33.

49. Hegedus, C., et al., *PARP1 Inhibition Augments UVB-Mediated Mitochondrial Changes-Implications for UV-Induced DNA Repair and Photocarcinogenesis.* Cancers (Basel), 2019. **12**(1).

50. Lakatos, P., et al., *3-Aminobenzamide protects primary human keratinocytes from UV-induced cell death by a poly(ADP-ribosyl)ation independent mechanism.* Biochim Biophys Acta, 2013. **1833**(3): p. 743-51.

51. Sistigu, A., et al., *Trial watch - inhibiting PARP enzymes for anticancer therapy.* Mol Cell Oncol, 2016. **3**(2): p. e1053594.

52. de Vries, A., et al., *Increased susceptibility to ultraviolet-B and carcinogens of mice lacking the DNA excision repair gene XPA.* Nature, 1995. **377**(6545): p. 169-73.

53. Nakane, H., et al., *High incidence of ultraviolet-B-or chemical-carcinogen-induced skin tumours in mice lacking the xeroderma pigmentosum group A gene.* Nature, 1995. **377**(6545): p. 165-8.

54. Sands, A.T., et al., *High susceptibility to ultraviolet-induced carcinogenesis in mice lacking XPC.* Nature, 1995. **377**(6545): p. 162-5.

55. Itoh, T., et al., *DDB2 gene disruption leads to skin tumors and resistance to apoptosis after exposure to ultraviolet light but not a chemical carcinogen.* Proc Natl Acad Sci U S A, 2004. **101**(7): p. 2052-7.

56. Yoon, T., et al., *Tumor-prone phenotype of the DDB2-deficient mice.* Oncogene, 2005. **24**(3): p. 469-78.

57. Martin-Oliva, D., et al., *Crosstalk between PARP-1 and NF-kappaB modulates the promotion of skin neoplasia.* Oncogene, 2004. **23**(31): p. 5275-83.

58. Martin-Oliva, D., et al., *Inhibition of poly(ADP-ribose) polymerase modulates tumor-related gene expression, including hypoxia-inducible factor-1 activation, during skin carcinogenesis.* Cancer Res, 2006. **66**(11): p. 5744-56.

59. Schwarz, M., P.A. Munzel, and A. Braeuning, *Non-melanoma skin cancer in mouse and man.* Arch Toxicol, 2013. **87**(5): p. 783-98.

60. Kraus, W.L., *PARPs and ADP-Ribosylation: 50 Years ... and Counting.* Mol Cell, 2015. **58**(6): p. 902-10.

61. Yi, M., et al., *Advances and perspectives of PARP inhibitors.* Exp Hematol Oncol, 2019. **8**: p. 29.

62. To, C., et al., *The PARP inhibitors, veliparib and olaparib, are effective chemopreventive agents for delaying mammary tumor development in BRCA1-deficient mice.* Cancer Prev Res (Phila), 2014. **7**(7): p. 698-707.

63. Garcovich, S., et al., *Skin Cancer Epidemics in the Elderly as An Emerging Issue in Geriatric Oncology.* Aging Dis, 2017. **8**(5): p. 643-661.

64. Young, A.R., J. Claveau, and A.B. Rossi, *Ultraviolet radiation and the skin: Photobiology and sunscreen photoprotection.* J Am Acad Dermatol, 2017. **76**(3S1): p. S100-S109.

65. Chand, S.N., et al., *PARP inhibitors for chemoprevention--letter.* Cancer Prev Res (Phila), 2014. **7**(11): p. 1170-1.

66. Mitchell, D.L., et al., *Effects of chronic low-dose ultraviolet B radiation on DNA damage and repair in mouse skin.* Cancer Res, 1999. **59**(12): p. 2875-84.

67. Ouhtit, A., et al., *Loss of Fas-ligand expression in mouse keratinocytes during UV carcinogenesis.* Am J Pathol, 2000. **157**(6): p. 1975-81.

68. Ziegler, A., et al., *Sunburn and p53 in the onset of skin cancer.* Nature, 1994. **372**(6508): p. 773-6.

69. Jiao, J., et al., *Cell-type-specific roles for COX-2 in UVB-induced skin cancer.* Carcinogenesis, 2014. **35**(6): p. 1310-9.

70. Cho, S.H., et al., *Bax gene disruption alters the epidermal response to ultraviolet irradiation and in vivo induced skin carcinogenesis.* Int J Mol Med, 2001. **7**(3): p. 235-41.

71. Hart, P.H. and M. Norval, *Ultraviolet radiation-induced immunosuppression and its relevance for skin carcinogenesis.* Photochem Photobiol Sci, 2018. **17**(12): p. 1872-1884.

72. Farkas, B., et al., *Reduction of acute photodamage in skin by topical application of a novel PARP inhibitor.* Biochem Pharmacol, 2002. **63**(5): p. 921-32.

73. Apalla, Z., et al., Skin Cancer: Epidemiology, Disease Burden, Pathophysiology, Diagnosis, and Therapeutic Approaches. Dermatol Ther (Heidelb), 2017. **7**(Suppl 1): p. 5-19.

74. Rodriguez, M.I., et al., PARP-1 regulates metastatic melanoma through modulation of vimentin-induced malignant transformation. PLoS Genet, 2013. **9**(6): p. e1003531.

75. Adashek, J.J., R.K. Jain, and J. Zhang, Clinical Development of PARP Inhibitors in Treating Metastatic Castration-Resistant Prostate Cancer. Cells, 2019. **8**(8).

76. De Gruijl, F.R., J.B. Van Der Meer, and J.C. Van Der Leun, Dose-time dependency of tumor formation by chronic UV exposure. Photochem Photobiol, 1983. **37**(1): p. 53-62.

77. Shah, G.M., et al., Approaches to detect PARP-1 activation in vivo, in situ, and in vitro. Methods Mol Biol, 2011. **780**: p. 3-34.

4.11. Acknowledgement

This work was supported by Discovery Grant RGPIN-2016-05868 and Discovery Accelerator Grant RGPAS-492875-2016 (to G.M.S.) from the Natural Sciences and Engineering Research Council of Canada. N.K.P. received a foreign student fee-waiver scholarship from the Québec Government and Shastri Indo-Canadian Institute and the graduate scholarships from the Neuroscience Axis of Centre Hospitalier Universitaire de Québec Research Center-Université Laval. We acknowledge the timely help from Dr. Mihaela Robu, Rashmi Shah and Dr. Samuel Adant for the animal photography and sample harvesting for this study.

Conflict of interest

Authors have no conflict of interest to declare.

Chapter 5. General discussion

Since its discovery, PARP1 has continued to amaze the scientific community with the diversity of its functions in mammalian cells. In recent past, studies from our group and others have decisively ended the debate about whether PARP1 has any role in the NER of DNA damage that is devoid of strand breaks, i.e., CPD and 6-4PP (Section E.2). These DNA damage (Section N.1.2) are frequently caused in human skin by solar UV exposure (Section D.1) and PARP1 is implicated from DNA damage recognition to post-incision steps of their repair via GG-NER sub-pathway. In the present thesis, we further unravel the DNA binding characteristics of PARP1 at the direct DNA damage site and provide structural basis for the reported interaction of PARP1 with DDB2 during the DNA damage recognition step of GG-NER sub-pathway by using two novel assays (Chapter 1), as discussed further in section 5.1.

Defective NER of direct DNA damage is associated with increased susceptibility to UVB-induced SCC in knockout mouse models of key NER pathway proteins such as DDB2, XPC and XPA [87, 497-500]. Consistently, enhanced repair of UVB-induced CPD in transgenic mice expressing CPD photolyase significantly reduced UVB-induced SCC development [519]. However, despite defective NER in the skin, PARPi [820] and KO (Fig. 4.8A) mice exhibited reduced UVB-induced SCC development (Figs. 4.3, 4.5 and 4.6). In view of the oncosuppressive role of PARP1 in spontaneous and/or alkylating agent-induced *de novo* tumorigenesis [861, 910], our observation was a bolt from the blue. To rationalize this result, we discuss the mechanism which could account for the reduced UVB-induced SCC development in PARPi and KO (PARP1-impaired) mice vis a vis NER protein-KO mouse models in section 5.2. We also discuss the possibility for the application of PARPi as a chemopreventive agent for cancer in Section 5.3.

5.1. Development of two novel assays to characterize PARP1-DDB2 interaction at the DNA damage

Several questions about the binding of PARP1 at direct DNA damage site during DNA damage recognition step of GG-NER need to be addressed. No prior study had clearly shown that the PAR formation coinciding at UV-lesion site is mediated by PARP1. Nonetheless, based on the indirect evidence that both, PARP1-depleted and PARP inhibited cells exhibited absence of UVC-induced PAR and a similar delay in NER kinetics, our study suggested that PARP1 is the main PARP implicated in facilitating NER [820]. In view of this, we developed an “in situ fractionation” technique, which uses detergents and salt to extract free cytoplasmic and nucleoplasmic proteins, while retaining the chromatin-bound proteins (Chapter 1). Combining this technique with an

immunocytological method, we reduced the background noise of the abundant unbound PARP1 in the nuclei of locally UVC-irradiated cells to be able to visualize the co-localization of PARP1 at the TT CPD lesion sites (Fig.1.2a). This technique also allowed us to demonstrate the co-localization of PARP1 and DDB2 in locally irradiated cell nuclei (Fig.1.1e), which was in agreement with the previously observed association between them at the UVC-damaged chromatin [820, 821].

My colleagues had shown that PARP1 and DDB2 co-immunoprecipitated in the chromatin-bound extract from UVC-irradiated cells in the presence of ethidium bromide [820], thereby indicating that PARP1 and DDB2 interact with each other on the same DNA strand. Earlier crystallographic studies have shown that DDB2 directly binds to CPD or 6-4PP while making a footprint of 2 nt upstream of these lesions [169, 189, 225]. Therefore, PARP1 must be binding somewhere nearby DDB2 to account for their interaction on the same strand. Our lab earlier showed that PARP1 binds to UVB-irradiated dsDNA *in vitro* and is enriched in chromatin fragments containing TT CPD isolated from UVB-irradiated cells [814]. However, since these larger DNA fragments could contain multiple adjacent dipyrimidines, it was difficult to determine with the nucleotide level resolution whether PARP1 and DDB2 bound to the same lesion or to different but nearby CPD lesions on DNA. Therefore, we created a model biotin-labelled 40 mer or 60 mer oligos with (UV-DNA) or without (control-DNA) a single defined UV-lesion surrounded by multiple unique restriction enzyme sites. The top strand of these DNA contained a single adjacent pyrimidine pair, i.e., thymine, which upon UVC-irradiation largely resulted in formation of TT CPD rather than TT 6-4PP (Suppl. Fig.S1.2b). This was in agreement with the previous report that 6-4PP are induced 1000 times slower and 3-5 times lesser as compared to CPD by UVC [41, 45, 50]. We validated the use of our model oligos for the protein binding and footprinting assays by demonstrating that DDB2 exhibited similar binding affinity (Fig.1.3b, top panel) and footprint (Figs.1.4 a-b) on UV-DNA, as reported earlier [169, 189, 225, 911]. The UV-DNA bound DDB2 permitted the access of CPD photolyase to the damage (Fig.1.4e), thereby indicating that the binding mode of DDB2 to our model UV-oligo was similar to that observed in the cells in an earlier study [232].

The subsequent protein binding studies revealed that PARP1 bound 1.5-1.7 times more to UV-DNA than the control-DNA (Fig.1.3b, bottom panel), which is in agreement with previously reported affinity of PARP1 for the DNA containing altered structures without any strand breaks [629, 631-636]. PARP1-DBD (Zn1-Zn2) was sufficient to recognize the direct DNA damage (Fig.1.2b), possibly via the ability of Zn1 and Zn2 to interact with the unpaired bases opposite the TT/6-4PP or any other exposed nucleotide in the vicinity, as demonstrated for SSB and DSB [648, 649]. The footprinting studies of PARP1 on the UV-DNA revealed that PARP1 has -12 to +9 nt asymmetric

bilateral footprint around the defined UV-damaged site (Figs.1.4a-c). This footprint of PARP1 around TT/6-4PP is reminiscent of its bilateral footprint around SSB [640, 649]. While PARP1 footprint around CPD/6-4PP site in our model is compatible with previously reported monomeric [628, 638-642] or dimeric [620, 643-647] binding of PARP1 at DNA strand breaks, further studies are required to determine if one or two molecules of PARP1 can bind simultaneously around CPD/6-4PP site. In this regard, our most recent study does indicate the possibility of co-existence of two PARP1 molecules at the CPD/6-4PP site, one alone whereas other is recruited in complex with XPC (Appendix 3) [912].

We further analyzed the simultaneous binding of PARP1 and DDB2 to UV-DNA (Fig.1.4d, left panel). The observed no change in the footprint of PARP1 on UV-DNA in presence of DDB2 suggests that they have non-interfering binding sites on the UV-DNA (Fig.1.4d, right panel), which can allow their independent recruitment at the damage site, as reported earlier [820, 821]. Moreover, the proximity of PARP1 (-12 to +9 nt) and DDB2 (-2 nt) footprints on UV-DNA (Figs. 1.4 a-b and Fig. 1.5b) accounts for their previously reported association in the vicinity of the damage [820, 821] and co-localization in locally UVC-irradiated cell nuclei (Fig.1.1e). We also observed that the binding of DDB2 to UV-DNA increased 2.4 times in presence of PARP1 as compared to that in absence of PARP1 (Fig.1.4d, left panel), thereby suggesting that an early arrival of PARP1 at the CPD/6-4PP site can facilitate the binding of incoming DDB2 at this site,. On the contrary, the presence of DDB2 on UV-DNA reduced the binding of incoming PARP1 by half (Fig.1.4d, left panel). Since PARP1 ($0.5\text{-}2\times10^6$ molecules per cell [614]) is much more abundant than DDB2 ($\sim1\times10^5$ per cell [913]) in mammalian cells, it is highly possible that PARP1 encounters the direct DNA damage prior to DDB2 [223, 641]. This possibility was also proposed in previous studies including one from my laboratory [820, 821]. While further studies are required to gain insight in this aspect of PARP1 and DDB2 recruitment at CPD/6-4PP site, it is reasonable to assume that DDB2 can access CPD in presence of PARP1 since CPD photolyase has been shown to repair TT-CPD that is bound to PARP1 (Fig.1.4e).

The binding of PARP1 to UV-DNA resulted in stronger activation of PARP1 as compared to control-DNA (Fig.1.5a, left panel), similar to that observed for PARP1 activation with DNA containing altered structures without strand break [631, 633, 636]. Moreover, activation of PARP1 was stronger when it bound to 24 mer oligo containing TT 6-4PP as compared to that containing TT CPD (Fig. 1.5, right panel). Higher helical distortion of DNA induced by the 6-4PP as compared to CPD [67] can result in greater extent of unfolding of restrictive helical regions within HD subdomain of PARP1 which can account for this increased activation. While this proposed model is based on a recent study which associated the extent of unfolding within HD with the degree of catalytic activation of PARP1

[650], it needs to be demonstrated experimentally. This mechanism can also indirectly account for the observed stimulation of PARP1 activity by DDB2 in presence of DNA that largely contained TT CPD *in vitro* in our previous study [820] because binding of DDB2 at CPD site bends the DNA at an angle of 40-45º [169, 189]. However, this also needs to be verified experimentally.

In conclusion, the co-existence of PARP1 and DDB2 on UV-DNA can be accounted for by proposed model (Chapter 1) in which DDB2 attaches directly to the CPD/6-4PP whereas PARP1 makes an asymmetric bilateral contact from -12 to +9 nt around the CPD/6-4PP site. However, we do not rule out the possibility that the PARP1 footprint at CPD/6-4PP site may vary when it binds to them in complex with XPC in presence or absence of DDB2 [912], in the context of chromatin or when there are multiple UV-lesions in close proximity.

5.2. Why PARP1-impaired mice exhibit reduced UVB-induced SCC development despite defective NER in their skin?

Two enabling characteristics of carcinogenesis are the genomic instability and inflammation [859]. PARP1 can act as both, a friend and a foe of carcinogenesis due to its proinflammatory and genomic stability maintenance functions, respectively (Section P). Intriguingly, we observed that despite delayed NER of UVB-induced direct DNA damage (Fig.4.8A and [820]), the initiation and/or promotion of UVB-induced SCC development was reduced in PARP1-impaired SKH-1 mice (Chapter 4). This is in contrast to not only the known oncosuppressive role of PARP1 in carcinogenesis (Section P), but also to the observed increase in UVB-induced SCC development in NER protein-KO mouse models such as XPA [87], XPC [498] and DDB2 [499].

This discrepancy between PARP1-impaired mice and NER protein-KO mice for UVB-induced SCC development can be partially explained by the difference in the level of UVB-induced apoptosis observed in their epidermis (Table 5.1). The epidermis of GG-NER defective XPC-KO and DDB2-KO mice exhibited resistance to apoptosis as compared to the WT mice in response to single [86, 914] or chronic UVB exposure [915, 916]. Consistently, the epidermis from XPC-KO mice [915] and DDB2 deficient hamster cell line V79 [231] exhibited increased UV-induced mutagenesis. Conversely, we demonstrated increased apoptosis in the epidermis of PARP1-impaired mice as compared to WT mice in response to single UVB exposure (Fig.4.8B). Since the UVB-damaged KC are the potential progenitors of SCC (Section J.2.1.1), their increased apoptosis can reduce the frequency of mutated KC, and hence the initiation of UVB-induced tumorigenesis in the PARP1-impaired epidermis. Our proposed mechanism is supported by a recent study, which showed that inhibition of PARP1 activity reduced UVB-induced mutagenesis in CHO cells [917]. Nonetheless,

the frequency of UVB-induced mutations in the epidermis of chronic UVB-irradiated PARP1-impaired mice remains to be determined.

Mice	Defective NER	Apoptosis	Frequency of UVB-induced mutagenesis	Inflammation (erythema)	Immuno-suppression	SCC development
XPC-KO	✓	Reduced [86, 915]	Increased [915]	No change [918]	No change [918]	Increased [498]
DDB2-KO	✓	Reduced [914, 916]	Increased* [231]	No change [914]	?	Increased [499]
XPA-KO	✓	Increased [86]	Increased (low UVB dose) or No change (high UVB dose)# [919]	Increased [918, 920]	Increased [918, 920]	Increased [87, 497, 921]
PARP1-KO or PARPi-treated	✓·	Increased·	Decreased* [917]	?	Reduced in PARPi mice [810]	Reduced·

Table 5.1. UVB-induced responses in the skin of NER protein-KO mice and PARP1-impaired mice relative to WT mice.
** indicates the observation made in cultured cells, # indicates that the observation changes with the dose of UVB, • indicates observation made in chapter 4, and ? indicates yet to be examined in response to UVB.*

Our proposed model of increased apoptosis induced reduced SCC development in chronic UVB irradiated PARP1-impaired mice is contradicted by the observed increase in UVB-induced SCC development despite increased apoptosis in the epidermis of NER defective XPA-KO mice [86, 87, 497, 921]. Interestingly, epidermis of XPA-KO mice had a higher frequency of UVB-induced mutations compared to WT mice but only at low UVB dose (50 J/m^2), whereas at high dose, mutation frequency between them was similar [919]. The authors suggested that the latter observation could be explained by the observed increase in apoptosis in the epidermis of XPA-KO mice as compared to that in the epidermis of WT mice at higher dose of UVB. However, the apoptosis in the epidermis of XPA-KO mice was determined only after single exposure to UVB [86]. Since apoptotic capacity of KC reduces with chronic UVB exposures as compared to that after single UVB exposure [490, 491], it is important to examine the level of apoptosis in epidermis post chronic UVB irradiation of these mice including our PARP1-impaired mice.

The increased SCC in XPA-KO mice despite lack of difference in UVB-induced mutagenesis can be explained by the factors facilitating SCC promotion and progression, such as UVB-induced inflammation and immunosuppression (Table 5.1) (Section J.2.4 and J.2.5). XPA-KO mice, which have abrogation of both the NER sub-pathways, exhibit increased UVB-induced inflammation and immunosuppression as compared to the WT mice [918, 920]. This suggests that despite same mutation frequency in the epidermis of XPA-KO and WT mice, the enhanced UVB-induced immune modulations facilitate increased SCC development in XPA-KO mice. Notably, GG-NER-deficient XPC-KO and TC-NER deficient CSB-KO mice exhibit no significant difference in these UVB-induced immune modulations in their skin as compared to their WT counterparts [918]. In contrast, the skin of PARP1-impaired mice exhibit reduced inflammatory response after topical application of chemical carcinogen [841, 842] and reduced immunosuppression in response to single UVB exposure [810]. Since inflammatory mediators also foster progression stage of SCC (section J.2.5), our data of no difference in progression phase between PARP1-impaired and WT mice (Figs. 4.7C-D) suggests that UVB-induced inflammation does not contribute to this phase of SCC. While we do not rule out the possibility for their role during promotion stage of SCC development, further studies are warranted on how PARP1 impairment affects the UVB-induced inflammation and immunosuppression in mouse skin.

5.3. Can PARPi be used for chemoprevention of cancer?

The reduced initiation and/or promotion of UVB-induced SCC development in PARPi mice suggest chemopreventive role of PARPi. To our knowledge, only one other study has pointed out a chemopreventive application of PARPi for spontaneous *de novo* mammary tumorigenesis in BRCA1-deficient mice [922]. Interestingly, this study also related the reduced mammary tumorigenesis to increased apoptosis observed in the mammary glands of BRCA1-deficient mice. Yet another study has reported reduced number of diethyl-nitrosamine-induced preneoplastic foci formation in the liver of C57BL/6 mice injected with the PARPi DPQ [923]. Even though the authors attributed this to chemotherapeutic effect of PARPi in hepatocellular carcinoma, it could also be explained as a chemopreventive role for PARPi, similar to that reported in our study.

The chemopreventive use of PARPi for the solar UV-induced SCC will be the translational application of our study. Furthermore, reduced UVB-induced mutagenicity in PARPi-treated CHO cells [917] that are deficient in DDB2 suggests that the PARPi can be exploited for the chemoprevention of UV-induced SCC in XP patients [494-496], which exhibit high susceptibility to these cancers. Hence, further studies are warranted to examine the susceptibility of PARPi-treated NER protein-KO mice to UV-induced SCC.

Conclusion

a. "Updated" model for role of PARP1 during the DNA damage recognition step of GG-NER sub-pathway

The "updated" working model that encompasses the results in the chapter 1 and annex 4 of the present thesis, for the role of PARP1 during the DNA damage recognition step of GG-NER sub-pathway is as follows (Fig. a). In undamaged mammalian cells, PARP1 either exists in unbound state in nucleoplasm or nucleosome-bound state in chromatin [628]. Since number of molecules of PARP1 ($0.5\text{-}2\times10^6$/cell [614]) are much higher than that of XPC ($\sim3\times10^4$/cell [275]), nucleoplasmic PARP1 can be either free or in complex with XPC (PARP1-XPC) [912]. Owing to their affinity for DNA, PARP1 or PARP1-XPC can constantly scan otherwise intact DNA. PARP1 scans DNA for damage three dimensionally via monkey bar mechanism [641, 776] whereas XPC scans one-dimensionally by hopping [209]. Their mode of DNA scanning when they are in complex still needs to be determined.

Upon UV-induced direct DNA damage in the mammalian cells, PARP1 or PARP1-XPC complex could be the first ones to arrive and bind around the CPD/6-4PP lesions in the chromatin due to the abundance of PARP1 [614], its swiftness in scanning DNA [641, 776] and its association with chromatin [628]. The capacity of its Zn1 and Zn2 to interact with the unpaired nucleotide bases could be exploited by PARP1 for the recognition of CPD/6-4PP (Section 5.1), similar to that shown for PARP1 at SSB or DSB [648, 649]. Binding of PARP1 at this damage can result in its basal activation and formation of PAR in the vicinity of damage [820].

While the footprint of PARP1 in the chromatin context or in complex with XPC is yet to be determined, free PARP1 casts asymmetric and bilateral footprint around CPD or 6-4PP sites on the naked DNA [924]. Since this mode of PARP1 binding also allows access at CPD/6-4PP site by other proteins, the binding of DDB2 (in UV-DDB ligase complex) could either accompany or follow the PARP1 binding at lesion site [924]. In the latter case, PARP1 can facilitate DDB2 binding at CPD/6-4PP site [924]. The resulting DNA distortion around CPD site due to DDB2 binding [169, 189] can further stimulate the activity of PARP1 (Section 5.1), which in turn can prolong the retention time of DDB2 at the CPD/6-4PP site [821]. As explained in section N.1.2, the catalytic activity of PARP1 has been shown to facilitate the recruitment of XPC by mediating chromatin remodeling around CPD/6-4PP by directly PARylating histones, DDB2 and recruiting "PAR-readers" such as ALC1.

In our most recent study, we showed that this PARylation activity by PARP1 ("first" PARP1)

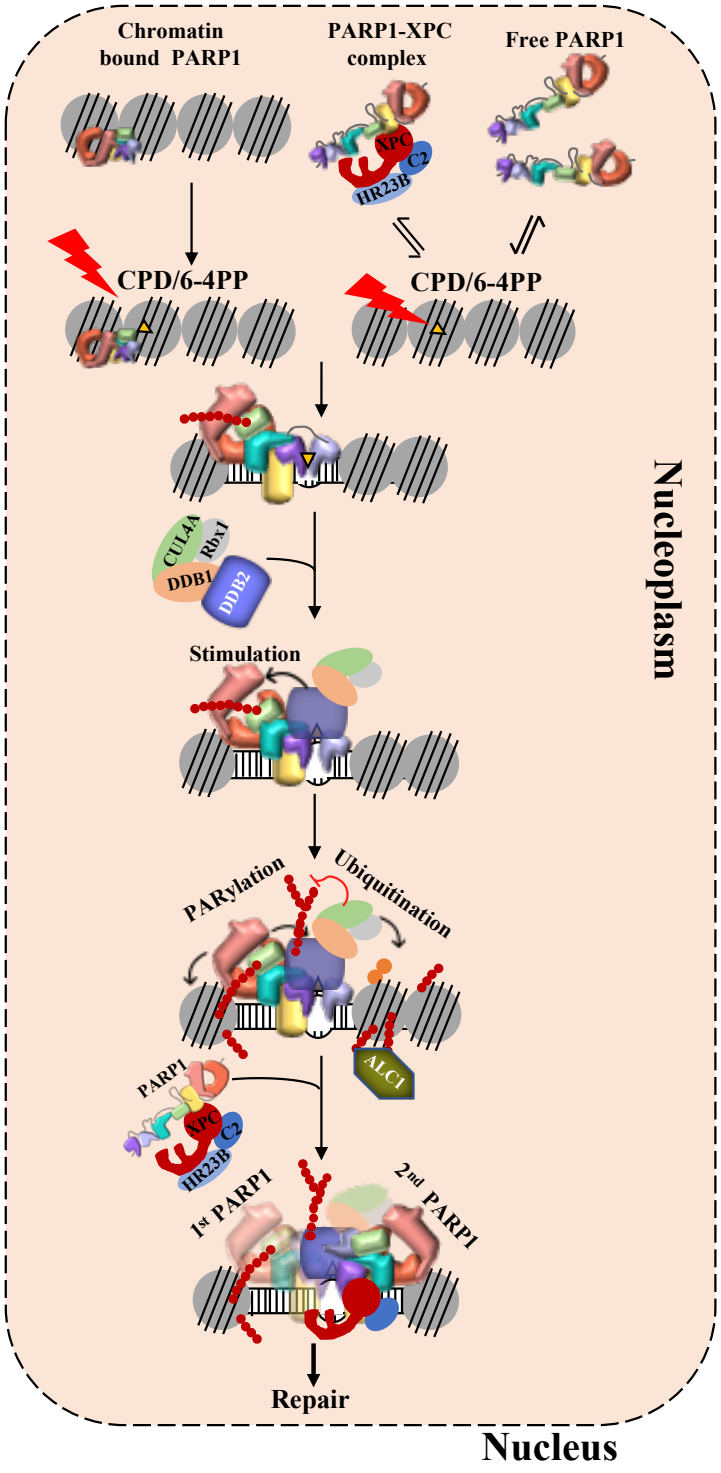

Figure a. "Updated" working model for the roles of PARP1 during DNA damage recognition phase of GG-NER sub-pathway
Figure created by Nupur Purohit.

facilitates the recruitment of the PARP1-XPC complex at CPD/6-4PP site; thus the arrival of "second" PARP1 [912]. It still needs to be determined if two PARP1 are present at the same time at the CPD/6-4PP site. In view of the known PAR-reading capacity of both PARP1 and XPC [701, 710], we propose that PARP1-XPC complex arrives at the site of damage as PAR-seeking molecules [912]. The functional relevance of preformed PARP1-XPC complex in nucleoplasm is that PARP1 can facilitate the damage search by XPC by escorting and depositing it preferably at the CPD/6-4PP sites that are bound by UV-DDB ligase complex [912]. At CPD/6-4PP sites, PARP1 facilitates XPC recruitment even in absence of DDB2 as demonstrated by using PARPi-treated XP-E cells which are devoid of DDB2 [912]. To conclude, PARP1 facilitates XPC recruitment by mediating DDB2-dependent and independent chromatin remodeling activities at the CPD/6-4PP sites and by escorting XPC to these sites.

b. "Proposed" mechanisms for the reduced initiation and/or promotion of UVB-induced SCC development in PARP1-impaired mice.

Our study in PARP1-impaired mice indicates that PARP1 functions are co-opted for the initiation and/or promotion of UVB-induced SCC development and that PARPi could be a potential chemopreventive agent for the SCC development (Chapter 4 and Sections 5.2–5.3). Based on our results placed in the context of previous studies, I propose that delayed NER of UVB-induced direct DNA damage sensitizes PARP1-impaired KC to UVB-induced apoptosis [820, 822, 833, 917]. This results in increased elimination of premutagenic KC from the epidermis, and hence reduces the number of mutated KC and initiation of SCC development in PARP1-impaired mice (Fig.b.1). Furthermore, chronic UVB-induced inflammation could also be alleviated in PARP1-impaired mice skin (Section O). Since inflammatory mediators trigger survival and proliferation of initiated KC during the promotion stage (Section J.2.4 and Fig.b.2), this could be another potential mechanism by which the UVB-induced SCC development is averted in PARP1-impaired mice. Finally, since PARPi decreases the extent of UVB-induced immunosuppression in the skin of SKH-1 mice [810], PARP1-impaired mouse skin may be capable of launching a robust immune response to eliminate cancer cells and thus decrease the susceptibility to develop NMSC. While it is intriguing that the genome integrity maintenance function of PARP1 (via NER pathway) does not protect against the occurrence of SCC in our study, our hypothesized tumor promoting pro-inflammatory role of PARP1 is in agreement with the previous reports.

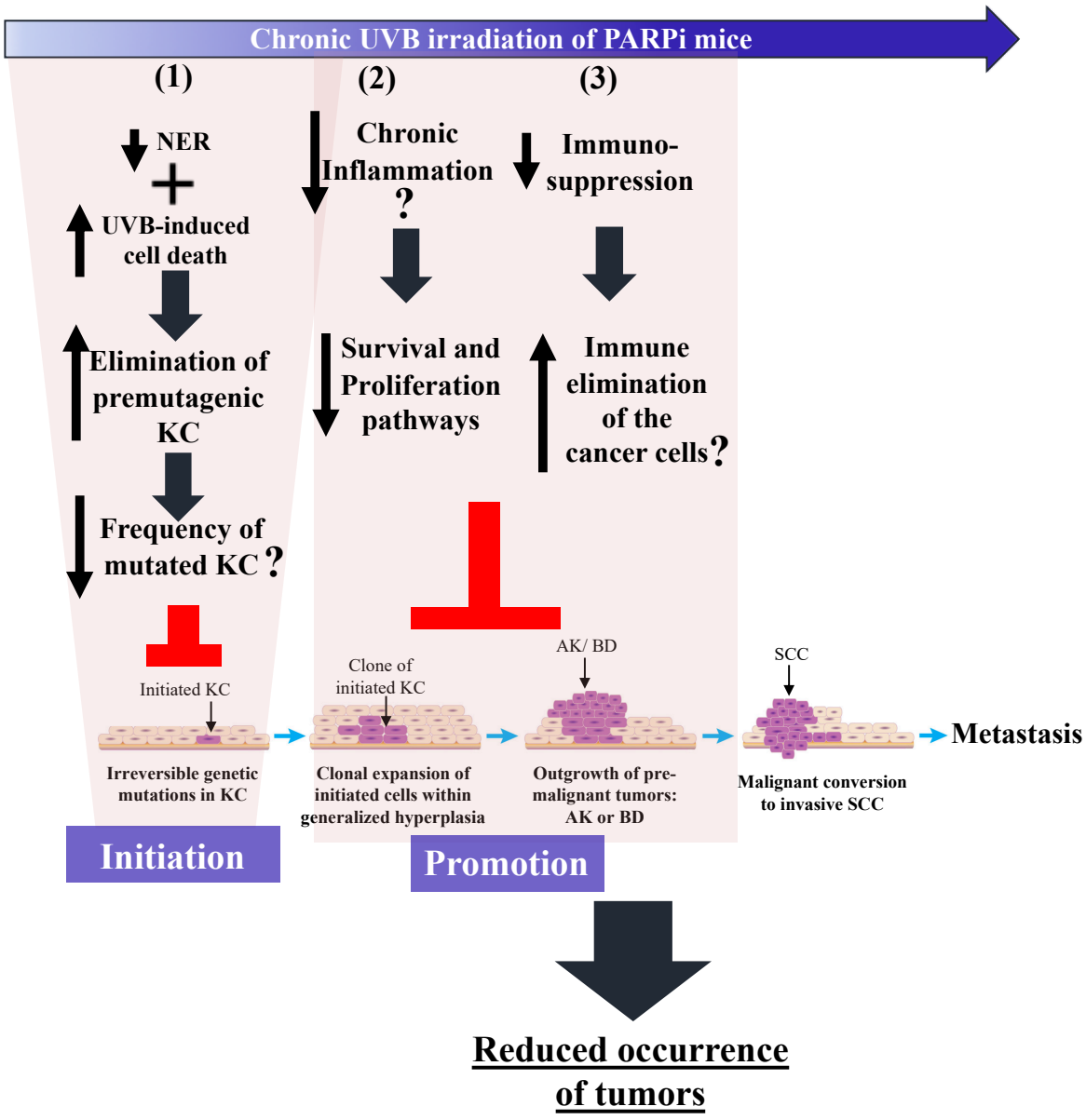

Figure b. Proposed model for reduced UVB-induced SCC development in PARP1-impaired mice

Figure created by Nupur Purohit.

Future perspectives

The discovery of the role of PARP1 in facilitating the repair of UV-induced direct DNA damage opened the door to explore its implication in the development of UV-induced skin cancers. My doctoral study demonstrates that impairing PARP1 in SKH-1 mice reduces their susceptibility to UVB-induced SCC development due to increased death of premutagenic KC from the skin of PARP1-impaired mice. Moreover, previous studies indicate that immune functions of PARP1 could also be implicated in the reduction of UVB-induced SCC development in PARP1-impaired mice. However, these mechanisms are based on the observations made after single exposure to UVB (Chapter 4 and [810, 820]) or that made in the cultured keratinocytes [833, 917]. Therefore, further studies are required to validate them *in vivo* in response to chronic UVB-exposure. In addition to UVB, the terrestrial solar UV also constitutes UVA, which can also contribute to SCC development, albeit at much higher dose than UVB. Therefore, it is important to validate reduced susceptibility in PARPi mouse to SCC development in response to solar simulated UV (SSUV), which mimics the terrestrial solar UV. Since we used second generation PARPi (PJ-34) in our study (Chapter 4), validating our data of SCC development using FDA-approved PARPi such as olaparib and talazoparib merits further studies. Moreover, examining the effect of PARPi on UV-induced skin cancer susceptibility of mouse models with KO for XP family of genes could allow us to treat the XP-patients [494-496] with PARPi to reduce their susceptibility to cancer. Bearing in mind that terrestrial solar UV is also one of the factors that can cause melanoma and BCC, determining the role of PARP1 in *de novo* development of these cancers can open up additional avenues for use of PARPi as a chemopreventive agent in sunscreens.

Identifying the mechanism by which PARP1-impaired mice exhibit reduced initiation and/or promotion of UVB-induced SCC development *in vivo*

As proposed in section b, reduced initiation and/or promotion of UVB-induced SCC development in PARP1-impaired SKH-1 mice could be via one or more of the three proposed mechanisms, which can be validated as follows.

First proposed mechanism: Reduced occurrence of SCC in PARP1-impaired mice is due to increased death of UVB-damaged or premutagenic KC from their skin. To test whether the increased level of cell death in the epidermis of PARP1-impaired mice alleviated the occurrence of tumors in them (Fig. 1.b), the adjacent non-tumor bearing skin samples collected from the KO, PARPi and WT mice at the end of chronic UVB protocols (Section 4.9) can be used for TUNEL staining assay. The reduced UVB-mutagenesis in the PARPi treated CHO cells [917] can be validated in the epidermis of PARP1-

impaired mice by the immunohistochemical (IHC) assessment of the mutant p53 in the adjacent non-tumor bearing skin samples using monoclonal p53 antibody PAb240, which recognizes only mutant p53 protein [528]. The mutation frequency in these three groups of mice can be determined by calculating the number of mutant p53-positive cells per unit epidermal area. The NER capacity of the PARP1-impaired epidermis following chronic UVB irradiation can be determined by IHC assessment of CPD in the skin samples harvested at 3 time points (0 h, 36 h and 72 h) after the last chronic UVB irradiation at 5-week intervals until 20 weeks of irradiation.

Alternatively, *in vitro* progression model of UVB-induced skin carcinogenesis, which uses transformed human keratinocytes (HaCaT cells), can also be used to assess the NER capacity and level of cell death [925]. For this, the PARP1-KO (using CRISPR Cas9 technique), PARPi treated (PARPi) and WT HaCaT cells irradiated with 300 J/m^2 UVB can be used to create the 3, 8, 12 and 16 week sublines as described by Tyagi et al [925]. To assess the NER capacity of each subline, CPD levels at the various time points (0, 2, 6 and 24h) post last UVB-irradiation can be determined by using immunofluorescence technique as described previously by us [820, 912]. Determining the cell viability by trypan blue cell count method or CellTiter-Blue® Cell Viability Assay can be employed to assess the cell death capacity of PARP1-KO, PARPi and WT sublines following the last UVB-irradiation. Various apoptosis markers such as cleaved caspase-3 and -7 can be analyzed by Western blotting in the extracts of PARP1-KO, PARPi and WT HaCaT cells at the appropriate time points after the last UVB irradiation for each sublines. To examine that the premutagenic CPD bearing KC are the ones that are undergoing apoptosis, the CPD dot blot can be performed using the DNA isolated from the floater cells harvested from the UVB-irradiated PARP1-KO, PARPi and WT HaCaT cells.

Second and third proposed mechanisms: Reduced occurrence of SCC in PARP1-impaired mice can also be due to abrogation of UVB-induced inflammation and reduction in UVB-induced immunosuppression. The Luminex method with mouse cytokine array allows quantification of the levels of pro-inflammatory cytokine such as IL-1β, IL-6 and TNFα as well as immunosuppressive cytokines such as IL-10 and IL-4 in the protein extracts of harvested tumor and adjacent non-tumor bearing part of the skin from KO, PARPi and WT mice of the chronic UVB-irradiation protocol (Section 4.9). Other parameters for UVB-induced inflammation and immunosuppression are the infiltration of pro-inflammatory macrophages and neutrophils as well as the generation of Treg, respectively (Sections I and J.2.5). The macrophages and neutrophils can be detected in the above mentioned samples via IHC using antibodies (Ab) against Ly6g and F4/80 [926], respectively [926]. Treg can also be detected via double IHC analysis using Ab against Foxp3 and CD25 in these samples

[582]. Furthermore, examining the intratumoral infiltration of Tc cells using Ab against CD8+ can allow to determine immune effectiveness in PARP1-impaired mice [582].

To determine the susceptibility of olaparib or talazoparib treated WT and NER protein-KO mice to SSUV-induced SCC development

To do this, chronic SSUV irradiation of XPC-KO, DDB2-KO, XPA-KO and WT mice treated or not with olaparib or talazoparib can be carried out as described in previous report [927]. The tumor data acquisition and cancer severity analysis as described in chapter 2 and 3 will allow determination of the susceptibility of PARPi (olaparib or talazoparib)-treated mice as compared to non-treated mice to SSUV-induced SCC development. Olaparib and talazoparib have been reported to exhibit toxic side effects when injected in the human cancer patients [902, 928]. Therefore, it is important to examine whether their prolonged topical application has any toxic effects on the skin and other internal organs. To do this, they can be topically applied to the various strains of mice until their natural death and several harvested tissue samples including skin can be analysed and compared with respective untreated mice.

Examining the susceptibility of PARPi-treated mice to the development of UV-induced melanoma and BCC

While previous studies have demonstrated that PARP1 promotes the tumorigenic potential of melanoma cells in mice [875, 876], till date, no study has examined the role of PARP1 in the *de novo* melanoma tumorigenesis. To do this, $Braf^{V600E}$ transgenic mouse model for SSUV-induced *de novo* melanoma tumorigenesis can be used. Chronic SSUV irradiation of adult $Braf^{V600E}$ mice topically treated or not with olaparib or talazoparib before each irradiation can be carried out as described before [929]. The epidemiological data suggest that malignant melanoma may arise as a consequence of intense and intermittent exposure of the skin to solar UV in childhood [930]. To address the role of PARP1 in this, single SSUV-irradiation of neonatal $Braf^{V600E}$ mice topically treated or not with olaparib or talazoparib before and after irradiation can be carried out [931]. Unlike melanoma, the role of PARP1 in *de novo* BCC tumorigenesis was studied in $Ptch1^{+/-}$ transgenic mouse model, albeit with X-rays [877]. However, chronic UV has also been shown to induce BCC tumorigenesis in $Ptch1^{+/-}$ transgenic mice [932]. To examine the susceptibility of PARPi-treated mice to UV-induced BCC, chronic SSUV irradiation of $Ptch1^{+/-}$ transgenic mice treated or not with olaparib or talazoparib can be carried out. Since the $Ptch1^{+/-}$ transgenic mice develop SCC and fibrosarcoma type of tumors in addition to BCC [932], the histological assessment of each tumor will be required to determine the susceptibility for each type of skin cancer. In these cancer models, the tumor data acquisition and the

cancer severity analysis as described in chapter 2 and 3 will determine the susceptibility of PARPi-treated mice to SSUV-induced melanoma.

To conclude, the research in the present thesis opens a newer avenue, where PARPi can be potentially exploited as chemopreventive agent against UV-induced non-melanoma skin cancers in addition to its well-known clinical application as chemotherapeutic agent for specific cancers. It will be interesting to test whether PARPi can be included as a chemopreventive agent in sunscreens to increase their efficacy for the prevention of SCC. Further studies are also required to explore whether PARPi can show a chemopreventive effect against the development of other types of cancers.

Bibliography

1. Kanitakis, J., *Anatomy, histology and immunohistochemistry of normal human skin.* Eur J Dermatol, 2002. **12**(4): p. 390-9; quiz 400-1.

2. D'Orazio, J., S. Jarrett, A. Amaro-Ortiz, and T. Scott, *UV radiation and the skin.* Int J Mol Sci, 2013. **14**(6): p. 12222-48.

3. A. J. Kolarsick, P., M. Ann Kolarsick, and C. Goodwin, *Anatomy and Physiology of the Skin*. Vol. 3. 2011. 203-213.

4. Nestle, F.O., P. Di Meglio, J.Z. Qin, and B.J. Nickoloff, *Skin immune sentinels in health and disease.* Nat Rev Immunol, 2009. **9**(10): p. 679-91.

5. Bos, J.D. and M.L. Kapsenberg, *The skin immune system Its cellular constituents and their interactions.* Immunol Today, 1986. **7**(7-8): p. 235-40.

6. Mann, E., K. Smith, D. Bernardo, H. Al-Hassi, and S. Knight, *Review: skin and the immune system.* J Clin Exp Dermatol Res S, 2012. **2**: p. 003.

7. Matejuk, A., *Skin Immunity.* Arch Immunol Ther Exp (Warsz), 2018. **66**(1): p. 45-54.

8. Streilein, J.W., *Skin-associated lymphoid tissues (SALT): origins and functions.* J Invest Dermatol, 1983. **80 Suppl**: p. 12s-16s.

9. Maverakis, E., Y. Miyamura, M.P. Bowen, G. Correa, Y. Ono, and H. Goodarzi, *Light, including ultraviolet.* J Autoimmun, 2010. **34**(3): p. J247-57.

10. Diffey, B.L., *What is light?* Photodermatol Photoimmunol Photomed, 2002. **18**(2): p. 68-74.

11. Bruls, W.A. and J.C. van der Leun, *Forward scattering properties of human epidermal layers.* Photochem Photobiol, 1984. **40**(2): p. 231-42.

12. Bruls, W.A., H. Slaper, J.C. van der Leun, and L. Berrens, *Transmission of human epidermis and stratum corneum as a function of thickness in the ultraviolet and visible wavelengths.* Photochem Photobiol, 1984. **40**(4): p. 485-94.

13. Valejo Coelho, M.M., T.R. Matos, and M. Apetato, *The dark side of the light: mechanisms of photocarcinogenesis.* Clin Dermatol, 2016. **34**(5): p. 563-70.

14. Juzeniene, A. and J. Moan, *Beneficial effects of UV radiation other than via vitamin D production.* Dermatoendocrinol, 2012. **4**(2): p. 109-17.

15. Wacker, M. and M.F. Holick, *Sunlight and Vitamin D: A global perspective for health.* Dermatoendocrinol, 2013. **5**(1): p. 51-108.

16. Radack, K.P., M.E. Farhangian, K.L. Anderson, and S.R. Feldman, *A review of the use of tanning beds as a dermatological treatment.* Dermatol Ther (Heidelb), 2015. **5**(1): p. 37-51.

17. Wong, T., L. Hsu, and W. Liao, *Phototherapy in psoriasis: a review of mechanisms of action.* J Cutan Med Surg, 2013. **17**(1): p. 6-12.

18. Young, A.R., J. Claveau, and A.B. Rossi, *Ultraviolet radiation and the skin: Photobiology and sunscreen photoprotection.* J Am Acad Dermatol, 2017. **76**(3S1): p. S100-S109.

19. Young, A.R., *Chromophores in human skin.* Phys Med Biol, 1997. **42**(5): p. 789-802.

20. Bikle, D.D., *Vitamin D metabolism and function in the skin.* Mol Cell Endocrinol, 2011. **347**(1-2): p. 80-9.

21. Baden, H.P. and M.A. Pathak, *The metabolism and function of urocanic acid in skin.* J Invest Dermatol, 1967. **48**(1): p. 11-7.

22. Baden, H.P., M.A. Pathak, and D. Butler, *Trans to cis isomerization of urocanic acid.* Nature, 1966. **210**(5037): p. 732-3.

23. Mullenders, L.H.F., *Solar UV damage to cellular DNA: from mechanisms to biological effects.* Photochem Photobiol Sci, 2018. **17**(12): p. 1842-1852.

24. Regensburger, J., A. Knak, T. Maisch, M. Landthaler, and W. Baumler, *Fatty acids and vitamins generate singlet oxygen under UVB irradiation.* Exp Dermatol, 2012. **21**(2): p. 135-9.

25. Knak, A., J. Regensburger, T. Maisch, and W. Baumler, *Exposure of vitamins to UVB and UVA radiation generates singlet oxygen.* Photochem Photobiol Sci, 2014. **13**(5): p. 820-9.

26. Davies, M.J. and R.J. Truscott, *Photo-oxidation of proteins and its role in cataractogenesis.* J Photochem Photobiol B, 2001. **63**(1-3): p. 114-25.

27. Cadet, J. and T. Douki, *Formation of UV-induced DNA damage contributing to skin cancer development.* Photochem Photobiol Sci, 2018. **17**(12): p. 1816-1841.

28. Marathe, G.K., C. Johnson, S.D. Billings, M.D. Southall, Y. Pei, D. Spandau*, et al.*, *Ultraviolet B radiation generates platelet-activating factor-like phospholipids underlying cutaneous damage.* J Biol Chem, 2005. **280**(42): p. 35448-57.

29. Alappatt, C., C.A. Johnson, K.L. Clay, and J.B. Travers, *Acute keratinocyte damage stimulates platelet-activating factor production.* Arch Dermatol Res, 2000. **292**(5): p. 256-9.

30. Fritsche, E., C. Schafer, C. Calles, T. Bernsmann, T. Bernshausen, M. Wurm*, et al.*, *Lightening up the UV response by identification of the arylhydrocarbon receptor as a cytoplasmatic target for ultraviolet B radiation.* Proc Natl Acad Sci U S A, 2007. **104**(21): p. 8851-6.

31. Pattison, D.I., A.S. Rahmanto, and M.J. Davies, *Photo-oxidation of proteins.* Photochemical & Photobiological Sciences, 2012. **11**(1): p. 38-53.

32. Lu, Y.P., Y.R. Lou, P. Yen, D. Mitchell, M.T. Huang, and A.H. Conney, *Time course for early adaptive responses to ultraviolet B light in the epidermis of SKH-1 mice.* Cancer Res, 1999. **59**(18): p. 4591-602.

33. Kunisada, M., K. Sakumi, Y. Tominaga, A. Budiyanto, M. Ueda, M. Ichihashi*, et al.*, *8-Oxoguanine formation induced by chronic UVB exposure makes Ogg1 knockout mice susceptible to skin carcinogenesis.* Cancer Res, 2005. **65**(14): p. 6006-10.

34. Kumar, S., N.D. Sharma, R.J. Davies, D.W. Phillipson, and J.A. McCloskey, *The isolation and characterisation of a new type of dimeric adenine photoproduct in UV-irradiated deoxyadenylates.* Nucleic Acids Res, 1987. **15**(3): p. 1199-216.

35. Banyasz, A., L. Martinez-Fernandez, T.M. Ketola, A. Munoz-Losa, L. Esposito, D. Markovitsi*, et al.*, *Excited State Pathways Leading to Formation of Adenine Dimers.* J Phys Chem Lett, 2016. **7**(11): p. 2020-3.

36. Asgatay, S., A. Martinez, S. Coantic-Castex, D. Harakat, C. Philippe, T. Douki*, et al.*, *UV-induced TA photoproducts: formation and hydrolysis in double-stranded DNA.* J Am Chem Soc, 2010. **132**(30): p. 10260-1.

37. Kielbassa, C., L. Roza, and B. Epe, *Wavelength dependence of oxidative DNA damage induced by UV and visible light.* Carcinogenesis, 1997. **18**(4): p. 811-6.

38. Schreier, W.J., T.E. Schrader, F.O. Koller, P. Gilch, C.E. Crespo-Hernandez, V.N. Swaminathan*, et al.*, *Thymine dimerization in DNA is an ultrafast photoreaction.* Science, 2007. **315**(5812): p. 625-9.

39. Markovitsi, D., *UV-induced DNA Damage: The Role of Electronic Excited States.* Photochem Photobiol, 2016. **92**(1): p. 45-51.

40. Banyasz, A., T. Douki, R. Improta, T. Gustavsson, D. Onidas, I. Vaya*, et al.*, *Electronic excited states responsible for dimer formation upon UV absorption directly by thymine strands: joint experimental and theoretical study.* J Am Chem Soc, 2012. **134**(36): p. 14834-45.

41. Douki, T. and J. Cadet, *Individual determination of the yield of the main UV-induced dimeric pyrimidine photoproducts in DNA suggests a high mutagenicity of CC photolesions.* Biochemistry, 2001. **40**(8): p. 2495-501.

42. Cadet, J., A. Grand, and T. Douki, *Solar UV radiation-induced DNA Bipyrimidine photoproducts: formation and mechanistic insights.* Top Curr Chem, 2015. **356**: p. 249-75.

43. Ben-Hur, E. and R. Ben-Ishai, *Trans-syn thymine dimers in ultraviolet-irradiated denatured DNA: identification and photoreactivability.* Biochim Biophys Acta, 1968. **166**(1): p. 9-15.

44. Rahn, R.O. and L.C. Landry, *Pyrimidine dimer formation in poly (d-dT) and apurinic acid.* Biochim Biophys Acta, 1971. **247**(2): p. 197-206.

45. Bryan, D.S., M. Ransom, B. Adane, K. York, and J.R. Hesselberth, *High resolution mapping of modified DNA nucleobases using excision repair enzymes.* Genome Res, 2014. **24**(9): p. 1534-42.

46. Mouret, S., C. Baudouin, M. Charveron, A. Favier, J. Cadet, and T. Douki, *Cyclobutane pyrimidine dimers are predominant DNA lesions in whole human skin exposed to UVA radiation.* Proc Natl Acad Sci U S A, 2006. **103**(37): p. 13765-70.

47. Richa, R.P. Sinha, and D.P. Hader, *Physiological aspects of UV-excitation of DNA.* Top Curr Chem, 2015. **356**: p. 203-48.

48. Law, Y.K., R.A. Forties, X. Liu, M.G. Poirier, and B. Kohler, *Sequence-dependent thymine dimer formation and photoreversal rates in double-stranded DNA.* Photochem Photobiol Sci, 2013. **12**(8): p. 1431-9.

49. Cadet, J. and T. Douki, *Formation of UV-induced DNA damage contributing to skin cancer development.* Photochem Photobiol Sci, 2018.

50. Marguet, S. and D. Markovitsi, *Time-resolved study of thymine dimer formation.* J Am Chem Soc, 2005. **127**(16): p. 5780-1.

51. Kan, L.S., L. Voituriez, and J. Cadet, *The Dewar valence isomer of the (6-4) photoadduct of thymidylyl-(3'-5')-thymidine monophosphate: formation, alkaline lability and conformational properties.* J Photochem Photobiol B, 1992. **12**(4): p. 339-57.

52. Douki, T. and E. Sage, *Dewar valence isomers, the third type of environmentally relevant DNA photoproducts induced by solar radiation.* Photochem Photobiol Sci, 2016. **15**(1): p. 24-30.

53. Taylor, J.S., H.F. Lu, and J.J. Kotyk, *Quantitative conversion of the (6-4) photoproduct of TpdC to its Dewar valence isomer upon exposure to simulated sunlight.* Photochem Photobiol, 1990. **51**(2): p. 161-7.

54. Perdiz, D., P. Grof, M. Mezzina, O. Nikaido, E. Moustacchi, and E. Sage, *Distribution and repair of bipyrimidine photoproducts in solar UV-irradiated mammalian cells. Possible role of Dewar photoproducts in solar mutagenesis.* J Biol Chem, 2000. **275**(35): p. 26732-42.

55. Chadwick, C.A., C.S. Potten, O. Nikaido, T. Matsunaga, C. Proby, and A.R. Young, *The detection of cyclobutane thymine dimers, (6-4) photolesions and the Dewar photoisomers in sections of UV-irradiated human skin using specific antibodies, and the demonstration of depth penetration effects.* J Photochem Photobiol B, 1995. **28**(2): p. 163-70.

56. Han, C., A.K. Srivastava, T. Cui, Q.E. Wang, and A.A. Wani, *Differential DNA lesion formation and repair in heterochromatin and euchromatin.* Carcinogenesis, 2016. **37**(2): p. 129-38.

57. Gale, J.M. and M.J. Smerdon, *UV induced (6-4) photoproducts are distributed differently than cyclobutane dimers in nucleosomes.* Photochem Photobiol, 1990. **51**(4): p. 411-7.

58. Niggli, H.J. and P.A. Cerutti, *Nucleosomal distribution of thymine photodimers following far- and near-ultraviolet irradiation.* Biochem Biophys Res Commun, 1982. **105**(3): p. 1215-23.

59. Brown, D.W., L.J. Libertini, C. Suquet, E.W. Small, and M.J. Smerdon, *Unfolding of nucleosome cores dramatically changes the distribution of ultraviolet photoproducts in DNA.* Biochemistry, 1993. **32**(40): p. 10527-31.

60. Gale, J.M., K.A. Nissen, and M.J. Smerdon, *UV-induced formation of pyrimidine dimers in nucleosome core DNA is strongly modulated with a period of 10.3 bases.* Proc Natl Acad Sci U S A, 1987. **84**(19): p. 6644-8.

61. Rochette, P.J. and D.E. Brash, *Human telomeres are hypersensitive to UV-induced DNA Damage and refractory to repair.* PLoS Genet, 2010. **6**(4): p. e1000926.

62. Pfeifer, G.P., R. Drouin, and G.P. Holmquist, *Detection of DNA adducts at the DNA sequence level by ligation-mediated PCR.* Mutat Res, 1993. **288**(1): p. 39-46.

63. Bastien, N., J.P. Therrien, and R. Drouin, *Cytosine containing dipyrimidine sites can be hotspots of cyclobutane pyrimidine dimer formation after UVB exposure.* Photochem Photobiol Sci, 2013. **12**(8): p. 1544-54.

64. Mitchell, D.L., J. Jen, and J.E. Cleaver, *Sequence specificity of cyclobutane pyrimidine dimers in DNA treated with solar (ultraviolet B) radiation.* Nucleic Acids Res, 1992. **20**(2): p. 225-9.

65. Tommasi, S., M.F. Denissenko, and G.P. Pfeifer, *Sunlight induces pyrimidine dimers preferentially at 5-methylcytosine bases.* Cancer Res, 1997. **57**(21): p. 4727-30.

66. Rochette, P.J., S. Lacoste, J.P. Therrien, N. Bastien, D.E. Brash, and R. Drouin, *Influence of cytosine methylation on ultraviolet-induced cyclobutane pyrimidine dimer formation in genomic DNA.* Mutat Res, 2009. **665**(1-2): p. 7-13.

67. Kim, J.K., D. Patel, and B.S. Choi, *Contrasting structural impacts induced by cis-syn cyclobutane dimer and (6-4) adduct in DNA duplex decamers: implication in mutagenesis and repair activity.* Photochem Photobiol, 1995. **62**(1): p. 44-50.

68. Mouret, S., M. Charveron, A. Favier, J. Cadet, and T. Douki, *Differential repair of UVB-induced cyclobutane pyrimidine dimers in cultured human skin cells and whole human skin.* DNA Repair (Amst), 2008. **7**(5): p. 704-12.

69. Cadet, J., T. Douki, J.L. Ravanat, and P. Di Mascio, *Sensitized formation of oxidatively generated damage to cellular DNA by UVA radiation.* Photochem Photobiol Sci, 2009. **8**(7): p. 903-11.

70. Schuch, A.P., N.C. Moreno, N.J. Schuch, C.F.M. Menck, and C.C.M. Garcia, *Sunlight damage to cellular DNA: Focus on oxidatively generated lesions.* Free Radic Biol Med, 2017. **107**: p. 110-124.

71. Dedon, P.C., *The chemical toxicology of 2-deoxyribose oxidation in DNA.* Chem Res Toxicol, 2008. **21**(1): p. 206-19.

72. Caldecott, K.W., *Single-strand break repair and genetic disease.* Nat Rev Genet, 2008. **9**(8): p. 619-31.

73. Foote, C.S., *Definition of type I and type II photosensitized oxidation.* Photochem Photobiol, 1991. **54**(5): p. 659.

74. Creed, D., *THE PHOTOPHYSICS AND PHOTOCHEMISTRY OF THE NEAR-UV ABSORBING AMINO ACIDS–I. TRYPTOPHAN AND ITS SIMPLE DERIVATIVES.* Photochemistry and Photobiology, 1984. **39**(4): p. 537-562.

75. Tedesco, A.C., L. Martinez, and S. Gonzalez, *Photochemistry and photobiology of actinic erythema: defensive and reparative cutaneous mechanisms.* Braz J Med Biol Res, 1997. **30**(5): p. 561-75.

76. Ravanat, J.L., P. Di Mascio, G.R. Martinez, M.H. Medeiros, and J. Cadet, *Singlet oxygen induces oxidation of cellular DNA.* J Biol Chem, 2000. **275**(51): p. 40601-4.

77. Cadet, J., J.R. Wagner, V. Shafirovich, and N.E. Geacintov, *One-electron oxidation reactions of purine and pyrimidine bases in cellular DNA.* Int J Radiat Biol, 2014. **90**(6): p. 423-32.

78. Douki, T., D. Perdiz, P. Grof, Z. Kuluncsics, E. Moustacchi, J. Cadet*, et al.*, *Oxidation of guanine in cellular DNA by solar UV radiation: biological role.* Photochem Photobiol, 1999. **70**(2): p. 184-90.

79. Premi, S., S. Wallisch, C.M. Mano, A.B. Weiner, A. Bacchiocchi, K. Wakamatsu*, et al.*, *Photochemistry. Chemiexcitation of melanin derivatives induces DNA photoproducts long after UV exposure.* Science, 2015. **347**(6224): p. 842-7.

80. Gajula, R.P. and S. Gaddameedhi, *Commentary: Chemiexcitation of melanin derivatives induces DNA photoproducts long after UV exposure.* Front Physiol, 2015. **6**: p. 276.

81. Wischermann, K., S. Popp, S. Moshir, K. Scharfetter-Kochanek, M. Wlaschek, F. de Gruijl*, et al.*, *UVA radiation causes DNA strand breaks, chromosomal aberrations and tumorigenic transformation in HaCaT skin keratinocytes.* Oncogene, 2008. **27**(31): p. 4269-80.

82. Rizzo, J.L., J. Dunn, A. Rees, and T.M. Runger, *No formation of DNA double-strand breaks and no activation of recombination repair with UVA.* J Invest Dermatol, 2011. **131**(5): p. 1139-48.

83. Greinert, R., B. Volkmer, S. Henning, E.W. Breitbart, K.O. Greulich, M.C. Cardoso*, et al.*, *UVA-induced DNA double-strand breaks result from the repair of clustered oxidative DNA damages.* Nucleic Acids Res, 2012. **40**(20): p. 10263-73.

84. Garinis, G.A., J.R. Mitchell, M.J. Moorhouse, K. Hanada, H. de Waard, D. Vandeputte*, et al.*, *Transcriptome analysis reveals cyclobutane pyrimidine dimers as a major source of UV-induced DNA breaks.* EMBO J, 2005. **24**(22): p. 3952-62.

85. Berg, R.J., H.J. Ruven, A.T. Sands, F.R. de Gruijl, and L.H. Mullenders, *Defective global genome repair in XPC mice is associated with skin cancer susceptibility but not with sensitivity to UVB induced erythema and edema.* J Invest Dermatol, 1998. **110**(4): p. 405-9.

86. van Oosten, M., H. Rebel, E.C. Friedberg, H. van Steeg, G.T. van der Horst, H.J. van Kranen*, et al.*, *Differential role of transcription-coupled repair in UVB-induced G2 arrest and apoptosis in mouse epidermis.* Proc Natl Acad Sci U S A, 2000. **97**(21): p. 11268-73.

87. Nakane, H., S. Takeuchi, S. Yuba, M. Saijo, Y. Nakatsu, H. Murai*, et al.*, *High incidence of ultraviolet-B-or chemical-carcinogen-induced skin tumours in mice lacking the xeroderma pigmentosum group A gene.* Nature, 1995. **377**(6545): p. 165-8.

88. Dianov, G., C. Bischoff, J. Piotrowski, and V.A. Bohr, *Repair pathways for processing of 8-oxoguanine in DNA by mammalian cell extracts.* J Biol Chem, 1998. **273**(50): p. 33811-6.

89. Markkanen, E., *Not breathing is not an option: How to deal with oxidative DNA damage.* DNA Repair (Amst), 2017. **59**: p. 82-105.

90. Wilson, S.H. and T.A. Kunkel, *Passing the baton in base excision repair.* Nat Struct Biol, 2000. **7**(3): p. 176-8.

91. Mol, C.D., T. Izumi, S. Mitra, and J.A. Tainer, *DNA-bound structures and mutants reveal abasic DNA binding by APE1 and DNA repair coordination [corrected].* Nature, 2000. **403**(6768): p. 451-6.

92. Frosina, G., P. Fortini, O. Rossi, F. Carrozzino, G. Raspaglio, L.S. Cox*, et al.*, *Two pathways for base excision repair in mammalian cells.* J Biol Chem, 1996. **271**(16): p. 9573-8.

93. Bruner, S.D., D.P. Norman, and G.L. Verdine, *Structural basis for recognition and repair of the endogenous mutagen 8-oxoguanine in DNA.* Nature, 2000. **403**(6772): p. 859-66.

94. Radicella, J.P., C. Dherin, C. Desmaze, M.S. Fox, and S. Boiteux, *Cloning and characterization of hOGG1, a human homolog of the OGG1 gene of Saccharomyces cerevisiae.* Proc Natl Acad Sci U S A, 1997. **94**(15): p. 8010-5.

95. Mosbaugh, D.W. and S. Linn, *Further characterization of human fibroblast apurinic/apyrimidinic DNA endonucleases. The definition of two mechanistic classes of enzyme.* J Biol Chem, 1980. **255**(24): p. 11743-52.

96. Li, M. and D.M. Wilson, 3rd, *Human apurinic/apyrimidinic endonuclease 1.* Antioxid Redox Signal, 2014. **20**(4): p. 678-707.

97. Fortini, P., E. Parlanti, O.M. Sidorkina, J. Laval, and E. Dogliotti, *The type of DNA glycosylase determines the base excision repair pathway in mammalian cells.* J Biol Chem, 1999. **274**(21): p. 15230-6.

98. Pascucci, B., G. Maga, U. Hubscher, M. Bjoras, E. Seeberg, I.D. Hickson*, et al.*, *Reconstitution of the base excision repair pathway for 7,8-dihydro-8-oxoguanine with purified human proteins.* Nucleic Acids Res, 2002. **30**(10): p. 2124-30.

99. Dianov, G., A. Price, and T. Lindahl, *Generation of single-nucleotide repair patches following excision of uracil residues from DNA.* Mol Cell Biol, 1992. **12**(4): p. 1605-12.

100. Dianov, G. and T. Lindahl, *Reconstitution of the DNA base excision-repair pathway.* Curr Biol, 1994. **4**(12): p. 1069-76.

101. Matsumoto, Y. and K. Kim, *Excision of deoxyribose phosphate residues by DNA polymerase beta during DNA repair.* Science, 1995. **269**(5224): p. 699-702.

102. Marsin, S., A.E. Vidal, M. Sossou, J. Menissier-de Murcia, F. Le Page, S. Boiteux*, et al.*, *Role of XRCC1 in the coordination and stimulation of oxidative DNA damage repair initiated by the DNA glycosylase hOGG1.* J Biol Chem, 2003. **278**(45): p. 44068-74.

103. Abbotts, R. and D.M. Wilson, 3rd, *Coordination of DNA single strand break repair.* Free Radic Biol Med, 2017. **107**: p. 228-244.

104. Beard, W.A., R. Prasad, and S.H. Wilson, *Activities and mechanism of DNA polymerase beta.* Methods Enzymol, 2006. **408**: p. 91-107.

105. Cappelli, E., R. Taylor, M. Cevasco, A. Abbondandolo, K. Caldecott, and G. Frosina, *Involvement of XRCC1 and DNA ligase III gene products in DNA base excision repair.* J Biol Chem, 1997. **272**(38): p. 23970-5.

106. Markkanen, E., B. Castrec, G. Villani, and U. Hubscher, *A switch between DNA polymerases delta and lambda promotes error-free bypass of 8-oxo-G lesions.* Proc Natl Acad Sci U S A, 2012. **109**(50): p. 20401-6.

107. Picher, A.J. and L. Blanco, *Human DNA polymerase lambda is a proficient extender of primer ends paired to 7,8-dihydro-8-oxoguanine.* DNA Repair (Amst), 2007. **6**(12): p. 1749-56.

108. Shibutani, S., M. Takeshita, and A.P. Grollman, *Insertion of specific bases during DNA synthesis past the oxidation-damaged base 8-oxodG.* Nature, 1991. **349**(6308): p. 431-4.

109. Maga, G., G. Villani, E. Crespan, U. Wimmer, E. Ferrari, B. Bertocci*, et al.*, *8-oxo-guanine bypass by human DNA polymerases in the presence of auxiliary proteins.* Nature, 2007. **447**(7144): p. 606-8.

110. Krahn, J.M., W.A. Beard, H. Miller, A.P. Grollman, and S.H. Wilson, *Structure of DNA polymerase beta with the mutagenic DNA lesion 8-oxodeoxyguanine reveals structural insights into its coding potential.* Structure, 2003. **11**(1): p. 121-7.

111. Efrati, E., G. Tocco, R. Eritja, S.H. Wilson, and M.F. Goodman, *"Action-at-a-distance" mutagenesis. 8-oxo-7, 8-dihydro-2'-deoxyguanosine causes base substitution errors at neighboring template sites when copied by DNA polymerase beta.* J Biol Chem, 1999. **274**(22): p. 15920-6.

112. Hsu, G.W., M. Ober, T. Carell, and L.S. Beese, *Error-prone replication of oxidatively damaged DNA by a high-fidelity DNA polymerase.* Nature, 2004. **431**(7005): p. 217-21.

113. Markkanen, E., J. Dorn, and U. Hubscher, *MUTYH DNA glycosylase: the rationale for removing undamaged bases from the DNA.* Front Genet, 2013. **4**: p. 18.

114. Burak, M.J., K.E. Guja, E. Hambardjieva, B. Derkunt, and M. Garcia-Diaz, *A fidelity mechanism in DNA polymerase lambda promotes error-free bypass of 8-oxo-dG.* EMBO J, 2016. **35**(18): p. 2045-59.

115. Maga, G., E. Crespan, U. Wimmer, B. van Loon, A. Amoroso, C. Mondello*, et al.*, *Replication protein A and proliferating cell nuclear antigen coordinate DNA polymerase selection in 8-oxo-guanine repair.* Proc Natl Acad Sci U S A, 2008. **105**(52): p. 20689-94.

116. van Loon, B. and U. Hubscher, *An 8-oxo-guanine repair pathway coordinated by MUTYH glycosylase and DNA polymerase lambda.* Proc Natl Acad Sci U S A, 2009. **106**(43): p. 18201-6.

117. Storici, F., G. Henneke, E. Ferrari, D.A. Gordenin, U. Hubscher, and M.A. Resnick, *The flexible loop of human FEN1 endonuclease is required for flap cleavage during DNA replication and repair.* EMBO J, 2002. **21**(21): p. 5930-42.

118. Liu, Y., H.I. Kao, and R.A. Bambara, *Flap endonuclease 1: a central component of DNA metabolism.* Annu Rev Biochem, 2004. **73**: p. 589-615.

119. Mozzherin, D.J., S. Shibutani, C.K. Tan, K.M. Downey, and P.A. Fisher, *Proliferating cell nuclear antigen promotes DNA synthesis past template lesions by mammalian DNA polymerase delta.* Proc Natl Acad Sci U S A, 1997. **94**(12): p. 6126-31.

120. Kuzminov, A., *Single-strand interruptions in replicating chromosomes cause double-strand breaks.* Proc Natl Acad Sci U S A, 2001. **98**(15): p. 8241-6.

121. Caldecott, K.W., *DNA single-strand break repair.* Exp Cell Res, 2014. **329**(1): p. 2-8.

122. Sukhanova, M.V., S. Abrakhi, V. Joshi, D. Pastre, M.M. Kutuzov, R.O. Anarbaev*, et al.*, *Single molecule detection of PARP1 and PARP2 interaction with DNA strand breaks and their poly(ADP-ribosyl)ation using high-resolution AFM imaging.* Nucleic Acids Res, 2016. **44**(6): p. e60.

123. Ray Chaudhuri, A. and A. Nussenzweig, *The multifaceted roles of PARP1 in DNA repair and chromatin remodelling.* Nat Rev Mol Cell Biol, 2017. **18**(10): p. 610-621.

124. Satoh, M.S. and T. Lindahl, *Role of poly(ADP-ribose) formation in DNA repair.* Nature, 1992. **356**(6367): p. 356-8.

125. Hanzlikova, H., W. Gittens, K. Krejcikova, Z. Zeng, and K.W. Caldecott, *Overlapping roles for PARP1 and PARP2 in the recruitment of endogenous XRCC1 and PNKP into oxidized chromatin.* Nucleic Acids Res, 2017. **45**(5): p. 2546-2557.

126. Fisher, A.E., H. Hochegger, S. Takeda, and K.W. Caldecott, *Poly(ADP-ribose) polymerase 1 accelerates single-strand break repair in concert with poly(ADP-ribose) glycohydrolase.* Mol Cell Biol, 2007. **27**(15): p. 5597-605.

127. Woodhouse, B.C., Dianova, II, J.L. Parsons, and G.L. Dianov, *Poly(ADP-ribose) polymerase-1 modulates DNA repair capacity and prevents formation of DNA double strand breaks.* DNA Repair (Amst), 2008. **7**(6): p. 932-40.

128. Okano, S., L. Lan, K.W. Caldecott, T. Mori, and A. Yasui, *Spatial and temporal cellular responses to single-strand breaks in human cells.* Mol Cell Biol, 2003. **23**(11): p. 3974-81.

129. Masson, M., C. Niedergang, V. Schreiber, S. Muller, J. Menissier-de Murcia, and G. de Murcia, *XRCC1 is specifically associated with poly(ADP-ribose) polymerase and negatively regulates its activity following DNA damage.* Mol Cell Biol, 1998. **18**(6): p. 3563-71.

130. El-Khamisy, S.F., M. Masutani, H. Suzuki, and K.W. Caldecott, *A requirement for PARP-1 for the assembly or stability of XRCC1 nuclear foci at sites of oxidative DNA damage.* Nucleic Acids Res, 2003. **31**(19): p. 5526-33.

131. Breslin, C., P. Hornyak, A. Ridley, S.L. Rulten, H. Hanzlikova, A.W. Oliver*, et al.*, *The XRCC1 phosphate-binding pocket binds poly (ADP-ribose) and is required for XRCC1 function.* Nucleic Acids Res, 2015. **43**(14): p. 6934-44.

132. Polo, L.M., Y. Xu, P. Hornyak, F. Garces, Z. Zeng, R. Hailstone*, et al.*, *Efficient Single-Strand Break Repair Requires Binding to Both Poly(ADP-Ribose) and DNA by the Central BRCT Domain of XRCC1.* Cell Rep, 2019. **26**(3): p. 573-581 e5.

133. Caldecott, K.W., *XRCC1 protein; Form and function.* DNA Repair (Amst), 2019: p. 102664.

134. Whitehouse, C.J., R.M. Taylor, A. Thistlethwaite, H. Zhang, F. Karimi-Busheri, D.D. Lasko*, et al.*, *XRCC1 stimulates human polynucleotide kinase activity at damaged DNA termini and accelerates DNA single-strand break repair.* Cell, 2001. **104**(1): p. 107-17.

135. Karimi-Busheri, F., G. Daly, P. Robins, B. Canas, D.J. Pappin, J. Sgouros*, et al.*, *Molecular characterization of a human DNA kinase.* J Biol Chem, 1999. **274**(34): p. 24187-94.

136. Jilani, A., D. Ramotar, C. Slack, C. Ong, X.M. Yang, S.W. Scherer*, et al.*, *Molecular cloning of the human gene, PNKP, encoding a polynucleotide kinase 3'-phosphatase and evidence for its role in repair of DNA strand breaks caused by oxidative damage.* J Biol Chem, 1999. **274**(34): p. 24176-86.

137. Winters, T.A., M. Weinfeld, and T.J. Jorgensen, *Human HeLa cell enzymes that remove phosphoglycolate 3'-end groups from DNA.* Nucleic Acids Res, 1992. **20**(10): p. 2573-80.

138. Winters, T.A., W.D. Henner, P.S. Russell, A. McCullough, and T.J. Jorgensen, *Removal of 3'-phosphoglycolate from DNA strand-break damage in an oligonucleotide substrate by recombinant human apurinic/apyrimidinic endonuclease 1.* Nucleic Acids Res, 1994. **22**(10): p. 1866-73.

139. Chen, D.S., T. Herman, and B. Demple, *Two distinct human DNA diesterases that hydrolyze 3'-blocking deoxyribose fragments from oxidized DNA.* Nucleic Acids Res, 1991. **19**(21): p. 5907-14.

140. Izumi, T., T.K. Hazra, I. Boldogh, A.E. Tomkinson, M.S. Park, S. Ikeda*, et al.*, *Requirement for human AP endonuclease 1 for repair of 3'-blocking damage at DNA single-strand breaks induced by reactive oxygen species.* Carcinogenesis, 2000. **21**(7): p. 1329-34.

141. Parsons, J.L., Dianova, II, and G.L. Dianov, *APE1 is the major 3'-phosphoglycolate activity in human cell extracts.* Nucleic Acids Res, 2004. **32**(12): p. 3531-6.

142. Kim, Y.J. and D.M. Wilson, 3rd, *Overview of base excision repair biochemistry.* Curr Mol Pharmacol, 2012. **5**(1): p. 3-13.

143. Scharer, O.D., *Nucleotide excision repair in eukaryotes.* Cold Spring Harb Perspect Biol, 2013. **5**(10): p. a012609.

144. Rastogi, R.P., Richa, A. Kumar, M.B. Tyagi, and R.P. Sinha, *Molecular mechanisms of ultraviolet radiation-induced DNA damage and repair.* J Nucleic Acids, 2010. **2010**: p. 592980.

145. Rasmussen, R.E. and R.B. Painter, *Evidence for Repair of Ultra-Violet Damaged Deoxyribonucleic Acid in Cultured Mammalian Cells.* Nature, 1964. **203**: p. 1360-2.

146. Setlow, R.B. and W.L. Carrier, *The Disappearance of Thymine Dimers from DNA: An Error-Correcting Mechanism.* Proc Natl Acad Sci U S A, 1964. **51**: p. 226-31.

147. Araujo, S.J., F. Tirode, F. Coin, H. Pospiech, J.E. Syvaoja, M. Stucki*, et al.*, *Nucleotide excision repair of DNA with recombinant human proteins: definition of the minimal set of factors, active forms of TFIIH, and modulation by CAK.* Genes Dev, 2000. **14**(3): p. 349-59.

148. Volker, M., M.J. Mone, P. Karmakar, A. van Hoffen, W. Schul, W. Vermeulen*, et al.*, *Sequential assembly of the nucleotide excision repair factors in vivo.* Mol Cell, 2001. **8**(1): p. 213-24.

149. Spivak, G., *Nucleotide excision repair in humans.* DNA Repair (Amst), 2015. **36**: p. 13-18.

150. Bohr, V.A., C.A. Smith, D.S. Okumoto, and P.C. Hanawalt, *DNA repair in an active gene: removal of pyrimidine dimers from the DHFR gene of CHO cells is much more efficient than in the genome overall.* Cell, 1985. **40**(2): p. 359-69.

151. Mellon, I., V.A. Bohr, C.A. Smith, and P.C. Hanawalt, *Preferential DNA repair of an active gene in human cells.* Proc Natl Acad Sci U S A, 1986. **83**(23): p. 8878-82.

152. Madhani, H.D., V.A. Bohr, and P.C. Hanawalt, *Differential DNA repair in transcriptionally active and inactive proto-oncogenes: c-abl and c-mos.* Cell, 1986. **45**(3): p. 417-23.

153. Vermeulen, W. and M. Fousteri, *Mammalian transcription-coupled excision repair.* Cold Spring Harb Perspect Biol, 2013. **5**(8): p. a012625.

154. Venema, J., A. van Hoffen, A.T. Natarajan, A.A. van Zeeland, and L.H. Mullenders, *The residual repair capacity of xeroderma pigmentosum complementation group C fibroblasts is highly specific for transcriptionally active DNA.* Nucleic Acids Res, 1990. **18**(3): p. 443-8.

155. Spivak, G., *Transcription-coupled repair: an update.* Arch Toxicol, 2016. **90**(11): p. 2583-2594.

156. Gregersen, L.H. and J.Q. Svejstrup, *The Cellular Response to Transcription-Blocking DNA Damage.* Trends Biochem Sci, 2018. **43**(5): p. 327-341.

157. Geijer, M.E. and J.A. Marteijn, *What happens at the lesion does not stay at the lesion: Transcription-coupled nucleotide excision repair and the effects of DNA damage on transcription in cis and trans.* DNA Repair (Amst), 2018. **71**: p. 56-68.

158. van den Boom, V., E. Citterio, D. Hoogstraten, A. Zotter, J.M. Egly, W.A. van Cappellen*, et al.*, *DNA damage stabilizes interaction of CSB with the transcription elongation machinery.* J Cell Biol, 2004. **166**(1): p. 27-36.

159. Nakazawa, Y., K. Sasaki, N. Mitsutake, M. Matsuse, M. Shimada, T. Nardo*, et al.*, *Mutations in UVSSA cause UV-sensitive syndrome and impair RNA polymerase IIo processing in transcription-coupled nucleotide-excision repair.* Nat Genet, 2012. **44**(5): p. 586-92.

160. Schwertman, P., W. Vermeulen, and J.A. Marteijn, *UVSSA and USP7, a new couple in transcription-coupled DNA repair.* Chromosoma, 2013. **122**(4): p. 275-84.

161. Zhang, X., K. Horibata, M. Saijo, C. Ishigami, A. Ukai, S. Kanno*, et al.*, *Mutations in UVSSA cause UV-sensitive syndrome and destabilize ERCC6 in transcription-coupled DNA repair.* Nat Genet, 2012. **44**(5): p. 593-7.

162. Selby, C.P., R. Drapkin, D. Reinberg, and A. Sancar, *RNA polymerase II stalled at a thymine dimer: footprint and effect on excision repair.* Nucleic Acids Res, 1997. **25**(4): p. 787-93.

163. Garinis, G.A., L.M. Uittenboogaard, H. Stachelscheid, M. Fousteri, W. van Ijcken, T.M. Breit*, et al.*, *Persistent transcription-blocking DNA lesions trigger somatic growth attenuation associated with longevity.* Nat Cell Biol, 2009. **11**(5): p. 604-15.

164. Beerens, N., J.H. Hoeijmakers, R. Kanaar, W. Vermeulen, and C. Wyman, *The CSB protein actively wraps DNA.* J Biol Chem, 2005. **280**(6): p. 4722-9.

165. Lake, R.J. and H.Y. Fan, *Structure, function and regulation of CSB: a multi-talented gymnast.* Mech Ageing Dev, 2013. **134**(5-6): p. 202-11.

166. Lake, R.J., A. Geyko, G. Hemashettar, Y. Zhao, and H.Y. Fan, *UV-induced association of the CSB remodeling protein with chromatin requires ATP-dependent relief of N-terminal autorepression.* Mol Cell, 2010. **37**(2): p. 235-46.

167. Xu, J., I. Lahiri, W. Wang, A. Wier, M.A. Cianfrocco, J. Chong*, et al.*, *Structural basis for the initiation of eukaryotic transcription-coupled DNA repair.* Nature, 2017. **551**(7682): p. 653-657.

168. Fousteri, M., W. Vermeulen, A.A. van Zeeland, and L.H. Mullenders, *Cockayne syndrome A and B proteins differentially regulate recruitment of chromatin remodeling and repair factors to stalled RNA polymerase II in vivo.* Mol Cell, 2006. **23**(4): p. 471-82.

169. Fischer, E.S., A. Scrima, K. Bohm, S. Matsumoto, G.M. Lingaraju, M. Faty*, et al.*, *The molecular basis of CRL4DDB2/CSA ubiquitin ligase architecture, targeting, and activation.* Cell, 2011. **147**(5): p. 1024-39.

170. Groisman, R., J. Polanowska, I. Kuraoka, J. Sawada, M. Saijo, R. Drapkin*, et al.*, *The ubiquitin ligase activity in the DDB2 and CSA complexes is differentially regulated by the COP9 signalosome in response to DNA damage.* Cell, 2003. **113**(3): p. 357-67.

171. Groisman, R., I. Kuraoka, O. Chevallier, N. Gaye, T. Magnaldo, K. Tanaka*, et al.*, *CSA-dependent degradation of CSB by the ubiquitin-proteasome pathway establishes a link between complementation factors of the Cockayne syndrome.* Genes Dev, 2006. **20**(11): p. 1429-34.

172. Fei, J. and J. Chen, *KIAA1530 protein is recruited by Cockayne syndrome complementation group protein A (CSA) to participate in transcription-coupled repair (TCR).* J Biol Chem, 2012. **287**(42): p. 35118-26.

173. Tornaletti, S., D. Reines, and P.C. Hanawalt, *Structural characterization of RNA polymerase II complexes arrested by a cyclobutane pyrimidine dimer in the transcribed strand of template DNA.* J Biol Chem, 1999. **274**(34): p. 24124-30.

174. Citterio, E., S. Rademakers, G.T. van der Horst, A.J. van Gool, J.H. Hoeijmakers, and W. Vermeulen, *Biochemical and biological characterization of wild-type and ATPase-deficient Cockayne syndrome B repair protein.* J Biol Chem, 1998. **273**(19): p. 11844-51.

175. Citterio, E., V. Van Den Boom, G. Schnitzler, R. Kanaar, E. Bonte, R.E. Kingston*, et al.*, *ATP-dependent chromatin remodeling by the Cockayne syndrome B DNA repair-transcription-coupling factor.* Mol Cell Biol, 2000. **20**(20): p. 7643-53.

176. Muftuoglu, M., S. Sharma, T. Thorslund, T. Stevnsner, M.M. Soerensen, R.M. Brosh, Jr.*, et al.*, *Cockayne syndrome group B protein has novel strand annealing and exchange activities.* Nucleic Acids Res, 2006. **34**(1): p. 295-304.

177. Trieschmann, L., B. Martin, and M. Bustin, *The chromatin unfolding domain of chromosomal protein HMG-14 targets the N-terminal tail of histone H3 in nucleosomes.* Proc Natl Acad Sci U S A, 1998. **95**(10): p. 5468-73.

178. Lim, J.H., K.L. West, Y. Rubinstein, M. Bergel, Y.V. Postnikov, and M. Bustin, *Chromosomal protein HMGN1 enhances the acetylation of lysine 14 in histone H3.* EMBO J, 2005. **24**(17): p. 3038-48.

179. Birger, Y., K.L. West, Y.V. Postnikov, J.H. Lim, T. Furusawa, J.P. Wagner*, et al.*, *Chromosomal protein HMGN1 enhances the rate of DNA repair in chromatin.* EMBO J, 2003. **22**(7): p. 1665-75.

180. Dinant, C., G. Ampatziadis-Michailidis, H. Lans, M. Tresini, A. Lagarou, M. Grosbart*, et al.*, *Enhanced chromatin dynamics by FACT promotes transcriptional restart after UV-induced DNA damage.* Mol Cell, 2013. **51**(4): p. 469-79.

181. Lans, H., J.A. Marteijn, and W. Vermeulen, *ATP-dependent chromatin remodeling in the DNA-damage response.* Epigenetics Chromatin, 2012. **5**: p. 4.

182. Cho, I., P.F. Tsai, R.J. Lake, A. Basheer, and H.Y. Fan, *ATP-dependent chromatin remodeling by Cockayne syndrome protein B and NAP1-like histone chaperones is required for efficient transcription-coupled DNA repair.* PLoS Genet, 2013. **9**(4): p. e1003407.

183. Mullenders, L., *DNA damage mediated transcription arrest: Step back to go forward.* DNA Repair (Amst), 2015. **36**: p. 28-35.

184. Nakatsu, Y., H. Asahina, E. Citterio, S. Rademakers, W. Vermeulen, S. Kamiuchi*, et al.*, *XAB2, a novel tetratricopeptide repeat protein involved in transcription-coupled DNA repair and transcription.* J Biol Chem, 2000. **275**(45): p. 34931-7.

185. Kuraoka, I., S. Ito, T. Wada, M. Hayashida, L. Lee, M. Saijo*, et al.*, *Isolation of XAB2 complex involved in pre-mRNA splicing, transcription, and transcription-coupled repair.* J Biol Chem, 2008. **283**(2): p. 940-50.

186. Venema, J., L.H. Mullenders, A.T. Natarajan, A.A. van Zeeland, and L.V. Mayne, *The genetic defect in Cockayne syndrome is associated with a defect in repair of UV-induced DNA damage in transcriptionally active DNA.* Proc Natl Acad Sci U S A, 1990. **87**(12): p. 4707-11.

187. van Hoffen, A., A.T. Natarajan, L.V. Mayne, A.A. van Zeeland, L.H. Mullenders, and J. Venema, *Deficient repair of the transcribed strand of active genes in Cockayne's syndrome cells.* Nucleic Acids Res, 1993. **21**(25): p. 5890-5.

188. Troelstra, C., A. van Gool, J. de Wit, W. Vermeulen, D. Bootsma, and J.H. Hoeijmakers, *ERCC6, a member of a subfamily of putative helicases, is involved in Cockayne's syndrome and preferential repair of active genes.* Cell, 1992. **71**(6): p. 939-53.

189. Scrima, A., R. Konickova, B.K. Czyzewski, Y. Kawasaki, P.D. Jeffrey, R. Groisman*, et al.*, *Structural basis of UV DNA-damage recognition by the DDB1-DDB2 complex.* Cell, 2008. **135**(7): p. 1213-23.

190. Nemzow, L., A. Lubin, L. Zhang, and F. Gong, *XPC: Going where no DNA damage sensor has gone before.* DNA Repair (Amst), 2015. **36**: p. 19-27.

191. Kusakabe, M., Y. Onishi, H. Tada, F. Kurihara, K. Kusao, M. Furukawa*, et al.*, *Mechanism and regulation of DNA damage recognition in nucleotide excision repair.* Genes Environ, 2019. **41**: p. 2.

192. Mu, H., N.E. Geacintov, S. Broyde, J.E. Yeo, and O.D. Scharer, *Molecular basis for damage recognition and verification by XPC-RAD23B and TFIIH in nucleotide excision repair.* DNA Repair (Amst), 2018. **71**: p. 33-42.

193. Venema, J., A. van Hoffen, V. Karcagi, A.T. Natarajan, A.A. van Zeeland, and L.H. Mullenders, *Xeroderma pigmentosum complementation group C cells remove pyrimidine dimers selectively from the transcribed strand of active genes.* Mol Cell Biol, 1991. **11**(8): p. 4128-34.

194. Sugasawa, K., C. Masutani, A. Uchida, T. Maekawa, P.J. van der Spek, D. Bootsma*, et al.*, *HHR23B, a human Rad23 homolog, stimulates XPC protein in nucleotide excision repair in vitro.* Mol Cell Biol, 1996. **16**(9): p. 4852-61.

195. Ng, J.M., W. Vermeulen, G.T. van der Horst, S. Bergink, K. Sugasawa, H. Vrieling*, et al.*, *A novel regulation mechanism of DNA repair by damage-induced and RAD23-dependent stabilization of xeroderma pigmentosum group C protein.* Genes Dev, 2003. **17**(13): p. 1630-45.

196. Dantuma, N.P., C. Heinen, and D. Hoogstraten, *The ubiquitin receptor Rad23: at the crossroads of nucleotide excision repair and proteasomal degradation.* DNA Repair (Amst), 2009. **8**(4): p. 449-60.

197. Bergink, S., W. Toussaint, M.S. Luijsterburg, C. Dinant, S. Alekseev, J.H. Hoeijmakers*, et al.*, *Recognition of DNA damage by XPC coincides with disruption of the XPC-RAD23 complex.* J Cell Biol, 2012. **196**(6): p. 681-8.

198. Min, J.H. and N.P. Pavletich, *Recognition of DNA damage by the Rad4 nucleotide excision repair protein.* Nature, 2007. **449**(7162): p. 570-5.

199. Araki, M., C. Masutani, M. Takemura, A. Uchida, K. Sugasawa, J. Kondoh*, et al.*, *Centrosome protein centrin 2/caltractin 1 is part of the xeroderma pigmentosum group C complex that initiates global genome nucleotide excision repair.* J Biol Chem, 2001. **276**(22): p. 18665-72.

200. Nishi, R., Y. Okuda, E. Watanabe, T. Mori, S. Iwai, C. Masutani*, et al.*, *Centrin 2 stimulates nucleotide excision repair by interacting with xeroderma pigmentosum group C protein.* Mol Cell Biol, 2005. **25**(13): p. 5664-74.

201. Hey, T., G. Lipps, K. Sugasawa, S. Iwai, F. Hanaoka, and G. Krauss, *The XPC-HR23B complex displays high affinity and specificity for damaged DNA in a true-equilibrium fluorescence assay.* Biochemistry, 2002. **41**(21): p. 6583-7.

202. Sugasawa, K., T. Okamoto, Y. Shimizu, C. Masutani, S. Iwai, and F. Hanaoka, *A multistep damage recognition mechanism for global genomic nucleotide excision repair.* Genes Dev, 2001. **15**(5): p. 507-21.

203. Shell, S.M., E.K. Hawkins, M.S. Tsai, A.S. Hlaing, C.J. Rizzo, and W.J. Chazin, *Xeroderma pigmentosum complementation group C protein (XPC) serves as a general sensor of damaged DNA.* DNA Repair (Amst), 2013. **12**(11): p. 947-53.

204. Hess, M.T., D. Gunz, N. Luneva, N.E. Geacintov, and H. Naegeli, *Base pair conformation-dependent excision of benzo[a]pyrene diol epoxide-guanine adducts by human nucleotide excision repair enzymes.* Mol Cell Biol, 1997. **17**(12): p. 7069-76.

205. Camenisch, U., D. Trautlein, F.C. Clement, J. Fei, A. Leitenstorfer, E. Ferrando-May*, et al.*, *Two-stage dynamic DNA quality check by xeroderma pigmentosum group C protein.* EMBO J, 2009. **28**(16): p. 2387-99.

206. Chen, X., Y. Velmurugu, G. Zheng, B. Park, Y. Shim, Y. Kim*, et al.*, *Kinetic gating mechanism of DNA damage recognition by Rad4/XPC.* Nat Commun, 2015. **6**: p. 5849.

207. Velmurugu, Y., X. Chen, P. Slogoff Sevilla, J.H. Min, and A. Ansari, *Twist-open mechanism of DNA damage recognition by the Rad4/XPC nucleotide excision repair complex.* Proc Natl Acad Sci U S A, 2016. **113**(16): p. E2296-305.

208. Kong, M., L. Liu, X. Chen, K.I. Driscoll, P. Mao, S. Bohm*, et al.*, *Single-Molecule Imaging Reveals that Rad4 Employs a Dynamic DNA Damage Recognition Process.* Mol Cell, 2016. **64**(2): p. 376-387.

209. Cheon, N.Y., H.S. Kim, J.E. Yeo, O.D. Scharer, and J.Y. Lee, *Single-molecule visualization reveals the damage search mechanism for the human NER protein XPC-RAD23B.* Nucleic Acids Res, 2019.

210. Paul, D., H. Mu, H. Zhao, O. Ouerfelli, P.D. Jeffrey, S. Broyde*, et al.*, *Structure and mechanism of pyrimidine-pyrimidone (6-4) photoproduct recognition by the Rad4/XPC nucleotide excision repair complex.* Nucleic Acids Res, 2019. **47**(12): p. 6015-6028.

211. Sugasawa, K., Y. Shimizu, S. Iwai, and F. Hanaoka, *A molecular mechanism for DNA damage recognition by the xeroderma pigmentosum group C protein complex.* DNA Repair (Amst), 2002. **1**(1): p. 95-107.

212. Buterin, T., C. Meyer, B. Giese, and H. Naegeli, *DNA quality control by conformational readout on the undamaged strand of the double helix.* Chem Biol, 2005. **12**(8): p. 913-22.

213. Trego, K.S. and J.J. Turchi, *Pre-steady-state binding of damaged DNA by XPC-hHR23B reveals a kinetic mechanism for damage discrimination.* Biochemistry, 2006. **45**(6): p. 1961-9.

214. Maillard, O., S. Solyom, and H. Naegeli, *An aromatic sensor with aversion to damaged strands confers versatility to DNA repair.* PLoS Biol, 2007. **5**(4): p. e79.

215. Zhang, E.T., Y. He, P. Grob, Y.W. Fong, E. Nogales, and R. Tjian, *Architecture of the human XPC DNA repair and stem cell coactivator complex.* Proc Natl Acad Sci U S A, 2015. **112**(48): p. 14817-22.

216. Kusumoto, R., C. Masutani, K. Sugasawa, S. Iwai, M. Araki, A. Uchida*, et al.*, *Diversity of the damage recognition step in the global genomic nucleotide excision repair in vitro.* Mutat Res, 2001. **485**(3): p. 219-27.

217. Sugasawa, K., Y. Okuda, M. Saijo, R. Nishi, N. Matsuda, G. Chu*, et al.*, *UV-induced ubiquitylation of XPC protein mediated by UV-DDB-ubiquitin ligase complex.* Cell, 2005. **121**(3): p. 387-400.

218. Fitch, M.E., I.V. Cross, and J.M. Ford, *p53 responsive nucleotide excision repair gene products p48 and XPC, but not p53, localize to sites of UV-irradiation-induced DNA damage, in vivo.* Carcinogenesis, 2003. **24**(5): p. 843-50.

219. Wakasugi, M., A. Kawashima, H. Morioka, S. Linn, A. Sancar, T. Mori*, et al.*, *DDB accumulates at DNA damage sites immediately after UV irradiation and directly stimulates nucleotide excision repair.* J Biol Chem, 2002. **277**(3): p. 1637-40.

220. Wang, Q.E., Q. Zhu, G. Wani, J. Chen, and A.A. Wani, *UV radiation-induced XPC translocation within chromatin is mediated by damaged-DNA binding protein, DDB2.* Carcinogenesis, 2004. **25**(6): p. 1033-43.

221. Moser, J., M. Volker, H. Kool, S. Alekseev, H. Vrieling, A. Yasui*, et al.*, *The UV-damaged DNA binding protein mediates efficient targeting of the nucleotide excision repair complex to UV-induced photo lesions.* DNA Repair (Amst), 2005. **4**(5): p. 571-82.

222. Nishi, R., S. Alekseev, C. Dinant, D. Hoogstraten, A.B. Houtsmuller, J.H. Hoeijmakers*, et al.*, *UV-DDB-dependent regulation of nucleotide excision repair kinetics in living cells.* DNA Repair (Amst), 2009. **8**(6): p. 767-76.

223. Ghodke, H., H. Wang, C.L. Hsieh, S. Woldemeskel, S.C. Watkins, V. Rapic-Otrin*, et al.*, *Single-molecule analysis reveals human UV-damaged DNA-binding protein (UV-DDB) dimerizes on DNA via multiple kinetic intermediates.* Proc Natl Acad Sci U S A, 2014. **111**(18): p. E1862-71.

224. Batty, D., V. Rapic'-Otrin, A.S. Levine, and R.D. Wood, *Stable binding of human XPC complex to irradiated DNA confers strong discrimination for damaged sites.* J Mol Biol, 2000. **300**(2): p. 275-90.

225. Yeh, J.I., A.S. Levine, S. Du, U. Chinte, H. Ghodke, H. Wang*, et al.*, *Damaged DNA induced UV-damaged DNA-binding protein (UV-DDB) dimerization and its roles in chromatinized DNA repair.* Proc Natl Acad Sci U S A, 2012. **109**(41): p. E2737-46.

226. Osakabe, A., H. Tachiwana, W. Kagawa, N. Horikoshi, S. Matsumoto, M. Hasegawa*, et al.*, *Structural basis of pyrimidine-pyrimidone (6-4) photoproduct recognition by UV-DDB in the nucleosome.* Sci Rep, 2015. **5**: p. 16330.

227. Matsumoto, S., S. Cavadini, R.D. Bunker, R.S. Grand, A. Potenza, J. Rabl*, et al.*, *DNA damage detection in nucleosomes involves DNA register shifting.* Nature, 2019. **571**(7763): p. 79-84.

228. Kulaksiz, G., J.T. Reardon, and A. Sancar, *Xeroderma pigmentosum complementation group E protein (XPE/DDB2): purification of various complexes of XPE and analyses of their damaged DNA binding and putative DNA repair properties.* Mol Cell Biol, 2005. **25**(22): p. 9784-92.

229. He, Y.J., C.M. McCall, J. Hu, Y. Zeng, and Y. Xiong, *DDB1 functions as a linker to recruit receptor WD40 proteins to CUL4-ROC1 ubiquitin ligases.* Genes Dev, 2006. **20**(21): p. 2949-54.

230. Hwang, B.J., J.M. Ford, P.C. Hanawalt, and G. Chu, *Expression of the p48 xeroderma pigmentosum gene is p53-dependent and is involved in global genomic repair.* Proc Natl Acad Sci U S A, 1999. **96**(2): p. 424-8.

231. Tang, J.Y., B.J. Hwang, J.M. Ford, P.C. Hanawalt, and G. Chu, *Xeroderma pigmentosum p48 gene enhances global genomic repair and suppresses UV-induced mutagenesis.* Mol Cell, 2000. **5**(4): p. 737-44.

232. Fitch, M.E., S. Nakajima, A. Yasui, and J.M. Ford, *In vivo recruitment of XPC to UV-induced cyclobutane pyrimidine dimers by the DDB2 gene product.* J Biol Chem, 2003. **278**(47): p. 46906-10.

233. Wakasugi, M., M. Shimizu, H. Morioka, S. Linn, O. Nikaido, and T. Matsunaga, *Damaged DNA-binding protein DDB stimulates the excision of cyclobutane pyrimidine dimers in vitro in concert with XPA and replication protein A.* J Biol Chem, 2001. **276**(18): p. 15434-40.

234. Fei, J., N. Kaczmarek, A. Luch, A. Glas, T. Carell, and H. Naegeli, *Regulation of nucleotide excision repair by UV-DDB: prioritization of damage recognition to internucleosomal DNA.* PLoS Biol, 2011. **9**(10): p. e1001183.

235. Krasikova, Y.S., N.I. Rechkunova, E.A. Maltseva, R.O. Anarbaev, P.E. Pestryakov, K. Sugasawa*, et al.*, *Human and yeast DNA damage recognition complexes bind with high affinity DNA structures mimicking in size transcription bubble.* J Mol Recognit, 2013. **26**(12): p. 653-61.

236. Luijsterburg, M.S., M. Lindh, K. Acs, M.G. Vrouwe, A. Pines, H. van Attikum*, et al.*, *DDB2 promotes chromatin decondensation at UV-induced DNA damage.* J Cell Biol, 2012. **197**(2): p. 267-81.

237. Datta, A., S. Bagchi, A. Nag, P. Shiyanov, G.R. Adami, T. Yoon*, et al.*, *The p48 subunit of the damaged-DNA binding protein DDB associates with the CBP/p300 family of histone acetyltransferase.* Mutat Res, 2001. **486**(2): p. 89-97.

238. Rapic-Otrin, V., M.P. McLenigan, D.C. Bisi, M. Gonzalez, and A.S. Levine, *Sequential binding of UV DNA damage binding factor and degradation of the p48 subunit as early events after UV irradiation.* Nucleic Acids Res, 2002. **30**(11): p. 2588-98.

239. Martinez, E., V.B. Palhan, A. Tjernberg, E.S. Lymar, A.M. Gamper, T.K. Kundu*, et al.*, *Human STAGA complex is a chromatin-acetylating transcription coactivator that interacts with pre-mRNA splicing and DNA damage-binding factors in vivo.* Mol Cell Biol, 2001. **21**(20): p. 6782-95.

240. Jiang, Y., X. Wang, S. Bao, R. Guo, D.G. Johnson, X. Shen*, et al.*, *INO80 chromatin remodeling complex promotes the removal of UV lesions by the nucleotide excision repair pathway.* Proc Natl Acad Sci U S A, 2010. **107**(40): p. 17274-9.

241. Zhao, Q., Q.E. Wang, A. Ray, G. Wani, C. Han, K. Milum*, et al.*, *Modulation of nucleotide excision repair by mammalian SWI/SNF chromatin-remodeling complex.* J Biol Chem, 2009. **284**(44): p. 30424-32.

242. Zhang, L., Q. Zhang, K. Jones, M. Patel, and F. Gong, *The chromatin remodeling factor BRG1 stimulates nucleotide excision repair by facilitating recruitment of XPC to sites of DNA damage.* Cell Cycle, 2009. **8**(23): p. 3953-9.

243. Kapetanaki, M.G., J. Guerrero-Santoro, D.C. Bisi, C.L. Hsieh, V. Rapic-Otrin, and A.S. Levine, *The DDB1-CUL4ADDB2 ubiquitin ligase is deficient in xeroderma pigmentosum group E and targets histone H2A at UV-damaged DNA sites.* Proc Natl Acad Sci U S A, 2006. **103**(8): p. 2588-93.

244. Wang, H., L. Zhai, J. Xu, H.Y. Joo, S. Jackson, H. Erdjument-Bromage*, et al.*, *Histone H3 and H4 ubiquitylation by the CUL4-DDB-ROC1 ubiquitin ligase facilitates cellular response to DNA damage.* Mol Cell, 2006. **22**(3): p. 383-94.

245. Puumalainen, M.R., P. Ruthemann, J.H. Min, and H. Naegeli, *Xeroderma pigmentosum group C sensor: unprecedented recognition strategy and tight spatiotemporal regulation.* Cell Mol Life Sci, 2016. **73**(3): p. 547-66.

246. Chitale, S. and H. Richly, *Timing of DNA lesion recognition: Ubiquitin signaling in the NER pathway.* Cell Cycle, 2017. **16**(2): p. 163-171.

247. Bertolaet, B.L., D.J. Clarke, M. Wolff, M.H. Watson, M. Henze, G. Divita*, et al.*, *UBA domains of DNA damage-inducible proteins interact with ubiquitin.* Nat Struct Biol, 2001. **8**(5): p. 417-22.

248. Lan, L., S. Nakajima, M.G. Kapetanaki, C.L. Hsieh, M. Fagerburg, K. Thickman*, et al.*, *Monoubiquitinated histone H2A destabilizes photolesion-containing nucleosomes with concomitant release of UV-damaged DNA-binding protein E3 ligase.* J Biol Chem, 2012. **287**(15): p. 12036-49.

249. El-Mahdy, M.A., Q. Zhu, Q.E. Wang, G. Wani, M. Praetorius-Ibba, and A.A. Wani, *Cullin 4A-mediated proteolysis of DDB2 protein at DNA damage sites regulates in vivo lesion recognition by XPC.* J Biol Chem, 2006. **281**(19): p. 13404-11.

250. Puumalainen, M.R., D. Lessel, P. Ruthemann, N. Kaczmarek, K. Bachmann, K. Ramadan*, et al.*, *Chromatin retention of DNA damage sensors DDB2 and XPC through loss of p97 segregase causes genotoxicity.* Nat Commun, 2014. **5**: p. 3695.

251. van Cuijk, L., G.J. van Belle, Y. Turkyilmaz, S.L. Poulsen, R.C. Janssens, A.F. Theil*, et al.*, *SUMO and ubiquitin-dependent XPC exchange drives nucleotide excision repair.* Nat Commun, 2015. **6**: p. 7499.

252. Poulsen, S.L., R.K. Hansen, S.A. Wagner, L. van Cuijk, G.J. van Belle, W. Streicher*, et al.*, *RNF111/Arkadia is a SUMO-targeted ubiquitin ligase that facilitates the DNA damage response.* J Cell Biol, 2013. **201**(6): p. 797-807.

253. Akita, M., Y.S. Tak, T. Shimura, S. Matsumoto, Y. Okuda-Shimizu, Y. Shimizu*, et al.*, *SUMOylation of xeroderma pigmentosum group C protein regulates DNA damage recognition during nucleotide excision repair.* Sci Rep, 2015. **5**: p. 10984.

254. Yokoi, M., C. Masutani, T. Maekawa, K. Sugasawa, Y. Ohkuma, and F. Hanaoka, *The xeroderma pigmentosum group C protein complex XPC-HR23B plays an important role in the recruitment of transcription factor IIH to damaged DNA.* J Biol Chem, 2000. **275**(13): p. 9870-5.

255. Riedl, T., F. Hanaoka, and J.M. Egly, *The comings and goings of nucleotide excision repair factors on damaged DNA.* EMBO J, 2003. **22**(19): p. 5293-303.

256. Bunick, C.G., M.R. Miller, B.E. Fuller, E. Fanning, and W.J. Chazin, *Biochemical and structural domain analysis of xeroderma pigmentosum complementation group C protein.* Biochemistry, 2006. **45**(50): p. 14965-79.

257. Compe, E. and J.M. Egly, *Nucleotide Excision Repair and Transcriptional Regulation: TFIIH and Beyond.* Annu Rev Biochem, 2016. **85**: p. 265-90.

258. Okuda, M., Y. Nakazawa, C. Guo, T. Ogi, and Y. Nishimura, *Common TFIIH recruitment mechanism in global genome and transcription-coupled repair subpathways.* Nucleic Acids Res, 2017. **45**(22): p. 13043-13055.

259. Nocentini, S., F. Coin, M. Saijo, K. Tanaka, and J.M. Egly, *DNA damage recognition by XPA protein promotes efficient recruitment of transcription factor II H.* J Biol Chem, 1997. **272**(37): p. 22991-4.

260. Marteijn, J.A., J.H. Hoeijmakers, and W. Vermeulen, *Check, Check ...Triple Check: Multi-Step DNA Lesion Identification by Nucleotide Excision Repair.* Mol Cell, 2015. **59**(6): p. 885-6.

261. Li, C.L., F.M. Golebiowski, Y. Onishi, N.L. Samara, K. Sugasawa, and W. Yang, *Tripartite DNA Lesion Recognition and Verification by XPC, TFIIH, and XPA in Nucleotide Excision Repair.* Mol Cell, 2015. **59**(6): p. 1025-34.

262. Sugasawa, K., J. Akagi, R. Nishi, S. Iwai, and F. Hanaoka, *Two-step recognition of DNA damage for mammalian nucleotide excision repair: Directional binding of the XPC complex and DNA strand scanning.* Mol Cell, 2009. **36**(4): p. 642-53.

263. Fadda, E., *Role of the XPA protein in the NER pathway: A perspective on the function of structural disorder in macromolecular assembly.* Comput Struct Biotechnol J, 2016. **14**: p. 78-85.

264. Sugitani, N., R.M. Sivley, K.E. Perry, J.A. Capra, and W.J. Chazin, *XPA: A key scaffold for human nucleotide excision repair.* DNA Repair (Amst), 2016. **44**: p. 123-135.

265. Kokic, G., A. Chernev, D. Tegunov, C. Dienemann, H. Urlaub, and P. Cramer, *Structural basis of TFIIH activation for nucleotide excision repair.* Nat Commun, 2019. **10**(1): p. 2885.

266. Greber, B.J., D.B. Toso, J. Fang, and E. Nogales, *The complete structure of the human TFIIH core complex.* Elife, 2019. **8**.

267. Evans, E., J.G. Moggs, J.R. Hwang, J.M. Egly, and R.D. Wood, *Mechanism of open complex and dual incision formation by human nucleotide excision repair factors.* EMBO J, 1997. **16**(21): p. 6559-73.

268. Li, L., X. Lu, C.A. Peterson, and R.J. Legerski, *An interaction between the DNA repair factor XPA and replication protein A appears essential for nucleotide excision repair.* Mol Cell Biol, 1995. **15**(10): p. 5396-402.

269. You, J.S., M. Wang, and S.H. Lee, *Biochemical analysis of the damage recognition process in nucleotide excision repair.* J Biol Chem, 2003. **278**(9): p. 7476-85.

270. Krasikova, Y.S., N.I. Rechkunova, E.A. Maltseva, I.O. Petruseva, and O.I. Lavrik, *Localization of xeroderma pigmentosum group A protein and replication protein A on damaged DNA in nucleotide excision repair.* Nucleic Acids Res, 2010. **38**(22): p. 8083-94.

271. Sijbers, A.M., W.L. de Laat, R.R. Ariza, M. Biggerstaff, Y.F. Wei, J.G. Moggs*, et al.*, *Xeroderma pigmentosum group F caused by a defect in a structure-specific DNA repair endonuclease.* Cell, 1996. **86**(5): p. 811-22.

272. Li, L., S.J. Elledge, C.A. Peterson, E.S. Bales, and R.J. Legerski, *Specific association between the human DNA repair proteins XPA and ERCC1.* Proc Natl Acad Sci U S A, 1994. **91**(11): p. 5012-6.

273. Li, L., C.A. Peterson, X. Lu, and R.J. Legerski, *Mutations in XPA that prevent association with ERCC1 are defective in nucleotide excision repair.* Mol Cell Biol, 1995. **15**(4): p. 1993-8.

274. Tsodikov, O.V., D. Ivanov, B. Orelli, L. Staresincic, I. Shoshani, R. Oberman*, et al.*, *Structural basis for the recruitment of ERCC1-XPF to nucleotide excision repair complexes by XPA.* EMBO J, 2007. **26**(22): p. 4768-76.

275. Araujo, S.J., E.A. Nigg, and R.D. Wood, *Strong functional interactions of TFIIH with XPC and XPG in human DNA nucleotide excision repair, without a preassembled repairosome.* Mol Cell Biol, 2001. **21**(7): p. 2281-91.

276. Zotter, A., M.S. Luijsterburg, D.O. Warmerdam, S. Ibrahim, A. Nigg, W.A. van Cappellen*, et al.*, *Recruitment of the nucleotide excision repair endonuclease XPG to sites of UV-induced dna damage depends on functional TFIIH.* Mol Cell Biol, 2006. **26**(23): p. 8868-79.

277. Ito, S., I. Kuraoka, P. Chymkowitch, E. Compe, A. Takedachi, C. Ishigami*, et al.*, *XPG stabilizes TFIIH, allowing transactivation of nuclear receptors: implications for Cockayne syndrome in XP-G/CS patients.* Mol Cell, 2007. **26**(2): p. 231-43.

278. Wakasugi, M., J.T. Reardon, and A. Sancar, *The non-catalytic function of XPG protein during dual incision in human nucleotide excision repair.* J Biol Chem, 1997. **272**(25): p. 16030-4.

279. Mocquet, V., J.P. Laine, T. Riedl, Z. Yajin, M.Y. Lee, and J.M. Egly, *Sequential recruitment of the repair factors during NER: the role of XPG in initiating the resynthesis step.* EMBO J, 2008. **27**(1): p. 155-67.

280. Ogi, T., S. Limsirichaikul, R.M. Overmeer, M. Volker, K. Takenaka, R. Cloney*, et al.*, *Three DNA polymerases, recruited by different mechanisms, carry out NER repair synthesis in human cells.* Mol Cell, 2010. **37**(5): p. 714-27.

281. Staresincic, L., A.F. Fagbemi, J.H. Enzlin, A.M. Gourdin, N. Wijgers, I. Dunand-Sauthier*, et al.*, *Coordination of dual incision and repair synthesis in human nucleotide excision repair.* EMBO J, 2009. **28**(8): p. 1111-20.

282. Kemp, M.G., J.T. Reardon, L.A. Lindsey-Boltz, and A. Sancar, *Mechanism of release and fate of excised oligonucleotides during nucleotide excision repair.* J Biol Chem, 2012. **287**(27): p. 22889-99.

283. Huang, J.C., D.L. Svoboda, J.T. Reardon, and A. Sancar, *Human nucleotide excision nuclease removes thymine dimers from DNA by incising the 22nd phosphodiester bond 5' and the 6th phosphodiester bond 3' to the photodimer.* Proc Natl Acad Sci U S A, 1992. **89**(8): p. 3664-8.

284. Moser, J., H. Kool, I. Giakzidis, K. Caldecott, L.H. Mullenders, and M.I. Fousteri, *Sealing of chromosomal DNA nicks during nucleotide excision repair requires XRCC1 and DNA ligase III alpha in a cell-cycle-specific manner.* Mol Cell, 2007. **27**(2): p. 311-23.

285. Herrlich, P., M. Karin, and C. Weiss, *Supreme EnLIGHTenment: damage recognition and signaling in the mammalian UV response.* Mol Cell, 2008. **29**(3): p. 279-90.

286. Feehan, R.P. and L.M. Shantz, *Molecular signaling cascades involved in nonmelanoma skin carcinogenesis.* Biochem J, 2016. **473**(19): p. 2973-94.

287. Zou, L. and S.J. Elledge, *Sensing DNA damage through ATRIP recognition of RPA-ssDNA complexes.* Science, 2003. **300**(5625): p. 1542-8.

288. Vrouwe, M.G., A. Pines, R.M. Overmeer, K. Hanada, and L.H. Mullenders, *UV-induced photolesions elicit ATR-kinase-dependent signaling in non-cycling cells through nucleotide excision repair-dependent and -independent pathways.* J Cell Sci, 2011. **124**(Pt 3): p. 435-46.

289. Jiang, G. and A. Sancar, *Recruitment of DNA damage checkpoint proteins to damage in transcribed and nontranscribed sequences.* Mol Cell Biol, 2006. **26**(1): p. 39-49.

290. Derheimer, F.A., H.M. O'Hagan, H.M. Krueger, S. Hanasoge, M.T. Paulsen, and M. Ljungman, *RPA and ATR link transcriptional stress to p53.* Proc Natl Acad Sci U S A, 2007. **104**(31): p. 12778-83.

291. Abraham, R.T., *Cell cycle checkpoint signaling through the ATM and ATR kinases.* Genes Dev, 2001. **15**(17): p. 2177-96.

292. Yajima, H., K.J. Lee, and B.P. Chen, *ATR-dependent phosphorylation of DNA-dependent protein kinase catalytic subunit in response to UV-induced replication stress.* Mol Cell Biol, 2006. **26**(20): p. 7520-8.

293. Park, J.S., S.J. Park, X. Peng, M. Wang, M.A. Yu, and S.H. Lee, *Involvement of DNA-dependent protein kinase in UV-induced replication arrest.* J Biol Chem, 1999. **274**(45): p. 32520-7.

294. Yajima, H., K.J. Lee, S. Zhang, J. Kobayashi, and B.P. Chen, *DNA double-strand break formation upon UV-induced replication stress activates ATM and DNA-PKcs kinases.* J Mol Biol, 2009. **385**(3): p. 800-10.

295. Sancar, A., L.A. Lindsey-Boltz, K. Unsal-Kacmaz, and S. Linn, *Molecular mechanisms of mammalian DNA repair and the DNA damage checkpoints.* Annu Rev Biochem, 2004. **73**: p. 39-85.

296. Blackford, A.N. and S.P. Jackson, *ATM, ATR, and DNA-PK: The Trinity at the Heart of the DNA Damage Response.* Mol Cell, 2017. **66**(6): p. 801-817.

297. Kamata, H., S. Honda, S. Maeda, L. Chang, H. Hirata, and M. Karin, *Reactive oxygen species promote TNFalpha-induced death and sustained JNK activation by inhibiting MAP kinase phosphatases.* Cell, 2005. **120**(5): p. 649-61.

298. Zhang, Y., W.Y. Ma, A. Kaji, A.M. Bode, and Z. Dong, *Requirement of ATM in UVA-induced signaling and apoptosis.* J Biol Chem, 2002. **277**(5): p. 3124-31.

299. Reinhardt, H.C., A.S. Aslanian, J.A. Lees, and M.B. Yaffe, *p53-deficient cells rely on ATM- and ATR-mediated checkpoint signaling through the p38MAPK/MK2 pathway for survival after DNA damage.* Cancer Cell, 2007. **11**(2): p. 175-89.

300. Reinhardt, H.C. and M.B. Yaffe, *Kinases that control the cell cycle in response to DNA damage: Chk1, Chk2, and MK2.* Curr Opin Cell Biol, 2009. **21**(2): p. 245-55.

301. Bode, A.M. and Z. Dong, *Mitogen-activated protein kinase activation in UV-induced signal transduction.* Sci STKE, 2003. **2003**(167): p. RE2.

302. Tokino, T., S. Thiagalingam, W.S. el-Deiry, T. Waldman, K.W. Kinzler, and B. Vogelstein, *p53 tagged sites from human genomic DNA.* Hum Mol Genet, 1994. **3**(9): p. 1537-42.

303. Benjamin, C.L., S.E. Ullrich, M.L. Kripke, and H.N. Ananthaswamy, *p53 tumor suppressor gene: a critical molecular target for UV induction and prevention of skin cancer.* Photochem Photobiol, 2008. **84**(1): p. 55-62.

304. Decraene, D., K. Smaers, D. Maes, M. Matsui, L. Declercq, and M. Garmyn, *A low UVB dose, with the potential to trigger a protective p53-dependent gene program, increases the resilience of keratinocytes against future UVB insults.* J Invest Dermatol, 2005. **125**(5): p. 1026-31.

305. Ouhtit, A., H.K. Muller, D.W. Davis, S.E. Ullrich, D. McConkey, and H.N. Ananthaswamy, *Temporal events in skin injury and the early adaptive responses in ultraviolet-irradiated mouse skin.* Am J Pathol, 2000. **156**(1): p. 201-7.

306. Courtois, S.J., C.D. Woodworth, H. Degreef, and M. Garmyn, *Early ultraviolet B-induced G1 arrest and suppression of the malignant phenotype by wild-type p53 in human squamous cell carcinoma cells.* Exp Cell Res, 1997. **233**(1): p. 135-44.

307. Williams, A.B. and B. Schumacher, *p53 in the DNA-Damage-Repair Process.* Cold Spring Harb Perspect Med, 2016. **6**(5).

308. Adimoolam, S. and J.M. Ford, *p53 and DNA damage-inducible expression of the xeroderma pigmentosum group C gene.* Proc Natl Acad Sci U S A, 2002. **99**(20): p. 12985-90.

309. Hastak, K., S. Adimoolam, N.D. Trinklein, R.M. Myers, and J.M. Ford, *Identification of a Functional In Vivo p53 Response Element in the Coding Sequence of the Xeroderma Pigmentosum Group C Gene.* Genes Cancer, 2012. **3**(2): p. 131-40.

310. Ford, J.M. and P.C. Hanawalt, *Li-Fraumeni syndrome fibroblasts homozygous for p53 mutations are deficient in global DNA repair but exhibit normal transcription-coupled repair and enhanced UV resistance.* Proc Natl Acad Sci U S A, 1995. **92**(19): p. 8876-80.

311. Ford, J.M. and P.C. Hanawalt, *Expression of wild-type p53 is required for efficient global genomic nucleotide excision repair in UV-irradiated human fibroblasts.* J Biol Chem, 1997. **272**(44): p. 28073-80.

312. Mirzayans, R., L. Enns, K. Dietrich, R.D. Barley, and M.C. Paterson, *Faulty DNA polymerase delta/epsilon-mediated excision repair in response to gamma radiation or ultraviolet light in p53-deficient fibroblast strains from affected members of a cancer-prone family with Li-Fraumeni syndrome.* Carcinogenesis, 1996. **17**(4): p. 691-8.

313. Rubbi, C.P. and J. Milner, *p53 is a chromatin accessibility factor for nucleotide excision repair of DNA damage.* EMBO J, 2003. **22**(4): p. 975-86.

314. Offer, H., I. Zurer, G. Banfalvi, M. Reha'k, A. Falcovitz, M. Milyavsky*, et al.*, *p53 modulates base excision repair activity in a cell cycle-specific manner after genotoxic stress.* Cancer Res, 2001. **61**(1): p. 88-96.

315. Achanta, G. and P. Huang, *Role of p53 in sensing oxidative DNA damage in response to reactive oxygen species-generating agents.* Cancer Res, 2004. **64**(17): p. 6233-9.

316. Chatterjee, A., E. Mambo, M. Osada, S. Upadhyay, and D. Sidransky, *The effect of p53-RNAi and p53 knockout on human 8-oxoguanine DNA glycosylase (hOgg1) activity.* FASEB J, 2006. **20**(1): p. 112-4.

317. Oka, S., J. Leon, D. Tsuchimoto, K. Sakumi, and Y. Nakabeppu, *MUTYH, an adenine DNA glycosylase, mediates p53 tumor suppression via PARP-dependent cell death.* Oncogenesis, 2015. **4**: p. e142.

318. Zhou, J., J. Ahn, S.H. Wilson, and C. Prives, *A role for p53 in base excision repair.* EMBO J, 2001. **20**(4): p. 914-23.

319. Seo, Y.R., M.L. Fishel, S. Amundson, M.R. Kelley, and M.L. Smith, *Implication of p53 in base excision DNA repair: in vivo evidence.* Oncogene, 2002. **21**(5): p. 731-7.

320. Woodcock, A. and I.A. Magnus, *The sunburn cell in mouse skin: preliminary quantitative studies on its production.* Br J Dermatol, 1976. **95**(5): p. 459-468.

321. Van Laethem, A., M. Garmyn, and P. Agostinis, *Starting and propagating apoptotic signals in UVB irradiated keratinocytes.* Photochem Photobiol Sci, 2009. **8**(3): p. 299-308.

322. Ziegler, A., A.S. Jonason, D.J. Leffell, J.A. Simon, H.W. Sharma, J. Kimmelman*, et al.*, *Sunburn and p53 in the onset of skin cancer.* Nature, 1994. **372**(6508): p. 773-6.

323. Aubrey, B.J., G.L. Kelly, A. Janic, M.J. Herold, and A. Strasser, *How does p53 induce apoptosis and how does this relate to p53-mediated tumour suppression?* Cell Death Differ, 2018. **25**(1): p. 104-113.

324. Wu, Y., D. Xing, L. Liu, and B. Gao, *Regulation of Bax activation and apoptotic response to UV irradiation by p53 transcription-dependent and -independent pathways.* Cancer Lett, 2008. **271**(2): p. 231-9.

325. Holley, A.K. and D.K. St Clair, *Watching the watcher: regulation of p53 by mitochondria.* Future Oncol, 2009. **5**(1): p. 117-30.

326. Lee, C.H., S.B. Wu, C.H. Hong, H.S. Yu, and Y.H. Wei, *Molecular Mechanisms of UV-Induced Apoptosis and Its Effects on Skin Residential Cells: The Implication in UV-Based Phototherapy.* Int J Mol Sci, 2013. **14**(3): p. 6414-35.

327. Aragane, Y., D. Kulms, D. Metze, G. Wilkes, B. Poppelmann, T.A. Luger*, et al.*, *Ultraviolet light induces apoptosis via direct activation of CD95 (Fas/APO-1) independently of its ligand CD95L.* J Cell Biol, 1998. **140**(1): p. 171-82.

328. Schwarz, A., R. Bhardwaj, Y. Aragane, K. Mahnke, H. Riemann, D. Metze*, et al.*, *Ultraviolet-B-induced apoptosis of keratinocytes: evidence for partial involvement of tumor necrosis factor-alpha in the formation of sunburn cells.* J Invest Dermatol, 1995. **104**(6): p. 922-7.

329. Tobin, D., M. van Hogerlinden, and R. Toftgard, *UVB-induced association of tumor necrosis factor (TNF) receptor 1/TNF receptor-associated factor-2 mediates activation of Rel proteins.* Proc Natl Acad Sci U S A, 1998. **95**(2): p. 565-9.

330. Qin, J.Z., P. Bacon, J. Panella, L.A. Sitailo, M.F. Denning, and B.J. Nickoloff, *Low-dose UV-radiation sensitizes keratinocytes to TRAIL-induced apoptosis.* J Cell Physiol, 2004. **200**(1): p. 155-66.

331. Stevens, C., L. Smith, and N.B. La Thangue, *Chk2 activates E2F-1 in response to DNA damage.* Nat Cell Biol, 2003. **5**(5): p. 401-9.

332. Lin, W.C., F.T. Lin, and J.R. Nevins, *Selective induction of E2F1 in response to DNA damage, mediated by ATM-dependent phosphorylation.* Genes Dev, 2001. **15**(14): p. 1833-44.

333. Van Laethem, A., S. Van Kelst, S. Lippens, W. Declercq, P. Vandenabeele, S. Janssens*, et al.*, *Activation of p38 MAPK is required for Bax translocation to mitochondria, cytochrome c release and apoptosis induced by UVB irradiation in human keratinocytes.* FASEB J, 2004. **18**(15): p. 1946-8.

334. Nys, K., A. Van Laethem, C. Michiels, N. Rubio, J.G. Piette, M. Garmyn*, et al.*, *A p38(MAPK)/HIF-1 pathway initiated by UVB irradiation is required to induce Noxa and apoptosis of human keratinocytes.* J Invest Dermatol, 2010. **130**(9): p. 2269-76.

335. Van Laethem, A., K. Nys, S. Van Kelst, S. Claerhout, H. Ichijo, J.R. Vandenheede*, et al.*, *Apoptosis signal regulating kinase-1 connects reactive oxygen species to p38 MAPK-induced mitochondrial apoptosis in UVB-irradiated human keratinocytes.* Free Radic Biol Med, 2006. **41**(9): p. 1361-71.

336. Nadeau, P.J., S.J. Charette, M.B. Toledano, and J. Landry, *Disulfide Bond-mediated multimerization of Ask1 and its reduction by thioredoxin-1 regulate H(2)O(2)-induced c-Jun NH(2)-terminal kinase activation and apoptosis.* Mol Biol Cell, 2007. **18**(10): p. 3903-13.

337. Wang, X., W.R. Chen, and D. Xing, *A pathway from JNK through decreased ERK and Akt activities for FOXO3a nuclear translocation in response to UV irradiation.* J Cell Physiol, 2012. **227**(3): p. 1168-78.

338. Weinberg, R.L., D.B. Veprintsev, M. Bycroft, and A.R. Fersht, *Comparative binding of p53 to its promoter and DNA recognition elements.* J Mol Biol, 2005. **348**(3): p. 589-96.

339. Schlereth, K., R. Beinoraviciute-Kellner, M.K. Zeitlinger, A.C. Bretz, M. Sauer, J.P. Charles*, et al.*, *DNA binding cooperativity of p53 modulates the decision between cell-cycle arrest and apoptosis.* Mol Cell, 2010. **38**(3): p. 356-68.

340. Li, G. and V.C. Ho, *p53-dependent DNA repair and apoptosis respond differently to high- and low-dose ultraviolet radiation.* Br J Dermatol, 1998. **139**(1): p. 3-10.

341. Decraene, D., P. Agostinis, A. Pupe, P. de Haes, and M. Garmyn, *Acute response of human skin to solar radiation: regulation and function of the p53 protein.* J Photochem Photobiol B, 2001. **63**(1-3): p. 78-83.

342. Lane, D.P., *Cancer. p53, guardian of the genome.* Nature, 1992. **358**(6381): p. 15-6.

343. Koehler, M.J., K. Kellner, U.C. Hipler, and M. Kaatz, *Acute UVB-induced epidermal changes assessed by multiphoton laser tomography.* Skin Res Technol, 2015. **21**(2): p. 137-43.

344. Tong, X., S. Mirzoeva, D. Veliceasa, B.B. Bridgeman, P. Fitchev, M.L. Cornwell*, et al.*, *Chemopreventive apigenin controls UVB-induced cutaneous proliferation and angiogenesis through HuR and thrombospondin-1.* Oncotarget, 2014. **5**(22): p. 11413-27.

345. El-Abaseri, T.B., S. Putta, and L.A. Hansen, *Ultraviolet irradiation induces keratinocyte proliferation and epidermal hyperplasia through the activation of the epidermal growth factor receptor.* Carcinogenesis, 2006. **27**(2): p. 225-31.

346. El-Abaseri, T.B., J. Fuhrman, C. Trempus, I. Shendrik, R.W. Tennant, and L.A. Hansen, *Chemoprevention of UV light-induced skin tumorigenesis by inhibition of the epidermal growth factor receptor.* Cancer Res, 2005. **65**(9): p. 3958-65.

347. Knebel, A., H.J. Rahmsdorf, A. Ullrich, and P. Herrlich, *Dephosphorylation of receptor tyrosine kinases as target of regulation by radiation, oxidants or alkylating agents.* EMBO J, 1996. **15**(19): p. 5314-25.

348. Gross, S., A. Knebel, T. Tenev, A. Neininger, M. Gaestel, P. Herrlich*, et al.*, *Inactivation of protein-tyrosine phosphatases as mechanism of UV-induced signal transduction.* J Biol Chem, 1999. **274**(37): p. 26378-86.

349. Meng, T.C., T. Fukada, and N.K. Tonks, *Reversible oxidation and inactivation of protein tyrosine phosphatases in vivo.* Mol Cell, 2002. **9**(2): p. 387-99.

350. Gulati, P., B. Markova, M. Gottlicher, F.D. Bohmer, and P.A. Herrlich, *UVA inactivates protein tyrosine phosphatases by calpain-mediated degradation.* EMBO Rep, 2004. **5**(8): p. 812-7.

351. Xu, Y., J.J. Voorhees, and G.J. Fisher, *Epidermal growth factor receptor is a critical mediator of ultraviolet B irradiation-induced signal transduction in immortalized human keratinocyte HaCaT cells.* Am J Pathol, 2006. **169**(3): p. 823-30.

352. Pastore, S., F. Mascia, V. Mariani, and G. Girolomoni, *The epidermal growth factor receptor system in skin repair and inflammation.* J Invest Dermatol, 2008. **128**(6): p. 1365-74.

353. Gazon, H., B. Barbeau, J.M. Mesnard, and J.M. Peloponese, Jr., *Hijacking of the AP-1 Signaling Pathway during Development of ATL.* Front Microbiol, 2017. **8**: p. 2686.

354. Cooper, S.J. and G.T. Bowden, *Ultraviolet B regulation of transcription factor families: roles of nuclear factor-kappa B (NF-kappaB) and activator protein-1 (AP-1) in UVB-induced skin carcinogenesis.* Curr Cancer Drug Targets, 2007. **7**(4): p. 325-34.

355. McCubrey, J.A., L.S. Steelman, W.H. Chappell, S.L. Abrams, E.W. Wong, F. Chang*, et al.*, *Roles of the Raf/MEK/ERK pathway in cell growth, malignant transformation and drug resistance.* Biochim Biophys Acta, 2007. **1773**(8): p. 1263-84.

356. Feehan, R.P. and L.M. Shantz, *Negative regulation of the FOXO3a transcription factor by mTORC2 induces a pro-survival response following exposure to ultraviolet-B irradiation.* Cell Signal, 2016. **28**(8): p. 798-809.

357. Brunet, A., A. Bonni, M.J. Zigmond, M.Z. Lin, P. Juo, L.S. Hu*, et al.*, *Akt promotes cell survival by phosphorylating and inhibiting a Forkhead transcription factor.* Cell, 1999. **96**(6): p. 857-68.

358. Zhang, X., N. Tang, T.J. Hadden, and A.K. Rishi, *Akt, FoxO and regulation of apoptosis.* Biochim Biophys Acta, 2011. **1813**(11): p. 1978-86.

359. Xie, Q., J. Chen, and Z. Yuan, *Post-translational regulation of FOXO.* Acta Biochim Biophys Sin (Shanghai), 2012. **44**(11): p. 897-901.

360. Akunda, J.K., K.S. Chun, A.R. Sessoms, H.C. Lao, S.M. Fischer, and R. Langenbach, *Cyclooxygenase-2 deficiency increases epidermal apoptosis and impairs recovery following acute UVB exposure.* Mol Carcinog, 2007. **46**(5): p. 354-62.

361. El-Abaseri, T.B., B. Hammiller, S.K. Repertinger, and L.A. Hansen, *The epidermal growth factor receptor increases cytokine production and cutaneous inflammation in response to ultraviolet irradiation.* ISRN Dermatol, 2013. **2013**: p. 848705.

362. Xu, Y., Y. Shao, J. Zhou, J.J. Voorhees, and G.J. Fisher, *Ultraviolet irradiation-induces epidermal growth factor receptor (EGFR) nuclear translocation in human keratinocytes.* J Cell Biochem, 2009. **107**(5): p. 873-80.

363. Wang, S.C. and M.C. Hung, *Nuclear translocation of the epidermal growth factor receptor family membrane tyrosine kinase receptors.* Clin Cancer Res, 2009. **15**(21): p. 6484-9.

364. Lin, S.Y., K. Makino, W. Xia, A. Matin, Y. Wen, K.Y. Kwong*, et al.*, *Nuclear localization of EGF receptor and its potential new role as a transcription factor.* Nat Cell Biol, 2001. **3**(9): p. 802-8.

365. Wang, S.C., H.C. Lien, W. Xia, I.F. Chen, H.W. Lo, Z. Wang*, et al.*, *Binding at and transactivation of the COX-2 promoter by nuclear tyrosine kinase receptor ErbB-2.* Cancer Cell, 2004. **6**(3): p. 251-61.

366. Wang, S.C., Y. Nakajima, Y.L. Yu, W. Xia, C.T. Chen, C.C. Yang*, et al.*, *Tyrosine phosphorylation controls PCNA function through protein stability.* Nat Cell Biol, 2006. **8**(12): p. 1359-68.

367. Sterenborg, H.J., F.R. de Gruijl, and J.C. van der Leun, *UV-induced epidermal hyperplasia in hairless mice.* Photodermatol, 1986. **3**(4): p. 206-14.

368. Suh, K.S., H.J. Roh, S.Y. Choi, Y.S. Jeon, K.S. Doh, J.H. Bae*, et al.*, *A long-term evaluation of erythema and pigmentation induced by ultraviolet radiations of different wavelengths.* Skin Res Technol, 2007. **13**(4): p. 360-8.

369. Cui, R., H.R. Widlund, E. Feige, J.Y. Lin, D.L. Wilensky, V.E. Igras*, et al.*, *Central role of p53 in the suntan response and pathologic hyperpigmentation.* Cell, 2007. **128**(5): p. 853-64.

370. D'Orazio, J.A., T. Nobuhisa, R. Cui, M. Arya, M. Spry, K. Wakamatsu*, et al.*, *Topical drug rescue strategy and skin protection based on the role of Mc1r in UV-induced tanning.* Nature, 2006. **443**(7109): p. 340-4.

371. Rouzaud, F., A.L. Kadekaro, Z.A. Abdel-Malek, and V.J. Hearing, *MC1R and the response of melanocytes to ultraviolet radiation.* Mutat Res, 2005. **571**(1-2): p. 133-52.

372. Swope, V.B. and Z.A. Abdel-Malek, *MC1R: Front and Center in the Bright Side of Dark Eumelanin and DNA Repair.* Int J Mol Sci, 2018. **19**(9).

373. Friedmann, P.S. and B.A. Gilchrest, *Ultraviolet radiation directly induces pigment production by cultured human melanocytes.* J Cell Physiol, 1987. **133**(1): p. 88-94.

374. Stierner, U., I. Rosdahl, A. Augustsson, and B. Kagedal, *UVB irradiation induces melanocyte increase in both exposed and shielded human skin.* J Invest Dermatol, 1989. **92**(4): p. 561-4.

375. van Schanke, A., M.J. Jongsma, R. Bisschop, G.M. van Venrooij, H. Rebel, and F.R. de Gruijl, *Single UVB overexposure stimulates melanocyte proliferation in murine skin, in contrast to fractionated or UVA-1 exposure.* J Invest Dermatol, 2005. **124**(1): p. 241-7.

376. Nguyen, N.T. and D.E. Fisher, *MITF and UV responses in skin: From pigmentation to addiction.* Pigment Cell Melanoma Res, 2019. **32**(2): p. 224-236.

377. Hirobe, T., R. Furuya, S. Akiu, O. Ifuku, and M. Fukuda, *Keratinocytes control the proliferation and differentiation of cultured epidermal melanocytes from ultraviolet radiation B-induced pigmented spots in the dorsal skin of hairless mice.* Pigment Cell Res, 2002. **15**(5): p. 391-9.

378. D'Mello, S.A., G.J. Finlay, B.C. Baguley, and M.E. Askarian-Amiri, *Signaling Pathways in Melanogenesis.* Int J Mol Sci, 2016. **17**(7).

379. Kim, M., T. Shibata, S. Kwon, T.J. Park, and H.Y. Kang, *Ultraviolet-irradiated endothelial cells secrete stem cell factor and induce epidermal pigmentation.* Sci Rep, 2018. **8**(1): p. 4235.

380. Gange, R.W., A.D. Blackett, E.A. Matzinger, B.M. Sutherland, and I.E. Kochevar, *Comparative protection efficiency of UVA- and UVB-induced tans against erythema and formation of endonuclease-sensitive sites in DNA by UVB in human skin.* J Invest Dermatol, 1985. **85**(4): p. 362-4.

381. Young, A.R., C.S. Potten, C.A. Chadwick, G.M. Murphy, J.L. Hawk, and A.J. Cohen, *Photoprotection and 5-MOP photochemoprotection from UVR-induced DNA damage in humans: the role of skin type.* J Invest Dermatol, 1991. **97**(5): p. 942-8.

382. Potten, C.S., C.A. Chadwick, A.J. Cohen, O. Nikaido, T. Matsunaga, N.W. Schipper*, et al.*, *DNA damage in UV-irradiated human skin in vivo: automated direct measurement by image analysis (thymine dimers) compared with indirect measurement (unscheduled DNA synthesis) and protection by 5-methoxypsoralen.* Int J Radiat Biol, 1993. **63**(3): p. 313-24.

383. Kaidbey, K.H., P.P. Agin, R.M. Sayre, and A.M. Kligman, *Photoprotection by melanin--a comparison of black and Caucasian skin.* J Am Acad Dermatol, 1979. **1**(3): p. 249-60.

384. Brenner, M. and V.J. Hearing, *The protective role of melanin against UV damage in human skin.* Photochem Photobiol, 2008. **84**(3): p. 539-49.

385. Garibyan, L. and D.E. Fisher, *How sunlight causes melanoma.* Curr Oncol Rep, 2010. **12**(5): p. 319-26.

386. Montagna, W. and K. Carlisle, *The architecture of black and white facial skin.* J Am Acad Dermatol, 1991. **24**(6 Pt 1): p. 929-37.

387. Kobayashi, N., A. Nakagawa, T. Muramatsu, Y. Yamashina, T. Shirai, M.W. Hashimoto*, et al.*, *Supranuclear melanin caps reduce ultraviolet induced DNA photoproducts in human epidermis.* J Invest Dermatol, 1998. **110**(5): p. 806-10.

388. Bustamante, J., L. Bredeston, G. Malanga, and J. Mordoh, *Role of melanin as a scavenger of active oxygen species.* Pigment Cell Res, 1993. **6**(5): p. 348-53.

389. Bernard, J.J., R.L. Gallo, and J. Krutmann, *Photoimmunology: how ultraviolet radiation affects the immune system.* Nat Rev Immunol, 2019.

390. Hart, P.H. and M. Norval, *Ultraviolet radiation-induced immunosuppression and its relevance for skin carcinogenesis.* Photochem Photobiol Sci, 2018. **17**(12): p. 1872-1884.

391. Gibbs, N.K. and M. Norval, *Photoimmunosuppression: a brief overview.* Photodermatol Photoimmunol Photomed, 2013. **29**(2): p. 57-64.

392. Ullrich, S.E. and S.N. Byrne, *The immunologic revolution: photoimmunology.* J Invest Dermatol, 2012. **132**(3 Pt 2): p. 896-905.

393. Prasad, R. and S.K. Katiyar, *Crosstalk Among UV-Induced Inflammatory Mediators, DNA Damage and Epigenetic Regulators Facilitates Suppression of the Immune System.* Photochem Photobiol, 2017. **93**(4): p. 930-936.

394. Bernard, J.J., C. Cowing-Zitron, T. Nakatsuji, B. Muehleisen, J. Muto, A.W. Borkowski*, et al.*, *Ultraviolet radiation damages self noncoding RNA and is detected by TLR3.* Nat Med, 2012. **18**(8): p. 1286-90.

395. Gallo, R.L. and J.J. Bernard, *Innate immune sensors stimulate inflammatory and immunosuppressive responses to UVB radiation.* J Invest Dermatol, 2014. **134**(6): p. 1508-1511.

396. Trautinger, F., I. Kindas-Mugge, R.M. Knobler, and H. Honigsmann, *Stress proteins in the cellular response to ultraviolet radiation.* J Photochem Photobiol B, 1996. **35**(3): p. 141-8.

397. Johnson, K.E., B.C. Wulff, T.M. Oberyszyn, and T.A. Wilgus, *Ultraviolet light exposure stimulates HMGB1 release by keratinocytes.* Arch Dermatol Res, 2013. **305**(9): p. 805-15.

398. Kawasaki, T. and T. Kawai, *Toll-like receptor signaling pathways.* Front Immunol, 2014. **5**: p. 461.

399. Halliday, G.M. and J.G. Lyons, *Inflammatory doses of UV may not be necessary for skin carcinogenesis.* Photochem Photobiol, 2008. **84**(2): p. 272-83.

400. Yarosh, D.B., *The role of DNA damage and UV-induced cytokines in skin cancer.* J Photochem Photobiol B, 1992. **16**(1): p. 91-4.

401. Angst, M.S., J.D. Clark, B. Carvalho, M. Tingle, M. Schmelz, and D.C. Yeomans, *Cytokine profile in human skin in response to experimental inflammation, noxious stimulation, and administration of a COX-inhibitor: a microdialysis study.* Pain, 2008. **139**(1): p. 15-27.

402. Quist, S.R., I. Wiswedel, J. Quist, and H.P. Gollnick, *Kinetic Profile of Inflammation Markers in Human Skin In vivo Following Exposure to Ultraviolet B Indicates Synchronic Release of Cytokines and Prostanoids.* Acta Derm Venereol, 2016. **96**(7): p. 910-916.

403. Hou, G.R., K. Zeng, H.M. Lan, and Q. Wang, *Juglanin ameliorates UVBinduced skin carcinogenesis via antiinflammatory and proapoptotic effects in vivo and in vitro.* Int J Mol Med, 2018. **42**(1): p. 41-52.

404. *Severe sunburn.* Nursing, 2014. **44**(7): p. 35.

405. Lopes, D.M. and S.B. McMahon, *Ultraviolet Radiation on the Skin: A Painful Experience?* CNS Neurosci Ther, 2016. **22**(2): p. 118-26.

406. Clydesdale, G.J., G.W. Dandie, and H.K. Muller, *Ultraviolet light induced injury: immunological and inflammatory effects.* Immunol Cell Biol, 2001. **79**(6): p. 547-68.

407. Warren, J.B., *Nitric oxide and human skin blood flow responses to acetylcholine and ultraviolet light.* FASEB J, 1994. **8**(2): p. 247-51.

408. Hawk, J.L., G.M. Murphy, and C.A. Holden, *The presence of neutrophils in human cutaneous ultraviolet-B inflammation.* Br J Dermatol, 1988. **118**(1): p. 27-30.

409. Reefman, E., M.C. de Jong, H. Kuiper, M.F. Jonkman, P.C. Limburg, C.G. Kallenberg*, et al.*, *Is disturbed clearance of apoptotic keratinocytes responsible for UVB-induced inflammatory skin lesions in systemic lupus erythematosus?* Arthritis Res Ther, 2006. **8**(6): p. R156.

410. Meunier, L., Z. Bata-Csorgo, and K.D. Cooper, *In human dermis, ultraviolet radiation induces expansion of a CD36+ CD11b+ CD1- macrophage subset by infiltration and proliferation; CD1+ Langerhans-like dendritic antigen-presenting cells are concomitantly depleted.* J Invest Dermatol, 1995. **105**(6): p. 782-8.

411. Cotran, R.S. and M.A. Pathak, *The pattern of vascular leakage induced by monochromatic UV irradiation in rats, guinea pigs and hairless mice.* J Invest Dermatol, 1968. **51**(3): p. 155-64.

412. Permatasari, F., B. Zhou, and D. Luo, *Epidermal barrier: Adverse and beneficial changes induced by ultraviolet B irradiation depending on the exposure dose and time (Review).* Exp Ther Med, 2013. **6**(2): p. 287-292.

413. Haratake, A., Y. Uchida, M. Schmuth, O. Tanno, R. Yasuda, J.H. Epstein*, et al.*, *UVB-induced alterations in permeability barrier function: roles for epidermal hyperproliferation and thymocyte-mediated response.* J Invest Dermatol, 1997. **108**(5): p. 769-75.

414. Holleran, W.M., Y. Uchida, L. Halkier-Sorensen, A. Haratake, M. Hara, J.H. Epstein*, et al.*, *Structural and biochemical basis for the UVB-induced alterations in epidermal barrier function.* Photodermatol Photoimmunol Photomed, 1997. **13**(4): p. 117-28.

415. Takagi, Y., H. Nakagawa, H. Kondo, Y. Takema, and G. Imokawa, *Decreased levels of covalently bound ceramide are associated with ultraviolet B-induced perturbation of the skin barrier.* J Invest Dermatol, 2004. **123**(6): p. 1102-9.

416. Chen, G.Y. and G. Nunez, *Sterile inflammation: sensing and reacting to damage.* Nat Rev Immunol, 2010. **10**(12): p. 826-37.

417. Rundhaug, J.E. and S.M. Fischer, *Molecular mechanisms of mouse skin tumor promotion.* Cancers (Basel), 2010. **2**(2): p. 436-82.

418. Pathak, M.A. and D.L. Fanselow, *Photobiology of melanin pigmentation: dose/response of skin to sunlight and its contents.* J Am Acad Dermatol, 1983. **9**(5): p. 724-33.

419. Kripke, M.L. and M.S. Fisher, *Immunologic parameters of ultraviolet carcinogenesis.* J Natl Cancer Inst, 1976. **57**(1): p. 211-5.

420. Kripke, M.L. and M.S. Fisher, *Immunologic aspects of tumor induction by ultraviolet radiation.* Natl Cancer Inst Monogr, 1978(50): p. 179-83.

421. Hart, P.H., S. Gorman, and J.J. Finlay-Jones, *Modulation of the immune system by UV radiation: more than just the effects of vitamin D?* Nat Rev Immunol, 2011. **11**(9): p. 584-96.

422. Vieyra-Garcia, P.A. and P. Wolf, *From Early Immunomodulatory Triggers to Immunosuppressive Outcome: Therapeutic Implications of the Complex Interplay Between the Wavebands of Sunlight and the Skin.* Front Med (Lausanne), 2018. **5**: p. 232.

423. Timares, L., S.K. Katiyar, and C.A. Elmets, *DNA damage, apoptosis and langerhans cells--Activators of UV-induced immune tolerance.* Photochem Photobiol, 2008. **84**(2): p. 422-36.

424. Elmets, C.A., C.M. Cala, and H. Xu, *Photoimmunology.* Dermatol Clin, 2014. **32**(3): p. 277-90, vii.

425. Elmets, C.A., P.R. Bergstresser, R.E. Tigelaar, P.J. Wood, and J.W. Streilein, *Analysis of the mechanism of unresponsiveness produced by haptens painted on skin exposed to low dose ultraviolet radiation.* J Exp Med, 1983. **158**(3): p. 781-94.

426. Byrne, S.N. and G.M. Halliday, *B cells activated in lymph nodes in response to ultraviolet irradiation or by interleukin-10 inhibit dendritic cell induction of immunity.* J Invest Dermatol, 2005. **124**(3): p. 570-8.

427. Matsumura, Y., S.N. Byrne, D.X. Nghiem, Y. Miyahara, and S.E. Ullrich, *A role for inflammatory mediators in the induction of immunoregulatory B cells.* J Immunol, 2006. **177**(7): p. 4810-7.

428. Sleijffers, A., J. Garssen, F.R. de Gruijl, G.J. Boland, J. van Hattum, W.A. van Vloten*, et al.*, *UVB exposure impairs immune responses after hepatitis B vaccination in two different mouse strains.* Photochem Photobiol, 2002. **75**(5): p. 541-6.

429. El-Ghorr, A.A. and M. Norval, *The UV waveband dependencies in mice differ for the suppression of contact hypersensitivity, delayed-type hypersensitivity and cis-urocanic acid formation.* J Invest Dermatol, 1999. **112**(5): p. 757-62.

430. Halliday, G.M., D.L. Damian, S. Rana, and S.N. Byrne, *The suppressive effects of ultraviolet radiation on immunity in the skin and internal organs: implications for autoimmunity.* J Dermatol Sci, 2012. **66**(3): p. 176-82.

431. Apalla, Z., D. Nashan, R.B. Weller, and X. Castellsague, *Skin Cancer: Epidemiology, Disease Burden, Pathophysiology, Diagnosis, and Therapeutic Approaches.* Dermatol Ther (Heidelb), 2017. **7**(Suppl 1): p. 5-19.

432. Apalla, Z., A. Lallas, E. Sotiriou, E. Lazaridou, and D. Ioannides, *Epidemiological trends in skin cancer.* Dermatol Pract Concept, 2017. **7**(2): p. 1-6.

433. Liu-Smith, F., J. Jia, and Y. Zheng, *UV-Induced Molecular Signaling Differences in Melanoma and Non-melanoma Skin Cancer.* Adv Exp Med Biol, 2017. **996**: p. 27-40.

434. Lipozencic, J., R. Jurakic-Toncic, J. Rados, and D. Celic, *Epidemiology of nonmelanoma and melanoma skin cancer in Zagreb, Croatia.* Acta Dermatovenerol Croat, 2008. **16**(4): p. 193-203.

435. Geller, A.C. and G.D. Annas, *Epidemiology of melanoma and nonmelanoma skin cancer.* Semin Oncol Nurs, 2003. **19**(1): p. 2-11.

436. Fernandes, A.R., A.C. Santos, E. Sanchez-Lopez, A.B. Kovacevic, M. Espina, A.C. Calpena*, et al.*, *Neoplastic Multifocal Skin Lesions: Biology, Etiology, and Targeted Therapies for Nonmelanoma Skin Cancers.* Skin Pharmacol Physiol, 2018. **31**(2): p. 59-73.

437. Albert, M.R. and M.A. Weinstock, *Keratinocyte carcinoma.* CA Cancer J Clin, 2003. **53**(5): p. 292-302.

438. Karimkhani, C., L.N. Boyers, R.P. Dellavalle, and M.A. Weinstock, *It's time for "keratinocyte carcinoma" to replace the term "nonmelanoma skin cancer".* J Am Acad Dermatol, 2015. **72**(1): p. 186-7.

439. Burton, K.A., K.A. Ashack, and A. Khachemoune, *Cutaneous Squamous Cell Carcinoma: A Review of High-Risk and Metastatic Disease.* Am J Clin Dermatol, 2016. **17**(5): p. 491-508.

440. Nagarajan, P., M.M. Asgari, A.C. Green, S.M. Guhan, S.T. Arron, C.M. Proby*, et al.*, *Keratinocyte Carcinomas: Current Concepts and Future Research Priorities.* Clin Cancer Res, 2019. **25**(8): p. 2379-2391.

441. Rees, J.R., M.S. Zens, M.O. Celaya, B.L. Riddle, M.R. Karagas, and J.L. Peacock, *Survival after squamous cell and basal cell carcinoma of the skin: A retrospective cohort analysis.* Int J Cancer, 2015. **137**(4): p. 878-884.

442. Gurney, B. and C. Newlands, *Management of regional metastatic disease in head and neck cutaneous malignancy. 1. Cutaneous squamous cell carcinoma.* Br J Oral Maxillofac Surg, 2014. **52**(4): p. 294-300.

443. Lomas, A., J. Leonardi-Bee, and F. Bath-Hextall, *A systematic review of worldwide incidence of nonmelanoma skin cancer.* Br J Dermatol, 2012. **166**(5): p. 1069-80.

444. Karia, P.S., J. Han, and C.D. Schmults, *Cutaneous squamous cell carcinoma: estimated incidence of disease, nodal metastasis, and deaths from disease in the United States, 2012.* J Am Acad Dermatol, 2013. **68**(6): p. 957-66.

445. Schmults, C.D., P.S. Karia, J.B. Carter, J. Han, and A.A. Qureshi, *Factors predictive of recurrence and death from cutaneous squamous cell carcinoma: a 10-year, single-institution cohort study.* JAMA Dermatol, 2013. **149**(5): p. 541-7.

446. Fransen, M., A. Karahalios, N. Sharma, D.R. English, G.G. Giles, and R.D. Sinclair, *Non-melanoma skin cancer in Australia.* Med J Aust, 2012. **197**(10): p. 565-8.

447. Mudigonda, T., D.J. Pearce, B.A. Yentzer, P. Williford, and S.R. Feldman, *The economic impact of non-melanoma skin cancer: a review.* J Natl Compr Canc Netw, 2010. **8**(8): p. 888-96.

448. Didona, D., G. Paolino, U. Bottoni, and C. Cantisani, *Non Melanoma Skin Cancer Pathogenesis Overview.* Biomedicines, 2018. **6**(1).

449. Lucas, R.M., S. Yazar, A.R. Young, M. Norval, F.R. de Gruijl, Y. Takizawa*, et al.*, *Human health in relation to exposure to solar ultraviolet radiation under changing stratospheric ozone and climate.* Photochem Photobiol Sci, 2019. **18**(3): p. 641-680.

450. Bray, F., J. Ferlay, I. Soerjomataram, R.L. Siegel, L.A. Torre, and A. Jemal, *Global cancer statistics 2018: GLOBOCAN estimates of incidence and mortality worldwide for 36 cancers in 185 countries.* CA Cancer J Clin, 2018. **68**(6): p. 394-424.

451. Radenska-Lopovok, S.G., T.M. Reshetniak, Y. Zabek, and B. Voizekhovska, *[Blood vessels morphology in antiphospholipid syndrome].* Arkh Patol, 2001. **63**(6): p. 8-11.

452. Lucas, R.M., M. Norval, R.E. Neale, A.R. Young, F.R. de Gruijl, Y. Takizawa*, et al.*, *The consequences for human health of stratospheric ozone depletion in association with other environmental factors.* Photochem Photobiol Sci, 2015. **14**(1): p. 53-87.

453. Madigan, L.M. and H.W. Lim, *Tanning beds: Impact on health, and recent regulations.* Clin Dermatol, 2016. **34**(5): p. 640-8.

454. Garcovich, S., G. Colloca, P. Sollena, B. Andrea, L. Balducci, W.C. Cho*, et al.*, *Skin Cancer Epidemics in the Elderly as An Emerging Issue in Geriatric Oncology.* Aging Dis, 2017. **8**(5): p. 643-661.

455. Armstrong, B.K. and A. Kricker, *The epidemiology of UV induced skin cancer.* J Photochem Photobiol B, 2001. **63**(1-3): p. 8-18.

456. Subramaniam, P., C.M. Olsen, B.S. Thompson, D.C. Whiteman, R.E. Neale, Q.S. Sun*, et al.*, *Anatomical Distributions of Basal Cell Carcinoma and Squamous Cell Carcinoma in a Population-Based Study in Queensland, Australia.* JAMA Dermatol, 2017. **153**(2): p. 175-182.

457. Green, A., G. Williams, R. Neale, V. Hart, D. Leslie, P. Parsons*, et al.*, *Daily sunscreen application and betacarotene supplementation in prevention of basal-cell and squamous-cell carcinomas of the skin: a randomised controlled trial.* Lancet, 1999. **354**(9180): p. 723-9.

458. van der Pols, J.C., G.M. Williams, N. Pandeya, V. Logan, and A.C. Green, *Prolonged prevention of squamous cell carcinoma of the skin by regular sunscreen use.* Cancer Epidemiol Biomarkers Prev, 2006. **15**(12): p. 2546-8.

459. Urbach, F., P.D. Forbes, R.E. Davies, and D. Berger, *Cutaneous photobiology: past, present and future.* J Invest Dermatol, 1976. **67**(1): p. 209-24.

460. de Gruijl, F.R. and P.D. Forbes, *UV-induced skin cancer in a hairless mouse model.* Bioessays, 1995. **17**(7): p. 651-60.

461. El Ghissassi, F., R. Baan, K. Straif, Y. Grosse, B. Secretan, V. Bouvard*, et al.*, *A review of human carcinogens--part D: radiation.* Lancet Oncol, 2009. **10**(8): p. 751-2.

462. Kelfkens, G., F.R. de Gruijl, and J.C. van der Leun, *Tumorigenesis by short-wave ultraviolet A: papillomas versus squamous cell carcinomas.* Carcinogenesis, 1991. **12**(8): p. 1377-82.

463. de Gruijl, F.R. and P. Voskamp, *Photocarcinogenesis--DNA damage and gene mutations.* Cancer Treat Res, 2009. **146**: p. 101-8.

464. Boukamp, P., *Non-melanoma skin cancer: what drives tumor development and progression?* Carcinogenesis, 2005. **26**(10): p. 1657-67.

465. Ratushny, V., M.D. Gober, R. Hick, T.W. Ridky, and J.T. Seykora, *From keratinocyte to cancer: the pathogenesis and modeling of cutaneous squamous cell carcinoma.* J Clin Invest, 2012. **122**(2): p. 464-72.

466. Paolino, G., M. Donati, D. Didona, S.R. Mercuri, and C. Cantisani, *Histology of Non-Melanoma Skin Cancers: An Update.* Biomedicines, 2017. **5**(4).

467. Azimi, A., K.L. Kaufman, M. Ali, J. Arthur, S. Kossard, and P. Fernandez-Penas, *Differential proteomic analysis of actinic keratosis, Bowen's disease and cutaneous squamous cell carcinoma by label-free LC-MS/MS.* J Dermatol Sci, 2018. **91**(1): p. 69-78.

468. Yanofsky, V.R., S.E. Mercer, and R.G. Phelps, *Histopathological variants of cutaneous squamous cell carcinoma: a review.* J Skin Cancer, 2011. **2011**: p. 210813.

469. Fernandez Figueras, M.T., *From actinic keratosis to squamous cell carcinoma: pathophysiology revisited.* J Eur Acad Dermatol Venereol, 2017. **31 Suppl 2**: p. 5-7.

470. Carless, M.A. and L.R. Griffiths, *Cytogenetics of melanoma and nonmelanoma skin cancer.* Adv Exp Med Biol, 2014. **810**: p. 160-81.

471. Wikonkal, N.M. and D.E. Brash, *Ultraviolet radiation induced signature mutations in photocarcinogenesis.* J Investig Dermatol Symp Proc, 1999. **4**(1): p. 6-10.

472. Armstrong, J.D. and B.A. Kunz, *Site and strand specificity of UVB mutagenesis in the SUP4-o gene of yeast.* Proc Natl Acad Sci U S A, 1990. **87**(22): p. 9005-9.

473. Brash, D.E., *UV signature mutations.* Photochem Photobiol, 2015. **91**(1): p. 15-26.

474. Ikehata, H., R. Okuyama, E. Ogawa, S. Nakamura, A. Usami, T. Mori*, et al.*, *Influences of p53 deficiency on the apoptotic response, DNA damage removal and mutagenesis in UVB-exposed mouse skin.* Mutagenesis, 2010. **25**(4): p. 397-405.

475. Ikehata, H., T. Ono, K. Tanaka, and T. Todo, *A model for triplet mutation formation based on error-prone translesional DNA synthesis opposite UV photolesions.* DNA Repair (Amst), 2007. **6**(5): p. 658-68.

476. Wang, F., Y. Saito, T. Shiomi, S. Yamada, T. Ono, and H. Ikehata, *Mutation spectrum in UVB-exposed skin epidermis of a mildly-affected Xpg-deficient mouse.* Environ Mol Mutagen, 2006. **47**(2): p. 107-16.

477. Ikehata, H., F. Yanase, T. Mori, O. Nikaido, K. Tanaka, and T. Ono, *Mutation spectrum in UVB-exposed skin epidermis of Xpa-knockout mice: frequent recovery of triplet mutations.* Environ Mol Mutagen, 2007. **48**(1): p. 1-13.

478. Ikehata, H., Y. Saito, F. Yanase, T. Mori, O. Nikaido, and T. Ono, *Frequent recovery of triplet mutations in UVB-exposed skin epidermis of Xpc-knockout mice.* DNA Repair (Amst), 2007. **6**(1): p. 82-93.

479. Ikehata, H. and T. Ono, *The mechanisms of UV mutagenesis.* J Radiat Res, 2011. **52**(2): p. 115-25.

480. Drobetsky, E.A., J. Turcotte, and A. Chateauneuf, *A role for ultraviolet A in solar mutagenesis.* Proc Natl Acad Sci U S A, 1995. **92**(6): p. 2350-4.

481. Cheng, K.C., D.S. Cahill, H. Kasai, S. Nishimura, and L.A. Loeb, *8-Hydroxyguanine, an abundant form of oxidative DNA damage, causes G----T and A----C substitutions.* J Biol Chem, 1992. **267**(1): p. 166-72.

482. Epe, B., *Genotoxicity of singlet oxygen.* Chem Biol Interact, 1991. **80**(3): p. 239-60.

483. Kappes, U.P., D. Luo, M. Potter, K. Schulmeister, and T.M. Runger, *Short- and long-wave UV light (UVB and UVA) induce similar mutations in human skin cells.* J Invest Dermatol, 2006. **126**(3): p. 667-75.

484. Katiyar, S.K., M.S. Matsui, and H. Mukhtar, *Kinetics of UV light-induced cyclobutane pyrimidine dimers in human skin in vivo: an immunohistochemical analysis of both epidermis and dermis.* Photochem Photobiol, 2000. **72**(6): p. 788-93.

485. Mitchell, D.L., R. Greinert, F.R. de Gruijl, K.L. Guikers, E.W. Breitbart, M. Byrom*, et al.*, *Effects of chronic low-dose ultraviolet B radiation on DNA damage and repair in mouse skin.* Cancer Res, 1999. **59**(12): p. 2875-84.

486. de Gruijl, F.R. and R.J. Berg, *In situ molecular dosimetry and tumor risk: UV-induced DNA damage and tumor latency time.* Photochem Photobiol, 1998. **68**(4): p. 555-60.

487. Sreevidya, C.S., A. Fukunaga, N.M. Khaskhely, T. Masaki, R. Ono, C. Nishigori*, et al.*, *Agents that reverse UV-Induced immune suppression and photocarcinogenesis affect DNA repair.* J Invest Dermatol, 2010. **130**(5): p. 1428-37.

488. Montaner, B., P. O'Donovan, O. Reelfs, C.M. Perrett, X. Zhang, Y.Z. Xu*, et al.*, *Reactive oxygen-mediated damage to a human DNA replication and repair protein.* EMBO Rep, 2007. **8**(11): p. 1074-9.

489. Guven, M., R. Brem, P. Macpherson, M. Peacock, and P. Karran, *Oxidative Damage to RPA Limits the Nucleotide Excision Repair Capacity of Human Cells.* J Invest Dermatol, 2015. **135**(11): p. 2834-2841.

490. Ouhtit, A., A. Gorny, H.K. Muller, L.L. Hill, L. Owen-Schaub, and H.N. Ananthaswamy, *Loss of Fas-ligand expression in mouse keratinocytes during UV carcinogenesis.* Am J Pathol, 2000. **157**(6): p. 1975-81.

491. Ouhtit, A., H.K. Muller, A. Gorny, and H.N. Ananthaswamy, *UVB-induced experimental carcinogenesis: dysregulation of apoptosis and p53 signalling pathway.* Redox Rep, 2000. **5**(2-3): p. 128-9.

492. McAdam, E., R. Brem, and P. Karran, *Oxidative Stress-Induced Protein Damage Inhibits DNA Repair and Determines Mutation Risk and Therapeutic Efficacy.* Mol Cancer Res, 2016. **14**(7): p. 612-22.

493. Matsumura, Y. and H.N. Ananthaswamy, *Short-term and long-term cellular and molecular events following UV irradiation of skin: implications for molecular medicine.* Expert Rev Mol Med, 2002. **4**(26): p. 1-22.

494. DiGiovanna, J.J. and K.H. Kraemer, *Shining a light on xeroderma pigmentosum.* J Invest Dermatol, 2012. **132**(3 Pt 2): p. 785-96.

495. Bradford, P.T., A.M. Goldstein, D. Tamura, S.G. Khan, T. Ueda, J. Boyle*, et al.*, *Cancer and neurologic degeneration in xeroderma pigmentosum: long term follow-up characterises the role of DNA repair.* J Med Genet, 2011. **48**(3): p. 168-76.

496. Cleaver, J.E., E.T. Lam, and I. Revet, *Disorders of nucleotide excision repair: the genetic and molecular basis of heterogeneity.* Nat Rev Genet, 2009. **10**(11): p. 756-68.

497. de Vries, A., C.T. van Oostrom, F.M. Hofhuis, P.M. Dortant, R.J. Berg, F.R. de Gruijl*, et al.*, *Increased susceptibility to ultraviolet-B and carcinogens of mice lacking the DNA excision repair gene XPA.* Nature, 1995. **377**(6545): p. 169-73.

498. Sands, A.T., A. Abuin, A. Sanchez, C.J. Conti, and A. Bradley, *High susceptibility to ultraviolet-induced carcinogenesis in mice lacking XPC.* Nature, 1995. **377**(6545): p. 162-5.

499. Itoh, T., D. Cado, R. Kamide, and S. Linn, *DDB2 gene disruption leads to skin tumors and resistance to apoptosis after exposure to ultraviolet light but not a chemical carcinogen.* Proc Natl Acad Sci U S A, 2004. **101**(7): p. 2052-7.

500. Yoon, T., A. Chakrabortty, R. Franks, T. Valli, H. Kiyokawa, and P. Raychaudhuri, *Tumor-prone phenotype of the DDB2-deficient mice.* Oncogene, 2005. **24**(3): p. 469-78.

501. Jansen, J.G., P. Temviriyanukul, N. Wit, F. Delbos, C.A. Reynaud, H. Jacobs*, et al.*, *Redundancy of mammalian Y family DNA polymerases in cellular responses to genomic DNA lesions induced by ultraviolet light.* Nucleic Acids Res, 2014. **42**(17): p. 11071-82.

502. Yeeles, J.T., J. Poli, K.J. Marians, and P. Pasero, *Rescuing stalled or damaged replication forks.* Cold Spring Harb Perspect Biol, 2013. **5**(5): p. a012815.

503. Courdavault, S., C. Baudouin, M. Charveron, B. Canguilhem, A. Favier, J. Cadet*, et al.*, *Repair of the three main types of bipyrimidine DNA photoproducts in human keratinocytes exposed to UVB and UVA radiations.* DNA Repair (Amst), 2005. **4**(7): p. 836-44.

504. Mitchell, D.L., C.A. Haipek, and J.M. Clarkson, *(6-4)Photoproducts are removed from the DNA of UV-irradiated mammalian cells more efficiently than cyclobutane pyrimidine dimers.* Mutat Res, 1985. **143**(3): p. 109-12.

505. Young, A.R., C.A. Chadwick, G.I. Harrison, J.L. Hawk, O. Nikaido, and C.S. Potten, *The in situ repair kinetics of epidermal thymine dimers and 6-4 photoproducts in human skin types I and II.* J Invest Dermatol, 1996. **106**(6): p. 1307-13.

506. You, Y.H., D.H. Lee, J.H. Yoon, S. Nakajima, A. Yasui, and G.P. Pfeifer, *Cyclobutane pyrimidine dimers are responsible for the vast majority of mutations induced by UVB irradiation in mammalian cells.* J Biol Chem, 2001. **276**(48): p. 44688-94.

507. Jans, J., W. Schul, Y.G. Sert, Y. Rijksen, H. Rebel, A.P. Eker*, et al.*, *Powerful skin cancer protection by a CPD-photolyase transgene.* Curr Biol, 2005. **15**(2): p. 105-15.

508. Wood, R.D., *Pyrimidine dimers are not the principal pre-mutagenic lesions induced in lambda phage DNA by ultraviolet light.* J Mol Biol, 1985. **184**(4): p. 577-85.

509. Otoshi, E., T. Yagi, T. Mori, T. Matsunaga, O. Nikaido, S.T. Kim*, et al.*, *Respective roles of cyclobutane pyrimidine dimers, (6-4)photoproducts, and minor photoproducts in ultraviolet mutagenesis of repair-deficient xeroderma pigmentosum A cells.* Cancer Res, 2000. **60**(6): p. 1729-35.

510. Ikehata, H., T. Mori, T. Douki, J. Cadet, and M. Yamamoto, *Quantitative analysis of UV photolesions suggests that cyclobutane pyrimidine dimers produced in mouse skin by UVB are more mutagenic than those produced by UVC.* Photochem Photobiol Sci, 2018. **17**(4): p. 404-413.

511. Martincorena, I., A. Roshan, M. Gerstung, P. Ellis, P. Van Loo, S. McLaren*, et al.*, *Tumor evolution. High burden and pervasive positive selection of somatic mutations in normal human skin.* Science, 2015. **348**(6237): p. 880-6.

512. South, A.P., K.J. Purdie, S.A. Watt, S. Haldenby, N. den Breems, M. Dimon*, et al.*, *NOTCH1 mutations occur early during cutaneous squamous cell carcinogenesis.* J Invest Dermatol, 2014. **134**(10): p. 2630-2638.

513. Pacifico, A. and G. Leone, *Role of p53 and CDKN2A inactivation in human squamous cell carcinomas.* J Biomed Biotechnol, 2007. **2007**(3): p. 43418.

514. Owens, D.M. and F.M. Watt, *Contribution of stem cells and differentiated cells to epidermal tumours.* Nat Rev Cancer, 2003. **3**(6): p. 444-51.

515. Martin, M.T., A. Vulin, and J.H. Hendry, *Human epidermal stem cells: Role in adverse skin reactions and carcinogenesis from radiation.* Mutat Res, 2016. **770**(Pt B): p. 349-368.

516. Sanchez-Danes, A. and C. Blanpain, *Deciphering the cells of origin of squamous cell carcinomas.* Nat Rev Cancer, 2018. **18**(9): p. 549-561.

517. Mitchell, D.L., B. Volkmer, E.W. Breitbart, M. Byrom, M.G. Lowery, and R. Greinert, *Identification of a non-dividing subpopulation of mouse and human epidermal cells exhibiting high levels of persistent ultraviolet photodamage.* J Invest Dermatol, 2001. **117**(3): p. 590-5.

518. Nijhof, J.G., C. van Pelt, A.A. Mulder, D.L. Mitchell, L.H. Mullenders, and F.R. de Gruijl, *Epidermal stem and progenitor cells in murine epidermis accumulate UV damage despite NER proficiency.* Carcinogenesis, 2007. **28**(4): p. 792-800.

519. Jans, J., G.A. Garinis, W. Schul, A. van Oudenaren, M. Moorhouse, M. Smid*, et al.*, *Differential role of basal keratinocytes in UV-induced immunosuppression and skin cancer.* Mol Cell Biol, 2006. **26**(22): p. 8515-26.

520. Berg, R.J., H.J. van Kranen, H.G. Rebel, A. de Vries, W.A. van Vloten, C.F. Van Kreijl*, et al.*, *Early p53 alterations in mouse skin carcinogenesis by UVB radiation: immunohistochemical detection of mutant p53 protein in clusters of preneoplastic epidermal cells.* Proc Natl Acad Sci U S A, 1996. **93**(1): p. 274-8.

521. Rebel, H., L.O. Mosnier, R.J. Berg, A. Westerman-de Vries, H. van Steeg, H.J. van Kranen*, et al.*, *Early p53-positive foci as indicators of tumor risk in ultraviolet-exposed hairless mice: kinetics of induction, effects of DNA repair deficiency, and p53 heterozygosity.* Cancer Res, 2001. **61**(3): p. 977-83.

522. Zhang, W., E. Remenyik, D. Zelterman, D.E. Brash, and N.M. Wikonkal, *Escaping the stem cell compartment: sustained UVB exposure allows p53-mutant keratinocytes to colonize adjacent epidermal proliferating units without incurring additional mutations.* Proc Natl Acad Sci U S A, 2001. **98**(24): p. 13948-53.

523. Jonason, A.S., S. Kunala, G.J. Price, R.J. Restifo, H.M. Spinelli, J.A. Persing*, et al.*, *Frequent clones of p53-mutated keratinocytes in normal human skin.* Proc Natl Acad Sci U S A, 1996. **93**(24): p. 14025-9.

524. Nakazawa, H., D. English, P.L. Randell, K. Nakazawa, N. Martel, B.K. Armstrong*, et al.*, *UV and skin cancer: specific p53 gene mutation in normal skin as a biologically relevant exposure measurement.* Proc Natl Acad Sci U S A, 1994. **91**(1): p. 360-4.

525. Mudgil, A.V., N. Segal, F. Andriani, Y. Wang, N.E. Fusenig, and J.A. Garlick, *Ultraviolet B irradiation induces expansion of intraepithelial tumor cells in a tissue model of early cancer progression.* J Invest Dermatol, 2003. **121**(1): p. 191-7.

526. Zhang, W., A.N. Hanks, K. Boucher, S.R. Florell, S.M. Allen, A. Alexander*, et al.*, *UVB-induced apoptosis drives clonal expansion during skin tumor development.* Carcinogenesis, 2005. **26**(1): p. 249-57.

527. Brash, D.E., W. Zhang, D. Grossman, and S. Takeuchi, *Colonization of adjacent stem cell compartments by mutant keratinocytes.* Semin Cancer Biol, 2005. **15**(2): p. 97-102.

528. Kramata, P., Y.P. Lu, Y.R. Lou, R.N. Singh, S.M. Kwon, and A.H. Conney, *Patches of mutant p53-immunoreactive epidermal cells induced by chronic UVB Irradiation harbor the same p53 mutations as squamous cell carcinomas in the skin of hairless SKH-1 mice.* Cancer Res, 2005. **65**(9): p. 3577-85.

529. Knatko, E.V., B. Praslicka, M. Higgins, A. Evans, K.J. Purdie, C.A. Harwood*, et al.*, *Whole-Exome Sequencing Validates a Preclinical Mouse Model for the Prevention and Treatment of Cutaneous Squamous Cell Carcinoma.* Cancer Prev Res (Phila), 2017. **10**(1): p. 67-75.

530. Rebel, H., N. Kram, A. Westerman, S. Banus, H.J. van Kranen, and F.R. de Gruijl, *Relationship between UV-induced mutant p53 patches and skin tumours, analysed by mutation spectra and by induction kinetics in various DNA-repair-deficient mice.* Carcinogenesis, 2005. **26**(12): p. 2123-30.

531. Ren, Z.P., A. Hedrum, F. Ponten, M. Nister, A. Ahmadian, J. Lundeberg*, et al.*, *Human epidermal cancer and accompanying precursors have identical p53 mutations different from p53 mutations in adjacent areas of clonally expanded non-neoplastic keratinocytes.* Oncogene, 1996. **12**(4): p. 765-73.

532. Nelson, M.A., J.G. Einspahr, D.S. Alberts, C.A. Balfour, J.A. Wymer, K.L. Welch*, et al.*, *Analysis of the p53 gene in human precancerous actinic keratosis lesions and squamous cell cancers.* Cancer Lett, 1994. **85**(1): p. 23-9.

533. Campbell, C., A.G. Quinn, Y.S. Ro, B. Angus, and J.L. Rees, *p53 mutations are common and early events that precede tumor invasion in squamous cell neoplasia of the skin.* J Invest Dermatol, 1993. **100**(6): p. 746-8.

534. Albibas, A.A., M.J.J. Rose-Zerilli, C. Lai, R.J. Pengelly, G.A. Lockett, J. Theaker*, et al.*, *Subclonal Evolution of Cancer-Related Gene Mutations in p53 Immunopositive Patches in Human Skin.* J Invest Dermatol, 2018. **138**(1): p. 189-198.

535. Pierceall, W.E., M.L. Kripke, and H.N. Ananthaswamy, *N-ras mutation in ultraviolet radiation-induced murine skin cancers.* Cancer Res, 1992. **52**(14): p. 3946-51.

536. van Kranen, H.J., F.R. de Gruijl, A. de Vries, Y. Sontag, P.W. Wester, H.C. Senden*, et al.*, *Frequent p53 alterations but low incidence of ras mutations in UV-B-induced skin tumors of hairless mice.* Carcinogenesis, 1995. **16**(5): p. 1141-7.

537. van Kranen, H.J., A. Westerman, R.J. Berg, N. Kram, C.F. van Kreijl, P.W. Wester*, et al.*, *Dose-dependent effects of UVB-induced skin carcinogenesis in hairless p53 knockout mice.* Mutat Res, 2005. **571**(1-2): p. 81-90.

538. Remenyik, E., N.M. Wikonkal, W. Zhang, V. Paliwal, and D.E. Brash, *Antigen-specific immunity does not mediate acute regression of UVB-induced p53-mutant clones.* Oncogene, 2003. **22**(41): p. 6369-76.

539. Yilmaz, A.S., H.G. Ozer, J.L. Gillespie, D.C. Allain, M.N. Bernhardt, K.C. Furlan*, et al.*, *Differential mutation frequencies in metastatic cutaneous squamous cell carcinomas versus primary tumors.* Cancer, 2017. **123**(7): p. 1184-1193.

540. Marks, R., G. Rennie, and T.S. Selwood, *Malignant transformation of solar keratoses to squamous cell carcinoma.* Lancet, 1988. **1**(8589): p. 795-7.

541. De Gruijl, F.R., J.B. Van Der Meer, and J.C. Van Der Leun, *Dose-time dependency of tumor formation by chronic UV exposure.* Photochem Photobiol, 1983. **37**(1): p. 53-62.

542. Campos, M.A., S. Macedo, M. Fernandes, A. Pestana, J. Pardal, R. Batista*, et al.*, *TERT promoter mutations are associated with poor prognosis in cutaneous squamous cell carcinoma.* J Am Acad Dermatol, 2019. **80**(3): p. 660-669 e6.

543. Nindl, I. and F. Rosl, *Molecular pathogenesis of squamous cell carcinoma.* Cancer Treat Res, 2009. **146**: p. 205-11.

544. Cheng, J.B. and R.J. Cho, *Emergence and Evolution of Mutational Hotspots in Sun-Damaged Skin.* J Invest Dermatol, 2018. **138**(1): p. 16-17.

545. Wilgus, T.A., A.T. Koki, B.S. Zweifel, D.F. Kusewitt, P.A. Rubal, and T.M. Oberyszyn, *Inhibition of cutaneous ultraviolet light B-mediated inflammation and tumor formation with topical celecoxib treatment.* Mol Carcinog, 2003. **38**(2): p. 49-58.

546. Pentland, A.P., J.W. Schoggins, G.A. Scott, K.N. Khan, and R. Han, *Reduction of UV-induced skin tumors in hairless mice by selective COX-2 inhibition.* Carcinogenesis, 1999. **20**(10): p. 1939-44.

547. Fischer, S.M., H.H. Lo, G.B. Gordon, K. Seibert, G. Kelloff, R.A. Lubet*, et al.*, *Chemopreventive activity of celecoxib, a specific cyclooxygenase-2 inhibitor, and indomethacin against ultraviolet light-induced skin carcinogenesis.* Mol Carcinog, 1999. **25**(4): p. 231-40.

548. Burns, E.M., K.L. Tober, J.A. Riggenbach, D.F. Kusewitt, G.S. Young, and T.M. Oberyszyn, *Differential effects of topical vitamin E and C E Ferulic(R) treatments on ultraviolet light B-induced cutaneous tumor development in Skh-1 mice.* PLoS One, 2013. **8**(5): p. e63809.

549. Gensler, H.L. and M. Magdaleno, *Topical vitamin E inhibition of immunosuppression and tumorigenesis induced by ultraviolet irradiation.* Nutr Cancer, 1991. **15**(2): p. 97-106.

550. Burns, E.M., K.L. Tober, J.A. Riggenbach, D.F. Kusewitt, G.S. Young, and T.M. Oberyszyn, *Extended UVB Exposures Alter Tumorigenesis and Treatment Efficacy in a Murine Model of Cutaneous Squamous Cell Carcinoma.* J Skin Cancer, 2013. **2013**: p. 246848.

551. Gensler, H.L., B.N. Timmermann, S. Valcic, G.A. Wachter, R. Dorr, K. Dvorakova*, et al.*, *Prevention of photocarcinogenesis by topical administration of pure epigallocatechin gallate isolated from green tea.* Nutr Cancer, 1996. **26**(3): p. 325-35.

552. Bowden, G.T., *Prevention of non-melanoma skin cancer by targeting ultraviolet-B-light signalling.* Nat Rev Cancer, 2004. **4**(1): p. 23-35.

553. Sluyter, R. and G.M. Halliday, *Enhanced tumor growth in UV-irradiated skin is associated with an influx of inflammatory cells into the epidermis.* Carcinogenesis, 2000. **21**(10): p. 1801-7.

554. Avramoiu, I., I.O. Petrescu, M.E. Ciurea, A. Bold, I. Silosi, M.M. tanTu*, et al.*, *Peritumoral inflammatory reaction in non-melanoma skin cancers - histological and immunohistochemical study.* Rom J Morphol Embryol, 2016. **57**(3): p. 943-950.

555. Dickinson, S.E., E.R. Olson, J. Zhang, S.J. Cooper, T. Melton, P.J. Criswell*, et al.*, *p38 MAP kinase plays a functional role in UVB-induced mouse skin carcinogenesis.* Mol Carcinog, 2011. **50**(6): p. 469-78.

556. Cooper, S.J., J. MacGowan, J. Ranger-Moore, M.R. Young, N.H. Colburn, and G.T. Bowden, *Expression of dominant negative c-jun inhibits ultraviolet B-induced squamous cell carcinoma number and size in an SKH-1 hairless mouse model.* Mol Cancer Res, 2003. **1**(11): p. 848-54.

557. Kim, D.J., J.M. Angel, S. Sano, and J. DiGiovanni, *Constitutive activation and targeted disruption of signal transducer and activator of transcription 3 (Stat3) in mouse epidermis reveal its critical role in UVB-induced skin carcinogenesis.* Oncogene, 2009. **28**(7): p. 950-60.

558. Kim, H., A. Casta, X. Tang, C.T. Luke, A.L. Kim, D.R. Bickers*, et al.*, *Loss of hairless confers susceptibility to UVB-induced tumorigenesis via disruption of NF-kappaB signaling.* PLoS One, 2012. **7**(6): p. e39691.

559. Jiao, J., C. Mikulec, T.O. Ishikawa, C. Magyar, D.S. Dumlao, E.A. Dennis*, et al.*, *Cell-type-specific roles for COX-2 in UVB-induced skin cancer.* Carcinogenesis, 2014. **35**(6): p. 1310-9.

560. Starcher, B., *Role for tumour necrosis factor-alpha receptors in ultraviolet-induced skin tumours.* Br J Dermatol, 2000. **142**(6): p. 1140-7.

561. Tober, K.L., T.A. Wilgus, D.F. Kusewitt, J.M. Thomas-Ahner, T. Maruyama, and T.M. Oberyszyn, *Importance of the EP(1) receptor in cutaneous UVB-induced inflammation and tumor development.* J Invest Dermatol, 2006. **126**(1): p. 205-11.

562. Filip, G.A., I.D. Postescu, C. Tatomir, A. Muresan, and S. Clichici, *Calluna vulgaris extract modulates NF-kappaB/ERK signaling pathway and matrix metalloproteinase expression in SKH-1 hairless mice skin exposed to ultraviolet B irradiation.* J Physiol Pharmacol, 2012. **63**(4): p. 423-32.

563. Kim, S.Y., S. Lamichhane, J.H. Ju, and J. Yun, *Protective Effect of Octylmethoxycinnamate against UV-Induced Photoaging in Hairless Mouse via the Regulation of Matrix Metalloproteinases.* Int J Mol Sci, 2018. **19**(7).

564. Martins, V.L., J.J. Vyas, M. Chen, K. Purdie, C.A. Mein, A.P. South*, et al.*, *Increased invasive behaviour in cutaneous squamous cell carcinoma with loss of basement-membrane type VII collagen.* J Cell Sci, 2009. **122**(Pt 11): p. 1788-99.

565. de Oliveira Poswar, F., C.A. de Carvalho Fraga, E.S. Gomes, L.C. Farias, L.W. Souza, S.H. Santos*, et al.*, *Protein expression of MMP-2 and MT1-MMP in actinic keratosis, squamous cell carcinoma of the skin, and basal cell carcinoma.* Int J Surg Pathol, 2015. **23**(1): p. 20-5.

566. Maru, G.B., K. Gandhi, A. Ramchandani, and G. Kumar, *The role of inflammation in skin cancer.* Adv Exp Med Biol, 2014. **816**: p. 437-69.

567. Gonzalez, H., C. Hagerling, and Z. Werb, *Roles of the immune system in cancer: from tumor initiation to metastatic progression.* Genes Dev, 2018. **32**(19-20): p. 1267-1284.

568. Barr, B.B., E.C. Benton, K. McLaren, M.H. Bunney, I.W. Smith, K. Blessing*, et al.*, *Human papilloma virus infection and skin cancer in renal allograft recipients.* Lancet, 1989. **1**(8630): p. 124-9.

569. Hartevelt, M.M., J.N. Bavinck, A.M. Kootte, B.J. Vermeer, and J.P. Vandenbroucke, *Incidence of skin cancer after renal transplantation in The Netherlands.* Transplantation, 1990. **49**(3): p. 506-9.

570. Bavinck, J.N., A. De Boer, B.J. Vermeer, M.M. Hartevelt, F.J. van der Woude, F.H. Claas*, et al.*, *Sunlight, keratotic skin lesions and skin cancer in renal transplant recipients.* Br J Dermatol, 1993. **129**(3): p. 242-9.

571. Mackenzie, K.A., J.E. Wells, K.L. Lynn, J.W. Simcock, B.A. Robinson, J.A. Roake*, et al.*, *First and subsequent nonmelanoma skin cancers: incidence and predictors in a population of New Zealand renal transplant recipients.* Nephrol Dial Transplant, 2010. **25**(1): p. 300-6.

572. Carroll, R.P., D.S. Segundo, K. Hollowood, T. Marafioti, T.G. Clark, P.N. Harden*, et al.*, *Immune phenotype predicts risk for posttransplantation squamous cell carcinoma.* J Am Soc Nephrol, 2010. **21**(4): p. 713-22.

573. Hope, C.M., B.S. Grace, K.R. Pilkington, P.T. Coates, I.P. Bergmann, and R.P. Carroll, *The immune phenotype may relate to cancer development in kidney transplant recipients.* Kidney Int, 2014. **86**(1): p. 175-83.

574. Harwood, C.A., A.E. Toland, C.M. Proby, S. Euvrard, G.F.L. Hofbauer, M. Tommasino*, et al.*, *The pathogenesis of cutaneous squamous cell carcinoma in organ transplant recipients.* Br J Dermatol, 2017. **177**(5): p. 1217-1224.

575. Lanz, J., J.N. Bouwes Bavinck, M. Westhuis, K.D. Quint, C.A. Harwood, S. Nasir*, et al.*, *Aggressive Squamous Cell Carcinoma in Organ Transplant Recipients.* JAMA Dermatol, 2019. **155**(1): p. 66-71.

576. Brewer, J.D., T.M. Habermann, and T.D. Shanafelt, *Lymphoma-associated skin cancer: incidence, natural history, and clinical management.* Int J Dermatol, 2014. **53**(3): p. 267-74.

577. Silverberg, M.J., W. Leyden, E.M. Warton, C.P. Quesenberry, Jr., E.A. Engels, and M.M. Asgari, *HIV infection status, immunodeficiency, and the incidence of non-melanoma skin cancer.* J Natl Cancer Inst, 2013. **105**(5): p. 350-60.

578. Jensen, A.O., A.B. Olesen, C. Dethlefsen, H.T. Sorensen, and M.R. Karagas, *Chronic diseases requiring hospitalization and risk of non-melanoma skin cancers--a population based study from Denmark.* J Invest Dermatol, 2008. **128**(4): p. 926-31.

579. Agnew, K.L., R. Ruchlemer, D. Catovsky, E. Matutes, and C.B. Bunker, *Cutaneous findings in chronic lymphocytic leukaemia.* Br J Dermatol, 2004. **150**(6): p. 1129-35.

580. Asgari, M.M., G.T. Ray, C.P. Quesenberry, Jr., K.A. Katz, and M.J. Silverberg, *Association of Multiple Primary Skin Cancers With Human Immunodeficiency Virus Infection, CD4 Count, and Viral Load.* JAMA Dermatol, 2017. **153**(9): p. 892-896.

581. Nasti, T.H., O. Iqbal, I.A. Tamimi, J.T. Geise, S.K. Katiyar, and N. Yusuf, *Differential roles of T-cell subsets in regulation of ultraviolet radiation induced cutaneous photocarcinogenesis.* Photochem Photobiol, 2011. **87**(2): p. 387-98.

582. Azzimonti, B., E. Zavattaro, M. Provasi, M. Vidali, A. Conca, E. Catalano*, et al.*, *Intense Foxp3+ CD25+ regulatory T-cell infiltration is associated with high-grade cutaneous squamous cell carcinoma and counterbalanced by CD8+/Foxp3+ CD25+ ratio.* Br J Dermatol, 2015. **172**(1): p. 64-73.

583. Lai, C., S. August, A. Albibas, R. Behar, S.Y. Cho, M.E. Polak*, et al.*, *OX40+ Regulatory T Cells in Cutaneous Squamous Cell Carcinoma Suppress Effector T-Cell Responses and Associate with Metastatic Potential.* Clin Cancer Res, 2016. **22**(16): p. 4236-48.

584. Hope, C.M., P.T. Coates, and R.P. Carroll, *Immune profiling and cancer post transplantation.* World J Nephrol, 2015. **4**(1): p. 41-56.

585. Kosmidis, M., P. Dziunycz, M. Suarez-Farinas, B. Muhleisen, L. Scharer, S. Lauchli*, et al.*, *Immunosuppression affects CD4+ mRNA expression and induces Th2 dominance in the microenvironment of cutaneous squamous cell carcinoma in organ transplant recipients.* J Immunother, 2010. **33**(5): p. 538-46.

586. Zhang, S., H. Fujita, H. Mitsui, V.R. Yanofsky, J. Fuentes-Duculan, J.S. Pettersen*, et al.*, *Increased Tc22 and Treg/CD8 ratio contribute to aggressive growth of transplant associated squamous cell carcinoma.* PLoS One, 2013. **8**(5): p. e62154.

587. Wang, D. and R.N. DuBois, *Immunosuppression associated with chronic inflammation in the tumor microenvironment.* Carcinogenesis, 2015. **36**(10): p. 1085-93.

588. Benavides, F., T.M. Oberyszyn, A.M. VanBuskirk, V.E. Reeve, and D.F. Kusewitt, *The hairless mouse in skin research.* J Dermatol Sci, 2009. **53**(1): p. 10-8.

589. BROOKE, H.C., *HAIRLESS MICE.* Journal of Heredity, 1926. **17**(5): p. 173-174.

590. Stoye, J.P., S. Fenner, G.E. Greenoak, C. Moran, and J.M. Coffin, *Role of endogenous retroviruses as mutagens: the hairless mutation of mice.* Cell, 1988. **54**(3): p. 383-91.

591. Cachon-Gonzalez, M.B., I. San-Jose, A. Cano, J.A. Vega, N. Garcia, T. Freeman*, et al.*, *The hairless gene of the mouse: relationship of phenotypic effects with expression profile and genotype.* Dev Dyn, 1999. **216**(2): p. 113-26.

592. Panteleyev, A.A., C. van der Veen, T. Rosenbach, S. Muller-Rover, V.E. Sokolov, and R. Paus, *Towards defining the pathogenesis of the hairless phenotype.* J Invest Dermatol, 1998. **110**(6): p. 902-7.

593. Demidova-Rice, T.N., E.V. Salomatina, A.N. Yaroslavsky, I.M. Herman, and M.R. Hamblin, *Low-level light stimulates excisional wound healing in mice.* Lasers Surg Med, 2007. **39**(9): p. 706-15.

594. Kligman, L.H., *The hairless mouse model for photoaging.* Clin Dermatol, 1996. **14**(2): p. 183-95.

595. Moon, J.M., S.H. Park, K.H. Jhee, and S.A. Yang, *Protection against UVB-Induced Wrinkle Formation in SKH-1 Hairless Mice: Efficacy of Tricin Isolated from Enzyme-Treated Zizania latifolia Extract.* Molecules, 2018. **23**(9).

596. Nishimura, H., H. Yasui, and H. Sakurai, *Generation and distribution of reactive oxygen species in the skin of hairless mice under UVA: studies on in vivo chemiluminescent detection and tape stripping methods.* Exp Dermatol, 2006. **15**(11): p. 891-9.

597. Bussau, L.J., L.T. Vo, P.M. Delaney, G.D. Papworth, D.H. Barkla, and R.G. King, *Fibre optic confocal imaging (FOCI) of keratinocytes, blood vessels and nerves in hairless mouse skin in vivo.* J Anat, 1998. **192 (Pt 2)**: p. 187-94.

598. Matsumura, Y., A.M. Moodycliffe, D.X. Nghiem, S.E. Ullrich, and H.N. Ananthaswamy, *Resistance of CD1d-/- mice to ultraviolet-induced skin cancer is associated with increased apoptosis.* Am J Pathol, 2004. **165**(3): p. 879-87.

599. Schul, W., J. Jans, Y.M. Rijksen, K.H. Klemann, A.P. Eker, J. de Wit*, et al.*, *Enhanced repair of cyclobutane pyrimidine dimers and improved UV resistance in photolyase transgenic mice.* EMBO J, 2002. **21**(17): p. 4719-29.

600. Michel, A., A. Kopp-Schneider, H. Zentgraf, A.D. Gruber, and E.M. de Villiers, *E6/E7 expression of human papillomavirus type 20 (HPV-20) and HPV-27 influences proliferation and differentiation of the skin in UV-irradiated SKH-hr1 transgenic mice.* J Virol, 2006. **80**(22): p. 11153-64.

601. Forbes, P.D., H.F. Blum, and R.E. Davies, *Photocarcinogenesis in hairless mice: dose-response and the influence of dose-delivery.* Photochem Photobiol, 1981. **34**(3): p. 361-5.

602. de Gruijl, F.R., H.J. Sterenborg, P.D. Forbes, R.E. Davies, C. Cole, G. Kelfkens*, et al.*, *Wavelength dependence of skin cancer induction by ultraviolet irradiation of albino hairless mice.* Cancer Res, 1993. **53**(1): p. 53-60.

603. Gallagher, C.H., P.J. Canfield, G.E. Greenoak, and V.E. Reeve, *Characterization and histogenesis of tumors in the hairless mouse produced by low-dosage incremental ultraviolet radiation.* J Invest Dermatol, 1984. **83**(3): p. 169-74.

604. An, K.P., M. Athar, X. Tang, S.K. Katiyar, J. Russo, J. Beech*, et al.*, *Cyclooxygenase-2 expression in murine and human nonmelanoma skin cancers: implications for therapeutic approaches.* Photochem Photobiol, 2002. **76**(1): p. 73-80.

605. Athar, M., K.P. An, K.D. Morel, A.L. Kim, M. Aszterbaum, J. Longley*, et al.*, *Ultraviolet B(UVB)-induced cox-2 expression in murine skin: an immunohistochemical study.* Biochem Biophys Res Commun, 2001. **280**(4): p. 1042-7.

606. Schaffer, B.S., M.H. Grayson, J.M. Wortham, C.B. Kubicek, A.T. McCleish, S.I. Prajapati, *et al.*, *Immune competency of a hairless mouse strain for improved preclinical studies in genetically engineered mice.* Mol Cancer Ther, 2010. **9**(8): p. 2354-64.

607. Kim, T.H., H.N. Ananthaswamy, M.L. Kripke, and S.E. Ullrich, *Advantages of using hairless mice versus haired mice to test sunscreen efficacy against photoimmune suppressions.* Photochem Photobiol, 2003. **78**(1): p. 37-42.

608. Thomas-Ahner, J.M., B.C. Wulff, K.L. Tober, D.F. Kusewitt, J.A. Riggenbach, and T.M. Oberyszyn, *Gender differences in UVB-induced skin carcinogenesis, inflammation, and DNA damage.* Cancer Res, 2007. **67**(7): p. 3468-74.

609. Chilampalli, C., R. Guillermo, X. Zhang, R.S. Kaushik, A. Young, D. Zeman, *et al.*, *Effects of magnolol on UVB-induced skin cancer development in mice and its possible mechanism of action.* BMC Cancer, 2011. **11**: p. 456.

610. Sapi, J., L. Kovacs, D.A. Drexler, P. Kocsis, D. Gajari, and Z. Sapi, *Tumor Volume Estimation and Quasi-Continuous Administration for Most Effective Bevacizumab Therapy.* PLoS One, 2015. **10**(11): p. e0142190.

611. Ayers, G.D., E.T. McKinley, P. Zhao, J.M. Fritz, R.E. Metry, B.C. Deal, *et al.*, *Volume of preclinical xenograft tumors is more accurately assessed by ultrasound imaging than manual caliper measurements.* J Ultrasound Med, 2010. **29**(6): p. 891-901.

612. Gaddameedhi, S., C.P. Selby, W.K. Kaufmann, R.C. Smart, and A. Sancar, *Control of skin cancer by the circadian rhythm.* Proc Natl Acad Sci U S A, 2011. **108**(46): p. 18790-5.

613. Lu, Y.P., Y.R. Lou, J.G. Xie, Q.Y. Peng, J. Liao, C.S. Yang, *et al.*, *Topical applications of caffeine or (-)-epigallocatechin gallate (EGCG) inhibit carcinogenesis and selectively increase apoptosis in UVB-induced skin tumors in mice.* Proc Natl Acad Sci U S A, 2002. **99**(19): p. 12455-60.

614. Yamanaka, H., C.A. Penning, E.H. Willis, D.B. Wasson, and D.A. Carson, *Characterization of human poly(ADP-ribose) polymerase with autoantibodies.* J Biol Chem, 1988. **263**(8): p. 3879-83.

615. Sugimura, T. and M. Miwa, *Poly(ADP-ribose): historical perspective.* Mol Cell Biochem, 1994. **138**(1-2): p. 5-12.

616. Ame, J.C., C. Spenlehauer, and G. de Murcia, *The PARP superfamily.* Bioessays, 2004. **26**(8): p. 882-93.

617. Hottiger, M.O., *SnapShot: ADP-Ribosylation Signaling.* Mol Cell, 2015. **58**(6): p. 1134-1134 e1.

618. Bai, P., *Biology of Poly(ADP-Ribose) Polymerases: The Factotums of Cell Maintenance.* Mol Cell, 2015. **58**(6): p. 947-58.

619. Langelier, M.F. and J.M. Pascal, *PARP-1 mechanism for coupling DNA damage detection to poly(ADP-ribose) synthesis.* Curr Opin Struct Biol, 2013. **23**(1): p. 134-43.

620. Alemasova, E.E. and O.I. Lavrik, *Poly(ADP-ribosyl)ation by PARP1: reaction mechanism and regulatory proteins.* Nucleic Acids Res, 2019. **47**(8): p. 3811-3827.

621. Langelier, M.F., T. Eisemann, A.A. Riccio, and J.M. Pascal, *PARP family enzymes: regulation and catalysis of the poly(ADP-ribose) posttranslational modification.* Curr Opin Struct Biol, 2018. **53**: p. 187-198.

622. Pascal, J.M., *The comings and goings of PARP-1 in response to DNA damage.* DNA Repair (Amst), 2018. **71**: p. 177-182.

623. Gibson, B.A. and W.L. Kraus, *New insights into the molecular and cellular functions of poly(ADP-ribose) and PARPs.* Nat Rev Mol Cell Biol, 2012. **13**(7): p. 411-24.

624. Burkle, A. and L. Virag, *Poly(ADP-ribose): PARadigms and PARadoxes.* Mol Aspects Med, 2013. **34**(6): p. 1046-65.

625. Benjamin, R.C. and D.M. Gill, *Poly(ADP-ribose) synthesis in vitro programmed by damaged DNA. A comparison of DNA molecules containing different types of strand breaks.* J Biol Chem, 1980. **255**(21): p. 10502-8.

626. Ohgushi, H., K. Yoshihara, and T. Kamiya, *Bovine thymus poly(adenosine diphosphate ribose) polymerase. Physical properties and binding to DNA.* J Biol Chem, 1980. **255**(13): p. 6205-11.

627. Sastry, S.S., K.G. Buki, and E. Kun, *Binding of adenosine diphosphoribosyltransferase to the termini and internal regions of linear DNAs.* Biochemistry, 1989. **28**(13): p. 5670-80.

628. Clark, N.J., M. Kramer, U.M. Muthurajan, and K. Luger, *Alternative modes of binding of poly(ADP-ribose) polymerase 1 to free DNA and nucleosomes.* J Biol Chem, 2012. **287**(39): p. 32430-9.

629. Gradwohl, G., A. Mazen, and G. de Murcia, *Poly(ADP-ribose) polymerase forms loops with DNA.* Biochem Biophys Res Commun, 1987. **148**(3): p. 913-9.

630. Khodyreva, S.N., R. Prasad, E.S. Ilina, M.V. Sukhanova, M.M. Kutuzov, Y. Liu*, et al.*, *Apurinic/apyrimidinic (AP) site recognition by the 5'-dRP/AP lyase in poly(ADP-ribose) polymerase-1 (PARP-1).* Proc Natl Acad Sci U S A, 2010. **107**(51): p. 22090-5.

631. Chasovskikh, S., A. Dimtchev, M. Smulson, and A. Dritschilo, *DNA transitions induced by binding of PARP-1 to cruciform structures in supercoiled plasmids.* Cytometry A, 2005. **68**(1): p. 21-7.

632. Soldatenkov, V.A., S. Chasovskikh, V.N. Potaman, I. Trofimova, M.E. Smulson, and A. Dritschilo, *Transcriptional repression by binding of poly(ADP-ribose) polymerase to promoter sequences.* J Biol Chem, 2002. **277**(1): p. 665-70.

633. Lonskaya, I., V.N. Potaman, L.S. Shlyakhtenko, E.A. Oussatcheva, Y.L. Lyubchenko, and V.A. Soldatenkov, *Regulation of poly(ADP-ribose) polymerase-1 by DNA structure-specific binding.* J Biol Chem, 2005. **280**(17): p. 17076-83.

634. Galande, S. and T. Kohwi-Shigematsu, *Poly(ADP-ribose) polymerase and Ku autoantigen form a complex and synergistically bind to matrix attachment sequences.* J Biol Chem, 1999. **274**(29): p. 20521-8.

635. Sastry, S.S. and E. Kun, *The interaction of adenosine diphosphoribosyl transferase (ADPRT) with a cruciform DNA.* Biochem Biophys Res Commun, 1990. **167**(2): p. 842-7.

636. Potaman, V.N., L.S. Shlyakhtenko, E.A. Oussatcheva, Y.L. Lyubchenko, and V.A. Soldatenkov, *Specific binding of poly(ADP-ribose) polymerase-1 to cruciform hairpins.* J Mol Biol, 2005. **348**(3): p. 609-15.

637. Kim, M.Y., S. Mauro, N. Gevry, J.T. Lis, and W.L. Kraus, *NAD+-dependent modulation of chromatin structure and transcription by nucleosome binding properties of PARP-1.* Cell, 2004. **119**(6): p. 803-14.

638. Lilyestrom, W., M.J. van der Woerd, N. Clark, and K. Luger, *Structural and biophysical studies of human PARP-1 in complex with damaged DNA.* J Mol Biol, 2010. **395**(5): p. 983-94.

639. Langelier, M.F., J.L. Planck, S. Roy, and J.M. Pascal, *Structural basis for DNA damage-dependent poly(ADP-ribosyl)ation by human PARP-1.* Science, 2012. **336**(6082): p. 728-32.

640. Menissier-de Murcia, J., M. Molinete, G. Gradwohl, F. Simonin, and G. de Murcia, *Zinc-binding domain of poly(ADP-ribose)polymerase participates in the recognition of single strand breaks on DNA.* J Mol Biol, 1989. **210**(1): p. 229-33.

641. Liu, L., M. Kong, N.R. Gassman, B.D. Freudenthal, R. Prasad, S. Zhen*, et al.*, *PARP1 changes from three-dimensional DNA damage searching to one-dimensional diffusion after auto-PARylation or in the presence of APE1.* Nucleic Acids Res, 2017. **45**(22): p. 12834-12847.

642. Eustermann, S., H. Videler, J.C. Yang, P.T. Cole, D. Gruszka, D. Veprintsev*, et al.*, *The DNA-binding domain of human PARP-1 interacts with DNA single-strand breaks as a monomer through its second zinc finger.* J Mol Biol, 2011. **407**(1): p. 149-70.

643. Pion, E., G.M. Ullmann, J.C. Ame, D. Gerard, G. de Murcia, and E. Bombarda, *DNA-induced dimerization of poly(ADP-ribose) polymerase-1 triggers its activation.* Biochemistry, 2005. **44**(44): p. 14670-81.

644. Ali, A.A.E., G. Timinszky, R. Arribas-Bosacoma, M. Kozlowski, P.O. Hassa, M. Hassler*, et al.*, *The zinc-finger domains of PARP1 cooperate to recognize DNA strand breaks.* Nat Struct Mol Biol, 2012. **19**(7): p. 685-692.

645. Panzeter, P.L. and F.R. Althaus, *DNA strand break-mediated partitioning of poly(ADP-ribose) polymerase function.* Biochemistry, 1994. **33**(32): p. 9600-5.

646. Langelier, M.F., K.M. Servent, E.E. Rogers, and J.M. Pascal, *A third zinc-binding domain of human poly(ADP-ribose) polymerase-1 coordinates DNA-dependent enzyme activation.* J Biol Chem, 2008. **283**(7): p. 4105-14.

647. Langelier, M.F., D.D. Ruhl, J.L. Planck, W.L. Kraus, and J.M. Pascal, *The Zn3 domain of human poly(ADP-ribose) polymerase-1 (PARP-1) functions in both DNA-dependent poly(ADP-ribose) synthesis activity and chromatin compaction.* J Biol Chem, 2010. **285**(24): p. 18877-87.

648. Langelier, M.F., J.L. Planck, S. Roy, and J.M. Pascal, *Crystal structures of poly(ADP-ribose) polymerase-1 (PARP-1) zinc fingers bound to DNA: structural and functional insights into DNA-dependent PARP-1 activity.* J Biol Chem, 2011. **286**(12): p. 10690-701.

649. Eustermann, S., W.F. Wu, M.F. Langelier, J.C. Yang, L.E. Easton, A.A. Riccio*, et al.*, *Structural Basis of Detection and Signaling of DNA Single-Strand Breaks by Human PARP-1.* Mol Cell, 2015. **60**(5): p. 742-754.

650. Dawicki-McKenna, J.M., M.F. Langelier, J.E. DeNizio, A.A. Riccio, C.D. Cao, K.R. Karch*, et al.*, *PARP-1 Activation Requires Local Unfolding of an Autoinhibitory Domain.* Mol Cell, 2015. **60**(5): p. 755-768.

651. Steffen, J.D., M.M. McCauley, and J.M. Pascal, *Fluorescent sensors of PARP-1 structural dynamics and allosteric regulation in response to DNA damage.* Nucleic Acids Res, 2016. **44**(20): p. 9771-9783.

652. Langelier, M.F., L. Zandarashvili, P.M. Aguiar, B.E. Black, and J.M. Pascal, *NAD(+) analog reveals PARP-1 substrate-blocking mechanism and allosteric communication from catalytic center to DNA-binding domains.* Nat Commun, 2018. **9**(1): p. 844.

653. Cohen-Armon, M., *PARP-1 activation in the ERK signaling pathway.* Trends Pharmacol Sci, 2007. **28**(11): p. 556-60.

654. Cohen-Armon, M., L. Visochek, D. Rozensal, A. Kalal, I. Geistrikh, R. Klein*, et al.*, *DNA-independent PARP-1 activation by phosphorylated ERK2 increases Elk1 activity: a link to histone acetylation.* Mol Cell, 2007. **25**(2): p. 297-308.

655. Cohen-Armon, M., A. Yeheskel, and J.M. Pascal, *Signal-induced PARP1-Erk synergism mediates IEG expression.* Signal Transduct Target Ther, 2019. **4**: p. 8.

656. Wright, R.H., G. Castellano, J. Bonet, F. Le Dily, J. Font-Mateu, C. Ballare*, et al.*, *CDK2-dependent activation of PARP-1 is required for hormonal gene regulation in breast cancer cells.* Genes Dev, 2012. **26**(17): p. 1972-83.

657. Rajamohan, S.B., V.B. Pillai, M. Gupta, N.R. Sundaresan, K.G. Birukov, S. Samant*, et al.*, *SIRT1 promotes cell survival under stress by deacetylation-dependent deactivation of poly(ADP-ribose) polymerase 1.* Mol Cell Biol, 2009. **29**(15): p. 4116-29.

658. Loseva, O., A.S. Jemth, H.E. Bryant, H. Schuler, L. Lehtio, T. Karlberg*, et al.*, *PARP-3 is a mono-ADP-ribosylase that activates PARP-1 in the absence of DNA.* J Biol Chem, 2010. **285**(11): p. 8054-60.

659. Ruf, A., J. Mennissier de Murcia, G. de Murcia, and G.E. Schulz, *Structure of the catalytic fragment of poly(AD-ribose) polymerase from chicken.* Proc Natl Acad Sci U S A, 1996. **93**(15): p. 7481-5.

660. Ruf, A., V. Rolli, G. de Murcia, and G.E. Schulz, *The mechanism of the elongation and branching reaction of poly(ADP-ribose) polymerase as derived from crystal structures and mutagenesis.* J Mol Biol, 1998. **278**(1): p. 57-65.

661. Miwa, M., N. Saikawa, Z. Yamaizumi, S. Nishimura, and T. Sugimura, *Structure of poly(adenosine diphosphate ribose): identification of 2'-[1"-ribosyl-2"-(or 3")-(1"'-ribosyl)]adenosine-5',5",5"'-tris(phosphate) as a branch linkage.* Proc Natl Acad Sci U S A, 1979. **76**(2): p. 595-9.

662. D'Amours, D., S. Desnoyers, I. D'Silva, and G.G. Poirier, *Poly(ADP-ribosyl)ation reactions in the regulation of nuclear functions.* Biochem J, 1999. **342 (Pt 2)**: p. 249-68.

663. Juarez-Salinas, H., V. Levi, E.L. Jacobson, and M.K. Jacobson, *Poly(ADP-ribose) has a branched structure in vivo.* J Biol Chem, 1982. **257**(2): p. 607-9.

664. Clark, J.B., G.M. Ferris, and S. Pinder, *Inhibition of nuclear NAD nucleosidase and poly ADP-ribose polymerase activity from rat liver by nicotinamide and 5'-methyl nicotinamide.* Biochim Biophys Acta, 1971. **238**(1): p. 82-5.

665. Curtin, N.J. and C. Szabo, *Therapeutic applications of PARP inhibitors: anticancer therapy and beyond.* Mol Aspects Med, 2013. **34**(6): p. 1217-56.

666. Jain, P.G. and B.D. Patel, *Medicinal chemistry approaches of poly ADP-Ribose polymerase 1 (PARP1) inhibitors as anticancer agents - A recent update.* Eur J Med Chem, 2019. **165**: p. 198-215.

667. Steffen, J.D., J.R. Brody, R.S. Armen, and J.M. Pascal, *Structural Implications for Selective Targeting of PARPs.* Front Oncol, 2013. **3**: p. 301.

668. Wahlberg, E., T. Karlberg, E. Kouznetsova, N. Markova, A. Macchiarulo, A.G. Thorsell*, et al.*, *Family-wide chemical profiling and structural analysis of PARP and tankyrase inhibitors.* Nat Biotechnol, 2012. **30**(3): p. 283-8.

669. Passeri, D., E. Camaioni, P. Liscio, P. Sabbatini, M. Ferri, A. Carotti*, et al.*, *Concepts and Molecular Aspects in the Polypharmacology of PARP-1 Inhibitors.* ChemMedChem, 2016. **11**(12): p. 1219-26.

670. Pommier, Y., M.J. O'Connor, and J. de Bono, *Laying a trap to kill cancer cells: PARP inhibitors and their mechanisms of action.* Sci Transl Med, 2016. **8**(362): p. 362ps17.

671. Murai, J., S.Y. Huang, A. Renaud, Y. Zhang, J. Ji, S. Takeda*, et al.*, *Stereospecific PARP trapping by BMN 673 and comparison with olaparib and rucaparib.* Mol Cancer Ther, 2014. **13**(2): p. 433-43.

672. Murai, J., S.Y. Huang, B.B. Das, A. Renaud, Y. Zhang, J.H. Doroshow*, et al.*, *Trapping of PARP1 and PARP2 by Clinical PARP Inhibitors.* Cancer Res, 2012. **72**(21): p. 5588-99.

673. Kraus, W.L., *PARPs and ADP-Ribosylation: 50 Years ... and Counting.* Mol Cell, 2015. **58**(6): p. 902-10.

674. Zhen, Y. and Y. Yu, *Proteomic Analysis of the Downstream Signaling Network of PARP1.* Biochemistry, 2018. **57**(4): p. 429-440.

675. Kalisch, T., J.C. Ame, F. Dantzer, and V. Schreiber, *New readers and interpretations of poly(ADP-ribosyl)ation.* Trends Biochem Sci, 2012. **37**(9): p. 381-90.

676. Barkauskaite, E., G. Jankevicius, A.G. Ladurner, I. Ahel, and G. Timinszky, *The recognition and removal of cellular poly(ADP-ribose) signals.* FEBS J, 2013. **280**(15): p. 3491-507.

677. Krietsch, J., M. Rouleau, E. Pic, C. Ethier, T.M. Dawson, V.L. Dawson*, et al.*, *Reprogramming cellular events by poly(ADP-ribose)-binding proteins.* Mol Aspects Med, 2013. **34**(6): p. 1066-87.

678. Alvarez-Gonzalez, R., *3'-Deoxy-NAD+ as a substrate for poly(ADP-ribose)polymerase and the reaction mechanism of poly(ADP-ribose) elongation.* J Biol Chem, 1988. **263**(33): p. 17690-6.

679. Mendoza-Alvarez, H. and R. Alvarez-Gonzalez, *Poly(ADP-ribose) polymerase is a catalytic dimer and the automodification reaction is intermolecular.* J Biol Chem, 1993. **268**(30): p. 22575-80.

680. Desmarais, Y., L. Menard, J. Lagueux, and G.G. Poirier, *Enzymological properties of poly(ADP-ribose)polymerase: characterization of automodification sites and NADase activity.* Biochim Biophys Acta, 1991. **1078**(2): p. 179-86.

681. Nishikimi, M., K. Ogasawara, I. Kameshita, T. Taniguchi, and Y. Shizuta, *Poly(ADP-ribose) synthetase. The DNA binding domain and the automodification domain.* J Biol Chem, 1982. **257**(11): p. 6102-5.

682. Ushiro, H., Y. Yokoyama, and Y. Shizuta, *Purification and characterization of poly (ADP-ribose) synthetase from human placenta.* J Biol Chem, 1987. **262**(5): p. 2352-7.

683. Kameshita, I., Z. Matsuda, T. Taniguchi, and Y. Shizuta, *Poly (ADP-Ribose) synthetase. Separation and identification of three proteolytic fragments as the substrate-binding domain, the DNA-binding domain, and the automodification domain.* J Biol Chem, 1984. **259**(8): p. 4770-6.

684. Sharifi, R., R. Morra, C.D. Appel, M. Tallis, B. Chioza, G. Jankevicius*, et al.*, *Deficiency of terminal ADP-ribose protein glycohydrolase TARG1/C6orf130 in neurodegenerative disease.* EMBO J, 2013. **32**(9): p. 1225-37.

685. Chapman, J.D., J.P. Gagne, G.G. Poirier, and D.R. Goodlett, *Mapping PARP-1 auto-ADP-ribosylation sites by liquid chromatography-tandem mass spectrometry.* J Proteome Res, 2013. **12**(4): p. 1868-80.

686. Tao, Z., P. Gao, and H.W. Liu, *Identification of the ADP-ribosylation sites in the PARP-1 automodification domain: analysis and implications.* J Am Chem Soc, 2009. **131**(40): p. 14258-60.

687. Gagne, J.P., C. Ethier, D. Defoy, S. Bourassa, M.F. Langelier, A.A. Riccio*, et al.*, *Quantitative site-specific ADP-ribosylation profiling of DNA-dependent PARPs.* DNA Repair (Amst), 2015. **30**: p. 68-79.

688. Daniels, C.M., S.E. Ong, and A.K. Leung, *Phosphoproteomic approach to characterize protein mono- and poly(ADP-ribosyl)ation sites from cells.* J Proteome Res, 2014. **13**(8): p. 3510-22.

689. Daniels, C.M., S.E. Ong, and A.K. Leung, *The Promise of Proteomics for the Study of ADP-Ribosylation.* Mol Cell, 2015. **58**(6): p. 911-24.

690. Jungmichel, S., F. Rosenthal, M. Altmeyer, J. Lukas, M.O. Hottiger, and M.L. Nielsen, *Proteome-wide identification of poly(ADP-Ribosyl)ation targets in different genotoxic stress responses.* Mol Cell, 2013. **52**(2): p. 272-85.

691. Teloni, F. and M. Altmeyer, *Readers of poly(ADP-ribose): designed to be fit for purpose.* Nucleic Acids Res, 2016. **44**(3): p. 993-1006.

692. Gibson, B.A., Y. Zhang, H. Jiang, K.M. Hussey, J.H. Shrimp, H. Lin*, et al.*, *Chemical genetic discovery of PARP targets reveals a role for PARP-1 in transcription elongation.* Science, 2016. **353**(6294): p. 45-50.

693. Altmeyer, M., S. Messner, P.O. Hassa, M. Fey, and M.O. Hottiger, *Molecular mechanism of poly(ADP-ribosyl)ation by PARP1 and identification of lysine residues as ADP-ribose acceptor sites.* Nucleic Acids Res, 2009. **37**(11): p. 3723-38.

694. Hottiger, M.O., *Nuclear ADP-Ribosylation and Its Role in Chromatin Plasticity, Cell Differentiation, and Epigenetics.* Annu Rev Biochem, 2015. **84**: p. 227-63.

695. Leslie Pedrioli, D.M., M. Leutert, V. Bilan, K. Nowak, K. Gunasekera, E. Ferrari*, et al.*, *Comprehensive ADP-ribosylome analysis identifies tyrosine as an ADP-ribose acceptor site.* EMBO Rep, 2018. **19**(8).

696. Larsen, S.C., I.A. Hendriks, D. Lyon, L.J. Jensen, and M.L. Nielsen, *Systems-wide Analysis of Serine ADP-Ribosylation Reveals Widespread Occurrence and Site-Specific Overlap with Phosphorylation.* Cell Rep, 2018. **24**(9): p. 2493-2505 e4.

697. Zhang, Y., J. Wang, M. Ding, and Y. Yu, *Site-specific characterization of the Asp- and Glu-ADP-ribosylated proteome.* Nat Methods, 2013. **10**(10): p. 981-4.

698. Talhaoui, I., N.A. Lebedeva, G. Zarkovic, C. Saint-Pierre, M.M. Kutuzov, M.V. Sukhanova*, et al.*, *Poly(ADP-ribose) polymerases covalently modify strand break termini in DNA fragments in vitro.* Nucleic Acids Res, 2016. **44**(19): p. 9279-9295.

699. Karlberg, T., M.F. Langelier, J.M. Pascal, and H. Schuler, *Structural biology of the writers, readers, and erasers in mono- and poly(ADP-ribose) mediated signaling.* Mol Aspects Med, 2013. **34**(6): p. 1088-108.

700. Pleschke, J.M., H.E. Kleczkowska, M. Strohm, and F.R. Althaus, *Poly(ADP-ribose) binds to specific domains in DNA damage checkpoint proteins.* J Biol Chem, 2000. **275**(52): p. 40974-80.

701. Gagne, J.P., M. Isabelle, K.S. Lo, S. Bourassa, M.J. Hendzel, V.L. Dawson*, et al.*, *Proteome-wide identification of poly(ADP-ribose) binding proteins and poly(ADP-ribose)-associated protein complexes.* Nucleic Acids Res, 2008. **36**(22): p. 6959-76.

702. Ahel, I., D. Ahel, T. Matsusaka, A.J. Clark, J. Pines, S.J. Boulton*, et al.*, *Poly(ADP-ribose)-binding zinc finger motifs in DNA repair/checkpoint proteins.* Nature, 2008. **451**(7174): p. 81-5.

703. Feijs, K.L., A.H. Forst, P. Verheugd, and B. Luscher, *Macrodomain-containing proteins: regulating new intracellular functions of mono(ADP-ribosyl)ation.* Nat Rev Mol Cell Biol, 2013. **14**(7): p. 443-51.

704. Karras, G.I., G. Kustatscher, H.R. Buhecha, M.D. Allen, C. Pugieux, F. Sait*, et al.*, *The macro domain is an ADP-ribose binding module.* EMBO J, 2005. **24**(11): p. 1911-20.

705. Rack, J.G., D. Perina, and I. Ahel, *Macrodomains: Structure, Function, Evolution, and Catalytic Activities.* Annu Rev Biochem, 2016. **85**: p. 431-54.

706. Wang, Z., G.A. Michaud, Z. Cheng, Y. Zhang, T.R. Hinds, E. Fan*, et al.*, *Recognition of the iso-ADP-ribose moiety in poly(ADP-ribose) by WWE domains suggests a general mechanism for poly(ADP-ribosyl)ation-dependent ubiquitination.* Genes Dev, 2012. **26**(3): p. 235-40.

707. Li, M., L.Y. Lu, C.Y. Yang, S. Wang, and X. Yu, *The FHA and BRCT domains recognize ADP-ribosylation during DNA damage response.* Genes Dev, 2013. **27**(16): p. 1752-68.

708. Zhang, F., Y. Chen, M. Li, and X. Yu, *The oligonucleotide/oligosaccharide-binding fold motif is a poly(ADP-ribose)-binding domain that mediates DNA damage response.* Proc Natl Acad Sci U S A, 2014. **111**(20): p. 7278-83.

709. Zhang, F., J. Shi, C. Bian, and X. Yu, *Poly(ADP-Ribose) Mediates the BRCA2-Dependent Early DNA Damage Response.* Cell Rep, 2015. **13**(4): p. 678-689.

710. Maltseva, E.A., N.I. Rechkunova, M.V. Sukhanova, and O.I. Lavrik, *Poly(ADP-ribose) Polymerase 1 Modulates Interaction of the Nucleotide Excision Repair Factor XPC-RAD23B with DNA via Poly(ADP-ribosyl)ation.* J Biol Chem, 2015. **290**(36): p. 21811-20.

711. Chambon, P., J.D. Weill, and P. Mandel, *Nicotinamide mononucleotide activation of new DNA-dependent polyadenylic acid synthesizing nuclear enzyme.* Biochem Biophys Res Commun, 1963. **11**: p. 39-43.

712. de Murcia, G., J. Jongstra-Bilen, M.E. Ittel, P. Mandel, and E. Delain, *Poly(ADP-ribose) polymerase auto-modification and interaction with DNA: electron microscopic visualization.* EMBO J, 1983. **2**(4): p. 543-8.

713. Alvarez-Gonzalez, R. and M.K. Jacobson, *Characterization of polymers of adenosine diphosphate ribose generated in vitro and in vivo.* Biochemistry, 1987. **26**(11): p. 3218-24.

714. Hayashi, K., M. Tanaka, T. Shimada, M. Miwa, and T. Sugimura, *Size and shape of poly(ADP-ribose): examination by gel filtration, gel electrophoresis and electron microscopy.* Biochem Biophys Res Commun, 1983. **112**(1): p. 102-7.

715. Minaga, T. and E. Kun, *Spectral analysis of the conformation of polyadenosine diphosphoribose. Evidence indicating secondary structure.* J Biol Chem, 1983. **258**(2): p. 725-30.

716. Reeder, R.H., K. Ueda, T. Honjo, Y. Nishizuka, and O. Hayaishi, *Studies on the polymer of adenosine diphosphate ribose. II. Characterization of the polymer.* J Biol Chem, 1967. **242**(13): p. 3172-9.

717. Sugimura, T., S. Fujimura, S. Hasegawa, and Y. Kawamura, *Polymerization of the adenosine 5'-diphosphate ribose moiety of NAD by rat liver nuclear enzyme.* Biochim Biophys Acta, 1967. **138**(2): p. 438-41.

718. Kang, H.C., Y.I. Lee, J.H. Shin, S.A. Andrabi, Z. Chi, J.P. Gagne*, et al.*, *Iduna is a poly(ADP-ribose) (PAR)-dependent E3 ubiquitin ligase that regulates DNA damage.* Proc Natl Acad Sci U S A, 2011. **108**(34): p. 14103-8.

719. DaRosa, P.A., Z. Wang, X. Jiang, J.N. Pruneda, F. Cong, R.E. Klevit*, et al.*, *Allosteric activation of the RNF146 ubiquitin ligase by a poly(ADP-ribosyl)ation signal.* Nature, 2015. **517**(7533): p. 223-6.

720. Abd Elmageed, Z.Y., A.S. Naura, Y. Errami, and M. Zerfaoui, *The poly(ADP-ribose) polymerases (PARPs): new roles in intracellular transport.* Cell Signal, 2012. **24**(1): p. 1-8.

721. Yu, S.W., S.A. Andrabi, H. Wang, N.S. Kim, G.G. Poirier, T.M. Dawson*, et al.*, *Apoptosis-inducing factor mediates poly(ADP-ribose) (PAR) polymer-induced cell death.* Proc Natl Acad Sci U S A, 2006. **103**(48): p. 18314-9.

722. Wang, Y., N.S. Kim, J.F. Haince, H.C. Kang, K.K. David, S.A. Andrabi*, et al.*, *Poly(ADP-ribose) (PAR) binding to apoptosis-inducing factor is critical for PAR polymerase-1-dependent cell death (parthanatos).* Sci Signal, 2011. **4**(167): p. ra20.

723. Kurgina, T.A., R.O. Anarbaev, M.V. Sukhanova, and O.I. Lavrik, *A rapid fluorescent method for the real-time measurement of poly(ADP-ribose) polymerase 1 activity.* Anal Biochem, 2018. **545**: p. 91-97.

724. Ferro, A.M. and B.M. Olivera, *Poly(ADP-ribosylation) in vitro. Reaction parameters and enzyme mechanism.* J Biol Chem, 1982. **257**(13): p. 7808-13.

725. Asher, G., H. Reinke, M. Altmeyer, M. Gutierrez-Arcelus, M.O. Hottiger, and U. Schibler, *Poly(ADP-ribose) polymerase 1 participates in the phase entrainment of circadian clocks to feeding.* Cell, 2010. **142**(6): p. 943-53.

726. Barkauskaite, E., G. Jankevicius, and I. Ahel, *Structures and Mechanisms of Enzymes Employed in the Synthesis and Degradation of PARP-Dependent Protein ADP-Ribosylation.* Mol Cell, 2015. **58**(6): p. 935-46.

727. Alvarez-Gonzalez, R. and F.R. Althaus, *Poly(ADP-ribose) catabolism in mammalian cells exposed to DNA-damaging agents.* Mutat Res, 1989. **218**(2): p. 67-74.

728. Miwa, M. and T. Sugimura, *Splitting of the ribose-ribose linkage of poly(adenosine diphosphate-robose) by a calf thymus extract.* J Biol Chem, 1971. **246**(20): p. 6362-4.

729. Ueda, K., J. Oka, S. Naruniya, N. Miyakawa, and O. Hayaishi, *Poly ADP-ribose glycohydrolase from rat liver nuclei, a novel enzyme degrading the polymer.* Biochem Biophys Res Commun, 1972. **46**(2): p. 516-23.

730. Oka, S., J. Kato, and J. Moss, *Identification and characterization of a mammalian 39-kDa poly(ADP-ribose) glycohydrolase.* J Biol Chem, 2006. **281**(2): p. 705-13.

731. Dunstan, M.S., E. Barkauskaite, P. Lafite, C.E. Knezevic, A. Brassington, M. Ahel*, et al.*, *Structure and mechanism of a canonical poly(ADP-ribose) glycohydrolase.* Nat Commun, 2012. **3**: p. 878.

732. Brochu, G., C. Duchaine, L. Thibeault, J. Lagueux, G.M. Shah, and G.G. Poirier, *Mode of action of poly(ADP-ribose) glycohydrolase.* Biochim Biophys Acta, 1994. **1219**(2): p. 342-50.

733. Desnoyers, S., G.M. Shah, G. Brochu, J.C. Hoflack, A. Verreault, and G.G. Poirier, *Biochemical properties and function of poly(ADP-ribose) glycohydrolase.* Biochimie, 1995. **77**(6): p. 433-8.

734. Barkauskaite, E., A. Brassington, E.S. Tan, J. Warwicker, M.S. Dunstan, B. Banos*, et al.*, *Visualization of poly(ADP-ribose) bound to PARG reveals inherent balance between exo- and endo-glycohydrolase activities.* Nat Commun, 2013. **4**: p. 2164.

735. Mashimo, M., J. Kato, and J. Moss, *Structure and function of the ARH family of ADP-ribosyl-acceptor hydrolases.* DNA Repair (Amst), 2014. **23**: p. 88-94.

736. Mueller-Dieckmann, C., S. Kernstock, M. Lisurek, J.P. von Kries, F. Haag, M.S. Weiss*, et al.*, *The structure of human ADP-ribosylhydrolase 3 (ARH3) provides insights into the reversibility of protein ADP-ribosylation.* Proc Natl Acad Sci U S A, 2006. **103**(41): p. 15026-31.

737. Niere, M., M. Mashimo, L. Agledal, C. Dolle, A. Kasamatsu, J. Kato*, et al.*, *ADP-ribosylhydrolase 3 (ARH3), not poly(ADP-ribose) glycohydrolase (PARG) isoforms, is responsible for degradation of mitochondrial matrix-associated poly(ADP-ribose).* J Biol Chem, 2012. **287**(20): p. 16088-102.

738. Mashimo, M., J. Kato, and J. Moss, *ADP-ribosyl-acceptor hydrolase 3 regulates poly (ADP-ribose) degradation and cell death during oxidative stress.* Proc Natl Acad Sci U S A, 2013. **110**(47): p. 18964-9.

739. Takada, T., I.J. Okazaki, and J. Moss, *ADP-ribosylarginine hydrolases.* Mol Cell Biochem, 1994. **138**(1-2): p. 119-22.

740. Takada, T., K. Iida, and J. Moss, *Cloning and site-directed mutagenesis of human ADP-ribosylarginine hydrolase.* J Biol Chem, 1993. **268**(24): p. 17837-43.

741. Fontana, P., J.J. Bonfiglio, L. Palazzo, E. Bartlett, I. Matic, and I. Ahel, *Serine ADP-ribosylation reversal by the hydrolase ARH3.* Elife, 2017. **6**.

742. Abplanalp, J., M. Leutert, E. Frugier, K. Nowak, R. Feurer, J. Kato*, et al.*, *Proteomic analyses identify ARH3 as a serine mono-ADP-ribosylhydrolase.* Nat Commun, 2017. **8**(1): p. 2055.

743. Jankevicius, G., M. Hassler, B. Golia, V. Rybin, M. Zacharias, G. Timinszky*, et al.*, *A family of macrodomain proteins reverses cellular mono-ADP-ribosylation.* Nat Struct Mol Biol, 2013. **20**(4): p. 508-14.

744. Rosenthal, F., K.L. Feijs, E. Frugier, M. Bonalli, A.H. Forst, R. Imhof*, et al.*, *Macrodomain-containing proteins are new mono-ADP-ribosylhydrolases.* Nat Struct Mol Biol, 2013. **20**(4): p. 502-7.

745. Daniels, C.M., P. Thirawatananond, S.E. Ong, S.B. Gabelli, and A.K. Leung, *Nudix hydrolases degrade protein-conjugated ADP-ribose.* Sci Rep, 2015. **5**: p. 18271.

746. Palazzo, L., B. Thomas, A.S. Jemth, T. Colby, O. Leidecker, K.L. Feijs*, et al.*, *Processing of protein ADP-ribosylation by Nudix hydrolases.* Biochem J, 2015. **468**(2): p. 293-301.

747. Palazzo, L., C.M. Daniels, J.E. Nettleship, N. Rahman, R.L. McPherson, S.E. Ong*, et al.*, *ENPP1 processes protein ADP-ribosylation in vitro.* FEBS J, 2016. **283**(18): p. 3371-88.

748. Cohen, M.S. and P. Chang, *Insights into the biogenesis, function, and regulation of ADP-ribosylation.* Nat Chem Biol, 2018. **14**(3): p. 236-243.

749. Koh, D.W., A.M. Lawler, M.F. Poitras, M. Sasaki, S. Wattler, M.C. Nehls*, et al.*, *Failure to degrade poly(ADP-ribose) causes increased sensitivity to cytotoxicity and early embryonic lethality.* Proc Natl Acad Sci U S A, 2004. **101**(51): p. 17699-704.

750. Virag, L., *50Years of poly(ADP-ribosyl)ation.* Mol Aspects Med, 2013. **34**(6): p. 1043-5.

751. Quenet, D., R. El Ramy, V. Schreiber, and F. Dantzer, *The role of poly(ADP-ribosyl)ation in epigenetic events.* Int J Biochem Cell Biol, 2009. **41**(1): p. 60-5.

752. Muthurajan, U.M., M.R. Hepler, A.R. Hieb, N.J. Clark, M. Kramer, T. Yao*, et al.*, *Automodification switches PARP-1 function from chromatin architectural protein to histone chaperone.* Proc Natl Acad Sci U S A, 2014. **111**(35): p. 12752-7.

753. Posavec Marjanovic, M., K. Crawford, and I. Ahel, *PARP, transcription and chromatin modeling.* Semin Cell Dev Biol, 2017. **63**: p. 102-113.

754. Dantzer, F. and R. Santoro, *The expanding role of PARPs in the establishment and maintenance of heterochromatin.* FEBS J, 2013. **280**(15): p. 3508-18.

755. Thomas, C. and A.V. Tulin, *Poly-ADP-ribose polymerase: machinery for nuclear processes.* Mol Aspects Med, 2013. **34**(6): p. 1124-37.

756. Kraus, W.L. and M.O. Hottiger, *PARP-1 and gene regulation: progress and puzzles.* Mol Aspects Med, 2013. **34**(6): p. 1109-23.

757. Ke, Y., J. Zhang, X. Lv, X. Zeng, and X. Ba, *Novel insights into PARPs in gene expression: regulation of RNA metabolism.* Cell Mol Life Sci, 2019. **76**(17): p. 3283-3299.

758. Robert, I., F. Dantzer, and B. Reina-San-Martin, *Parp1 facilitates alternative NHEJ, whereas Parp2 suppresses IgH/c-myc translocations during immunoglobulin class switch recombination.* J Exp Med, 2009. **206**(5): p. 1047-56.

759. Xu, Z., H. Zan, E.J. Pone, T. Mai, and P. Casali, *Immunoglobulin class-switch DNA recombination: induction, targeting and beyond.* Nat Rev Immunol, 2012. **12**(7): p. 517-31.

760. Wang, Z.Q., B. Auer, L. Stingl, H. Berghammer, D. Haidacher, M. Schweiger*, et al.*, *Mice lacking ADPRT and poly(ADP-ribosyl)ation develop normally but are susceptible to skin disease.* Genes Dev, 1995. **9**(5): p. 509-20.

761. de Murcia, J.M., C. Niedergang, C. Trucco, M. Ricoul, B. Dutrillaux, M. Mark*, et al.*, *Requirement of poly(ADP-ribose) polymerase in recovery from DNA damage in mice and in cells.* Proc Natl Acad Sci U S A, 1997. **94**(14): p. 7303-7.

762. Masutani, M., T. Nozaki, E. Nishiyama, T. Shimokawa, Y. Tachi, H. Suzuki*, et al.*, *Function of poly(ADP-ribose) polymerase in response to DNA damage: gene-disruption study in mice.* Mol Cell Biochem, 1999. **193**(1-2): p. 149-52.

763. Shall, S. and G. de Murcia, *Poly(ADP-ribose) polymerase-1: what have we learned from the deficient mouse model?* Mutat Res, 2000. **460**(1): p. 1-15.

764. Piskunova, T.S., M.N. Yurova, A.I. Ovsyannikov, A.V. Semenchenko, M.A. Zabezhinski, I.G. Popovich*, et al.*, *Deficiency in Poly(ADP-ribose) Polymerase-1 (PARP-1) Accelerates Aging and Spontaneous Carcinogenesis in Mice.* Curr Gerontol Geriatr Res, 2008: p. 754190.

765. Luo, X. and W.L. Kraus, *On PAR with PARP: cellular stress signaling through poly(ADP-ribose) and PARP-1.* Genes Dev, 2012. **26**(5): p. 417-32.

766. Gupte, R., Z. Liu, and W.L. Kraus, *PARPs and ADP-ribosylation: recent advances linking molecular functions to biological outcomes.* Genes Dev, 2017. **31**(2): p. 101-126.

767. Schuhwerk, H., R. Atteya, K. Siniuk, and Z.Q. Wang, *PARPing for balance in the homeostasis of poly(ADP-ribosyl)ation.* Semin Cell Dev Biol, 2017. **63**: p. 81-91.

768. Martin-Hernandez, K., J.M. Rodriguez-Vargas, V. Schreiber, and F. Dantzer, *Expanding functions of ADP-ribosylation in the maintenance of genome integrity.* Semin Cell Dev Biol, 2017. **63**: p. 92-101.

769. HamediRad, M., S. Weisberg, R. Chao, J. Lian, and H. Zhao, *Highly Efficient Single-Pot Scarless Golden Gate Assembly.* ACS Synth Biol, 2019. **8**(5): p. 1047-1054.

770. Kunze, F.A. and M.O. Hottiger, *Regulating Immunity via ADP-Ribosylation: Therapeutic Implications and Beyond.* Trends Immunol, 2019. **40**(2): p. 159-173.

771. Rodriguez-Vargas, J.M., F.J. Oliver-Pozo, and F. Dantzer, *PARP1 and Poly(ADP-ribosyl)ation Signaling during Autophagy in Response to Nutrient Deprivation.* Oxid Med Cell Longev, 2019. **2019**: p. 2641712.

772. Virag, L., A. Robaszkiewicz, J.M. Rodriguez-Vargas, and F.J. Oliver, *Poly(ADP-ribose) signaling in cell death.* Mol Aspects Med, 2013. **34**(6): p. 1153-67.

773. Aredia, F. and A.I. Scovassi, *Poly(ADP-ribose): a signaling molecule in different paradigms of cell death.* Biochem Pharmacol, 2014. **92**(1): p. 157-63.

774. Liu, Y., F.A. Kadyrov, and P. Modrich, *PARP-1 enhances the mismatch-dependence of 5'-directed excision in human mismatch repair in vitro.* DNA Repair (Amst), 2011. **10**(11): p. 1145-53.

775. Robert, I., O. Karicheva, B. Reina San Martin, V. Schreiber, and F. Dantzer, *Functional aspects of PARylation in induced and programmed DNA repair processes: preserving genome integrity and modulating physiological events.* Mol Aspects Med, 2013. **34**(6): p. 1138-52.

776. Rudolph, J., J. Mahadevan, P. Dyer, and K. Luger, *Poly(ADP-ribose) polymerase 1 searches DNA via a 'monkey bar' mechanism.* Elife, 2018. **7**.

777. Altmeyer, M., K.J. Neelsen, F. Teloni, I. Pozdnyakova, S. Pellegrino, M. Grofte*, et al.*, *Liquid demixing of intrinsically disordered proteins is seeded by poly(ADP-ribose).* Nat Commun, 2015. **6**: p. 8088.

778. Ma, W., C.J. Halweg, D. Menendez, and M.A. Resnick, *Differential effects of poly(ADP-ribose) polymerase inhibition on DNA break repair in human cells are revealed with Epstein-Barr virus.* Proc Natl Acad Sci U S A, 2012. **109**(17): p. 6590-5.

779. Mortusewicz, O., J.C. Ame, V. Schreiber, and H. Leonhardt, *Feedback-regulated poly(ADP-ribosyl)ation by PARP-1 is required for rapid response to DNA damage in living cells.* Nucleic Acids Res, 2007. **35**(22): p. 7665-75.

780. Caldecott, K.W., *Protein ADP-ribosylation and the cellular response to DNA strand breaks.* DNA Repair (Amst), 2014. **19**: p. 108-13.

781. Gibbs-Seymour, I., P. Fontana, J.G.M. Rack, and I. Ahel, *HPF1/C4orf27 Is a PARP-1-Interacting Protein that Regulates PARP-1 ADP-Ribosylation Activity.* Mol Cell, 2016. **62**(3): p. 432-442.

782. Bonfiglio, J.J., P. Fontana, Q. Zhang, T. Colby, I. Gibbs-Seymour, I. Atanassov*, et al.*, *Serine ADP-Ribosylation Depends on HPF1.* Mol Cell, 2017. **65**(5): p. 932-940 e6.

783. Leung, A.K., *SERious Surprises for ADP-Ribosylation Specificity: HPF1 Switches PARP1 Specificity to Ser Residues.* Mol Cell, 2017. **65**(5): p. 777-778.

784. Okano, S., L. Lan, A.E. Tomkinson, and A. Yasui, *Translocation of XRCC1 and DNA ligase IIIalpha from centrosomes to chromosomes in response to DNA damage in mitotic human cells.* Nucleic Acids Res, 2005. **33**(1): p. 422-9.

785. Campalans, A., T. Kortulewski, R. Amouroux, H. Menoni, W. Vermeulen, and J.P. Radicella, *Distinct spatiotemporal patterns and PARP dependence of XRCC1 recruitment to single-strand break and base excision repair.* Nucleic Acids Res, 2013. **41**(5): p. 3115-29.

786. Ahel, D., Z. Horejsi, N. Wiechens, S.E. Polo, E. Garcia-Wilson, I. Ahel*, et al.*, *Poly(ADP-ribose)-dependent regulation of DNA repair by the chromatin remodeling enzyme ALC1.* Science, 2009. **325**(5945): p. 1240-3.

787. Rulten, S.L., F. Cortes-Ledesma, L. Guo, N.J. Iles, and K.W. Caldecott, *APLF (C2orf13) is a novel component of poly(ADP-ribose) signaling in mammalian cells.* Mol Cell Biol, 2008. **28**(14): p. 4620-8.

788. Mehrotra, P.V., D. Ahel, D.P. Ryan, R. Weston, N. Wiechens, R. Kraehenbuehl*, et al.*, *DNA repair factor APLF is a histone chaperone.* Mol Cell, 2011. **41**(1): p. 46-55.

789. Wei, L., S. Nakajima, C.L. Hsieh, S. Kanno, M. Masutani, A.S. Levine*, et al.*, *Damage response of XRCC1 at sites of DNA single strand breaks is regulated by phosphorylation and ubiquitylation after degradation of poly(ADP-ribose).* J Cell Sci, 2013. **126**(Pt 19): p. 4414-23.

790. Flohr, C., A. Burkle, J.P. Radicella, and B. Epe, *Poly(ADP-ribosyl)ation accelerates DNA repair in a pathway dependent on Cockayne syndrome B protein.* Nucleic Acids Res, 2003. **31**(18): p. 5332-7.

791. Noren Hooten, N., K. Kompaniez, J. Barnes, A. Lohani, and M.K. Evans, *Poly(ADP-ribose) polymerase 1 (PARP-1) binds to 8-oxoguanine-DNA glycosylase (OGG1).* J Biol Chem, 2011. **286**(52): p. 44679-90.

792. Cistulli, C., O.I. Lavrik, R. Prasad, E. Hou, and S.H. Wilson, *AP endonuclease and poly(ADP-ribose) polymerase-1 interact with the same base excision repair intermediate.* DNA Repair (Amst), 2004. **3**(6): p. 581-91.

793. Prasad, R., J.K. Horton, P.D. Chastain, 2nd, N.R. Gassman, B.D. Freudenthal, E.W. Hou*, et al.*, *Suicidal cross-linking of PARP-1 to AP site intermediates in cells undergoing base excision repair.* Nucleic Acids Res, 2014. **42**(10): p. 6337-51.

794. Prasad, R., N. Dyrkheeva, J. Williams, and S.H. Wilson, *Mammalian Base Excision Repair: Functional Partnership between PARP-1 and APE1 in AP-Site Repair.* PLoS One, 2015. **10**(5): p. e0124269.

795. Moor, N.A., I.A. Vasil'eva, N.A. Kuznetsov, and O.I. Lavrik, *Human apurinic/apyrimidinic endonuclease 1 is modified in vitro by poly(ADP-ribose) polymerase 1 under control of the structure of damaged DNA.* Biochimie, 2019.

796. Reynolds, P., S. Cooper, M. Lomax, and P. O'Neill, *Disruption of PARP1 function inhibits base excision repair of a sub-set of DNA lesions.* Nucleic Acids Res, 2015. **43**(8): p. 4028-38.

797. Prasad, R., D.D. Shock, W.A. Beard, and S.H. Wilson, *Substrate channeling in mammalian base excision repair pathways: passing the baton.* J Biol Chem, 2010. **285**(52): p. 40479-88.

798. Dantzer, F., V. Schreiber, C. Niedergang, C. Trucco, E. Flatter, G. De La Rubia*, et al.*, *Involvement of poly(ADP-ribose) polymerase in base excision repair.* Biochimie, 1999. **81**(1-2): p. 69-75.

799. Dantzer, F., G. de La Rubia, J. Menissier-De Murcia, Z. Hostomsky, G. de Murcia, and V. Schreiber, *Base excision repair is impaired in mammalian cells lacking Poly(ADP-ribose) polymerase-1.* Biochemistry, 2000. **39**(25): p. 7559-69.

800. Sukhanova, M., S. Khodyreva, and O. Lavrik, *Poly(ADP-ribose) polymerase 1 regulates activity of DNA polymerase beta in long patch base excision repair.* Mutat Res, 2010. **685**(1-2): p. 80-9.

801. Oei, S.L. and M. Ziegler, *ATP for the DNA ligation step in base excision repair is generated from poly(ADP-ribose).* J Biol Chem, 2000. **275**(30): p. 23234-9.

802. Petermann, E., M. Ziegler, and S.L. Oei, *ATP-dependent selection between single nucleotide and long patch base excision repair.* DNA Repair (Amst), 2003. **2**(10): p. 1101-14.

803. Berger, N.A., G.W. Sikorski, S.J. Petzold, and K.K. Kurohara, *Association of poly(adenosine diphosphoribose) synthesis with DNA damage and repair in normal human lymphocytes.* J Clin Invest, 1979. **63**(6): p. 1164-71.

804. Berger, N.A., G.W. Sikorski, S.J. Petzold, and K.K. Kurohara, *Defective poly(adenosine diphosphoribose) synthesis in xeroderma pigmentosum.* Biochemistry, 1980. **19**(2): p. 289-93.

805. McCurry, L.S. and M.K. Jacobson, *Poly(ADP-ribose) synthesis following DNA damage in cells heterozygous or homozygous for the xeroderma pigmentosum genotype.* J Biol Chem, 1981. **256**(2): p. 551-3.

806. Cleaver, J.E., W.J. Bodell, W.F. Morgan, and B. Zelle, *Differences in the regulation by poly(ADP-ribose) of repair of DNA damage from alkylating agents and ultraviolet light according to cell type.* J Biol Chem, 1983. **258**(15): p. 9059-68.

807. Jacobson, E.L., K.M. Antol, H. Juarez-Salinas, and M.K. Jacobson, *Poly(ADP-ribose) metabolism in ultraviolet irradiated human fibroblasts.* J Biol Chem, 1983. **258**(1): p. 103-7.

808. Yoon, Y.S., J.W. Kim, K.W. Kang, Y.S. Kim, K.H. Choi, and C.O. Joe, *Poly(ADP-ribosyl)ation of histone H1 correlates with internucleosomal DNA fragmentation during apoptosis.* J Biol Chem, 1996. **271**(15): p. 9129-34.

809. Chang, H., C.S. Sander, C.S. Muller, P. Elsner, and J.J. Thiele, *Detection of poly(ADP-ribose) by immunocytochemistry: a sensitive new method for the early identification of UVB- and H2O2-induced apoptosis in keratinocytes.* Biol Chem, 2002. **383**(3-4): p. 703-8.

810. Farkas, B., M. Magyarlaki, B. Csete, J. Nemeth, G. Rabloczky, S. Bernath*, et al.*, *Reduction of acute photodamage in skin by topical application of a novel PARP inhibitor.* Biochem Pharmacol, 2002. **63**(5): p. 921-32.

811. Molinete, M., W. Vermeulen, A. Burkle, J. Menissier-de Murcia, J.H. Kupper, J.H. Hoeijmakers*, et al.*, *Overproduction of the poly(ADP-ribose) polymerase DNA-binding domain blocks alkylation-induced DNA repair synthesis in mammalian cells.* EMBO J, 1993. **12**(5): p. 2109-17.

812. Stevnsner, T., R. Ding, M. Smulson, and V.A. Bohr, *Inhibition of gene-specific repair of alkylation damage in cells depleted of poly(ADP-ribose) polymerase.* Nucleic Acids Res, 1994. **22**(22): p. 4620-4.

813. Schreiber, V., D. Hunting, C. Trucco, B. Gowans, D. Grunwald, G. De Murcia*, et al.*, *A dominant-negative mutant of human poly(ADP-ribose) polymerase affects cell recovery, apoptosis, and sister chromatid exchange following DNA damage.* Proc Natl Acad Sci U S A, 1995. **92**(11): p. 4753-7.

814. Vodenicharov, M.D., M.M. Ghodgaonkar, S.S. Halappanavar, R.G. Shah, and G.M. Shah, *Mechanism of early biphasic activation of poly(ADP-ribose) polymerase-1 in response to ultraviolet B radiation.* J Cell Sci, 2005. **118**(Pt 3): p. 589-99.

815. Mone, M.J., M. Volker, O. Nikaido, L.H. Mullenders, A.A. van Zeeland, P.J. Verschure*, et al.*, *Local UV-induced DNA damage in cell nuclei results in local transcription inhibition.* EMBO Rep, 2001. **2**(11): p. 1013-7.

816. Tang, J. and G. Chu, *Xeroderma pigmentosum complementation group E and UV-damaged DNA-binding protein.* DNA Repair (Amst), 2002. **1**(8): p. 601-16.

817. Ghodgaonkar, M.M., N. Zacal, S. Kassam, A.J. Rainbow, and G.M. Shah, *Depletion of poly(ADP-ribose) polymerase-1 reduces host cell reactivation of a UV-damaged adenovirus-encoded reporter gene in human dermal fibroblasts.* DNA Repair (Amst), 2008. **7**(4): p. 617-32.

818. Hastak, K., E. Alli, and J.M. Ford, *Synergistic chemosensitivity of triple-negative breast cancer cell lines to poly(ADP-Ribose) polymerase inhibition, gemcitabine, and cisplatin.* Cancer Res, 2010. **70**(20): p. 7970-80.

819. Hartman, A.R. and J.M. Ford, *BRCA1 induces DNA damage recognition factors and enhances nucleotide excision repair.* Nat Genet, 2002. **32**(1): p. 180-4.

820. Robu, M., R.G. Shah, N. Petitclerc, J. Brind'Amour, F. Kandan-Kulangara, and G.M. Shah, *Role of poly(ADP-ribose) polymerase-1 in the removal of UV-induced DNA lesions by nucleotide excision repair.* Proc Natl Acad Sci U S A, 2013. **110**(5): p. 1658-63.

821. Pines, A., M.G. Vrouwe, J.A. Marteijn, D. Typas, M.S. Luijsterburg, M. Cansoy*, et al.*, *PARP1 promotes nucleotide excision repair through DDB2 stabilization and recruitment of ALC1.* J Cell Biol, 2012. **199**(2): p. 235-49.

822. King, B.S., K.L. Cooper, K.J. Liu, and L.G. Hudson, *Poly(ADP-ribose) contributes to an association between poly(ADP-ribose) polymerase-1 and xeroderma pigmentosum complementation group A in nucleotide excision repair.* J Biol Chem, 2012. **287**(47): p. 39824-33.

823. Fischer, J.M., O. Popp, D. Gebhard, S. Veith, A. Fischbach, S. Beneke*, et al.*, *Poly(ADP-ribose)-mediated interplay of XPA and PARP1 leads to reciprocal regulation of protein function.* FEBS J, 2014. **281**(16): p. 3625-41.

824. Gottschalk, A.J., R.D. Trivedi, J.W. Conaway, and R.C. Conaway, *Activation of the SNF2 family ATPase ALC1 by poly(ADP-ribose) in a stable ALC1.PARP1.nucleosome intermediate.* J Biol Chem, 2012. **287**(52): p. 43527-32.

825. Pines, A., L.H. Mullenders, H. van Attikum, and M.S. Luijsterburg, *Touching base with PARPs: moonlighting in the repair of UV lesions and double-strand breaks.* Trends Biochem Sci, 2013. **38**(6): p. 321-30.

826. Krishnakumar, R. and W.L. Kraus, *The PARP side of the nucleus: molecular actions, physiological outcomes, and clinical targets.* Mol Cell, 2010. **39**(1): p. 8-24.

827. Fahrer, J., R. Kranaster, M. Altmeyer, A. Marx, and A. Burkle, *Quantitative analysis of the binding affinity of poly(ADP-ribose) to specific binding proteins as a function of chain length.* Nucleic Acids Res, 2007. **35**(21): p. e143.

828. Popp, O., S. Veith, J. Fahrer, V.A. Bohr, A. Burkle, and A. Mangerich, *Site-specific noncovalent interaction of the biopolymer poly(ADP-ribose) with the Werner syndrome protein regulates protein functions.* ACS Chem Biol, 2013. **8**(1): p. 179-88.

829. Thorslund, T., C. von Kobbe, J.A. Harrigan, F.E. Indig, M. Christiansen, T. Stevnsner*, et al.*, *Cooperation of the Cockayne syndrome group B protein and poly(ADP-ribose) polymerase 1 in the response to oxidative stress.* Mol Cell Biol, 2005. **25**(17): p. 7625-36.

830. Soldani, C. and A.I. Scovassi, *Poly(ADP-ribose) polymerase-1 cleavage during apoptosis: an update.* Apoptosis, 2002. **7**(4): p. 321-8.

831. Narne, P., V. Pandey, P.K. Simhadri, and P.B. Phanithi, *Poly(ADP-ribose)polymerase-1 hyperactivation in neurodegenerative diseases: The death knell tolls for neurons.* Semin Cell Dev Biol, 2017. **63**: p. 154-166.

832. Kandan-Kulangara, F., *Poly(ADP-ribose) polymerase-1 (PARP-1) and RNA interference (RNAi) during cell death*, in *Faculté de médecine*. 2013, Université Laval.

833. Lakatos, P., E. Szabo, C. Hegedus, G. Hasko, P. Gergely, P. Bai*, et al.*, *3-Aminobenzamide protects primary human keratinocytes from UV-induced cell death by a poly(ADP-ribosyl)ation independent mechanism.* Biochim Biophys Acta, 2013. **1833**(3): p. 743-51.

834. Brind'Amour, J., *Rôle de la poly(ADP-ribose) polymérase dans les réponses précoces aux rayons ultraviolets B dans l'épiderme de souris SKH-1*, in *Département de biologie cellulaire et moléculaire, Faculté de médecine*. 2005, Université Laval.

835. Valenzuela, M.T., R. Guerrero, M.I. Nunez, J.M. Ruiz De Almodovar, M. Sarker, G. de Murcia*, et al.*, *PARP-1 modifies the effectiveness of p53-mediated DNA damage response.* Oncogene, 2002. **21**(7): p. 1108-16.

836. Won, J., S.Y. Chung, S.B. Kim, B.H. Byun, Y.S. Yoon, and C.O. Joe, *Dose-dependent UV stabilization of p53 in cultured human cells undergoing apoptosis is mediated by poly(ADP-ribosyl)ation.* Mol Cells, 2006. **21**(2): p. 218-23.

837. Kanai, M., K. Hanashiro, S.H. Kim, S. Hanai, A.H. Boulares, M. Miwa*, et al.*, *Inhibition of Crm1-p53 interaction and nuclear export of p53 by poly(ADP-ribosyl)ation.* Nat Cell Biol, 2007. **9**(10): p. 1175-83.

838. Malanga, M., J.M. Pleschke, H.E. Kleczkowska, and F.R. Althaus, *Poly(ADP-ribose) binds to specific domains of p53 and alters its DNA binding functions.* J Biol Chem, 1998. **273**(19): p. 11839-43.

839. Fischbach, A., A. Kruger, S. Hampp, G. Assmann, L. Rank, M. Hufnagel*, et al.*, *The C-terminal domain of p53 orchestrates the interplay between non-covalent and covalent poly(ADP-ribosyl)ation of p53 by PARP1.* Nucleic Acids Res, 2018. **46**(2): p. 804-822.

840. Mabley, J.G., R. Wallace, P. Pacher, K. Murphy, and C. Szabo, *Inhibition of poly(adenosine diphosphate-ribose) polymerase by the active form of vitamin D.* Int J Mol Med, 2007. **19**(6): p. 947-52.

841. Martin-Oliva, D., R. Aguilar-Quesada, F. O'Valle, J.A. Munoz-Gamez, R. Martinez-Romero, R. Garcia Del Moral*, et al.*, *Inhibition of poly(ADP-ribose) polymerase modulates tumor-related gene expression, including hypoxia-inducible factor-1 activation, during skin carcinogenesis.* Cancer Res, 2006. **66**(11): p. 5744-56.

842. Martin-Oliva, D., F. O'Valle, J.A. Munoz-Gamez, M.T. Valenzuela, M.I. Nunez, M. Aguilar*, et al.*, *Crosstalk between PARP-1 and NF-kappaB modulates the promotion of skin neoplasia.* Oncogene, 2004. **23**(31): p. 5275-83.

843. Brady, P.N., A. Goel, and M.A. Johnson, *Poly(ADP-Ribose) Polymerases in Host-Pathogen Interactions, Inflammation, and Immunity.* Microbiol Mol Biol Rev, 2019. **83**(1).

844. El-Hamoly, T., C. Hegedus, P. Lakatos, K. Kovacs, P. Bai, M.A. El-Ghazaly*, et al.*, *Activation of poly(ADP-ribose) polymerase-1 delays wound healing by regulating keratinocyte migration and production of inflammatory mediators.* Mol Med, 2014. **20**: p. 363-71.

845. Ha, H.C., L.D. Hester, and S.H. Snyder, *Poly(ADP-ribose) polymerase-1 dependence of stress-induced transcription factors and associated gene expression in glia.* Proc Natl Acad Sci U S A, 2002. **99**(5): p. 3270-5.

846. Davidovich, P., C.J. Kearney, and S.J. Martin, *Inflammatory outcomes of apoptosis, necrosis and necroptosis.* Biol Chem, 2014. **395**(10): p. 1163-71.

847. Robinson, N., R. Ganesan, C. Hegedus, K. Kovacs, T.A. Kufer, and L. Virag, *Programmed necrotic cell death of macrophages: Focus on pyroptosis, necroptosis, and parthanatos.* Redox Biol, 2019. **26**: p. 101239.

848. Krukenberg, K.A., S. Kim, E.S. Tan, Z. Maliga, and T.J. Mitchison, *Extracellular poly(ADP-ribose) is a pro-inflammatory signal for macrophages.* Chem Biol, 2015. **22**(4): p. 446-452.

849. Oliver, F.J., J. Menissier-de Murcia, C. Nacci, P. Decker, R. Andriantsitohaina, S. Muller*, et al.*, *Resistance to endotoxic shock as a consequence of defective NF-kappaB activation in poly (ADP-ribose) polymerase-1 deficient mice.* EMBO J, 1999. **18**(16): p. 4446-54.

850. Damian, D.L., C.R. Patterson, M. Stapelberg, J. Park, R.S. Barnetson, and G.M. Halliday, *UV radiation-induced immunosuppression is greater in men and prevented by topical nicotinamide.* J Invest Dermatol, 2008. **128**(2): p. 447-54.

851. Gensler, H.L., *Prevention of photoimmunosuppression and photocarcinogenesis by topical nicotinamide.* Nutr Cancer, 1997. **29**(2): p. 157-62.

852. Gensler, H.L., T. Williams, A.C. Huang, and E.L. Jacobson, *Oral niacin prevents photocarcinogenesis and photoimmunosuppression in mice.* Nutr Cancer, 1999. **34**(1): p. 36-41.

853. Damian, D.L., *Photoprotective effects of nicotinamide.* Photochem Photobiol Sci, 2010. **9**(4): p. 578-85.

854. Surjana, D., G.M. Halliday, and D.L. Damian, *Role of nicotinamide in DNA damage, mutagenesis, and DNA repair.* J Nucleic Acids, 2010. **2010**.

855. Damian, D.L., *Nicotinamide for skin cancer chemoprevention.* Australas J Dermatol, 2017. **58**(3): p. 174-180.

856. Nasta, F., F. Laudisi, M. Sambucci, M.M. Rosado, and C. Pioli, *Increased Foxp3+ regulatory T cells in poly(ADP-Ribose) polymerase-1 deficiency.* J Immunol, 2010. **184**(7): p. 3470-7.

857. Zhang, P., T. Maruyama, J.E. Konkel, B. Abbatiello, B. Zamarron, Z.Q. Wang*, et al.*, *PARP-1 controls immunosuppressive function of regulatory T cells by destabilizing Foxp3.* PLoS One, 2013. **8**(8): p. e71590.

858. Brunyanszki, A., C. Hegedus, M. Szanto, K. Erdelyi, K. Kovacs, V. Schreiber*, et al.*, *Genetic ablation of PARP-1 protects against oxazolone-induced contact hypersensitivity by modulating oxidative stress.* J Invest Dermatol, 2010. **130**(11): p. 2629-37.

859. Hanahan, D. and R.A. Weinberg, *Hallmarks of cancer: the next generation.* Cell, 2011. **144**(5): p. 646-74.

860. Dulaney, C., S. Marcrom, J. Stanley, and E.S. Yang, *Poly(ADP-ribose) polymerase activity and inhibition in cancer.* Semin Cell Dev Biol, 2017. **63**: p. 144-153.

861. Masutani, M. and H. Fujimori, *Poly(ADP-ribosyl)ation in carcinogenesis.* Mol Aspects Med, 2013. **34**(6): p. 1202-16.

862. Wang, L., C. Liang, F. Li, D. Guan, X. Wu, X. Fu*, et al.*, *PARP1 in Carcinomas and PARP1 Inhibitors as Antineoplastic Drugs.* Int J Mol Sci, 2017. **18**(10).

863. Mitsuko Masutani, A.G., Masahiro Tsutsumi, Kumiko Ogawa, Nobuo Kamada, Tomoyuki Shirai, Kou-ichi Jishage, Hitoshi Nakagama, and Takashi Sugimura., *Role of Poly-ADP-Ribosylation in Cancer Development.* 2000-2013: Austin (TX): Landes Bioscience.

864. Tong, W.M., Y.G. Yang, W.H. Cao, D. Galendo, L. Frappart, Y. Shen*, et al.*, *Poly(ADP-ribose) polymerase-1 plays a role in suppressing mammary tumourigenesis in mice.* Oncogene, 2007. **26**(26): p. 3857-67.

865. Shibata, A., D. Maeda, H. Ogino, M. Tsutsumi, T. Nohmi, H. Nakagama*, et al.*, *Role of Parp-1 in suppressing spontaneous deletion mutation in the liver and brain of mice at adolescence and advanced age.* Mutat Res, 2009. **664**(1-2): p. 20-7.

866. Simbulan-Rosenthal, C.M., B.R. Haddad, D.S. Rosenthal, Z. Weaver, A. Coleman, R. Luo*, et al.*, *Chromosomal aberrations in PARP(-/-) mice: genome stabilization in immortalized cells by reintroduction of poly(ADP-ribose) polymerase cDNA.* Proc Natl Acad Sci U S A, 1999. **96**(23): p. 13191-6.

867. Piskunova, T.S., M.A. Zabezhinskii, I.G. Popovich, M.L. Tyndyk, M.N. Iurova, and V.N. Anisimov, *[Diethylnitrosamine-induced carcinogenesis in PARP-1(-/-) and PARP-1(+/+) mice].* Vopr Onkol, 2009. **55**(5): p. 608-11.

868. Tsutsumi, M., M. Masutani, T. Nozaki, O. Kusuoka, T. Tsujiuchi, H. Nakagama*, et al.*, *Increased susceptibility of poly(ADP-ribose) polymerase-1 knockout mice to nitrosamine carcinogenicity.* Carcinogenesis, 2001. **22**(1): p. 1-3.

869. Nozaki, T., H. Fujihara, M. Watanabe, M. Tsutsumi, K. Nakamoto, O. Kusuoka*, et al.*, *Parp-1 deficiency implicated in colon and liver tumorigenesis induced by azoxymethane.* Cancer Sci, 2003. **94**(6): p. 497-500.

870. Shibata, A., N. Kamada, K. Masumura, T. Nohmi, S. Kobayashi, H. Teraoka*, et al.*, *Parp-1 deficiency causes an increase of deletion mutations and insertions/rearrangements in vivo after treatment with an alkylating agent.* Oncogene, 2005. **24**(8): p. 1328-37.

871. Feng, F.Y., J.S. de Bono, M.A. Rubin, and K.E. Knudsen, *Chromatin to Clinic: The Molecular Rationale for PARP1 Inhibitor Function.* Mol Cell, 2015. **58**(6): p. 925-34.

872. Sistigu, A., G. Manic, F. Obrist, and I. Vitale, *Trial watch - inhibiting PARP enzymes for anticancer therapy.* Mol Cell Oncol, 2016. **3**(2): p. e1053594.

873. Staibano, S., S. Pepe, L. Lo Muzio, P. Somma, M. Mascolo, G. Argenziano*, et al.*, *Poly(adenosine diphosphate-ribose) polymerase 1 expression in malignant melanomas from photoexposed areas of the head and neck region.* Hum Pathol, 2005. **36**(7): p. 724-31.

874. Dorsam, B., N. Seiwert, S. Foersch, S. Stroh, G. Nagel, D. Begaliew*, et al.*, *PARP-1 protects against colorectal tumor induction, but promotes inflammation-driven colorectal tumor progression.* Proc Natl Acad Sci U S A, 2018. **115**(17): p. E4061-E4070.

875. Tentori, L., A. Muzi, A.S. Dorio, S. Bultrini, E. Mazzon, P.M. Lacal*, et al.*, *Stable depletion of poly (ADP-ribose) polymerase-1 reduces in vivo melanoma growth and increases chemosensitivity.* Eur J Cancer, 2008. **44**(9): p. 1302-14.

876. Rodriguez, M.I., A. Peralta-Leal, F. O'Valle, J.M. Rodriguez-Vargas, A. Gonzalez-Flores, J. Majuelos-Melguizo*, et al.*, *PARP-1 regulates metastatic melanoma through modulation of vimentin-induced malignant transformation.* PLoS Genet, 2013. **9**(6): p. e1003531.

877. Tanori, M., M. Mancuso, E. Pasquali, S. Leonardi, S. Rebessi, V. Di Majo*, et al.*, *PARP-1 cooperates with Ptc1 to suppress medulloblastoma and basal cell carcinoma.* Carcinogenesis, 2008. **29**(10): p. 1911-9.

878. Borek, C., W.F. Morgan, A. Ong, and J.E. Cleaver, *Inhibition of malignant transformation in vitro by inhibitors of poly(ADP-ribose) synthesis.* Proc Natl Acad Sci U S A, 1984. **81**(1): p. 243-7.

879. Epstein, J.H. and J.E. Cleaver, *3-Aminobenzamide can act as a cocarcinogen for ultraviolet light-induced carcinogenesis in mouse skin.* Cancer Res, 1992. **52**(14): p. 4053-4.

880. Lu, Y., Y. Liu, Y. Pang, K. Pacak, and C. Yang, *Double-barreled gun: Combination of PARP inhibitor with conventional chemotherapy.* Pharmacol Ther, 2018. **188**: p. 168-175.

881. Mangerich, A. and A. Burkle, *How to kill tumor cells with inhibitors of poly(ADP-ribosyl)ation.* Int J Cancer, 2011. **128**(2): p. 251-65.

882. Durkacz, B.W., O. Omidiji, D.A. Gray, and S. Shall, *(ADP-ribose)n participates in DNA excision repair.* Nature, 1980. **283**(5747): p. 593-6.

883. Ben-Hur, E., H. Utsumi, and M.M. Elkind, *Inhibitors of poly(ADP-ribose) synthesis enhance X-ray killing of log-phase Chinese hamster cells.* Radiat Res, 1984. **97**(3): p. 546-55.

884. Ben-Hur, E., C.C. Chen, and M.M. Elkind, *Inhibitors of poly(adenosine diphosphoribose) synthetase, examination of metabolic perturbations, and enhancement of radiation response in Chinese hamster cells.* Cancer Res, 1985. **45**(5): p. 2123-7.

885. Drean, A., C.J. Lord, and A. Ashworth, *PARP inhibitor combination therapy.* Crit Rev Oncol Hematol, 2016. **108**: p. 73-85.

886. Mateo, J., C.J. Lord, V. Serra, A. Tutt, J. Balmana, M. Castroviejo-Bermejo*, et al.*, *A decade of clinical development of PARP inhibitors in perspective.* Ann Oncol, 2019. **30**(9): p. 1437-1447.

887. Lesueur, P., F. Chevalier, J.B. Austry, W. Waissi, H. Burckel, G. Noel*, et al.*, *Poly-(ADP-ribose)-polymerase inhibitors as radiosensitizers: a systematic review of pre-clinical and clinical human studies.* Oncotarget, 2017. **8**(40): p. 69105-69124.

888. Li, A., M. Yi, S. Qin, Q. Chu, S. Luo, and K. Wu, *Prospects for combining immune checkpoint blockade with PARP inhibition.* J Hematol Oncol, 2019. **12**(1): p. 98.

889. Bryant, H.E., N. Schultz, H.D. Thomas, K.M. Parker, D. Flower, E. Lopez*, et al.*, *Specific killing of BRCA2-deficient tumours with inhibitors of poly(ADP-ribose) polymerase.* Nature, 2005. **434**(7035): p. 913-7.

890. Farmer, H., N. McCabe, C.J. Lord, A.N. Tutt, D.A. Johnson, T.B. Richardson*, et al.*, *Targeting the DNA repair defect in BRCA mutant cells as a therapeutic strategy.* Nature, 2005. **434**(7035): p. 917-21.

891. Dobzhansky, T., *Genetics of natural populations; recombination and variability in populations of Drosophila pseudoobscura.* Genetics, 1946. **31**: p. 269-90.

892. Scott, C.L., E.M. Swisher, and S.H. Kaufmann, *Poly (ADP-ribose) polymerase inhibitors: recent advances and future development.* J Clin Oncol, 2015. **33**(12): p. 1397-406.

893. D'Andrea, A.D., *Mechanisms of PARP inhibitor sensitivity and resistance.* DNA Repair (Amst), 2018. **71**: p. 172-176.

894. Lin, K.Y. and W.L. Kraus, *PARP Inhibitors for Cancer Therapy.* Cell, 2017. **169**(2): p. 183.

895. Lord, C.J. and A. Ashworth, *PARP inhibitors: Synthetic lethality in the clinic.* Science, 2017. **355**(6330): p. 1152-1158.

896. Kim, G., G. Ison, A.E. McKee, H. Zhang, S. Tang, T. Gwise*, et al.*, *FDA Approval Summary: Olaparib Monotherapy in Patients with Deleterious Germline BRCA-Mutated Advanced Ovarian Cancer Treated with Three or More Lines of Chemotherapy.* Clin Cancer Res, 2015. **21**(19): p. 4257-61.

897. *First PARP Inhibitor Ok'd for Breast Cancer.* Cancer Discov, 2018. **8**(3): p. 256-257.

898. Guney Eskiler, G., *Talazoparib to treat BRCA-positive breast cancer.* Drugs Today (Barc), 2019. **55**(7): p. 459-467.

899. Scott, L.J., *Niraparib: First Global Approval.* Drugs, 2017. **77**(9): p. 1029-1034.

900. Ison, G., L.J. Howie, L. Amiri-Kordestani, L. Zhang, S. Tang, R. Sridhara*, et al.*, *FDA Approval Summary: Niraparib for the Maintenance Treatment of Patients with Recurrent Ovarian Cancer in Response to Platinum-Based Chemotherapy.* Clin Cancer Res, 2018. **24**(17): p. 4066-4071.

901. Balasubramaniam, S., J.A. Beaver, S. Horton, L.L. Fernandes, S. Tang, H.N. Horne*, et al.*, *FDA Approval Summary: Rucaparib for the Treatment of Patients with Deleterious BRCA Mutation-Associated Advanced Ovarian Cancer.* Clin Cancer Res, 2017. **23**(23): p. 7165-7170.

902. Hoy, S.M., *Talazoparib: First Global Approval.* Drugs, 2018. **78**(18): p. 1939-1946.

903. McCann, K.E., *Advances in the use of PARP inhibitors for BRCA1/2-associated breast cancer: talazoparib.* Future Oncol, 2019. **15**(15): p. 1707-1715.

904. Adashek, J.J., R.K. Jain, and J. Zhang, *Clinical Development of PARP Inhibitors in Treating Metastatic Castration-Resistant Prostate Cancer.* Cells, 2019. **8**(8).

905. Lord, C.J. and A. Ashworth, *BRCAness revisited.* Nat Rev Cancer, 2016. **16**(2): p. 110-20.

906. Turner, N., A. Tutt, and A. Ashworth, *Hallmarks of 'BRCAness' in sporadic cancers.* Nat Rev Cancer, 2004. **4**(10): p. 814-9.

907. Jiang, X., W. Li, X. Li, H. Bai, and Z. Zhang, *Current status and future prospects of PARP inhibitor clinical trials in ovarian cancer.* Cancer Manag Res, 2019. **11**: p. 4371-4390.

908. Available from: https://www.who.int/news-room/fact-sheets/detail/cancer.

909. Tong, W.M., U. Cortes, and Z.Q. Wang, *Poly(ADP-ribose) polymerase: a guardian angel protecting the genome and suppressing tumorigenesis.* Biochim Biophys Acta, 2001. **1552**(1): p. 27-37.

910. Wang, J., A. Sato, H. Fujimori, Y. Miki, and M. Masutani, *PARP and Carcinogenesis*, in *PARP Inhibitors for Cancer Therapy*, N.J. Curtin and R.A. Sharma, Editors. 2015, Springer International Publishing: Cham. p. 99-124.

911. Wittschieben, B.O., S. Iwai, and R.D. Wood, *DDB1-DDB2 (xeroderma pigmentosum group E) protein complex recognizes a cyclobutane pyrimidine dimer, mismatches, apurinic/apyrimidinic sites, and compound lesions in DNA.* J Biol Chem, 2005. **280**(48): p. 39982-9.

912. Robu, M., R.G. Shah, N.K. Purohit, P. Zhou, H. Naegeli, and G.M. Shah, *Poly(ADP-ribose) polymerase 1 escorts XPC to UV-induced DNA lesions during nucleotide excision repair.* Proc Natl Acad Sci U S A, 2017. **114**(33): p. E6847-E6856.

913. Keeney, S., G.J. Chang, and S. Linn, *Characterization of a human DNA damage binding protein implicated in xeroderma pigmentosum E.* J Biol Chem, 1993. **268**(28): p. 21293-300.

914. Alekseev, S., H. Kool, H. Rebel, M. Fousteri, J. Moser, C. Backendorf*, et al.*, *Enhanced DDB2 expression protects mice from carcinogenic effects of chronic UV-B irradiation.* Cancer Res, 2005. **65**(22): p. 10298-306.

915. Ananthaswamy, H.N., A. Ouhtit, R.L. Evans, A. Gorny, P. Khaskina, A.T. Sands*, et al.*, *Persistence of p53 mutations and resistance of keratinocytes to apoptosis are associated with the increased susceptibility of mice lacking the XPC gene to UV carcinogenesis.* Oncogene, 1999. **18**(51): p. 7395-8.

916. Stoyanova, T., N. Roy, S. Bhattacharjee, D. Kopanja, T. Valli, S. Bagchi*, et al.*, *p21 cooperates with DDB2 protein in suppression of ultraviolet ray-induced skin malignancies.* J Biol Chem, 2012. **287**(5): p. 3019-28.

917. Hegedus, C., G. Boros, E. Fidrus, G.N. Kis, M. Antal, T. Juhasz*, et al.*, *PARP1 Inhibition Augments UVB-Mediated Mitochondrial Changes-Implications for UV-Induced DNA Repair and Photocarcinogenesis.* Cancers (Basel), 2019. **12**(1).

918. Garssen, J., H. van Steeg, F. de Gruijl, J. de Boer, G.T. van der Horst, H. van Kranen*, et al.*, *Transcription-coupled and global genome repair differentially influence UV-B-induced acute skin effects and systemic immunosuppression.* J Immunol, 2000. **164**(12): p. 6199-205.

919. Murai, H., S. Takeuchi, Y. Nakatsu, M. Ichikawa, M. Yoshino, Y. Gondo*, et al.*, *Studies of in vivo mutations in rpsL transgene in UVB-irradiated epidermis of XPA-deficient mice.* Mutat Res, 2000. **450**(1-2): p. 181-92.

920. Miyauchi-Hashimoto, H., K. Tanaka, and T. Horio, *Enhanced inflammation and immunosuppression by ultraviolet radiation in xeroderma pigmentosum group A (XPA) model mice.* J Invest Dermatol, 1996. **107**(3): p. 343-8.

921. de Vries, A., R.J. Berg, S. Wijnhoven, A. Westerman, P.W. Wester, C.F. van Kreijl*, et al.*, *XPA-deficiency in hairless mice causes a shift in skin tumor types and mutational target genes after exposure to low doses of U.V.B.* Oncogene, 1998. **16**(17): p. 2205-12.

922. To, C., E.H. Kim, D.B. Royce, C.R. Williams, R.M. Collins, R. Risingsong*, et al.*, *The PARP inhibitors, veliparib and olaparib, are effective chemopreventive agents for delaying mammary tumor development in BRCA1-deficient mice.* Cancer Prev Res (Phila), 2014. **7**(7): p. 698-707.

923. Quiles-Perez, R., J.A. Munoz-Gamez, A. Ruiz-Extremera, F. O'Valle, L. Sanjuan-Nunez, A.B. Martin-Alvarez*, et al.*, *Inhibition of poly adenosine diphosphate-ribose polymerase decreases hepatocellular carcinoma growth by modulation of tumor-related gene expression.* Hepatology, 2010. **51**(1): p. 255-66.

924. Purohit, N.K., M. Robu, R.G. Shah, N.E. Geacintov, and G.M. Shah, *Characterization of the interactions of PARP-1 with UV-damaged DNA in vivo and in vitro.* Sci Rep, 2016. **6**: p. 19020.

925. Tyagi, N., A. Bhardwaj, S.K. Srivastava, S. Arora, S. Marimuthu, S.K. Deshmukh*, et al.*, *Development and Characterization of a Novel in vitro Progression Model for UVB-Induced Skin Carcinogenesis.* Sci Rep, 2015. **5**: p. 13894.

926. Rodero, M.P., H.Y. Handoko, R.M. Villani, G.J. Walker, and K. Khosrotehrani, *Differential effects of ultraviolet irradiation in neonatal versus adult mice are not explained by defective macrophage or neutrophil infiltration.* J Invest Dermatol, 2014. **134**(7): p. 1991-1997.

927. Yang, G., Y. Fu, M. Malakhova, I. Kurinov, F. Zhu, K. Yao*, et al.*, *Caffeic acid directly targets ERK1/2 to attenuate solar UV-induced skin carcinogenesis.* Cancer Prev Res (Phila), 2014. **7**(10): p. 1056-66.

928. Bitler, B.G., Z.L. Watson, L.J. Wheeler, and K. Behbakht, *PARP inhibitors: Clinical utility and possibilities of overcoming resistance.* Gynecol Oncol, 2017. **147**(3): p. 695-704.

929. Viros, A., B. Sanchez-Laorden, M. Pedersen, S.J. Furney, J. Rae, K. Hogan*, et al.*, *Ultraviolet radiation accelerates BRAF-driven melanomagenesis by targeting TP53.* Nature, 2014. **511**(7510): p. 478-482.

930. Whiteman, D.C., C.A. Whiteman, and A.C. Green, *Childhood sun exposure as a risk factor for melanoma: a systematic review of epidemiologic studies.* Cancer Causes Control, 2001. **12**(1): p. 69-82.

931. Luo, C., J. Sheng, M.G. Hu, F.G. Haluska, R. Cui, Z. Xu*, et al.*, *Loss of ARF sensitizes transgenic BRAFV600E mice to UV-induced melanoma via suppression of XPC.* Cancer Res, 2013. **73**(14): p. 4337-48.

932. Aszterbaum, M., J. Epstein, A. Oro, V. Douglas, P.E. LeBoit, M.P. Scott*, et al.*, *Ultraviolet and ionizing radiation enhance the growth of BCCs and trichoblastomas in patched heterozygous knockout mice.* Nat Med, 1999. **5**(11): p. 1285-91.

Annexes

Annexe 1: Characterization of the interactions of PARP-1 with UV-damaged DNA in vivo and in vitro

SCIENTIFIC REPORTS

OPEN

Characterization of the interactions of PARP-1 with UV-damaged DNA *in vivo* and *in vitro*

Received: 05 August 2015
Accepted: 02 December 2015
Published: 12 January 2016

Nupur K. Purohit[1,*], Mihaela Robu[1,*], Rashmi G. Shah[1,*], Nicholas E. Geacintov[2] & Girish M. Shah[1]

The existing methodologies for studying robust responses of poly (ADP-ribose) polymerase-1 (PARP-1) to DNA damage with strand breaks are often not suitable for examining its subtle responses to altered DNA without strand breaks, such as UV-damaged DNA. Here we describe two novel assays with which we characterized the interaction of PARP-1 with UV-damaged DNA *in vivo* and *in vitro*. Using an *in situ* fractionation technique to selectively remove free PARP-1 while retaining the DNA-bound PARP-1, we demonstrate a direct recruitment of the endogenous or exogenous PARP-1 to the UV-lesion site *in vivo* after local irradiation. In addition, using the model oligonucleotides with single UV lesion surrounded by multiple restriction enzyme sites, we demonstrate *in vitro* that DDB2 and PARP-1 can simultaneously bind to UV-damaged DNA and that PARP-1 casts a bilateral asymmetric footprint from −12 to +9 nucleotides on either side of the UV-lesion. These techniques will permit characterization of different roles of PARP-1 in the repair of UV-damaged DNA and also allow the study of normal housekeeping roles of PARP-1 with undamaged DNA.

The abundance of poly (ADP-ribose) polymerase-1 (PARP-1) in mammalian cells and its rapid catalytic activation to form polymers of ADP-ribose (PAR) in the presence of various types of DNA damages with or without strand breaks has made it an ideal first responder at the lesion site to influence downstream events[1,2]. Apart from DNA damages, PARP-1 is also recruited to DNA during normal physiological processes such as transcription and chromatin remodeling[3], which do not involve overt DNA damage but just altered DNA structures. While we know much more about how PARP-1 rapidly recognizes and binds to single or double strand breaks in DNA, we know very little about how PARP-1 interacts with DNA damages or altered DNA structures without strand breaks. The key reason is that the existing methodologies that readily identify interactions of PARP-1 with DNA strand breaks are not sufficiently sensitive to study the relatively weaker responses of PARP-1 to DNA damage without strand breaks. The response of PARP-1 to UVC-induced direct photolesions, such as cyclobutane pyrimidine dimers (CPD) that are formed without any DNA strand breaks exemplifies this problem.

Recent studies from others and our team have shown the involvement of PARP-1 in the host cell reactivation[4] and specifically in the nucleotide excision repair (NER) of UV-damaged DNA through its interaction with early NER protein DDB2[5–7]. Additional studies have shown that downstream NER proteins XPA[8,9] and XPC[10] are PARylated. Thus, PARP-1 possibly has multiple roles in NER, but we do not yet fully understand its interactions with UV-damaged DNA or other NER proteins due to two major challenges. The first challenge is that unlike for many NER proteins, the abundance of endogenous PARP-1 in the nucleus makes it nearly impossible to visualize its dynamics of recruitment to UV-damaged DNA *in situ* using conventional immunocytological methods. To circumvent this challenge, the detection of its activation product PAR has been used as a proxy for PARP-1 recruitment at UV-lesion[5,11]. However, PAR may underestimate the role of PARP-1 in response to UV-damage due to weak activation of PARP-1 by UV[4,12], short half-life of PAR[2], and technical limitations in combining the detection of PAR with other proteins[13,14]. PAR detection will also not reveal participation of PARP-1 in protein-protein interactions without formation of PAR. Thus, there is a need for methods that permit direct visualization of recruitment of PARP-1 to UV-induced DNA lesions.

[1]Laboratory for Skin Cancer Research, CHU-Q (CHUL) Quebec University Hospital Research Centre & Laval University, 2705, Laurier Boulevard, Québec (QC) Canada G1V 4G2. [2]New York University, Department of Chemistry, New York, NY, USA. *These authors contributed equally to this work. Correspondence and requests for materials should be addressed to G.M.S. (email: girish.shah@crchul.ulaval.ca)

The second major challenge is that we do not know the exact footprint of PARP-1 at the UV-lesion site that could explain its interaction with different NER proteins. We have earlier shown that PARP-1 binds to UV-damaged large oligonucleotide *in vitro* or to chromatin fragments containing T-T lesions *in vivo*[11]. We also showed that PARP-1 and DDB2 associate with each other on the chromatin of UV-irradiated cells and that DDB2 stimulates catalytic activity of PARP-1 in the presence of UV-damaged DNA[7]. However, these assays lack the nucleotide level resolution to reveal whether PARP-1 was bound directly to the UV-damaged bases or to any other base in those long pieces of DNA and whether PARP-1 and DDB2 have sufficient space to co-exist around UV-induced DNA lesion. To address these challenges, here, we describe two novel assays. The first assay is an *in situ* fractionation technique that allows a direct visualization of PARP-1 recruited to UV-damaged DNA *in vivo*. The second assay involves use of model oligonucleotides with a defined UV-damage surrounded by multiple restriction enzyme sites that reveals a bilateral asymmetric footprint of PARP-1 around the UV-lesion.

Results and Discussion

Novel *in situ* fractionation protocol to reveal recruitment of endogenous PARP-1 to UV-induced DNA lesion. We first determined whether different permeabilization-fixation protocols conventionally used for PARP-1 could reveal a direct recruitment of PARP-1 to UVC-induced DNA photolesions *in situ*. There was no change in the pattern of abundant PARP-1 signal before or after global UVC-irradiation using formaldehyde-methanol protocol despite using three different antibodies to PARP-1 (Fig. 1a, left panel). Unlike global irradiation, local UVC-irradiation produces defined subnuclear spots of UV-damaged DNA that could be identified either by immunodetection of T-T lesions or DDB2 that is recruited very rapidly to these lesions (Supplementary Fig. S1a). Therefore, we examined whether the formaldehyde-methanol protocol could reveal localization of PARP-1 to subnuclear UV-damaged DNA spots after local irradiation. Once again, we could not observe colocalization of PARP-1 with the subnuclear spots of DDB2 (Fig. 1a, right panel). Next, we tried previously described formaldehyde-Triton protocol[8] which was shown to display a punctate pattern of PARP-1. However, we noted that this pattern did not correlate with recruitment of PARP-1 to UV-damaged DNA, because it was observed in both the unirradiated control and globally UVC-irradiated cells; and none of the spots of PARP-1 were co-incident with DDB2, i.e., UV-damaged DNA in the cells after local UVC-irradiation (Supplementary Fig. S1b).

In view of these challenges in the immunocytological detection of PARP-1 bound to UV-damaged DNA due to the background "noise" created by rest of the nuclear PARP-1, we designed a novel *in situ* fractionation technique to selectively deplete unbound or "free" PARP-1 from the nuclei while leaving behind the PARP-1 that is bound and cross-linked to the UV-damaged DNA. We used CSK buffer (C) with Triton (C+T) as the basic conditions, which have been used earlier to extract majority of the cellular proteins without destroying the cellular architecture and permit visualization of NER and other repair proteins recruited to the damaged DNA[15–18]. To this buffer, we added 0.42 M NaCl (C+T+S), since we had earlier seen that 0.42 M NaCl retained chromatin-bound PARP-1 during cell fractionation *in vitro*[7] whereas 1.6 M NaCl was shown to strip almost all PARP-1 from cells[19]. We first compared the efficiency of these three protocols (i.e., C, C+T and C+T+S) for the extraction of PARP-1 and DDB2 from unirradiated control cells. The immunoblotting of cell pellet and supernatant from each protocol revealed that while C+T protocol could efficiently remove majority of the free DDB2, a significant extraction of the free PARP-1 from cell pellet required C+T+S protocol (Fig. 1c). Next, we compared the capacity of these three protocols for the *in situ* extraction of PARP-1 from control and global UVC-irradiated cells. The immunocytological visualization confirmed that C+T+S buffer extracted most of the "free" PARP-1 from the control and UVC-irradiated cells, while leaving behind residual PARP-1 that would be interacting with DNA for normal physiological functions in control cells and relatively stronger punctate pattern of PARP-1 in UV-irradiated nuclei (Fig. 1d).

When the three protocols were compared after local irradiation, we observed that the C+T+S protocol offered the best extraction condition for visualization of the recruitment of PARP-1 to the subnuclear spots of DDB2 (Fig. 1e, left panel). The pooled data from at least 100 subnuclear spots revealed that each additional step of extraction with detergent and salt improved our ability to discern colocalization of PARP-1 with DDB2 (Fig. 1e, left chart). Since the initial irradiation conditions were identical prior to extraction with each of the protocols, the improved detection of colocalization of PARP-1 with DDB2 could only be due to a more efficient removal of rest of the nuclear "free PARP-1" by the C+T+S protocol. This was evident when PARP-1 signal at the irradiated site was corrected for the background signal from an equivalent area of the unirradiated part of the same nucleus for all techniques (Fig. 1e, right chart).

Validation of the *in situ* fractionation protocol with GFP-tagged exogenous PARP-1 or its N-terminal DNA binding domain. We compared the efficiency of each of the three protocols in revealing the recruitment of exogenous GFP-tagged PARP-1 to UV-induced T-T lesion in locally UV-irradiated cells (Fig. 2a). The C protocol was inefficient in revealing the co-localization of GFP signal with T-T spots especially in the cells expressing higher levels of exogenous PARP-1. The C+T and C+T+S protocols increasingly resolved this problem by removing "free" PARP-1, thus giving a background-corrected signal for GFP-PARP-1 at T-T lesion that was 1.9 and 2.7 times better than the C protocol, respectively (Fig. 2a, chart). The additional advantage was that this co-localization could be readily observed whether these cells initially expressed high or low levels of GFP-PARP-1.

The N-terminal DNA binding domain (DBD) of PARP-1 containing first two zinc fingers was shown to be sufficient for its recruitment to different types of DNA damages caused by laser irradiation of cells[20,21]. In the cells transiently transfected with GFP-DBD, the colocalization of DBD with T-T was evident only in low DBD-expressers, as shown in low and high exposure panels of C-protocol (Fig. 2b). The ability to discern co-localization of GFP-DBD to T-T lesion sites was significantly improved by 1.5 and 2.1 times with C+T protocol and C+T+S protocol, respectively (Fig. 2b, chart). Immunoblotting for GFP-DBD and endogenous untagged

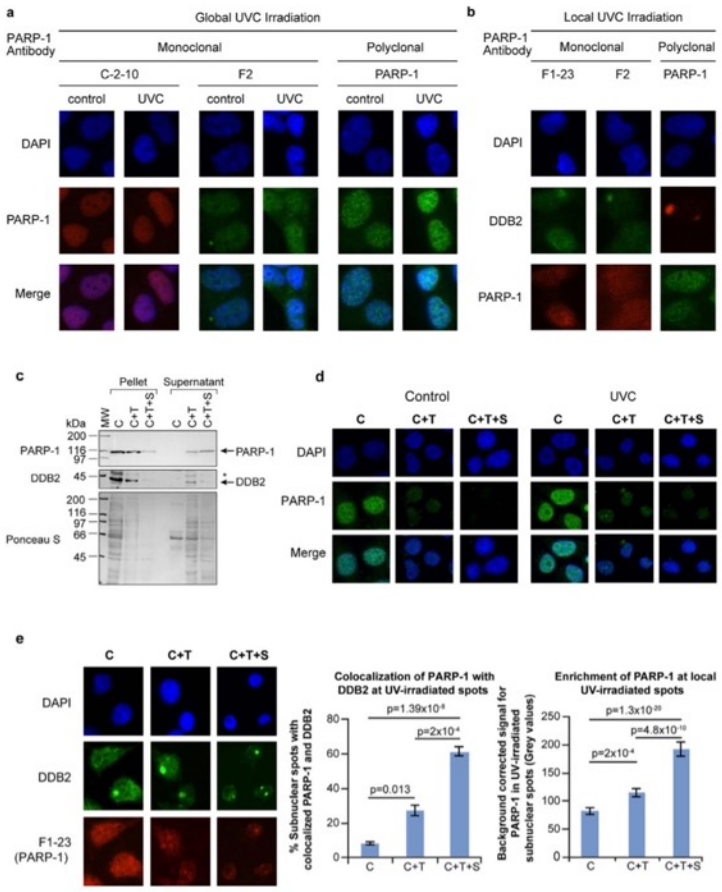

Figure 1. ***In situ*** **fractionation to reveal the recruitment of endogenous PARP-1 to UV-induced DNA lesion site.** (**a**,**b**) Unchanged pattern of nuclear staining for PARP-1 after global or local UVC-irradiation of cells processed with conventional immunocytological techniques. Human skin fibroblasts were exposed either to global (panel a) or local (panel b) irradiation with UVC, fixed with formaldehyde-methanol and probed for PARP-1 (global and local UVC) and DDB2 (local UVC) using specified antibodies. DAPI staining was carried out to define nuclei. (**c**) Efficiency of extraction of free PARP-1 and DDB2 from adherent control GMU6 cells. The pellets and supernatants obtained from equivalent cell numbers after extraction with CSK buffer (C), CSK+0.5% Triton (C+T) or CSK + 0.5% Triton + 0.42 M NaCl (C+T+S) were immunoblotted for PARP-1 and DDB2. The *refers to non-specific signal in DDB2 probing and Ponceau S staining reflected the residual protein content in cell pellets and supernatant at the end of each protocol. (**d**) Comparison of the efficiency of three protocols for extraction of the endogenous PARP-1 from adherent control and UV-irradiated cells. The GMU6 human skin fibroblasts were globally irradiated with 10 J/m^2 UVC (or control), extracted 10 min later with the three protocols and probed for PARP-1 using polyclonal PARP-1 antibody. (**e**) Colocalization of endogenous PARP-1 with DDB2 at local UVC-induced DNA damage. GMU6 cells were irradiated locally with 100 J/m^2 and after 10 min subjected to the three protocols (C, C+T and C+T+S) followed by visualization of PARP-1 (F1-23, red) and DDB2 (green). The left chart represents the percent of subnuclear PARP-1 spots that colocalize with DDB2. The right chart represents the quantification of the PARP-1 intensity at the DDB2 spots after subtraction of background signal intensity for PARP-1 from an equivalent area of unirradiated part of the same nucleus. Data of the charts are pooled from three experiments (n = 120–150 spots, data points are mean ± s.e.).

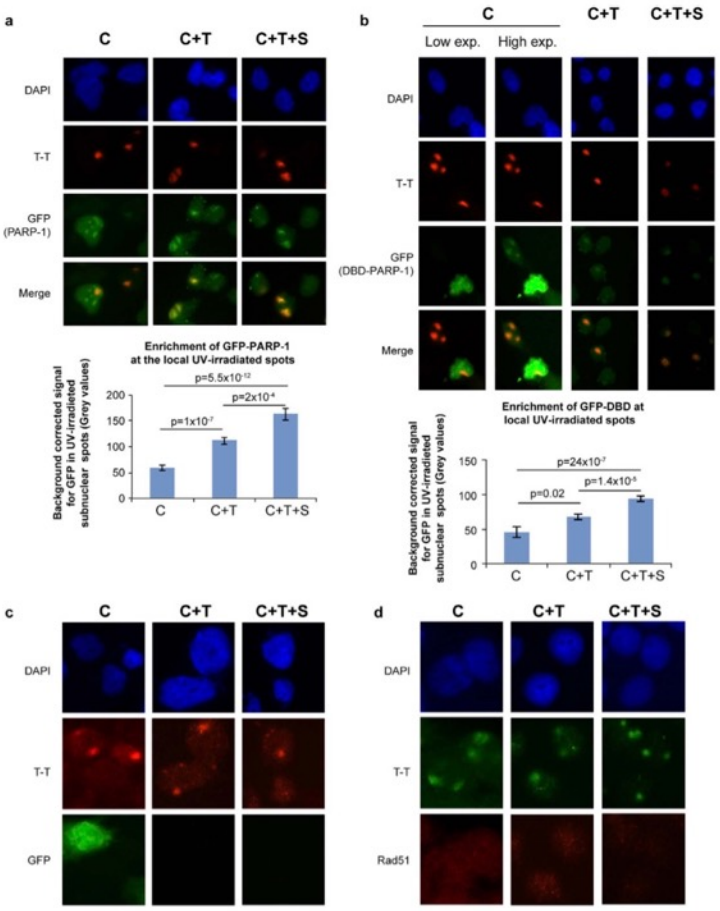

Figure 2. ***In situ*** **fractionation improves detection of exogenous GFP-PARP-1 or its DNA binding domain at local UV-irradiated spots. (a,b)** Recruitment of GFP-PARP-1 or its DBD to UV-induced T-T lesions. GMU6 cells were transfected with GFP- PARP-1 or GFP-DBD of PARP-1 for 24 h. The cells were locally irradiated and processed by C, C+T or C+T+S protocols. GFP-PARP-1 or GFP-DBD (green) and T-T (red) were visualized in DAPI-stained nuclei by immunofluorescence microscopy. The charts represent the quantification of GFP intensity for GFP- PARP-1 or GFP-DBD of PARP-1 at the T-T spots after background correction. (n = 80–150 spots, data points are mean ± s.e.). **(c,d)** Specificity of ***in situ*** extraction protocol: unrelated nuclear proteins (GFP and Rad51) do not colocalize with UV-damaged DNA. GMU6 cells were locally irradiated with 100 J/m^2 UVC and subjected 10 min later to ***in situ*** fractionation using the three protocols. For panel-c, the cells were transfected with GFP expressing plasmid 24 h before irradiation and protein extraction. The cells were processed for immunofluorescence detection of GFP, Rad51 (green) and T-T (red). DAPI staining was carried out to define nuclei.

PARP-1 in control cell pellets in these extraction protocols revealed that the extent of removal of exogenous GFP-DBD at each step was similar to that of the endogenous cellular PARP-1 (Supplementary Fig. S1c). Our results show that the N-terminal DBD of PARP-1 is sufficient to recognize and bind to UVC-induced DNA damage.

To assess the specificity of the new protocol, we examined the status of UV-induced colocalization of unrelated proteins, such as the exogenous tag protein GFP (Fig. 2c) or the cellular DNA double strand break-repair protein Rad51 (Fig. 2d) at UV-lesion spots after processing with all three protocols. Although C+T and C+T+S protocols progressively removed both of these proteins from the cells, neither GFP nor Rad51 colocalized with UV-induced T-T lesions. Thus, our results show that the C+T+S protocol does not cause an artifact of random

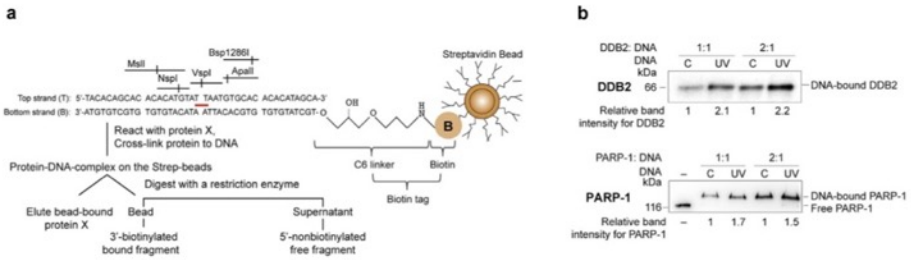

Figure 3. Strategy to study binding and footprint of proteins on UV-DNA. (a) The experimental design for determining the extent of binding of proteins to UV-DNA and analyses of protection of DNA during restriction digestion. The control and UV-DNA were immobilized on streptavidin beads via their biotin tag and reacted with purified PARP-1 or DDB2. The unreacted proteins were removed and bound proteins were cross-linked. The beads were then either analysed for bound-proteins by eluting the protein in Laemmli buffer, followed by SDS-PAGE, transfer and probe with specific antibodies or they were subjected to restriction digestion followed by analyses of the released DNA fragments on 10–15% native PAGE stained with gel red. **(b)** DDB2 and PARP-1 bind more to UV-DNA than control DNA. PARP-1 and DDB2 were reacted with 50 ng of control or UV-DNA at 1:1 or 1:2 (DNA:protein) molar ratios. The proteins were eluted from the beads, resolved on SDS-PAGE and analyzed by immunoblotting as shown in (**a**). The band intensities of protein bound to UV-DNA are shown as relative to signal for protein bound to control DNA.

colocalization of unrelated proteins with UV-damaged DNA. This simple yet selective *in situ* fractionation protocol to reveal PARP-1 at UV-lesion site would be useful in studying other NER-related roles of PARP-1 with or without its catalytic activation at the site of UV-damaged DNA.

An oligo with defined UV-lesion for restriction mapping of PARP-1. To determine the exact footprint of PARP-1 at the UV-lesion site, we created biotin-tagged 40 mer oligonucleotides with or without a single defined UV-lesion surrounded by multiple unique restriction enzyme sites (Fig. 3a and Supplementary Fig. S2a). The UVC-irradiation of the top strand of the oligo, which has only one pair of adjacent Ts and no other adjacent pyrimidines (T or C), resulted largely in the formation of T-T rather than 6–4PP lesions (Supplementary Fig. S2b). The inability of restriction enzymes to digest through UV-induced CPD[22,23] was exploited for purification of UV-DNA with VspI enzyme to remove all DNA molecules that did not form T-T at this site (Supplementary Fig. S2c). The biotin-tagged complementary strand for both control and UV-DNA allowed a common procedure for their immobilization to streptavidin beads (Fig. 3a). We reasoned that any protein bound at or around the UV-lesion site would prevent the restriction enzyme from digesting the DNA at that site; and thus decrease the quantity of non-biotinylated 5′-restriction fragment released from bead-bound DNA into the supernatant. This model allowed us to compare the extent of binding of proteins to control versus UV-DNA and also provide a non-isotopic method to footprint proteins on UV-DNA.

PARP-1 and DDB2 bind more to UV-DNA than control DNA. We had shown in the cells and *in vitro* that PARP-1 not only binds to UV-damaged DNA[11], but also interacts with DDB2 in the vicinity of UV-induced DNA lesions[7]. Using the model oligo described in Fig. 3a, we examined the extent of binding of PARP-1 and DDB2 to control and UV-DNA at two different molar ratios of protein : DNA (Fig. 3b). The 2.1—2.2× fold higher binding of DDB2 to UV-DNA than the control-DNA at these two molar ratios is in agreement with a previous report[24]. The binding of PARP-1 to UV-DNA was also 1.5—1.7× fold more than the control-DNA (Fig. 3b). We confirmed that PARP-1 did not bind to the beads per se unless DNA was attached to it (Supplementary Fig. S3a: left panel). To determine the site of PARP-1 binding to the control DNA without UV-lesion, we digested PARP-1-bound control DNA with VspI or NspI and noted that PARP-1 was attached more to the bead-bound 3′-end than to the 5′-end that is released after the restriction digestion (Supplementary Fig. S3a: right panel). This could be due to the linker attached biotin providing a pseudo-overhang at the 3′-end unlike blunt 5′-end, because PARP-1 has higher affinity for overhangs as compared to the blunt ends of DNA[25]. However, since the same 3′ and 5′-ends exist in both control and UV-DNA, any increase in PARP-1 binding to UV-DNA as compared to control-DNA must be due to the interaction of PARP-1 with UV-lesion, which we footprinted using a series of restriction enzymes that digest on either side of the lesion.

Restriction protection profile of PARP-1 is distinct from that of DDB2 on either side of the T-T lesion. We established the optimal amount of DNA required in the assay for detection of DNA fragments released after digestion with restriction enzyme (Supplementary Fig. S3b) and also confirmed that both the control and UV-DNA without bound protein could be digested by all the restriction enzymes used in our footprinting assays (Supplementary Fig. S3c,d). Thus, any restriction protection offered to DNA after reaction with protein could be attributed to the footprint of the protein. During the restriction digestion by NspI and MslI that recognize sequences from −2 to −12nt on the 5′-side of the T-T lesion, PARP-1 offered more protection to UV-DNA than control DNA, as seen from a significant PARP-1 dose-dependent decrease in the corresponding

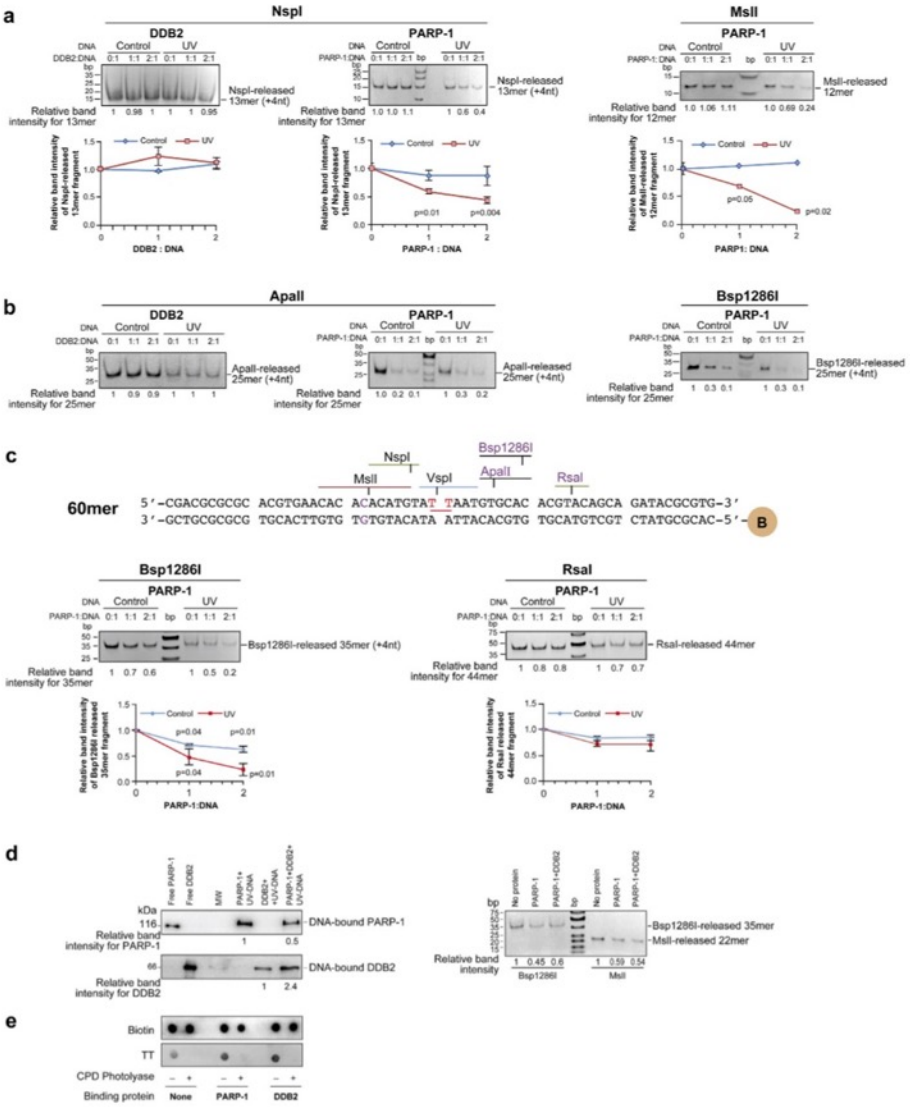

Figure 4. Footprinting of PARP-1 and DDB2 at UV-lesion site. (a) Restriction mapping of proteins on the 5′of the UV-lesion on 40mer DNA. 100 ng of bead-bound control or UV-DNA were reacted with DDB2 or PARP-1 at different DNA: protein ratios and digested at 37 °C with NspI (30 min) or MslI (15 min). The released 5′-fragments were resolved on 15% native PAGE and band intensities were measured. Each data point derived from three independent experiments represents mean ± s.d. for relative band intensity from three experiments for the fragment released from protein-bound versus protein-free DNA, with *P* values shown in the chart. **(b)** Mapping of proteins on the 3′-side of the UV-lesion on 40mer DNA. The protein-bound DNA was digested with ApaII (60 min) and Bsp1286I (20 min), and released 5′-fragments were resolved on 12% native PAGE. The data derived from two independent experiments is represented in the chart as described in panel-a. **(c)** *Top panel*-Structure of 60mer oligo with defined UV-damage. The 60mer oligo sequence was based on 40mer oligo but with a new RsaI site near 3′-end. *Bottom panels*- Restriction mapping of proteins on the 3′-side of the UV-lesion on 60mer DNA. The protein-bound DNA was digested with Bsp1286I (20 min) and

RsaI (30 min) and released 5′-fragments were analysed by 12% native PAGE. The data derived from three independent experiments is represented in the chart as described in panel-a. **(d)** Simultaneous binding and footprint of DDB2 and PARP-1 on 60mer UV-DNA. PARP-1 and DDB2 were reacted either separately or together with bead-bound UV-DNA (50 ng), at 2:1 molar ratio of protein:DNA. The proteins bound to the beads were detected by immunoblotting (left panels), and footprint of proteins on DNA was examined by restriction digestion with Bsp1286I and MslI (right panels). **(e)** Repair of T-T by CPD photolyase despite binding of DDB2 or PARP-1 to UV-DNA. Bead-bound 40mer UV-DNA was reacted (or not) with DDB2 or PARP-1, and subjected to repair (or not) by CPD photolyase. The DNA was eluted and immunodot-blotted for T-T. The data represents identical results obtained in three independent experiments.

5′-fragments released by these enzymes (Fig. 4a). Thus, the footprint of PARP-1 on UV-DNA extended from 2–12nt upstream of the lesion site. In contrast, DDB2 failed to protect UV-DNA against NspI (−2 to −7 nt), indicating that its footprint stays within 2nt on the 5′-side of T-T, as reported earlier[26].

PARP-1 has been shown to have a bilateral footprint of 7nt on either side of DNA single strand breaks[27]. Therefore, we compared the protections offered by PARP-1 and DDB2 against the restriction enzymes ApaII and Bsp1286I that target from 3 to 9nt on the 3′-side of the T-T lesion. The DDB2 did not offer any protection to control or UV-DNA against ApaII (Fig. 4b), indicating that its footprint does not exceed beyond 3nt on 3′-side of T-T, as reported earlier[26]. In contrast, PARP-1 offered a strong but equal protection to both UV and control oligos against both the enzymes, possibly due to PARP-1 bound to 3′-ends of both types of DNA, as noted earlier (Supplementary Fig. S3a: right panel). Thus using 40mer oligo, it was difficult to discern additional protection, if any, offered by PARP-1 that is bound at or near T-T site from the protection offered by PARP-1 that is bound to the 3′-end of the oligo.

To resolve this issue, we extended the size of 40 mer oligo on either ends to create a 60 mer, in which 3′-end was significantly separated from these two restriction sites and added a new RsaI restriction site at +11 nt from T-T (Fig. 4c, top panel). PARP-1 significantly protected 60mer UV-DNA against digestion by Bsp1286I as compared to control DNA, confirming its footprint up to +9nt from T-T lesion. Moreover, the lack of any additional protection by PARP-1 to UV-DNA against digestion by RsaI defined that PARP-1 footprint does not reach up to +11nt from T-T site (Fig. 4c). Thus using restriction-mapping technique on our model oligo, we show that PARP-1 bound at or near the T-T lesion extends asymmetric bilateral protection against restriction digestion from −12 to +9nt around the lesion.

Next, we examined whether PARP-1 and DDB2 can simultaneously bind to UV-DNA and whether DDB2 bound at the T-T lesion would alter the footprint of PARP-1 around the lesion. Using 60mer oligo, we noted that when incubated together, both DDB2 and PARP-1 could bind to UV-DNA (Fig. 4d, left panel). We observed in two independent experiments that the presence of PARP-1 increased the binding of DDB2 to UV-DNA, whereas that of DDB2 reduced the binding of PARP-1. However, the presence of DDB2 did not affect the restriction footprint of PARP-1 on UV-DNA, because PARP-1 offered identical protection to UV-DNA against restriction digestion on either side of the lesion site by MslI and Bsp1286I in the absence or the presence of DDB2 (Fig. 4d, right panel). Thus, the footprint of PARP-1 around the lesion was not compromised in the presence of DDB2 whereas DDB2 was more stabilized in the presence of PARP-1.

No effect of PARP-1 and DDB2 binding on CPD-photolyase mediated repair of T-T in UV-DNA. Unlike restriction enzymes that cleave the DNA in the sugar phosphate backbone, the CPD photolyase directly removes the cross-linking of adjacent pyrimidines in the CPD photolesions such as T-T[28]. Structural studies have revealed that DDB2 has a protein fold that flips out and maintains contact with T-T[26], and our results indicate that PARP-1 also remains in the vicinity of T-T lesion. Hence, we examined whether binding of DDB2 or PARP-1 to UV-DNA could influence the repair of T-T by CPD photolyase (Fig. 4e). The immunodot-blot of DNA with or without photolyase treatment revealed that binding of DDB2 or PARP-1 to DNA could not inhibit the ability of photolyase to repair the T-T lesions, indicating that these two proteins do not exclude other repair proteins from accessing the lesion. This is also in agreement with a previous report that binding of DDB2 to UV-DNA does not prevent CPD photolyase from repairing the UV-lesion[29].

Catalytic activation of PARP-1 is stronger with 6–4PP than T-T lesion. We used the model oligos for further characterization of the interaction of PARP-1 with UV-damaged DNA. Since the catalytic activation of PARP-1 is more with damaged DNA than with undamaged DNA[14], we examined the extent of activation of PARP-1 with 40mer control or UV-oligo *in vitro* as an additional indicator of the extent of binding of PARP-1 to these DNA. A stronger PARP-1 activation with UV-DNA was observed as compared to control-DNA at two different molar ratios of PARP-1 to DNA (Fig. 5a, left panel). Thus the binding of PARP-1 to UV-lesion caused stronger stimulation of its catalytic activity as compared to its binding to either the 3′ or 5′-ends of both the control and UV-DNA. To compare the capacity of different UV-induced direct damages for activation of PARP-1, we assessed the efficacy of 24mer oligo containing a single chemically synthesized T-T or 6–4PP lesion[30] in the PARP-1 activation assay *in vitro* (Fig. 5a, right panel). Both the DNA containing defined UV-lesions were stronger activator of PARP-1 than the 24mer control-DNA at two different molar ratios of PARP-1 to DNA. Moreover, 6–4PP, which is known to cause a higher degree of helical distortion, was a stronger stimulator of the catalytic activity of PARP-1 than T-T.

Model for the interaction of PARP-1 and DDB2 with UV-damaged DNA. Based on the current results of *in situ* visualization and footprinting of PARP-1 and DDB2 at UV-induced DNA lesion site, we propose

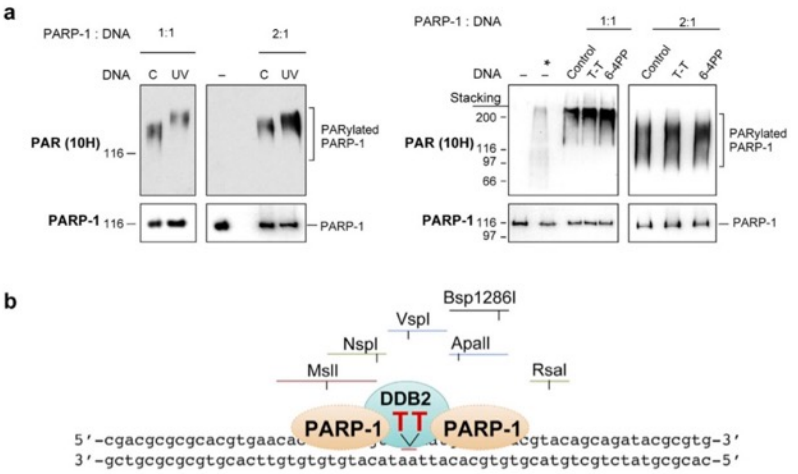

Figure 5. Catalytic activation of PARP-1 with defined UV-damaged DNA and a model for footprint of PARP-1 and DDB2 on UV-lesion site. **(a)** Stimulation of catalytic activity of PARP-1 by various defined UV-damaged DNA *in vitro*. PARP-1 activation assay was performed using 40 mer control or UV-DNA (left panel) or using 24mer DNA with no damage (control) or with a single defined T-T and 6–4PP (right panel) at 1:1 or 1:2 molar ratio of DNA:protein. After resolution on SDS-PAGE, immunoprobing for PARP-1 and PARylated PARP-1 (10H antibody) was carried out. The *refers to the cell extract containing H_2O_2-activated PARP-1. Panel represents one of three identical experiments. **(b)** Model for binding of PARP-1 and DDB2 to the UV-lesion site on 60mer oligo (see Results and Discussion section for details).

that DDB2 attaches directly at the UV-lesion site whereas PARP-1 makes an asymmetric bilateral contact from −12 to +9nt around the lesion (Fig. 5b). This footprint is compatible with either one or two PARP-1 molecules enveloping around the UV-lesion, similar to the reported binding of either one[31] or two[21] PARP-1 molecules at the site of DNA strand breaks. The N-terminal DNA binding domain of PARP-1 that is known to be recruited to DNA strand breaks[20] was also recruited to UV-lesions without strand breaks, indicating more general property of this domain of PARP-1 to bind to different types of DNA damages. Our model is also consistent with previously reported interactions of DDB2 and PARP-1 at the UV-lesion site[5,7]. We have earlier shown that PARP-1 and DDB2 co-immunoprecipitate at the UV-damaged chromatin in the presence of ethidium bromide, indicating their direct interaction on the same DNA strand[7]. Here, we confirm that PARP-1 and DDB2 can co-exist at the UV-lesion site and the presence of DDB2 does not alter the footprint of PARP-1 around the lesion. Our results do not exclude the possibility that PARP-1 footprint may vary when the damaged DNA is in the context of chromatin or when there are multiple UV-lesions in close proximity. We had earlier shown that PARP-1 is weakly activated by UV in the DDB2-deficient XP-E cells, but introduction of DDB2 in these cells strongly stimulates PARP-1 catalytic activity in response to UV[7]. Moreover, we had also observed that DDB2 stimulates catalytic activity of PARP-1 *in vitro* with UV-damaged DNA that largely contains T-T lesions[7], and here we show that PARP-1 activation was much stronger with 6–4PP than with T-T. Since the 6–4PP by itself causes larger distortion of DNA as compared to T-T, whereas the binding of DDB2 to T-T increases the distortion of DNA[26], collectively these results indicate that the extent of DNA distortion could be the determinant for PARP-1 activation with UV-damaged DNA. Our results show that PARP-1 and DDB2 do not prevent access to the lesion site by other repair proteins such as CPD photolyase, and may even be more flexible and accommodating in the *in vivo* conditions as compared to our *in vitro* condition in which damaged DNA is anchored to beads and interacting proteins are cross-linked to the DNA. Together, these two novel assays will open new avenues to study the ever-expanding roles of PARP-1 in NER and housekeeping functions in which PARP-1 shows subtle interactions with DNA without strand breaks.

Material and Methods

Antibodies. For Western blotting: Monoclonal 6–4PP (KTM50) and T-T (KTM53) (1:5,000), polyclonal PARP-1 (1:5,000), PARP-1 monoclonal (F2, 1:500), GFP monoclonal (1:5,000), DDB2 anti goat (1:500), PAR monoclonal (10H, 1:1,000), HRP-conjugated secondary antibodies (1:2,500). For immunocytology: T-T (KTM53, 1:2,000), polyclonal PARP-1 (1:5,000), PARP-1 monoclonal F2 (1:500), PARP-1 monoclonal C2-10 (1:500), F1-23 monoclonal (1:500), DDB2 anti goat (1:200), Rad51 polyclonal (1:500) and secondary fluorescent antibodies (1:500).

Cell culture. Cells were grown in 5% humidified incubator at 37 °C in αMEM medium supplemented with 10% FBS, penicillin and streptomycin and 200 μg/ml hygromycin. The creation of GM637-derived PARP-1 replete GMU6 cells were described earlier[32].

Expression Plasmids. The pGFP-hPARP-1 was a gift from V. Schreiber, pGFP-DBD of PARP-1 was generated by subcloning the 0.7 kb SacI (blunted) and HindIII-fragment of PARP31 cDNA into NheI (blunt)/HindIII sites of pEGFP-N1 plasmid.

Transfection and UVC-irradiation. GMU6 cells were transfected with pEGFP-hPARP-1, pEGFP-DBD-PARP-1 and pEGFP-N1 plasmid using Turbofect reagent. After 24 h, cells were irradiated for global UVC (10 J/m^2) or through polycarbonate filter with 5 μm pores for local (100 J/m^2) UVC[11].

Indirect immunofluorescence detection *in situ*. The cells adherent on the coverslip were processed by one of the three protocols: *C protocol:* After washing with CSK buffer (100 mM NaCl, 300 mM sucrose, 10 mM PIPES pH 6.8, 3 mM $MgCl_2$, 1 mM EGTA), cells were fixed with 3% formaldehyde (10 min, ambient temperature), rinsed with PBS, permeabilized with 100% methanol (−30 °C, 10 min), rinsed with PBS, blocked for 30 min with 5% BSA in PBS-0.1% Triton-X-100 followed by reaction with primary antibodies given below. *C+T protocol:* Cells were washed twice with CSK buffer, extracted with 0.5% Triton in CSK buffer for 8 min at ambient temperature, fixed and blocked as in C protocol. *C+T+S protocol:* After C+T protocol fixation step, cells were washed and extracted with 0.5% Triton in high salt CSK buffer (420 mM NaCl, 300 mM sucrose, 10 mM PIPES pH 6.8, 3 mM $MgCl_2$, 1 mM EGTA) for 20 min on ice. After DNA denaturation in 0.07 N NaOH for 8 min at ambient temperature, immunoprobing was carried out for all three protocols as follows: The cells were incubated for 1 h with primary antibodies in the blocking buffer, washed with PBS containing 0.1% Tween 20 and incubated for 30 min with Alexa 488 or 594-linked secondary antibodies. After washing with PBS-0.1% Tween 20, coverslips were incubated in PBS-0.25 μg/ml DAPI for 5 min and mounted with ProLong Gold Antifade. Images were captured with Zeiss Axiovert 200 and AxioCam MRm and the brightness and contrast were uniformly adjusted across the panels with Photoshop CS5.5. The fluorescent intensity of PARP-1 at the irradiated spots was analyzed with AxioVision 4.7 and corrected for background signal for similar area in the unirradiated zone of nucleus, where specified.

Statistical analyses for immunocytology. Data for intensity of at least 100 foci from three independent experiments were pooled to create mean ± s.e., and subjected to the unpaired two-tailed t-tests to determine the significance of difference. The significant P-values <0.05 are stated in the charts.

Oligos. The ss-24mer oligos with T-T or 6–4PP were chemically synthesized and hybridized with the complementary ss-24mer to get 24mer ds oligo with T-T or 6–4PP lesions. The creation of 40 or 60mer oligos are described in Figs. 3a, 4c, and Supplementary Fig. S2a.

VspI-purification of 25 kJ/m^2 UVC irradiated oligo. The UVC irradiated 40mer or 60mer ds oligos were digested with VspI for 1 h at 37 °C, followed by VspI-inactivation at 65 °C for 5 min. The VspI-resistant 40 or 60mer UV-DNA were separated on 12% PAGE from the digested fragments of DNA without UV-damage, cut from the gel and eluted with PAGE elution buffer (0.5 M ammonium acetate, 10 mM magnesium acetate and 1 mM EDTA) overnight at 37 °C. The eluted UV-DNA were cleaned by passage through ULTRAFREE–DA filter units, concentrated in Microcon YM-10 followed by purification in Zymo Research oligo clean and concentrator columns.

The protein-DNA interactions, restriction mapping and CPD photolyase assays for bead-bound oligos with proteins. The control or UV-DNA with biotin tag was immobilized on Dynabeads MyOne streptavidin T1. (i) The binding of PARP-1 or DDB2 to control or UV-oligos immobilized on the magnetic streptavidin beads: The bead-bound oligos (50–100 ng) were reacted with PARP-1 or DDB2 at 1:1 or 1:2 molar ratio. PARP-1 was reacted at 25 °C for 15 min in 10 μL of Na-PO_4 reaction mixture (20 mM of Na-PO_4 buffer pH 7.4, 5 mM $MgCl_2$, 150 mM NaCl, 5% glycerol, 1 mM DTT, 0.01% Triton, 20 μM Zn-acetate and 1× protease inhibitor). DDB2 was reacted at 25 °C for 30 min in Tris reaction mixture (100 mM Tris buffer pH 8.0, 10 mM $MgCl_2$, 10% glycerol, 150 mM NaCl, 1.5 mM DTT and 1× protease inhibitor). The simultaneous binding of PARP-1 and DDB2 was carried out in Tris reaction mixture for 15 min at 25 °C. The unbound proteins were removed and the bound proteins were crosslinked to oligo with 1% formalin in Na-PO_4 reaction mixture for 10 min at ambient temperature. After quenching formalin with 250 mM Tris-HCl pH 8.0, the beads were washed twice with Tris-reaction mixture and subjected to following steps.

(ii) Assessment of binding of proteins with DNA: The proteins that were attached to bead-bound DNA were extracted with Laemmli buffer at 95 °C for 10 min. The eluted proteins were resolved on SDS-PAGE for immunoblotting of the protein. The band quantification for immunoblots was carried out with ChemiGenius 2 using SynGene software.

(iii) Restriction protection assay of protein-bound oligos: For the restriction protection assay, the magnetic streptavidin beads bound control or UV-DNA with or without bound protein were digested with the specified Fast-digest or CutSmart restriction enzyme in 10 μL reaction buffer at 37 °C for specified time. The DNA fragments released in the supernatant were resolved on 10–15% native PAGE and stained with gel red for identification and quantification with ChemiGenius2 using SynGene software. The relative band intensities were derived by comparing the intensities of the fragments released from the protein-bound DNA with that from protein-free

DNA. The significance was calculated by unpaired two-tailed t-test and the P values <0.05 were considered significant.

(iv) CPD photolyase repair assays: The bead-bound UV-DNA with or without attached proteins was split into two aliquots; one subjected to repair by CPD photolyase and the other was mock-treated. The CPD repair was carried out in 20 μL CPD photolyase binding mix (20 mM Tris buffer pH 7.5, 1 mM DTT, 0.2 mg/ml BSA, 125 mM NaCl) with 0.2 μL Oryza sativa CPD photolyase and incubated for 15 min in dark at ambient temperature, followed by exposure for 15 min to UVA (Spectrolinker XL-1500, 363 nm, 15 watts). DNA was eluted with 95% formamide, 10 mM EDTA pH 8.0 for 5 min at 95 °C, dot-blotted on the Hybond N^+ and probed for T-T.

PARP-1 activation assay *in vitro*. In a 10 μL reaction mixture containing 100 mM Tris-HCl pH 8.0, 10 mM $MgCl_2$, 10% glycerol, 1.5 mM DTT, 1× protease inhibitor and 10 μM NAD, purified PARP-1 was reacted at 25 °C for 30 min with specified DNA for each reaction. After adding an equal volume of 2× Laemmli buffer, samples were resolved on SDS-PAGE and immunoblotted for PAR (10H) and PARP-1 [14].

Immuno-Dot-blot. DNA samples were heated at 95 °C for 5 min, chilled on ice for 5 min and adjusted to final concentration of 6× SSC. Samples were dot-blotted on Hybond N+ membrane, baked at 80 °C for 1–2 h and processed for antibody probing.

References

1. Robert, I., Karicheva, O., Reina San Martin, B., Schreiber, V. & Dantzer, F. Functional aspects of PARylation in induced and programmed DNA repair processes: Preserving genome integrity and modulating physiological events. *Mol. Aspects Med.* **34,** 1138–1152 (2013).
2. Pascal, J. M. & Ellenberger, T. The rise and fall of poly(ADP-ribose): An enzymatic perspective. *DNA Repair (Amst)* **32,** 10–16 (2015).
3. Kim, M. Y., Mauro, S., Gevry, N., Lis, J. T. & Kraus, W. L. NAD+-dependent modulation of chromatin structure and transcription by nucleosome binding properties of PARP-1. *Cell* **119,** 803–814 (2004).
4. Ghodgaonkar, M. M., Zacal, N. J., Kassam, S. N., Rainbow, A. J. & Shah, G. M. Depletion of poly(ADP-ribose) polymerase-1 reduces host cell reactivation for UV-treated adenovirus in human dermal fibroblasts. *DNA Repair (Amst)* **7,** 617–632 (2008).
5. Pines, A. *et al.* PARP1 promotes nucleotide excision repair through DDB2 stabilization and recruitment of ALC1. *J. Cell Biol.* **199,** 235–249 (2012).
6. Luijsterburg, M. S. *et al.* DDB2 promotes chromatin decondensation at UV-induced DNA damage. *J. Cell Biol.* **197,** 267–281 (2012).
7. Robu, M. *et al.* Role of poly(ADP-ribose) polymerase-1 in the removal of UV-induced DNA lesions by nucleotide excision repair. *Proc. Natl. Acad. Sci. USA* **110,** 1658–1663 (2013).
8. King, B. S., Cooper, K. L., Liu, K. J. & Hudson, L. G. Poly (ADP-ribose) contributes to an association between Poly(ADP-ribose) polymerase-1 and Xeroderma pigmentosum complementation group A in nucleotide excision repair. *J. Biol. Chem.* **287,** 39824–39833 (2012).
9. Fischer, J. M. *et al.* Poly(ADP-ribose)-mediated interplay of XPA and PARP1 leads to reciprocal regulation of protein function. *FEBS J.* **281,** 3625–3641 (2014).
10. Maltseva, E. A., Rechkunova, N. I., Sukhanova, M. V. & Lavrik, O. I. Poly(ADP-ribose) polymerase 1 Modulates Interaction of the Nucleotide Excision Repair Factor XPC-RAD23B with DNA via Poly(ADP-ribosyl) ation. *J. Biol. Chem.* **290,** 21811–21820 (2015).
11. Vodenicharov, M. D., Ghodgaonkar, M. M., Halappanavar, S. S., Shah, R. G. & Shah, G. M. Mechanism of early biphasic activation of poly(ADP-ribose) polymerase-1 in response to ultraviolet B radiation. *J. Cell Sci.* **118,** 589–599 (2005).
12. Berger, N. A. & Sikorski, G. W. Poly(adenosine diphosphoribose) synthesis in ultraviolet-irradiated xeroderma pigmentosum cells reconstituted with Micrococcus luteus UV endonuclease. *Biochemistry* **20,** 3610–3614 (1981).
13. Kawamitsu, H. *et al.* Monoclonal antibodies to poly(adenosine diphosphate ribose) recognize different structures. *Biochemistry* **23,** 3771–3777 (1984).
14. Shah, G. M. *et al.* Approaches to detect PARP-1 activation *in vivo*, *in situ*, and *in vitro*. *Methods Mol. Biol.* **780,** 3–34 (2011).
15. Mirzoeva, O. K. & Petrini, J. H. DNA damage-dependent nuclear dynamics of the Mre11 complex. *Mol. Cell. Biol.* **21,** 281–288 (2001).
16. Balajee, A. S. & Geard, C. R. Chromatin-bound PCNA complex formation triggered by DNA damage occurs independent of the ATM gene product in human cells. *Nucleic Acids Res.* **29,** 1341–1351 (2001).
17. Zhu, Q. *et al.* Chromatin restoration following nucleotide excision repair involves the incorporation of ubiquitinated H2A at damaged genomic sites. *DNA Repair* **8,** 262–273 (2009).
18. Fey, E. G., Wan, K. M. & Penman, S. Epithelial cytoskeletal framework and nuclear matrix-intermediate filament scaffold: three-dimensional organization and protein composition. *J. Cell Biol.* **98,** 1973–1984 (1984).
19. Kaufmann, S. H. *et al.* Association of poly(ADP-ribose) polymerase with the nuclear matrix: the role of intermolecular disulfide bond formation, RNA retention, and cell type. *Exp. Cell Res.* **192,** 524–535 (1991).
20. Mortusewicz, O., Ame, J. C., Schreiber, V. & Leonhardt, H. Feedback-regulated poly(ADP-ribosyl) ation by PARP-1 is required for rapid response to DNA damage in living cells. *Nucleic Acids Res.* **35,** 7665–7675 (2007).
21. Ali, A. A. *et al.* The zinc-finger domains of PARP1 cooperate to recognize DNA strand breaks. *Nat. Struct. Mol. Biol.* **19,** 685–692 (2012).
22. Hall, R. K. & Larcom, L. L. Blockage of restriction endonuclease cleavage by thymine dimers. *Photochem. Photobiol.* **36,** 429–432 (1982).
23. Cleaver, J. E. Restriction enzyme cleavage of ultraviolet-damaged simian virus 40 and pBR322 DNA. *J. Mol. Biol.* **170,** 305–317 (1983).
24. Wittschieben, B. O., Iwai, S. & Wood, R. D. DDB1-DDB2 (xeroderma pigmentosum group E) protein complex recognizes a cyclobutane pyrimidine dimer, mismatches, apurinic/apyrimidinic sites, and compound lesions in DNA. *J. Biol. Chem.* **280,** 39982–39989 (2005).
25. Clark, N. J., Kramer, M., Muthurajan, U. M. & Luger, K. Alternative modes of binding of poly(ADP-ribose) polymerase 1 to free DNA and nucleosomes. *J. Biol. Chem.* **287,** 32430–32439 (2012).
26. Fischer, E. S. *et al.* The molecular basis of CRL4DDB2/CSA ubiquitin ligase architecture, targeting, and activation. *Cell* **147,** 1024–1039 (2011).
27. Menissier-de Murcia, J., Molinete, M., Gradwohl, G., Simonin, F. & de Murcia, G. Zinc-binding domain of poly(ADP-ribose) polymerase participates in the recognition of single strand breaks on DNA. *J. Mol. Biol.* **210,** 229–233 (1989).
28. Sancar, A. & Sancar, G. B. DNA repair enzymes. *Annu. Rev. Biochem.* **57,** 29–67 (1988).
29. Fitch, M. E., Nakajima, S., Yasui, A. & Ford, J. M. *In vivo* recruitment of XPC to UV-induced cyclobutane pyrimidine dimers by the DDB2 gene product. *J. Biol. Chem.* **278,** 46906–46910 (2003).

30. Hendel, A., Ziv, O., Gueranger, Q., Geacintov, N. & Livneh, Z. Reduced efficiency and increased mutagenicity of translesion DNA synthesis across a TT cyclobutane pyrimidine dimer, but not a TT 6–4 photoproduct, in human cells lacking DNA polymerase eta. *DNA Repair (Amst)* **7,** 1636–1646 (2008).
31. Langelier, M. F. & Pascal, J. M. PARP-1 mechanism for coupling DNA damage detection to poly(ADP-ribose) synthesis. *Curr. Opin. Struct. Biol.* **23,** 134–143 (2013).
32. Shah, R. G., Ghodgaonkar, M. M., Affar el, B. & Shah, G. M. DNA vector-based RNAi approach for stable depletion of poly(ADP-ribose) polymerase-1. *Biochem Biophys Res Commun* **331,** 167–174 (2005).

Acknowledgements

We are thankful to V. Schreiber for GFP-PARP-1, K. Hitomi for the CPD photolyase and J. Brind'Amour for creating cDNA for GFP-DBD. We thank M. Miwa, National Cancer Center Research Institute, Tokyo, for permission to receive 10H hybridoma through the Riken cell bank. This work was supported equally by the two grant to GMS: Discovery Grant 155257-2011 from NSERC, Canada and Grant IMH-131569 from the Canadian Institutes of Health Research: Priority Announcement of Musculoskeletal Health, Arthritis, Skin and Oral Health. The work related to the site-specifically modified oligonucleotides was supported by the National Institutes of Health Grant CA-168469 to NEG. NP received the scholarship support from Quebec Government and Shastri Indo-Canadian Institute from foreign student fee waiver program and MR received graduate scholarship from the Fonds de recherche du Québec-Santé.

Author Contributions

The first three authors (N.K.P., M.R. and R.G.S.) contributed equally to performing all the experiments and preparing the figures. N.E.G. provided material support and guidance in planning the experiments with synthetically defined UV-damaged oligo. All authors contributed towards writing and reviewing the manuscript.

Additional Information

Supplementary information accompanies this paper at http://www.nature.com/srep

Competing financial interests: The authors declare no competing financial interests.

How to cite this article: Purohit, N. K. *et al.* Characterization of the interactions of PARP-1 with UV-damaged DNA *in vivo* and *in vitro*. *Sci. Rep.* **6,** 19020; doi: 10.1038/srep19020 (2016).

Annexe 2: Comprehensive measurement of UVB-induced non-Melanoma skin cancer burden in mice using photographic images as a substitute for the caliper method

PLOS ONE

RESEARCH ARTICLE

Comprehensive measurement of UVB-induced non-melanoma skin cancer burden in mice using photographic images as a substitute for the caliper method

Marc Bazin, Nupur K. Purohit, Girish M. Shah*

Laboratory for Skin Cancer Research, CHU-Q (CHUL) Quebec University Hospital Research Centre, Laval University, Québec City, Québec, Canada

* girish.shah@crchul.ulaval.ca

Citation: Bazin M, Purohit NK, Shah GM (2017) Comprehensive measurement of UVB-induced non-melanoma skin cancer burden in mice using photographic images as a substitute for the caliper method. PLoS ONE 12(2): e0171875. doi:10.1371/journal.pone.0171875

Editor: Amanda Ewart Toland, Ohio State University Wexner Medical Center, UNITED STATES

Received: November 1, 2016

Accepted: January 26, 2017

Published: February 10, 2017

Data Availability Statement: All relevant data are within the paper and its Supporting Information files.

Funding: This work was supported by the grants to GMS from Natural Sciences and Engineering Research Council of Canada (Discovery Grants # RGPIN-2016-05868 and Discovery Accelerator Grant # RGPAS-492875-2016). NKP received a foreign student fee-waiver scholarship from Quebec Government and Shastri Indo-Canadian

Abstract

The vernier caliper has been used as a gold standard to measure the length, width and height of skin tumors to calculate their total area and volume. It is a simple method for collecting data on a few tumors at a time, but becomes tedious, time-consuming and stressful for the animals and the operator when used for measuring multiple tumors in a large number of animals in protocols such as UVB-induced non-melanoma skin cancer (NMSC) in SKH-1 mice. Here, we show that photographic images of these mice taken within a few minutes under optimized conditions can be subjected to computerized analyses to determine tumor volume and area as accurately and precisely as the caliper method. Unlike the caliper method, the photographic method also records the incidence and multiplicity of tumors, thus permitting comprehensive measurement of tumor burden in the animal. The simplicity and ease of this method will permit more frequent monitoring of tumor burden in long protocols, resulting in the creation of additional data about dynamic changes in progression of cancer or the efficacy of therapeutic intervention. The photographic method can broadly substitute the caliper method for quantifying other skin pathologies.

Introduction

In mouse models that examine the causes and cures of chronic ultraviolet B (UVB)-induced non-melanoma skin cancers (NMSC), the tumor burden is quantified as the incidence (proportion of mice with or without tumor), multiplicity (number of tumors), tumor area and tumor volume [1–7]. While the first two parameters are visually noted and recorded, the last two parameters are measured using the vernier caliper, which is a simple yet accurate instrument to manually measure the length, width and height of tumors. The use of digital calipers with 0.01 mm accuracy is perfect for collecting data for one or two tumors per animal and for few animals at a time. However, it becomes time-consuming and challenging for measuring dimensions of hundreds of tumors. For example, the chronic UVB-irradiated SKH-1 albino hairless mice develop numerous papillomas, keratocanthomas, carcinomas-in-situ and

Institute. NKP was also a recipient of the graduate scholarships from the Neuroscience Axis of CR-CHU-Q. The funders had no role in study design, data collection and analysis, decision to publish, or preparation of the manuscript.

Competing interests: The authors have declared that no competing interests exist.

carcinomas over a period of 10–40 weeks; and caliper method would take 5–30 min per mouse and several days for each cycle of measurement for a large number of mice. Moreover, the repetitive and tedious nature of this work and stress-related movements of forcibly restrained mice increase the chances of errors in caliper measurement. Therefore, although frequent measurement of tumor dimensions throughout the NMSC protocol would provide valuable information about the dynamic state of the disease, few studies report weekly or biweekly measurement of tumor volume [2, 3], while most studies measure tumor volume only at the end of the protocol [4–7]. Some studies do not measure smaller tumors [1, 8] or height of the tumors [1, 9], while others do not report any measurement of tumor size but only the incidence [10]. All these studies produced valid data, but availability of a convenient yet accurate and reproducible alternative to caliper method would permit frequent measurement of tumor area and volume revealing more information about the disease.

In subcutaneous tumor models, the magnetic resonance imaging [11] or ultrasound imaging [12] were shown to be more accurate in measuring tumor volume than caliper method. However, these techniques would be expensive, require each mouse to be anesthetised and impractical for NMSC protocol with large number of mice. In studies related to healing of skin wounds, the area measurements are made with a foot-ruler or tracing of wound shapes on transparent sheets with a grid and scale-pattern, or by spectrophotogrammetry or spectophotography methods that use multiple cameras or video-camera with customized software in a special equipment [13–16]. For NMSC measurement, the transparency method would not save much time over caliper method, and photo or videography-based methods would be costly and perhaps even more time consuming than caliper method. Nonetheless, the photographic methods were more accurate in measurement of wound area, and an earlier NMSC study reported use of photography to determine tumor area [9], although the technique was not validated with caliper method, and it did not report tumor volume possibly because height could not be measured in their technique. Here, we provide detailed description of a fully validated simple photography method that allows measurement of area and volume of skin tumors as accurately as the caliper method, while avoiding potentially error-inducing limitations of the caliper method. This method also permits measurement of the incidence and multiplicity of tumors, thus providing a comprehensive method to measure tumor burden in UVB-induced NMSC protocols, and could broadly substitute caliper method for quantifying other skin pathologies.

Materials and methods

Chronic UVB-induced NMSC in SKH-1 hairless mice

All animal studies were approved by the Animal Protection Committee of Laval University and were conducted by the personnel who were trained and certified for animal work. The 5-week old SKH-1 albino hairless mice obtained from Charles River Canada were irradiated thrice a week for 20 weeks at 800 J/m^2 UVB (280–320 nm). Five weeks after last irradiation, mice were sacrificed under anaesthesia with isoflurane followed by exposure to CO_2 and cervical dislocation. The unrestrained mice were irradiated in an open cage placed in a Spectrolinker XL-1500 (Spectronics Corp.) equipped with six 15W UVB tube-lights, which delivered 800 J/m^2 within 2 to 3 min at a flux of 5.9 J/m^2/sec. During irradiation, the cages were covered from the top with a Kodacel filter to remove the contaminating UVC radiations (230–280 nm) [17]. The UVA wavelengths (320–400 nm) accounted for 20% of the energy, as measured by UVX radiometer (UVP Inc.) equipped with UV-A, B and C-specific probes. Mice were monitored weekly for tumor burden, as described below.

Caliper method to measure tumor dimensions

The tumors were visible from 12–15 weeks and all data presented in this study are from measurements between 20 to 25 weeks. The pre-neoplastic foci that persisted and progressed over time to form proper tumors were taken into account for the final tumor burden. In contrast, very few cysts that appeared on the skin were identified and excluded from data sets as they either did not change in appearance or disappeared in few weeks. Mice were held in hand for measuring all three dimensions of each tumor using the digital caliper with 0.01 mm precision (Mitutoyo). The length was measured along its longest linear dimension on the skin and the width was measured along the axis perpendicular to the length axis. The height was measured at the tallest point of the tumor. For the length and width that are measured along the flat skin, we could maintain the accuracy of 0.1 mm. However, the heights below 0.5 mm posed practical difficulties in judging accurate placement of the caliper jaws from skin to the top of the tumor; therefore using visual cues and caliper readout, the near-flat tumors were assigned 0.1 mm height and progressively raised tumors were assigned 0.25 or 0.5 mm heights. All heights above 0.5 mm were actual caliper readouts. Assuming hemi-ellipsoidal shape of the tumors, the tumor burden was determined as the area ($\frac{\pi}{4} \times length \times width$) and volume ($\frac{\pi}{6} \times length \times width \times height$) [6]. The statistical difference in values by two methods was derived using Origin Pro 2015 with the Wilcoxon signed rank test.

Photographic method to measure tumor dimensions

Photography set-up for mice in laminar hood. The measurement of tumor dimensions with photographs requires a set-up with known distances from the camera to the mouse skin and reference scale-bars, as well as an environment that keeps the mouse calm for few minutes to take the pictures of the tumors (Fig 1A). We used a laminar flow cabinet open on both sides for the ease of operations by two persons standing on either side of the cabinet. The cabinet was illuminated with diffused light from a top fluorescent lamp and two 5000 K fluorescent tubes from the sides. We designed a stand that permitted the camera to be steadily positioned so that the lens of the camera was exactly 130 mm above the frosted glass plate that was placed in the cabinet on top of a black paper and two rulers that would flank the mouse in the picture (Fig 1B). Since mouse becomes restless on the glass that does not provide any grip for their paws, we affixed a broad grid fabric tape on which mouse could obtain a secure grip and remain steady for the duration of the photography session. We used a reflex Canon EOS Rebel T5 camera equipped with a Canon EFS 24 mm lens having a fixed focal length and took all the pictures without flash. To avoid shaking the camera or alarming the mouse with hand movement, the pictures were taken using a commercially available remote shutter control cable for the camera.

Photography of mice. The mouse was gently placed over the glass plate and the tail was slightly tugged, which resulted in a relatively stable posture of the mouse with a straight spine and nearly flat dorsal skin containing almost all the tumors. In this situation, the tumors on back of mouse were at an average distance of 104 mm from the camera, whereas the reference scales below the glass plate were at 130 mm from the camera; and these two values were taken into account for calculation of scale factor in images (Fig 1B). Within 30 seconds, 3–5 top view pictures were taken without flashlight that would allow measurement of length and width (Fig 2A, top image). The camera was then removed from the stand to rapidly take several profile pictures of the mouse within 2 min from various angles that would allow measurement of heights of tumors (Fig 2A, bottom images). For profile pictures, it was impractical to use vertical scales or keep a fixed distance between camera and the tumors, as this would unduly

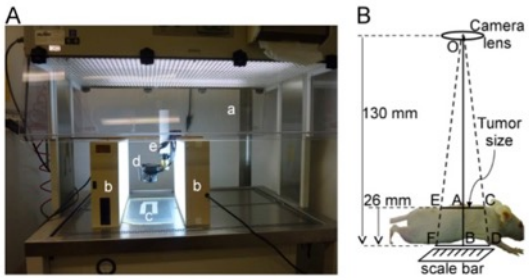

Fig 1. The optimized photography set-up for imaging mice. (A) The photography set-up. In a laminar flow cabinet with dual opening (a), illuminated by two additional fluorescent lights on the side (b), mice were placed one at a time on a frosted glass plate with a broad-grid fabric tape that was positioned above black paper and two scale bars (c). The remote shutter controlled camera (d) was positioned 130 mm above the glass plate on a telescopic support (e). **(B)** Representation of the imaging set-up with distances. The camera lens (O) was placed 130 mm above the glass plate, which resulted in a height difference of 26 mm between the scale bar below the glass plate (BD) and tumor (AC) on the dorsal skin of the mouse from the camera lens. The length or width dimension of the tumor (AC) was calculated using Thales' theorem to determine the scale factor of OA/OB = 0.8 = AC/BD. Since tumors were distributed broadly over the dorsal skin of the mouse, each tumor was carefully calibrated against the nearest portion of the scale bar for better accuracy of measurement. For example, the tumors in EC region of the skin were calibrated against FD segment of the scale.

doi:10.1371/journal.pone.0171875.g001

prolong picture session. Moreover, the distances in profile pictures could be calibrated against the top picture, as described below.

Measurement of the length, width and height of tumors from the top and profile pictures. We used freely available AxioVision SE64-4.9.1 image analysis software (Zeiss) to process the pictures for determining the tumor dimensions, although any other image analyses software that allows correlation of pixel distances in the pictures with actual size based on a scale bar in the same picture is suitable for this analysis. For each mouse, the top picture with scale bars was analyzed first to establish the correlation of pixel to distance in mm using Scaling wizard function in the "Measure/Scaling" menu of the software (Fig 2A, top image). A scale correction factor of 0.8 was applied to account for the difference in the distance from camera to the tumors (OA = 104 mm) and the nearest scale bar (OB = 130 mm) as per Thales' intercept theorem that OA/OB = AC/BD, where AC is the tumor dimension on the back of mouse and BD is the distance on the scale below the glass plate (Fig 1B). The calibrated pixel distance in the picture allowed measurement of length and width of the tumor using the measure "length" menu of the software (Fig 2A). The photographic method with zooming of pictures on the computer screen allowed better definition of the tumor boundaries and more accurate measurement of distances. For profile pictures, since scale bars and distances were not fixed, we calibrated the pixel distance of either the length or width of the tumor in profile image with the known value of this parameter in the top picture and used the revised scale to measure height of the tumor in the profile picture (Fig 2A, circled images of tumors #b and c in top and profile images). For multiple tumors in close proximity, the calibration made with one tumor could be easily applied to measure dimensions of other tumors of similar size. The area and volume of tumors and statistical analyses were carried out as described for caliper method. The average time for measuring dimensions of a single tumor on the computer by the photography method was about 1–2 min, which is similar to the time required for the caliper method. However, for a mouse with 30 tumors, the actual photography session with mouse would take about 3 min and tumor measurements on computer would be about 30–60 min,

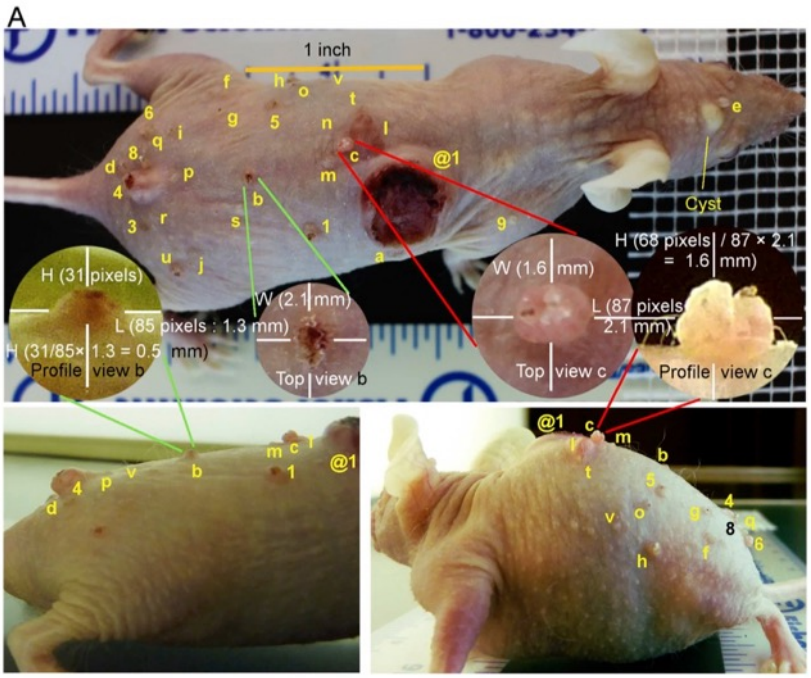

Fig 2. Measurement of tumor dimensions and total tumor burden in mice by two methods. (A) Top and profile view pictures of a mouse with multiple UVB-induced skin cancers for photographic method of measuring tumor dimensions. The top views of the mouse with scale bars (top image) were used for detecting tumors (incidence) and for counting the tumors to determine the multiplicity. The magnified images of individual tumors from top view, as shown here for tumors # b and c, were used for measuring the length and width of tumors. The profile pictures of the mouse (bottom images) allowed measurement of heights of all tumors, as shown here for encircled magnified images of these two tumors in different profile images. The calibration of pixel to distance in profile pictures was achieved by comparing either the length or width

dimension of a given tumor in both top and profile magnified images. The newly calibrated pixel distances in profile picture now allowed accurate measurement of height of this tumor in profile images. The cysts such as the one seen between eyes were identified as described in the caliper method were excluded in tumor counts. **(B)** Comparison of time-course of increasing total tumor burden (area) in mice as measured by the caliper and photography methods. The total tumor burden (area) in three different mice was monitored from 20 to 25 weeks of the protocol by caliper and photography methods.

doi:10.1371/journal.pone.0171875.g002

whereas in the caliper method, the entire period of 30–60 min would have to be spent with a mouse in hand.

Results

Photographic method accurately reflects caliper method for total tumor burden in terms of area and volume per mouse

In a single mouse with 30 tumors of different sizes, the photographic and caliper methods were used for measuring length, width and height of each tumor (Fig 1A). Evidently, the top picture of the mouse enlarged on the computer screen allowed us to note the tumor incidence and identify and count tumor multiplicity. The three dimensions of each tumor were used for determining total tumor volume and area by each method. Both the methods produced statistically similar values for total tumor burden, measured as total area or volume of all the tumors in the mouse (Table 1 and S1 Table). To examine whether photographic method was accurate for all sizes of tumors, we sorted these tumors by volume as small (<2 mm^3) or large (>2 mm^3); and observed that the photography and caliper methods once again produced statistically similar total collective volume or area for small or large size tumors (Table 1, bottom panel). We noted that volume of individual smaller tumors often differed significantly between two methods because of differences in height rather than length or width values (S1 Table). This could be attributed to approximation of heights assigned to smaller tumors below 0.5 mm in caliper method (see Materials and Methods), whereas the photographic method using enlarged images allowed precise determination of heights below 0.5 mm. Nonetheless, the global impact of the differences in heights of smaller tumors by two methods was negligible to the total tumor burden on the mouse, which is mostly determined by larger tumors. Thus, photographic method allowed measurement of all four parameters of tumor burden, namely the incidence, multiplicity, area and volume, with last two parameters accurately reflecting the values obtained by the caliper method.

The individual volume and area measurements of 30 tumors were derived from the data of all three dimensions of each tumor by both the methods as shown in S1 Table. The small and large tumors (2 mm cut-off by caliper volume) are separated by a double-line. The two methods were compared for measuring the total volume or area for all (n = 30), small (n = 24) or large (n = 6) tumors. The statistical significance of difference between two methods was calculated using Wilcoxon signed rank test.

To confirm our observation that the tumor dimensions measured by photographic method are comparable to those measured by caliper; we examined total tumor area in five additional mice by both the methods. The mice had variable tumor area that ranged from 34 to 200 mm^2. Once again the photography method produced statistically similar tumor burden data as the caliper method for each mouse (Table 2 and S2 Table).

Total tumor area for 6 mice was calculated from the length and width of all tumors measured by the caliper and photographic methods. The data for individual tumors in each mouse is shown in S2 Table. The differences between two methods for total tumor burden varied from 0.05–6.5%, but it was statistically not different, as determined by Wilcoxon signed rank test.

Table 1. Comparison of tumor volume and area of 30 tumors by caliper and photographic methods.

	Volume (mm^3)		Area (mm^2)	
Tumor ID	**Caliper**	**Photography**	**Caliper**	**Photography**
v	0.05	0.08	0.82	0.57
o	0.07	0.28	1.04	1.41
j	0.09	0.09	1.38	1.41
3	0.13	0.13	1.88	1.90
r	0.14	0.04	0.85	0.57
m	0.16	0.30	0.95	1.13
9	0.17	0.19	0.50	0.95
8	0.18	0.35	1.10	1.33
i	0.22	0.31	1.30	1.56
n	0.22	0.04	1.33	0.63
p	0.27	0.45	1.63	1.70
g	0.46	0.65	1.38	2.42
e	0.55	0.90	0.64	1.13
t	0.79	0.37	2.36	1.84
a	0.85	1.20	5.09	4.52
8	0.89	1.27	0.64	0.95
l (letter)	0.98	1.35	5.87	6.74
q	1.07	1.33	1.34	1.53
f	1.23	0.80	1.84	2.00
5	1.39	0.66	2.97	2.47
h	1.65	1.42	2.47	2.67
b	1.72	0.71	3.68	2.14
d	1.76	1.68	2.94	2.51
1	1.85	1.91	3.97	4.08
u	2.17	1.76	3.61	3.30
6	2.26	2.40	2.26	2.40
c	2.67	2.81	2.67	2.64
k	3.18	3.36	5.96	5.61
4	35.26	31.76	19.59	17.01
@1(2+7)	276.08	274.66	118.32	121.17
All tumors n = 30	338.5	333.3	200.4	200.3
% Difference	1.5%		0.05%	
P-value	0.98		0.97	
Small tumors n = 24, <2 mm^3	16.9	16.5	48.0	48.2
% Difference	0.2%		0.4%	
P-value	0.23		0.84	
Large tumors n = 6, >2 mm^3	321.6	316.8	152.4	152.1
% Difference	1.5%		0.2%	
P-value	0.44		0.69	

doi:10.1371/journal.pone.0171875.t001

Finally, we compared the two methods for measuring the changes in total tumor burden in three mice over a period of six weeks (Fig 2B). Although the total tumor area changed in each mouse by 5–7 fold from 20^{th} to 25^{th} week, both the methods produced similar values for total tumor burden at three different time-points in this period. Thus the photography method produced total tumor burden data similar to the caliper method in multiple mice carrying

Table 2. Comparison of total tumor burden on 6 mice using photographic and caliper methods.

Mouse #	Number of tumors	Total area by caliper (mm^2)	Total area from photography (mm^2)	*P-value*	% Difference
1151	10	34.3	33.0	0.30	3.9%
1154	17	132.3	140.9	1	6.5%
1157	12	43.4	458	0.31	5.4%
1158	22	67.5	68.7	0.36	1.7%
1152	24	69.9	72.5	0.30	3.7%
1680	30	200.4	200.3	0.97	0.05%

doi:10.1371/journal.pone.0171875.t002

Table 3. Accuracy and precision of the photography and caliper methods.

		Small tumor (~1 mm length)		Large tumor (~5 mm length)	
		Caliper	Photography	Caliper	Photography
Mean Length (mm)		1.03	1.04	5.36	5.32
Standard Deviation		0.16	0.10	0.19	0.10
Precision	Relative standard variation	15.9	9.30	3.50	1.90
Accuracy	(Photography/Caliper) × 100	100.97		99.30	

doi:10.1371/journal.pone.0171875.t003

different sizes of tumors and for assessing growth of the same set of tumors over several weeks in a given mouse.

Accuracy and precision of photography and caliper methods

Next, we compared the accuracy and precision of photography and caliper method by taking 10 replicate measures of the length of a small tumor (~1 mm) and a medium size tumor (~5 mm) by two methods (Table 3 and S3 Table). The average length from 10 measurements by photography method accurately reflected within 1% the average length derived by the caliper method. The precision of a method refers to the reproducibility of result in repeated measurements, and this is derived from relative standard deviation of replicate values (SD / mean × 100) with lower value showing greater precision. The relative standard deviation values revealed that measurements by both the methods were less precise with smaller tumors as compared to larger tumors. Interestingly, the photography method showed better precision than the caliper method for both 1 and 5 mm dimensions. In summary, if caliper is the gold standard for measurement of tumor dimensions, then photography method accurately and precisely measures the true dimensions of the tumors.

The length of a small and medium size tumors were measured 10 times by the same operator under optimum conditions, and averages shown here were derived from the dataset shown in S3 Table. Accuracy of photography method was reflected in providing average length value that is very close to the mean obtained by the caliper method. The precision was derived from the relative standard deviation of repeat measures (SD as % of mean value), which decreases when precision increases.

Discussion

Our results clearly show that the photographic method is simple, cheap and accurate alternative to the caliper method for measuring tumor burden in terms of area and volume of all sizes of NMSC. In addition, the photographs allow measurement of the incidence as well as multiplicity of tumors, thus providing a comprehensive measure of tumor burden in the animal. Most importantly, our photography method allows measurement of the tumor height and

therefore the tumor volume. Since height of NMSC often indicates its degree of progression, measuring the actual height of each tumor has an advantage of integrating the severity of cancer in the volume data. The biggest advantage of photography method is that it splits the total task of caliper method in two distinct components. The first one involves handling of the animals to collect raw data in the form of pictures which are taken within few minutes; while the second task of tumor dimension measurement is handled away from the animals and using computerized methods which can be performed at any other time by the operator who handled the animal or by anybody else with computer skills. Thus, a quick photo session is less stressful to the animal and decreases the operator fatigue. Moreover, the photography method offers more reproducibility and accuracy than the caliper method in volume measurement of even smaller tumors with heights below 0.5 mm. In our experience, the operators who are properly trained in both the methods are able to generate unbiased data for total tumor volume or area from multiple tumors that differ by less than 5% between two methods for each mouse. Thus, while being as accurate as the caliper method, photographic method avoids major error-inducing factors of caliper method even when used for measuring the tumor burden in a large number of animals.

The photography method offers additional advantages, such as reducing the cost associated with using the animal house facilities during long hours of caliper measurement in time-shared laminar flow cabinets. The splitting of tasks for animal handling for picture session and computerized measurement of tumor dimensions permits better work distribution and time-management among personnel with animal and computer skills. Most importantly, the photographs serve as a permanent record of data for regulatory purposes, and could be subjected to repeated analyses for verification or correction of data, as well as for any additional analyses in future. A series of weekly photographs during the protocol could provide useful data for determining the growth rate of tumors from pre-neoplastic foci to full tumors or for regression of tumors in response to therapy. Among few limitations of photography method is the need for a skilled photographer and a well-trained person in computer skills for dimension measurement, as well as the creation of simple photography set-up in the animal facility. In view of its simplicity, the photography method would also be suitable for quantification of skin lesions in the models of melanoma, subcutaneous tumors, wound healing, inflammatory responses and other pathologies of skin.

Supporting information

S1 Table. Three dimensions of 30 individual tumors measured by the caliper and photography methods.
(DOCX)

S2 Table. The total tumor area (mm^2) by the caliper (C) and photography (P) methods for six mice bearing 10–30 tumors.
(DOCX)

S3 Table. Ten replicate measurements of length of a small and a medium size tumor to determine accuracy and precision of the photography and caliper methods.
(DOCX)

Acknowledgments

NKP received a foreign student fee-waiver scholarship from Quebec Government and Shastri Indo-Canadian Institute. NKP was also a recipient of the graduate scholarships from the Neuroscience Axis of CR-CHU-Q.

Author Contributions

Conceptualization: MB NKP GMS.

Data curation: MB NKP GMS.

Formal analysis: MB NKP GMS.

Funding acquisition: GMS.

Investigation: MB NKP.

Methodology: MB NKP GMS.

Project administration: MB NKP.

Resources: MB NKP GMS.

Software: MB.

Supervision: GMS.

Validation: MB NKP GMS.

Visualization: MB NKP GMS.

Writing – original draft: MB NKP GMS.

Writing – review & editing: MB NKP GMS.

References

1. Thomas-Ahner JM, Wulff BC, Tober KL, Kusewitt DF, Riggenbach JA, Oberyszyn TM. Gender differences in UVB-induced skin carcinogenesis, inflammation, and DNA damage. Cancer Res. 2007; 67 (7):3468–74. doi: 10.1158/0008-5472.CAN-06-3798 PMID: 17389759
2. Lou YR, Peng QY, Li T, Medvecky CM, Lin Y, Shih WJ, et al. Effects of high-fat diets rich in either omega-3 or omega-6 fatty acids on UVB-induced skin carcinogenesis in SKH-1 mice. Carcinogenesis. 2011; 32(7):1078–84. doi: 10.1093/carcin/bgr074 PMID: 21525235
3. Lu YP, Lou YR, Xie JG, Peng QY, Liao J, Yang CS, et al. Topical applications of caffeine or (-)-epigallocatechin gallate (EGCG) inhibit carcinogenesis and selectively increase apoptosis in UVB-induced skin tumors in mice. Proc Natl Acad Sci U S A. 2002; 99(19):12455–60. doi: 10.1073/pnas.182429899 PMID: 12205293
4. Katiyar SK, Korman NJ, Mukhtar H, Agarwal R. Protective effects of silymarin against photocarcinogenesis in a mouse skin model. J Natl Cancer Inst. 1997; 89(8):556–66. PMID: 9106644
5. Pentland AP, Schoggins JW, Scott GA, Khan KN, Han R. Reduction of UV-induced skin tumors in hairless mice by selective COX-2 inhibition. Carcinogenesis. 1999; 20(10):1939–44. PMID: 10506108
6. Vaid M, Singh T, Prasad R, Katiyar SK. Intake of high-fat diet stimulates the risk of ultraviolet radiation-induced skin tumors and malignant progression of papillomas to carcinoma in SKH-1 hairless mice. Toxicol Appl Pharmacol. 2014; 274(1):147–55. doi: 10.1016/j.taap.2013.10.030 PMID: 24211275
7. Tsai KD, Lin JC, Yang SM, Tseng MJ, Hsu JD, Lee YJ, et al. Curcumin Protects against UVB-Induced Skin Cancers in SKH-1 Hairless Mouse: Analysis of Early Molecular Markers in Carcinogenesis. Evid Based Complement Alternat Med. 2012; 2012:593952, doi: 10.1155/2012/593952 PMID: 22888366
8. Gaddameedhi S, Selby CP, Kaufmann WK, Smart RC, Sancar A. Control of skin cancer by the circadian rhythm. Proc Natl Acad Sci U S A. 2011; 108(46):18790–5. doi: 10.1073/pnas.1115249108 PMID: 22025708
9. Chilampalli C, Guillermo R, Zhang X, Kaushik RS, Young A, Zeman D, et al. Effects of magnolol on UVB-induced skin cancer development in mice and its possible mechanism of action. BMC Cancer. 2011; 11:456. Epub 2011/10/22. doi: 10.1186/1471-2407-11-456 PMID: 22014088
10. Singh A, Singh A, Sand JM, Bauer SJ, Hafeez BB, Meske L, et al. Topically applied Hsp90 inhibitor 17AAG inhibits UVR-induced cutaneous squamous cell carcinomas. J Invest Dermatol. 2015; 135 (4):1098–107. doi: 10.1038/jid.2014.460 PMID: 25337691

11. Sapi J, Kovacs L, Drexler DA, Kocsis P, Gajari D, Sapi Z. Tumor Volume Estimation and Quasi-Continuous Administration for Most Effective Bevacizumab Therapy. PLoS One. 2015; 10(11):e0142190. doi: 10.1371/journal.pone.0142190 PMID: 26540189

12. Ayers GD, McKinley ET, Zhao P, Fritz JM, Metry RE, Deal BC, et al. Volume of preclinical xenograft tumors is more accurately assessed by ultrasound imaging than manual caliper measurements. J Ultrasound Med. 2010; 29(6):891–901. PMID: 20498463

13. Wysocki AB. Wound measurement. Int J Dermatol. 1996; 35(2):82–91. PMID: 8850032

14. Griffin JW, Tolley EA, Tooms RE, Reyes RA, Clifft JK. A comparison of photographic and transparency-based methods for measuring wound surface area. Physical therapy. 1993; 73(2):117–22. PMID: 8421717

15. Gilman T. Wound outcomes: the utility of surface measures. Int J Low Extrem Wounds. 2004; 3(3):125–32. doi: 10.1177/1534734604264419 PMID: 15866803

16. Chang AC, Dearman B, Greenwood JE. A comparison of wound area measurement techniques: visitrak versus photography. Eplasty. 2011; 11:e18 PMID: 21559060

17. Vodenicharov MD, Ghodgaonkar MM, Halappanavar SS, Shah RG, Shah GM. Mechanism of early biphasic activation of poly(ADP-ribose) polymerase-1 in response to ultraviolet B radiation. J Cell Sci. 2005; 118(Pt 3):589–99. Epub 2005/01/20. doi: 10.1242/jcs.01636 PMID: 15657079

Annexe 3: A panel of criteria for comprehensive assessment of severity of ultraviolet B radiation-induced non-Melanoma skin cancers in SKH-1 mice

Journal of Photochemistry & Photobiology, B: Biology 205 (2020) 111847

Contents lists available at ScienceDirect

Journal of Photochemistry & Photobiology, B: Biology

journal homepage: www.elsevier.com/locate/jphotobiol

A panel of criteria for comprehensive assessment of severity of ultraviolet B radiation-induced non-melanoma skin cancers in SKH-1 mice

Marc Bazin[a,c], Nupur K. Purohit[a,c], Marine A. Merlin[a,c], Girish M. Shah[a,b,c,*]

[a] CHU de Quebec-Laval University Research Center, Neuroscience and Cancer Axes, Laboratory for Skin Cancer Research, 2705, Boulevard Laurier, Quebec (QC), Canada
[b] Department of Molecular Biology, Medical Biochemistry and Pathology, Faculty of Medicine, Laval University, Quebec (QC), Canada
[c] Université Laval Cancer Research Center, Quebec (QC), Canada

ARTICLE INFO

Keywords:
Ultraviolet B (UVB) radiation
Non-melanoma skin cancers (NMSC)
SKH-1 mouse model
Assessment of cancer burden
Methods/tools/techniques

ABSTRACT

The study of causes and cures for ultraviolet B radiation (UVB)-induced non-melanoma skin cancers (NMSC) has been greatly facilitated by use of the albino SKH-1 hairless mice. These mice develop multiple tumors of different sizes and the severity of cancer is often measured by one or more of the four criteria, namely the prevalence, multiplicity, area and volume of tumors. However, there are inherent limitations of each criterion: the prevalence and number do not account for size differences among tumors, area measurement ignores the tumor height, and volume measurement overcompensates for the height at the cost of planar dimensions. Here, using our dataset from an ongoing NMSC study, we discuss the limitations of these four criteria, and suggest refinements in measuring prevalence. We recommend the use of three more criteria, namely the Knud Thomsen tridimensional surface that apportions optimal weightage to three tumor dimensions, weekly occurrence of new tumors and tumor growth-rate to reveal initiation and growth of tumors in early and late phase of NMSC development, respectively. Together, use of this comprehensive panel of seven criteria can provide an accurate assessment of severity of NMSC and lead to a testable hypothesis whether the experimental manipulation of mice has affected the early initiation or growth phase of NMSC tumors.

1. Introduction

All studies that examine the genetic, pharmacological and other causes or cures for different cancers in animal models need to assess and compare severity of the disease with or without the proposed intervention. Unlike cancers that are within the body, skin cancers offer multiple options to physically measure its severity. As an example, the study of various factors influencing solar ultraviolet B radiation (UVB)-induced non-melanoma skin cancers (NMSC) has been greatly facilitated by use of the albino SKH-1 hairless mouse model [1–4]. This model results in mice carrying variable number of small to large, flat or raised tumors appearing at different time in the protocol, and severity of their cancer burden is routinely assessed by one or more of the following four criteria. The first criterion is the prevalence [5,6] or the tumor-free survival fraction [7,8] that represents the fraction of mice carrying tumors or free from tumors in a given group, respectively. Second criterion is the multiplicity or the average number of tumors per mouse [7,9]. The last two criteria describe the size of the tumor burden in the form of average tumor area per mouse measured from the length and width [10] or diameter [5] of the tumors, or the average tumor volume per mouse derived from the length, width and height of the tumors [6,8].

Each criterion provides key information about the severity of the disease, but inherently contains limitations that restrict its capacity to represent the full picture of tumor burden. The prevalence and multiplicity account for the presence of a tumor but ignore the difference in size of tumors. The area measurement ignores height, whereas volume measurement places more emphasis on height at the expense of contributions from length and width of tumor, although clinically all three dimensions contribute significantly to the severity of NMSC. Since most published papers with this model do not provide all four criteria of tumor burden, it is a significant challenge to compare conclusions drawn from studies that use different criterion for measuring the severity of cancer. Hence, it is important to assess the advantages and limitations of each of these criteria and improve the panel to more accurately reflect the status of disease.

Here, using selected dataset from our ongoing experiments with UVB-induced NMSC model, we highlight the problem that each of these

* Corresponding author at: CHU de Quebec-Laval University Research Center, Neuroscience and Cancer Axes, Laboratory for Skin Cancer Research, 2705, Boulevard Laurier, Quebec (QC), Canada.
E-mail address: girish.shah@crchul.ulaval.ca (G.M. Shah).

https://doi.org/10.1016/j.jphotobiol.2020.111847
Received 22 August 2019; Received in revised form 18 February 2020; Accepted 3 March 2020
Available online 04 March 2020
1011-1344/

four routinely used criteria may not always lead to an identical conclusion about the severity of tumor burden. We demonstrate that a more accurate estimate of tumor size can be obtained by using a fifth criterion, namely Knud Thomsen three-dimensional (KT-3D) tumor surface area, which is used in many other disciplines but not in NMSC research. We also show that analyzing the weekly appearance of new tumors during the protocol and a modified version of a rarely used criterion of tumor growth-rate [5] together should be used to measure the frequency of initiation of measurable tumors and changes in the growth characteristics of cancer with time. Together, the four old and three new criteria can provide not just a numerical but a more comprehensive picture of the UVB-induced NMSC.

2. Materials and Methods

2.1. Chronic UVB-Induced NMSC in SKH-1 Mice and Weekly Measurement of Tumors

All animal studies were approved by the Animal Protection Committee of Laval University and were conducted by the personnel who were trained and certified for animal work. The animal protocol was carried out as described earlier [11]. Briefly, the 5-week old SKH-1 albino hairless mice were irradiated thrice a week with 800 J/m^2 of UVB filtered through Kodacel (to remove UVC) for 20 weeks. Mice were photographed weekly at the same time to build a database of weekly tumor appearance as well as the length, width, and height of each tumor over the 20-week protocol. The transient lesions that did not last for the entire protocol were excluded and merger of adjacent tumors was accounted for to determine the multiplicity of tumors. This database was subjected to analyses by OriginPro 2015 software (OriginLab Corp.) for assessment of severity of cancers by seven different criteria, as described below. Similar analyses could be conducted using more commonly used software for statistical and linear regression analyses, such as Microsoft Excel, R and LibreOffice Calc.

2.2. Measurement of Tumor Prevalence or Tumor-Free Survival Fraction

The tumor prevalence (P) is the proportion of mice with at least one or two (as improved criterion described here) tumors at a given time. The tumor-free survival fraction was calculated as 1-P. The tumor-free survival graphs were analyzed using a Kaplan-Meier estimator with a log-rank test to calculate mean time when a mouse group develops the first or first two tumors and the median time when 50% of the mice in a group are affected.

2.3. Measurement of Multiplicity, Area and Volume of Tumors

Multiplicity of tumors was determined as average number of tumors per mouse. The area and volume were derived from length, width and height of the tumors using following formulae:

$$Area = \frac{\pi}{4} \times length \times width$$

$$Volume = \frac{\pi}{6} \times length \times width \times height$$

The tumor burden per mouse for each criterion was calculated from the sum of all tumor values for each mouse in the group in a given week, and presented as time-course of the burden value over the duration of the protocol.

2.4. Knud Thomsen's Three-Dimensional (KT-3D) Tumor Surface Area

The three-dimensional tumor surface area was determined by KT-3D formula:

$$KT\text{-}3D\ surface = \pi \left(\frac{length^p height^p + width^p height^p + \frac{1}{2^p} length^p width^p}{3} \right)^{\frac{1}{p}}$$

where $p = 1.6075$. From Klamkin's mathematical expression of the boundaries of an ellipsoidal surface [12], Knud Thomsen identified the best optimization to approximate this surface (with 1.061% error) [13]. In this formula, the two first terms in the numerator are the height contribution and the last term is the base area (length and width) contribution. The collective tumor burden by KT-3D surface area for each group was measured in the same way as described in Section 2.3 for area and volume criteria.

2.5. Weekly Occurrence of New Tumors and Tumor Growth-Rate

The occurrence of new tumors in a given week was derived by deducting multiplicity number of the previous week from the given week. Since tumor grows exponentially with cell division, its growth-rate was defined by the exponent of the exponential growth. The KT-3D surface data for each tumor at each time was log-transformed to generate linear data from which the slope represents the growth-rate of the given tumor. The growth-rates of the merged tumors were not assessed and corresponding tumors were excluded from this analysis. The average growth-rates of tumors appearing at week 13 were calculated for three periods: 13–20 weeks (total period); 13–16 weeks (initial phase) and 17–20 weeks (late phase). We also calculated growth-rate of tumors appearing at week 17 for the period of 17–20 weeks (early phase of late appearing tumors). The statistical differences were calculated using a two-sample *t*-test.

2.6. Statistical Analyses for Comparisons of Groups

For each group, the data are presented as the mean burden per animal with standard error of the mean (SEM). The tumor burden data are calculated from the week where at least one mouse in any of the experimental groups developed a tumor. The tumor burden curves for different groups were compared with the ANOVA 2 factors test for repeated measures using OriginPro 2015 software where the factors are the group treatment and time (week) of the protocol. To determine the significance of difference between two groups at any given time, data were transformed to obtain a linear response of each factor with time. First, the data were converted by small numerical values when null, otherwise by a root function: square root for areas and KT-3D surfaces, and cubical root for volumes. Next, these quantities as well as the multiplicity and new tumor numbers were transformed by a natural logarithm function. Multiple linear regression method was performed on the transformed data to check the normality distribution. The data sphericity was calculated using the Greenhouse-Geisser and the Huynh-Feldt corrections to estimate the factor interaction. The multiple comparisons, if required, were done with a Holm-Bonferroni post-hoc test. In all the statistical tests, the *p*-value below 0.05 was considered as a statistically significant difference.

3. Results and Discussion

3.1. Discordance among Four Conventional Criteria for Determining the Severity of NMSC

We first examined whether all four conventionally used assessment criteria, i.e., prevalence, multiplicity, area and volume, would provide an identical conclusion regarding differences in the severity of tumor burden among different groups that were chosen from our large ongoing experimental dataset using this model. We selected five groups of 9–12 mice that had a predominance of small (groups 1 and 2), medium (group 3), large and flat (group 4) or large and raised (group 5) tumors (Suppl. Fig. 1). For each group, the weekly tumor data for all four

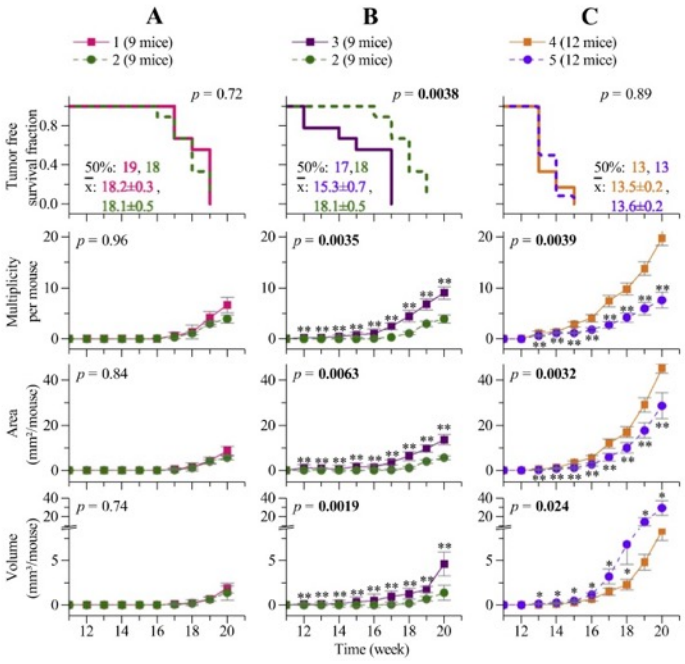

Fig. 1. Four commonly used criteria for assessment of severity of NMSC. The severity of cancer burden mice from five groups is presented as comparison pair A (groups 1 and 2), pair B (groups 2 and 3) and pair C (groups 4 and 5). The results are presented as pairwise comparison of two selected groups with *p*-values (*p*), medians (50%) and means ($\bar{x}$). Multiple comparison results are annotated with * for significant, ** for very significant, and *** for highly significant difference. Error bars are means ± SEM.

criteria were collected using our photographic method [11]. We divided these five groups of mice in three pairs for comparison, namely pair A (groups 1 and 2), pair B (groups 2 and 3) and pair C (groups 4 and 5). For each pair, we compared the difference in severity of cancer by each of the four criteria.

In pair A containing groups 1 and 2 with mainly small tumors, all four criteria revealed an identical conclusion that there was no significant difference in severity of cancer in these two groups (Fig. 1, pair A). In pair B, when we compared the group 2 mice with smaller tumors to group 3 mice with moderate size tumors, once again all four criteria unequivocally identified that group 3 had significantly more severe cancer as compared to group 2 (Fig. 1, pair B). Thus, if there are two groups with either very similar or distinctly different size tumors, all four conventional criteria would provide an identical conclusion about severity of cancer in these groups.

In contrast, when we compared group 4 mice carrying mainly large flat tumors with group 5 mice having largely tall tumors with small footprint on the skin (Fig. 1, pair C), the four criteria produced three different conclusions regarding which group had more severe cancer burden. The prevalence criterion indicated no significant difference with the mean tumor-free survival period around 13.5 weeks for both the groups. The multiplicity criterion at week 20 revealed that average number of tumors per mouse was 2.6 times more in group 4 (19.7 tumors) than in group 5 (7.6 tumors). The area criterion also gave similar indication that group 4 (45.1 mm^2) had significantly higher (1.6 times) average area of tumors per mouse than group 5 (28.6 mm^2). In contrast, the tumor volume criterion produced a diametrically opposite result that group 5 (29.1 mm^3) had almost 3.5 times more severe cancer burden than group 4 (8.4 mm^3).

This discrepancy among four commonly used criteria in the estimation of severity of cancer poses a significant challenge in drawing an accurate conclusion about the influence of genes and other interventions on the susceptibility to NMSC that tend to generate situation such as that described in pair C. As we described earlier [11], this problem is even more acute since many studies do not report all four criteria but report the results with only prevalence and number of tumors, whereas other studies report area and that too after excluding tumors below an arbitrary cut-off dimension, and very few studies report volume of tumors. Thus, reporting of results based on only one or two criteria could introduce an unintended bias in the interpretations of results. In addition, even the use of all four conventional criteria does not guarantee a uniform conclusion for at least some of the data in NMSC studies, such as pair C. Hence, there is a need for additional criteria for a more reliable and consistent estimate of severity of cancer burden.

3.2. Knud Thomsen Three-Dimensional Surface as a Fifth Criterion of Tumor Burden

The formulae for area and volume measurement are made with an assumption of a hemi-ellipsoidal shape for NMSC tumors. However, for such a shape, the KT-3D formula to calculate the tridimensional surface area strikes an optimum balance between the contributions by the length and width against its height. This formula, developed by Knud Thomsen [13] through optimization of the original formula of Klamkin [12] for ellipsoid shapes, is extensively used in many different disciplines ranging from medicine [14–16], veterinary medicine [17], medical imaging [18], cell biology [19,20], immunology [21], plant biology [22], plant pathogen interactions [23,24], evolutionary ecology [25], biophysics [26], oceanography [27], physical chemistry [28], engineering and applied sciences [29], aeronautics [30], geology [31], hydrodynamic [32], and thermodynamics [33]. More specifically in the above studies, the KT-3D formula was used for calculating the three-dimensional surface area of a vast variety of ellipsoid or hemi-ellipsoid

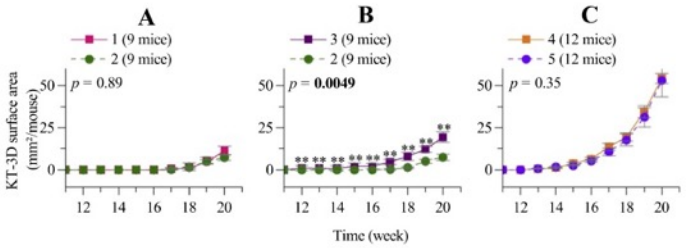

Fig. 2. Assessment of cancer burden by KT-3D surface area. The severity of tumor burden was measured as KT-3D surface area for five groups of mice divided in three comparison pairs (A, B and C) described in Fig. 1.

objects, such as osteosarcoma, retinal myocytes, zone affected by mitral valve regurgitation, areas of brain, dendritic cells in brain, bacterial shape during cell-cycle, insect puparium, beetles, plasma membrane of plant cells that transport nutrients, rhodolith beds of algae in marine sediments, and gas-filled airships.

In view of the widespread acceptance of KT-3D formula as a true measure of tridimensional surface area of a hemi-ellipsoid object, we used it as a fifth criterion for measuring NMSC tumor burden in the same three comparison groups (Fig. 2). First of all, this criterion validated the observations described in Fig. 1 that there was no significant difference between groups 1 and 2 (Fig. 2A); and that group 3 had a significantly higher tumor burden than group 2 (Fig. 2B). On the other hand, KT-3D surface measurement revealed no statistically significant difference between groups 4 and 5 (Fig. 2C), an assessment of tumor burden that was a compromise between two opposite results observed with area and volume criteria in Fig. 1C. In view of the limitations of the formulae used for area and volume, we propose that conclusion drawn by KT-3D surface criteria is a more reasonable comparison of tumor burden between these two groups.

To more clearly demonstrate how each of the three dimensions of tumor influence the estimation of severity of burden as measured by area, volume and KT-3D surface, we compared the severity of cancer burden in two mice, one (mouse #1) carrying multiple small and near-flat tumors and another (mouse #2) carrying one very large and few small tumors (Suppl. Fig. 2). The mouse #1 had 4.9 times more tumor burden by area but 11.4 times less burden by volume than mouse #2, whereas KT-3D surface once again moderated between these two criteria to indicate that mouse #1 had 1.9 times more severe tumor burden than mouse #2. Thus, the area measurement undervalues the importance of a large and tall tumor with small footprint on the skin, whereas volume measurement undervalues contribution of numerous small but flat tumors to tumor burden. Since all three dimensions are clinically important determinants of severity of cancer, and since KT-3D surface criterion is universally recognized to apportion optimal weightage to all three dimensions of ellipsoid and hemi-ellipsoid structures, we propose that KT-3D surface represents the most accurate estimation of the severity of cancer in this model.

3.3. Occurrence of New Tumors and Growth-Rate of Tumors as Two Additional Criteria

The net increase in tumor burden over time is due to two distinct factors, the number of new tumors added each week which represents continuing cancer initiation events, and weekly increase in size of tumors which represents growth of tumors at different stages after initiation. However, these two key aspects of cancer burden are not readily discernible in the cumulative weekly data for different criteria, as presented in Figs. 1 and 2. The presentation of weekly multiplicity data in Fig. 1 reveals a total number of tumors each week, irrespective of whether they were pre-existing tumors from earlier weeks or new tumors that appeared in that week. Similarly, weekly tumor area and volume data shown in Fig. 1 or weekly KT-3D surface area curves shown in Fig. 2 provide an average growth rate of newly formed tumors during that week pooled with that of the tumors that had appeared weeks earlier in the protocol.

Here, we propose two more criteria to measure occurrence of new tumors and growth rate of new versus old tumors by mining our exhaustive weekly dataset on multiplicity and KT-3D surface area as shown in Figs. 1 and 2. The weekly data for the multiplicity in pair C was transformed to determine the occurrence of new tumors each week during the protocol (Fig. 3, left panel). While both groups developed ~1–2 new tumors each week up to 16th week, the occurrence of new tumors jumped significantly from week 17 for group 4 but not for group 5. These results suggest that the experimental intervention in group 4

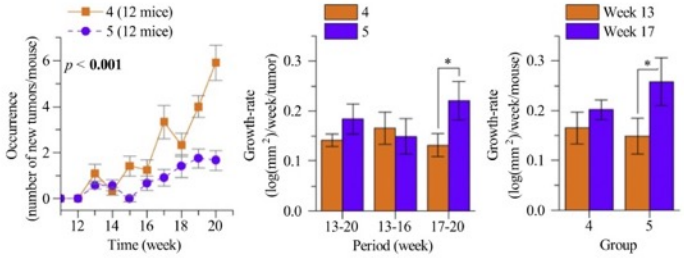

Fig. 3. Weekly occurrence and growth-rate of tumors. Left panel: Weekly occurrence of new tumors per mouse for groups 4 and 5. The group description and *p*-value for difference between two groups are same as described for Fig. 1. Middle panel: Growth-rate in initial and late phase of tumors. For the tumors in groups 4 and 5 that appeared in week 13, their growth-rates in two groups were compared for the periods of 13–20 week (total period), 13–16 weeks (initial growth) and 17–20 weeks (late growth). Right panel: Growth-rate of early and late appearing tumors within a group. Comparison within each group for only the initial growth-rate of tumors over first four weeks after their first appearance in either 13th week (early tumors) or in 17th week (late tumors). The *p*-value indicates the significance of the occurrence group comparison. The * indicates statistically significant difference.

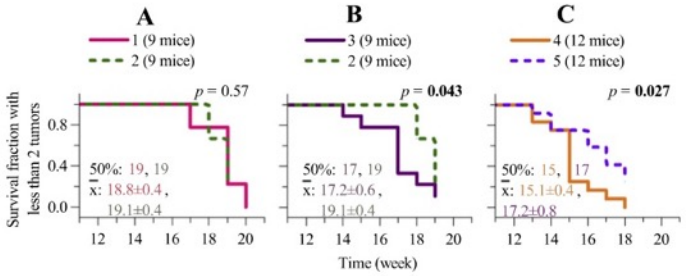

Fig. 4. Tumor survival graphs with two-tumor cut-off for same three comparison pairs described in Fig. 1.

had influence over tumor initiation events, as compared to intervention in group 5.

The variation in growth-rate of cancers after their initial appearance on the skin was determined by analyses of tumor dimension data collected on weekly basis, as suggested by Gruijl et al. [5]. We used KT-3D surface data to determine the average tumor growth-rate per week in entire period of 13–20 weeks, or only in the initial (13–16 weeks) or late (17–20 weeks) phase of tumor growth (Fig. 3, middle panel). The global average growth-rate for the tumors from their first appearance in 13th week to the last week of the protocol (week 20) showed no significant difference between groups 4 and 5. However, stratification of this data into early (13–16 weeks) and late (17–20 weeks) phases revealed that tumors in group 5 had a significantly higher growth-rate than group 4 tumors only in the late phase but not in the initial phase.

Next, we examined if initial 4-week growth-rate of tumors would be same in a given group whether tumors appeared either early (13th week) or late (17th week) period of the protocol (Fig. 3, right panel). The main difference between these two types of tumors would be that late appearing tumors would have received four extra weeks of irradiation before they first appeared as tumors in the 17th week. The initial growth-rate of early and late tumors was not significantly different in group 4, but for tumors in group 5, growth-rate of late tumors was significantly higher as compared to early tumors. Collectively, these two new criteria revealed key mechanistic differences in development of NMSC in these two groups of mice. Mice in group 4 had tendency to promote more frequent appearance of new tumors but not alter the growth-rate of tumors over time. In contrast, mice in group 5 exhibited stable occurrence of new tumors throughout the protocol, but accelerated the growth of tumors at later stage of the protocol. Thus, use of these two new criteria could reveal experimentally testable hypothesis for explaining the differences in NMSC development in groups 4 and 5.

3.4. Improved Method to Calculate Tumor-Free Survival Fraction

Gruijl et al. had earlier shown a mathematical relationship between the prevalence and multiplicity in UVB-induced NMSC in SKH-1 mice [34]. In Fig. 1, this correlation of higher prevalence and multiplicity was evident for comparison pairs A and B. However, for pair C, although prevalence was not different, the multiplicity was more in group 4 than in group 5. Normally, prevalence is based on the appearance of the first tumor, but we noted that appearance of a minimum of two tumors is a better indicator of a stable disease. Therefore, we recalculated the prevalence based on the presence of two tumors in a mouse rather than the first tumor (Fig. 4). This revised method of calculating prevalence or tumor-free survival correlated very well with multiplicity in all three pairs described in Fig. 1. Thus, our results indicate that tumor-free survival fraction based on two-tumor cut-off could serve as a better criterion for prevalence that is more aligned with multiplicity measure of tumor burden.

The SKH-1 mouse model has been very useful to study solar UVB-induced NMSC despite its limitations. These experiments are time-consuming, expensive and require a significant manpower. As a result, it is understandable that many studies do not analyze tumor burden each week and report only few criteria to assess and compare severity of cancer in different groups. Earlier, we have shown that the use of a simple yet accurate photographic method to capture weekly three-dimensional tumor data for measuring tumor burden on an ongoing basis can solve most of the manpower and time problem in collecting the weekly tumor data from a large number of mice in this protocol [11]. Here, we show that our combined panel of seven criteria can provide a comprehensive picture of NMSC severity and lead to further studies to understand mechanistic explanations for the influence of experimental treatment on development of NMSC. Our panel could also be applied for the study of NMSC in other mouse strains, if they develop UVB-induced NMSC because not all mouse strains have similar photosensitive response to UVB [35]. Finally, our panel can be more broadly used for measuring changes in other skin lesions such as psoriasis or wound or for other cancers in internal organs, as long as they can be counted and measured by any means for calculating area, volume and KT 3D-surface with formulae suitable for the shape of the lesion or tumor.

Declaration of Competing Interest

Authors have no conflict of interest to declare.

Acknowledgement

We are thankful to Mihaela Robu and Rashmi Shah for help in measurement of tumor dimensions. This work was supported by the Discovery Grant (RGPIN 2016–05868) and the Discovery Accelerator Supplement Grants (RGPA-492875-2016) to GMS from the Natural Sciences and Engineering Research Council of Canada. NKP received a graduate student scholarship from the CHU de Quebec Research Centre as well as a foreign student supplemental tuition fee waiver from Quebec Government and the Shastri Indo-Canadian Institute.

Appendix A. Supplementary data

Supplementary data to this article can be found online at https://doi.org/10.1016/j.jphotobiol.2020.111847.

References

[1] F. Benavides, T.M. Oberyszyn, A.M. VanBuskirk, V.E. Reeve, D.F. Kusewitt, The hairless mouse in skin research, J. Dermatol. Sci. 53 (2009) 10–18.
[2] A.Y. Voigt, M. Michaud, K.Y. Tsai, J. Oh, J.P. Sundberg, Differential hairless mouse strain-specific susceptibility to skin cancer and sunburn, J. Invest. Dermatol. 139 (2019) 1837–1840 (e1833).
[3] S. Chilampalli, X. Zhang, H. Fahmy, R.S. Kaushik, D. Zeman, M.B. Hildreth, C. Dwivedi, Chemopreventive effects of honokiol on UVB-induced skin cancer

development, Anticancer Res. 30 (2010) 777–783.
[4] C.K. Singh, C.A. Mintie, M.A. Ndiaye, G. Chhabra, P.P. Dakup, T. Ye, M. Yu, N. Ahmad, Chemoprotective effects of dietary grape powder on UVB radiation-mediated skin carcinogenesis in SKH-1 hairless mice, J. Invest. Dermatol. 139 (2019) 552–561.
[5] F.R. de Gruijl, J.B. Van Der Meer, J.C. Van Der Leun, Dose-time dependency of tumor formation by chronic UV exposure, Photochem. Photobiol. 37 (1983) 53–62.
[6] M. Vaid, T. Singh, R. Prasad, S.K. Katiyar, Intake of high-fat diet stimulates the risk of ultraviolet radiation-induced skin tumors and malignant progression of papillomas to carcinoma in SKH-1 hairless mice, Toxicol. Appl. Pharmacol. 274 (2014) 147–155.
[7] J.M. Thomas-Ahner, B.C. Wulff, K.L. Tober, D.F. Kusewitt, J.A. Riggenbach, T.M. Oberyszyn, Gender differences in UVB-induced skin carcinogenesis, inflammation, and DNA damage, Cancer Res. 67 (2007) 3468–3474.
[8] Y.R. Lou, Q.Y. Peng, T. Li, C.M. Medvecky, Y. Lin, W.J. Shih, A.H. Conney, S. Shapses, G.C. Wagner, Y.P. Lu, Effects of high-fat diets rich in either omega-3 or omega-6 fatty acids on UVB-induced skin carcinogenesis in SKH-1 mice, Carcinogenesis 32 (2011) 1078–1084.
[9] R.B. Cope, C. Loehr, R. Dashwood, N.I. Kerkvliet, Ultraviolet radiation-induced non-melanoma skin cancer in the Crl:SKH1:hr-BR hairless mouse: augmentation of tumor multiplicity by chlorophyllin and protection by indole-3-carbinol, Photochem. Photobiol. Sci. 5 (2006) 499–507.
[10] D.M. Euhus, C. Hudd, M.C. LaRegina, F.E. Johnson, Tumor measurement in the nude mouse, J. Surg. Oncol. 31 (1986) 229–234.
[11] M. Bazin, N.K. Purohit, G.M. Shah, Comprehensive measurement of UVB-induced non-melanoma skin cancer burden in mice using photographic images as a substitute for the caliper method, PLoS One 12 (2017) e0171875.
[12] M.S. Klamkin, Elementary approximations to the area of N-dimensional ellipsoids, Am. Math. Mon. 78 (1971) 280–283.
[13] L. Cao, Biological model representation and analysis, Thesis of Mathematics and Natural Science, Leiden University, Section Imaging & BioInformatics, Leiden Insitute of Advanced Computer Science, Faculty of Science, Leiden University, 2014.
[14] E. Ashikhmina, D. Shook, F. Cobey, B. Bollen, J. Fox, X. Liu, A. Worthington, P. Song, S. Shernan, Three-dimensional versus two-dimensional echocardiographic assessment of functional mitral regurgitation proximal isovelocity surface area, Anesth. Analg. 120 (2015) 534–542.
[15] S.L. Cotter, V. Klika, L. Kimpton, S. Collins, A.E. Heazell, A stochastic model for early placental development, J. R. Soc. Interface 11 (2014) 20140149.
[16] J.J. Tukker, B. Lasztoczi, L. Katona, J.D. Roberts, E.K. Pissadaki, Y. Dalezios, L. Marton, L. Zhang, T. Klausberger, P. Somogyi, Distinct dendritic arborization and in vivo firing patterns of parvalbumin-expressing basket cells in the hippocampal area CA3, J. Neurosci. 33 (2013) 6809–6825.
[17] R.A. Sternberg, H.C. Pondenis, X. Yang, M.A. Mitchell, R.T. O'Brien, L.D. Garrett, W.G. Helferich, W.E. Hoffmann, T.M. Fan, Association between absolute tumor burden and serum bone-specific alkaline phosphatase in canine appendicular osteosarcoma, J. Vet. Intern. Med. 27 (2013) 955–963.
[18] D. Xu, J. Cui, R. Bansal, X. Hao, J. Liu, W. Chen, B.S. Peterson, The ellipsoidal area ratio: an alternative anisotropy index for diffusion tensor imaging, Magn. Reson. Imaging 27 (2009) 311–323.
[19] M.K. McGahon, J.M. Dawicki, A. Arora, D.A. Simpson, T.A. Gardiner, A.W. Stitt, C.N. Scholfield, J.G. McGeown, T.M. Curtis, Kv1.5 is a major component underlying the A-type potassium current in retinal arteriolar smooth muscle, Am. J. Physiol. Heart Circ. Physiol. 292 (2007) H1001–H1008.
[20] J.M. Monteiro, P.B. Fernandes, F. Vaz, A.R. Pereira, A.C. Tavares, M.T. Ferreira, P.M. Pereira, H. Veiga, E. Kuru, M.S. VanNieuwenhze, Y.V. Brun, S.R. Filipe, M.G. Pinho, Cell shape dynamics during the staphylococcal cell cycle, Nat. Commun. 6 (2015) 8055.
[21] S.L. Harwood, A. Alvarez-Cienfuegos, N. Nuñez-Prado, M. Compte, S. Hernández-Pérez, N. Merino, J. Bonet, R. Navarro, P.M.P. Van Bergen en Henegouwen, S. Lykkemark, K. Mikkelsen, K. Mølgaard, F. Jabs, L. Sanz, F.J. Blanco, P. Roda-Navarro, L. Alvarez-Vallina, ATTACK, a novel bispecific T cell-recruiting antibody with trivalent EGFR binding and monovalent CD3 binding for cancer immunotherapy, OncoImmunology 7 (1) (2017) e1377874.
[22] D. Pugh, C. Offler, M. Talbot, Y.-L. Ruan, Evidence for the role of transfer cells in the evolutionary increase in seed and fiber biomass yield in cotton, Mol. Plant 3 (2010) 1075–1086.
[23] S.A. Broski, B.H. King, Drilling-in and chewing-out of hosts by the Parasitoid wasp Spalangia endius (Hymenoptera: Pteromalidae) when parasitizing Musca domestica (Diptera: Muscidae), Environ. Entomol. 44 (2015) 1116–1124.
[24] B. Mori, H. Proctor, D. Walter, M. Evenden, Phoretic mite associates of mountain pine beetle at the leading edge of an infestation in northwestern Alberta, Canada, Can. Entomol. 143 (2011) 44–55.
[25] A. Ansart, A. Guiller, O. Moine, M.C. Martin, L. Madec, Is cold hardiness size-constrained? A comparative approach in land snails, Evol. Ecol. 28 (2014) 471–493.
[26] C. Ihueze, C. Okafor, P. Ogbobe, Finite design for critical stresses of compressed biomaterials under transportation, Proceedings of the World Congress on Engineering (WCE) July 3–5 2013, SSRN, London, U.K, 2013(Available at SSRN).
[27] K. Millar, P. Gagnon, Mechanism of stability of rhodolith beds: sedimentological aspects, Mar. Ecol. Prog. Ser. 594 (2018) 65–83.
[28] S. Manet, A.S. Cuvier, C. Valotteau, G.C. Fadda, J. Perez, E. Karakas, S. Abel, N. Baccile, Structure of bolaamphiphile sophorolipid micelles characterized with SAXS, SANS, and MD simulations, J. Phys. Chem. B 119 (2015) 13113–13133.
[29] R. Noerhidajat, Z.A. Yunus, S. Zurina, T.S. Syafiie, Chang, Modeling and simulation of heat and mass transfer in oil palm fruit digestion process, J. Emerg. Trends Eng. Appl. Sci. 6 (2015) 136–143.
[30] M. Bonnici, A. Tacchini, D. Vucinic, Long permanence high altitude airships: the opportunity of hydrogen, Eur. Transp. Res. Rev. 6 (2014) 253–266.
[31] Z. Jin, Z.Y. Yin, P. Kotronis, Y.F. Jin, Numerical investigation on evolving failure of caisson foundation in sand using the combined Lagrangian-SPH method, Mar. Georesour. Geotechnol. 37 (2018) 23–35.
[32] P.M. Mwasame, N.J. Wagner, A.N. Beris, On the macroscopic modelling of dilute emulsions under flow, J. Fluid Mech. 831 (2017) 433–473.
[33] F.E. Benedetto, H. Zolotucho, M.O. Prado, Critical assessment of the surface tension determined by the maximum pressure bubble method, Mater. Res. 18 (2015) 9–14.
[34] F.R. de Gruijl, P.D. Forbes, UV-induced skin cancer in a hairless mouse model, Bioessays 17 (1995) 651–660.
[35] N. Gyongyosi, K. Lorincz, A. Keszeg, D. Haluszka, A. Banvolgyi, E. Tatrai, S. Karpati, N.M. Wikonkal, Photosensitivity of murine skin greatly depends on the genetic background: clinically relevant dose as a new measure to replace minimal erythema dose in mouse studies, Exp. Dermatol. 25 (2016) 519–525.

Annexe 4: Poly(ADP-ribose) Polymerase 1 escorts XPC to UV-induced DNA lesions during nucleotide excision repair

Poly(ADP-ribose) polymerase 1 escorts XPC to UV-induced DNA lesions during nucleotide excision repair

Mihaela Robu[a,1], Rashmi G. Shah[a,1], Nupur K. Purohit[a], Pengbo Zhou[b], Hanspeter Naegeli[c], and Girish M. Shah[a,2]

[a]Laboratory for Skin Cancer Research, Neuroscience Axis, Centre Hospitalier Universitaire de Québec Research Center-Université Laval, Québec, QC, Canada G1V 4G2; [b]Department of Pathology and Molecular Medicine, Weill Cornell Medical College, New York, NY 10065; and [c]Institute of Pharmacology and Toxicology, University of Zurich, Zurich, CH-8057, Switzerland

Edited by James E. Cleaver, University of California, San Francisco, CA, and approved July 5, 2017 (received for review April 26, 2017)

Xeroderma pigmentosum C (XPC) protein initiates the global genomic subpathway of nucleotide excision repair (GG-NER) for removal of UV-induced direct photolesions from genomic DNA. The XPC has an inherent capacity to identify and stabilize at the DNA lesion sites, and this function is facilitated in the genomic context by UV-damaged DNA-binding protein 2 (DDB2), which is part of a multiprotein UV–DDB ubiquitin ligase complex. The nuclear enzyme poly(ADP-ribose) polymerase 1 (PARP1) has been shown to facilitate the lesion recognition step of GG-NER via its interaction with DDB2 at the lesion site. Here, we show that PARP1 plays an additional DDB2-independent direct role in recruitment and stabilization of XPC at the UV-induced DNA lesions to promote GG-NER. It forms a stable complex with XPC in the nucleoplasm under steady-state conditions before irradiation and rapidly escorts it to the damaged DNA after UV irradiation in a DDB2-independent manner. The catalytic activity of PARP1 is not required for the initial complex formation with XPC in the nucleoplasm but it enhances the recruitment of XPC to the DNA lesion site after irradiation. Using purified proteins, we also show that the PARP1–XPC complex facilitates the handover of XPC to the UV-lesion site in the presence of the UV–DDB ligase complex. Thus, the lesion search function of XPC in the genomic context is controlled by XPC itself, DDB2, and PARP1. Our results reveal a paradigm that the known interaction of many proteins with PARP1 under steady-state conditions could have functional significance for these proteins.

PARP1 | XPC | NER | DDB2 | UV

Nucleotide excision repair (NER) is a versatile pathway that removes a wide variety of DNA lesions including UV radiation (UV)-induced cyclobutane pyrimidine dimers (CPD) and 6–4 pyrimidine-pyrimidone photoproducts (6-4PP). There are two subpathways of NER: the global genomic NER (GG-NER) that removes the majority of lesions from the entire genome and the transcription-coupled NER that repairs the minority of total lesions that occur on the transcribed strand (1). The GG-NER process is dependent on the Xeroderma pigmentosum C (XPC) protein, the arrival and stabilization of which at the lesion site, followed by its timely departure, are crucial for permitting the downstream NER events (2). XPC accomplishes some of these tasks on its own or with the help of processes initiated by two proteins that independently reach the lesion site very rapidly, namely UV-damaged DNA-binding protein 2 (DDB2) and poly(ADP-ribose) polymerase 1 (PARP1). It is known that once XPC reaches the vicinity of the DNA lesion site, the UV–DDB ubiquitin ligase complex containing DDB1, DDB2, Cul4A, and Rbx1 regulates its specific binding and stabilization at the site (2). However, we have the least understanding of the ability of XPC to rapidly search for and arrive at the very few lesions surrounded by a vast majority of undamaged bases in the chromatin structure (3).

There are three proposed mechanisms by which XPC could be rapidly recruited to the lesion site in the genomic context. The first mechanism is based on XPC's inherent capacity to interrogate the DNA for verifying the presence or absence of a lesion. It has been suggested that XPC searches for the lesion-induced helical distortion in the genome (1) by association and quick dissociation until it encounters the lesion site where it stabilizes due to a stronger association (4). Since the yeast ortholog of XPC forms identical crystal structures with normal and UV-damaged DNA (5), it is proposed that the discrimination between normal and damaged DNA depends on the difference in the kinetics of twisting and opening of the helix by XPC at these two sites (5, 6). Although this physical verification mechanism could work rapidly in vitro with small and naked DNA, it would be too slow to explain the rapid recruitment of XPC that is known to occur within minutes at UV-lesion sites in a complex eukaryotic chromatin. Therefore, the second proposed mechanism is that DDB2 helps XPC in finding the UV lesions in the genomic context. This is based on the observation that the Xeroderma pigmentosum group E (XP-E) cells, which are deficient in DDB2 but proficient in XPC, can slowly repair 6–4PP lesions but fail to remove CPD lesions, which constitute the majority of the lesions formed by UV radiation (7, 8). Based on the phenotype of XP-E cells and the biochemical studies of XPC with these two types of lesions (2), it is proposed that, although XPC can directly recognize the greater degree of helical distortion in DNA induced by 6–4PP lesions, it cannot recognize the smaller degree of distortion caused by CPD lesions until DDB2 binds to these lesions and increases the degree of helical distortion at the site (3). Finally, the third proposed mechanism is that XPC recognizes the remodeled chromatin at the lesion site, which is the result of events initiated by ubiquitination of histones by the UV–DDB ligase complex (9). This is supported by the observations that decreased histone ubiquitination impairs the eviction of the UV–DDB ligase

Significance

Repair of the majority of UV-induced DNA damage in mammalian cells by the nucleotide excision repair pathway starts with rapid recruitment of Xeroderma pigmentosum C (XPC) protein to the lesion. However, rapidity of XPC recruitment to the lesion site in a genomic context cannot be fully explained by the known properties of XPC or its partner protein DDB2. Here, we show that the DNA damage-detecting nuclear protein PARP1 forms a stable complex with XPC before DNA damage and transfers it very rapidly to the DNA lesion site if other repair conditions are present. Since PARP1 is known to interact with many proteins under steady-state conditions, our results reveal a paradigm that an association with PARP1 could confer a functional advantage to these proteins.

Author contributions: M.R., R.G.S., N.K.P., and G.M.S. designed research; M.R., R.G.S., and N.K.P. performed research; M.R., R.G.S., N.K.P., P.Z., and H.N. contributed new reagents/analytic tools; M.R., R.G.S., N.K.P., P.Z., H.N., and G.M.S. analyzed data; and M.R., R.G.S., N.K.P., P.Z., H.N., and G.M.S. wrote the paper.

The authors declare no conflict of interest.

This article is a PNAS Direct Submission.

Freely available online through the PNAS open access option.

[1]M.R. and R.G.S. contributed equally to this work.

[2]To whom correspondence should be addressed. Email: girish.shah@crchul.ulaval.ca.

This article contains supporting information online at www.pnas.org/lookup/suppl/doi:10.1073/pnas.1706981114/-/DCSupplemental.

complex (10) and recruitment of XPC to the lesions site (11). Thus, apart from the direct recognition of the DNA damage by XPC, all other mechanisms to explain XPC's ability to rapidly reach most of the UV lesions in the genomic context depend on DDB2. However, XPC must have some DDB2-independent mechanism of recruitment to lesions other than 6–4PP. For example, CPD are recognized and repaired even after DDB2 is degraded (12) or when the number of lesion sites exceeds the number of DDB2 molecules in the cell (13). In addition, XPC recognizes and starts NER at other types of DNA damages, such as bulky adducts and cross-links that are not likely to be recognized by DDB2, because these lesions cannot be accommodated in DDB2's recognition pocket (14–16).

Earlier, we showed that PARP1, an abundant nuclear enzyme in higher eukaryotes, is recruited very early to the UV-lesion site and catalytically activated to form polymers of ADP-ribose (PAR) (17, 18). It has been shown by others and our team that PARP1 and DDB2 reach the lesion site in the same time frame and cooperate with each other to increase the efficiency of GG-NER. More specifically, DDB2 has been shown to stimulate catalytic activity of PARP1, which in turn PARylates DDB2 and DDB1 (18, 19). The inhibition of PARylation has been shown to block the turnover of DDB2 at UV-damaged chromatin (18) and to decrease total cellular levels of DDB2 (19). Additionally, the activated PARP1 promotes chromatin decondensation by DDB2 (20) via recruitment of the remodeler protein ALC1 at the UV-lesion site (19). Together, these studies suggest that the interplay of PARP1 and DDB2 at UV-damaged DNA could be a mechanism for recruitment and stabilization of XPC at UV-damaged chromatin (18, 20). Recent studies have shown PARylation of XPC in vitro (21) and in the cells responding to oxidative DNA damage (22). However, the significance of the PARylation of XPC in NER of UV-induced DNA damage is not clear since the higher affinity of XPC for larger PAR chains shown in vitro (21) would repel XPC from DNA, and in vivo PARylation of XPC was not observed in UV-irradiated cells (22). Thus, studies to date have not shown an unequivocal direct DDB2-independent role for PARP1 and PARylation in recruitment of XPC in GG-NER.

Here, we show that PARP1 stably interacts with XPC in the nucleoplasm under unchallenged conditions, i.e., in the absence of any type of exogenously induced DNA damage. The functionally important DNA-binding region of XPC is involved in its interaction with PARP1. Using various cellular models and in vitro assays with purified proteins, we show that, after UV irradiation, PARP1 rapidly escorts XPC to the UV-lesion site and facilitates its handover to the damaged DNA in the presence of the UV–DDB ligase complex. We also show that, although the PARP1 catalytic function does not influence the initial interaction between these two proteins in the nucleoplasm, it is required for efficient recruitment of their complex to the lesion site. Our results reveal that the interaction of XPC with PARP1 in nucleoplasm under steady-state conditions facilitates the search function of XPC for DNA damage in the genomic context.

Results

DDB2-Independent Nucleoplasmic Interaction of PARP1 with XPC Before and After DNA Damage. Within minutes after UV irradiation, XPC, DDB2, and PARP1 are present at the UV-induced DNA lesions in cells. Although independent interactions of DDB2 with XPC (18, 23) or PARP1 (18, 19) at the lesion site are known, here we examined whether XPC interacts directly with PARP1 on the UV-damaged chromatin. The FLAG-PARP1–expressing human skin fibroblasts (GMRSiP) were fractionated before and after UV irradiation to prepare cytoplasm, nucleoplasm, and chromatin-bound protein fractions (Fig. 1*A*), as described earlier (18). In this protocol, the chromatin proteins such as histone H3 do not leak in the nucleoplasmic fraction but are extracted in the chromatin-bound protein fraction. Moreover, we further validated this fractionation protocol by confirming our earlier observation (18) that DDB2 accumulates in the chromatin fraction after UV irradiation (Fig. 1*A*). The XPC-immunoprecipitation (IP) of chromatin extracts with equal protein content from control and UV-irradiated cells revealed a significant increase in UV-induced association of PARP1 with XPC on the chromatin (Fig. 1*B*, *Left*). We also observed a UV-induced increase in the interaction of DDB2 with XPC at the chromatin, which is in agreement with our previous observation of this interaction identified by DDB2-IP (18). The reciprocal PARP1-IP using FLAG antibody revealed a strong UV-induced association of XPC with PARP1 in the chromatin-bound fraction (Fig. 1*B*, *Middle*). Since PARP1 and XPC are present in the nucleoplasm before and after irradiation (Fig. 1*A*), we examined whether they also interact with each other in this subnuclear fraction. The reciprocal IP for XPC and PARP1 in the nucleoplasmic fraction revealed a strong association of these two proteins not just after UV irradiation but also under control conditions before irradiation (Fig. 1*C*). Both the IPs failed to pull down DDB2 from control nucleoplasm, indicating a DDB2-independent nature of PARP1–XPC nucleoplasmic interaction before irradiation. Even after UV irradiation, XPC-IP confirmed its lack of interaction with DDB2 in nucleoplasm, whereas PARP1-IP revealed a feeble interaction of PARP1 with DDB2 (Fig. 1*C*), reflecting some turnover of the PARP1–DDB2 complex from postirradiation chromatin to nucleoplasm.

The interaction between PARP1 and XPC in UV-irradiated chromatin was expected, as both are known to bind to UV-damaged DNA. However, their interaction in nucleoplasm under steady-state conditions before UV challenge was unexpected; therefore, we examined this interaction in further detail using multiple cellular and in vitro models. To exclude the possibility that this could be an artifact of the expression of exogenous FLAG-tagged PARP1 in the above model, we examined this interaction in HEK293T cells that express endogenous XPC, PARP1, and DDB2. The mass spectrometry of the proteins that coimmunoprecipitate (co-IP) with XPC from the lysates of unirradiated HEK293T cells confirmed the presence of PARP1 as well as two known partners of XPC, namely HR23B and Centrin2 (Fig. 1*D*). The reciprocal IP for PARP1 and XPC validated the interaction of even the endogenous PARP1 with XPC in this fraction (Fig. 1*E*). Interestingly, the mass spectrometry of XPC eluate did not reveal the presence of DDB2, confirming its lack of interaction with XPC under control conditions. The DDB2-independent interaction between endogenous PARP1 and endogenous XPC was further confirmed in the nucleoplasm of DDB2-deficient XP-E cells (Fig. 1*F*). Thus, using different cellular models expressing endogenous or exogenous PARP1, and the variable status of DDB2, we consistently observed a DDB2-independent interaction between XPC and PARP1 in the nucleoplasm before and after irradiation and an increased interaction at the chromatin after irradiation.

Direct Interaction of XPC and PARP1. PARP1 and XPC are DNA-binding proteins; therefore, we examined the possibility that DNA could be mediating their interaction in the nucleoplasm. Unlike chromatin fraction, the nucleoplasmic fraction of the unirradiated HEK293T cells contained undetectable levels of DNA (Fig. S1). Very high doses of micrococcal nuclease (MNase) or benzonase are often used for digesting DNA from chromatin preparations to demonstrate direct interactions of proteins. In our IP studies, we prepared a chromatin-bound protein fraction after treatment of chromatin pellets with very low-dose MNase (25 U/mL). Since treatment of HeLa cell extracts with high-dose MNase was shown to digest the DNA to mononucleosomes (23), we treated the chromatin fraction of HEK293T cells with different doses of MNase up to 4,000 U/mL or benzonase up to 50 U/mL to digest it down to mononucleosomal DNA at 147 bp (Fig. S1). Although there was no detectable DNA in the nucleoplasmic fraction, we still treated this fraction from control or UV-treated HEK293T cells with 4,000 U/mL MNase before subjecting it to XPC-IP and observed that MNase did not break the association of XPC with

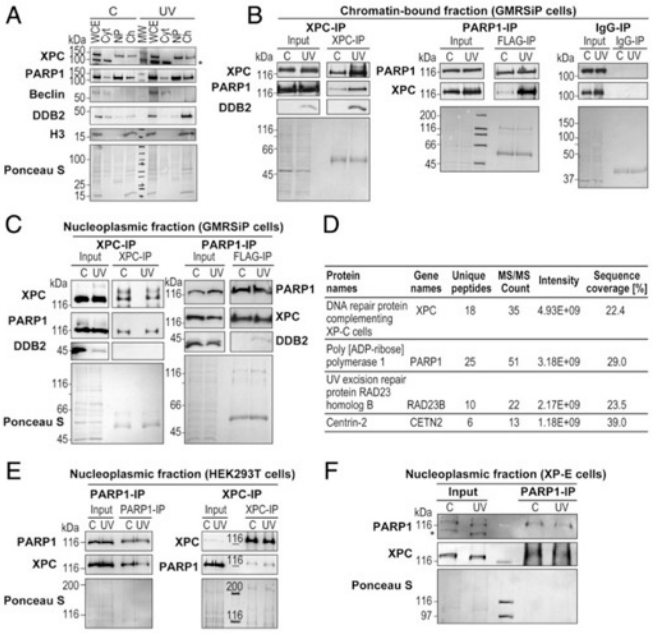

Fig. 1. PARP1 interacts with XPC in the nucleoplasmic and chromatin fractions. (*A*) The GMRSiP cells expressing FLAG-tagged PARP1 were irradiated with 30 J/m^2 UVC (or control), and whole-cell extracts (WCE) were fractionated to obtain cytoplasm (Cyt), nucleoplasm (Np), and chromatin-bound (Ch) fractions. The proteins from each fraction were immunoblotted for XPC, PARP1, and DDB2. Beclin and histone H3 were used as cytoplasmic and chromatin markers, respectively. The asterisk indicates a nonspecific band. The Ponceau S staining reflects the protein content at the end of each fractionation step. (*B* and *C*) The chromatin (*B*) and nucleoplasm fractions (*C*) of GMRSiP cells prepared as described above were subjected to IP for XPC, FLAG (PARP1), and mouse IgG (negative control), followed by the detection of PARP1, XPC, and DDB2. (*D*) Table showing the XPC-interacting proteins identified after XPC-IP of HEK293T cells followed by mass spectrometry analysis. (*E*) PARP1-IP and XPC-IP were performed in the Np fractions of control and UVC-treated HEK293T cells as shown in *C*. The Input and IP eluates were probed for XPC and PARP1. (*F*) PARP1-IP was performed in the Np fractions of control, and UVC-treated XP-E cells as described above. The Input and IP eluates were probed for XPC and PARP1. For *B*, *C*, *E*, and *F* the Ponceau S staining was used as loading control, and results shown here are representative of results from two to four experiments.

PARP1 (Fig. 2*A*), confirming DNA-independent interaction of these two proteins in the nucleoplasm.

To identify the domains of XPC involved in interaction with PARP1, we expressed GFP-tagged XPC and its five different partially overlapping fragments in HEK293T cells (Fig. 2*B*, *Top*). The extracts from these cells under control conditions were subjected to PARP1-IP followed by immunoblotting for GFP. Since the expression levels of full-length XPC and its fragments varied greatly after transfection (Fig. 2*B*, Input lanes), the strength of interaction of each XPC fragment with PARP1 was measured as a fraction of total input protein that coimmunoprecipitated with PARP1 and expressed relative to the interaction of full-length XPC with PARP1 (Fig. 2*B*, *Lower*). While control GFP protein did not interact with PARP1, four of the XPC fragments that span from 427 to 940 aa showed an interaction with PARP1 similar to that seen with full-length XPC, whereas a comparatively weaker interaction was observed with an N-terminal fragment (1–495 aa).

The interaction observed above between XPC or its fragments and PARP1 after PARP1-IP could not exclude the possibility that PARP1-interacting proteins may be indirectly mediating their interaction. Therefore, we examined the interaction of purified PARP1 in vitro with equimolar amounts of three purified fragments of XPC, namely GST-tagged 141–250 aa (XPC-N), His-tagged 496–734 aa (XPC-C1), and His-tagged 734–933 aa (XPC-C2) (Fig. 2*C*, *Top*). The PARP1-IP of above reaction mixtures revealed a strong interaction of PARP1 with XPC-C1 fragment, a weak interaction with XPC-C2 fragment and no interaction with XPC-N fragment, indicating that 496–734 aa is key region of XPC that interacts with PARP1 (Fig. 2*C*, *Lower*). These results are in agreement with the above in vivo data (Fig. 2*B*) showing a comparatively weaker interaction with PARP1 for the N-terminal XPC fragment (1–495 aa) compared with a strong interaction seen with full-length XPC or four of its fragments that contain the central region of XPC. The results with purified proteins and in vivo data with cells expressing XPC fragments strongly indicate an interaction of the central portion of the XPC protein spanning 496 to 734 aa with PARP1 without intervention of other proteins or DNA.

To identify the domains of PARP1 implicated in this interaction, its N-terminal (1–232 aa) fragment was expressed in GMSiP cells in which endogenous PARP1 was depleted by shRNA, whereas the C-terminal (232–1014 aa) fragment of PARP1 was expressed in PARP1$^{-/-}$ A1 cells. For control, we used GMRSiP cells that express FLAG-tagged full-length PARP1 in the GMSiP cells (Fig. 2*D*, *Top*). The XPC-IP of the extracts of these cells revealed that the C-terminal fragment of PARP1 is implicated in its interaction with XPC (Fig. 2*D*, *Lower*). Collectively, these results demonstrate that the region of XPC that is involved in its interaction with DNA, DDB2, and HR23B (2) is also involved in its interaction with PARP1.

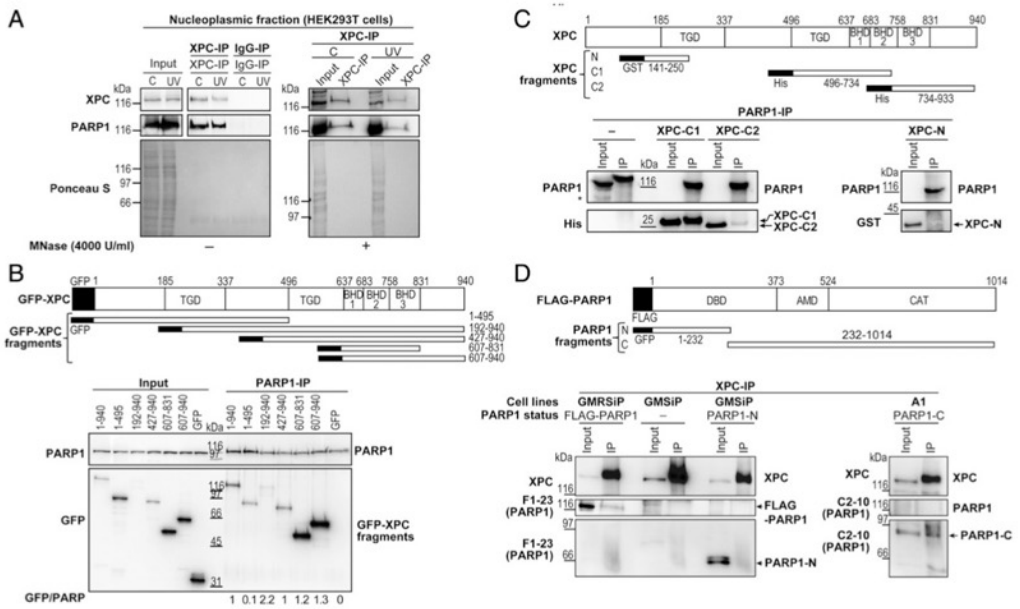

Fig. 2. Identification of the domains implicated in the interaction between PARP1 and XPC. (*A, Left*) IP for XPC and rabbit IgG were performed in the nucleoplasm of HEK293T cells prepared as described in Fig. 1*E*. (*A, Right*) Nucleoplasmic extracts were also treated with 4,000 U/mL MNase and subjected to XPC-IP. The Input and eluates were probed for XPC and PARP1. Ponceau S was used as loading control. (*B, Top*) Pictogram of GFP-tagged full-length XPC and its five fragments used in the study. The domains marked as TGD and BHD1-3 represent the transglutaminase homology domain and β hairpin domains 1–3. (*B, Lower*) The HEK293T cells were transiently transfected with GFP-tagged full-length XPC or its fragments for 48 h, and cell extracts were subjected to PARP1-IP. The Input and the IP eluates were analyzed for GFP (XPC) and PARP1. The relative intensity of the IP band was measured as a fraction of the total input protein. The strength of the interaction between XPC fragments and PARP1 was expressed as relative to the interaction of full-length XPC with PARP1. (*C, Top*) The pictogram of the full-length XPC and its fragments used in this study. (*C, Lower*) The XPC fragments were reacted with pure PARP1 for 30 min at 25 °C, followed by PARP1-IP on magnetic beads. The bead elutes were probed for PARP1, GST (XPC-N), and histidine (XPC-C1 and XPC-C2). (*D, Top*) Pictogram showing the domains of full-length PARP1 and its N- or C-terminal fragments used in this study. The DBD, AMD, and CAT are the DNA-binding, automodification, and catalytic domains, respectively. (*D, Lower*) The PARP1-depleted GMSiPs were transiently transfected with the full-length FLAG-PARP1 or its N-terminal fragment (GFP-DBD) and the PARP1$^{-/-}$ A1 cells with the C-terminal fragment for 48 h. The cell extracts were subjected to XPC-IP, and the bead eluates were analyzed for XPC and PARP1 or its fragments (F1-23 and C2-10). The data represent similar results observed in two experiments.

Roles of the PARP1–XPC Complex and Catalytic Activity of PARP1 in Recruitment of XPC to UV-Damaged DNA. PARP1 is known to rapidly reach damaged DNA in the chromatin context; hence, the PARP1–XPC complex formed in the nucleoplasm before irradiation could have a role in rapidly escorting XPC to the DNA lesion site after UV irradiation. To trace the intranuclear movement of PARP1-bound XPC, we used the proximity-dependent biotin identification (Bio-ID) technique (24). The FLAG-PARP1 was cloned in the myc-tagged biotin ligase BirA vector to create a new Bio-ID-PARP1 vector. The expression of Bio-ID-PARP1 in GMSiP cells depleted of endogenous PARP1 in the nuclear fraction (Fig. S2*A*) ensured that any nuclear protein that stably associates with or stays within 10 nm of the cloned PARP1 would be stably biotinylated. The absence of endogenous PARP1 in these cells eliminated the possibility that any PARP1-associated protein would not be biotinylated. For optimal biotinylation, we incubated these cells for 16–18 h with biotin before irradiation (24) and confirmed biotinylation of XPC and auto-biotinylation of PARP1 in XPC-IP eluates of the nucleoplasm of control and UV-irradiated cells (Fig. S2*B*). To examine the role of the catalytic activity of PARP1 in this interaction, we also treated the cells with PARPi PJ-34 under conditions that abolished the signal for PAR-modified proteins in control or UV-irradiated cells (Fig. S2*C*). Interestingly, the presence of PARPi did not abolish the interaction between XPC and PARP1, indicating that catalytic function of PARP1 is not required for this interaction in the nucleoplasm (Fig. S2*B*). Using this model, we tracked UV-induced movement of biotinylated XPC and PARP1 from the nucleoplasmic to chromatin fractions of control or UV-treated cells (Fig. 3*A*). In the streptavidin-IP of nucleoplasm, both PARP1 and XPC were detectable before and after irradiation, confirming biotinylation of XPC and auto-biotinylation of Bio-ID-PARP1 (Fig. 3*A*, *Left*, and Fig. S2*D*). The decrease in signal for biotinylated XPC after UV irradiation suggested a movement of XPC away from this fraction. Interestingly, PARPi blocked the reduction in the signal for XPC after UV irradiation, indicating a potential role of catalytic activity of PARP1 in the movement of XPC from the nucleoplasmic fraction to damaged DNA. The absence of biotinylated DDB2 in streptavidin-IP (Fig. 3*A*, *Left*), once again confirmed that DDB2 did not interact with Bio-ID-PARP1 or its complex with XPC in the nucleoplasm.

To examine whether the biotinylated nucleoplasmic XPC reaches the UV-damaged DNA, we performed the streptavidin-IP of corresponding chromatin fractions from these cells (Fig. 3*A*, *Right*). There was some signal for biotinylated XPC under steady-state conditions, which represents a basal level of interrogation of

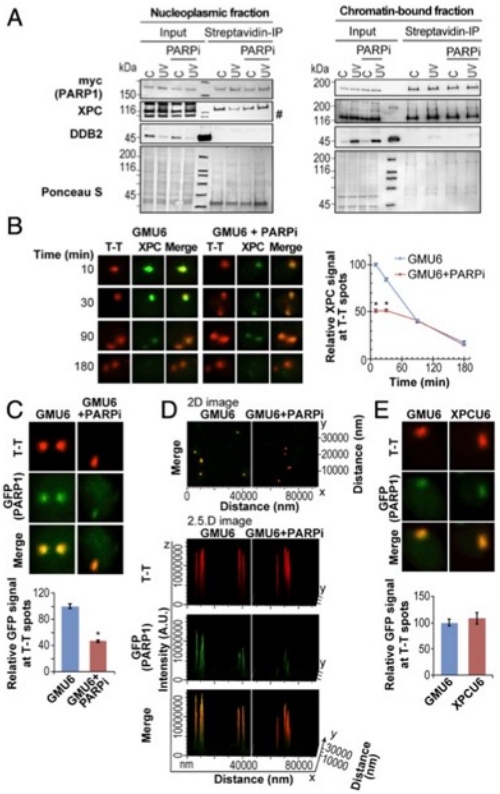

Fig. 3. Efficient recruitment of PARP1 and XPC to the UV lesion requires PARP1 catalytic activity. (*A*) Bio-ID-PARP1 cells expressing myc-Bio-ID-FLAG-PARP1 were irradiated (30 J/m^2 UVC or control) with or without PARPi (PJ-34). The nucleoplasm (*Left*) and chromatin-bound (*Right*) fractions were subjected to streptavidin-IP. The eluates were analyzed for myc (PARP1), XPC, and DDB2. The data represent similar results observed in three experiments, and Ponceau staining provides loading control. The "#" refers to a nonspecific band. (*B*) The XPC kinetics at the UV lesions were monitored in GMU6 cells up to 180 min after local UVC irradiation with 100 J/m^2 UVC through 5-μm pores of a polycarbonate filter with or without PARPi PJ-34. The background-corrected signal for XPC (green) at T-T spots (red) relative to the 10-min signal is represented as mean ± SEM (200–500 spots from three experiments). Note: In all panels of this and subsequent figures, an asterisk (*) denotes a statistically significant difference with P value < 0.05 with unpaired two-tailed t test. (*C* and *D*) The GMU6 cells were transiently transfected with GFP-PARP1 for 24 h and locally irradiated with 100 J/m^2 UVC in the absence or presence of PARPi PJ-34. (*C*) The GFP (PARP1) signals at local T-T spots (red) after background correction were pooled from 200 to 300 spots derived from three experiments and expressed relative to the signal observed in cells not treated with PARPi. (*D*) A representative 2D-merged image for GFP (PARP1) and T-T (red) colocalization and the orthogonal view (2.5D image) for the same field is shown to visualize signal intensity of T-T and GFP. The x and y axis represent distance in nanometers, and the z axis represents fluorescence intensity in arbitrary units. (*E*) The accumulation of the GFP (PARP1) at T-T lesions was monitored in GMU6 and XPCU6 cells 10 min after irradiation with UVC at 100 J/m^2. The background-corrected GFP signal at lesion sites relative to the signal observed in GMU6 cells is expressed as mean ± SEM derived from ≥150 spots from two experiments.

DNA at all times by the multifunctional XPC protein and an increase in this signal in UV-treated cells, which was suppressed by PARPi (Fig. 3*A*, *Right*). Our results are in agreement with a previous report that XPC constantly associates–dissociates with chromatin under steady-state conditions; an additional association of XPC is seen with chromatin after UV-induced DNA damage (4). The UV-mediated increase in biotinylated XPC at chromatin with a corresponding decrease in nucleoplasm suggests that either PARP1-bound XPC moved from nucleoplasm to UV-damaged chromatin or a completely independent XPC arrived at the lesion site and was biotinylated by PARP1 within 30 min after irradiation when the samples were harvested. However, within the same time period of 30 min postirradiation, DDB2, which is known to closely interact with PARP1 at the chromatin immediately after UV irradiation (18, 19), was not strongly biotinylated by Bio-ID-PARP1 (Fig. 3*A*, *Right*). Thus, the biotinylated XPC that is deposited on the UV-damaged chromatin must have originated from nucleoplasmic PARP1–XPC complexes formed before UV damage, and PARPi suppressed this movement.

To validate the inhibitory effect of PARPi on the movement of XPC from nucleoplasm to chromatin, we used immunocytological methods to visualize XPC at the site of local ultraviolet C (UVC) irradiation up to 3 h in the NER-proficient GMU6 human skin fibroblasts with or without treatment with PARPi (Fig. 3*B*). The GMU6 fibroblasts were locally irradiated with UVC through 5-μm pores in a polycarbonate filter, which produces distinct subnuclear areas of irradiation that are surrounded by unirradiated zones in the nucleus (25). Unlike Western blot data that reveal total XPC molecules that are bound to both UV-damaged and undamaged portions of chromatin, the immunocytological data with local irradiation reflect the status of XPC only in the irradiated subnuclear zones, thus excluding the "noise" of XPC signals from the unirradiated portions of the nucleus. In the subnuclear irradiated zones identified by staining with thymine dimer (T-T) CPD-specific antibody, the endogenous XPC followed a normal kinetics, i.e., initial strong accumulation at 10 min followed by a steady decline to 40% of initial levels in 90 min. The treatment of cells with PARPi, which could abolish the signal for PAR-modified proteins in control or UV-irradiated cells (Fig. S2*E*), also suppressed the initial recruitment of XPC at 10 min by 50%. Moreover, PARPi slowed down the departure of XPC from the lesion site in the first 90 min, compared with the rapid turnover of XPC in cells not treated with PARPi (Fig. 3*B*, *Right*). Thus, the major impact of PARP inhibition was in partially suppressing the initial recruitment of XPC to UV-lesion sites.

Since XPC is in a complex with PARP1 in the nucleoplasm, we examined the effect of PARPi on the recruitment of PARP1 itself to UV-damaged chromatin. Using cells expressing GFP-PARP1 and a recently developed in situ extraction technique that can selectively identify DNA-bound PARP1 (26), we observed that PARPi PJ-34 suppressed by 50% the initial recruitment of GFP-PARP1 to local UV-irradiated subnuclear zones, which were identified by immunostaining for T-T (Fig. 3*C*, *Lower*). The Z-stack images (Fig. S3*A*) and their orthogonal view (Fig. S3*B*) of the locally irradiated GMU6 cells confirmed the spatial colocalization of the GFP-PARP1 with T-T (Fig. 3*C*). The immunofluorescence image with multiple locally irradiated cells presented in 2D and 2.5D format revealed that PARPi treatment significantly reduced the intensity of colocalized signal for GFP-PARP1 at the site of DNA damage (Fig. 3*D*). Interestingly, the recruitment of PARP1 itself to a UV-lesion site is not dependent on XPC because it occurs to an identical extent in both XPC-proficient (GMU6) and -deficient (XP-C) cells (Fig. 3*E*). Collectively, our results indicate that the initial phase of the basal level of recruitment of PARP1 and XPC to UV-damaged DNA does not require catalytic activity of PARP1, whereas the second phase occurs in response to PARP1 activation.

PARP1-Mediated Recruitment of XPC to UV-Lesion Sites Is Independent of DDB2. DDB2 is known to recruit XPC to the UV-lesion site, and since DDB2 and PARP1 interact with each other to facilitate NER (27), our results of suppressed XPC recruitment to the UV-lesion site could also be an indirect effect of PARPi on the role of DDB2 in recruiting XPC. To exclude this possibility, we used DDB2-deficient XP-E cells to examine the effect of PARPi on colocalization of XPC with 6–4PP lesions after local UV irradiation. At the lesion sites, the signal for XPC declined rapidly by 50–60% from 10 to 60 min (Fig. 4*A*). In contrast, PARPi treatment not only reduced the initial recruitment of XPC at lesion site by 50%, but also slowed down XPC turnover up to 60 min, a trend that was also observed in DDB2-proficient GM cells (Fig. 3*B*). An identical profile of suppression of XPC recruitment and turnover in DDB2-proficient and -deficient cells indicates that the suppression of XPC recruitment by PARPi is not mediated via DDB2. The biological end-point of XPC recruitment to the lesion site is the repair of UV-damaged DNA. Therefore, we measured the kinetics of removal of 6–4PP lesions up to 8 h following global UV irradiation in XP-E cells. As expected, almost all 6–4PP lesions were removed in XP-E cells by 8 h, but the treatment with PARPi significantly slowed down this repair process (Fig. 4*B*). Since the depletion of PARP1 completely suppressed any PAR formation in response to UV irradiation without affecting PARP2 expression (18, 28, 29), these results indicate that XPC recruitment is partially controlled by the catalytic activity of PARP1 in a DDB2-independent manner. Collectively, our findings demonstrate that the inhibition of PARP1 activity reduces recruitment of XPC to UV damage with a direct negative consequence on the repair of UV-induced lesions.

To determine the extent of the contribution of DDB2 and PARP1 in the recruitment of XPC to DNA lesions, we used four different cell lines described earlier (29) (Fig. 4*C*): CHOSiP cells (deficient in both PARP1 and DDB2); CHOU6 cells (deficient only in DDB2); GMSiP cells (deficient only in PARP1); and GMU6 (proficient in both DDB2 and PARP1). In each cell type, we examined the early accumulation of XPC at the local UV-lesion site (Fig. 4*C*, *Right*). The CHOSiP cells displayed a basal level of accumulation of XPC at the UV-lesion site, which represents the inherent capacity of XPC to reach the lesions without the help of DDB2 or PARP1. Relative to this basal level, the presence of only PARP1 (CHOU6) or only DDB2 (GMSiP) increased XPC recruitment by about 40%. However, the presence of both DDB2 and PARP1 in GMU6 cells nearly doubled the XPC accumulation compared with the CHOSiP model, strongly supporting independent roles of DDB2 and PARP1 in this process.

The total cellular levels of XPC in PARP1-depleted GMSiP and CHOSiP cell lines were similar to PARP1-proficient GMU6 and CHOU6 cells (Fig. 4*D*); therefore, the suppression of the recruitment of XPC to the damaged site in PARP1-depleted cells was not an artifact of reduced XPC expression in these cells. Since the recruitment of the downstream NER proteins depends on XPC loading and stabilization at the damage site (1), we measured the accumulation of Xeroderma pigmentosum A (XPA) protein on the chromatin-bound fraction of these cells up to 4 h after damage (Fig. 4*E*). In each of these cellular models, the kinetics of XPA recruitment reflected the status of XPC at the UV-damaged chromatin. The XPA accumulation was robust in GMU6 cells and reduced in the absence of PARP1 (GMSiP cells) or DDB2 (CHO cells), whereas the weakest accumulation and a rapid turnover of XPA were seen in the CHOSiP cells devoid of both DDB2 and PARP1. Collectively, our results show that there are three components of recruitment of XPC to a DNA lesion site: the first is a basal level of recruitment controlled by XPC itself; the second is dependent on PARP1 or DDB2 proteins; and the last component depends on the catalytic activation of PARP1.

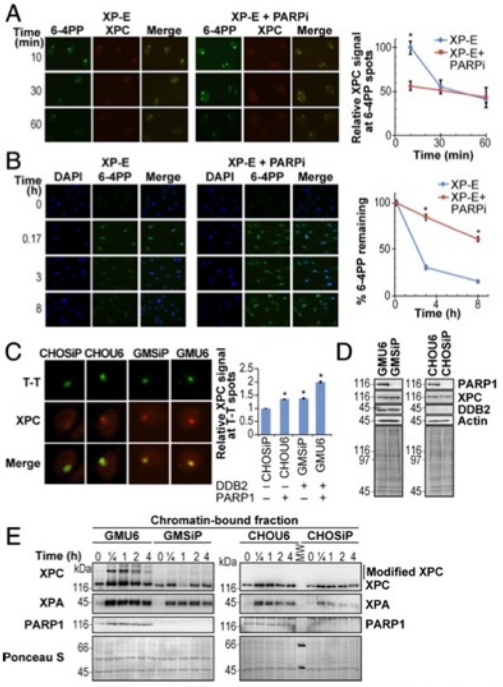

Fig. 4. XPC recruitment to UV lesions by PARP1 is DDB2-independent. (*A*) XP-E cells with or without PARPi (ABT-888) were locally irradiated with 100 J/m^2 UVC and probed for XPC (red) and 6–4PP sites (green) at different times. The background-corrected signal for XPC at 6–4PP spots is represented as mean ± SEM (300 spots derived from three experiments). (*B*) The DDB2-deficient XP-E cells, with or without PARPi ABT-888, were globally irradiated with 10 J/m^2 UVC and immunostained for 6–4PP lesions to determine its repair kinetics up to 8 h. The data are presented as signal intensity relative to the maximum signal at 10 min (mean ± SEM, $n \geq 300$ nuclei from three experiments). (*C*) The four cell lines with differing status of PARP1 and DDB2, as shown at the *Right*, were locally irradiated with 100 J/m^2 and probed for T-T and XPC at 10 min after irradiation. Background-corrected signal for XPC at the T-T under identical exposure conditions was calculated as mean ± SEM derived from 300 to 700 spots from three experiments. The accumulation of the XPC at the T-T lesion in CHOU6, GMSiP, and GMU6 is expressed as fold increase over that observed in CHOSiP. (*D*) The total cell extracts of the four indicated cell lines were separated on the SDS/PAGE and probed for PARP1, XPC, and DDB2. Actin and Ponceau S were used as loading controls. (*E*) The four cell lines from above were globally irradiated with 30 J/m^2 UVC and fractionated after the time indicated. The chromatin extracts with equal protein content were separated on SDS/PAGE and probed for XPC, XPA, and PARP1. Ponceau S staining was used as loading control.

Characterization of the Handover of XPC from Its Complex with PARP1 to UV-Damaged DNA. Our results show that PARP1 and XPC form a complex in the nucleoplasm, and the biotin tag on XPC at the UV-lesion site indicates a physical handover of XPC from its complex with PARP1 to UV-damaged DNA. To explore the mechanistic aspect of this transfer in vivo, we carried out GFP (XPC)-IP of chromatin fractions from HEK293T cells expressing GFP-tagged XPC up to 3 h after irradiation and examined the state of association of PARP1 with XPC (Fig. 5*A*, *Left*). The IP revealed a normal kinetics of recruitment and departure of XPC at the UV-damaged chromatin with a strong accumulation at 30 min and a significant reduction by 3 h. In contrast, the amount of PARP1 that

is associated with GFP-XPC decreased rapidly from 30 to 90 min, and no signal was detected at 180 min. It is noteworthy that, although a significant amount of PARP1 was still present in the chromatin fraction from 30 to 180 min (as seen in the Input samples in Fig. 5*A*, *Left*), it was not associated with XPC after the peak period of recruitment of XPC to the lesion. A similar kinetics of association and dissociation of XPC and PARP1 was observed in chromatin over 3-h period after exposure to 30 J/m^2 UVC in GM cells that express endogenous XPC and PARP1 (Fig. 5*A*, *Middle*), demonstrating the general nature of this observation. Moreover, XPC-IP of the chromatin-bound fraction of the same GM cells 10 min after exposure to various UVC doses up to 100 J/m^2 revealed a dose-dependent increase in the interaction between XPC and PARP1 at the chromatin (Fig. 5*A*, *Right*). On the other hand, despite an abundance of DDB2 in the input chromatin fraction at all doses, there was a dose-dependent decrease in association of DDB2 with XPC (Fig. 5*A*, *Right*). The dose-dependent increase in association of XPC and PARP1 at an early time point and their dissociation at a later time support a model that early recruitment of XPC occurs as a complex with PARP1 but, having reached the lesion site, XPC gradually dissociates from PARP1 to continue with its functions in NER.

To explore the conditions required for XPC to dissociate from its complex with PARP1 and bind to UV-damaged DNA, we designed in vitro assays using the factors prevalent at the lesion site in vivo, namely UV-damaged DNA, DDB2, PARP1, and XPC represented by its key fragment 496–734 aa (ΔXPC) that interacts with PARP1 (Figs. 5 *B–D*). To examine the endogenous properties of these three proteins to bind to UV-damaged DNA, we reacted them singly or in combinations with UVC-irradiated plasmid DNA, which was immobilized on the magnetic beads via T-T antibody (Fig. S4). All of the proteins could bind to UV-damaged DNA on their own and even in combination with other proteins (Fig. 5*B*). Although this assay confirms the inherent capacity of XPC, DDB2, and PARP1 to bind to UV-damaged DNA, it does not reveal how DDB2 or PARP1, which are recruited before XPC, could participate in the loading of XPC to the lesion site.

Since XPC exists as a complex with PARP1 in the nucleoplasm before reaching UV-damaged chromatin, we examined whether this PARP1–XPC complex would simulate conditions for in vivo loading of XPC to UV-DNA. We immobilized the PARP1–ΔXPC complex on the agarose beads with PARP1 antibody (A beads) and reacted it with the above-described UV-damaged DNA bound to magnetic beads (M1) in the presence of either PARP1

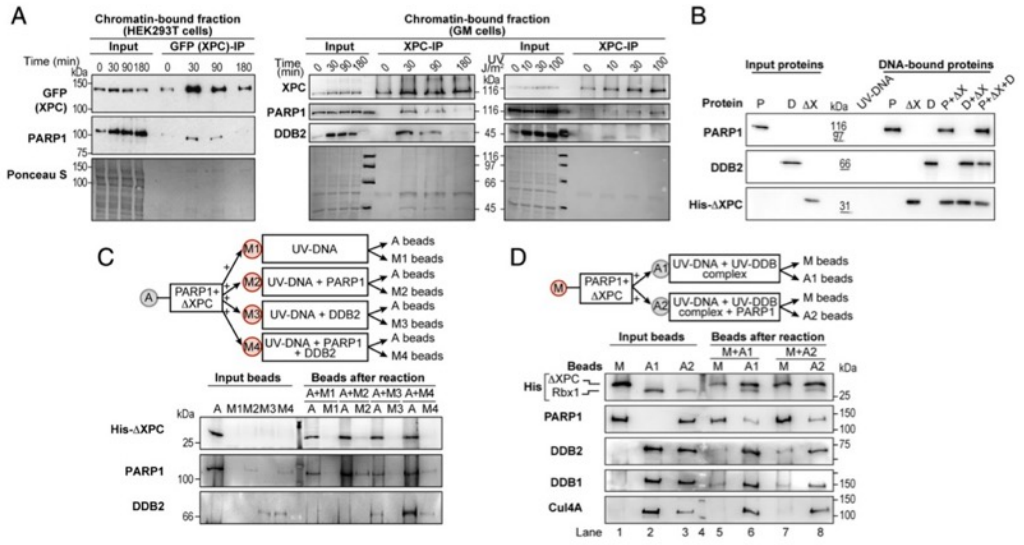

Fig. 5. Role of PARP1 and the UV–DDB ligase complex in the handover of XPC to the lesion site. (*A*, *Left*) HEK293T cells transfected with GFP-XPC plasmid were irradiated 48 h later with 30 J/m^2 UVC (or control) and fractionated to isolate chromatin-bound fraction, which was subjected to IP with GFP-trap beads. The eluates were probed with PARP1 and GFP antibody. (*A*, *Middle* and *Right*) GMU6 cells were irradiated with either 30 J/m^2 UVC (*Middle*) or different UVC doses as indicated (*Right*) and fractionated after the time indicated for the *Middle* panel or at 10 min for the *Right* panel. The chromatin-bound protein fraction was used for immunoprecipitation of XPC. The IP eluates were resolved on the SDS/PAGE and probed for XPC, PARP1, and DDB2. The Ponceau S staining was used as loading control, and each panel is representative of results from two experiments. (*B*) UVC-DNA was bound to magnetic beads via T-T antibody and reacted with the pure proteins PARP1 (P), XPC fragment (ΔX), DDB2 (D), and different protein combinations for 15 min at 25 °C. The beads were washed, and the bound proteins were eluted, separated on SDS/PAGE, and probed with their respective antibodies. (*C* and *D*, *Top*) The *Top* panels represent schematic of the different conditions used in the in vitro assays for examining the separation of XPC from the PARP1–XPC complex and its handover to UV-DNA. The gray and red circles represent agarose and magnetic beads, respectively. The bead-bound PARP1–ΔXPC complex was prepared either on magnetic or agarose beads as described in Fig. 2*C*. The representative results for each model from two to three experiments are shown. (*C*, *Lower*) The PARP1–ΔXPC complex was prepared on agarose beads (*A*), and magnetic bead-bound UV-DNA (M1) was reacted with PARP1 (M2), DDB2 (M3), or both (M4), as described for *B*. The beads were mixed as indicated in the *Top* panel, reacted for 15 min at 25 °C in buffer, separated, washed, and eluted, and the elution was separated on SDS/PAGE and probed with specified antibodies. (*D*, *Lower*) The PARP1–ΔXPC complex was prepared on magnetic beads (M), and the agarose bead-bound UV–DDB ligase complex without (A1) or with (A2) second PARP1 was prepared by prereacting the agarose bead-bound Cul4A–Rbx1 complex with free UV-DNA, DDB1, and DDB2 for 15 min at 25 °C. The beads were mixed, reacted for 15 min at 25 °C in buffer, separated, washed, and eluted, and the elution was separated on SDS/PAGE and probed with specified antibodies.

(M2 beads) or DDB2 (M3 beads) or both PARP1 and DDB2 (M4) (Fig. 5*C*, *Top*). After each reaction, the agarose (A beads) and magnetic beads (M1–M4) were separated and washed, and the proteins present in each of these beads were examined by immunoblotting of bead eluates. The immunoprobing for ΔXPC in the agarose and magnetic beads after the reaction revealed that none of the above conditions could dissociate ΔXPC from its complex with PARP1 (Fig. 5*C*).

At the UV-lesion site on DNA, DDB2 is not recruited alone but as a UV–DDB ligase complex containing DDB2, DDB1, Cul4A, and Rbx1. In addition, DDB2 interacts with PARP1 at the lesion site. Therefore, we examined whether the entire UV–DDB complex as well as PARP1 are required for loading of XPC to UV-DNA (Fig. 5*D*, *Top*). We recreated this complex by loading purified Cul4A–Rbx1 on agarose beads and reacted it with purified DDB1, DDB2, and UV-DNA in the absence (A1) or presence of PARP1 (A2). On the other hand, the PARP1–ΔXPC complex was immobilized via PARP1 antibody on the magnetic beads (M). The immunoblotting confirmed the presence or absence of each of the six designated proteins in the input beads M, A1, and A2 (Fig. 5*D*, Input lanes). The PARP1–ΔXPC (M) beads were reacted with A1 or A2 agarose beads, and the beads were separated and washed followed by immunoblotting of each of the beads for detection of the six proteins. The immunoprobing for His-ΔXPC in the magnetic and agarose beads revealed that the UV–DDB ligase complex with UV-DNA provided favorable conditions for promoting the dissociation of ΔXPC from its complex with PARP1 on magnetic beads (Fig. 5*D*, compare lane 1 with lane 5) as well as loading of ΔXPC onto the UV-DNA on A1 agarose beads (Fig. 5*D*, compare lane 2 with lane 6). Addition of PARP1 to the UV–DDB complex on A2 agarose beads in the above reaction did not confer any additional movement of ΔXPC to UV-DNA on agarose beads (Fig. 5*D*, compare lane 6 with lane 8). Collectively, these in vitro assays with purified proteins reveal that, although free XPC has an inherent capacity to efficiently bind to UV-DNA, its presence as a complex with PARP1 before irradiation ensures that XPC is preferably deposited at the UV-damaged sites that contain the UV–DDB ligase complex.

Discussion

For the last 15 years, focused efforts have been made to understand how XPC, with or without the help of other proteins, rapidly searches for its target lesions scattered across the entire genome in higher-order chromatin structure. Many studies indicated a role for DDB2 in the proper functioning of XPC with an indirect role for PARP1 via its ability to participate in chromatin remodeling (20, 27). The present study reveals a paradigm for the functional role of physical interaction of PARP1 with XPC before DNA damage in the initial recruitment and handover of XPC at UV-induced DNA lesions. Using various cell lines with exogenous or endogenous PARP1 and XPC, we show that PARP1 and XPC interact in the nucleoplasmic fraction of the cells even in the absence of DNA damage and that this interaction is independent of DDB2 and catalytic activation of PARP1. By using the PARP1 proximity-mediated biotinylation model in vivo, we also show that XPC from the nucleoplasmic PARP1–XPC complex is deposited at the DNA lesion site after UV irradiation. Using PJ-34 as PARPi, we observed that PARP inhibition partially suppresses the initial recruitment of XPC and PARP1 to the UV-lesion site, which is in agreement with earlier reports showing decreased recruitment of PARP1 to the site of microirradiation-induced DNA damage in the presence of PARPi such as PJ-34 (30) and NU-1025 (31). Another study reported an increased signal for PARP1 at damaged DNA after treatment with the PARPi 4-amino-1,8-naphthalimide (32). The difference in the end results among these studies could be attributed to the time of harvesting of the samples after treatment and the capacity of different PARPi to immobilize PARP1 on the DNA lesion sites (30, 33). Since PARP1 depletion reduces XPC recruitment to the lesion site, and PARPi reduces the rapid colocalization of PARP1 and XPC to the lesion site in vivo, our results indicate that both PARP1 and its catalytic function determine the movement of the PARP1–XPC complex from nucleoplasm to chromatin after irradiation.

In XP-E cells deficient in DDB2 function, the repair of 6–4PP is attributed to the inherent property of XPC to recognize 6–4PP lesions. Nonetheless, some studies demonstrated a reduced level of recruitment of XPC to UV damage in these cells compared with DDB2-proficient cells (7, 8). Additionally, we show that PARPi not only causes further reduction in initial recruitment of XPC to local spots of UV-induced DNA lesions but also significantly hampers the repair of 6–4PP lesions in these cells. Thus, in the XP-E model, our results clearly reveal a DDB2-independent role of PARP1 in facilitating XPC recruitment to the UV lesions and repair of 6–4PP by NER. It has been shown that XP-E cells have very low levels of PAR and that both ubiquitination and ALC1-mediated chromatin remodeling are absent in these cells (19). Hence, the decrease in recruitment of XPC by PARPi could not be related to ubiquitination or chromatin remodeling at the damaged site but instead due mainly to the suppression of movement of the PARP1–XPC complex from nucleoplasm to the lesion site on chromatin in XP-E cells. Using cells that are DDB2-deficient, PARP1-depleted, or treated with PARPi, we identified that the recruitment of XPC to the UV-lesion site in the genomic context is the sum of efforts by multiple factors including XPC itself, DDB2, PARP1, and the catalytic activity of PARP1. In a cell line that is devoid of functional DDB2 and PARP1 (CHO-SiP), there is a basal level of recruitment of XPC to the lesion site, indicating that XPC has some inherent capacity to reach the DNA lesion site that is not dependent on DDB2 or PARP1 or its activation. The reduced level of XPC translates to an impaired accumulation of XPA at the lesion site. Nonetheless, adding PARP1 alone in this DDB2-deficient background (CHOU6 cells) or DDB2 alone in a PARP1-deficient background (GMSiP) improves the recruitment of XPC above the basal level, indicating that each of these two proteins independently participates in XPC recruitment and stabilization. Finally, in the cells with PARP1 and DDB2, it is the DDB2-stimulated catalytic activation of PARP1 (18) that provides the last boost for recruitment of XPC to the lesion.

PARP1 has many characteristics that would facilitate the search function of XPC in NER: (*i*) PARP1 is an abundant protein in the mammalian nucleus that is rapidly recruited to all types of DNA damages (34) including UV-induced DNA lesions (26). Hence, an association with PARP1 will allow XPC to be quickly recruited to different types of DNA lesions anywhere in the genome. (*ii*) PARP1 can detect lesions and become activated to form PAR and create a protein-recruiting PAR platform (35), which in turn can bring in more PARP1 with XPC and other PAR-seeking proteins to the site. (*iii*) Like XPC, the binding of PARP1 to damaged DNA is independent of the sequence or the chemical nature of DNA damage (1, 36). Moreover, both XPC and PARP1 have affinity for unusual DNA structures with nonhydrogen-bonded bases, such as hairpins, stem loops, bubbles, and overhangs (1, 37). Thus, PARP1 could rapidly recruit XPC to all types of damages that are repaired by NER irrespective of their recognition by DDB2 (38). (*iv*) PARP1 is a part of the chromatin structure with preference for binding to the internucleosomal linker region (39). The chromatin-bound PARP1 can bind rapidly to lesions in this region and help recruit the nucleoplasmic PARP1–XPC complex. Additionally, the presence of the UV–DDB ligase complex in the linker (23) will allow handover and stabilization of XPC at this site. (*v*) Finally, the role of PARP1 activation in chromatin remodeling at the lesion site via recruitment of ALC1 (19) and PARylation of histones (34) would subsequently permit XPC to repair less accessible intranucleosomal lesions.

It has been shown that the handover of the UV lesion from the UV–DDB complex to XPC requires a transient physical interaction

between DDB2 and the central region of XPC (496–679 aa) containing the domains required for its interaction with DNA (23). Interestingly, our in vitro studies have identified that the same central domain of XPC (496–734 aa) mediates its interaction with PARP1. This indicates a dynamic and cooperative process in which XPC is released from its complex with PARP1 and transferred to the lesion site containing the UV–DDB complex. Thus, our in vitro model faithfully replicates the sequence of events surrounding efficient stabilization of XPC to the lesion site, which starts with its dissociation from the complex formed with PARP1, followed by the formation of a new complex with UV–DDB. The requirement of the UV–DDB ligase complex at the lesion site ensures that PARP1-escorted XPC is preferably released at a site that is primed for GG-NER due to ubiquitination and chromatin-remodeling events initiated by the UV–DDB ligase complex. Our data do not exclude the role of the PARylation of proteins as well as changes in the structure of DNA at the lesion site toward dissociation of the PARP1–XPC complex and stabilization of XPC. These factors could play a key role in delivering XPC from its complex with PARP1 to the damage site in the absence of DDB2. Such events have been shown to play a role in dissociation of PARP1 from XRCC1 or APE1 during base excision repair (40, 41).

We propose a model for the roles of PARP1 in the lesion recognition function of XPC (Fig. 6). Before UV irradiation, PARP1 and XPC coexist as a complex in the nucleoplasm, and DDB2 is not part of this complex. Since PARP1 is a more abundant protein compared with XPC (9, 42), there will still be sufficient free PARP1 molecules to separately interact with DDB2 at the lesion site. The free PARP1 molecules as well as the PARP1–XPC complex will scan the intact DNA due to the affinity of PARP1 and XPC for DNA, which explains the presence of basal levels of biotinylated XPC and PARP1 in chromatin-bound protein fractions from control cells. However, the transient binding of the complex to control DNA will not result in separation of XPC from PARP1 because the UV–DDB ligase complex is not recruited to chromatin until DNA damage occurs. Upon UV irradiation, free PARP1 as well as XPC-bound PARP1 molecules will reach the lesion site and may deposit XPC from the complex to the lesion site with the help of other factors. However, the optimum deposition of XPC from its complex with PARP1 to the UV-lesion site would occur when the UV–DDB ligase complex is present at the lesion site, a condition that would be observed in normal DDB2-competent cells. The formation of PAR by DDB2-stimulated PARP1 (18) provides a platform for additional PAR-seeking molecules to accumulate at the damaged site, including more of the nucleoplasmic PARP1–XPC complex. The presence of the UV–DDB complex at the lesion site in the linker region (23) or in the core region (43) would facilitate prioritization of these sites for initial recruitment of XPC and the repair. Additionally, the PARylation, DDB2, and UV–DDB ubiquitin ligase complex-mediated chromatin-remodeling events opens the nucleosomal structure to allow the arrival of downstream proteins to complete the process of NER at all of the remaining lesions in the genome.

Much effort has gone into understanding the interaction of PAR and PARP1 with different proteins in the cells after DNA damage. However, not much is known about the importance of the interaction of PARP1 with multiple cellular proteins in steady-state conditions before DNA damage, which has been reported in the proteomics study (44). Here, we clearly show that the interaction of PARP1 with XPC before DNA damage is not a random phenomenon, but serves a definitive purpose of delivering XPC to the site of DNA damage within minutes after irradiation for efficient NER-mediated repair by XPC. We suggest that similar functional roles are possible for the steady-state interaction of other proteins with PARP1. Our study also highlights the fact that proteins move from one subnuclear compartment to another and thus that they may carry old partners into a new compartment or make new partners in the new location. Hence, the proteomic studies of PARP1 interactors would be much more informative if these analyses were performed before and after DNA damage and in different subnuclear compartments.

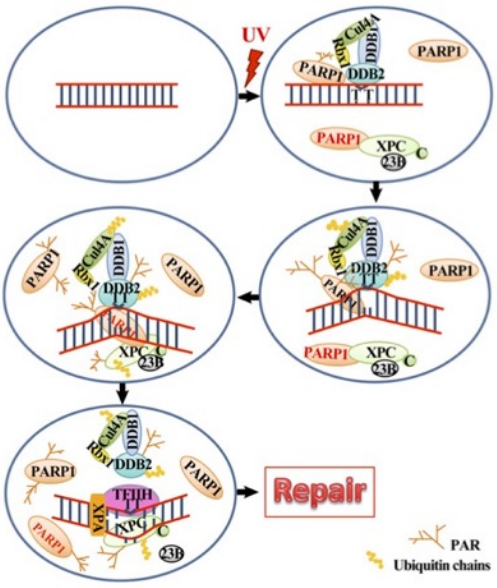

Fig. 6. Model for the role of PARP1 in recruitment and stabilization of XPC in NER. See details in *Discussion*.

Materials and Methods

Full details are provided in *SI Materials and Methods*.

Cell Lines, Clones, Plasmids, and Cloning. The SV-40 immortalized GM637 and primary XP-E (GM01389) human skin fibroblasts were obtained from Coriell. HEK293T and CHO cells were from ATCC. The clones PARP1-replete (GMU6, CHOU6), PARP1-depleted (GMSiP, CHOSiP), and FLAG-tagged PARP1-expressing (GMRSiP) were described earlier (18, 29). The Bio-ID-PARP1–expressing plasmid was generated in pcDNA3.1 mycBioID backbone from Addgene (24) and used for creating Bio-ID-PARP1 cell lines in the PARP1-depleted GMSiP cells. The creation of the pGFP-DBD vector expressing the N-terminal fragment of PARP1 (1–232 aa) was described earlier (26). The vector expressing the C-terminal fragment of PARP1 (232–1,014 aa) was cloned from PARP31 vector.

UV Irradiation and Immunofluorescence Microscopy Studies. The local UVC irradiation using a 5-μm polycarbonate filter (Millipore), global UVC irradiation, the repair kinetics assays for 6–4PP, recruitment of NER proteins and GFP-PARP1 to local UVC-induced DNA damage, the image acquisition and analyses and software used for analyses of images, and full details of the statistical analyses of images are described in *SI Materials and Methods*.

Cell Fractionation and co-IP of Proteins in the Cell Fractions. Cell fractionation to obtain nucleoplasmic and chromatin-bound protein fractions and the IP protocols followed by immunoprobing for proteins in these fractions were described earlier (18) and are explained in *SI Materials and Methods*. For streptavidin-IP, cells were incubated with 50 μM biotin in the medium for 16–18 h before UV treatment.

Identification of XPC-Interacting Proteins by Mass Spectrometry. The preparation of the cell extracts from HEK293T cells, the XPC-IP, the identification XPC-interacting proteins using LC-MS/MS, along with their quantification using the appropriate software and the threshold limits, were described earlier (45) and also in *SI Materials and Methods*.

In Vitro Studies to Examine the Handover of XPC from PARP1 to UV-Damaged DNA. Use of purified bovine PARP1 (Apartosis), XPC fragments (Antibodies online), GST-DDB1 and GST-DDB2 (Abnova), purification of full-length human Cul4A, binding of UVC-DNA and proteins to magnetic or agarose beads through their respective antibodies, and the handover assays are described in *SI Materials and Methods*.

ACKNOWLEDGMENTS. We thank V. Schreiber for GFP-PARP1 and M. Miwa for permission to receive 10H hybridoma and F. M. Boisvert and D. Levesque for interpretation of the proteomics data generated at Université de Sherbrooke. This work was supported by Discovery Grant RGPIN-2016-05868 and Discovery Accelerator Grant RGPAS-492875-2016 (to G.M.S.) from the Natural Sciences and Engineering Research Council of Canada. N.K.P. received a foreign student fee-waiver scholarship from the Québec Government and Shastri Indo-Canadian Institute. M.R. and N.K.P. were recipients of graduate scholarships from the Fonds de Recherche du Québec-Santé and Neuroscience Axis of Centre Hospitalier Universitaire de Québec Research Center-Université Laval, respectively.

1. Schärer OD (2013) Nucleotide excision repair in eukaryotes. *Cold Spring Harb Perspect Biol* 5:a012609.
2. Puumalainen MR, Rüthemann P, Min JH, Naegeli H (2016) Xeroderma pigmentosum group C sensor: Unprecedented recognition strategy and tight spatiotemporal regulation. *Cell Mol Life Sci* 73:547–566.
3. Sugasawa K (2016) Molecular mechanisms of DNA damage recognition for mammalian nucleotide excision repair. *DNA Repair (Amst)* 44:110–117.
4. Hoogstraten D, et al. (2008) Versatile DNA damage detection by the global genome nucleotide excision repair protein XPC. *J Cell Sci* 121:2850–2859.
5. Chen X, et al. (2015) Kinetic gating mechanism of DNA damage recognition by Rad4/XPC. *Nat Commun* 6:5849.
6. Velmurugu Y, Chen X, Slogoff Sevilla P, Min JH, Ansari A (2016) Twist-open mechanism of DNA damage recognition by the Rad4/XPC nucleotide excision repair complex. *Proc Natl Acad Sci USA* 113:E2296–E2305.
7. Moser J, et al. (2005) The UV-damaged DNA binding protein mediates efficient targeting of the nucleotide excision repair complex to UV-induced photo lesions. *DNA Repair (Amst)* 4:571–582.
8. Oh KS, et al. (2011) Nucleotide excision repair proteins rapidly accumulate but fail to persist in human XP-E (DDB2 mutant) cells. *Photochem Photobiol* 87:729–733.
9. Luijsterburg MS, et al. (2007) Dynamic in vivo interaction of DDB2 E3 ubiquitin ligase with UV-damaged DNA is independent of damage-recognition protein XPC. *J Cell Sci* 120:2706–2716.
10. Lan L, et al. (2012) Monoubiquitinated histone H2A destabilizes photolesion-containing nucleosomes with concomitant release of UV-damaged DNA-binding protein E3 ligase. *J Biol Chem* 287:12036–12049.
11. Wang H, et al. (2006) Histone H3 and H4 ubiquitylation by the CUL4-DDB-ROC1 ubiquitin ligase facilitates cellular response to DNA damage. *Mol Cell* 22:383–394.
12. El-Mahdy MA, et al. (2006) Cullin 4A-mediated proteolysis of DDB2 protein at DNA damage sites regulates in vivo lesion recognition by XPC. *J Biol Chem* 281:13404–13411.
13. Nishi R, et al. (2009) UV-DDB-dependent regulation of nucleotide excision repair kinetics in living cells. *DNA Repair (Amst)* 8:767–776.
14. Shell SM, et al. (2013) Xeroderma pigmentosum complementation group C protein (XPC) serves as a general sensor of damaged DNA. *DNA Repair (Amst)* 12:947–953.
15. Payne A, Chu G (1994) Xeroderma pigmentosum group E binding factor recognizes a broad spectrum of DNA damage. *Mutat Res* 310:89–102.
16. Scrima A, et al. (2008) Structural basis of UV DNA-damage recognition by the DDB1-DDB2 complex. *Cell* 135:1213–1223.
17. Vodenicharov MD, Ghodgaonkar MM, Halappanavar SS, Shah RG, Shah GM (2005) Mechanism of early biphasic activation of poly(ADP-ribose) polymerase-1 in response to ultraviolet B radiation. *J Cell Sci* 118:589–599.
18. Robu M, et al. (2013) Role of poly(ADP-ribose) polymerase-1 in the removal of UV-induced DNA lesions by nucleotide excision repair. *Proc Natl Acad Sci USA* 110:1658–1663.
19. Pines A, et al. (2012) PARP1 promotes nucleotide excision repair through DDB2 stabilization and recruitment of ALC1. *J Cell Biol* 199:235–249.
20. Luijsterburg MS, et al. (2012) DDB2 promotes chromatin decondensation at UV-induced DNA damage. *J Cell Biol* 197:267–281.
21. Maltseva EA, Rechkunova NI, Sukhanova MV, Lavrik OI (2015) Poly(ADP-ribose)polymerase 1 modulates interaction of the nucleotide excision repair factor XPC-RAD23B with DNA via poly(ADP-ribosyl)ation. *J Biol Chem* 290:21811–21820.
22. Jungmichel S, et al. (2013) Proteome-wide identification of poly(ADP-ribosyl)ation targets in different genotoxic stress responses. *Mol Cell* 52:272–285.
23. Fei J, et al. (2011) Regulation of nucleotide excision repair by UV-DDB: Prioritization of damage recognition to internucleosomal DNA. *PLoS Biol* 9:e1001183.
24. Roux KJ, Kim DI, Raida M, Burke B (2012) A promiscuous biotin ligase fusion protein identifies proximal and interacting proteins in mammalian cells. *J Cell Biol* 196:801–810.
25. Moné MJ, et al. (2001) Local UV-induced DNA damage in cell nuclei results in local transcription inhibition. *EMBO Rep* 2:1013–1017.
26. Purohit NK, Robu M, Shah RG, Geacintov NE, Shah GM (2016) Characterization of the interactions of PARP-1 with UV-damaged DNA in vivo and in vitro. *Sci Rep* 6:19020.
27. Pines A, Mullenders LH, van Attikum H, Luijsterburg MS (2013) Touching base with PARPs: Moonlighting in the repair of UV lesions and double-strand breaks. *Trends Biochem Sci* 38:321–330.
28. Ghodgaonkar MM, Zacal N, Kassam S, Rainbow AJ, Shah GM (2008) Depletion of poly(ADP-ribose) polymerase-1 reduces host cell reactivation of a UV-damaged adenovirus-encoded reporter gene in human dermal fibroblasts. *DNA Repair (Amst)* 7:617–632.
29. Shah RG, Ghodgaonkar MM, Affar B, Shah GM (2005) DNA vector-based RNAi approach for stable depletion of poly(ADP-ribose) polymerase-1. *Biochem Biophys Res Commun* 331:167–174.
30. Hanssen-Bauer A, et al. (2011) XRCC1 coordinates disparate responses and multiprotein repair complexes depending on the nature and context of the DNA damage. *Environ Mol Mutagen* 52:623–635.
31. Mortusewicz O, Amé JC, Schreiber V, Leonhardt H (2007) Feedback-regulated poly(ADP-ribosyl)ation by PARP-1 is required for rapid response to DNA damage in living cells. *Nucleic Acids Res* 35:7665–7675.
32. Godon C, et al. (2008) PARP inhibition versus PARP-1 silencing: Different outcomes in terms of single-strand break repair and radiation susceptibility. *Nucleic Acids Res* 36:4454–4464.
33. Gassman NR, Wilson SH (2015) Micro-irradiation tools to visualize base excision repair and single-strand break repair. *DNA Repair (Amst)* 31:52–63.
34. Luo X, Kraus WL (2012) On PAR with PARP: Cellular stress signaling through poly(ADP-ribose) and PARP-1. *Genes Dev* 26:417–432.
35. Pascal JM, Ellenberger T (2015) The rise and fall of poly(ADP-ribose): An enzymatic perspective. *DNA Repair (Amst)* 32:10–16.
36. Langelier MF, Pascal JM (2013) PARP-1 mechanism for coupling DNA damage detection to poly(ADP-ribose) synthesis. *Curr Opin Struct Biol* 23:134–143.
37. Lonskaya I, et al. (2005) Regulation of poly(ADP-ribose) polymerase-1 by DNA structure-specific binding. *J Biol Chem* 280:17076–17083.
38. Sugasawa K, et al. (2005) UV-induced ubiquitylation of XPC protein mediated by UV-DDB-ubiquitin ligase complex. *Cell* 121:387–400.
39. Clark NJ, Kramer M, Muthurajan UM, Luger K (2012) Alternative modes of binding of poly (ADP-ribose) polymerase 1 to free DNA and nucleosomes. *J Biol Chem* 287:32430–32439.
40. Moor NA, Vasil'eva IA, Anarbaev RO, Antson AA, Lavrik OI (2015) Quantitative characterization of protein-protein complexes involved in base excision DNA repair. *Nucleic Acids Res* 43:6009–6022.
41. Wei L, et al. (2013) Damage response of XRCC1 at sites of DNA single strand breaks is regulated by phosphorylation and ubiquitylation after degradation of poly(ADP-ribose). *J Cell Sci* 126:4414–4423.
42. Kraus WL, Lis JT (2003) PARP goes transcription. *Cell* 113:677–683.
43. Osakabe A, et al. (2015) Structural basis of pyrimidine-pyrimidone (6-4) photoproduct recognition by UV-DDB in the nucleosome. *Sci Rep* 5:16330.
44. Isabelle M, et al. (2010) Investigation of PARP-1, PARP-2, and PARG interactomes by affinity-purification mass spectrometry. *Proteome Sci* 8:22.
45. Dubois ML, Bastin C, Lévesque D, Boisvert FM (2016) Comprehensive characterization of minichromosome maintenance complex (MCM) protein interactions using affinity and proximity purifications coupled to mass spectrometry. *J Proteome Res* 15:2924–2934.

Annexe 5: Potentiation of ^{177}Lu-octreotate peptide receptor radionuclide therapy of human neuroendocrine tumor cells by PARP inhibitor

www.oncotarget.com Oncotarget, 2018, Vol. 9, (No. 37), pp: 24693-24706

Research Paper

Potentiation of ^{177}Lu-octreotate peptide receptor radionuclide therapy of human neuroendocrine tumor cells by PARP inhibitor

Nupur K. Purohit[1,2,3], Rashmi G. Shah[1,2,3], Samuel Adant[1,2,3,4,5], Michael Hoepfner[6], Girish M. Shah[1,2,3,*] and Jean-Mathieu Beauregard[2,4,5,*]

[1]Department of Molecular Biology, Medical Biochemistry and Pathology, Université Laval, Quebec City, Canada

[2]Cancer Research Center, Université Laval, Quebec City, Canada

[3]Neurosciences and Oncology Branches of CHU de Québec, Université Laval Research Center, Quebec City, Canada

[4]Department of Radiology and Nuclear Medicine, Université Laval, Quebec City, Canada

[5]Oncology Branch of CHU de Québec, Université Laval Research Center, Quebec City, Canada

[6]Institute of Physiology, Charité-Universitätsmedizin Berlin, Berlin, Germany

[*]Senior authorship

Correspondence to: *Jean-Mathieu Beauregard,* ***email:*** *jean-mathieu.beauregard@chudequebec.ca*

Keywords: *peptide receptor radionuclide therapy; ^{177}Lu-octreotate; neuroendocrine tumors; PARP inhibitor; radiosensitization*

Received: *November 08, 2017* ***Accepted:*** *April 06, 2018* ***Published:*** *May 15, 2018*

ABSTRACT

For patients with inoperable neuroendocrine tumors (NETs) expressing somatostatin receptors, peptide receptor radionuclide therapy (PRRT) with ^{177}Lu-[DOTA0-Tyr3]-octreotate (^{177}Lu-octreotate) is one of the most promising targeted therapeutic options but it rarely achieves cure. Therefore, different approaches are being tested to increase the efficacy of ^{177}Lu-octreotate PRRT in NET patients. Using the gastroenteropancreatic BON-1 and the bronchopulmonary NCI-H727 as NET cell models, here we report that pharmacological inhibitors of DNA repair-associated enzyme poly(ADP-ribose) polymerase-1 (PARPi) potentiate the cytotoxic effect of ^{177}Lu-octreotate on 2D monolayer and 3D spheroid models of these two types of NET cells. PARPi mediates this effect by enhancing ^{177}Lu-octreotate-induced cell cycle arrest and cell death. Thus, the use of PARPi may offer a novel option for improving the therapeutic efficacy of ^{177}Lu-octreotate PRRT of NETs.

INTRODUCTION

Neuroendocrine tumors (NETs) originate from enterochromaffin cells of the diffuse neuroendocrine system and form a heterogeneous family of neoplasms. While NETs generally display an indolent behavior, they can significantly impair the quality of life, particularly when they cause hormonal syndromes [1]. About 68% of NETs arise from the gastroenteropancreatic system (GEP-NETs), and approximately 25% from the bronchopulmonary system (BP-NETs). In the last decade, their incidence has markedly increased by 6.4 fold, from 1.09 to 6.98 cases per 100,000 individuals per year [2–4]. Complete surgical resection remains the only cure, but it is not an option for all NET patients. Hence other treatment modalities, such as regional therapies, systemic chemotherapy, somatostatin analogues, interferon alpha, molecular targeted therapy and peptide receptor radionuclide therapy (PRRT) are employed [5]. Among these treatments, PRRT is one of the most promising in terms of survival, response rates and low toxicity [6]. PRRT uses radiolabeled somatostatin analogues, which preferably bind to somatostatin receptor (SSTR) subtypes 2 and 5 (SSTR2, SSTR5), which are overexpressed on the plasma membrane of NET cells [7, 8]. The ionizing radiations released by the particle-emitting PRRT

radiopharmaceuticals cause cytotoxicity by inducing DNA damage, such as single and double strand breaks (SSBs and DSBs, respectively) [9]. To date, [^{177}Lu-DOTA^{0},Tyr^{3}]-octreotate (^{177}Lu-octreotate) is the most widely used PRRT radiopharmaceutical and has shown favorable objective response rates, progression-free survival (PFS), overall survival and limited side effects [6, 8, 10]. However, complete remission following ^{177}Lu-octreotate PRRT in patients with metastasized NET is still rare, and therefore there is a need for improvement. NETs are also sensitive to some cytotoxic and/or molecular targeted chemotherapies [11, 12], hence combining them with PRRT offers new possibilities for more effective treatments. Combination of capecitabine and temozolomide with ^{177}Lu-octreotate has resulted in encouraging PFS with modest hematological toxicity in a clinical trial of progressive metastatic NETs [13]. Another trial of mTOR inhibitor everolimus along with ^{177}Lu-octreotate is underway in NET patients [14].

Another class of molecularly targeted antitumor drugs are pharmacological inhibitors of poly(ADP-ribose) polymerase-1 (PARPi). These mediate their therapeutic effects by inhibiting the catalytic activity of the mammalian enzymes, poly(ADP-ribose) polymerases (PARPs), of which PARP1 is the most abundant member that accounts for about 80% of cellular PARP activity [15]. In mammalian cells, PARP1 is among the earliest proteins to detect and bind to different types of DNA damages, which results in its catalytic activation [16]. The activated PARP1 utilizes the substrate nicotinamide adenine dinucleotide (NAD^{+}) to synthesize polymers of ADP-ribose (PAR) that post-translationally modify (PARylate) itself and other target proteins in the vicinity of DNA damage. The activation of PARP1 and PARylation of proteins have been shown to influence DNA damage responses such as DNA repair, chromatin remodeling and cell death [17]. Overall, PARP1 plays an important role in various types of DNA damage repair pathways including base excision repair of SSBs and homologous recombination repair (HRR) or nonhomologous end joining of DSBs [18]. Currently, the role of PARP1 in the base excision repair of DNA SSBs and abasic sites has been the basis for the use of PARPi as synthetic lethal monotherapy for BRCA1/2 mutant cancers that are defective in HRR pathway, or in combination with chemicals or external radiation for cancers with apparently normal DNA repair capacity [19–21].

With respect to the internal radiotherapy of cancer, PARPi was reported to potentiate radionuclide therapy using noradrenaline transporter-targeted radioiodinated metaiodobenzylguanidine in neuroblastoma cells [22]. A recent study has reported potentiation of ^{177}Lu-octreotate PRRT by PARPi in a rat pancreatic adenocarcinoma cell line that endogenously expresses SSTR2, and in the human osteosarcoma cell line U2OS that was modified to express exogenous SSTR2 [23]. Since these are non-NET cancer models and expression of exogenous SSTR may not represent true pathophysiological response of NET cells that endogenously express SSTR, it still needs to be determined whether this effect of PARPi on ^{177}Lu-octreotate-based PRRT will be observed in human NET cells. In the present study, we used 2D and 3D cell culture models of a human-derived GEP-NET and BP-NET cell lines, to show that PARPi potentiates therapeutic efficacy of ^{177}Lu-octreotate PRRT in NET.

RESULTS

^{177}Lu-octreotate uptake and PARP1 activation in NET cells

We first screened a panel of selected NET and non-NET cell lines for the expression of mRNA of SSTR2 and SSTR5 by RT-PCR. Two human NET cell lines, BON-1 and NCI-H727 cells, were found to express both the receptors (Supplementary Figure 1A), confirming their reported receptor status [24, 25]. The functional state of these receptors was verified by comparing the intracellular uptake of two ^{177}Lu radiochemicals, namely ^{177}Lu-octreotate that is internalized via the SSTR and ^{177}Lu-diethylenetriaminepentaacetic acid (^{177}Lu-DTPA), a carrier of ^{177}Lu that cannot penetrate inside the cell. There was a 5 to 20-fold increase in the intracellular uptake of ^{177}Lu when these cells were incubated for five days with ^{177}Lu-octreotate as compared to ^{177}Lu-DTPA (Figure 1A), confirming the specificity of the SSTR-mediated internalization of ^{177}Lu-octreotate. In BON-1 cells, although the intracellular uptake of ^{177}Lu-octreotate was higher than ^{177}Lu-DTPA even after 3h incubation (Supplementary Figure 1B), the 5-day incubation regime with ^{177}Lu-octreotate resulted in a significantly higher toxicity as compared to 3h exposure, and this increased toxicity was not seen with ^{177}Lu-DTPA (Supplementary Figure 1C). To assess whether the toxic effect was due to intracellular uptake of ^{177}Lu-octreotate, we incubated both the cell lines for five more days after removal of each of the radiolabel at day 5 and compared the toxicity at 5th and 10th day (Figure 1B and 1C). There was a significant increase in toxicity of ^{177}Lu-octreotate at day 10 as compared to day 5 in both BON-1 (Figure 1B) and H727 cells (Figure 1C). In contrast, a marginal toxicity attributable to external radiation by ^{177}Lu-DTPA in the medium during 5-day exposure did not increase by day 10 (Figure 1B and 1C). Thus, the effect of ^{177}Lu-octreotate was mostly attributable to its specific cellular internalization and intracellular retention rather than extracellular irradiation from ^{177}Lu suspended in the medium.

Next, we examined the status of catalytic activation of PARP1 in response to DNA damage caused by irradiation from ^{177}Lu-octreotate (Figure 1D). In both the cell lines, the immunoblotting of cell extracts up to 1 h after exposure to ^{177}Lu-octreotate revealed a smear of heterogeneously PAR-modified proteins above 100 kDa up to 1 h. Moreover, the treatment with PARPi 1,5-dihydroxyisoquinoline (DHQ) before exposure

to ^{177}Lu-octreotate completely suppressed the signal of PAR in both the cell types. Our results indicate that the intracellular uptake of ^{177}Lu-octreotate resulted in damage to DNA and PARylation of proteins that could be efficiently suppressed by PARPi; thus, PARPi has the potential to influence different cellular responses to radiation-induced DNA damage.

Potentiation of ^{177}Lu-octreotate by PARPi in BON-1 cell monolayers

We assessed the influence of suppression of PARP1 activation on the cytotoxic effect of ^{177}Lu-octreotate in BON-1 cells using multiple parameters. Treatment with ^{177}Lu-octreotate or DHQ alone reduced the fraction of

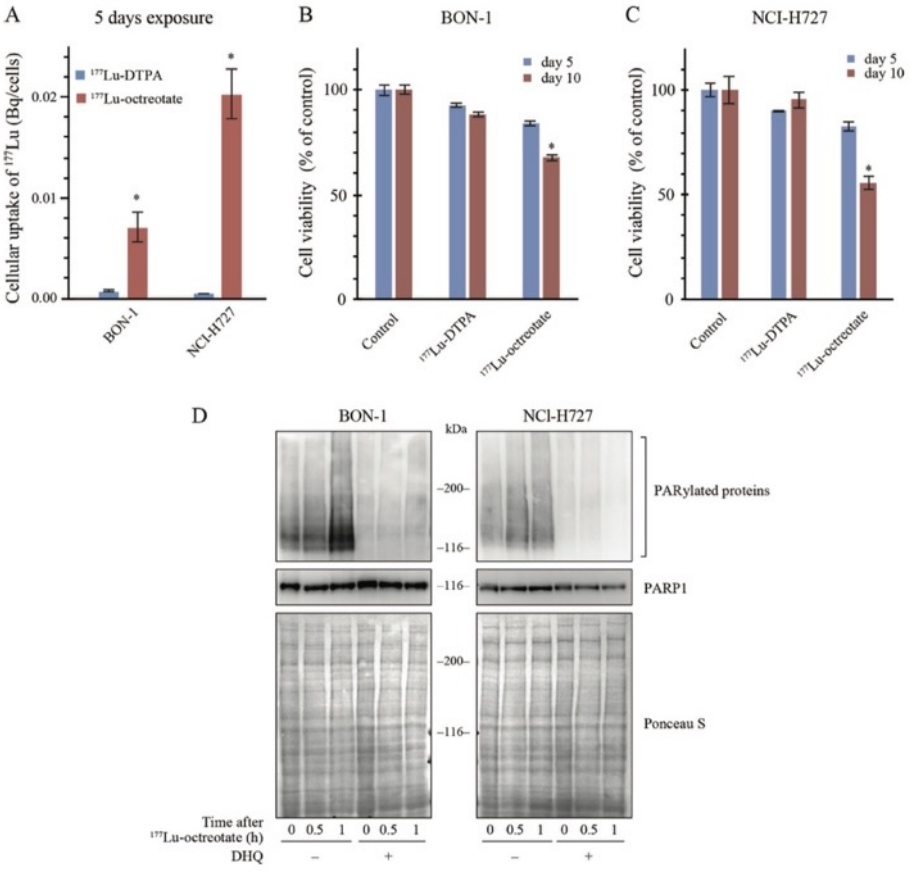

Figure 1: ^{177}Lu-octreotate uptake and PARylation of proteins in BON-1 and NCI-H727 cells. (**A**) Uptake of ^{177}Lu-octreotate in BON-1 and NCI-H727 cells. Both the cell lines were exposed to 2.75 MBq/mL of ^{177}Lu-octreotate or 2.75 MBq/mL of ^{177}Lu-DTPA for 5 days. Each data point, derived from six replicates per experimental condition, represents mean ± SEM. The * indicates significant differences ($P \leq 0.05$) in uptake of ^{177}Lu-octreotate as compared to that of ^{177}Lu-DTPA in both the cell lines. (**B-C**) ^{177}Lu-octreotate-induced reduction in cell viability of BON-1 and NCI-H727 cells. Both the cell lines were exposed to 2.75 MBq/mL of ^{177}Lu-octreotate or 2.75 MBq/mL of ^{177}Lu-DTPA for 5 days followed by five more days of incubation of cells in medium without radiolabel. The viability was determined at day 5 and day 10 of the protocol. The cell count in each treatment group is expressed as percent of number of viable cells in untreated control. The average of six replicates per experimental condition is plotted as mean ± SEM, with * indicating a significant difference in %viability of cells on day 5 and day 10 in each treatment group. (**D**) PARP inhibitor DHQ inhibits the PAR formation by PARP1 induced by ^{177}Lu-octreotate in BON-1 and NCI-H727 cells. Both the cell lines were treated with 2.75 MBq/mL of ^{177}Lu-octreotate in presence and absence of DHQ for indicated time points and the cell extracts were immunoblotted for PAR and PARP1.

viable cells to 63.4 % and 73.5 %, respectively, whereas these two agents together significantly reduced the viability to 40.4 % (Figure 2A). None of the treatments reduced the number of viable cells below the number of cells at the start of treatment, indicating growth-suppressive effect of the single or combination treatment. Moreover, this effect was due to radiolabel attached to octreotate because no toxicity was observed after treatment of cells with up to 200 nM unlabeled [DOTA^0-Tyr^3]-octreotate (Supplementary Figure 2A). The low-level cytotoxicity of PARPi observed with DHQ in BON-1 cells was also observed with two other PARPi: PJ-34 and ABT-888 (veliparib) (Supplementary Figure 2B). We also confirmed that treatment of BON-1 cells with the three different PARPi did not increase the intracellular uptake of ^{177}Lu-octreotate (Supplementary Figure 2C). This indicates that the effect of PARPi, when combined with of ^{177}Lu-octreotate was mainly due to its influence on biological events following intracellular irradiation.

To characterize the growth suppressive effect of ^{177}Lu-octreotate and PARPi, we examined the proportion of cells in each phase of the cell cycle (Figure 2B and Supplementary Figure 3, left panel). ^{177}Lu-octreotate treatment increased the cell population in sub-G1, S and G2/M phases by 4.8, 2.6 and 2.8 folds, respectively. Since sub-G1 phase represents apoptotic cells with reduced DNA content [26], these results indicate a combination of cell death and cell cycle arrest in S and G2/M phases in response to ^{177}Lu-octreotate. While PARPi treatment alone did not cause a significant increase in sub-G1 population, its presence with ^{177}Lu-octreotate significantly increased sub-G1 fraction of cells (12 folds), accompanied by an increased S-phase arrest (4.5 folds). Thus, ^{177}Lu-octreotate induced apoptosis and cell cycle arrest, which were augmented by co-treatment with PARPi.

Mechanisms of the potentiation of ^{177}Lu-octreotate by PARPi in BON-1 cells

To examine the consequences of DNA damage induced by irradiation from ^{177}Lu-octreotate, we assessed the phosphorylation status of histone H2AFX (γH2AX) and of TP53 (p53) [27]. Treatment with ^{177}Lu-octreotate increased the levels of γH2AX and phospho-p53. While PARPi alone did not alter these parameters, it significantly increased the levels of ^{177}Lu-octreotate-induced γH2AX and phospho-p53 (Figure 2C). The phosphorylation of p53 is known to promote its accrual [28], which was observed following treatment with ^{177}Lu-octreotate, PARPi, and the combination of the two (Figure 2C). Furthermore, while ^{177}Lu-octreotate alone caused a modest upregulation of the cell cycle inhibitor CDKN1A (p21), PARPi alone or in combination with ^{177}Lu-octreotate caused a significant increase in p21 levels. These results demonstrate the effect of PARPi in causing the persistence of damaged DNA and cell cycle arrest.

The increased sub-G1- population of ^{177}Lu-octreotate-treated cells with or without PARPi indicates an involvement of apoptosis [29]. The immunoblotting revealed that all three caspases 3, 7 and 9 were significantly activated after treatment with ^{177}Lu-octreotate, but not with PARPi (Figure 2C). However, the presence of PARPi further upregulated ^{177}Lu-octreotate-induced activation of all three caspases. There was a corresponding increase in cleavage of PARP1 to its signature 89-kDa fragment by caspases 3 and 7 in these samples (Figure 2C). Together, the changes in parameters that assess cellular responses to DNA damage, stalled stalled cell cycle (increased p21), and cell death (subG1 cells, and activation of caspases), indicate that PARPi potentiated cytotoxicity of ^{177}Lu-octreotate in BON-1 cells by upregulating cell cycle arrest and apoptosis.

Potentiation of ^{177}Lu-octreotate by PARPi in BON-1 cell spheroids

The 3D spheroids mimic physiological and biological properties of *in vivo* tumors better than 2D cell monolayers for testing anti-cancer therapeutics [30]. We examined the PARPi (DHQ)-mediated potentiation of cytotoxicity of ^{177}Lu-octreotate in a 3D model of BON-1 cells (Figure 3A). We first confirmed the uptake of ^{177}Lu-octreotate by BON-1 spheroids and noted that the presence of PARPi did not significantly change the extent of uptake of ^{177}Lu-octreotate by spheroids (Supplementary Figure 4A). Next, we determined the effect of ^{177}Lu-octreotate with or without PARPi on the growth of spheroids (Figure 3B). Over 15 days, while the volume of untreated spheroids increased by 16 folds (100%), the spheroids treated with ^{177}Lu-octreotate, PARPi alone or ^{177}Lu-octreotate plus PARPi increased by 5.0 (30%), 11.0 (70%) and 1.9 folds (12%), respectively. The reduction in spheroid growth with ^{177}Lu-octreotate appeared specific to ^{177}Lu because the unlabeled [DOTA^0-Tyr^3]-octreotate up to 200 nM had no effect on the growth of spheroids. (Supplementary Figure 4B). Thus, like in the 2D model, the combination of PARPi and ^{177}Lu-octreotate was more effective than ^{177}Lu-octreotate alone in suppressing the growth of 3D cultures of BON-1 cells *in vitro*.

The levels of cell proliferation marker MKI67 (Ki67) is an important indicator of tumor growth and aggressiveness used for grading NETs [31]. The immunoblotting revealed reduced levels of Ki67 in ^{177}Lu-octreotate- or PARPi-treated spheroids as compared to untreated spheroids (Figure 3C). Once again, the combined treatment was most effective in reducing the Ki67 level as compared to the individual treatments. This is consistent with a stronger suppression of growth of BON-1 spheroids in the presence of ^{177}Lu-octreotate plus PARPi.

In order to further understand the mechanisms by which ^{177}Lu-octreotate and PARPi affected the spheroids growth, we examined DNA damage and cell death

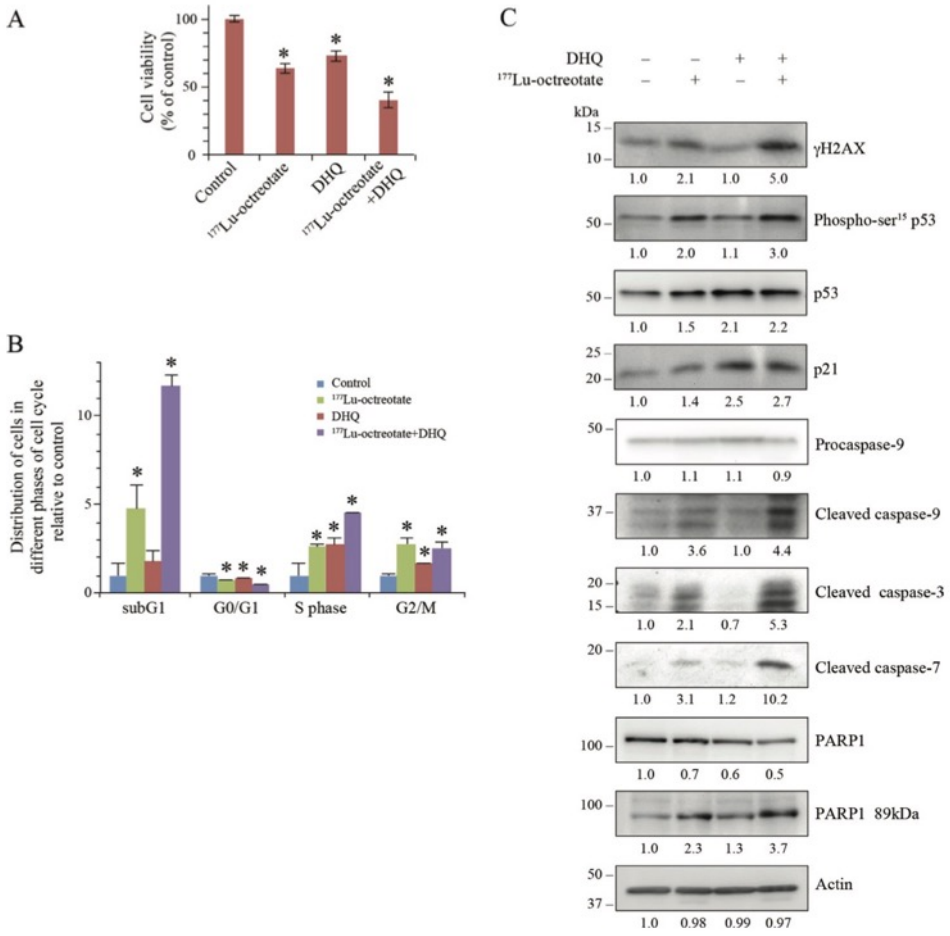

Figure 2: Effect of ^{177}Lu-octreotate and PARPi on BON-1 cell monolayers. (**A**) PARPi augments the ^{177}Lu-octreotate-induced reduction in cell viability. The cells were treated in six replicates for five days with ^{177}Lu-octreotate and DHQ independently and in combination followed by 10 more days of incubation of cells in medium without radiolabel and viable cell count was taken on the 10th day. The cell count is expressed as percent of viable cell count as compared to the untreated control. The number of cells seeded at the start of the experiment was 3.82% of the number of control cells on day of harvest. The average of six replicates per experimental condition are plotted as mean ± SEM and * indicates a significant difference from % viability of control cells. (**B**) PARPi potentiates ^{177}Lu-octreotate-induced cell death and cell cycle arrest in BON-1 cells. The cells treated as above for panel-A were harvested at day 10 and analyzed by flow-cytometry after staining with propidium iodide. The data of each cell cycle phase (sub-G1, G1, S, and G2/M) is derived from triplicates per experimental condition and are plotted as mean ± SD of the fold change of the cell population relative to that of control of same phase of the cell cycle in the untreated controls and * indicates a significant difference from control cells in the given phase of cell cycle. (**C**) PARPi increases the downstream effects of ^{177}Lu-octreotate–induced DNA damage on cell cycle arrest and apoptosis. The cells were treated in six replicates as indicated for panel A, harvested and pooled together for immunoblotting of parameters of DNA damage (γH2AX and phospho-p53), cell cycle arrest (p53 and p21) and apoptosis (Cleaved caspase 9, 3, 7 and PARP1 89kDa). Their band densities in arbitrary units were measured using GeneTools analysis software (Syngene) and normalized with the band density of actin from the corresponding samples. The fold change in the normalized band density of each protein in each treatment groups relative to control is indicated below each immunoblot. The panel for each immunoblot represents one of the two independent identical experiments with similar results.

parameters 15 days after treatment (Figure 3C). The immunoblotting of spheroid extracts revealed that ^{177}Lu-octreotate alone caused an induction of DNA damage markers γH2AX and phospho-p53. PARPi alone did not affect the phosphorylation of either marker but, in combination with ^{177}Lu-octreotate, a pronounced increase was observed. PARPi treatment resulted in upregulation of p53 and p21 with and without ^{177}Lu-octreotate. Regarding

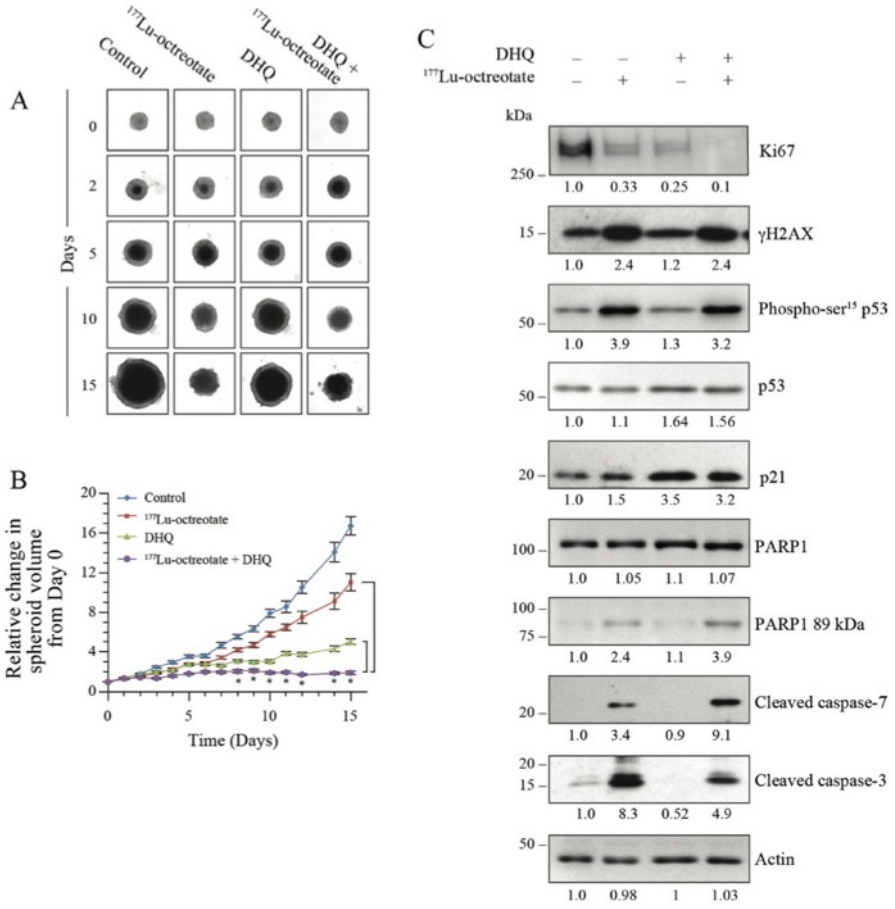

Figure 3: Effect of ^{177}Lu-octreotate and PARPi on BON-1 spheroids. (**A**) The 12 control and 24 treatment spheroids of BON-1 cells were treated with ^{177}Lu-octreotate and DHQ independently and in combination for 5 days followed by 10 more days of incubation of cells in medium without radiolabel. The representative image of 12 to 24 spheroids over time course of treatment from two independent experiments is shown here. The black core and the peripheral grey zones represent dead and viable parts of the spheroid, respectively. (**B**) The data pooled from time-course of changes in spheroid volume from 12 to 24 spheroids from two independent experiments described for panel A is plotted as mean ± SEM of fold change in the spheroid volume relative to that at the start of treatment, i.e. Day 0. * indicates that all the data points are significantly different between DHQ alone and ^{177}Lu-octreotate + DHQ treatment groups as well as between ^{177}Lu-octreotate and ^{177}Lu-octreotate + DHQ treatment groups from each other from day 8 onwards with *P*-values ≤ 0.01. (**C**) Analyses of different parameters of cell proliferation, DNA damage, cell cycle arrest and apoptosis. The 12 control and 24 treatment spheroids were treated as indicated for panel A and harvested on day 15 for immunoblotting proliferation marker Ki67 and other indicated parameters and band intensities were measured and expressed for each panel as described for Figure 2C. The panel for each immunoblot represents one of the two independent identical experiments with similar results.

cell death parameters, ^{177}Lu-octreotate by itself increased the cleaved caspase 3. The combined treatment resulted in higher amount of cleaved caspase 7 with a concomitant increase in PARP1 cleavage. In summary, the results with the 2D and 3D models of BON-1 cells indicate that ^{177}Lu-octreotate suppressed cell growth, caused DNA damage, cell cycle arrest and cell death, and these effects were augmented in the presence of PARPi.

Potentiation of ^{177}Lu-octreotate by PARPi in H727 cell models

Using trypan blue dye exclusion assay, we observed that the growth of H727 monolayer cells was reduced to 59.4 % by ^{177}Lu-octreotate and to 25.5 % by PARPi DHQ (Figure 4A). The combination treatment reduced the growth to 8.5 % of control. In comparison, the treatment of cells with unlabeled [DOTA^0-Tyr^3]-octreotate up to 200 nM did not result in any toxicity (Supplementary Figure 2D), confirming that the effect of ^{177}Lu-octreotate was due to the internalized radiolabel. We confirmed the above results in H727 cells using two other PARP inhibitors: PJ-34 and ABT-888 (Supplementary Figure 2E). Moreover, as in BON-1 cells, the presence of PARPi did not affect the uptake of ^{177}Lu-octreotate by H727 cells (Supplementary Figure 2F). The FACS analyses revealed that the growth reduction in these cells at 10 days under all treatment conditions largely manifested as cell death (Figure 4B and Supplementary Figure 3, right panel). The augmentation of population in sub-G1 phase in the presence of ^{177}Lu-octreotate, PARPi, and ^{177}Lu-octreotate plus PARPi was 8.2, 6.8 and 18.1 folds over the control, respectively. At the time of harvesting, none of the treatment conditions exhibited much difference in proportion of cells in other phases of cell cycle. The DNA damage parameters such as γH2AX and phospho-p53 increased in the presence of ^{177}Lu-octreotate or PARPi alone, and there was an additive effect following the combined treatment (Figure 4C and 4D). Conversely, levels of p53 remained unaffected by any of the three treatments and PARPi lowered the levels of p21 in these cells. Since we observed a significant percentage of H727 cells in sub-G1 phase which represents apoptotic population of the cells [26], we also verified the markers of apoptosis in these cells. We observed that in the three treatment groups, there was an activation of caspase 9 as compared to control (Figure 4C and 4D). Moreover, both the downstream caspases 3 and 7 were activated in H727 cells. PARPi caused an increase in cleaved caspase 3, demonstrating its toxicity in these cells, but the combined treatment yielded much higher levels of activated caspase 3 than single treatment. The cleavage of PARP1 to its 89-kDa fragment correlated with caspase 3 activation in these cells.

In the 3D spheroid model of H727 cells, we first confirmed the uptake of ^{177}Lu-octreotate (Supplementary Figure 4C). There was a trend toward higher uptake of ^{177}Lu-octreotate in the presence of PARPi, but this was not statistically significant. The control spheroids exhibited a 11.4-fold (100%) growth over 15 days, whereas those treated with ^{177}Lu-octreotate, PARPi, and ^{177}Lu-octreotate + PARPi grew by, 4.6 (23%), 3.5 (30%) and 2.8 folds (18%), respectively (Figure 5A and 5B). Unlabeled [DOTA^0-Tyr^3]-octreotate by itself had no effect on the growth of spheroids (Supplementary Figure 3D). ^{177}Lu-octreotate and PARPi caused a reduction of Ki67 level, which was further reduced with the combination treatment (Figure 5C and 5D). γH2AX and phospho-p53 were increased with ^{177}Lu-octreotate alone, but not with PARPi alone, while the combination treatment yielded levels comparable to those following ^{177}Lu-octreotate alone (Figure 5C). Like in the 2D monolayers, p53 levels remained unchanged in the 3D model. ^{177}Lu-octreotate by itself caused some activation of caspase 3, and the combined treatment further enhanced it. We observed PARP1 cleavage in all the four groups, but it was higher in the spheroids treated with ^{177}Lu-octreotate and ^{177}Lu-octreotate plus PARPi. Collectively, the results of the 2D and the 3D models of H727 cells indicated that PARPi alone was generally toxic by itself, and it further increased inherent capacity of ^{177}Lu-octreotate to cause cell death.

DISCUSSION

^{177}Lu-octreotate PRRT, when coupled with molecular imaging of SSTR, is one of the most promising theranostic applications for the treatment of inoperable NETs. Different approaches are being investigated to improve the antitumor efficacy of ^{177}Lu-octreotate PRRT and one of them is combining it with radiosensitizing chemotherapeutic drugs [13, 14, 32]. In the present study, we utilized NET patient-derived GEP-NET and BP-NET cell lines that endogenously express SSTR2 and 5, to show that ^{177}Lu-octreotate is internalized by these cells and results in PARylation of proteins indicating the catalytic activation of PARP1 in response to DNA damage caused by internalized ^{177}Lu-octreotate. We also demonstrated that the pharmacological suppression of PARP-activation response results in a potentiation of cytotoxic effects of ^{177}Lu-octreotate. We also show that PARPi did not increase uptake of ^{177}Lu-octreotate by the cells, but augmented consequences of radiation-induced damage to DNA, such as blocked cell cycle, increased signal for γH2AX or phosphorylated p53. These observations are in agreement with known biological function of PARP1 activation in facilitating the downstream processes such as the repair of DNA damage [17]. More specifically, PARPi has been shown to inhibit repair of DNA damage via trapping PARP1 at the lesion site and convert unrepaired SSBs to DSBs leading to cell death [21, 33]. Our data is in agreement with a recent report that PARPi increases the signal for TP53BP1, a marker of DSB, in the biopsy tissues of NET patients treated with ^{177}Lu-octreotate [23].

The increased DNA damage is known to result in the phosphorylation-induced activation and accumulation of p53 via the ATM, ATR and DNA PKcs pathways [27, 28], which can lead to cell cycle arrest and/or apoptosis [34]. Our data suggest that p53 accumulation and its phosphorylation could be the reason for the observed cell cycle arrest and apoptosis in GEP-NET BON-1 cells. In contrast, in BP-NET H727 cells, there was increased phosphorylation of p53 but not its accumulation, which may be due to mutations reported in p53 gene in H727 cells [35, 36]. The lack of p53 or p21 accumulation in H727 cells may also be due to the greater tendency to execute apoptosis rather than remain stalled in cell cycle. The apoptotic cell death by PARPi and ^{177}Lu-octreotate

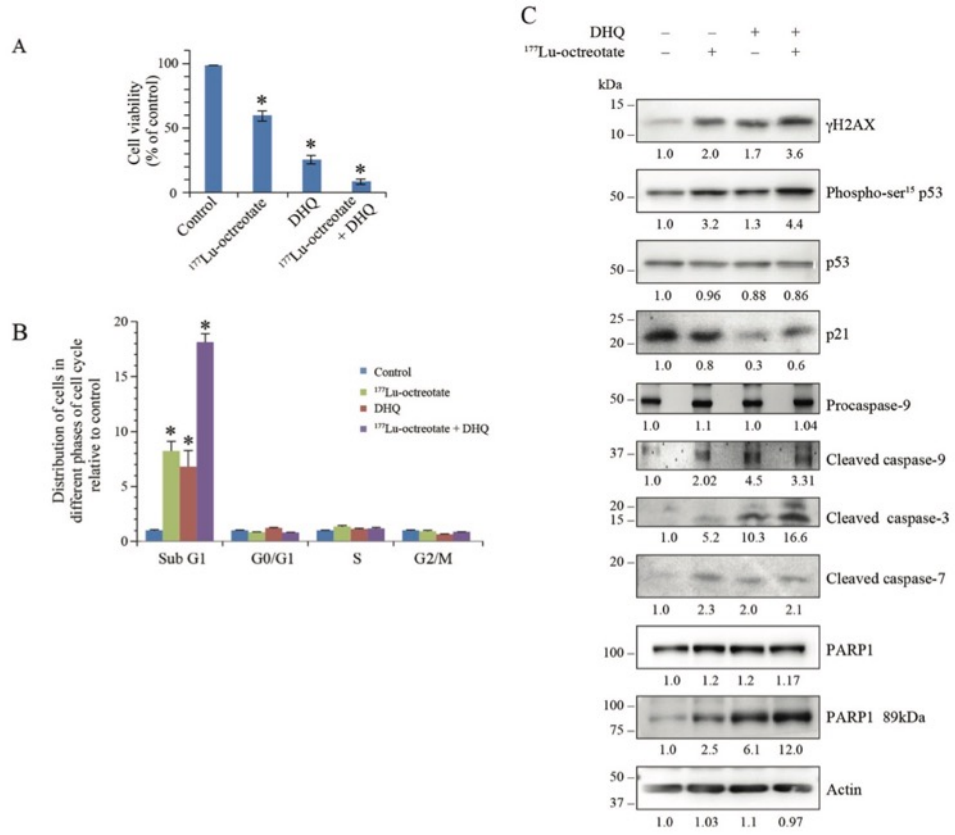

Figure 4: Effect of ^{177}Lu-octreotate and PARPi on NCI-H727 cell monolayers. (**A**) PARPi augments the ^{177}Lu-octreotate-induced reduced cell viability of NCI-H727 cells. The H727 cells were treated in six replicates for five days with ^{177}Lu-octreotate and DHQ independently and in combination as described for BON-1 cells in Figure 2. The average cell counts in each treatment groups from six independent experiments is derived and expressed as mean ± SEM exactly as described for Figure 2A. The number of cells seeded at the start of the experiment were 3.75% of the number of control cells on day of harvest. * indicates a significant difference from % viability of control cells. (**B**) PARPi potentiates the ^{177}Lu-octreotate-induced cell death and cell cycle arrest in H727 cells. The cells treated as above for panel-A were harvested at day 10 and analyzed by flow-cytometry after staining with propidium iodide. The data of each cell cycle phase (sub-G1, G1, S, and G2/M) is derived from triplicates per experimental condition and were plotted as means ± SD of fold change in the percent cell population relative to that of untreated controls. The * indicates a significant difference as compared to the control cells in the given cell cycle phase. (**C**) Analyses of DNA damage, cell cycle arrest and cell death parameters by western blotting in H727 cells. The cells treated in six replicates as indicated for panel A were harvested and pooled together for immunoblotting of various parameters. Band intensities were measured as described for Figure 2C. The panel for each immunoblot represents one of the two independent identical experiments with similar results.

treatment alone or in combination in H727 and BON-1 cells was evident from reduced cell viability and the presence of activated (cleaved) caspases 9, 3 and 7, and apoptosis signature cleavage of PARP1 to its 89-kDa fragment. Our results with these two NET cell lines suggest that PARPi could potentiate the cytotoxic responses to ^{177}Lu-octroetate in different NET tumors, which have normal or abnormal p53/p21 response to DNA damage.

We also observed that treatment of NCI-H727 cells with PARPi alone induced a relatively high level of cytotoxicity as compared to that seen in BON-1 cells, which could be due to the presence of missense mutations in BRCA1 gene in these cells [37]. In fact, PARPi are used in clinic as synthetic lethal monotherapy for BRCA-mutant ovarian tumors that are deficient in HRR of DSBs [19], although it needs to be confirmed whether the BRCA1 mutation affects the functional state of BRCA in H727 cells. In any case, ^{177}Lu-octreotate with PARPi caused more damage in BON-1 and NCI-H727 cells than either compound alone, indicating a collaborative action of these two agents. Thus, our studies strengthen the argument that PARPi can potentiate the therapeutic efficacy of DNA damaging agents, even in BON-1 cells that are not characterized by BRCAness, i.e. any known deficiency in DNA DSB repair.

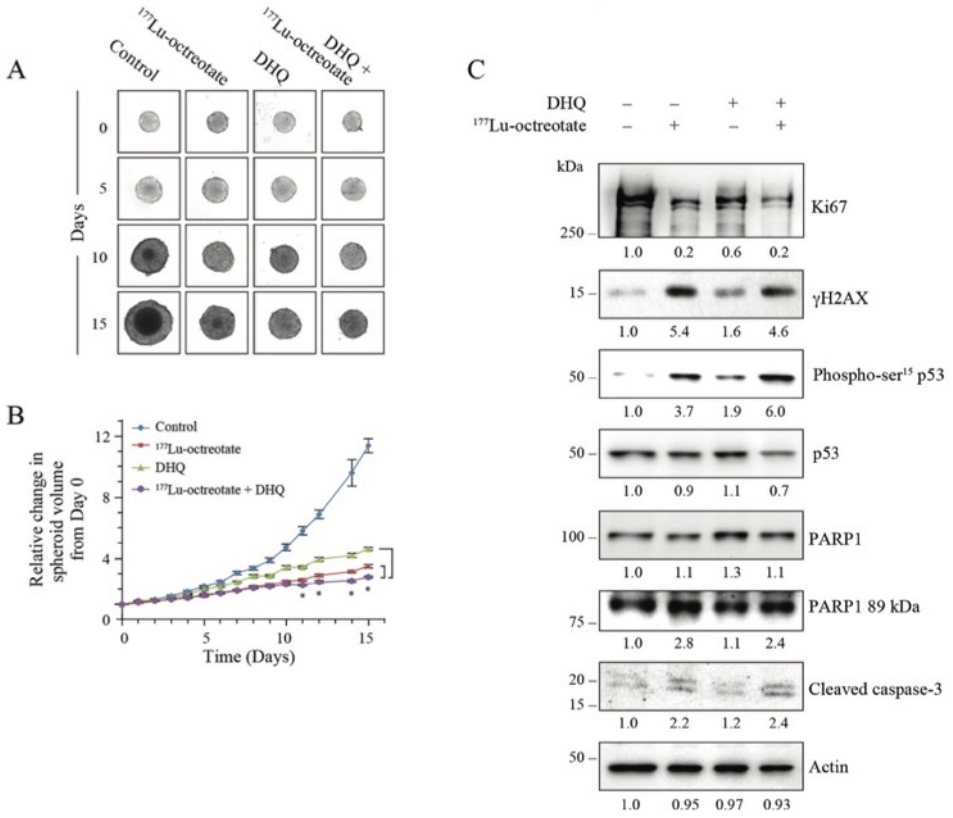

Figure 5: Effect of ^{177}Lu-octreotate and PARPi on NCI-H727 cell spheroids. All three panels represent data from H727 spheroids exactly treated as described for BON-1 spheroids in Figure 3. (**A**) The representative microscopic images of spheroids from each treatment group at indicated time points. (**B**) The time-course of change in spheroid volume from two independent experiments described for panel A is plotted as mean ± SEM of fold change in the spheroid volume relative to that at the start of treatment, i.e. Day 0. * indicates that all the data points are significantly different between DHQ alone and ^{177}Lu-octreotate + DHQ treatment groups as well as between ^{177}Lu-octreotate and ^{177}Lu-octreotate + DHQ treatment groups from each other from day 8 onwards with P-values ≤ 0.01. (**C**) Analysis of cell proliferation marker Ki-67, DNA damage, cell cycle arrest and apoptosis parameters by western blotting. The treatments, immunoblotting and data analyses were carried out as described for BON-1 spheroids in Figure 3C.

Radiosensitization by PARPi during the ^{177}Lu-octreotate-based PRRT of osteosarcoma cell line U2OS expressing exogenous SSTR2 and of rat pancreatic tumor cell line Ca20948 expressing endogenous SSTR2 has been recently reported [23]. However, osteosarcomas are not clinically treated with PRRT as they do not express SSTR, and artificially overexpressed SSTR may not reflect pathophysiological conditions in these cells. Further, the biology of osteosarcoma or of a rat pancreatic cancer of acinar origin [38] differs from that of NETs in many respects, as they do not have the same origin. In contrast, PRRT with ^{177}Lu-octreotate has become a standard therapeutic option for endogenously SSTR-expressing NETs in the clinic [39]. While the authors in this study clearly showed radiosensitization by PARPi of PRRT in SSTR-positive cells, our results now firmly establish that PARPi has the capacity to potentiate ^{177}Lu-octreotate-based PRRT in two human NET cell lines from common origins: gastroenteropancreatic and bronchopulmonary.

It may be challenging to directly translate the therapeutic effects seen with 2D monolayer cells to 3D tumors *in vivo,* which are comprised of a variety of cells that interact with each other, have a heterogeneous distribution of receptors on their surface, have diffusional limits to mass transport of drugs, nutrients and other factors, and may develop central necrosis and regions of hypoxia. These *in vivo* biological conditions can be partly recreated *in vitro* by using 3D spheroids of the cancer cell lines [30]. In our study, we showed that the radiosensitizing effects of PARPi observed in 3D spheroids were not only similar to those observed using monolayer culture (2D) of these cells, but also mediated via similar mechanisms of action. Moreover, the observed cytotoxic effects using PARPi and ^{177}Lu-octreotate alone or in combination directly correlated with the levels of cell proliferation marker Ki-67. Thus, our data with 3D spheroids supports the use of PARPi during PRRT in pre-clinical animal models of NET, and eventually in clinical trials in NET patients.

PRRT confers an advantage of limited long-term toxicity or acute and sub-acute side effects owing to its specificity towards the SSTRs, which are more concentrated in the NET lesions as compared to healthy organs [6]. Therefore, it would be beneficial to combine PRRT with a potentiating agent that is also specific and associated with limited toxicity that is not overlapping with that of PRRT. PARPi is one such agent that is known to have a favorable toxicity profile [40, 41], and also causes its radiosensitizing or chemo-potentiation effects preferentially in high-grade metastatic cancers [15, 16]. This is because PARPi-mediated suppression of repair of SSBs and conversion to DSBs can take place only in replicating cells. Thus, in the tumors containing a higher proportion of replicating cells that are defective in cell cycle checkpoint responses than normal tissues, PARPi can increase the therapeutic index of PRRT by specifically increasing DNA damage in actively replicating NET cells, while sparing non-cycling normal tissues. Hence, PARPi is not expected to potentiate ^{177}Lu-octreotate effects in organs with high radiation exposure but with lower proliferative activity, such as the kidney. However, some side effects could still potentially occur in the bone marrow, even if it receives relatively low absorbed radiation doses during PRRT, because of its high proliferation rate and radiosensitivity.

In summary, our study shows that PARPi potentiates PRRT in human NET cell lines via augmenting the downstream effect of ^{177}Lu-octreotate-induced DNA damage, such as cell cycle arrest and apoptosis. Since some PARP inhibitors such as olaparib are being used in the clinic for the treatment of other cancers, combining PARPi with ^{177}Lu-octreotate could rapidly offer a new opportunity for boosting the efficacy of PRRT in patients suffering from NET.

MATERIALS AND METHODS

Chemicals and other reagents

The chemicals used in preparing the buffers and other fine chemicals were purchased from Sigma. All the cell culture-related products were purchased from Life technology. Nitrocellulose ECL membrane was from Amersham and immobilon western chemiluminescent HRP substrate (WBKLS0500) was from Millipore. PARP inhibitors, 1,5-dihydroxyisoquinoline (DHQ) was from Sigma, PJ-34 was from Alexis Biochemicals and ABT-888 (veliparib) was from Santa Cruz Biotechnology.

Radiopharmaceuticals

^{177}Lu-octreotate radiolabeling was performed as previously described [42] and was used for clinical PRRT as well as for all the experiments. $^{177}LuCl_3$ was obtained from IDB Holland BV, and [DOTA^0,Tyr^3]-octreotate was generously provided by the Erasmus Medical Center (Rotterdam, The Netherlands). Radiochemical purity of ^{177}Lu-octreotate was >97%, and specific activities in different batches ranged from 22,015 to 85,100 MBq/μmole (50–100 nM octreotate delivered per 2.75 MBq typical treatment dose). The ^{177}Lu-DTPA was prepared by mixing $^{177}LuCl_3$ with DTPA at room temperature.

Cell culture and treatment

The BON-1 is a GEP-NET cell line established from a human pancreatic carcinoid tumor [43] which was maintained as described earlier [44]. The BP-NET NCI-H727 cells (CRL-5815) were obtained from ATCC and maintained as per the ATCC specifications.

Unless specified otherwise in the legends, BON-1 and H727 cells were seeded in monolayers at 10,000 cells/cm^2 and subjected to treatments after 2 days either individually or in combination with ^{177}Lu-octreotate and one of the different PARP inhibitors, 100 μM DHQ, 10 μM PJ-

34 or 2.5 μM ABT-888. For relevant treatment groups with PARPi, the cells were treated with PARPi starting 30 minutes prior to exposure to ^{177}Lu-octreotate (2.75 MBq/mL) for five days. The medium was removed after five days and cells were maintained for five more days in the presence of PARPi in relevant treatment groups. Similar experimental conditions were also used for treatment of cells with ^{177}Lu-DTPA individually, i.e. 5 days of treatment followed by the removal of treatment and maintaining cells for five more days.

Growth of spheroids

The 3D spheroids of BON-1 and H727 cells were grown as previously described [45]. After six days, when the spheroids reached 300–400 μM diameter, they were treated with ^{177}Lu-octreotate 2.75 MBq/mL medium (or mock) in the presence or absence of PARPi for five days. The treatment was terminated after five days with change of medium, and the spheroids were grown for an additional 10 days in the presence of PARPi, where required. The images of spheroids were captured at 20X magnification using Zeiss Axiovert 200 microscope and volume of spheroids was calculated ($v = 0.5 \times \text{length} \times (\text{width})^2$) from the dimensions measured using Axio Vision 4.9.1 Software. The average growth from six spheroids per treatment group up to 15 days was calculated as relative to the spheroid volume at the start of treatment (Day 0). For the analyses of ^{177}Lu-octreotate uptake and protein analyses by immunoblotting, 12–24 spheroids were pooled per treatment group at 15 days.

Measurement of ^{177}Lu-octreotate uptake

Cell monolayers growing in 6-well clusters were incubated with ^{177}Lu-octreotate and different PARP inhibitors for five days, as described above. The medium was removed and monolayers were washed thrice with phosphate buffered saline (PBS) to remove any unbound ^{177}Lu-octreotate. Cells were scrapped in 1 mL PBS and 0.2 mL aliquot was mixed with 5 mL of scintillating liquid for measuring radioactivity by liquid scintillation counter (Coulter). Another aliquot of cells was used for viable cell count. ^{177}Lu-octreotate uptake was presented as Bq per cell.

To measure ^{177}Lu-octreotate uptake by spheroids, 6–12 spheroids were collected per treatment group in 100 μL culture medium on a Millipore glass-fiber filter with 0.7 μm retention under vacuum. After two washes with PBS, radioactivity was measured as mentioned above. ^{177}Lu-octreotate uptake was presented as Bq/mm^3 volume of spheroid.

Cell viability by trypan blue

BON-1 and H727 cells in six-well clusters were treated with PARPi and ^{177}Lu-octreotate as described before. Six replicates per treatment group and per time point were used. At the specified time points, cells were trypsinized to prepare single-cell suspension from which an aliquot was mixed with equal volume of 0.4 % trypan blue (GIBCO) to count viable cells which exclude the dye.

Flow cytometric analysis of cell cycle

Cell monolayers of BON-1 and H727 treated as described above were trypsinized, washed twice and suspended in PBS. An aliquot representing one million cells from each sample was fixed with 70% ethanol on ice for 30 min and spun down at 500 *g* to remove ethanol. The pellet was washed twice with PBS, suspended in 500 μL of PBS containing 50 μg/mL propidium iodide and 50 μg/mL RNAase A and incubated at 37° C for 30 minutes. FACS analyses were carried out with a BD FACS Calibur flow cytometer, and the data were analyzed with BD FACSDiva software. The histograms were generated using FlowJo 7.6.1 software from Tree Star.

Western blotting

Cell monolayers of BON-1 and H727 treated as described above were scrapped in PBS, spun down, suspended in 1X Laemmli SDS-PAGE buffer and sonicated to prepare protein extracts for SDS-PAGE. In case of spheroids, 6–12 spheroids per treatment groups were collected on Day 15 in 100 μL volume and pooled into one tube. The spheroids were spun down and washed with PBS and suspended in 1X Laemmli SDS-PAGE buffer and sonicated to prepare protein extracts for SDS-PAGE. 10–20 μg of protein extracts from each treatment groups of cell monolayers or spheroids were resolved on 6–15% gradient SDS-PAGE or on individual 8 and 15% SDS-PAGE, transferred to nitrocellulose membrane and probed with specific antibodies as indicated. The immunoprobing for β-actin or staining of blot with Ponceau S were performed as the loading control. All Western blotting data were repeated twice from the extracts derived from two independent experiments. Their band densities in arbitrary units were derived using GeneTools analysis software from Syngene. All the band densities of different proteins are normalized with the band density of actin from the corresponding samples.

Antibodies

The following antibodies were used at specified dilutions for immunoblotting: polyclonal PARP1 antibody (1:5,000; Alexis Biochemicals), PARP1 monoclonal (F2, 1:500; Santacruz), PARP1 C-2-10 (1:1,000), PARP1 89kDa (1:1,000, Abcam), p53 (1:1,000, Boehringer), gH2AX (1:1,000, Millipore), phospho-p53 (1:2,000, NEB), p21 (1:1,000, NEB0), β-actin (1:20,000, Sigma), cleaved caspase-9 (1:1,000, Cell Signaling), cleaved caspase-3 (1:1,000, Cell Signaling), cleaved caspase-7

(1:200, Abcam), Ki-67 (1:100, Thermo scientific), PCNA (1:1,000, Neomarkers). Anti-pADPr monoclonal 10H was purified from the culture medium of 10H hybridoma obtained from Dr. M. Miwa, National Cancer Center Research Institute, Tokyo, through the Riken cell bank (1:500). The secondary HRP-conjugated antibodies (1:1,250) were purchased from Jackson Immunoresearch Laboratories.

RT-PCR for SSTR2 and SSTR5

Total RNA was extracted from BON-1 and NCI-H727 cells using RNeasy Mini Kit (Qiagen 74104), as per manufacturer's protocol. 1 ug RNA was used to synthesize cDNA in 10 µl volume by using RevertAid First Strand cDNA Synthesis Kit (Thermo scientific, K1621), as per as per manufacture's protocol. To carry out RT-PCR, 1:100 diluted cDNA was used. The PCR (35 cycles) was carried out for SSTR2 using forward primer: 5′-GATGATCACCATGGCTGTG-3′and reverse primer: 5′-CAGGCATGATCCCTCTTC-3′; for SSTR5 using forward primer: 5′-GCCGGCCTCTACTTCTTCGTG-3′and reverse primer: 5′-CCGTGGCGTCAGCGTCCTTGG-3′; and for GAPDH using forward primer: 5′-CTTCATTGACCTCAACTACATGG-3′ and reverse primer: 5′-GTCTGGGTGGCAGTGATG-3′.

Statistical analyses

All the graphs were generated and all the statistical analyses were done using Excel software (Microsoft Corporation). Comparisons were made using student's *t*-test and *P*-values < 0.05 were considered significant.

Abbreviations

BP: bronchopulmonary; DHQ: 1,5-dihydroxyisoquinoline; DSB: double strand break; DTPA: diethylenetriaminepentaacetic acid; GEP: gasrtroenteropancreatic; HRR: homologous recombination repair; NET: neuroendocrine tumor; PAR: polymer of ADP-ribose; PARP1: poly(ADP-ribose) polymerase 1; PARPi: PARP inhibitor; PRRT: peptide receptor radionuclide therapy; SSB: single strand break; SSTR: somatostatin receptor.

Author contributions

Nupur K. Purohit: concept, design, data collection and analysis, writing of manuscript. Rashmi G. Shah: concept, design, data collection and analysis, manuscript editing. Samuel Adant: data collection, manuscript editing. Michael Hoepfner: contributed new materials, manuscript editing. Girish M. Shah: concept, design, manuscript editing. Jean-Mathieu Beauregard: concept design, manuscript editing and final approval.

ACKNOWLEDGMENTS

This work was supported by the Mitzi & William Blahd, MD Pilot Research Grant from The Education and Research Foundation for Nuclear Medicine and Molecular Imaging, Pilot Project Grant from Quebec Bio-Imaging Network, a Cancer Research Grant from the The CHU de Québec-Université Laval Foundation, and a NET Research Grant from the Carcinoid-Neuro Endocrine Tumor Society (CNETS) Canada to JMB and GMS. JMB was supported by a Clinical Research Scholar award from the Fonds de recherche du Québec – Santé. SA was supported by the Joseph-Demers M.Sc. Scholarship and the Jean-François Bergeron Scholarship from Université Laval, and Canada Graduate Scholarships-Master's Grant from the Canadian Institutes of Health Research. NKP was recipient of a graduate scholarship from the Neurosciences Branch of the CHU de Québec – Université Laval Research Center, as well as a scholarship for exemption of Foreign Student Supplemental Tuition Fee from Shastri Indo-Canadian Institute and Fonds de recherche du Québec – Santé.

CONFLICTS OF INTEREST

We have no conflicts of interest to declare.

FUNDING

The Education and Research Foundation for Nuclear Medicine and Molecular Imaging, Quebec Bio-Imaging Network, The CHU de Québec-Université Laval Foundation, Carcinoid-NeuroEndocrine Tumor Society (CNETS) Canada.

REFERENCES

1. Caplin ME, Buscombe JR, Hilson AJ, Jones AL, Watkinson AF, Burroughs AK. Carcinoid tumour. Lancet. 1998; 352:799–805. https://doi.org/10.1016/S0140-6736(98)02286-7.
2. Yao JC, Hassan M, Phan A, Dagohoy C, Leary C, Mares JE, Abdalla EK, Fleming JB, Vauthey JN, Rashid A, Evans DB. One hundred years after "carcinoid": epidemiology of and prognostic factors for neuroendocrine tumors in 35,825 cases in the United States. J Clin Oncol. 2008; 26:3063–72. https://doi.org/10.1200/JCO.2007.15.4377.
3. Scherubl H, Streller B, Stabenow R, Herbst H, Hopfner M, Schwertner C, Steinberg J, Eick J, Ring W, Tiwari K, Zappe SM. Clinically detected gastroenteropancreatic neuroendocrine tumors are on the rise: epidemiological changes in Germany. World J Gastroenterol. 2013; 19:9012–9. https://doi.org/10.3748/wjg.v19.i47.9012.
4. Dasari A, Shen C, Halperin D, Zhao B, Zhou S, Xu Y, Shih T, Yao JC. Trends in the Incidence, Prevalence, and Survival

Outcomes in Patients With Neuroendocrine Tumors in the United States. JAMA Oncol. 2017; 3:1335–42. https://doi.org/10.1001/jamaoncol.2017.0589.

5. Mangano A, Lianos GD, Roukos DH, Mason SE, Kim HY, Dionigi G. New horizons for targeted treatment of neuroendocrine tumors. Future Oncol. 2016; 12:1059–65. https://doi.org/10.2217/fon.16.8.
6. Kwekkeboom DJ, Krenning EP. Peptide Receptor Radionuclide Therapy in the Treatment of Neuroendocrine Tumors. Hematol Oncol Clin North Am. 2016; 30:179–91. https://doi.org/10.1016/j.hoc.2015.09.009.
7. Reubi JC, Schar JC, Waser B, Wenger S, Heppeler A, Schmitt JS, Macke HR. Affinity profiles for human somatostatin receptor subtypes SST1-SST5 of somatostatin radiotracers selected for scintigraphic and radiotherapeutic use. Eur J Nucl Med. 2000; 27:273–82.
8. Sabet A, Biersack HJ, Ezziddin S. Advances in Peptide Receptor Radionuclide Therapy. Semin Nucl Med. 2016; 46:40–6. https://doi.org/10.1053/j.semnuclmed.2015.09.005.
9. Graf F, Fahrer J, Maus S, Morgenstern A, Bruchertseifer F, Venkatachalam S, Fottner C, Weber MM, Huelsenbeck J, Schreckenberger M, Kaina B, Miederer M. DNA double strand breaks as predictor of efficacy of the alpha-particle emitter Ac-225 and the electron emitter Lu-177 for somatostatin receptor targeted radiotherapy. PLoS One. 2014; 9:e88239. https://doi.org/10.1371/journal.pone.0088239.
10. Strosberg J, El-Haddad G, Wolin E, Hendifar A, Yao J, Chasen B, Mittra E, Kunz PL, Kulke MH, Jacene H, Bushnell D, O'Dorisio TM, Baum RP, et al. Phase 3 Trial of ^{177}Lu-Dotatate for Midgut Neuroendocrine Tumors. N Engl J Med. 2017; 376:125–35. https://doi.org/10.1056/NEJMoa1607427.
11. Gloesenkamp CR, Nitzsche B, Ocker M, Di Fazio P, Quint K, Hoffmann B, Scherubl H, Hopfner M. AKT inhibition by triciribine alone or as combination therapy for growth control of gastroenteropancreatic neuroendocrine tumors. Int J Oncol. 2012; 40:876–88. https://doi.org/10.3892/ijo.2011.1256.
12. Hopfner M, Schuppan D, Scherubl H. Treatment of gastrointestinal neuroendocrine tumors with inhibitors of growth factor receptors and their signaling pathways: recent advances and future perspectives. World J Gastroenterol. 2008; 14:2461–73.
13. Claringbold PG, Turner JH. Pancreatic Neuroendocrine Tumor Control: Durable Objective Response to Combination Lu-Octreotate-Capecitabine-Temozolomide Radiopeptide Chemotherapy. Neuroendocrinology. 2016; 103:432–9. https://doi.org/10.1159/000434723.
14. Claringbold PG, Turner JH. NeuroEndocrine Tumor Therapy with Lutetium-177-octreotate and Everolimus (NETTLE): A Phase I Study. Cancer Biother Radiopharm. 2015; 30:261–9. https://doi.org/10.1089/cbr.2015.1876.
15. Chalmers AJ, Lakshman M, Chan N, Bristow RG. Poly(ADP-ribose) polymerase inhibition as a model for synthetic lethality in developing radiation oncology targets. Semin Radiat Oncol. 2010; 20:274–81. https://doi.org/10.1016/j.semradonc.2010.06.001.
16. Ray Chaudhuri A, Nussenzweig A. The multifaceted roles of PARP1 in DNA repair and chromatin remodelling. Nat Rev Mol Cell Biol. 2017; 18:610–621. https://doi.org/10.1038/nrm.2017.53.
17. Wei H, Yu X. Functions of PARylation in DNA Damage Repair Pathways. Genomics Proteomics Bioinformatics. 2016; 14:131–9. https://doi.org/10.1016/j.gpb.2016.05.001.
18. Scott CL, Swisher EM, Kaufmann SH. Poly (ADP-ribose) polymerase inhibitors: recent advances and future development. J Clin Oncol. 2015; 33:1397–406. https://doi.org/10.1200/JCO.2014.58.8848.
19. Feng FY, de Bono JS, Rubin MA, Knudsen KE. Chromatin to Clinic: The Molecular Rationale for PARP1 Inhibitor Function. Mol Cell. 2015; 58:925–34. https://doi.org/10.1016/j.molcel.2015.04.016.
20. Montoni A, Robu M, Pouliot E, Shah GM. Resistance to PARP-Inhibitors in Cancer Therapy. Front Pharmacol. 2013; 4:18. https://doi.org/10.3389/fphar.2013.00018.
21. Lord CJ, Ashworth A. PARP inhibitors: Synthetic lethality in the clinic. Science. 2017; 355:1152–8. https://doi.org/10.1126/science.aam7344.
22. Nile DL, Rae C, Hyndman IJ, Gaze MN, Mairs RJ. An evaluation *in vitro* of PARP-1 inhibitors, rucaparib and olaparib, as radiosensitisers for the treatment of neuroblastoma. BMC Cancer. 2016; 16:621. https://doi.org/10.1186/s12885-016-2656-8.
23. Nonnekens J, van Kranenburg M, Beerens CE, Suker M, Doukas M, van Eijck CH, de Jong M, van Gent DC. Potentiation of Peptide Receptor Radionuclide Therapy by the PARP Inhibitor Olaparib. Theranostics. 2016; 6:1821–32. https://doi.org/10.7150/thno.15311.
24. Ono K, Suzuki T, Miki Y, Taniyama Y, Nakamura Y, Noda Y, Watanabe M, Sasano H. Somatostatin receptor subtypes in human non-functioning neuroendocrine tumors and effects of somatostatin analogue SOM230 on cell proliferation in cell line NCI-H727. Anticancer Res. 2007; 27:2231–9.
25. Sun L, Luo J, Mackey LV, Morris LM, Franko-Tobin LG, LePage KT, Coy DH. Investigation of cancer cell lines for peptide receptor-targeted drug development. J Drug Target. 2011; 19:719–30. https://doi.org/10.3109/1061186x.2011.558089.
26. Plesca D, Mazumder S, Almasan A. DNA damage response and apoptosis. Methods Enzymol. 2008; 446:107–22. https://doi.org/10.1016/S0076-6879(08)01606-6.
27. Marechal A, Zou L. DNA damage sensing by the ATM and ATR kinases. Cold Spring Harb Perspect Biol. 2013; 5. https://doi.org/10.1101/cshperspect.a012716.

28. Shieh SY, Ikeda M, Taya Y, Prives C. DNA damage-induced phosphorylation of p53 alleviates inhibition by MDM2. Cell. 1997; 91:325–34.
29. Schuler M, Green DR. Mechanisms of p53-dependent apoptosis. Biochem Soc Trans. 2001; 29:684–8.
30. Mehta G, Hsiao AY, Ingram M, Luker GD, Takayama S. Opportunities and challenges for use of tumor spheroids as models to test drug delivery and efficacy. J Control Release. 2012; 164:192–204. https://doi.org/10.1016/j.jconrel.2012.04.045.
31. Whitfield ML, George LK, Grant GD, Perou CM. Common markers of proliferation. Nat Rev Cancer. 2006; 6:99–106. https://doi.org/10.1038/nrc1802.
32. Lewin J, Cullinane C, Akhurst T, Waldeck K, Watkins DN, Rao A, Eu P, Mileshkin L, Hicks RJ. Peptide receptor chemoradionuclide therapy in small cell carcinoma: from bench to bedside. Eur J Nucl Med Mol Imaging. 2015; 42:25–32. https://doi.org/10.1007/s00259-014-2888-2.
33. Shah GM, Robu M, Purohit NK, Rajawat J, Tentori L, Graziani G. PARP Inhibitors in Cancer Therapy: Magic Bullets but Moving Targets. Front Oncol. 2013; 3:279. https://doi.org/10.3389/fonc.2013.00279.
34. Lakin ND, Jackson SP. Regulation of p53 in response to DNA damage. Oncogene. 1999; 18:7644–55. https://doi.org/10.1038/sj.onc.1203015.
35. Mitsudomi T, Steinberg SM, Nau MM, Carbone D, D'Amico D, Bodner S, Oie HK, Linnoila RI, Mulshine JL, Minna JD. p53 gene mutations in non-small-cell lung cancer cell lines and their correlation with the presence of ras mutations and clinical features. Oncogene. 1992; 7:171–80.
36. Degenhardt Y, Greshock J, Laquerre S, Gilmartin AG, Jing J, Richter M, Zhang X, Bleam M, Halsey W, Hughes A, Moy C, Liu-Sullivan N, Powers S, et al. Sensitivity of cancer cells to Plk1 inhibitor GSK461364A is associated with loss of p53 function and chromosome instability. Mol Cancer Ther. 2010; 9:2079–89. https://doi.org/10.1158/1535-7163.MCT-10-0095.
37. Boora GK, Kanwar R, Kulkarni AA, Pleticha J, Ames M, Schroth G, Beutler AS, Banck MS. Exome-level comparison of primary well-differentiated neuroendocrine tumors and their cell lines. Cancer Genet. 2015; 208:374–81. https://doi.org/10.1016/j.cancergen.2015.04.002.
38. Bernard BF, Krenning E, Breeman WA, Visser TJ, Bakker WH, Srinivasan A, de Jong M. Use of the rat pancreatic CA20948 cell line for the comparison of radiolabelled peptides for receptor-targeted scintigraphy and radionuclide therapy. Nucl Med Commun. 2000; 21:1079–85.
39. Dash A, Chakraborty S, Pillai MR, Knapp FF Jr. Peptide receptor radionuclide therapy: an overview. Cancer Biother Radiopharm. 2015; 30:47–71. https://doi.org/10.1089/cbr.2014.1741.
40. Fong PC, Yap TA, Boss DS, Carden CP, Mergui-Roelvink M, Gourley C, De Greve J, Lubinski J, Shanley S, Messiou C, A'Hern R, Tutt A, Ashworth A, et al. Poly(ADP)-ribose polymerase inhibition: frequent durable responses in BRCA carrier ovarian cancer correlating with platinum-free interval. J Clin Oncol. 2010; 28:2512–9. https://doi.org/10.1200/JCO.2009.26.9589.
41. Audeh MW, Carmichael J, Penson RT, Friedlander M, Powell B, Bell-McGuinn KM, Scott C, Weitzel JN, Oaknin A, Loman N, Lu K, Schmutzler RK, Matulonis U, et al. Oral poly(ADP-ribose) polymerase inhibitor olaparib in patients with BRCA1 or BRCA2 mutations and recurrent ovarian cancer: a proof-of-concept trial. Lancet. 2010; 376:245–51. https://doi.org/10.1016/S0140-6736(10)60893-8.
42. Kwekkeboom DJ, Bakker WH, Kooij PP, Konijnenberg MW, Srinivasan A, Erion JL, Schmidt MA, Bugaj JL, de Jong M, Krenning EP. [^{177}Lu-DOTA^{0}Tyr^{3}]octreotate: comparison with [^{111}In-DTPA^{0}]octreotide in patients. Eur J Nucl Med. 2001; 28:1319–25.
43. Evers BM, Ishizuka J, Townsend CM Jr, Thompson JC. The human carcinoid cell line, BON. A model system for the study of carcinoid tumors. Ann N Y Acad Sci. 1994; 733:393–406.
44. Gloesenkamp C, Nitzsche B, Lim AR, Normant E, Vosburgh E, Schrader M, Ocker M, Scherubl H, Hopfner M. Heat shock protein 90 is a promising target for effective growth inhibition of gastrointestinal neuroendocrine tumors. Int J Oncol. 2012; 40:1659–67. https://doi.org/10.3892/ijo.2012.1328.
45. Wong C, Vosburgh E, Levine AJ, Cong L, Xu EY. Human neuroendocrine tumor cell lines as a three-dimensional model for the study of human neuroendocrine tumor therapy. J Vis Exp. 2012; 66:e4218. https://doi.org/10.3791/4218.

Annexe 6: PARP inhibitors in cancer therapy: magic Bullets but moving targets

frontiers in ONCOLOGY

OPINION ARTICLE
published: 14 November 2013
doi: 10.3389/fonc.2013.00279

PARP inhibitors in cancer therapy: magic bullets but moving targets

Girish M. Shah[1], Mihaela Robu[1], Nupur K. Purohit[1], Jyotika Rajawat[1], Lucio Tentori[2] and Grazia Graziani[2]*

[1] *Laboratory for Skin Cancer Research, CHU-Q (CHUL) Research Centre, Laval University, Quebec City, QC, Canada*
[2] *Department of System Medicine, University of Rome "Tor Vergata", Rome, Italy*
**Correspondence: girish.shah@crchul.ulaval.ca*

Edited by:
Christina Annunziata, National Cancer Institute, USA

Reviewed by:
Daekyu Sun, University of Arizona, USA
Michael Witcher, McGill University, Canada

Keywords: poly(ADP-ribose) polymerase (PARP), PARP inhibitors (PARPi), cancer therapy, BRCA-mutant cancers, synthetic lethality, combination therapy, multiple targets of PARPi

The pharmacological inhibitors of poly(ADP-ribose) polymerase-1 (PARP-1) have reached the first milestone toward their inclusion in the arsenal of anti-cancer drugs by showing consistent benefits in clinical trials against BRCA-mutant cancers that are deficient in the homologous recombination repair (HRR) of DNA double strand breaks (DSB) (1, 2). PARP inhibitors (PARPi) also potentiate therapeutic efficacy of ionizing radiation and some chemotherapeutic agents (1). These effects of PARPi were initially linked to inhibition of the role of PARP-1 in base excision repair (BER) of DNA damaged by endogenous or exogenous agents, resulting in accumulation of single strand breaks (SSB), which upon conversion to toxic DSB lesions would kill cancer cells deficient in DSB repair (1, 3, 4). However, PARPi lethality in HRR-deficient cancers can also be explained by other mechanisms not involving a direct effect of PARPi on BER [reviewed in Ref. (5, 6)]. In addition, therapeutic benefits of PARPi with agents such as carboplatin in HRR-proficient and -deficient tumors [reviewed in Ref. (1, 7)], simply cannot be explained by BER inhibitory effect of PARPi. Therefore, PARPi are like magic bullets that can kill cancer cells under different circumstances, but to comprehend their global scope and limitations, here we discuss the full range of their targets and the possible impact of broad specificity of current PARPi during prolonged therapy of cancer patients.

MECHANISMS OF ACTION OF PARPi IN CANCER THERAPY: MAGIC BULLETS BUT MOVING TARGETS

It is not surprising that the mechanism of action of PARPi in killing cancer cells still remains an open question, because its principal target PARP-1 is a multifunctional protein implicated in various cellular responses to DNA damage ranging from different pathways of DNA repair and cell death to stress signaling, transcription, and genomic stability (8, 9), all of which could be affected by PARPi and thus influence outcome of cancer therapies. Following are various possibly overlapping mechanisms for the anti-cancer effect of PARPi.

BER/HRR NEXUS FOR SYNTHETIC LETHALITY OF PARPi IN BRCA-MUTANT CANCERS

It was first demonstrated by two teams (3, 4) that two individually non-lethal conditions, i.e., PARPi-mediated inhibition of PARP-1 and BRCA mutation-induced HRR deficiency in cancer cell, would become synthetic lethal when combined in a single cell [reviewed in Ref. (1, 5, 10, 11)] (**Figure 1A**). This model focuses on the role of PARP-1 in BER, the pathway that repairs abasic sites and SSB that are constantly created in the mammalian genome by endogenous oxidants. When PARPi suppress the role of PARP-1 in BER, the unrepaired SSB would accumulate and collapse the DNA replication fork to form potentially lethal DSB. The normal cells would survive by repairing these DSB by HRR, but the HRR-deficient BRCA-mutants would die due to unrepaired DSB or possibly due to excessive reliance on the error-prone non-homologous end-joining (NHEJ) repair pathway to remove DSB (**Figure 1A**). This model also covers minor variations of the central theme as reviewed recently (1, 10) (**Figure 1A**). For example, tumors with other conditions that cause HRR deficiency or "BRCAness" phenotype would also be susceptible to PARPi. It permits inclusion of PARP-2 and its role in BER as target of PARPi, because most current PARPi also inhibit PARP-2 (10). It also explains the potentiating effect of PARPi in the combination therapy with radiation or chemicals, such as temozolomide, irinotecan, or topotecan, because DNA damage caused by these agents is also repaired by BER.

ALTERNATIVE TARGETS OF PARPi IN BRCA-MUTANT CANCERS

However, the above mechanism is inadequate to explain all the effects of PARPi seen in BRCA-mutant cancers, which could be explained by the effect of PARPi on alternate targets, as reviewed earlier (5, 6, 10) (**Figure 1A**). In brief, (i) PARPi could be trapping PARP-1 or PARP-2 to SSB with resultant PARP-SSB complex that would be more toxic than unrepaired SSB or even knockdown of PARPs (5, 12). (ii) PARPi could act via upregulation of NHEJ pathway, which would presumably cause genomic instability and eventual lethality (13). (iii) PARPi could suppress the role of PARP-1 in reactivating DNA replication forks (5). Thus, apart from BER/HRR nexus, there could be NHEJ/HRR or DNA replication/HRR nexus to explain PARPi lethality in BRCA-mutant cancers.

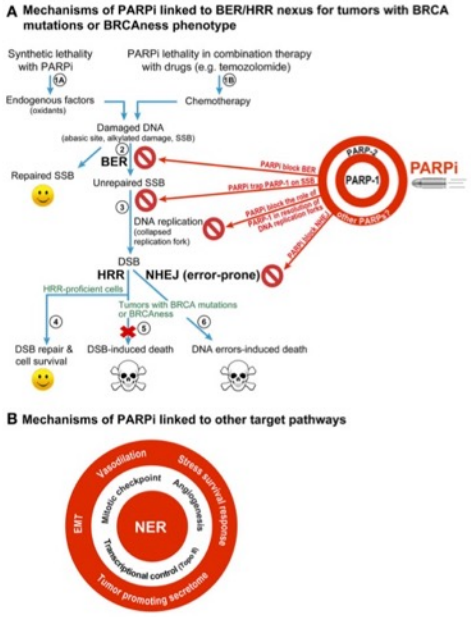

FIGURE 1 | Different mechanisms for therapeutic efficacy of PARPi in cancers. (A) BER/HRR model: this model focuses on the role of PARP-1, the principal target of PARPi, in BER that removes abasic sites and SSB created constantly in the mammalian genome by endogenous oxidants (steps 1A). During BER, the binding of PARP-1 to SSB leads to stimulation of its catalytic activity of forming polymers of ADP-ribose (PAR) from its substrate NAD^+. The PAR and PARP-1 interact with and recruit the key BER scaffold protein XRCC1, whereas PAR-modified PARP-1 loses its affinity to bind to SSB and vacates the site for BER to continue. When PARPi suppress the role of PARP-1 in BER (step 2), the unrepaired SSB would accumulate and collapse the DNA replication fork to form potentially lethal DSB (step 3). The normal cells would survive by repairing these DSB by HRR (step 4), but the HRR-deficient BRCA-mutants would die due to unrepaired DSB (step 5) or possibly due to excessive reliance on the error-prone NHEJ repair pathway to remove DSB (step 6). This BER/HRR nexus also explains the effectiveness of combination therapy of PARPi with drugs that cause DNA damage that is repaired by BER (step 1B). Since PARP-2 is also known to play a role in BER, and since current PARPi are also known to inhibit PARP-2, the effect of PARPi may also be mediated by targeting of the functions of PARP-2 in BER, as shown on the target board along with PARP-1. In addition, the inhibitory effect of PARPi on other PARPs could also influence therapeutic efficacy of PARPi (see target board), although their contribution to BER/HRR mediated therapeutic effect of PARPi is not yet fully assessed. **(B)** Other targets of PARPi that can confer therapeutic benefits of PARPi: PARPi could also be effective anticancer agents by targeting the role of PARP-1 in other DNA repair pathways, such as NER; or other cellular pathways, such as control over cell cycle, tumor angiogenesis, transcription, epithelial-mesenchymal transition (EMT), stress survival response, vasodilation, or tumor-promoting secretome.

EXPANDING UNIVERSE OF POTENTIAL TARGETS OF PARPi

Therapeutic effectiveness of PARPi seen with some drugs cannot be explained by any of the above models, e.g., the potentiating effects of PARPi on the platinum-based drugs such as carboplatin, cisplatin, or oxaliplatin on HRR-deficient or -proficient tumors [reviewed in Ref. (1, 7)] (**Figure 1B**). These observations were further supported by recent studies showing the potentiating effect of PARPi veliparib on carboplatin treatment of patients with BRCA-mutant breast cancers (14) or carboplatin and phosphoinositide 3-kinase mTOR inhibitor treatment of mouse xenografts of BRCA-competent triple negative breast cancer cells (15). Since platinum compounds cause DNA damage that is largely repaired by the nucleotide excision repair (NER) pathway and not BER, we need to think beyond BER for an explanation. Moreover, BER was shown to mediate toxicity of cisplatin by competing with the repair of cisplatin inter-strand cross-links and DSB caused by these links (16). Therefore, if PARPi effect was mainly via inhibition of BER, we should have observed less and not more toxicity of cisplatin.

One possible explanation is that PARPi could be causing vasodilation (**Figure 1B**) to improve intra-tumoral delivery of platinum drugs (1), although it needs to be confirmed if this generalized effect could also potentiate other drugs. On the other hand, recently discovered roles of PARP-1 in improving the efficiency of NER-mediated removal of UV-induced DNA damage (17–19) provides a more handy explanation for the PARPi-induced potentiation of platinum compound-based drugs, which also cause DNA damage that is repaired by NER (**Figure 1B**). This NER targeting effect of PARPi alone can account for death of HRR-proficient tumors, as seen in clinical trials [reviewed in Ref. (1, 7)] and supported by *in vitro* results showing that PARP-1 depletion (20) or inhibition (19) decreases clonogenic survival of UV-exposed human skin fibroblasts with no reported HRR-deficiencies. Of course, PARPi could have an additional effect in this model due to suppression of the role of PARP-1 in HRR pathway (21). In addition, in the PARPi-treated BRCA-mutant HRR-deficient tumors, the unrepaired DNA damage by platinum drugs could collapse the DNA replication fork to form DSB and cause lethality. Thus, the NER effect alone or NER-HRR nexus could be possible explanations for the lethality of PARPi/platinum compounds in HRR-proficient or -deficient tumors.

The clinical and preclinical studies have also revealed other targets of PARPi in cancer therapies that are linked to various roles of their multifunctional target PARP-1 in following cellular processes (**Figure 1B**). (i) Transcriptional control of drug-target genes: PARPi have been shown to increase toxicity of topoisomerase II-poison doxorubicin *in vitro* (22) or in xenografted tumors in mice (23). This effect could be

due to doxorubicin-induced decrease in expression and activity of PARP-1 (24) or PARPi-mediated increase in expression of topoisomerase II, because the transcription activator Sp1 loses its affinity for the topoisomerase II-promoter region upon modification by polymer of ADP-ribose (PAR) created by the activated PARP-1 (22). (ii) Mitotic checkpoint: the beneficial effects of PARPi with microtubule stabilizing mitotic inhibitor paclitaxel in patients with recurrent metastatic gastric cancers with BRCAness phenotype (25) could be linked to suppression of the role of PARP-1 in maintaining the mitotic checkpoint via PARylation of itself or the mitotic checkpoint protein CHFR (26, 27). An abrogation of mitotic checkpoint would kill cancer cells, because they will be forced to divide before resolution of the damage. (iii) Tumor-promoting secretome: PARPi-mediated suppression of the role of PARP-1 in elaborating tumor-promoting secretome containing cytokines and growth factors has been suggested as a cause for decreasing the resistance to another mitotic inhibitor docetaxel (28). (iv) Angiogenesis: the role of PARP-1 in promoting angiogenesis that fuels the growth of tumors can also be target of PARPi, because PARP-1 depletion or PARPi reduce vessel formation (29) and expression of markers of angiogenesis in melanoma (30) or endothelial cells (31). (v) Epithelial-mesenchymal transition (EMT) and metastasis: PARPi or PARP-1 depletion-induced reduction in aggressiveness and growth of metastatic melanoma in animal studies (30, 31) along with decreased markers for EMT (31, 32) suggest that the increase in progression-free survival of PARPi-treated patients could be due to reduction in the proliferation rate of the primary tumor and repression of its metastatic potential. (vi) Stress survival response: finally, cancer cells respond to any therapy by elaborating various stress responses to survive; and PARP-1 and its product PAR play key roles in these stress responses (9). Hence the suppression of pro-survival stress responses could explain the effectiveness of PARPi with any anti-cancer drug. An expanding list of potential targets of PARPi provides us with a much larger vision of the future applications of PARPi in cancer therapy.

BROAD SPECIFICITY OF PARPi: A KEY ISSUE FOR THE FUTURE OF PARPi THERAPY

There are two basic issues arising from the broad specificity of current PARPi.

(a) PARPi can inhibit more than one PARP ("they are bazookas not bullets"): many of the current PARPi in clinical trials display strong binding to PARPs 1–4 (33), and inhibit both PARP-1 and 2 at clinically relevant concentrations (10). Most studies assume that the effect of PARPi on both PARP-1 and 2 is important for therapy; however, this may not be the case. In fact, some studies using specific knockdown of PARPs showed that only the knockdown of PARP-1, but not PARP-2, replicates: (i) the synthetic lethal effect of PARPi on BRCA2 mutant cells (3); (ii) potentiation of cisplatin by PARPi in BRCA-proficient triple negative breast cancer cells (34); and (iii) sensitization of melanoma cells *in vitro* to temozolomide (35). On the other hand, the effect of PARPi on gemcitabine in the above breast cancer cells was replicated by PARP-2 knockdown and not PARP-1 knockdown (34). In contrast, the siRNA for PARP-1 could specifically prevent the growth of BRCA-deficient ovarian cancer cell-derived tumors in mice (36). Since the double knockout of PARP-1 and PARP-2 is embryonic lethal (37), we must verify the assumption that gratuitous inhibition of unrelated PARPs has no effect on the end-results.

(b) Indiscriminate inhibition of all the roles of a given PARP by PARPi ("we are nuking the entire PARP-landscape"): PARP-1, the principal target of PARPi, is a multifunctional protein that is implicated not only in DNA repair but also in various forms of cell death, transcription, epigenetic control of gene expression, and chromatin remodeling (8, 38). Hence even if we were to develop novel PARPi to specifically inhibit only PARP-1, it will still shut down most if not all the functions of PARP-1. Similar arguments can be made for PARPi-mediated suppression of different roles of PARP-2. Although adverse genomic consequences of PARPi therapy have not yet been reported, we need to consider that prolonged PARPi therapy may cause genome instability because PARP-$1^{-/-}$ mouse embryonic fibroblasts have a tendency to become tetraploid (39, 40), and the susceptibility of PARP-$1^{-/-}$ female mice to develop mammary carcinoma is enhanced if p53 is also mutated, a phenomenon frequently observed in cancers (41). In effect, PARPi are the magic bullets, but instead of doing precision targeting with them for the desired effect, we are simply nuking the entire spectrum of functions of that target PARP, which could result in unintended consequence during maintenance (prolonged) therapy with PARPi including survival of damaged cancer cells, development of secondary tumors as a consequence of genomic instability and resistance to PARPi. Thus, while the current broad specificity PARPi work properly for short-term cancer therapy, there is a need for development of new and more specific PARPi that are unique not only for a given PARP but also for a given function of that PARP related to its anti-cancer effect.

It is heartening that PARPi have shown some clinical benefit for BRCA-mutant cancer patients in clinical trials as monotherapy or as a combination therapy, but we need to do a lot more to understand the therapeutic effect of PARPi to establish them firmly in the arsenal of anti-tumor agents against variety of cancers.

ACKNOWLEDGMENTS

Mihaela Robu was recipient of the Pierre J. Durand doctoral scholarship award from Faculty of Medicine Laval University (2011–12) the Doctoral scholarship award Fonds de recherche Santé Québec (FRQ-S, # 27896 since 2013). Nupur K. Purohit was recipient of the foreign student supplemental fee waiver scholarship from Laval University and from the Shastri Indo-Canadian Institute (since 2012). This work was supported by the CIHR operating grant #89964 to Girish M. Shah.

REFERENCES

1. Curtin NJ, Szabo C. Therapeutic applications of PARP inhibitors: anticancer therapy and beyond. *Mol Aspects Med* (2013) **34**(6):1217–56. doi:10.1016/j.mam.2013.01.006
2. Do K, Chen AP. Molecular pathways: targeting PARP in cancer treatment. *Clin Cancer Res* (2013) **19**(5):977–84. doi:10.1158/1078-0432.CCR-12-0163
3. Bryant HE, Schultz N, Thomas HD, Parker KM, Flower D, Lopez E, et al. Specific killing of BRCA2-deficient tumours with inhibitors of poly(ADP-ribose) polymerase. *Nature* (2005) **434**(7035):913–7. doi:10.1038/nature03443
4. Farmer H, McCabe N, Lord CJ, Tutt AN, Johnson DA, Richardson TB, et al. Targeting the DNA repair defect in BRCA mutant cells as a therapeutic strategy. *Nature* (2005) **434**(7035):917–21. doi:10.1038/nature03445
5. Helleday T. The underlying mechanism for the PARP and BRCA synthetic lethality: clearing up the misunderstandings. *Mol Oncol* (2011) **5**(4):387–93. doi:10.1016/j.molonc.2011.07.001
6. De Lorenzo SB, Patel AG, Hurley RM, Kaufmann SH. The elephant and the blind men: making sense of PARP inhibitors in homologous recombination deficient tumor cells. *Front Oncol* (2013) **3**:228. doi:10.3389/fonc.2013.00228
7. Tentori L, Muzi A, Dorio AS, Dolci S, Campolo F, Vernole P, et al. MSH3 expression does not influence the sensitivity of colon cancer HCT116 cell line to oxaliplatin and poly(ADP-ribose) polymerase (PARP) inhibitor as monotherapy or in combination. *Cancer Chemother Pharmacol* (2013) **72**(1):117–25. doi:10.1007/s00280-013-2175-0
8. Gibson BA, Kraus WL. New insights into the molecular and cellular functions of poly(ADP-ribose) and PARPs. *Nat Rev Mol Cell Biol* (2012) **13**(7):411–24. doi:10.1038/nrm3376
9. Luo X, Kraus WL. On PAR with PARP: cellular stress signaling through poly(ADP-ribose) and PARP-1. *Genes Dev* (2012) **26**(5):417–32. doi:10.1101/gad.183509.111
10. Montoni A, Robu M, Pouliot E, Shah GM. Resistance to PARP-inhibitors in cancer therapy. *Front Pharmacol* (2013) **4**:18. doi:10.3389/fphar.2013.00018
11. Lord CJ, Ashworth A. The DNA damage response and cancer therapy. *Nature* (2012) **481**(7381):287–94. doi:10.1038/nature10760
12. Murai J, Huang SY, Das BB, Renaud A, Zhang Y, Doroshow JH, et al. Trapping of PARP1 and PARP2 by clinical PARP inhibitors. *Cancer Res* (2012) **72**(21):5588–99. doi:10.1158/0008-5472.CAN-12-2753
13. Patel AG, Sarkaria JN, Kaufmann SH. Nonhomologous end joining drives poly(ADP-ribose) polymerase (PARP) inhibitor lethality in homologous recombination-deficient cells. *Proc Natl Acad Sci U S A* (2011) **108**(8):3406–11. doi:10.1073/pnas.1013715108
14. Somlo G, Frankel PH, Luu TH, Ma C, Arun B, Garcia A, et al. Efficacy of the combination of ABT-888 (veliparib) and carboplatin in patients with BRCA-associated breast cancer. *J Clin Oncol* (2013) **31**(15-Suppl):1024.
15. Dey N, Sun Y, Carlson J, Friedman L, De P, Leyland-Jones B. A combination of dual PI3K-mTOR inhibitor, GDC-0980, with PARP inhibitor plus carboplatin blocked tumor growth of BRCA-competent triple-negative breast cancer cells. *J Clin Oncol* (2013) **31**(15-Suppl):2613.
16. Kothandapani A, Dangeti VS, Brown AR, Banze LA, Wang XH, Sobol RW, et al. Novel role of base excision repair in mediating cisplatin cytotoxicity. *J Biol Chem* (2011) **286**(16):14564–74. doi:10.1074/jbc.M111.225375
17. Robu M, Shah RG, Petitclerc N, Brind'Amour J, Kandan-Kulangara F, Shah GM. Role of poly(ADP-ribose) polymerase-1 in the removal of UV-induced DNA lesions by nucleotide excision repair. *Proc Natl Acad Sci U S A* (2013) **110**(5):1658–63. doi:10.1073/pnas.1209507110
18. Luijsterburg MS, Lindh M, Acs K, Vrouwe MG, Pines A, van Attikum H, et al. DDB2 promotes chromatin decondensation at UV-induced DNA damage. *J Cell Biol* (2012) **197**(2):267–81. doi:10.1083/jcb.201106074
19. Pines A, Vrouwe MG, Marteijn JA, Typas D, Luijsterburg MS, Cansoy M, et al. PARP1 promotes nucleotide excision repair through DDB2 stabilization and recruitment of ALC1. *J Cell Biol* (2012) **199**(2):235–49. doi:10.1083/jcb.201112132
20. Ghodgaonkar MM, Zacal NJ, Kassam SN, Rainbow AJ, Shah GM. Depletion of poly(ADP-ribose)polymerase-1 reduces host cell reactivation for UV-treated adenovirus in human dermal fibroblasts. *DNA Repair (Amst)* (2008) **7**:617–32. doi:10.1016/j.dnarep.2008.01.001
21. Helleday T, Bryant HE, Schultz N. Poly(ADP-ribose) polymerase (PARP-1) in homologous recombination and as a target for cancer therapy. *Cell Cycle* (2005) **4**(9):1176–8. doi:10.4161/cc.4.9.2031
22. Magan N, Isaacs RJ, Stowell KM. Treatment with the PARP-inhibitor PJ34 causes enhanced doxorubicin-mediated cell death in HeLa cells. *Anticancer Drugs* (2012) **23**(6):627–37. doi:10.1097/CAD.0b013e328350900f
23. Mason KA, Valdecanas D, Hunter NR, Milas L. INO-1001, a novel inhibitor of poly(ADP-ribose) polymerase, enhances tumor response to doxorubicin. *Invest New Drugs* (2008) **26**(1):1–5. doi:10.1007/s10637-007-9072-5
24. Zaremba T, Ketzer P, Cole M, Coulthard S, Plummer ER, Curtin NJ. Poly(ADP-ribose) polymerase-1 polymorphisms, expression and activity in selected human tumour cell lines. *Br J Cancer* (2009) **101**(2):256–62. doi:10.1038/sj.bjc.6605166
25. Bang Y-J, Im S-A, Lee K-W, Cho JY, Song E-K, Lee KH, et al. Olaparib plus paclitaxel in patients with recurrent or metastatic gastric cancer: a randomized, double-blind phase II study. *J Clin Oncol* (2013) **31**(15-Suppl):4013.
26. Ahel I, Ahel D, Matsusaka T, Clark AJ, Pines J, Boulton SJ, et al. Poly(ADP-ribose)-binding zinc finger motifs in DNA repair/checkpoint proteins. *Nature* (2008) **451**(7174):81–5. doi:10.1038/nature06420
27. Kashima L, Idogawa M, Mita H, Shitashige M, Yamada T, Ogi K, et al. CHFR protein regulates mitotic checkpoint by targeting PARP-1 protein for ubiquitination and degradation. *J Biol Chem* (2012) **287**(16):12975–84. doi:10.1074/jbc.M111.321828
28. Zhao S, Coleman I, Coleman R, Nelson P. Association of PARP inhibitors and docetaxel resistance through suppressing a tumor microenvironment-associated secretory program. *J Clin Oncol* (2013) **31**(15-Suppl):e22212.
29. Tentori L, Lacal PM, Muzi A, Dorio AS, Leonetti C, Scarsella M, et al. Poly(ADP-ribose) polymerase (PARP) inhibition or PARP-1 gene deletion reduces angiogenesis. *Eur J Cancer* (2007) **43**(14):2124–33. doi:10.1016/j.ejca.2007.07.010
30. Tentori L, Muzi A, Dorio AS, Bultrini S, Mazzon E, Lacal PM, et al. Stable depletion of poly (ADP-ribose) polymerase-1 reduces in vivo melanoma growth and increases chemosensitivity. *Eur J Cancer* (2008) **44**(9):1302–14. doi:10.1016/j.ejca.2008.03.019
31. Rodríguez MI, Peralta-Leal A, O'Valle F, Rodriguez-Vargas JM, Gonzalez-Flores A, Majuelos-Melguizo J, et al. PARP-1 regulates metastatic melanoma through modulation of vimentin-induced malignant transformation. *PLoS Genet* (2013) **9**(6):e1003531. doi:10.1371/journal.pgen.1003531
32. McPhee TR, McDonald PC, Oloumi A, Dedhar S. Integrin-linked kinase regulates E-cadherin expression through PARP-1. *Dev Dyn* (2008) **237**(10):2737–47. doi:10.1002/dvdy.21685
33. Wahlberg E, Karlberg T, Kouznetsova E, Markova N, Macchiarulo A, Thorsell AG, et al. Family-wide chemical profiling and structural analysis of PARP and tankyrase inhibitors. *Nat Biotechnol* (2012) **30**(3):283–8. doi:10.1038/nbt.2121
34. Hastak K, Alli E, Ford JM. Synergistic chemosensitivity of triple-negative breast cancer cell lines to poly(ADP-Ribose) polymerase inhibition, gemcitabine, and cisplatin. *Cancer Res* (2010) **70**(20):7970–80. doi:10.1158/0008-5472.CAN-09-4521
35. Tentori L, Muzi A, Dorio AS, Scarsella M, Leonetti C, Shah GM, et al. Pharmacological inhibition of poly(ADP-ribose) polymerase (PARP) activity in PARP-1 silenced tumour cells increases chemosensitivity to temozolomide and to a N3-adenine selective methylating agent. *Curr Cancer Drug Targets* (2010) **10**(4):368–83. doi:10.2174/156800910791208571
36. Goldberg MS, Xing D, Ren Y, Orsulic S, Bhatia SN, Sharp PA. Nanoparticle-mediated delivery of siRNA targeting Parp1 extends survival of mice bearing tumors derived from Brca1-deficient ovarian cancer cells. *Proc Natl Acad Sci U S A* (2011) **108**(2):745–50. doi:10.1073/pnas.1016538108
37. Menissier de Murcia J, Ricoul M, Tartier L, Niedergang C, Huber A, Dantzer F, et al. Functional interaction between PARP-1 and PARP-2 in chromosome stability and embryonic development in mouse. *EMBO J* (2003) **22**(9):2255–63. doi:10.1093/emboj/cdg206
38. Zampieri M, Guastafierro T, Calabrese R, Ciccarone F, Bacalini MG, Reale A, et al. ADP-ribose polymers localized on Ctcf-Parp1-Dnmt1 complex prevent methylation of Ctcf target sites. *Biochem J* (2012) **441**(2):645–52. doi:10.1042/BJ20111417

39. Simbulan-Rosenthal CM, Haddad BR, Rosenthal DS, Weaver Z, Coleman A, Luo R, et al. Chromosomal aberrations in PARP(-/-) mice: genome stabilization in immortalized cells by reintroduction of poly(ADP-ribose) polymerase cDNA. *Proc Natl Acad Sci U S A* (1999) **96**(23):13191–6. doi:10.1073/pnas.96.23.13191
40. Halappanavar S, Shah GM. Defective control of mitotic and post-mitotic checkpoints in Poly(ADP-ribose) polymerase-1(-/-) fibroblasts after mitotic spindle disruption. *Cell Cycle* (2004) **3**(3):335–42. doi:10.4161/cc.3.3.670
41. Tong WM, Yang YG, Cao WH, Galendo D, Frappart L, Shen Y, et al. Poly(ADP-ribose) polymerase-1 plays a role in suppressing mammary tumourigenesis in mice. *Oncogene* (2006) **26**(26):3857–67. doi:10.1038/sj.onc.1210156

Received: 16 October 2013; accepted: 29 October 2013; published online: 14 November 2013.
Citation: Shah GM, Robu M, Purohit NK, Rajawat J, Tentori L and Graziani G (2013) PARP inhibitors in cancer therapy: magic bullets but moving targets. Front. Oncol. 3:279. doi: 10.3389/fonc.2013.00279
This article was submitted to Cancer Molecular Targets and Therapeutics, a section of the journal Frontiers in Oncology.